Lehrstuhl für Aerodynamik und Strömungsmechanik
Technische Universität München

Small Disturbance Navier-Stokes Predictions of Low-Aspect-Ratio Wing Harmonic Loading

Alexander Nikolaus Pechloff

Vollständiger Abdruck der von der Fakultät für Maschinenwesen der Technischen Universität München zur Erlangung des akademischen Grades eines

Doktor-Ingenieurs

genehmigten Dissertation.

Vorsitzender:		Prof. Dr.-Ing. Florian Holzapfel
Prüfer der Dissertation:		
	1.	Prof. Dr.-Ing. Boris Laschka
	2.	apl. Prof. Dr.-Ing. Christian Breitsamter
	3.	Prof. Dr.-Ing. Lorenz Tichy

Die Dissertation wurde am 23.04.2018 bei der Technischen Universität München eingereicht und durch die Fakultät für Maschinenwesen am 24.10.2018 angenommen.

Preface

This dissertation originated while I was employed as a scientific assistant at the Institute for Fluid Mechanics of the Technische Universität München. It was completed at the successor institute, the Chair of Aerodynamics and Fluid Mechanics. In this regard, I would like to thank my advisor Prof. Dr.-Ing. Boris Laschka for having given me the opportunity to earn a doctorate. I am very grateful for his mentoring, counsel, and support over many years. During this time, apl. Prof. Dr.-Ing. Christian Breitsamter had been readily approachable as well, which I am very appreciative of. I would also like to thank him for having served as the second examiner. Furthermore, I would like to thank Prof. Dr.-Ing. Lorenz Tichy of the Technische Universität Braunschweig for having served as the external examiner and Prof. Dr.-Ing. Florian Holzapfel for having chaired the examination committee. Prof. Dr.-Ing. Nikolaus Adams gave me the opportunity to stay on as a guest at the Chair of Aerodynamics and Fluid Mechanics, providing me with a workplace as well as access to infrastructure and staff. For this I am very grateful. Additionally, I would like to thank all past and current institute members who had accompanied and supported me on my path. I am especially thankful to Dr.-Ing. Ulf Sickmüller and Dr.-Ing. Josef Fischer for having shown me how to best perform my teaching duties early on. I highly value the friendship that we share. Furthermore, I would like to thank Dr.-Ing. Michail Iatrou for the good scientific exchange that we had. I am also very appreciative of the friendship that has developed with Dipl.-Phys. Roman Reß, Dr.-Ing. Jan-Ulrich Klar, Dr.-Ing. Ulrich Jung, and Dr.-Ing. Dietmar Fleischer. My greatest thanks go to my parents, who had always encouraged the pursuit of a higher education, as well as to my sister Konstanze. Their enduring love and steadfast support were integral toward achieving my goal.

Dedicated to my parents, Jakob and Elisabeth Maria Pechloff

Munich, March 2019 Alexander Nikolaus Pechloff

Abstract

Aircraft flutter analysis within a production environment demands a numerical method that can accurately and yet efficiently predict the unsteady aerodynamic loading of the transonic speed range for a simple harmonic excitation. Both shocks and viscous phenomena need to be treatable. A method based on the frequency-domain solution of the small disturbance Navier-Stokes equations can satisfy this demand. To this effect, the research conducted at the Technical University of Munich has led to the small disturbance Navier-Stokes method FLM-SD.NS. In the dissertation at hand a derivation of the small disturbance Navier-Stokes equations through the triple decomposition of the instantaneous Navier-Stokes equations is presented. The amplitude dynamic eddy viscosity is provided through a small disturbance formulation of the Spalart-Allmaras one-equation turbulence model. For the particular incarnation of FLM-SD.NS, a solution algorithm utilizing multigrid-accelerated implicit pseudotime integration is implemented. The novel limitation of the amplitude Spalart-Allmaras conservative working variable allows for solution stability in cases of localized flow separation. The validity of the small disturbance Navier-Stokes approach as realized with FLM-SD.NS, its flow-topological versatility, and the attainable computational efficiency gain with respect to its unsteady Reynolds-averaged Navier-Stokes counterpart FLM-NS is substantiated for the low-aspect-ratio wing. It typifies an aircraft configuration of high speed and high maneuverability. Specifically, pitching- and flap-oscillation test cases of the experimentally investigated NASA Clipped Delta Wing are computed. These feature shocks of diverse strength and degree of motion, as well as a leading-edge vortex. Generally, the FLM-SD.NS results agree well with those gained from FLM-NS. Between the two methods, reductions up to an order of magnitude in computational time are ascertained. The superiority of the viscous consideration over the inviscid one is equally demonstrated.

Übersicht

Die Flatteranalyse eines Flugzeuges innerhalb einer Produktionsumgebung erfordert ein numerisches Verfahren, das die instationären Luftkräfte des transsonischen Geschwindigkeitsbereichs für eine einfache harmonische Anregung genau, aber dennoch effizient vorhersagen kann. Sowohl Verdichtungsstöße als auch viskose Phänomene müssen behandelbar sein. Ein Verfahren basierend auf der Frequenzbereichslösung der Navier-Stokes-Gleichungen bei kleinen Störungen kann diese Anforderung erfüllen. Diesbezüglich führte die an der Technischen Universität München betriebene Forschung zu dem Navier-Stokes-Verfahren kleiner Störungen FLM-SD.NS. In der vorliegenden Dissertation wird eine Herleitung der Navier-Stokes-Gleichungen bei kleinen Störungen durch die Dreifachdekomposition der instantanen Navier-Stokes-Gleichungen präsentiert. Die Amplitude der dynamischen Wirbelviskosität wird durch eine Formulierung des Spalart-Allmaras-Eingleichungsturbulenzmodells für kleine Störungen bereitgestellt. Für die spezifische FLM-SD.NS Version wird ein Lösungsalgorithmus implementiert, der eine, durch Mehrgittertechnik beschleunigte, implizite Pseudozeitintegration nutzt. Die neuartige Limitierung der Amplitude der Spalart-Allmaras konservativen Arbeitsvariable ermöglicht Lösungsstabilität in Fällen von örtlich begrenzter Strömungsablösung. Die Validität des Navier-Stokes-Ansatzes bei kleinen Störungen, wie mit FLM-SD.NS verwirklicht, und dessen strömungstopologische Vielseitigkeit sowie der erzielbare Recheneffizienzvorteil gegenüber dem instationären Reynolds-gemittelten Navier-Stokes-Verfahren FLM-NS wird für den Flügel kleiner Streckung nachgewiesen. Dieser repräsentiert die Flugzeugkonfiguration hoher Geschwindigkeit und hoher Wendigkeit. Hierfür werden Testfälle von Nick- und Klappenschwingungen des experimentell untersuchten NASA Clipped Delta Wing berechnet. Diese zeichnen sich durch Verdichtungsstöße unterschiedlicher Stärke und unterschiedlichem Bewegungsausmaßes sowie durch einen Vorderkantenwirbel aus. Grundsätzlich stimmen die FLM-SD.NS Ergebnisse gut mit denjenigen von FLM-NS überein, wobei eine Rechenzeitreduktion um bis zu einer Größenordnung festgestellt wird. Die Überlegenheit der viskosen Betrachtungsweise gegenber der nichtviskosen wird ebenso aufgezeigt

Contents

List of Figures

List of Tables

Nomenclature

Roman Symbol	Denotation
A	semi-span planform area, $\int_0^s c\,dy$
a	speed of sound
c	local chord length, $c(y/s)$
c_{av}	average chord length, A/s
$\mathbf{c}_f$	Cartesian skin-friction-coefficient vector
c_L	lift coefficient
c_M	pitching-moment coefficient
c_p	pressure coefficient
$c_{p,\,crit}$	critical pressure-coefficient, $c_p(Ma_\infty)$ at $Ma = 1.0$
c_r	root chord length, $c(0)$
c_t	tip chord length, $c(1)$
c_μ	reference chord length, $\int_0^s c^2\,dy/A$
$D_{\breve{\mu}}$	Spalart-Allmaras turbulence destruction term
d	distance to the nearest wall
$\mathbf{E}_\psi$	generalized curvilinear convective flux vector
$\mathbf{E}_{\mathbf{v}\,\psi}$	generalized curvilinear viscous flux vector
e	specific total energy
$\mathbf{F}$, $\mathbf{G}$, $\mathbf{H}$	convective flux vector, respectively, in ξ, η, ζ direction
$\mathbf{F_v}$, $\mathbf{G_v}$, $\mathbf{H_v}$	viscous flux vector respectively, in ξ, η, ζ direction
$F_{\breve{\mu}}$	Spalart-Allmaras turbulence first-order diffusion term
f	oscillation frequency
f_{v1}	Spalart-Allmaras first viscous damping function

Roman Symbol	**Denotation**
H	total enthalpy per unit volume
J	determinant of the coordinate transformation's Jacobian
$\mathbf{K}_{\psi}$	Jacobian matrix of the generalized convective flux vector
k	angular frequency
k_{red}	reduced frequency
$\breve{k}$	turbulence kinetic energy
L	reference length of the geometric nondimensionalization
L_{Re_∞}	characteristic length used in the formation of Re_∞
Ma	Mach number
$P_{\breve{\mu}}$	Spalart-Allmaras turbulence production term
Pr	Prandtl number
Pr_t	turbulent Prandtl number
p	static pressure
$\mathbf{Q}$	curvilinear state vector of dependent conservative variables
$\mathbf{q}$	Cartesian state vector of dependent conservative variables
q_x, q_y, q_z	elements of the Cartesian heat flux vector
Re	Reynolds number
$\mathbf{r}$	Cartesian position vector
S	Sutherland constant
$\mathbf{S}$	Cartesian physical surface normal vector of a cell interface
s	semi-span length
$\mathbf{T}$	Spalart-Allmaras turbulence source term vector
T	static temperature
t	physical time (Cartesian temporal coordinate)
u, v, w	Cartesian velocity, respectively, in x, y, z direction
$\mathbf{v}$	Cartesian velocity vector
x, y, z	global Cartesian spatial coordinates

Roman Symbol	**Denotation**
x	span-station-local chordwise coordinate, $x(y/s)$ ($= 0$: leading edge, $= c$: trailing edge)
x_h, z_h	global flap-hinge axis coordinates
x_p, z_p	global pitch axis coordinates
y	semi-span coordinate ($= 0$: root, $= s$: tip)

Greek Symbol	**Denotation**
α	angle of attack
Γ	inverse of the specific heat at constant volume
γ	ratio of specific heats
η	flap deflection angle
θ_ψ	generalized contravariant velocity (multiplied by J)
μ	dynamic molecular viscosity
μ_t	dynamic eddy viscosity
$\breve{\mu}$	Spalart-Allmaras conservative working variable
$\breve{\nu}$	Spalart-Allmaras primitive working variable
ξ, η, ζ	curvilinear spatial coordinates
Π_x, Π_y, Π_z	viscous energy fluxes, respectively, associated with the x, y, and z direction
ρ	density
τ	curvilinear temporal coordinate
τ°	pseudotime
τ_{xx}, τ_{xy}, τ_{xz}, τ_{yx}, τ_{yy}, τ_{yz}, τ_{zx}, τ_{zy}, τ_{zz}	elements of the Cartesian shear stress tensor
Φ	arbitrary instantaneous field quantity

Greek Symbol	**Denotation**
$\breve{\varphi}_{\hat{\chi}}$	phase angle of $\hat{\chi}$, with $\chi \in \{c_p,\, c_L,\, c_M\}$, $\left[\frac{\pi}{2}\frac{Im\,\hat{\chi}}{\lvert Im\,\hat{\chi}\rvert}\left(1-\frac{Re\,\hat{\chi}}{\lvert Re\,\hat{\chi}\,\rvert}\right)+\arctan\left(\frac{Im\,\hat{\chi}}{Re\,\hat{\chi}}\right)\right]\ 180\,\text{deg}\ /\,\pi$ (>0: $\tilde{\chi}$ leads the excitation, <0: $\tilde{\chi}$ lags the excitation, respectively, corresponding to $Im\,\hat{\chi}>0$, $Im\,\hat{\chi}<0$)
$\breve{\chi}$	argument of f_{v1}
ψ	generalized curvilinear coordinate

Operator	**Denotation**
$Re\,(\ )$	real part
$Im\,(\ )$	imaginary part
$\langle\,(\ )\,\rangle$	phase average
$\overline{(\ )}$	time average
$\mathbf{D}$	diagonal matrix
$\mathbf{L}$	lower-triangular matrix
$\mathbf{U}$	upper-triangular matrix
Δ	difference between lower- and upper-surface value, $\Delta(x/c)$; e.g., $\Delta c_p = c_{p,\,lower} - c_{p,\,upper}$

Subscript	**Denotation**
a	pertaining to the aerodynamic Cartesian coordinate system
b	pertaining to the body fixed Cartesian coordinate system
ext	pertaining to a first exterior cell at a block boundary
ffb	pertaining to a far-field-boundary cell-interface
$i,\, j,\, k$	cell/centroid index
$i \pm \frac{1}{2},\, j,\, k$	cell-local forward/backward interface index in the ξ direction
$i,\, j \pm \frac{1}{2},\, k$	cell-local forward/backward interface index in the η direction

Subscript	**Denotation**
i, j, $k \pm \frac{1}{2}$	cell-local forward/backward interface index in the ζ direction
int	pertaining to a first interior cell at a block face
n	block-face-/cell-interface-normal direction
ref	reference quantity of the nondimensionalization
$t1$, $t2$	block-face-/cell-interface-tangential directions
v	pertaining to a grid vertex
wb	pertaining to a wall-boundary cell-interface
x, y, z, t	Cartesian coordinate derivatives, respectively, $\partial/\partial x$, $\partial/\partial y$, $\partial/\partial z$, $\partial/\partial t$, if applied to a curvilinear coordinate
0	pertaining to the origin of the globally employed Cartesian coordinate system
ξ, η, ζ, τ	curvilinear coordinate derivatives, respectively, $\partial/\partial \xi$, $\partial/\partial \eta$, $\partial/\partial \zeta$, $\partial/\partial \tau$, if applied to a Cartesian coordinate
∞	freestream condition

Superscript	**Denotation**
CC	pertaining to a cell's centroid
EG	pertaining to the extremum grid
IC	pertaining to a cell interface's centroid
L	pertaining to the cell-interface-respective backward (left-side) state
n, $n+1$	current, subsequent superordinate pseudotime level
ν, $\nu+1$	current, subsequent grid-level-specific pseudotime level
R	pertaining to the cell-interface-respective forward (right-side) state
RG	pertaining to the reference grid
0	zeroth harmonic

Superscript	**Denotation**
1, 2, 3	first, second, third harmonic
(1)	homogenous in the periodic-perturbation/amplitude state vector
(2)	homogenous in the periodic-perturbation/amplitude geometric and kinematic entities

Modifier	**Denotation**
$\check{(\ )}$	dimensional
$\overline{(\ )}$	time-invariant mean
$\widetilde{(\ )}$	periodic perturbation
$(\ )'$	erratic fluctuation
$(\ )^*$	linearized with respect to the periodic perturbation
$\widehat{(\ )}$	perturbation amplitude
$\underline{(\ )}$	Roe average
$(\ )^\star$	normalized with the magnitude of the considered spatial metric vector

Acronym	**Denotation**
B/L	Baldwin-Lomax
CA	computational aeroelasticity
CFD	computational fluid dynamics
CPU	central processing unit
FEVA	frozen eddy-viscosity approach
FLM	Institute for Fluid Mechanics
FLM-Eu	FLM dynamically fully nonlinear Euler method
FLM-NS	FLM dynamically fully nonlinear RANS method
FLM-SDEu	FLM small disturbance Euler method

Acronym	**Denotation**
FLM-SD.NS	FLM small disturbance Navier-Stokes method
FTDW	Fighter-type Delta Wing
GAF	generalized aerodynamic force
GMRES	generalized minimal residual
ILU	incomplete lower-upper
LANNW	Lockheed Georgia, Air Force Flight Dynamics Laboratory NASA Langley Research Center, and National Aerospace Laboratory wing
LE	leading edge
LEV	LE vortex
LHS	left hand side
LU-SSOR	lower-upper symmetric successive overrelaxation
MUSCL	monotonic upstream-centered scheme for conservation laws
NCDW	NASA Clipped Delta Wing
PDE	partial differential equation
RANS	Reynolds-averaged Navier-Stokes
RHS	right hand side
RPM	recursive projection method
S/A	Spalart-Allmaras
TE	trailing edge
TUM	Technical University of Munich
URANS	unsteady RANS

Chapter 1

Introduction

Aircraft structures are not entirely rigid. Especially such components as the wing, the stabilizers, and the control surfaces are highly flexible. Under flight conditions, the aerodynamic loading of the structure leads to its deformation/deflection, which in turn alters the aerodynamic loading, and so forth. Dynamically, this behavior is governed by the reciprocity between the aerodynamic forces resultant from the flowfield, the inertial forces resultant from the structural mass distribution, and the elastic forces resultant from the structural stiffness distribution. The instability of this aeroelastic system corresponds to the phenomena of flutter. It is a structural oscillation of ever growing deformation/deflection amplitude due to a net transfer of energy by the aerodynamic forces into the structure for each individual cycle, eventually ending in component failure. As this can be catastrophic, aircraft must be shown to be free of flutter well beyond the intended flight envelope in order to achieve certification. The respective verification is conducted throughout the design process, minimizing expensive rectifications during flight testing; e.g., see Bisplinghoff et al. [13].

Within such a production environment, a computational aeroelasticity (CA) tool that performs a linear stability analysis of the structural equations of motion under the modal approach is still most commonly employed. In this regard, a numerical structural method initially renders the relevant structural eigenmodes, and then supplies the matrices of the discrete mass and stiffness distributions as generalized for the structural eigenmodes to the CA tool. Complementarily, a numerical aerodynamic method renders the unsteady loading for a simple harmonic oscillation of each structural eigenmode over a discrete reduced-frequency bandwidth for various flight conditions. Only the first harmonic inherent to the unsteady loading is relevant to the problem. This set of first harmonics is then supplied to the CA tool in the form of generalized aerodynamic force (GAF) matrices, as transitioned from the time to the frequency domain. The prerequisite is that the unsteady loading behaves dynamically linear: Its amplitude must be directly proportional to the excitation amplitude. No restriction, however, is placed on the fidelity of the flow

model (and thus the flow governing equation/equation system) drawn on by the numerical aerodynamic method. Ultimately, the CA tool iterates over both the reduced frequency and the flight conditions to identify the flight speeds at which the aeroelastic system requires zero artificial structural damping to maintain a simple harmonic oscillation. These flight speeds are known as the flutter velocities; e.g., see Hassig [46]. Both the accuracy and efficiency of the CA tool are primarily determined by the numerical aerodynamic method. It needs to account for the flow properties exhibited in the investigated speed range, while allowing for the computation of the necessary parameter variations under the constraints of a production environment. Often, these demands are incompatible. An extensive overview on this matter is provided by Schuster et al. [114] as well as Yurkovich [148], with a comprehensive discussion of the hierarchy of flow governing equations given by Bendiksen [10].

In the following, a brief overview of the utilized numerical aerodynamic methods for the various speed ranges is given, highlighting the lack of an accurate and efficient instance for the transonic viscous flow regime. It is elaborated how this gap can be closed by a small disturbance Navier-Stokes method, and the standard of knowledge summarized. Lastly, the research objectives of the dissertation at hand are formulated.

1.1 Numerical Aerodynamic Methods for Aircraft Flutter Analysis within a Production Environment

To date, the numerical aerodynamic methods utilized by a CA tool predominantly draw on the linearized potential equation. It is a linear partial differential equation (PDE) of second order for a velocity potential, and governs inviscid sub- or supersonic irrotational/isentropic flow over slender geometries. The linearity of the governing equation permits its decomposition into an instance for the steady flowfield respective the considered body's reference position and an instance for a minor perturbation about it, which are treatable independent from each other. On the basis of the perturbed flow governing equation, strictly first-harmonic loading can then be obtained for a simple harmonic excitation, computed directly in the frequency domain. This approach has proven to be sufficiently accurate and highly efficient: For the subsonic speed range, lifting surface kernel-function methods as originating from Laschka [76] (also see Sensburg and Laschka [118]), doublet lattice methods as originating from Albano and Rodden [2] (also see Kalman et al. [64]), and constant pressure panel methods, such as the instance within the ZONA Technology ZAERO suite of CA tools [151], have become the most established. For the supersonic speed range, however, a greater variety of methods had come into existence, and have

seen more or less frequent usage; i.a., Mach box methods, supersonic incarnations of the lifting-surface kernel function method and the doublet lattice method, as well as harmonic gradient methods [148].

Naturally, the preceding methods are not suitable for the transonic speed range: The linearized potential equation does not account for convective nonlinearities (shocks) in the flowfield. As described by Schuster et al. [114], the emergence of shocks can, however, be detrimental to the stability of the aeroelastic system. This circumstance is experienced as a substantial reduction of the flutter velocity, designated the transonic dip [114]. Numerical aerodynamic methods drawing on higher-tier flow governing equations, such as the transonic small disturbance equation, the full potential equation, and the Euler equations, allow for the first-harmonic loading to be obtained as influenced by the shocks. Both the transonic small disturbance equation and the full potential equation are nonlinear PDE of second order for a velocity potential, governing inviscid compressible irrotational/isentropic flow. The former is still restricted to slender geometries, while the latter permits more general ones. Only weak shocks can be accounted for in the flowfield, while being limited in their degree of motion. The Euler equations, however, are a coupled system of nonlinear PDEs of first order for the primitive field quantities (variables); i.e., the density, the velocity vector, and the specific total energy. The system embodies the fundamental physical principles of mass conservation, Newton's second law, and energy conservation. It is typically expressed in vector form, where a state vector for the primitive field variables is defined, and its time rate of change then equated to the negative sum of each convective flux vector's spatial rate of change. The Euler equations govern inviscid compressible rotational/nonisentropic flow over general geometries. Hence, shocks of arbitrary strength and degree of motion can be accounted for in the flowfield. Naturally, with the increasing fidelity of the flow model, the computational effort required by the associated method increases as well, exceedingly witnessed when transitioning from the full potential equation to the Euler equations. In addition, the nonlinearity of all three instances generally requires a solution in the time domain, and thus time-accurately, which further diminishes the associated method's efficiency.

Pursuant to Schuster et al. [114], the transonic dip can be predicted by these nonlinear inviscid methods per se, yet at varying accuracy. From the aspect of aircraft design, however, the low point of the transonic dip is commonly the critical characteristic, as it represents the minimum flutter velocity across the intended flight envelope. The low point is mostly contingent on the viscous phenomena exhibited by the flowfield; in particular, the degree of interaction between the shocks and the boundary layer. Neither the transonic small disturbance equation, the full potential equation nor the Euler equations, though, can account for viscous phenomena, with the associated methods typically leading to substantially lower minimum flutter velocities than would be the case in reality.

Hence, a structural design of excessive mass and/or stiffness may become realized [114]. As a remedy, both experimental and theoretical corrections of the supplied first-harmonic loading are often performed [148]. Coupling the preceding governing equations/equation system with the boundary layer equations has been employed likewise. All these measures, however, can not account for the influence of viscous phenomena in their generality. Numerical aerodynamic methods drawing on the transonic small disturbance equations have become the most established for the transonic speed range, as they offer the best trade-off between accuracy and efficiency; i.a., CAP-TSD originating from Batina et al. [9] of the NASA Langley Research Center (also see Bennett et al. [11]), as well as its boundary-layer-equations-coupled incarnation CAP-TSDV [40]. Over the last decade, the Euler equations have been more frequently drawn on, as the associated methods benefited from the substantial increase in processing power and storage capabilities at concurrently decreasing expenditure. The ZONA Euler unsteady solver (ZEUS) originating from Chen et al. [27] of ZONA Technology is such an instance. It realizes a time-domain solution with the option of coupling the boundary layer equations.

For a continuum, the highest tier of flow governing equations are the (instantaneous) Navier-Stokes equations. In contrast to the Euler equations, additional viscous flux vectors provide for friction and heat conduction under consideration of the fluid's material law. The state vector's time rate of change is equated to the summed difference between each viscous and convective flux vector's spatial rate of change, rendering a coupled system of nonlinear PDEs of second order for the primitive field variables. It allows for both shocks and viscous phenomena to be generally accounted for in the flowfield. A numerical aerodynamic method drawing on the instantaneous Navier-Stokes equations could inherently render boundary layer thickening, laminar/turbulent transition, flow separation, and turbulence per se, as long as all time and length scales are sufficiently resolved. Referred to as direct numerical simulation, it requires the utmost in processing power and storage capabilities even for the simplest geometries and low Reynolds numbers. Complex geometries at flight-realistic Reynolds numbers are currently not treatable and will not be so in the foreseeable future. This makes direct numerical simulation generally irrelevant to aircraft aerodynamics, and naturally to flutter analysis as well.

Requiring substantially less processing power and storage capabilities, a numerical aerodynamic method drawing on the Reynolds-averaged Navier-Stokes (RANS) equations can sufficiently account for the relevant occurrences of the transonic viscous flow regime. The RANS equations result from a statistical treatment of the instantaneous Navier-Stokes equations under the assumption that the time scales of turbulence are widely disjoined from the time scales of any organized unsteadiness inherent to the flowfield: The erratic fluctuations of the primitive field variables (as associated with turbulence) are averaged out, yielding a limited number of additional unknown terms within the equation

system governing the organized unsteadiness. Representing a problem of closure, these turbulent correlation terms are then either modeled directly or indirectly by amending the governing equation system with semi-empirical equations of algebraic and/or partial differential design. The direct approach is known as Reynolds stress modeling, while the indirect approach is known as eddy viscosity modeling. The latter is based on the Boussinesq approximation, which relates the turbulent correlation terms to the spatial derivatives of the averaged primitive field variables by introducing a dynamic eddy viscosity as a supplement to the dynamic molecular viscosity. For either approach, a wide array of models have been developed, allowing the influence of turbulence to be considered at varying degrees of fidelity and reasonable computational effort. A numerical aerodynamic method drawing on the RANS equations would be best suited to supply the first harmonic loading of a complex geometry at transonic speeds with respect to accuracy. Unfortunately, it would still not meet the efficiency demand of aircraft flutter analysis within a production environment, as will be elaborated in Section 1.2.

Numerical methods solving either the instantaneous Navier-Stokes equations, the RANS equations, the Euler equations, or even the boundary layer equations are designated computational fluid dynamics (CFD) methods. An overview of the fundamental schemes (spatial/temporal discretization, boundary conditions, solution techniques) and grid generation principles are provided by Anderson [6], Hoffmann and Chiang [49, 50], Blazek [16], as well as Hirsch [47, 48]. Hoffmann and Chiang [51] as well as Blazek [16] also give an overview of the most commonly employed turbulence models, with Wilcox [139] offering a more fundamental and detailed discussion. It should be noted that shock-capturing CFD methods (those where shocks emerge and interact as part of the solution process) typically draw on flow governing equations formulated in terms of conservative field variables; i.e., the mass, the momentum vector, and the total energy, all per unit volume. In combination with a finite volume spatial discretization, this allows for numerical robustness to be achieved despite the discontinuity of the primitive field variables across shocks. Recently, the CFD method designation has been extended to include potential-based methods, with the instances drawing on the linearized potential equation considered to be CFD methods of lowest order. In contrast, direct numerical simulation is the CFD method of highest order. Furthermore, the numerical aerodynamic method utilized by a CA tool is referred to as its CFD component.

1.2 Satisfying the Accuracy and Efficiency Demands for the Transonic Viscous Flow Regime

CFD methods that solve the RANS equations are nowadays well-established for steady and select unsteady problems of aircraft aerodynamic analysis in the transonic viscous

flow regime. Several instances have matured to the point where they prominently feature within research and industrial production environments; in particular, elsA [18] of the French Aerospace Laboratory (ONERA), FLOWer [74] and TAU [42, 115] of the German Aerospace Center (DLR), as well as CFL3D [112] and FUN3D (originating from Anderson and Bonhaus [7]) of the NASA Langley Research Center. Another such instance is FLM-NS (originating from Cvrlje et al. [32]) of the former Chair of Fluid Mechanics (FLM)[1], Department of Mechanical Engineering, Technical University of Munich (TUM); also see Cvrlje's [31] dissertation of 2001. These high-order CFD methods, however, are seldom employed for aircraft flutter analysis: Computing the unsteady loading of an elastic body's simple harmonic oscillation, or even that of a structural eigenmode, a time-domain solution of the RANS equations needs to be realized; e.g., see Lee-Rausch and Batina [77]. Referred to as the unsteady RANS (URANS) approach, a dynamically fully nonlinear flow response is generally rendered with it. A number of computational cost issues are inherent. Pechloff and Laschka summarized that

> [the d]ual[-]time-stepping schemes typically employed in the [URANS approach] must sequentially realize a pseudosteady solution at each incremental [deformation/]deflection (physical time step) of the elastic body's [simple harmonic oscillation]. As the unsteady flowfield's periodicity is typically gained only after the computation of several oscillatory cycles, the aggregate number of pseudosteady solutions represents the primary cost, a circumstance which becomes especially expensive at low frequencies. A secondary cost rests in the accompanied incremental deformation of the body-embedding computational grid. For each physical time step, the computational grid must be updated to the body's new position, a task which becomes all the more expensive as the geometric complexity of the body increases. Lastly, the effort associated with the acquired data's postprocessing has to be taken into account. Since the unsteady loading is obtained as a series in time, subsequent Fourier analysis becomes necessary to extract the harmonics of interest. In doing so, turnaround time and thus throughput of the overall process is further diminished. [103]

Considering the Mach number and the Reynolds number at freestream conditions, the attitude conditions, as well as M relevant structural eigenmodes, the flutter velocity's evaluation through GAF matrices for a reduced-frequency bandwidth given by N nodes would require $M \times N$ URANS-method executions; N reduced-frequency-specific instances of a complex $M \times M$ GAF matrix could then be provided to the CA tool. Any other parameter's variation would entail a correspondingly higher total of executions: The flutter velocity rendered as a function of the Mach number at freestream conditions is of particular interest. Permutations to account for an aircraft's variable geometry and/or the

[1]The FLM was reconstituted as the Institute of Aerodynamics in December 2004 under o. Prof. Dr.-Ing. Nikolaus Adams, and subsequently redesignated the Chair of Aerodynamics and Fluid Mechanics.

interference of exchangeable components need to be factored in as well. Overall, without a massive multiprocessor capability, the URANS approach becomes too inefficient within a production environment, notwithstanding its inherent accuracy in the transonic viscous flow regime; also see Pechloff and Laschka [100, 103]

Proposed by Pechloff et al. [98] in 2002, as well as by Pechloff and Laschka [100, 103] onward, a CFD method solving the small disturbance Navier-Stokes equations can be an efficient substitute for an URANS method, while keeping the latter's accuracy to a great extent. As established,

> [f]or problems of dynamic stability, the elastic body's [simple harmonic oscillation] can be regarded as being limited to minor [deformations/]deflections about a reference position. Consequently, the organized [fluctuation] inherent to the flowfield's instantaneous response can be presumed to be a predominantly dynamically linear perturbation about a [linearized] time-invariant[-]mean [(reference)] state. This would entail that the higher-order harmonics present within the response become negligible to the point where a generally phase-shifted first harmonic prevails. Under the preceding assumption, a system of statistically treated linear [PDEs] exclusively governing the complex amplitude of the [periodic perturbation] can be extracted from the instantaneous Navier-Stokes equations. With the elimination of time-dependency, time-accuracy and the accompanied incremental grid deformation are no longer an issue to the solution process. Thus, the necessary computational effort becomes comparable to the one involved with the steady-state solution of the RANS equations.
>
> The small disturbance Navier-Stokes solution embodies magnitude and phase-shift of the [periodic perturbation]. It develops contingent on a given oscillation frequency and amplitude surface [deformation/]deflection of the elastic body's [simple] harmonic [oscillation], as well as the reference [...] flowfield about which the [periodic perturbation] occurs. [...] The amplitude surface [deformation/]deflection [can be] numerically supplied by way of two computational grids. One embeds the elastic body at its reference position, while the other does so at its [deformed/]deflected extremum position. A steady-state RANS solution realized in the reference grid for the specific [freestream and attitude conditions] serves as the [reference] flowfield. For both [a structural] eigenmode and [reduced frequency] variation, it remains unchanged. [103]

In practice, the small disturbance Navier-Stokes method would intrinsically subtract the reference grid from its extremum counterpart once at initialization, yielding the required Cartesian amplitude coordinates of each vertex. The URANS method, on the other hand, would typically interpolate between the two grids or extrapolate from them in accordance with the time law, obtaining the grid instance of the considered physical time step. Furthermore, the steady-state RANS solution is merely employed to initialize the URANS computation process. Pechloff and Laschka further stated that

> [t]he small disturbance [Navier-Stokes] approach handles dynamically nonlinear phenomena that would emerge in the flowfield's instantaneous response as dynamically linear perturbations about a statically nonlinear state, as contained in the [reference] flowfield. [...] Contrary to the [URANS] approach, the unsteady loading is acquired directly. The obtained complex amplitude load represents the first-harmonic load resultant from the considered [structural] eigenmode's oscillation with [a particular reduced frequency], while the afore computed [reference] load embodies the zeroth-harmonic load. Naturally, the treatment of a body's elastic oscillations represents the most general case, the consideration of rigid[-body] oscillations for an a priori known frequency being equally feasible. In this instance, the amplitude surface [deformation/]deflection is replaced by the [amplitude] translational and/or rotational [deflection, ultimately yielding the dynamic stability derivatives of said motion.] [103]

At TUM, the small disturbance approach itself had been initially applied to the Euler equations for the given external flow problem by Kreiselmaier [70] in his dissertation of 1998; also see Kreiselmaier and Laschka [71]. As described by Pechloff and Laschka [100], it was based on original developments in the field of turbomachinery by Hall and Crawley [44] (1989), as well as Lindquist and Giles [81] (1994). The prediction accuracy and computational efficiency gain of the resulting small disturbance Euler method FLM-SDEu was substantiated with respect to its dynamically fully nonlinear counterpart FLM-Eu [70, 71] for various airfoil and wing cases. In this context, computational efficiency gain is defined as the inverse ratio of the computation times required by the small disturbance and the dynamically fully nonlinear method. The low-aspect-ratio wing of a high-speed/high-maneuverability aircraft configuration, designated the Fighter-type Delta Wing (FTDW), was particularly focused on. FLM-SDEu/FLM-Eu predictions of the harmonic loading for various FTDW eigenmodes were investigated by Sickmüller et al. [120] in 2001 as well as Weishäupl and Laschka [132] in 2004, with the latter publication also considering pitching and flap oscillations. Allen et al. [5] had further investigated flap oscillations for the FTDW with an external store [100]. Beyond the original FLM-SDEu incarnation, Sickmüller [119] had derived the governing equation of the second-harmonic flow response under the small disturbance premise in his 2005 dissertation, while implementing its solution and substantiating the validity of the approach per se. Furthermore, Sekar and Laschka [117] (2005), as well as Sekar [116] in his dissertation of 2006, realized an FLM-SDEu incarnation that coupled the small disturbance Euler equations with the boundary layer equations, allowing for a degree of interaction between predominantly viscous and predominantly inviscid flow. Eventually, the formulation of the small disturbance Euler equations provided by Kreiselmaier and Laschka [70] served ZONA Technology as the basis for the implementation of a proprietary method. Originally published by Zhang et al. [149] in 2012, it was realized as a derivative of ZEUS [27]: Unconventionally, ZEUS

utilizes an invariant Cartesian grid with a transpiration near-field boundary condition. It eliminates the need to generate an extremum grid for each structural eigenmode, while foregoing the time-accurate grid deformation as well. The reduction in computational cost due to the latter, however, may become compensated by the increase in computational cost due to the evaluation of the transpiration near-field boundary condition. The small disturbance incarnation of ZEUS retains this technique [149]. Of course, merely the benefit of not needing to generate an extremum grid for each structural eigenmode remains in the frequency domain.

Just as for a dynamically fully nonlinear Euler method, a small disturbance Euler method yields inaccurate predictions for cases where the unsteady loading is increasingly affected by viscous phenomena, even when coupling the boundary layer equations. The upgrade toward a small disturbance Navier-Stokes method is the self-evident remedy, e.g., as reasonably accomplished by means of the original FLM-SDEu [70]; also see Pechloff and Laschka [100]. In this context, Dowell et al. had already recognized the small disturbance approach per se as being "sufficient to assess the linear stability of the aeroelastic system[.]"[36] It was further stated that even the amplitude of a limit cycle oscillation can be predicted by this means as long as "the structural nonlinearities are dominant[.]"[36] In conclusion, the differences of the small disturbance approach to the dynamically fully nonlinear approach (in its deforming grid instance) are recapped through Figure 1.1 and Table 1.1.

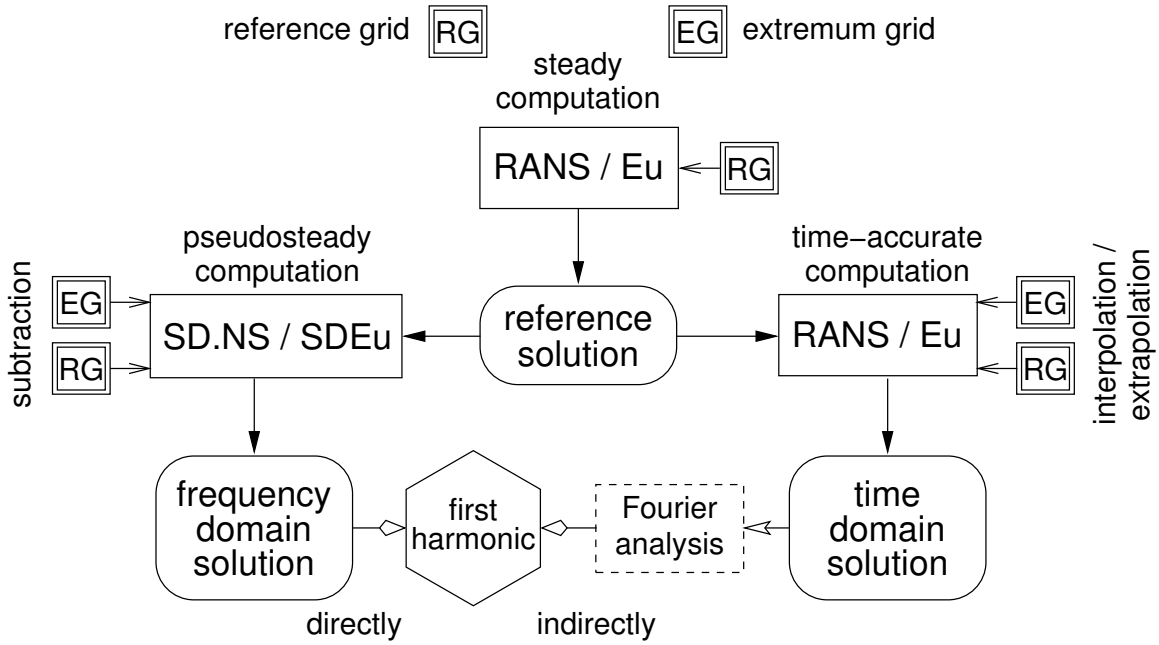

Figure 1.1: Comparison between the small disturbance (SD) and dynamically fully nonlinear computation process (NS: Navier-Stokes, Eu: Euler); based on [103], Fig. 1.

Aspect	Approach	
	Small disturbance	Dynamically fully nonlinear
Solution process	Single pseudosteady solution for the complex amplitude of the first harmonic	Time-accurate, typically requiring 300–400 successive pseudosteady solutions
Grid deformation	Unnecessary	Incremental
First-harmonic load	Obtained directly, in the scale of the disturbance	Fourier analysis[a]

[a] Considering the first-harmonic load to be an order of magnitude smaller than the zeroth-harmonic load, the former may be undesirably impacted by numerical errors incurred in its extraction as a small quantity from the entirety of the time-accurate periodic loading.

Table 1.1: Computational advantages of the small disturbance approach over the dynamically fully nonlinear instance; based on [103], Table 1

1.3 Standard of Knowledge

A continuous yet brief review of the development and the adoption of small disturbance Navier-Stokes methods has been conducted by Pechloff and Laschka since 2004 [99, 100, 101, 103, 102], and also by Pechloff [97] in 2012. As stated,

> [t]he small disturbance Navier-Stokes approach has its origin in the field of turbomachinery, where respective computational methods were developed to provide an accurate and yet efficient means of investigating unsteady viscous flow effects within a blade design environment. Also referred to as [...] time-linearized Navier-Stokes methods, pioneering work [was] conducted by Clark [[28]], who harnessed the approach for the analysis of [transonic forced response and subsonic] stall flutter in two-dimensional cascades [at Duke University in 1998]. [103]

From this starting point, a plethora of small disturbance Navier-Stokes methods have been brought to maturity, becoming the customary computational means for turbomachinery flutter analysis in a production environment [103]. For aircraft flutter analysis, however, such methods had not gained traction until 2010 [103]. Only a few endeavors were made, with established RANS methods being appropriated for the development of complementary small disturbance Navier-Stokes incarnations. They have been realized to varying degrees of intricacy and maturity. In the following, a detailed review of small disturbance Navier-Stokes methods employed in the field of turbomachinery aeroelasticity and in the field of aircraft aeroelasticity is conducted.

1.3.1 Small Disturbance Navier-Stokes Methods in the Field of Turbomachinery Aeroelasticity

The small disturbance Navier-Stokes methods employed in the field of turbomachinery aeroelasticity can be discerned on the basis of the implemented solution technique. The initial instances rely on conventional pseudotime integration, while the continuative instances utilize advanced schemes.

1.3.1.1 Initial Instances

In Clark's [28] pioneering work, the small disturbance Navier-Stokes equations' frequency-domain formulation was derived from two-dimensional RANS equations cast for a deforming grid approach. To this effect, both the conservative variables describing the flowfield and the spatial coordinates of the grid vertices were each decomposed into a time-invariant mean and a simple harmonic perturbation. The combined convective and viscous flux vector of each coordinate direction was then expanded through a first-order Taylor-series, with the individual Jacobian matrix being expressed analytically. The simple harmonic perturbation of the dynamic molecular viscosity and the dynamic eddy viscosity was fully accounted for, respectively, as governed by a small disturbance formulation of Sutherland's law and the Spalart-Allmaras (S/A) one-equation turbulence model [121]. Similarly, small disturbance formulations of the no-slip-/adiabatic-wall boundary condition were novelly derived. The far-field boundary condition was based on a Fourier-mode decomposition technique derived for an earlier developed small disturbance Euler method. It was said to yield a high degree of nonreflectivity for both the inflow and the outflow boundary. Likewise, the known frequency-domain formulation of the spatial-periodicity boundary condition was drawn on. Directly accounting for the considered interblade phase angle, merely a single blade-passage needs to be treated by a small disturbance method. A time-domain method, on the other hand, would need to treat an appropriate number of interconnected blade-passages to have the same effect [28].

Clark [28] realized the small disturbance Navier-Stokes equations' numerical solution by a finite volume structured method, which also supported a division of the computational domain into multiple blocks. The introduction of a pseudotime derivative respective the amplitude conservative state vector allowed for a solution by means of pseudotime integration. In this regard, a modified instance of the Lax-Wendroff (explicit) scheme was implemented. It was identified that the pseudotime integration of the small disturbance Navier-Stokes equations' frequency-domain formulation did not require temporal accuracy; i.e., equivalent to the pseudotime integration of the RANS equations toward a steady-state solution. Consequently, it was feasible to utilize the convergence acceleration techniques commonly employed with the latter: local pseudotime stepping, residual

smoothing, and multigriding. Spatial discretization was realized by means of a central vertex-centered scheme, which, however, is not inherently dissipative. Thus, artificial dissipation terms based on second- and fourth-differences were introduced, allowing shocks to be accurately resolved and spurious spatial oscillations of the field variables to be suppressed. A full small disturbance formulation of this scheme was implemented. Within the viscous flux vectors and the S/A turbulence source term vector, as well as within the pertinent Jacobian matrices, spatial derivatives of time-invariant-mean flowfield variables needed to be evaluated. This was handled by applying the gradient theorem, and led to overall second-order spatial accuracy. The S/A one-equation turbulence model [121] itself was fully integrated toward the wall boundary. Prescribing the inflow/outflow conditions, a steady-state solution of the RANS equations for the considered blade's time-invariant-mean position was utilized to supply the required time-invariant-mean flowfield. It was recognized, however, that if the dynamical nonlinearity of the actual flowfield were too high, its time-invariant mean would deviate from the steady-state flowfield per se. Since the latter serves as the basis for the small disturbance computation, the obtained amplitude flowfield would have effectively been impacted as well [28].

Clark [28] initially considered a cascade of NACA 2406 airfoils under transonic flow conditions to substantiate the validity of the small disturbance Navier-Stokes approach. It was deemed to be representative of a compressor section. A quasi-steady outflow-pressure perturbation (i.e., at nil-valued reduced frequency) was computed with the small disturbance Navier-Stokes method and compared with the corresponding divided-difference RANS result. It is the difference between the steady-state RANS solution for the positive amplitude increment of the nominal outflow pressure and its negative counterpart. The conformity of the obtained amplitude surface-pressure distributions essentially verified the consistency of the small disturbance method's implementation, while demonstrating the capability to accurately render a shock impulse. Additionally, the flowfield response to a torsional vibration at a 90 deg interblade phase angle was computed with the small disturbance Navier-Stokes method. It demonstrated the capability to account for an amplitude deformation of the grid. However, a comparison of the obtained first-harmonic surface-pressure distribution to experimental data, or a corresponding URANS-method result, was not actually provided. The computational efficiency gain achieved by the small disturbance Navier-Stokes method was said to be within one and two orders of magnitude respective a URANS method [28]. This corresponds to a reduction of computational time by 90% to 99%. Due to the lack of a comparative URANS computation, though, Clark [28] extrapolated these benchmarks from the underlying steady-state RANS computation. The computational efficiency gain was in part attributed to the feasibility of treating a multiple-blade-passage problem in the time domain as a single-blade-passage problem in the frequency domain. Specifically, the computationally treated physical domain had

become reduced to one quarter of its necessary time-domain size [28].

Clark [28] further investigated the feasibility of accurately computing the unsteady flow in a typical transonic turbine stage. The considered case was characterized by shocks and wakes that had emerged within the stator vane row and induced an unsteady flow response in the passing downstream rotor blade row. For the frequency-domain treatment, the computational domain embedding the single rotor-blade passage was isolated from its stator-vane counterpart. A steady-state RANS solution conducted within the stator-vane's computational domain allowed gust shapes of the characteristic variables (vorticity, entropy, and pressure) to be determined at the outflow boundary with respect to the rotor's frame of reference. Transformed to the frequency domain, they were applied at the inflow boundary of the rotor-blade's computational domain as the far-field boundary condition of the small disturbance Navier-Stokes computation. The necessary time-invariant-mean flowfield was again supplied by an isolated steady-state RANS solution therein. For this purpose, the steady conservative variables at the outflow boundary of the stator-vane's computational domain were converted to the rotor's frame of reference, and applied at the pertinent inflow boundary as the far-field boundary condition. Ultimately, the magnitude of the obtained first-harmonic surface-pressure distribution was compared to experimental data and a dynamically fully nonlinear computational result yielding from an established URANS method. It utilized a quasi three-dimensional approach, employed the Baldwin-Lomax (B/L) algebraic turbulence model [8], and induced the flowfield response by time-accurately translating the computational domain of the rotor-blade passage past its stator-vane counterpart. This was realized by means of an overset-grid technique. It was ascertained that the small disturbance Navier-Stokes method predicted the experimental data just as well as the URANS method [28]. A CPU-time ratio between the two methods, however, was not given.

Lastly, Clark [28] employed the small disturbance Navier-Stokes method to investigate the aeroelastic stability of a low-aspect-ratio fan-blade (the tip section) within a cascade. In particular, the effect of viscous phenomena on the flutter behavior was highlighted. Both a low and high inflow-angle case at incompressible flow conditions were considered, respectively, characterized by a predominantly attached and an extensively separated flow topology. For each case, the identical pitching oscillation about the midchord point at a specific reduced frequency and a 180 deg interblade phase angle was conducted, being representative of a torsional vibration. Experimentally, these cases are known as the Buffum-cascade cases, with first-harmonic surface-pressure-coefficient data having been acquired. Furthermore, dynamically fully nonlinear computational results yielding from another established URANS method were drawn on. This instance utilized a strictly two-dimensional approach, however, again employed the B/L algebraic turbulence model [8]. For the low inflow-angle case, it was ascertained that the small disturbance Navier-Stokes

prediction agreed quite well with the experimental data in both the real and imaginary part of the first-harmonic surface-pressure-coefficient distribution. The prediction was confirmed in principle by the URANS result, with greater deviations mainly emerging at the leading edge (LE). For the high inflow-angle case, it was ascertained that the small disturbance Navier-Stokes prediction agreed excellently with the experimental data, even on the suction surface, where the extensive flow separation occurred. The URANS result, on the other hand, merely conformed to the small disturbance Navier-Stokes prediction and the experimental data on the pressure surface. Substantial deviations emerged on the suction surface for both the real and imaginary part of the first-harmonic surface-pressure-coefficient distribution. These were partially attributed to the known deficits of the B/L algebraic turbulence model [8] in treating extensively separated flow. Furthermore, it was reported that a small disturbance Navier-Stokes computation attempted under discount of the amplitude dynamic eddy viscosity was not able to render a converged solution [28]. This discount is referred to as the frozen eddy-viscosity approach (FEVA).

For both the low and high inflow-angle condition, Clark [28] eventually conducted a variation on the pitching oscillation's reduced frequency, as well as a sweep over the entire interblade phase angle range. Under the small disturbance premise, the time-invariant-mean flowfield at a specific inflow condition will be independent of any variation of reduced frequency or interblade phase angle. Consequently, the pertinent small disturbance Navier-Stokes computations can all be conducted on the basis of the same steady-state RANS solution. Analyzing the aerodynamic work performed on the blade over the course of a pitching cycle for each case, it was ascertained that at the high inflow-angle condition (the stalled operating point) an increase in reduced frequency has a far more stabilizing effect than at the low inflow-angle condition (the nominal operating point). However, the maximum of the aerodynamic work performed on the blade, which corresponds to the instance of greatest instability, increased significantly for the stalled operating point, whereas it minorly decreased for its nominal counterpart [28]. A comparison with experimental data or a URANS result had not been provided. Excerpts of Clark's [28] dissertation had been presented by Clark and Hall [29] in 1999, and published in 2000 [30], with the Buffum-cascade cases being focused on therein.

Further pioneering work was concurrently presented by Holmes et al. [52] from General Electric Corporate R&D/Aircraft Engines. They had implemented a three-dimensional structured small disturbance Navier-Stokes method for forced response and flutter computations. It novelly employed a small disturbance formulation of the Wilcox k-omega two-equation turbulence model [138]. Considering a standardized compressor cascade (the Standard Configuration 10) in two-dimensional space, subsonic forced response investigations through acoustic wave perturbations at the outflow boundary had been conducted on the need to fully account for the amplitude viscous fluxes. Furthermore, the

need to fully account for the amplitude dynamic eddy viscosity in such an instance was studied as well. Because the investigations were limited to thin attached boundary layers, a wall function had been instated to bridge the near-wall and logarithmic region, instead of integrating the turbulence model entirely. Initially, the results of small disturbance Euler computations performed on the basis of a steady-state RANS solution for the reference conditions were put into comparison with their small disturbance Navier-Stokes counterparts. This demonstrated the need to fully account for the amplitude viscous fluxes. The need to fully account for the amplitude dynamic eddy viscosity was then identified toward the lower end of the excitation frequency spectrum. Toward the higher end, on the other hand, a FEVA sufficed [52].

As ascertained by Pechloff and Laschka, "[s]ince [the introduction of the small disturbance Navier-Stokes method], the dynamically linear treatment of unsteady viscous flow has proven to be applicable to a wide range of turbomachinery aeroelasticity problems." [103] In 2001 Sbardella and Imregun [113] from the Imperial College London novelly implemented a small disturbance Navier-Stokes method that employed a hybrid computational grid; i.e., using both structured and unstructured grid elements. They validated their approach in two-dimensional space by means of a subsonic attached-flow case and a transonic flow/separation bubble case pertaining to a standardized turbine cascade (the Standard Configuration 11), with a bending mode considered for both instances. In three-dimensional space, a transonic flow case for a rotor/stator assembly was investigated. A small disturbance formulation of the S/A one-equation turbulence model [121] was again employed. By default, it was integrated all the way toward a considered wall boundary. The FEVA was also made available, and could be applied with the option of a wall function to further reduce computational effort. Based on the two-dimensional cases, it was concluded that the need to fully account for the amplitude dynamic eddy viscosity is merely given when viscous effects become dominant; e.g., with the existence of a separation bubble. Consequently, it was suggested that the examination of the utilized steady-state RANS solution could allow this need to be a priori gauged. For the three-dimensional case, the steady-state RANS solution was merely rendered under employment of a wall function. Complementarily, the FEVA with wall function was applied for the small disturbance Navier-Stokes computation. The results were deemed acceptable in comparison to the experimental data. However, it was suggested that an improvement could be made by providing a small disturbance formulation of the wall function per se, hence permitting that the amplitude dynamic eddy viscosity again be fully accounted for. Absent of an actual comparative URANS computation, the computational efficiency gain of the small disturbance Navier-Stokes method was extrapolated from the steady-state RANS computation, resulting in a factor of 33 [113]. This corresponds to a reduction of computational time by 97%.

In 2003 Ning et al. [91] from ALSTOM Power UK Ltd. investigated the feasibility of employing a small disturbance Navier-Stokes method to predict the bladerow interactions in a multistage design. A subsonic turbine-stage case and a transonic counter-rotating shrouded propfan case supplied by DLR were considered in two-dimensional space. The employed structured method, however, was stated to already be implemented for three-dimensional treatments. The computations were conducted with the B/L algebraic turbulence model [8] under application of a FEVA. Comparison of the small disturbance Navier-Stokes results with both experimental data and the comparative URANS results allowed the prediction capability to be ascertained as sufficiently accurate. For the subsonic turbine-stage case, a reduction of computational time by two orders of magnitude (99%) with respect to the URANS computation was determined. For the transonic counter-rotating shrouded propfan case, a reduction by 75% was still achieved [91].

Actual three-dimensional investigations on bladerow interactions in a multistage design were presented by Ekici et al. [41] from Duke University in 2005. Both a modern front-stage compressor and the primary rotor/stator assembly of a two-stage fan (NASA Rotor 67) were considered under transonic flow conditions, with a flutter analysis being ultimately realized. The employed structured small disturbance Navier-Stokes method fully accounted for the amplitude dynamic eddy viscosity, again supplied by a small disturbance formulation of the S/A one-equation turbulence model [121]. The method was deemed to be accurate as well as highly efficient in the prediction of the particular unsteady viscous flow. Computational time was said to be in the same order of magnitude as for the treatment of comparative steady-flow cases. Novelly, it was determined that the computational time and memory requirements would scale linearly with the number of treated bladerows [41].

1.3.1.2 Continuative Instances

Equivalent to the original small disturbance Navier-Stokes method of Clark and Hall [30], the instances presented by Holmes et al. [52], Sbardella and Imregun [113], Ning et al. [91], and Ekici et al. [41] all employed a form of pseudotime integration, being either of explicit or implicit type. Referencing Campobasso and Giles [19] from Oxford University, it was stated by Pechloff and Laschka that "[g]enerally, this pseudotime integration yields a converged solution without difficulty. In cases[, however,] where the RANS supplied [steady-state] flowfield exhibits phenomena associated with inherent physical unsteadiness ([e.g., regions] of separation), solution divergence has sometimes been observed." [103] Already investigated in 2003, Campobasso and Giles [19] ascertained that even if the RANS-supplied steady-state flowfield satisfied a residual tolerance of sufficient accuracy, the actual solution process may have terminated in a state of low-level limit cycle. In such a case, the nonlinearity inherent to the RANS equations prevented the initial

instability from growing unchecked. A pseudotime integration of the small disturbance Navier-Stokes equations on the basis of such a steady-state flowfield, however, results in the exponential growth of the amplitude residual independent of the pseudotime step. Equating the pseudotime integration with the fixed-point iteration of a system of linear equations, stability analysis of the solution process for both the two-dimensional transonic flow/separation bubble case of the Standard Configuration 11 and a three-dimensional fan-rotor case revealed a small number of complex-conjugate eigenvalue-pairs that violated the convergence condition. It was further found that associated eigenmodes spatially correspond to the boundaries of the separation phenomena present in the steady-state flowfield. Consequently, the linearization about the low-level limit cycle of such instances could be identified as the cause of the amplitude residual's divergence [19]. As summarized,

> Campobasso and Giles[[19] also] show that the pseudotime integration can be stabilized by applying a generalized minimum residual (GMRES) approach to [the solution of] the derived [system of] linear equation[s ...] at each pseudotime step [...]. The tradeoff lies in a more intricate algorithm as well as substantially higher memory requirements than experienced with conventional pseudotime-integration techniques [[19]]. Incurring significantly less [memory] penalties than [the] GMRES [approach,]while being computationally competitive and equally robust, Campobasso and Giles [[20]] subsequently suggested the recursive projection method (RPM) as an alternative means of stabilization [...]. [103]

Beneficially, both the GMRES approach and the RPM accelerated convergence if the utilized steady-state flowfield terminated devoid of a low-level limit cycle [20].

In 2006 Chassaing et al. [25] from Université Pierre-et-Marie-Curie provided a fundamental investigation on the solution of the small disturbance Navier-Stokes equations sans pseudotime integration. To this effect, a GMRES approach was applied directly to the derived system of linear equations, and put into comparison with both an approximate factorization alternating directions implicit (AF-ADI) pseudotime-integration scheme and a nonfactorized GMRES-approach-stabilized instance. Differing preconditioning techniques were employed for each GMRES approach utilization. Turbulence closure was realized by incorporating a Reynolds stress model into the governing equation system. A two-dimensional test case for transonic flow in a channel was initially focused on. The channel geometry itself featured a convergent-divergent nozzle, which rendered a strong λ-shock toward the exit of the divergent portion, further incurring a sizeable region of flow separation. Computationally, unsteadiness was introduced into the flowfield through a back-pressure delta function, forced on the outflow boundary. This impulse was imposed free of phase shift, leading to a solution of the small disturbance Navier-Stokes equations entirely in the real field of numbers. It was shown that for a baseline spatial discretization the direct application of the GMRES approach produced amplitude surface-pressure dis-

tributions conforming to the instances gained with the AF-ADI pseudotime-integration scheme at a 66% reduction of computational time, while experiencing a 50% increase in memory requirements. However, under refinement of the spatial discretization, and thus better resolution of the flow separation, the AF-ADI pseudotime-integration scheme failed to converge. Surprisingly, the nonfactorized GMRES-approach-stabilized instance did so as well. Converged solutions were merely achieved by the direct application of the GMRES approach, with an incomplete lower-upper (ILU) factorization employed as preconditioner. In this regard, it was demonstrated that an increase in the number of vectors utilized for the Krylov basis can substantially accelerate convergence, and thus reduce computational time, however, while incurring an increase in memory requirements to a similar degree. Secondly, a three-dimensional test case was investigated. The channel geometry featured a planar symmetric Laval-nozzle, rendering a shock toward the exit of the divergent portion. Sizeable regions of flow separation emerged in vicinity of the wall corners. In order to ensure convergence of the AF-ADI pseudotime-integration scheme, merely a coarse spatial discretization was considered. A back-pressure delta function was again imposed. The solution through the direct application of the GMRES approach utilized a Jacobi/block-Jacobi preconditioner. Comparison of the obtained amplitude surface-pressure distributions eventually revealed very good conformity between both techniques [25].

In 2008 Chassaing and Gerolymos [24] revisited the preceding Laval-nozzle test case to further investigate the employed small disturbance Navier-Stokes method's shock-capturing capability. For this instance, unsteadiness was computationally introduced into the flowfield through a simple harmonic back-pressure oscillation, again imposed on the outflow boundary. Merely the AF-ADI pseudotime-integration scheme was employed. The first-harmonic results of the shock/boundary-layer interaction were compared to URANS-obtained counterparts and experimental data, which, however, were both based on a multiple-harmonic back-pressure oscillation. Four excitation frequencies of decreasing value were considered. The small disturbance Navier-Stokes computations were conducted under a frozen turbulence-scales assumption; i.e., both an amplitude and steady dynamic eddy viscosity were introduced, with an algebraic closure instated, ultimately foregoing the linearization of the underlying Reynolds stress model. The latter was still utilized to render the steady-state RANS solution. Across the frequency spectrum, good agreement between the computed amplitude surface-pressure distributions was ascertained, and was also given respective the experimental data. With decreasing frequency, however, deviations emerged at the shock location, likewise propagating into the computed surface load. This circumstance was primarily ascribed to the nonconsideration of harmonic interaction by the small disturbance Navier-Stokes method. However, the oversimplified treatment of the amplitude Reynolds stresses within the governing equation system was also made

responsible for not resolving details exhibited by the URANS-obtained amplitude surface-pressure distributions; e.g., the secondary shock-peak. Overall, a computational efficiency gain of up to an order of magnitude was demonstrated for the small disturbance Navier-Stokes method. It was again emphasized that in cases where the steady-state RANS solution was obtained with an inherent unsteadiness a pseudotime-integration scheme can lead to divergence of the small disturbance Navier-Stokes solution. A refinement of the spatial discretization, a reduction of the numerical dissipation, or a discount of the statistically unsteady contribution of the turbulence were stated to even facilitate this unwanted behavior. Thus, a solution of the small disturbance Navier-Stokes equations without employing pseudotime integration was generally recommended [24]; also referenced in [103].

For turbomachinery applications, Petrie-Repar [104] had realized a small disturbance Navier-Stokes method without pseudotime integration at DLR as early as 2002; published in 2004. Consistent with Chassaing et al. [25], the derived system of linear equations was solved by applying the GMRES approach directly; also stated in [103]. Likewise, an ILU factorization was employed as preconditioner. Similar to FLM-SDEu [71], an instance of Roe's approximate Riemann-solver [111] and Van Leer's monotonic upstream-centered scheme for conservation laws (MUSCL) [130] is utilized to construct the convective fluxes. A one-dimensional nonreflecting far-field boundary condition had been implemented at both the inflow and outflow boundary. Following Clark and Hall [30], the amplitude dynamic eddy viscosity was fully accounted for, and supplied by a small disturbance formulation of the S/A one-equation turbulence model [121]. The structured multiblock method was initially implemented for merely two dimensions. The approach was validated with the transonic flow/separation bubble bending-mode case of the Standard Configuration 11, which had originally been drawn on by Sbardella and Imregun [113]. Comparing the obtained magnitude and phase of the first-harmonic surface-pressure-coefficient distribution to the instances computed by Sbardella and Imregun [113], good conformity of the two methods was ascertained, as well as being mostly in agreement with the experimental data. Furthermore, an additional small disturbance Euler result substantiated the greater prediction accuracy of the viscous consideration. The realized small disturbance Navier-Stokes method was deemed to be both robust and computationally efficient [104]. However, a direct comparison to an incarnation employing pseudotime integration had not been provided. Likewise, comparative URANS computations had not been conducted, leaving the attainable CPU-time ratio and incurred memory penalty undisclosed. As published in 2006, Petrie-Repar [105] had extended the investigation on the small disturbance Navier-Stokes method by comparing the suitability of various convective flux evaluation schemes. Surprisingly, it was determined that the advection upstream splitting method should be preferred over Roe's approximate Riemann-solver. The more

dissipative nature of the former would suppress spurious oscillations in the first-harmonic surface-pressure-coefficient distribution near the shock location. Nevertheless, adverse effects on the boundary layer's development were not evident for the considered transonic flow/separation bubble bending-mode case of the Standard Configuration 11 [105].

In 2006 Petrie-Repar et al. [107] additionally presented a three-dimensional unstructured small disturbance Navier-Stokes method developed under the RPMTurbo consultancy; also discussed in 2007 [108]. The implementation again fully accounted for the amplitude dynamic eddy viscosity through a small disturbance formulation of the S/A one-equation turbulence model [121]. For the treatment of two-dimensional cases, an exact two-dimensional nonreflecting far-field boundary condition was employed at both the inflow and outflow boundary [107]. For the treatment of three-dimensional cases, however, merely a one-dimensional nonreflecting far-field boundary condition was initially utilized [108]. The solution scheme applied to the derived system of linear equations was left undisclosed. It was stated, however, that a computational efficiency gain of up to three orders of magnitude over a comparative URANS method was realizable [108]. Structured multiblock grids could be treated as well, and parallel execution of the code was made available [108]. The transonic flow/separation bubble bending-mode case of the Standard Configuration 11 was again drawn on to validate the approach for two-dimensional space. Subsequently, aerodynamic damping maps were computed for the Standard Configuration 10 [107]. In this regard, both a torsion and a bending mode were considered. It was shown that a flutter boundary obtained under the viscous treatment can significantly differ from the inviscid instance, possibly predicting an unstable operating condition where the other had not. In fact, occurrences of deep flutter were only predicted under the viscous treatment. This was the case for inflow conditions that rendered the underlying steady-state flowfield with separation [107]. Ultimately, a three-dimensional viscous flutter analysis was conducted for both a design (subsonic inflow) and an off-design (near stall) torsion-mode case of the Standard Configuration 10 [108]. In either instance the prediction was assessed to be superior in quality over its two-dimensional counterpart, as well as over a three-dimensional inviscid prediction. The three-dimensional viscous treatment was shown to yield stability behavior that differed from the other two treatments over a wide range of interblade phase angles. It was further ascertained that the implemented one-dimensional nonreflecting far-field boundary condition could render the stability behavior sufficiently independent of the employed far-field distance as long as the considered interblade phase angle was not in vicinity of the resonant instances [108]. To remedy this deficit, Petrie-Repar [106] developed an exact three-dimensional nonreflecting far-field boundary condition in 2010. It is based on the local decomposition of the unsteady flowfield into eigenmodes. These are numerically determined as a function of the supplied steady-state flowfield. In this manner, both restrictions on the far-field

boundary's geometry and the need for circumferential uniformity of the steady-state flow-field were eliminated. The amplitude of an incoming eigenmode was imposed, while being extrapolated for an outgoing instance. The validity of the approach was substantiated through a three-dimensional inviscid flutter analysis of the design torsion-mode case of the Standard Configuration 10, with the stability behavior now obtained independent of the employed far-field distance over the entire interblade phase angle range [106].

Further developments at DLR had led to the incorporation of the small disturbance approach into the Turbomachinery Research Aerodynamics Computational Environment (TRACE), as originally presented by Kersken et al. [66] in 2010. At that time, TRACE already was a well-established structured multiblock numerical method for solving the three-dimensional RANS equations in a rotating frame of reference either toward a steady state or time-accurately for an unsteady state, while potentially accounting for grid deformation. Within TRACE, the convective flux vectors were evaluated utilizing Roe's approximate Riemann-solver [111] and Van Leer's MUSCL [130]. The derivatives of the primitive variables in the viscous flux vectors were approximated by central differences; also see Nürnberger et al. [93]. The small disturbance incarnation of TRACE was based on a semi-analytical linearization of these spatially discrete RANS equations. It was conducted by means of a first-order Taylor-series expansion of the residual vector about the reference state. The arising analytical derivatives of the residual vector with respect to the state vector of conservative variables, as well as instances with respect to the spatial coordinates and the spatial coordinates' time rate of change, were not explicitly rendered, yet needed to be evaluated at the reference state. In case of the former, which actually is the residual's Jacobian matrix, a second-order finite difference approximation was employed. For this purpose, the RANS-employed convective and viscous flux vector evaluation was simply drawn on, however, considering a state vector perturbed from its reference value within the reference grid by the finite difference step-size. This technique, however, requires a case-dependent a priori determination of the appropriate instance, which can become computationally expensive. The analytical derivatives of the residual vector with respect to the spatial coordinates and the spatial coordinates' time rate of change both constitute the invariant right hand side (RHS) of the treated governing equation [66]. In this regard, it was merely stated that "[t]he [RHS] is computed by accumulating the perturbation of [the residual vector] when the grid coordinates are perturbed by [their actual amplitude] and the grid velocities by [their actual complex amplitude]."[66] The derived system of linear equations is again solved by applying the GMRES approach directly, while employing either an ILU factorization with fill-in or an m-step symmetric successive overrelaxation as preconditioner [66]. Exact nonreflecting far-field boundary conditions derived from the two-dimensional linearized Euler equations are imposed on bands of constant radius at both the inflow and outflow boundaries [66], with "the radial

distribution of the stagnation pressure and temperature, [as well as] the radial and circumferential flow angles,"[66] set at the former. A FEVA is instated on the basis of the Wilcox k-omega two-equation turbulence model [138]. If desired, the viscous fluxes can be discounted outright to render a strictly inviscid solution [66].

Ultimately, Kersken [66] et al. conducted a comparison between the small disturbance incarnation of TRACE and its dynamically fully nonlinear counterpart by means of the DLR-proprietary ultra-high-bypass-ratio fan-stage. Merely the first structural eigenmode was considered. The computations were all performed three-dimensionally and fully viscous, with a wall function instated for the turbulence model. Due to the computational efficiency of the small disturbance incarnation, it was possible to render the global aerodynamic damping for all interblade phase angles under the given project constraints. With the dynamically fully nonlinear incarnation, on the other hand, only three interblade phase angles (zero deg and $\pm$120 deg) could be equally rendered, as the low structural eigenfrequency incurred a very fine temporal discretization of the individual cycle, while also requiring numerous cycles to obtain flow periodicity. For these instances, the small-disturbance-computed global aerodynamic damping agreed very well with their dynamically fully nonlinear counterparts. Inversely, this substantiated that the considered amplitude of the structural eigenmode produced a predominantly dynamically linear flow response to the excitation. Global aerodynamic damping was revealed to be at its least for the zero deg interblade phase angle. An investigation of the local aerodynamic work performed on the individual blade further showed that the shock motion contributed strongly positive over a small surface region. Having an amplifying effect, the global aerodynamic damping had been reduced in kind. Again, the small-disturbance-computed local aerodynamic work agreed very well with its dynamically fully nonlinear counterpart. Typically, a reduction of computational time by two orders of magnitude was achieved with the small disturbance incarnation of TRACE [66]. Kersken et al. [67] eventually published their study in 2012. The advantage of the viscous consideration over the inviscid one, however, was not demonstrated.

To the preceding effect, May and Grübner [83] investigated the flutter behavior of a modern transonic axial compressor with both the small disturbance incarnation of TRACE and the MTU-Aero-Engines-proprietary small disturbance Euler method Lin3D in 2010. Reference solutions rendered by TRACE were likewise supplied to Lin3D; i.e., a small disturbance Euler computation was conducted on the basis of a RANS-obtained steady-state flowfield, as restricted to a coarser grid. For an operating point on the working line, it was ascertained that the small disturbance incarnation of TRACE and Lin3D agreed well in their prediction of stability. For an operating point near the surge line, on the other hand, the small disturbance incarnation of TRACE predicted flutter where Lin3D had not. This circumstance, however, was attributed to the coarseness of the Lin3D-employed

grid, and hence the differing resolution of the implied shock motion in the tip region of the blades, rather than to the inviscid consideration per se [83].

1.3.2 Small Disturbance Navier-Stokes Methods in the Field of Aircraft Aeroelasticity

Concurrent to the development of a small disturbance Navier-Stokes method at TUM, other instances had emerged at ONERA, DLR, and Dassault Aviation, with the latter being the sole industrial representative. A more unorthodox instance had been realized at the University of Liverpool on the basis of the 2012 implicit meshless scheme of Kennett et al. [65]. It is characterized by the evaluation of spatial derivatives with respect to a set of points instead with respect to a cell face. Utilizing a least squares approach, the conventional problem of generating an extremum grid for each structural eigenmode reduces in this manner to the local application of an appropriate stencil [65]. ZONA Technology, on the other hand, progressed toward the implementation of a small disturbance Navier-Stokes method by conducting a small disturbance Euler computation on the basis of a RANS-obtained reference solution, as supplied through FUN3D [7]. Originally presented by Yang et al. [142] in 2015, the realized method was designated the ZONA unstructured linearized unsteady solver (ZULUS). It utilizes a transpiration near-field boundary condition, which likewise eliminates the need to generate an extremum grid for each structural eigenmode [142]. The details of the implicit-meshless-scheme small disturbance Navier-Stokes method and of ZULUS, however, will not be elaborated on herein.

1.3.2.1 French Aerospace Laboratory

In 2003 Mortchéléwicz [90] had provided a viscous extension of his previously devised small disturbance Euler method REELC [88, 89] at ONERA. The well-established elsA method [18] was drawn on to supply the necessary steady-state RANS solution in the reference grid. Mortchéléwicz's small disturbance Navier-Stokes method was based on the RANS equations' deforming grid formulation, with an analytical linearization of its spatially discrete instance conducted by means of a first-order Taylor-series expansion of the constituting vectors about the reference state; i.e., the linearized periodic perturbation of the constituting vectors was explicitly rendered. Featuring a structured multiblock shock-capturing scheme, the evaluation of both the convective and viscous flux vectors was performed with second-order accuracy. The derived system of ordinary differential equations were then solved by the Jameson-Lerat scheme [79]. It embedded an explicit pseudotime integration based on the Runge-Kutta scheme into a full approximation storage multigrid algorithm for convergence acceleration. Furthermore, implicit residual smoothing had been applied to extend the utilizable pseudotime step beyond the

baseline scheme's stability limit. The implemented central difference discretization of the convective flux vectors had relied on the artificial dissipation technique of Jameson et al. [61] to resolve shocks accurately, while providing a base level of dissipation throughout the computational domain. Neither the amplitude dynamic molecular viscosity nor the amplitude dynamic eddy viscosity were accounted for in the small disturbance formulation of the spatially discrete RANS equations; i.e., both a frozen molecular-viscosity approach and a FEVA were employed. The elsA-supplied reference flowfield, and thus the steady dynamic eddy viscosity, had again been realized by means of the S/A one-equation turbulence model [121]. Mortchéléwicz put the validity of his small disturbance Navier-Stokes approach into evidence by means of the NACA 64A010 transonic pitching-oscillation case CT6 experimentally investigated by Davis [34], as well as the flutter analysis of a high-aspect-ratio wing in the transonic viscous flow regime. For the latter, the wing of the experimentally investigated Aeroelastic-Model-Programme transport-type wing-fuselage configuration [150] was drawn on. Merely its first bending and torsion mode needed to be considered at three successive excitation frequencies. In this regard, the small disturbance Navier-Stokes method's computational efficiency gain was assessed, however, without a comparison to a URANS counterpart actually being made. An improvement in the accuracy of the flutter prediction over REELC was stated to have occurred. Lastly, it should be noted that Mortchéléwicz simply referred to his small disturbance Navier-Stokes method as a linearized RANS method, consistent with his earlier linearized Euler method designation [90].

As presented by Liauzun et al. [80] in 2008, Mortchéléwicz's small disturbance Navier-Stokes method [90] had been recoded and incorporated into ONERA's elsA framework as a full-fledged CFD option. It complemented the already inherent URANS option. The numerical features of Mortchéléwicz's small disturbance Navier-Stokes method were fully retained, however, implemented through small disturbance formulations of elsA's dynamically fully nonlinear instances. Thus, numerical equivalence between the two options had been achieved. Naturally, the steady-state RANS option again supplies the necessary reference solution to the small disturbance Navier-Stokes computation, while also serving to initialize the comparative URANS computation. For all three CFD options, both the Jameson-Lerat scheme [79] and a multigrid-embedded implicit pseudotime integration are available. The latter is based on the lower-upper symmetric successive overrelaxation (LU-SSOR) scheme originating from Jameson and Turkel [62]. For the steady-state RANS/URANS option, the dynamic eddy viscosity can be supplied by either the S/A one-equation turbulence model [121] or the Menter shear stress transport two-equation turbulence model [86], as indicated by Dufour et al. [37] in 2010. Regarding the small disturbance Navier-Stokes option, both the frozen molecular-viscosity approach and the FEVA were employed. Once more, the Aeroelastic-Model-Programme transport-

type wing-fuselage configuration [150] was drawn on to investigate the validity of the small disturbance Navier-Stokes approach. Now, however, the entire configuration was utilized. For the investigation, the S/A one-equation turbulence model [121] was selected. The test case parameters originally considered by Mortchéléwicz [90] were used to compute the new geometry, with the flutter analysis then compared to the experimental data as before. Additionally, URANS results were provided. Good conformity to either instance was ultimately determined. Since the small disturbance Navier-Stokes and the URANS option are numerically equivalent, a direct comparison between the two was permissible. In this regard, a reduction of computational time by 80% was ascertained, however, while nearly doubling the amount of required memory [80]. It should be noted that elsA's small disturbance Navier-Stokes option is actually referred to as the linearized unsteady RANS (LUR) option, or elsA-LUR; i.e., designated consistently to elsA-URANS [37].

In 2010 Dufour et al. [37] further compared elsA-LUR, elsA-URANS, and the elsA inherent harmonic balance (HB) Navier-Stokes option, referred to as elsA-HB, with each other. For this purposes, the NACA 64A006 flap-oscillation test cases CT1 and CT6 experimentally investigated by Zwaan [152] were considered. They, respectively, feature sub- and transonic attached flow at a zero angle-of-attack. Additionally, a test case with positive angle-of-attack derived from the CT6 case, and featuring detached flow, was considered. It had no experimental equivalent. The attached-flow cases were computed with the S/A one-equation turbulence model [121], while the detached-flow case was computed with the Menter shear stress transport two-equation turbulence model [86]. For the CT1 case, elsA-LUR was deemed to be the most efficient, realizing an 86% reduction in computational time with respect to elsA-URANS, and a 57% reduction with respect to the single-harmonic elsA-HB (achieved at equal prediction accuracy). For the CT6 case, the computational efficiency gain was demonstrated to be even greater, however, with the elsA-LUR prediction of the zeroth- and first-harmonic harmonic surface-pressure-coefficient distribution now substantially deviating from its elsA-URANS counterpart in the shock region. To that effect, the single-harmonic elsA-HB prediction significantly improved on the the elsA-LUR instance, with total conformity to the elsA-URANS prediction achieved once both the second and the third harmonic were taken into account. It should be noted that the CT6 case per se exhibits a dynamically highly nonlinear flowfield. The shock alternately emerges and disappears on the upper and lower surface over the course of a cycle. In this regard, the steady-state RANS solution supplied to elsA-LUR for the airfoil's reference position naturally deviated from the time-invariant mean of the elsA-URANS solution. Consequently, the selection of the CT6 case for an intermethod comparison had favored elsA-HB from the outset. It was also shown, however, that the deviations of the elsA-LUR-obtained first-harmonic surface-pressure-coefficient distributions to their elsA-URANS counterparts had been mostly compensated in the

integration toward the GAF, differing by merely 5% in both magnitude and phase. For the CT6 detached-flow case, elsA-LUR failed to achieve a converged solution, as was to be expected when employing a conventional pseudotime-integration scheme. Contrarily, single-harmonic elsA-HB did render a solution. It conformed very well in the first-harmonic surface-pressure-coefficient distribution with its elsA-URANS counterpart, while realizing an 83% reduction of computational time. In this regard, either the implementation of the GMRES approach to stabilize the pseudotime-integration scheme or its direct application to the derived system of linear equations was recommended. Generally, the advantage of the single-harmonic elsA-HB to partially account for the dynamic nonlinearity inherent to the flowfield was established. The consideration of an increasing number of higher harmonics gradually improved the prediction accuracy of elsA-HB, however, also substantially reduced its computational efficiency gain over elsA-URANS [37].

1.3.2.2 German Aerospace Center

In 2010 Widhalm et al. [135] presented a small disturbance Navier-Stokes incarnation of DLR's well-established hybrid unstructured finite volume RANS method TAU [42, 115]. The realized method was again based on a semi-analytical linearization of the spatially discrete RANS equations in their deforming-grid formulation. It was conducted by means of a first-order Taylor-series expansion of the residual vector about the reference state. The arising analytical derivatives of the residual vector with respect to the state vector of conservative variables, as well as instances with respect to the spatial coordinates and the spatial coordinates' time rate of change, needed to be evaluated at the reference state. This conformed to the requirements of the TRACE-employed formulation [66]. In case of the former, which again actually is the residual's Jacobian matrix, an explicit instance had already been rendered and coded as part of the exact discrete adjoint incarnation of TAU [39, 38]; i.e., a full linearization of both the convective and viscous flux vectors, as well as the turbulence model, with respect to the state vector was inherently considered. In the presented small disturbance Navier-Stokes incarnation of TAU, however, the contribution of the viscous flux vectors to the residual's Jacobian matrix was discounted, perforce also eliminating the need to account for the amplitude dynamic eddy viscosity. The analytical derivatives of the residual vector with respect to the spatial coordinates and the spatial coordinates' time rate of change were not explicitly rendered. For their evaluation, central finite difference approximations were hence employed. As with TRACE [66], the need to determine the appropriate finite difference step-size remains a computational penalty. Ultimately, the derived system of linear equations is solved by a multigrid-embedded implicit pseudotime integration based on the lower-upper symmetric Gauss-Seidel (LU-SGS) scheme, which is identical to the LU-SSOR scheme, and actually is its original designation [16]. Optionally, the pseudotime integration can be stabilized by applying the

GRMES approach. The reference state is provided through a steady-state TAU solution for the reference grid, rendered under consideration of the S/A one-equation turbulence model [121]. It should be noted that the small disturbance Navier-Stokes incarnation of TAU is actually referred to as the linearized frequency-domain (LFD) incarnation, or TAU-LFD; i.e., designated consistently to its dynamically fully nonlinear counterpart TAU-URANS [135].

Widhalm et al. [135] substantiated the validity of their small disturbance Navier-Stokes approach for both two- and three-dimensional space. On one hand, the NACA 64A010 transonic pitching-oscillation test case CT8 experimentally investigated by Davis [34] was drawn on. On the other hand, the Lockheed Georgia, Air Force Flight Dynamics Laboratory, NASA Langley Research Center, and National Aerospace Laboratory wing (LANNW) spanwise λ-shock/attached-flow pitching-oscillation test case CT5 experimentally investigated by Zwaan [154] was drawn on; i.e., a high-aspect-ratio wing test case. Additionally, a transonic pitching-oscillation test case of the DLR-proprietary F12 transport aircraft configuration experimentally investigated by Hübner et al. [53] was considered. Comparing the TAU-LFD-obtained first-harmonic surface-pressure-coefficient distributions with their TAU-URANS counterparts, overall good agreement was ascertained for each case. A comparison with the experimentally obtained data, however, was merely conducted for the NACA 64A010 CT8 case: The quality of the prediction is identifiable as being good; in particular, outside of the shock region. Within the shock region, only a single experimental data point exists, leaving the quality of the prediction inconclusive. Overall, reductions of computational time beyond an order of magnitude were determined. At best, TAU-LFD required 94% less computational time than TAU-URANS; i.e., for the DLR F12 case [135]. In the opinion of the author, however, the computational time required by TAU-URANS for the three-dimensional cases was excessive, especially considering that a fully parallelized code was employed on multiple processors. This circumstance skewed the computational efficiency gain realized by TAU-LFD favorably.

A more extensive investigation on the capabilities of TAU-LFD was published by Thormann and Widhalm [128] in 2013. Now referred to as the linear frequency-domain incarnation of TAU, the contribution of both the convective and viscous flux vectors to the residual's Jacobian matrix were accounted for, with the amplitude dynamic eddy viscosity equally considered. Additionally, the cell volumes' derivative with respect to the spatial coordinates was reincorporated into the treated governing equation. The required evaluation at the reference state was again conducted by means of a central finite difference approximation. Novelly, a solution option without pseudotime integration was made available. In particular, the GMRES approach was directly applied to the derived system of linear equations, with an ILU factorization employed as preconditioner. Usage of the latter was based on observations made by McCracken et al. [85] in 2012 (published by

McCracken et al. [84] in 2013). A FEVA option was implemented as well, which, however, expanded on the original premise by wholly discounting the contribution of the viscous flux vector's turbulent elements to the residual's Jacobian matrix. Furthermore, the laminar elements were merely evaluated under the thin shear layer assumption, while the artificial dissipation terms of the central spatial scheme were considered to be invariant for a small disturbance [128].

Thormann and Widhalm [128] revisited the NACA 64A010 CT8 case [34], while further investigating derivative cases at an intermediate and highest reduced frequency. Additionally, the frequency response functions of the first-harmonic lift and pitching-moment coefficient were computed over an orders of magnitude range, yet at a lower pitching amplitude. Complementarily, the amplitude response functions were computed at the baseline reduced frequency. Comparing the TAU-LFD results to their URANS counterparts, excellent agreement was mostly observed. Deviations merely arose for the higher end of the amplitude response function range. This circumstance was attributed to the increasing dynamic nonlinearity inherent to the TAU-URANS-rendered flowfield for an increasing pitching amplitude. First-harmonic surface-pressure-coefficient distributions were also compared for the baseline, intermediate, and the highest reduced-frequency cases. Including a TAU-LFD-FEVA result as well, it was shown that the maximum absolute value of the shock peaks was underpredicted by this simplification, yet more so in the imaginary part than in the real one. Deviations, though, were observed to subside toward the highest reduced frequency. With the baseline reduced-frequency case it was further demonstrated that the pitching-moment coefficient is by far more sensitive to the FEVA than the lift coefficient. Substantial deviations between the TAU-LFD-FEVA result and its TAU-LFD/TAU-URANS counterparts emerged in both the magnitude and the phase angle of the former. An equivalent set of investigations was conducted for a higher angle-of-attack. These derivative cases were all characterized by shock-induced flow separation. Again, the comparison of the TAU-LFD results to their URANS counterparts revealed mostly excellent agreement, despite the more challenging flow topology. Similarly, deviations merely arose for the higher end of the amplitude response function range, however, occurring at significantly lesser pitching amplitude than for the zero angle-of-attack; i.e., under attached flow conditions. For the baseline, intermediate, and the highest reduced-frequency cases, the TAU-LFD-FEVA predictions of the first-harmonic surface-pressure-coefficient distributions now exhibited very substantial differences to their TAU-LFD counterparts in the shock region. Notably, TAU-LFD-FEVA predicted a reversal in phase for the shock motion at the baseline and intermediate reduced frequency. Again, agreement between the two predictions improved toward the highest reduced frequency. In contrast, the TAU-LFD prediction conformed excellently with its TAU-URANS counterpart for all instances. Unsurprisingly, TAU-LFD-FEVA was not able to properly repro-

duce either the lift or pitching-moment coefficient obtained from TAU-LFD in the baseline reduced-frequency case. However, true conformity between each TAU-LFD-rendered progression and its TAU-URANS counterpart was not given either. Higher harmonics had become influential under the dynamically fully nonlinear approach [128].

Thormann and Widhalm [128] revisited the LANNW CT5 case [154] as well, now showing that both TAU-LFD and TAU-URANS reproduced the first-harmonic surface-pressure-coefficient distributions of the experiment reasonably well. In this regard, the TAU-LFD result and its TAU-URANS counterpart exhibited near conformity. Merely the absolute value of the TAU-URANS-obtained shock peak was overpredicted at the outer-span station, in both its real and imaginary part. Computing an amplitude response function with TAU-URANS at the baseline reduced frequency, it was ascertained, however, that the first harmonic of the global load coefficients behaved dynamically linear for pitching amplitudes lower than a fifth of the baseline instance. Ultimately, the TAU-URANS result for a twenty-fifth of the baseline pitching amplitude was compared to the TAU-LFD baseline result. Normalized by the respective pitching amplitude, the first-harmonic surface-pressure-coefficient distributions had then become all but indistinguishable. For this particular pitching amplitude, derivative cases at an intermediate and highest reduced frequency were investigated as well. In both instances, excellent agreement between the TAU-LFD- and the TAU-URANS-rendered first-harmonic surface-pressure-coefficient distributions were again ascertained. Complementary TAU-LFD-FEVA computations revealed deviations at the baseline reduced frequency. They were especially observed in the imaginary part of the predicted shock peaks. With the increase in reduced frequency, however, the agreement to the TAU-URANS result improved considerably. The comparison of the TAU-LFD-, TAU-URANS-, and TAU-LFD-FEVA-obtained first harmonic of the global load coefficients (in magnitude and phase angle) presented equivalent characteristics [128].

Lastly, Thormann and Widhalm [128] performed a consistent comparison of computational efficiency between TAU-LFD and TAU-URANS for both the NACA 64A010 CT8 and the LANNW CT5 case. For the former, it was observed that TAU-LFD-FEVA employing the multigrid-accelerated LU-SGS scheme already achieved a computational efficiency gain by well over an order of magnitude respective TAU-URANS. Beyond the FEVA, TAU-LFD employing the GMRES-stabilized multigrid-accelerated LU-SGS scheme realized an improvement by nearly two orders of magnitude. The direct application of the GMRES approach in combination with the ILU factorization as preconditioner, however, led to the highest computational efficiency gain; i.e., well over two orders of magnitude, corresponding to a 99.6% reduction of the required computational time. For the LANNW CT5 case, the computational efficiency gains were generally lesser. TAU-LFD-FEVA employing the multigrid-accelerated LU-SGS scheme achieved an order of magnitude, while

TAU-LFD employing the GMRES-stabilized multigrid-accelerated LU-SGS scheme atypically realized only half an order of magnitude. The direct application of the GMRES approach in combination with the ILU factorization as preconditioner again led to the highest computational efficiency gain; i.e., nearly two orders of magnitude, corresponding to a 98.9% reduction of the required computational time. This instance, however, also allocated approximately ten times the memory of TAU-LFD-FEVA employing the multigrid-accelerated LU-SGS scheme, while requiring approximately 20 times the memory of TAU-URANS [128].

In 2012 additional investigations conducted by Thormann et al. [126] demonstrated the capability of TAU-LFD to render the resonance effect of the lift coefficient due to shock-separated flow for two-dimensional space, while concurrently exposing the failure of TAU-LFD-FEVA to do so. Widhalm et al. [136] also revisited the DLR-proprietary F12 transport aircraft configuration in 2012, further investigating the TAU-LFD capability to render the first-harmonic lift and pitching-moment coefficients for a pitching oscillation in the sub- and transonic viscous flow regime. Under direct application of the GMRES approach in combination with the ILU factorization as preconditioner, computational efficiency gains of one and a half orders of magnitude with respect to the comparative TAU-URANS computations were presented [136]. In 2013 Thormann and Widhalm [127] also showed that the modification of the standard preconditioner through weighting [85] led to increased robustness and higher computational efficiency of the GMRES approach in the case of three-dimensional shock-separated flow. To this end, the first bending mode of the DLR-proprietary generic transport aircraft FERMAT was considered under transonic flow conditions. A computational efficiency gain of nearly two orders of magnitude with respect to the comparative TAU-URANS computation was presented. Again, approximately 20 times the memory of TAU-URANS was required [127]. Investigations on the capability of TAU-LFD to accurately render the unsteady loading under massively separated flow for three-dimensional space had been documented by Widhalm and Thormann [137] in 2015, with the LANNW spanwise λ-shock/detached-flow pitching-oscillation test case CT9 [154] having been drawn on.

1.3.2.3 Dassault Aviation

In 2009 Daumas et al. [33] of Dassault Aviation presented a small disturbance Navier-Stokes method based on the proprietary hybrid unstructured finite element Navier-Stokes method AETHER [23]. The Navier-Stokes equations solved by AETHER are unorthodoxly formulated in terms of a mass-weighted entropy-variable state vector, as the method had originally been developed to treat chemically reacting hypersonic flows [22]. The considered small disturbance Navier-Stokes equations were derived from these Navier-Stokes equations' deforming-element instance by means of a first-order Taylor-series expansion.

The analytical derivatives of the considered Navier-Stokes equations' constituting vectors with respect to both the state vector and the state vector's time rate of change, as well as instances with respect to the spatial coordinates and the spatial coordinates' time rate of change, were not explicitly rendered. Their evaluation at the reference state is rather handled by code routines that were obtained through automatic differentiation of the AETHER instances employed in the evaluation of the considered Navier-Stokes equations' constituting vectors. Ultimately, the derived system of linear equations is solved by applying the GMRES approach directly. It is implied that the reference state is provided through a steady-state Navier-Stokes solution for the reference finite element distribution. A plethora of turbulence models can be selected to supply the dynamic eddy viscosity for either a steady-state or an unsteady Navier-Stokes solution. In this regard, the S/A one-equation turbulence model [121] and the Chen-Patel k-epsilon two-equation turbulence model [26] stand out. For a small disturbance Navier-Stokes solution, merely a FEVA was initially available. Typically, the small disturbance Navier-Stokes solutions are referred to as being linearized Navier-Stokes (LNS) solutions; i.e., rendered by AETHER-LNS. Unsteady Navier-Stokes solutions are referred to as being nonlinear Navier-Stokes (NLNS) solutions; i.e., rendered by AETHER-NLNS. Additionally, AETHER can provide small disturbance Euler solutions. They are consistently referred to as being linearized Euler (LEu) solutions; i.e., rendered by AETHER-LEu [33].

Daumas et al. [33] initially substantiated the validity of their small disturbance Navier-Stokes approach by means of a generic yet undesignated transport-type wing-fuselage configuration. Its swept wing utilizes a NACA 64A010 section across the semi-span. Merely employing the Chen-Patel k-epsilon two-equation turbulence model [26], pitching oscillations of the configuration in both the sub- and transonic viscous flow regime were considered. For each flow regime, a single case was computed with AETHER-LNS. The angle of attack, amplitude, and the excitation frequency were equal. The real and imaginary part of the resultant first-harmonic surface-pressure-coefficient distribution were presented for an inner- and an outer-span station, and put into comparison with results from AETHER-NLNS and AETHER-LEu, as well as the experimental data. For the subsonic case, the AETHER-LNS result conformed very well to its AETHER-NLNS counterpart, however, also to the AETHER-LEu result, revealing only a marginal improvement in prediction accuracy toward the experimental data under the viscous consideration. For the transonic case, which was said to feature a strong shock on both the upper and lower wing surface, AETHER-LNS and AETHER-NLNS rendered first-harmonic shock peaks that are situated distinctly upstream of the AETHER-LEu prediction, and are of differing magnitude to it. Significant deviations between the AETHER-LNS- and the AETHER-NLNS-obtained first-harmonic surface-pressure-coefficient distributions are only apparent in the shock region. For all three AETHER incarnations, however, the distributions ex-

hibit spurious oscillations at this locality. This circumstance is observed to be the most pronounced for AETHER-LEu. It serves as an indication that the implemented convective flux vector evaluation does not satisfy the total-variation-diminishing property. Overall, the AETHER-LNS prediction was ascertained to be the most accurate, despite only a limited number of experimental data points being available in the shock region [33].

Lastly, Daumas et al. [33] considered the transonic flutter case of the wing-fuselage configuration. Merely a representative bending mode and a representative torsion mode of the wing were employed. GAF matrices for three frequencies and five Mach numbers at freestream conditions (ranging from 0.7 to 0.9) were computed with AETHER-LNS, AETHER-NLNS, and AETHER-LEu. The respective GAF matrices were supplied to the CA tool ELFINI, subsequently yielding fitted progressions of the flutter-onset dynamic pressure over the Mach number. By default, ELFINI employs a doublet lattice method to internally provide the GAF matrices. It was utilized in this context to supply a comparative progression of a lower-order CFD method. The experimentally obtained progression was drawn on as well. Up to a Mach number of 0.8, the computed progressions all exhibit good conformity, while reproducing the experimentally obtained instance quite well. By 0.85, however, the progressions have deviated, with merely the AETHER-LNS- and AETHER-NLNS-obtained instances following the experimentally obtained progression's reversal in trend beyond it; i.e., evolving from a monotonically decreasing flutter-onset dynamic pressure to a monotonically increasing one. Assessing the Mach number at which the minimum flutter-onset dynamic pressure occurs, only a minor deviation between the AETHER-LNS- and the AETHER-NLNS-associated instance is witnessed. The minimum flutter-onset dynamic pressures, however, deviate substantially. In this regard, the AETHER-LNS-obtained progression exhibits a Mach number that is lower than the experimentally obtained instance, yet has a higher minimum flutter-onset dynamic pressure. In contrast, the AETHER-NLNS-obtained progression exhibits a Mach number that is higher than the experimentally obtained instance, yet has a lower minimum flutter-onset dynamic pressure; i.e., behaving inversely. The AETHER-LNS-associated minimum flutter-onset dynamic pressure, however, is closest to the experimentally associated instance. The deviation between the AETHER-LNS- and the AETHER-NLNS-obtained progression was attributed to an "unsufficient [sic] convergence in time step"[33] during the AETHER-NLNS computation. It was stated that AETHER-LNS achieved a reduction of computational time by an order of magnitude with respect to AETHER-NLNS, which, however, was not further quantified [33].

In 2011 Levasseur et al. [78] extended AETHER-LNS beyond the FEVA through a small disturbance formulation of both the S/A one-equation turbulence model [121] and the Chen-Patel k-epsilon two-equation turbulence model [26], allowing the amplitude dynamic eddy viscosity to be fully accounted for. The formulation itself was again based on

a first-order Taylor-series expansion, with the analytical derivatives of the constituting fluxes/source terms not explicitly rendered. Consistently, their evaluation at the reference state was handled by code routines that were obtained through automatic differentiation of the AETHER-NLNS instances. It was recognized, however, that the transport equation(s) of the turbulence model needed to be solved concurrently with the flow governing equations in order for AETHER-LNS to be computationally efficient. AETHER-NLNS, on the other hand, employs the commonly utilized staggered solution approach. In the time domain, its computational penalty is negligible with respect to the required overall effort. Ultimately, the need to account for the amplitude dynamic eddy viscosity when treating strong shock/boundary-layer interaction was demonstrated by means of a generic business-jet airfoil. A pitching oscillation at both a baseline and a higher frequency were considered. It was further ascertained that the need to account for the amplitude dynamic eddy viscosity is frequency-dependent [78], a circumstance originally identified by Holmes et al. [52] for subsonic internal flow. In 2011 Revalor et al. [109] additionally demonstrated the application readiness of AETHER-LNS for the treatment of full aircraft configurations, employing it for the flutter analysis of both a proprietary transport and a proprietary high-speed/high-maneuverability instance.

1.4 Research Objectives

Aircraft flutter analysis within a production environment demands a numerical method that can accurately and yet efficiently predict the unsteady aerodynamic loading of the transonic speed range for a simple harmonic excitation. Both shocks and viscous phenomena need to be treatable. A method based on the frequency-domain solution of the small disturbance Navier-Stokes equations was expected to satisfy this demand, and has the potential to become the preferred CFD component of a CA tool. To this effect, the research conducted at TUM from 1999 onward has led to the small disturbance Navier-Stokes method FLM-SD.NS; see Pechloff et al. [98], Pechloff and Laschka [100, 103], as well as Iatrou's [54] dissertation of 2009. With the research inception, the following objectives were formulated for the dissertation at hand:

- Firstly, derive the small disturbance Navier-Stokes equations in their closed frequency-domain formulation by way of the instantaneous Navier-Stokes equations' triple decomposition, as proposed by Laschka [75].

  This entails the expansion of each primitive field quantity into a time-invariant mean, a periodic perturbation, and an erratic fluctuation. Subsequently, the statistical treatment of the expanded equation system, the discounting of higher-order perturbation terms, and the resolution of turbulent correlation terms will yield an equation system governing the flowfield's perturbation response under the premise

of dynamic linearity [98, 100]. Closure to the introduced linearized time-invariant-mean and periodic-perturbation of the dynamic eddy viscosity is attained through the S/A one-equation turbulence model [121] [100]. Eventually, this equation system is again transitioned from the time domain to the frequency domain through a simple harmonic time law [70, 71] [98, 100].

- Secondly, cast the derived small disturbance Navier-Stokes equations into a mature numerical method that utilizes the established solution techniques of existing RANS methods.

  Designated FLM-SD.NS, the implementation should draw on both FLM-SDEu [70, 71] and FLM-NS [32, 31], rendering a viscous extension of the former, while allowing numerical equivalency to the latter [98, 100]. Novelly, a small disturbance formulation of the viscous flux vector evaluation and the near-field boundary condition inherent to FLM-NS, as well as a small disturbance formulation of the introduced S/A turbulence source term vector evaluation, needs to be implemented [98, 100]. Likewise, the LU-SSOR scheme employed by FLM-Eu/FLM-NS for implicit pseudotime integration [62, 70, 31] needs to be adapted, with the embedment into a geometric multigrid algorithm being proposed to accelerate convergence [100]. Stability issues known to arise in the small disturbance Navier-Stokes equations' pseudotime integration for cases where the supplied steady-state flowfield exhibits regions of separation are mitigated through the limitation of the amplitude S/A conservative working variable [103].

- Thirdly, substantiate the validity of the small disturbance Navier-Stokes approach as realized with FLM-SD.NS, its flow-topological versatility, and the attainable computational efficiency gain with respect to FLM-NS.

  For these purposes, experimentally investigated test cases are to be selectively computed. Induced flowfields must be characterized by shocks of diverse strength and degree of motion, as well as the severity of their boundary-layer interaction. In this regard, the low-aspect-ratio wing, which typifies the high-speed/high-maneuverability aircraft configuration, is focused on. Specifically, pitching- and flap-oscillation test cases of the NASA Clipped Delta Wing (NCDW) [12] are considered [103]. The superiority of the viscous consideration over the inviscid one is demonstrated as well; i.e., through direct comparison of FLM-SD.NS/FLM-NS-obtained results with their FLM-SDEu/FLM-Eu counterparts [103].

The realization of the preceding objectives is documented in the following chapters. In Chapter 2, the nondimensionalized instantaneous Navier-Stokes equations are given as formulated for a curvilinear coordinate system, with the reference quantities and similarity parameters being likewise defined. This sets up the Chapter 3 derivation of the small

disturbance Navier-Stokes equations in their closed frequency-domain instance. The numerical intricacies to cast them into FLM-SD.NS are subsequently provided in Chapter 4. Computational results for select pitching- and flap-oscillation test cases of the NCDW are discussed in Chapter 5. Lastly, Chapter 6 summarizes this dissertation and provides an outlook of continuative work. In completion, Appendix A and Appendix B, respectively, detail the necessary extensions of the existing FLM-SDEu implementation and the discrete evaluation of the considered body's local and global loading.

In this context, Iatrou [54] had provided a small disturbance formulation of the divergence theorem for the evaluation of the amplitude viscous flux vectors on the basis of Chakravarthy's [21] original utilization. Additionally, a small disturbance formulation of the no-slip-/adiabatic-wall boundary condition was given, and a FEVA employing the B/L algebraic turbulence model [8] instated. Ultimately, FLM-SD.NS-obtained results for oscillations of high-aspect-ratio wings and a nacelle-pylon-rectangular-wing assembly, both typifying the transport aircraft configuration, were presented. Comparisons to experimental data, as well as to FLM-NS- and FLM-SDEu-/FLM-Eu-obtained results were again made. Supplementally, a comparison between the two turbulence-model options was conducted [54].

Chapter 2

Fundamentals

Developing a structured finite volume shock-capturing numerical method for the computation of flows about aerodynamic geometries, the instantaneous Navier-Stokes equations are considered in their nondimensionalized strong conservation form, as cast for a boundary-fitted (curvilinear) coordinate system; also see Anderson [6], Hoffmann and Chiang [50], and Blazek [16]. Furthermore, the reference quantities utilized in the nondimensionalization are specified, as well as the similarity parameters pertinent to the problem introduced.

2.1 Nondimensionalized Instantaneous Navier-Stokes Equations Formulated for a Boundary-Fitted (Curvilinear) Coordinate System

In three-dimensional Cartesian space the instantaneous Navier-Stokes equations are comprised of the continuity equation, the three momentum equations respective the individual coordinate directions, and the energy equation. The Cartesian spatial coordinates x, y, z, as composited in the position vector

$$\mathbf{r} := (x,\, y,\, z)^T \;, \tag{2.1}$$

and the associated temporal coordinate t are originally classified as the independent variables; also see [6, 50, 16].

Through the introduction of a right-handed boundary-fitted coordinate system it becomes possible to utilize a nonuniform curvilinear grid for discretizing the treated physical Cartesian continuum, with individual interfaces of the computational cells naturally rendering the considered body's boundary. Furthermore, any deformation/deflection of the considered body's surface over time can be simply accounted for through the corresponding deformation/deflection of the surrounding computational cells in physical space. The boundary-fitted coordinate system is constituted by the curvilinear spatial coordinates ξ,

η, ζ, and the associated temporal coordinate τ. They replace the Cartesian coordinates as the independent variables:

$$x = x(\xi, \eta, \zeta, \tau)\,, \quad y = y(\xi, \eta, \zeta, \tau)\,, \quad z = z(\xi, \eta, \zeta, \tau)\,, \quad \text{and} \quad t = \tau\,. \tag{2.2}$$

The coordinate transformation itself is unique. Hence, the nonuniform curvilinear grid can be mapped from physical space to a uniform orthogonal grid in computational space; i.e., where planes perpendicular to the respective curvilinear coordinate direction ($\xi = const.$, $\eta = const.$, or $\zeta = const.$) become equidistant to each other. A numerical solution of the transformed PDEs obtained in discrete computational space can conversely be mapped back to discrete physical space. Whereas the Cartesian coordinate system is defined globally, the boundary-fitted coordinate system can be defined locally, allowing the physical Cartesian continuum to be subdivided into curvilinear blocks. Each block can then be discretized by an individual nonuniform curvilinear grid, for which the transformed PDEs are pertinently solved in discrete computational space. Typically, such multiblock topologies become necessary for the treatment of complex geometries. The boundary-fitted coordinate system can be equivalently referred to as the curvilinear coordinate system; also see [6, 50, 16].

Cast in nondimensionalized strong conservation form for the curvilinear coordinate system, the instantaneous Navier-Stokes equations become

$$\frac{\partial \mathbf{Q}}{\partial \tau} + \frac{\partial \mathbf{F}}{\partial \xi} + \frac{\partial \mathbf{G}}{\partial \eta} + \frac{\partial \mathbf{H}}{\partial \zeta} = \frac{\partial \mathbf{F_v}}{\partial \xi} + \frac{\partial \mathbf{G_v}}{\partial \eta} + \frac{\partial \mathbf{H_v}}{\partial \zeta}\,; \tag{2.3}$$

also see Pechloff and Laschka [100]. In this regard, $\mathbf{Q}$ represents the curvilinear state vector of dependent conservative variables, which are considered to be independent from one another. It is defined through its sought-after Cartesian counterpart $\mathbf{q}$; i.e.,

$$\mathbf{Q} := J\,\mathbf{q} = J\,(\rho,\, \rho u,\, \rho v,\, \rho w,\, \rho e)^T\,, \tag{2.4}$$

with J denoting the determinant of the coordinate transformation's Jacobian:

$$\begin{aligned} J &:= det\left[\frac{\partial(x, y, z, t)}{\partial(\xi, \eta, \zeta, \tau)}\right] \\ &= x_\xi(y_\eta z_\zeta - z_\eta y_\zeta) + y_\xi(z_\eta x_\zeta - x_\eta z_\zeta) + z_\xi(x_\eta y_\zeta - y_\eta x_\zeta)\,. \end{aligned} \tag{2.5}$$

The elements of the fluid's Cartesian velocity vector,

$$\mathbf{v} := (u,\, v,\, w)^T\,, \tag{2.6}$$

and the specific total energy e are identified as dependent primitive variables, while the density ρ serves as both a conservative and primitive instance. The former are straightforwardly gained as

$$u = \rho u/\rho\,, \quad v = \rho v/\rho\,, \quad w = \rho w/\rho\,, \quad e = \rho e/\rho\,. \tag{2.7}$$

Furthermore, $\mathbf{F}$, $\mathbf{G}$, and $\mathbf{H}$ represent the convective flux vectors, respectively, in ξ, η, and ζ direction, having $\mathbf{F_v}$, $\mathbf{G_v}$, and $\mathbf{H_v}$ as their viscous flux counterparts. Utilizing a generalized curvilinear coordinate ψ, both the convective flux vectors and the viscous flux vectors can each be universally formulated:

$$\mathbf{E}_\psi := \begin{pmatrix} \rho\,\theta_\psi & & \\ \rho u\,\theta_\psi & + & J\psi_x\,p \\ \rho v\,\theta_\psi & + & J\psi_y\,p \\ \rho w\,\theta_\psi & + & J\psi_z\,p \\ H\,\theta_\psi & - & J\psi_t\,p \end{pmatrix} \quad \text{and} \quad \mathbf{E}_{\mathbf{v}\,\psi} := \begin{pmatrix} 0 & & & & \\ J\psi_x\,\tau_{xx} & + & J\psi_y\,\tau_{yx} & + & J\psi_z\,\tau_{zx} \\ J\psi_x\,\tau_{xy} & + & J\psi_y\,\tau_{yy} & + & J\psi_z\,\tau_{zy} \\ J\psi_x\,\tau_{xz} & + & J\psi_y\,\tau_{yz} & + & J\psi_z\,\tau_{zz} \\ J\psi_x\,\Pi_x & + & J\psi_y\,\Pi_y & + & J\psi_z\,\Pi_z \end{pmatrix}, \tag{2.8}$$

with the substitution $\psi = \xi$, η, or ζ then, respectively, yielding $\mathbf{F} = \mathbf{E}_\xi$ and $\mathbf{F_v} = \mathbf{E}_{\mathbf{v}\,\xi}$, $\mathbf{G} = \mathbf{E}_\eta$ and $\mathbf{G_v} = \mathbf{E}_{\mathbf{v}\,\eta}$, or $\mathbf{H} = \mathbf{E}_\zeta$ and $\mathbf{H_v} = \mathbf{E}_{\mathbf{v}\,\zeta}$. Inherent to $\mathbf{E}_\psi$ of Eq. (2.8), θ_ψ represents the J-multiplied generalized contravariant velocity,

$$\theta_\psi := J\psi_x u + J\psi_y v + J\psi_z w + J\psi_t\,, \tag{2.9}$$

and p is the static pressure. Being the fifth element of $\mathbf{E}_\psi$, the ψ-directional convective energy flux is rendered by way of the total enthalpy per unit volume H; i.e.,

$$H := \rho e + p\,. \tag{2.10}$$

Inherent to $\mathbf{E}_{\mathbf{v}\,\psi}$ of Eq. (2.8), the elements of the Cartesian shear stress tensor are expressed for Newtonian fluids under consideration of the Stokes hypothesis:

$$\begin{aligned} \tau_{xx} &:= \frac{2}{3}\,\mu\left(2\frac{\partial u}{\partial x} - \frac{\partial v}{\partial y} - \frac{\partial w}{\partial z}\right), \qquad \tau_{xy} = \tau_{yx} := \mu\left(\frac{\partial u}{\partial y} + \frac{\partial v}{\partial x}\right), \\ \tau_{yy} &:= \frac{2}{3}\,\mu\left(2\frac{\partial v}{\partial y} - \frac{\partial u}{\partial x} - \frac{\partial w}{\partial z}\right), \qquad \tau_{xz} = \tau_{zx} := \mu\left(\frac{\partial u}{\partial z} + \frac{\partial w}{\partial x}\right), \\ \tau_{zz} &:= \frac{2}{3}\,\mu\left(2\frac{\partial w}{\partial z} - \frac{\partial u}{\partial x} - \frac{\partial v}{\partial y}\right), \qquad \tau_{yz} = \tau_{zy} := \mu\left(\frac{\partial v}{\partial z} + \frac{\partial w}{\partial y}\right), \end{aligned} \tag{2.11}$$

with the dynamic molecular viscosity μ. Being the fifth element of $\mathbf{E}_{\mathbf{v}\,\psi}$, the ψ-directional viscous energy flux is naturally constituted by its Cartesian counterparts, which compound shear stress work and heat transfer; i.e.,

$$\begin{aligned} \Pi_x &:= u\,\tau_{xx} + v\,\tau_{xy} + w\,\tau_{xz} - q_x\,, \\ \Pi_y &:= u\,\tau_{yx} + v\,\tau_{yy} + w\,\tau_{yz} - q_y\,, \\ \Pi_z &:= u\,\tau_{zx} + v\,\tau_{zy} + w\,\tau_{zz} - q_z\,. \end{aligned} \tag{2.12}$$

Therein, the elements of the Cartesian heat flux vector follow Fourier's law of heat conduction:

$$q_x := -\frac{\gamma}{\Gamma}\frac{\mu}{Pr}\frac{\partial T}{\partial x}\,, \quad q_y := -\frac{\gamma}{\Gamma}\frac{\mu}{Pr}\frac{\partial T}{\partial y}\,, \quad q_z := -\frac{\gamma}{\Gamma}\frac{\mu}{Pr}\frac{\partial T}{\partial z}\,, \quad \text{with} \quad \Gamma := \gamma - 1\,, \tag{2.13}$$

the ratio of specific heats γ, the Prandtl number Pr, and the static temperature T. Both γ and Pr are treated as constant for the particular fluid. Solely considering a calorically perfect gas, the thermal equation of state directly connects T to p:

$$p = \rho T \qquad \text{or} \qquad T = p/\rho\,. \tag{2.14}$$

Furthermore, e is defined as the sum of the specific internal energy, as given through the caloric equation of state, and the specific kinetic energy; i.e.,

$$e := T/\Gamma \,+\, \left(u^2 + v^2 + w^2\right)/\,2. \tag{2.15}$$

In conjunction, Eq. (2.14) and Eq. (2.15) yield the link between p and the conservative variables:

$$p(\mathbf{q}) = \Gamma\left\{\rho e - \left[(\rho u)^2 + (\rho v)^2 + (\rho w)^2\right]/(2\rho)\right\}\,. \tag{2.16}$$

Both p and T are considered to be derived primitive variables. Ultimately, the governing equation system is closed by way of Sutherland's law, which renders the dynamic molecular viscosity as an exclusive function of the static temperature:

$$\mu(T) = \mu_\infty\, T^{\frac{3}{2}}\,(1+S)\,/\,(T+S)\,, \tag{2.17}$$

wherein the dynamic molecular viscosity μ_∞ at freestream conditions and the Sutherland constant S are considered to be known; also see [100].

Both $\mathbf{E}_\psi$ and $\mathbf{E}_{\mathbf{v}\,\psi}$ are constituted through the J-multiplied generalized spatial metrics of the coordinate transformation $J\psi_x$, $J\psi_y$, and $J\psi_z$, respectively, with

$$\psi_x := \partial\psi/\partial x, \quad \psi_y := \partial\psi/\partial y, \quad \psi_z := \partial\psi/\partial z. \tag{2.18}$$

The J-multiplied generalized temporal metric of the coordinate transformation $J\psi_t$, on the other hand, is limited to $\mathbf{E}_\psi$, with

$$\psi_t := \partial\psi/\partial t. \tag{2.19}$$

Interpreting $J\psi_x$, $J\psi_y$, and $J\psi_z$ as the Cartesian components of a J-multiplied generalized spatial metric vector normal to a coordinate plane of $\psi = const.$,

$$\boldsymbol{J\psi} := \left(J\psi_x,\, J\psi_y,\, J\psi_z\right)^T\,, \tag{2.20}$$

$J\psi_t$ then equals the J-multiplied negative time rate of change for the position vector of $\boldsymbol{J\psi}$ in direction of ψ; i.e.,

$$J\psi_t = -\frac{\partial \mathbf{r}}{\partial \tau}\,\boldsymbol{J\psi}\,. \tag{2.21}$$

Hence, the J-multiplied generalized contravariant velocity can be alternatively formulated as

$$\theta_{\psi} = \boldsymbol{J\psi} \left(\mathbf{v} - \partial \mathbf{r} / \partial \tau \right) , \tag{2.22}$$

illustrating the manner in which the kinematics of the physical grid vertices are accounted for with respect to the kinematics of the flow. The explicit formulation of J, $\boldsymbol{J\xi}$, $\boldsymbol{J\eta}$, and $\boldsymbol{J\zeta}$ had already been provided by Kreiselmaier [70], as well as for merely two-dimensional space by Cvrlje [31], both on basis of Hoffmann and Chiang [50]. It had also been given by Sickmüller [119] and Iatrou [54]. Considering FLM-Eu [70] and FLM-NS [31], the constituting curvilinear spatial derivatives of the Cartesian spatial coordinates, however, are not actually evaluated to obtain J, $\boldsymbol{J\xi}$, $\boldsymbol{J\eta}$, and $\boldsymbol{J\zeta}$. Rather, consistency between the finite difference approximation of either the Euler and instantaneous Navier-Stokes equations' curvilinear differential form in computational space and the finite volume approximation of the particular Cartesian integral form in physical space had been invoked, pursuant to Hirsch [48]. To this end, the discrete instance of J for a computational cell of unity edge-lengths in computational space must become equal to the computational cell's volume in physical space [70, 100]. Furthermore, the directionally discrete instance of $\boldsymbol{J\psi}$ must become equal to the physical surface normal vector associated with the computational cell's $\psi = const.$ interface [70, 100] [48]. Consequently, $J\psi_t$ embodies the ψ-directional velocity of this cell interface's physical motion [70, 100]. Given that $\boldsymbol{J\psi}$ and $J\psi_t$ can be viewed as physical geometric and kinematic entities, it is admissible to consider J indivisible from either one. Thus, $\boldsymbol{J\psi}$ and $J\psi_t$ can be simply referred to as the generalized spatial metric vector and the generalized temporal metric, respectively. To that effect, θ_{ψ} will be redesignated as the generalized contravariant velocity.

Lastly, the Cartesian spatial derivatives constituting the elements of the Cartesian shear stress tensor and the elements of the Cartesian heat flux vector, respectively, Eq. (2.11) and Eq. (2.13), have not been transformed to the curvilinear coordinate system, as they can be evaluated in physical space by way of the divergence theorem [31, 100].

2.2 Reference Quantities and Similarity Parameters

Following Hoffmann and Chiang [50], the consideration of the nondimensionalized governing equation system allows a numerical solution for a model flow problem that achieves dynamic and energetic similarity to a real flow problem under given geometric similarity. Furthermore, the computed nondimensional field quantities can be kept within a reasonable numerical range; i.e., most desirably, between nil and unity [50]. The nondimensionalized governing equation system had resulted from its dimensional counterpart by formulating the dimensional instances of the Cartesian spatial and temporal coordinates, the primitive variables, as well as the dynamic molecular viscosity as products between

the corresponding nondimensional instances and appropriate dimensional reference quantities; i.e.,

$$\begin{aligned}
\check{x} &:= x\,\check{l}_{ref}\,, \quad & \check{y} &:= y\,\check{l}_{ref}\,, \quad & \check{z} &:= z\,\check{l}_{ref}\,, \quad & \check{t} &:= t\,\check{t}_{ref}\,, \\
\check{\rho} &:= \rho\,\check{\rho}_{ref}\,, \quad & \check{u} &:= u\,\check{u}_{ref}\,, \quad & \check{v} &:= v\,\check{u}_{ref}\,, \quad & \check{w} &:= w\,\check{u}_{ref}\,, \\
\check{e} &:= e\,\check{e}_{ref}\,, \quad & \check{p} &:= p\,\check{p}_{ref}\,, \quad & \check{T} &:= T\,\check{T}_{ref}\,, \quad & \check{\mu} &:= \mu\,\check{\mu}_{ref}\,.
\end{aligned} \tag{2.23}$$

The $(\check{\ })$ modifier denotes the dimensional quantities. Pursuant to dimensional analysis, specifying four physically independent dimensional reference quantities as known is then sufficient to determine the remaining instances. For the sake of consistency with the existing FLM methods [70, 31], the reference length, the reference density, the reference static pressure, and the reference static temperature were again adopted. They were assigned, respectively, a dimensional characteristic length, the dimensional density, the dimensional static pressure, and the dimensional static temperature, each at freestream conditions:

$$\check{l}_{ref} := \check{L}\,, \quad \check{\rho}_{ref} := \check{\rho}_{\infty}\,, \quad \check{p}_{ref} := \check{p}_{\infty}\,, \quad \check{T}_{ref} := \check{T}_{\infty}\,. \tag{2.24}$$

This had also been established in [100]. Consequently, the nondimensional characteristic length, the nondimensional density, the nondimensional static pressure, and the nondimensional static temperature, each at freestream conditions, all become unity. The remaining dimensional reference quantities were derived as

$$\check{t}_{ref} = \check{L}\sqrt{\check{\rho}_{\infty}/\check{p}_{\infty}}\,, \quad \check{u}_{ref} = \sqrt{\check{p}_{\infty}/\check{\rho}_{\infty}}\,, \quad \check{e}_{ref} = \check{p}_{\infty}/\check{\rho}_{\infty}\,, \quad \check{\mu}_{ref} = \check{L}\,\check{\rho}_{\infty}\sqrt{\check{p}_{\infty}/\check{\rho}_{\infty}}\,. \tag{2.25}$$

Compressible similarity was achieved through the setting of the Mach number at freestream conditions [70, 31, 100], which ultimately renders the magnitude of the corresponding nondimensional Cartesian velocity vector:

$$|\mathbf{v}_{\infty}| = \sqrt{\gamma}\,Ma_{\infty}\,. \tag{2.26}$$

Concurrent viscous similarity was achieved through the setting of the Reynolds number at freestream conditions [31, 100], which yields the corresponding nondimensional dynamic molecular viscosity employed in Sutherland's law, Eq. (2.17):

$$\mu_{\infty} = \sqrt{\gamma}\,Ma_{\infty}\,L_{Re_{\infty}}\,/\,Re_{\infty}\,. \tag{2.27}$$

In this regard, the dimensional characteristic length pertinent to the Reynolds number, $\check{L}_{Re_{\infty}}$, must not necessarily conform to $\check{L}$. Hence, $L_{Re_{\infty}}$ will not necessarily be equal to unity [100, 103]. Additionally, the nondimensional instance of Sutherland's constant is given through

$$S = \check{S}/\check{T}_{\infty} \tag{2.28}$$

[31, 100]. Similarity with respect to the relationship between molecular momentum diffusivity and molecular thermal diffusivity was achieved through the setting of the Prandtl number [31, 100], as factored into the elements of the Cartesian heat flux vector, Eq. (2.13). Overall, γ, Ma_∞, Re_∞, L_{Re_∞}, $\check{T}_\infty$, $\check{S}$ (in principle), and Pr need to be supplied by the user to treat a specific physical flow problem with FLM-NS [31, 100], while γ and Ma_∞ had sufficed for FLM-Eu and FLM-SDEu [70].

The prerequisite geometric similarity was achieved for all existing FLM methods by scaling the considered body's physical dimensions with $\check{L}$, and thus yielding the nondimensional model instance. The latter then serves as the basis on which the nonuniform curvilinear grid is constructed. Supplying this grid to the FLM method, $\check{L}$ becomes implicitly accounted for. Within the grid it is identifiable at the location where a nondimensional length, or L in particular, turns to unity.

Since the existing FLM methods are primarily employed to predict flow excited through the forced periodic motion of the considered body, an additional nondimensional parameter was required to achieve similarity with respect to the introduced unsteadiness. For this purpose, a nondimensional angular frequency k had been derived from a known dimensional excitation frequency $\check{f}$; i.e.,

$$k := 2\pi f = 2\pi \check{f}\, \check{L} \sqrt{\check{\rho}_\infty / \check{p}_\infty}\,, \tag{2.29}$$

with k set indirectly by the user [70, 31, 100].

Chapter 3

Small Disturbance Navier-Stokes Equations

On the basis of the instantaneous Navier-Stokes equations, a body undergoing a forced periodic oscillation in steady freestream conditions at flight-realistic Reynolds numbers will render a turbulent (instantaneous) flowfield response. As the time scales associated with the turbulence are generally orders of magnitude smaller than the problem-specific period of excitation, a statistical technique can be employed to extract an organized unsteadiness of equal periodicity. Similarly, a time-invariant mean of the instantaneous flowfield response can be gained over a single period of excitation. This subsequently allows a periodic perturbation to be extracted from the organized unsteadiness. If the body undergoes only minor deformations/deflections about its time-invariant-mean position, it can be postulated that the periodic perturbation inherent to the instantaneous flowfield response is dynamically fully linear. Under this premise, a system of linear PDEs governing the periodic perturbation contingent on the linearized time-invariant-mean state can be derived. Within these small disturbance Navier-Stokes equations the influence of turbulence is wholly compounded into statistical correlation terms. They represent a problem of closure, which, however, can be satisfied by equivalently linearizing a dynamically fully nonlinear modeling approach. Eventually, the small disturbance Navier-Stokes equations can be transitioned to the frequency domain, making a substantially more efficient numerical solution possible; see Pechloff et al. [98], as well as Pechloff and Laschka [100]. In the following, the steps involved with this derivation are elaborated. The nondimensionalized instantaneous Navier-Stokes equations formulated for a curvilinear coordinate system, Eqs. (2.3–2.21), serve as the starting point.

3.1 Overview

The small disturbance Navier-Stokes equations can be derived from the instantaneous Navier-Stokes equations through the triple decomposition of field quantities. Proposed by Laschka [75] in 1985 for treating the given external flow problem, Acharya [1] and Norris [92] had originally employed the approach in 1975 for treating turbulent channel flow under forced periodic excitation. Shortly thereafter Telionis [124, 125] appropriated the triple decomposition for more fundamental investigations on the unsteady behavior of turbulent boundary layers as well. Following Acharya [1], the triple decomposition renders a separation of a flowfield's instantaneous response into a time-invariant mean, a periodic perturbation, and an erratic fluctuation embodying the phenomena of turbulence. Mathematically, this is realized by separately applying two distinct statistical techniques, the phase average and the time average, to the instantaneous Navier-Stokes equations. The phase average itself conforms to the well-established ensemble average; i.e., an arithmetic average of an instantaneous quantity's phase-particular value over a large number of cycles. Thus, the phase-averaged flowfield retains time dependence, while being devoid of any erratic fluctuation. It embodies the organized unsteadiness inherent to the instantaneous response. The time average, on the other hand, considers an instantaneous quantity's value over a single cycle, with the time-averaged flowfield retaining no time dependence. It is the time-invariant mean of the flowfield's instantaneous response, as well as the time-invariant mean of the flowfield's underlying organized unsteadiness. Naturally, both averaging techniques are only effective if the frequency of the forced excitation, and hence the fundamental frequency of the organized unsteadiness, is known [1]; also see Pechloff et al. [98], as well as Pechloff and Laschka [100].

In this dissertation, the triple decomposition is performed by way of the constituting primitive variables. Each is individually expanded into a time-invariant mean, a periodic perturbation, and an erratic fluctuation [1, 98, 100]. Additionally, it must be taken into account that the considered body's motion generally introduces a dislocation of the physical grid vertices. Hence, their position vector can be dually decomposed into a time-invariant mean and a periodic perturbation, which ultimately leads to an equivalent decomposition of the determinant of the coordinate transformation's Jacobian, the spatial metric vectors, and the temporal metric [70, 100]. Having expanded the equation system in this manner, the separate application of the phase average and the time average under consideration of certain mathematical identities [1, 125] renders two new equation systems. The first governs the instantaneous flowfield's underlying organized unsteadiness and the second its time-invariant mean [98, 100]. In either equation system, the influence of turbulence has been exclusively reduced to averaged products between erratic fluctuations inherent to the instantaneous primitive variables [100]. Pursuant to Pechloff and Laschka, "[w]ith the emergence of these turbulent [correlation terms], additional unknowns [are] introduced

[...], presenting a problem of closure that will require further handling. By subtracting the time-averaged equation system from the phase-averaged one, the governing [equation system of] the [instantaneous flowfield's inherent] periodic [perturbation is] obtained." [100] As further established [98, 100], turbulent correlation terms arising from the phase average only occur in subtraction of the respective instance arising from the time average. Hence, a periodic perturbation inherent to the organized unsteady turbulent correlation term can be particularly defined. This problem of closure then becomes one of handling both the periodic perturbation inherent to the organized unsteady turbulent correlation term and its time-invariant mean [98, 100]. Following Acharya [1] as well as Norris [92], the Boussinesq approximation is drawn on to reduce this problem of closure: Both the periodic perturbation and the time-invariant mean of an organized unsteady dynamic eddy viscosity are introduced, allowing the periodic perturbation inherent to particular organized unsteady turbulent correlation terms and their time-invariant mean to be expressed through the periodic perturbation inherent to the organized unsteady primitive variables and their time-invariant mean [98, 100].

The governing equation system of the instantaneous flowfield's inherent periodic perturbation is still dynamically nonlinear, as products between periodic perturbation entities persist [100]. Invoking the premise of small disturbances, these higher-order perturbation terms are deemed negligible, and disregarded [100]. Effectively, a linearization of the governing equation system with respect to the perturbation occurs, the result being classified as the small disturbance Navier-Stokes equations in their unclosed time-domain formulation [100]. Closure with regard to the arisen linearized periodic-perturbation and linearized time-invariant-mean instances of the static temperature/pressure and dynamic molecular viscosity is, respectively, accomplished through a small disturbance formulation of the thermal equation of state and Sutherland's law [100]. Closure with regard to the linearized periodic-perturbation and linearized time-invariant-mean instances of the dynamic eddy viscosity, on the other hand, requires the selection of an eddy viscosity turbulence model that is per se receptive to a small disturbance formulation [100]. The S/A one-equation turbulence model [121] represents such an instance, and is accordingly incorporated into the governing equation system [100]. In this context, arisen linearized periodic-perturbation and linearized time-invariant-mean instances of the turbulence kinetic energy are permissibly disregarded. Ultimately, the closed frequency-domain formulation of the small disturbance Navier-Stokes equations is obtained by constraining the periodic perturbation of both the position vector and the primitive variables to a simple harmonic oscillation [98, 100]. This process follows the approach employed by Kreiselmaier [70] to obtain the frequency-domain formulation of the small disturbance Euler equations: All periodic-perturbation instances are expressed through a product between a particular time-invariant amplitude and the time law, with a formulation in the com-

plex field of numbers allowing a phase-shifted response of the primitive variables to be conveniently accounted for. Since the governing equation system is linear in the periodic-perturbation instances, the time law can be eliminated per se. Consequently, the initial unsteady problem reduces to a steady problem for the primitive variables' amplitude perturbation [70]; also see [98, 100]. The closed frequency-domain formulation of the small disturbance Navier-Stokes equations is cast in a strong conservation form utilizing a pseudotime derivative of the amplitude state vector [98, 100]. This again enables the implementation of a pseudotime-integration solution scheme [70]. A priori knowledge of both the linearized time-invariant-mean flowfield and the grid vertices' amplitude and linearized time-invariant-mean location are still prerequisite to any solution attempt [70, 98, 100].

The derivation of the small disturbance Navier-Stokes equations in their two-dimensional Cartesian partially closed time-domain formulation had been originally performed and documented by the author [94] in 2001. It had served as the basis for Iatrou's [58] formulation of the three-dimensional curvilinear coordinate system instance, and its subsequent transition to the frequency domain. As documented [58] in 2002, and eventually included in Iatrou's [54] dissertation of 2009, closure had been realized with the B/L algebraic turbulence model [8] under a FEVA. The derivation of the small disturbance Navier-Stokes equations presented by the author in the following differs, as the instantaneous Navier-Stokes equations in their three-dimensional curvilinear coordinate system formulation are expanded and statistically treated per se. Next to the S/A one-equation turbulence model closure provided in this dissertation, the Wilcox k-omega two-equation turbulence model closure [138] had been presented by Pechloff and Laschka [102] in 2010.

3.2 Triple Decomposition

The triple decomposition of the instantaneous Navier-Stokes equations requires a statistical treatment of the constituting field quantities [75, 1]. In the utilized curvilinear formulation, however, the statistical treatment extends to the constituting geometric and kinematic entities as well. The mathematical details involved with the triple decomposition are provided herein. They were originally mentioned by Pechloff et al. [98] in 2002 and partially shown by Pechloff and Laschka [99] in 2004. The latter was eventually published [100] in 2006.

3.2.1 Field Quantities

Following Pechloff and Laschka [100], an arbitrary instantaneous field quantity Φ is representatively considered. With the fundamental frequency of the inherent organized unsteadiness being equal to the known frequency of the forced excitation, two distinct sta-

tistical techniques can be applied to it. On one hand, this is the phase average

$$\langle \Phi(\xi,\eta,\zeta,\tau) \rangle = \langle \Phi \rangle(\xi,\eta,\zeta,\tau) := \lim_{N\to\infty} \frac{1}{N} \sum_{n=0}^{N} \Phi(\xi,\eta,\zeta,\tau + n\, T_{2\pi}) \,, \tag{3.1}$$

yielding

$$\langle \Phi \rangle(\xi,\eta,\zeta,\tau) = \langle \Phi \rangle(\xi,\eta,\zeta,\tau + n\, T_{2\pi}) \tag{3.2}$$

for the period of oscillation $T_{2\pi} = 2\pi/k$. It renders the organized unsteadiness inherent to the instantaneous field quantity. On the other hand, the time average

$$\overline{\Phi(\xi,\eta,\zeta,\tau)} = \bar{\Phi}(\xi,\eta,\zeta) := \frac{1}{T_{2\pi}} \int_{\tau}^{\tau+T_{2\pi}} \Phi(\xi,\eta,\zeta,\acute{\tau})\, d\acute{\tau} \tag{3.3}$$

renders the time-invariant mean of the instantaneous field quantity. Hence, the inherent periodic perturbation and the inherent erratic fluctuation can be, respectively, obtained through

$$\tilde{\Phi}(\xi,\eta,\zeta,\tau) := \langle \Phi \rangle(\xi,\eta,\zeta,\tau) - \bar{\Phi}(\xi,\eta,\zeta) \,, \tag{3.4}$$

with

$$\tilde{\Phi}(\xi,\eta,\zeta,\tau) = \tilde{\Phi}(\xi,\eta,\zeta,\tau + n\, T_{2\pi}) \,, \tag{3.5}$$

and

$$\Phi'(\xi,\eta,\zeta,\tau) := \Phi(\xi,\eta,\zeta,\tau) - \langle \Phi \rangle(\xi,\eta,\zeta,\tau) \,. \tag{3.6}$$

Eventually, adding Eq. (3.6) to Eq. (3.4) allows the instantaneous field quantity to be expanded into three parts:

$$\Phi(\xi,\eta,\tau) = \bar{\Phi}(\xi,\eta,\zeta) + \tilde{\Phi}(\xi,\eta,\zeta,\tau) + \Phi'(\xi,\eta,\zeta,\tau) \tag{3.7}$$

[100].

The instantaneous Navier-Stokes equations allow for a dynamically fully nonlinear organized unsteadiness to be inherent to the instantaneous response, even for a simple harmonic excitation. Hence, $\langle \Phi \rangle$ needs to be considered as being dynamically fully nonlinear a priori, which then follows through to $\tilde{\Phi}$ by way of Eq. (3.4). The special case of a strictly dynamically linear $\langle \Phi \rangle$ is utilized to illustrate the triple decomposition in Figure 3.1. On the basis of Eqs. (3.1–3.7) a set of mathematical identities can be derived with respect to the application of the phase average or the time average to an instantaneous field quantity's time-invariant mean, periodic perturbation, or erratic fluctuation, as well as products thereof. Originally established by Acharya [1], they are essential to extracting the governing equations of the instantaneous flowfield's inherent periodic perturbation; also see Telionis [125], as well as Pechloff and Laschka [100]. The mathematical identities are discussed in the following:

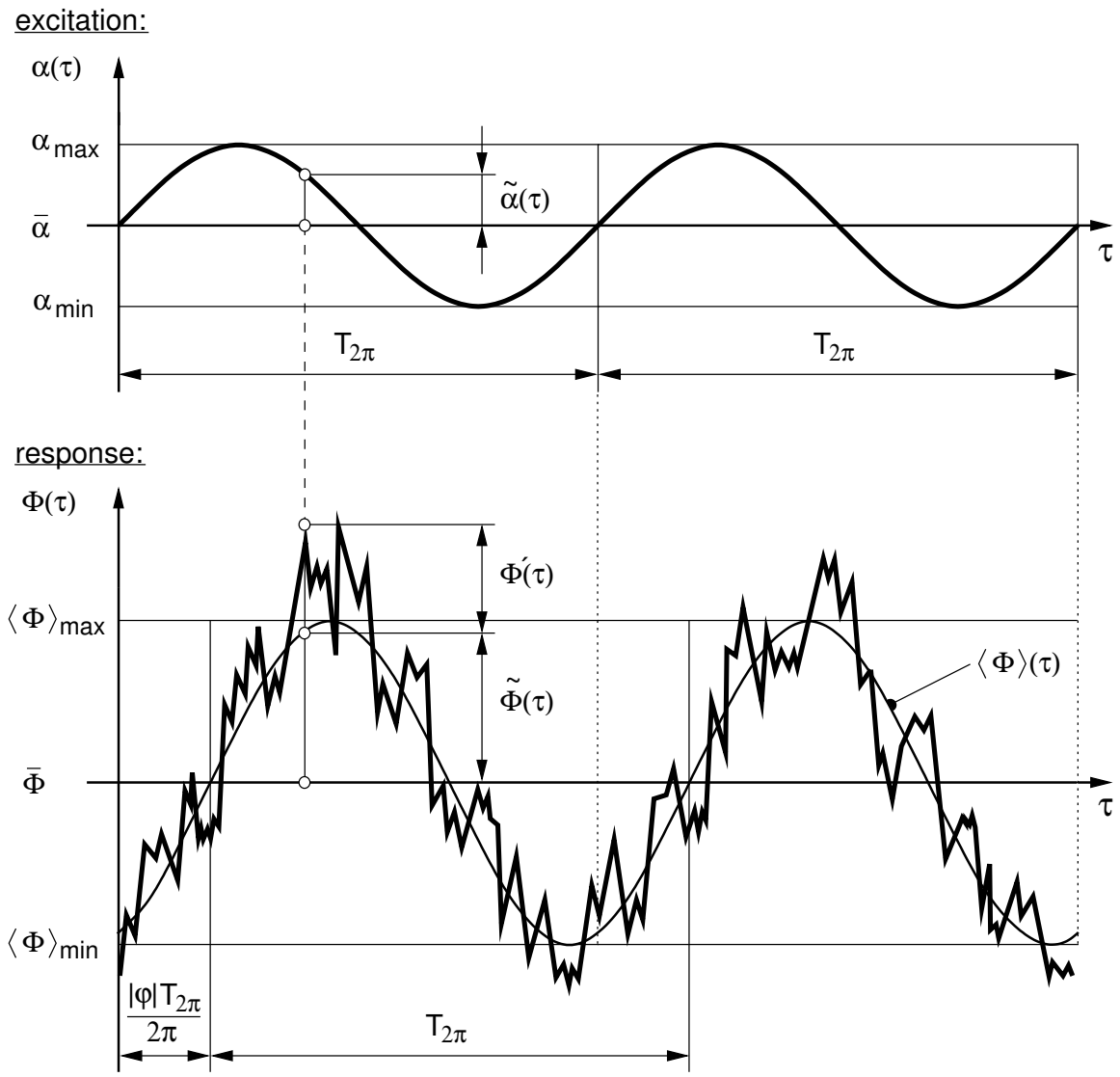

Figure 3.1: Triple decomposition of an arbitrary instantaneous field quantity Φ at fixed spatial coordinates for a generally phase-shifted flowfield response to a sinusoidal angle-of-attack oscillation under stipulation of a strictly dynamically linear inherent organized unsteadiness, with $\langle\Phi\rangle$ lagging by $|\varphi|$; based on Norris [92], Fig. 3.6.

- Since the phase average of an instantaneous field quantity renders the inherent $T_{2\pi}$-periodic organized unsteadiness, subsequent time-averaging renders the inherent time-invariant mean. Vice versa, phase-averaging an already time-averaged instantaneous field quantity is noneffective. The inherent time-invariant mean is again rendered; i.e., respectively,

$$\overline{\langle\Phi_A\rangle} = \overline{\Phi_A} \qquad \text{and} \qquad \langle\,\overline{\Phi_A}\,\rangle = \overline{\Phi_A} \tag{3.8}$$

[125].

- With the periodic perturbation inherent to the instantaneous field quantity being $T_{2\pi}$-periodic as well, phase-averaging is likewise noneffective. The periodic perturbation is again rendered. In contrast, time-averaging renders a nil value; i.e., respectively,

$$\langle \widetilde{\Phi_A} \rangle = \widetilde{\Phi_A} \qquad \text{and} \qquad \overline{\widetilde{\Phi_A}} = 0 \tag{3.9}$$

  [125].

- Furthermore, either phase-averaging or time-averaging the erratic fluctuation inherent to the instantaneous field quantity renders a nil value; i.e., respectively,

$$\langle \, (\Phi_A)' \, \rangle = 0 \qquad \text{and} \qquad \overline{(\Phi_A)'} = 0 \, . \tag{3.10}$$

  [125].

- Subsequently, an additional instantaneous field quantity Φ_B that generally differs in amplitude as well as phase from Φ_A yet is of equal periodicity is considered. Both the periodic perturbation and the time-invariant mean inherent to an instantaneous field quantity have been established as being constants with regard to the phase average. Hence, the phase average of a product between either instance and an additional instantaneous field quantity allows them to be factored out; i.e., respectively,

$$\langle \widetilde{\Phi_A} \, \Phi_B \rangle = \widetilde{\Phi_A} \, \langle \Phi_B \rangle \qquad \text{and} \qquad \langle \overline{\Phi_A} \, \Phi_B \rangle = \overline{\Phi_A} \, \langle \Phi_B \rangle \tag{3.11}$$

  [125].

- With regard to the time average, however, merely the time-invariant mean inherent to an instantaneous field quantity behaves as a constant. Hence, the time average of a product between the periodic perturbation inherent to an instantaneous field quantity and the time-invariant mean of an additional instantaneous field quantity allows the latter to be factored out. Ultimately, time-averaging the periodic perturbation by itself renders a nil value, and thus a nil value for the initial product's time average. In contrast, time-averaging a product between two time-invariant-mean instances is noneffective; i.e., respectively,

$$\overline{\widetilde{\Phi_A} \, \overline{\Phi_B}} = \overline{\widetilde{\Phi_A}} \, \overline{\Phi_B} = 0 \qquad \text{and} \qquad \overline{\overline{\Phi_A} \, \overline{\Phi_B}} = \overline{\Phi_A} \, \overline{\Phi_B} \tag{3.12}$$

  [125].

- Considering the product between the periodic perturbation inherent to an instantaneous field quantity and the erratic fluctuation inherent to an additional instantaneous field quantity, its time average can be said to be equal to time-averaging its phase average. Within the time average, the periodic perturbation can then be factored out from the phase average. Since the remaining phase average of the erratic

fluctuation is equal to a nil value, the initial product's time average is rendered to a nil value as well; i.e.,

$$\overline{\widetilde{\Phi_A}\,(\Phi_B)'} = \overline{\langle \widetilde{\Phi_A}\,(\Phi_B)' \rangle} = \overline{\widetilde{\Phi_A}\,\langle\,(\Phi_B)' \rangle} = 0 \tag{3.13}$$

[125].

- Lastly, both the time average and the phase average of a product between the two inherent erratic fluctuations can be shown to render a value other than nil; i.e., respectively,

$$\langle (\Phi_A)'\,(\Phi_B)' \rangle \neq 0 \qquad \text{and} \qquad \overline{(\Phi_A)'\,(\Phi_B)'} \neq 0 \tag{3.14}$$

[125], referred to as turbulent correlation terms.

Equations (3.8–3.14) are elementary, allowing an extension to the statistical treatment of products between several instantaneous field quantities. Products between the periodic perturbation of two or more instantaneous field quantities are referred to as higher-order perturbation terms.

3.2.2 Spatial Coordinates, Geometric and Kinematic Entities

Considering the instantaneous position vector $\mathbf{r}$ of an individual grid vertex, Eq. (2.1), an imposed $T_{2\pi}$-periodic displacement again permits both a phase average and a time average to be formulated; i.e., substituting $\mathbf{r}$ for Φ, respectively, in Eq. (3.1) and Eq. (3.3). Since there is no erratic fluctuation inherent to the instantaneous position vector, phase-averaging is noneffective per se:

$$\langle \mathbf{r} \rangle(\xi, \eta, \zeta, \tau) = \langle \mathbf{r} \rangle(\xi, \eta, \zeta, \tau + n\,T_{2\pi}) = \mathbf{r}(\xi, \eta, \zeta, \tau)\,. \tag{3.15}$$

Thus, the organized unsteadiness inherent to the instantaneous position vector is equal to the instantaneous position vector itself. As the time average of the instantaneous position vector again renders its time-invariant mean, the inherent periodic perturbation can be obtained through

$$\tilde{\mathbf{r}}(\xi, \eta, \zeta, \tau) := \langle \mathbf{r} \rangle(\xi, \eta, \zeta, \tau) - \bar{\mathbf{r}}(\xi, \eta, \zeta)\,, \tag{3.16}$$

with

$$\tilde{\mathbf{r}}(\xi, \eta, \zeta, \tau) = \tilde{\mathbf{r}}(\xi, \eta, \zeta, \tau + n\,T_{2\pi})\,. \tag{3.17}$$

This allows the instantaneous position vector to be expanded into two parts:

$$\mathbf{r}(\xi, \eta, \tau) = \bar{\mathbf{r}}(\xi, \eta, \zeta) + \tilde{\mathbf{r}}(\xi, \eta, \zeta, \tau)\,, \tag{3.18}$$

with

$$\begin{aligned} \bar{\mathbf{r}} &:= (\,\bar{x}(\xi, \eta, \zeta),\, \bar{y}(\xi, \eta, \zeta),\, \bar{z}(\xi, \eta, \zeta)\,)^T \qquad \text{and} \\ \tilde{\mathbf{r}} &:= (\,\tilde{x}(\xi, \eta, \zeta, \tau),\, \tilde{y}(\xi, \eta, \zeta, \tau),\, \tilde{z}(\xi, \eta, \zeta, \tau)\,)^T\,; \end{aligned} \tag{3.19}$$

based on Pechloff and Laschka [100]. Mathematical identities with respect to the application of the phase average and the time average to $\bar{\mathbf{r}}$ and $\tilde{\mathbf{r}}$ are straightforwardly obtained by substituting $\mathbf{r}$ for Φ_A in Eq. (3.8) and Eq. (3.9). Furthermore, mathematical identities with respect to the application of the phase average and the time average to products between the constituting Cartesian coordinates of $\bar{\mathbf{r}}$ and $\tilde{\mathbf{r}}$ are obtained by substituting x, y, z for Φ_A and Φ_B in Eq. (3.11) and Eq. (3.12) under permutation.

Since both the instantaneous determinant of the coordinate transformation's Jacobian and the instantaneous spatial metric vectors are constituted through the spatial curvilinear derivatives of the Cartesian coordinates, their decomposition into a time-invariant mean and periodic perturbation becomes possible as well. Focusing on the former, Eq. (2.5), the expansion of the constituting Cartesian spatial coordinates according to Eq. (3.18) yields

$$\begin{aligned}
J &= \bar{x}_\xi(\bar{y}_\eta\bar{z}_\zeta - \bar{z}_\eta\bar{y}_\zeta + \bar{y}_\eta\tilde{z}_\zeta - \bar{z}_\eta\tilde{y}_\zeta + \tilde{y}_\eta\bar{z}_\zeta - \tilde{z}_\eta\bar{y}_\zeta + \tilde{y}_\eta\tilde{z}_\zeta - \tilde{z}_\eta\tilde{y}_\zeta) \\
&+ \bar{y}_\xi(\bar{z}_\eta\bar{x}_\zeta - \bar{x}_\eta\bar{z}_\zeta + \bar{z}_\eta\tilde{x}_\zeta - \bar{x}_\eta\tilde{z}_\zeta + \tilde{z}_\eta\bar{x}_\zeta - \tilde{x}_\eta\bar{z}_\zeta + \tilde{z}_\eta\tilde{x}_\zeta - \tilde{x}_\eta\tilde{z}_\zeta) \\
&+ \bar{z}_\xi(\bar{x}_\eta\bar{y}_\zeta - \bar{y}_\eta\bar{x}_\zeta + \bar{x}_\eta\tilde{y}_\zeta - \bar{y}_\eta\tilde{x}_\zeta + \tilde{x}_\eta\bar{y}_\zeta - \tilde{y}_\eta\bar{x}_\zeta + \tilde{x}_\eta\tilde{y}_\zeta - \tilde{y}_\eta\tilde{x}_\zeta) \\
&+ \tilde{x}_\xi(\bar{y}_\eta\bar{z}_\zeta - \bar{z}_\eta\bar{y}_\zeta + \bar{y}_\eta\tilde{z}_\zeta - \bar{z}_\eta\tilde{y}_\zeta + \tilde{y}_\eta\bar{z}_\zeta - \tilde{z}_\eta\bar{y}_\zeta + \tilde{y}_\eta\tilde{z}_\zeta - \tilde{z}_\eta\tilde{y}_\zeta) \\
&+ \tilde{y}_\xi(\bar{z}_\eta\bar{x}_\zeta - \bar{x}_\eta\bar{z}_\zeta + \bar{z}_\eta\tilde{x}_\zeta - \bar{x}_\eta\tilde{z}_\zeta + \tilde{z}_\eta\bar{x}_\zeta - \tilde{x}_\eta\bar{z}_\zeta + \tilde{z}_\eta\tilde{x}_\zeta - \tilde{x}_\eta\tilde{z}_\zeta) \\
&+ \tilde{z}_\xi(\bar{x}_\eta\bar{y}_\zeta - \bar{y}_\eta\bar{x}_\zeta + \bar{x}_\eta\tilde{y}_\zeta - \bar{y}_\eta\tilde{x}_\zeta + \tilde{x}_\eta\bar{y}_\zeta - \tilde{y}_\eta\bar{x}_\zeta + \tilde{x}_\eta\tilde{y}_\zeta - \tilde{y}_\eta\tilde{x}_\zeta)\,.
\end{aligned} \tag{3.20}$$

On the basis of Eq. (3.15), phase-averaging Eq. (3.20) is noneffective; i.e.,

$$\langle J \rangle = J\,. \tag{3.21}$$

Thus, the organized unsteadiness inherent to the instantaneous determinant of the coordinate transformation's Jacobian is equal to the instantaneous determinant of the coordinate transformation's Jacobian itself. Time-averaging, on the other hand, renders

$$\begin{aligned}
\overline{J} &= \bar{x}_\xi(\bar{y}_\eta\bar{z}_\zeta - \bar{z}_\eta\bar{y}_\zeta + \overline{\tilde{y}_\eta\tilde{z}_\zeta} - \overline{\tilde{z}_\eta\tilde{y}_\zeta}) \\
&+ \bar{y}_\xi(\bar{z}_\eta\bar{x}_\zeta - \bar{x}_\eta\bar{z}_\zeta + \overline{\tilde{z}_\eta\tilde{x}_\zeta} - \overline{\tilde{x}_\eta\tilde{z}_\zeta}) \\
&+ \bar{z}_\xi(\bar{x}_\eta\bar{y}_\zeta - \bar{y}_\eta\bar{x}_\zeta + \overline{\tilde{x}_\eta\tilde{y}_\zeta} - \overline{\tilde{y}_\eta\tilde{x}_\zeta}) \\
&+ \bar{y}_\eta\overline{\tilde{x}_\xi\tilde{z}_\zeta} - \bar{z}_\eta\overline{\tilde{x}_\xi\tilde{y}_\zeta} + \overline{\tilde{x}_\xi\tilde{y}_\eta}\bar{z}_\zeta - \overline{\tilde{x}_\xi\tilde{z}_\eta}\bar{y}_\zeta + \overline{\tilde{x}_\xi\tilde{y}_\eta\tilde{z}_\zeta} - \overline{\tilde{x}_\xi\tilde{z}_\eta\tilde{y}_\zeta} \\
&+ \bar{z}_\eta\overline{\tilde{y}_\xi\tilde{x}_\zeta} - \bar{x}_\eta\overline{\tilde{y}_\xi\tilde{z}_\zeta} + \overline{\tilde{y}_\xi\tilde{z}_\eta}\bar{x}_\zeta - \overline{\tilde{y}_\xi\tilde{x}_\eta}\bar{z}_\zeta + \overline{\tilde{y}_\xi\tilde{z}_\eta\tilde{x}_\zeta} - \overline{\tilde{y}_\xi\tilde{x}_\eta\tilde{z}_\zeta} \\
&+ \bar{x}_\eta\overline{\tilde{z}_\xi\tilde{y}_\zeta} - \bar{y}_\eta\overline{\tilde{z}_\xi\tilde{x}_\zeta} + \overline{\tilde{z}_\xi\tilde{x}_\eta}\bar{y}_\zeta - \overline{\tilde{z}_\xi\tilde{y}_\eta}\bar{x}_\zeta + \overline{\tilde{z}_\xi\tilde{x}_\eta\tilde{y}_\zeta} - \overline{\tilde{z}_\xi\tilde{y}_\eta\tilde{x}_\zeta}\,;
\end{aligned} \tag{3.22}$$

i.e., the time-invariant mean. In analogy to Eq. (3.16), the periodic perturbation inherent to the determinant of the coordinate transformation's Jacobian is then obtained through

subtraction of the time-invariant mean from the organized unsteady instance:

$$\begin{aligned}
\widetilde{J} \;&:=\; \langle J \rangle - \overline{J} \\
&=\; \bar{x}_\xi(\bar{y}_\eta\tilde{z}_\zeta - \bar{z}_\eta\tilde{y}_\zeta + \tilde{y}_\eta\bar{z}_\zeta - \tilde{z}_\eta\bar{y}_\zeta + \tilde{y}_\eta\tilde{z}_\zeta - \tilde{z}_\eta\tilde{y}_\zeta - \overline{\tilde{y}_\eta\tilde{z}_\zeta} + \overline{\tilde{z}_\eta\tilde{y}_\zeta}) \\
&+\; \bar{y}_\xi(\bar{z}_\eta\tilde{x}_\zeta - \bar{x}_\eta\tilde{z}_\zeta + \tilde{z}_\eta\bar{x}_\zeta - \tilde{x}_\eta\bar{z}_\zeta + \tilde{z}_\eta\tilde{x}_\zeta - \tilde{x}_\eta\tilde{z}_\zeta - \overline{\tilde{z}_\eta\tilde{x}_\zeta} + \overline{\tilde{x}_\eta\tilde{z}_\zeta}) \\
&+\; \bar{z}_\xi(\bar{x}_\eta\tilde{y}_\zeta - \bar{y}_\eta\tilde{x}_\zeta + \tilde{x}_\eta\bar{y}_\zeta - \tilde{y}_\eta\bar{x}_\zeta + \tilde{x}_\eta\tilde{y}_\zeta - \tilde{y}_\eta\tilde{x}_\zeta - \overline{\tilde{x}_\eta\tilde{y}_\zeta} + \overline{\tilde{y}_\eta\tilde{x}_\zeta}) \\
&+\; \tilde{x}_\xi(\bar{y}_\eta\bar{z}_\zeta - \bar{z}_\eta\bar{y}_\zeta + \bar{y}_\eta\tilde{z}_\zeta - \bar{z}_\eta\tilde{y}_\zeta + \tilde{y}_\eta\bar{z}_\zeta - \tilde{z}_\eta\bar{y}_\zeta + \tilde{y}_\eta\tilde{z}_\zeta - \tilde{z}_\eta\tilde{y}_\zeta) \\
&+\; \tilde{y}_\xi(\bar{z}_\eta\bar{x}_\zeta - \bar{x}_\eta\bar{z}_\zeta + \bar{z}_\eta\tilde{x}_\zeta - \bar{x}_\eta\tilde{z}_\zeta + \tilde{z}_\eta\bar{x}_\zeta - \tilde{x}_\eta\bar{z}_\zeta + \tilde{z}_\eta\tilde{x}_\zeta - \tilde{x}_\eta\tilde{z}_\zeta) \\
&+\; \tilde{z}_\xi(\bar{x}_\eta\bar{y}_\zeta - \bar{y}_\eta\bar{x}_\zeta + \bar{x}_\eta\tilde{y}_\zeta - \bar{y}_\eta\tilde{x}_\zeta + \tilde{x}_\eta\bar{y}_\zeta - \tilde{y}_\eta\bar{x}_\zeta + \tilde{x}_\eta\tilde{y}_\zeta - \tilde{y}_\eta\tilde{x}_\zeta) \\
&-\; \bar{y}_\eta\overline{\tilde{x}_\xi\tilde{z}_\zeta} + \bar{z}_\eta\overline{\tilde{x}_\xi\tilde{y}_\zeta} - \overline{\tilde{x}_\xi\tilde{y}_\eta}\bar{z}_\zeta + \overline{\tilde{x}_\xi\tilde{z}_\eta}\bar{y}_\zeta - \overline{\tilde{x}_\xi\tilde{y}_\eta\tilde{z}_\zeta} + \overline{\tilde{x}_\xi\tilde{z}_\eta\tilde{y}_\zeta} \\
&-\; \bar{z}_\eta\overline{\tilde{y}_\xi\tilde{x}_\zeta} + \bar{x}_\eta\overline{\tilde{y}_\xi\tilde{z}_\zeta} - \overline{\tilde{y}_\xi\tilde{z}_\eta}\bar{x}_\zeta + \overline{\tilde{y}_\xi\tilde{x}_\eta}\bar{z}_\zeta - \overline{\tilde{y}_\xi\tilde{z}_\eta\tilde{x}_\zeta} + \overline{\tilde{y}_\xi\tilde{x}_\eta\tilde{z}_\zeta} \\
&-\; \bar{x}_\eta\overline{\tilde{z}_\xi\tilde{y}_\zeta} + \bar{y}_\eta\overline{\tilde{z}_\xi\tilde{x}_\zeta} - \overline{\tilde{z}_\xi\tilde{x}_\eta}\bar{y}_\zeta + \overline{\tilde{z}_\xi\tilde{y}_\eta}\bar{x}_\zeta - \overline{\tilde{z}_\xi\tilde{x}_\eta\tilde{y}_\zeta} + \overline{\tilde{z}_\xi\tilde{y}_\eta\tilde{x}_\zeta}\,.
\end{aligned} \tag{3.23}$$

This allows the instantaneous determinant of the coordinate transformation's Jacobian to be expanded into two parts:

$$J = \overline{J} + \widetilde{J} \tag{3.24}$$

[100].

Derived equivalently, the instantaneous generalized spatial metric vector, Eq. (2.20), is expanded as

$$\boldsymbol{J\psi} = \overline{\boldsymbol{J\psi}} + \widetilde{\boldsymbol{J\psi}} \tag{3.25}$$

[100], with

$$\overline{\boldsymbol{J\psi}} := \left(\overline{J\psi_x},\, \overline{J\psi_y},\, \overline{J\psi_z}\right)^T \quad \text{and} \quad \widetilde{\boldsymbol{J\psi}} := \langle \boldsymbol{J\psi} \rangle - \overline{\boldsymbol{J\psi}} = \left(\widetilde{J\psi_x},\, \widetilde{J\psi_y},\, \widetilde{J\psi_z}\right)^T , \tag{3.26}$$

respectively, being the time-invariant mean and the inherent periodic perturbation of the instantaneous generalized spatial metric vector.

Lastly, the insertion of both Eq. (3.18) and Eq. (3.25) into the instantaneous generalized temporal metric, Eq. (2.21), yields

$$J\psi_t = -\frac{\partial\tilde{\mathbf{r}}}{\partial\tau}\,\overline{\boldsymbol{J\psi}} - \frac{\partial\tilde{\mathbf{r}}}{\partial\tau}\,\widetilde{\boldsymbol{J\psi}}\,, \qquad \text{as} \qquad \frac{\partial\bar{\mathbf{r}}}{\partial\tau} = 0\,, \tag{3.27}$$

with the inherent organized unsteadiness being equal to it:

$$\langle J\psi_t \rangle = J\psi_t\,. \tag{3.28}$$

Complementarily, the time-invariant mean of the instantaneous generalized temporal metric becomes

$$\overline{J\psi_t} = -\overline{\frac{\partial\tilde{\mathbf{r}}}{\partial\tau}\,\widetilde{\boldsymbol{J\psi}}}\,, \qquad \text{as} \qquad \overline{\frac{\partial\tilde{\mathbf{r}}}{\partial\tau}} = 0\,, \tag{3.29}$$

rendering the inherent periodic perturbation:

$$\widetilde{J\psi_t} := \langle J\psi_t \rangle - \overline{J\psi_t} = -\frac{\partial \tilde{\mathbf{r}}}{\partial \tau}\,\overline{\boldsymbol{J\psi}} - \frac{\partial \tilde{\mathbf{r}}}{\partial \tau}\,\widetilde{\boldsymbol{J\psi}} + \overline{\frac{\partial \tilde{\mathbf{r}}}{\partial \tau}\,\widetilde{\boldsymbol{J\psi}}}\,. \tag{3.30}$$

The instantaneous generalized temporal metric can then be expanded into two parts:

$$J\psi_t = \overline{J\psi_t} + \widetilde{J\psi_t} \tag{3.31}$$

[100].

Evidently, J, $\boldsymbol{J\psi}$, and $J\psi_t$ behave dynamically fully nonlinearly even for an $\mathbf{r}$ governed by a simple harmonic. This circumstance follows through to $\widetilde{J}$, $\widetilde{\boldsymbol{J\psi}}$, and $\widetilde{J\psi_t}$, respectively, by way of Eq. (3.23), Eq. (3.26), and Eq. (3.30). Mathematical identities with respect to the application of the phase average and the time average to $\overline{J}$, $\overline{\boldsymbol{J\psi}}$, and $\overline{J\psi_t}$, as well as $\widetilde{J}$, $\widetilde{\boldsymbol{J\psi}}$, and $\widetilde{J\psi_t}$, are straightforwardly obtained by substituting J, $\boldsymbol{J\psi}$, or $J\psi_t$ for Φ_A in Eq. (3.8) and Eq. (3.9). Furthermore, mathematical identities with respect to the application of the phase average and the time average to products between $\overline{J}$, $\overline{\boldsymbol{J\psi}}$, $\overline{J\psi_t}$, as well as $\widetilde{J}$, $\widetilde{\boldsymbol{J\psi}}$, $\widetilde{J\psi_t}$, and an instantaneous field quantity are obtained by substituting J, $\boldsymbol{J\psi}$, or $J\psi_t$ for Φ_A in Eq. (3.11) and Eq. (3.12).

The preceding decomposition differs from the instance provided by Kreiselmaier [70], and subsequently utilized by Sickmüller [119] as well as Iatrou [54]. They had categorized the expanded geometric and kinematic entities into a steady (reference) and unsteady (perturbation) part, with the reference part being independent from the Cartesian coordinates' perturbation amplitude. In contrast, the geometric and kinematic entities' time-invariant mean is partially constituted by the curvilinear derivatives of the Cartesian coordinates' periodic perturbation. These make the geometric and kinematic entities' time-invariant mean dependent on the Cartesian coordinates' perturbation amplitude. Hence, the geometric and kinematic entities' time-invariant mean will generally differ from the categorized reference part. Naturally, their periodic perturbation will then differ from the categorized perturbation part as well.

3.3 Treatment of Higher-Order Perturbation and Turbulent Correlation Terms

The decomposition of the instantaneous Navier-Stokes equations is based on the expansion of the constituting primitive variables; see Pechloff and Laschka [99, 100]. For the stipulated problem, the turbulence structure inherent to a compressible wall-bounded flow can be considered equivalent to the turbulence structure inherent to an incompressible instance, as originally hypothesized by Morkovin [87]; also see Hoffmann and Chiang [51], as well as Wilcox [139]. Hence, it is permissible to omit the erratic fluctuation from the

expansion of the instantaneous density outright [100], which facilitates the decomposition substantially. Deviating from the process described in Sec. 3.1, the decomposition is performed on each element of the generalized instantaneous convective and viscous flux vector separately. Thus, neither the governing equation system of the organized unsteady flowfield nor its time-invariant-mean counterpart are explicitly formulated here. Furthermore, the small disturbance premise is invoked immediately after the particular statistical technique's application. With higher-order perturbation terms neglected, a linearized organized unsteady and a linearized time-invariant-mean instance of the considered element are rendered. The linearized periodic-perturbation instance is then simply obtained through subtraction of the latter from the former. Intermediately, emerging turbulent correlation terms are physically classified, and ultimately resolved as far as possible.

3.3.1 Mass Flux

The first element of the generalized convective flux vector, $E_{\psi\,1}$, embodies the ψ-directional mass flux. It is initially deconstructed into summation terms consistent with the generalized metrics:

$$\begin{aligned} E_{\psi\,1} \;:=\; \rho\,\theta_\psi \;&=\; J\psi_t\,\rho \;+\; J\psi_x\,\rho u \;+\; J\psi_y\,\rho v \;+\; J\psi_z\,\rho w \\ &=\; E_{\psi\,10} \;+\; E_{\psi\,11} \;+\; E_{\psi\,12} \;+\; E_{\psi\,13}\,. \end{aligned} \tag{3.32}$$

The generalized metrics, the instantaneous density, and the instantaneous Cartesian velocities are then expanded:

$$\begin{aligned} E_{\psi\,10} &= (\,\overline{J\psi_t} + \widetilde{J\psi_t}\,) \quad (\bar\rho + \tilde\rho)\,, \\ E_{\psi\,11} &= (\,\overline{J\psi_x} + \widetilde{J\psi_x}\,) \quad (\bar\rho\bar u + \bar\rho\tilde u + \bar\rho u' + \tilde\rho\bar u + \tilde\rho\tilde u + \tilde\rho u')\,, \\ E_{\psi\,12} &= (\,\overline{J\psi_y} + \widetilde{J\psi_y}\,) \quad (\bar\rho\bar v + \bar\rho\tilde v + \bar\rho v' + \tilde\rho\bar v + \tilde\rho\tilde v + \tilde\rho v')\,, \\ E_{\psi\,13} &= (\,\overline{J\psi_z} + \widetilde{J\psi_z}\,) \quad (\bar\rho\bar w + \bar\rho\tilde w + \bar\rho w' + \tilde\rho\bar w + \tilde\rho\tilde w + \tilde\rho w')\,. \end{aligned} \tag{3.33}$$

In a second step, the individual terms of Eq. (3.33) are phase-averaged. Taking into account the given mathematical identities, the statistical reduction

$$\begin{aligned} \langle E_{\psi\,10}\rangle &= (\,\overline{J\psi_t} + \widetilde{J\psi_t}\,) \quad (\bar\rho + \tilde\rho)\,, \\ \langle E_{\psi\,11}\rangle &= (\,\overline{J\psi_x} + \widetilde{J\psi_x}\,) \quad (\bar\rho\bar u + \bar\rho\tilde u + \tilde\rho\bar u + \tilde\rho\tilde u)\,, \\ \langle E_{\psi\,12}\rangle &= (\,\overline{J\psi_y} + \widetilde{J\psi_y}\,) \quad (\bar\rho\bar v + \bar\rho\tilde v + \tilde\rho\bar v + \tilde\rho\tilde v)\,, \\ \langle E_{\psi\,13}\rangle &= (\,\overline{J\psi_z} + \widetilde{J\psi_z}\,) \quad (\bar\rho\bar w + \bar\rho\tilde w + \tilde\rho\bar w + \tilde\rho\tilde w) \end{aligned} \tag{3.34}$$

is gained. Particularly, since the erratic fluctuation of each Cartesian velocity occurs only in a product with either the time-invariant-mean or periodic-perturbation density, no

turbulent correlation terms remain. Furthermore, both the time-invariant-mean and the periodic-perturbation generalized metrics are constants with respect to the phase average, allowing their factorization to be retained. Lastly, a number of higher-order perturbation terms exist in Eq. (3.34). They are constituted either through a product of periodic-perturbation primitive field quantities (e.g., $\overline{J\psi_x}\,\tilde{\rho}\tilde{u}$) or through a product of a periodic-perturbation generalized metric and a singly occurring periodic-perturbation primitive field quantity (e.g., $\widetilde{J\psi_x}\,\bar{\rho}\tilde{u}$) [100]. Additionally, both the time-invariant-mean and the periodic-perturbation generalized metrics are constituted by several summands qualifying as higher-order perturbation terms; i.e., they exhibit products between curvilinear coordinate derivatives of the periodic-perturbation Cartesian spatial coordinates and/or time-averaged instances thereof. Invoking the premise of small disturbances, said terms are considered insignificant, and subsequently discounted [100]. This procedure is equivalent to an entity's linearization with respect to the inherent periodic perturbation; in the following, indicated by the $(\ )^*$ modifier [100]. Thus, Eq. (3.34) eventually becomes

$$\begin{aligned}
\langle E_{\psi\,10}\rangle^* &= \overline{J\psi_t}^*(\bar{\rho}+\tilde{\rho}) &&+ \widetilde{J\psi_t}^*\,\bar{\rho}\,,\\
\langle E_{\psi\,11}\rangle^* &= \overline{J\psi_x}^*(\bar{\rho}\bar{u}+\bar{\rho}\tilde{u}+\tilde{\rho}\bar{u}) &&+ \widetilde{J\psi_x}^*\,\bar{\rho}\bar{u}\,,\\
\langle E_{\psi\,12}\rangle^* &= \overline{J\psi_y}^*(\bar{\rho}\bar{v}+\bar{\rho}\tilde{v}+\tilde{\rho}\bar{v}) &&+ \widetilde{J\psi_y}^*\,\bar{\rho}\bar{v}\,,\\
\langle E_{\psi\,13}\rangle^* &= \overline{J\psi_z}^*(\bar{\rho}\bar{w}+\bar{\rho}\tilde{w}+\tilde{\rho}\bar{w}) &&+ \widetilde{J\psi_z}^*\,\bar{\rho}\bar{w}\,.
\end{aligned} \tag{3.35}$$

In a third step, the individual terms of Eq. (3.33) are time-averaged. Again taking into account the given mathematical identities, the statistical reduction

$$\begin{aligned}
\overline{E_{\psi\,10}} &= \overline{J\psi_t}\,\bar{\rho} &&&&+ \overline{\widetilde{J\psi_t}\tilde{\rho}} &&,\\
\overline{E_{\psi\,11}} &= \overline{J\psi_x}\,(\bar{\rho}\bar{u}+\overline{\tilde{\rho}\tilde{u}}) &+ \bar{\rho}\,\overline{\widetilde{J\psi_x}\tilde{u}} &+ \bar{u}\,\overline{\widetilde{J\psi_x}\tilde{\rho}} &+ \overline{\widetilde{J\psi_x}\tilde{u}\tilde{\rho}}\,,\\
\overline{E_{\psi\,12}} &= \overline{J\psi_y}\,(\bar{\rho}\bar{v}+\overline{\tilde{\rho}\tilde{v}}) &+ \bar{\rho}\,\overline{\widetilde{J\psi_y}\tilde{v}} &+ \bar{v}\,\overline{\widetilde{J\psi_y}\tilde{\rho}} &+ \overline{\widetilde{J\psi_y}\tilde{v}\tilde{\rho}}\,,\\
\overline{E_{\psi\,13}} &= \overline{J\psi_z}\,(\bar{\rho}\bar{w}+\overline{\tilde{\rho}\tilde{w}}) &+ \bar{\rho}\,\overline{\widetilde{J\psi_z}\tilde{w}} &+ \bar{w}\,\overline{\widetilde{J\psi_z}\tilde{\rho}} &+ \overline{\widetilde{J\psi_z}\tilde{w}\tilde{\rho}}\,,
\end{aligned} \tag{3.36}$$

is complementarily gained. Equal to the phase average, the time average has eliminated the erratic fluctuations inherent to Eq. (3.33). The periodic-perturbation generalized metrics, however, are not constants with respect to the time average, disallowing their refactorization. Consequently, the higher-order perturbation terms of Eq. (3.36) are not only constituted by time-averaged products between periodic-perturbation primitive field quantities (e.g., $\overline{J\psi_x}\,\overline{\tilde{\rho}\tilde{u}}$), but also constituted by time-averaged products between periodic-perturbation generalized metrics and periodic-perturbation primitive field quantities (e.g., $\bar{\rho}\,\overline{\widetilde{J\psi_x}\tilde{u}}$). Linearization simplifies Eq. (3.36) substantially:

$$\overline{E_{\psi\,10}}^* = \overline{J\psi_t}^*\,\bar{\rho}\,,\quad \overline{E_{\psi\,11}}^* = \overline{J\psi_x}^*\,\bar{\rho}\bar{u}\,,\quad \overline{E_{\psi\,12}}^* = \overline{J\psi_y}^*\,\bar{\rho}\bar{v}\,,\quad \overline{E_{\psi\,13}}^* = \overline{J\psi_z}^*\,\bar{\rho}\bar{w}\,, \tag{3.37}$$

which are all exclusively products between a linearized time-invariant-mean generalized metric and time-invariant-mean primitive field quantities.

Ultimately, Eq. (3.37) is subtracted from Eq. (3.35); i.e.,

$$\begin{aligned}
\widetilde{E_{\psi\,10}}^{*} &:= \langle\, E_{\psi\,10}\,\rangle^{*} - \overline{E_{\psi\,10}}^{*} = \overline{J\psi_t}^{*}\,\tilde{\rho} + \widetilde{J\psi_t}^{*}\,\bar{\rho}\,,\\
\widetilde{E_{\psi\,11}}^{*} &:= \langle\, E_{\psi\,11}\,\rangle^{*} - \overline{E_{\psi\,11}}^{*} = \overline{J\psi_x}^{*}\,(\bar{\rho}\tilde{u} + \tilde{\rho}\bar{u}) + \widetilde{J\psi_x}^{*}\,\bar{\rho}\bar{u}\,,\\
\widetilde{E_{\psi\,12}}^{*} &:= \langle\, E_{\psi\,12}\,\rangle^{*} - \overline{E_{\psi\,12}}^{*} = \overline{J\psi_y}^{*}\,(\bar{\rho}\tilde{v} + \tilde{\rho}\bar{v}) + \widetilde{J\psi_y}^{*}\,\bar{\rho}\bar{v}\,,\\
\widetilde{E_{\psi\,13}}^{*} &:= \langle\, E_{\psi\,13}\,\rangle^{*} - \overline{E_{\psi\,13}}^{*} = \overline{J\psi_z}^{*}\,(\bar{\rho}\tilde{w} + \tilde{\rho}\bar{w}) + \widetilde{J\psi_z}^{*}\,\bar{\rho}\bar{w}\,,
\end{aligned} \tag{3.38}$$

eliminating the terms constituted by products between a linearized time-invariant-mean generalized metric and time-invariant-mean primitive field quantities. Hence, $\widetilde{E_{\psi\,10}}^{*}$, $\widetilde{E_{\psi\,11}}^{*}$, $\widetilde{E_{\psi\,12}}^{*}$, and $\widetilde{E_{\psi\,13}}^{*}$ are strictly linear in both the unknown periodic perturbation of the primitive field quantities and the known periodic perturbation of the Cartesian spatial coordinates as embodied by the linearized periodic-perturbation generalized metrics. Their summation renders the linearized periodic-perturbation mass flux in ψ direction, which is the first element of the linearized periodic-perturbation generalized convective flux vector:

$$\widetilde{E_{\psi\,1}}^{*} := \widetilde{E_{\psi\,10}}^{*} + \widetilde{E_{\psi\,11}}^{*} + \widetilde{E_{\psi\,12}}^{*} + \widetilde{E_{\psi\,13}}^{*} = \bar{\rho}\,\widetilde{\theta_\psi}^{*} + \tilde{\rho}\,\overline{\theta_\psi}^{*}\,, \tag{3.39}$$

having introduced the linearized periodic-perturbation generalized contravariant velocity

$$\widetilde{\theta_\psi}^{*} := \overline{J\psi_x}^{*}\,\tilde{u} + \overline{J\psi_y}^{*}\,\tilde{v} + \overline{J\psi_z}^{*}\,\tilde{w} + \widetilde{J\psi_x}^{*}\,\bar{u} + \widetilde{J\psi_y}^{*}\,\bar{v} + \widetilde{J\psi_z}^{*}\,\bar{w} + \widetilde{J\psi_t}^{*} \tag{3.40}$$

and its linearized time-invariant-mean counterpart

$$\overline{\theta_\psi}^{*} := \overline{J\psi_x}^{*}\,\bar{u} + \overline{J\psi_y}^{*}\,\bar{v} + \overline{J\psi_z}^{*}\,\bar{w} + \overline{J\psi_t}^{*}\,. \tag{3.41}$$

Both instances are verifiable through the decomposition and subsequent linearization of θ_ψ, Eq. (2.9), itself. They conform, respectively, to the linearized periodic-perturbation generalized contravariant velocity and its linearized time-invariant-mean counterpart in the small disturbance Euler equations' time-domain formulation [70].

The generalized viscous flux vector does not contribute to the mass-per-unit-volume's time rate of change. Consequently, its linearized periodic-perturbation instance does not either; i.e.,

$$E_{\mathrm{v}\,\psi\,1} = 0\,, \qquad \text{and thus} \qquad \widetilde{E_{\mathrm{v}\,\psi\,1}}^{*} := 0\,. \tag{3.42}$$

3.3.2 Momentum Flux

Both the generalized convective flux vector and the generalized viscous flux vector contribute to each Cartesian momentum-per-unit-volume's time rate of change through

momentum-flux elements. Specifically, these are the respective second, third, and fourth elements; i.e., $E_{\psi\,2}$, $E_{\psi\,3}$, and $E_{\psi\,4}$, as well as $E_{\mathrm{v}\,\psi\,2}$, $E_{\mathrm{v}\,\psi\,3}$, and $E_{\mathrm{v}\,\psi\,4}$. In the following, $E_{\psi\,2}$ and $E_{\mathrm{v}\,\psi\,2}$ are considered representatively. They embody the x-directional contribution of the ψ-directional convective and viscous momentum flux.

3.3.2.1 Convective Instance

The initial deconstruction of $E_{\psi\,2}$ into summation terms consistent with the generalized metrics becomes

$$\begin{aligned} E_{\psi\,2} \;:=\; \rho u\,\theta_{\psi} + J\psi_x\,p \;&=\; J\psi_t\,\rho u \;+\; J\psi_x\,(\rho u^2 + p) \;+\; J\psi_y\,\rho uv \;+\; J\psi_z\,\rho uw \\ &=\; E_{\psi\,20} \;+\; E_{\psi\,21} \;+\; E_{\psi\,22} \;+\; E_{\psi\,23}\,; \end{aligned} \tag{3.43}$$

based on [100]. Subsequently, the generalized metrics, the instantaneous density, the instantaneous Cartesian velocities, and the instantaneous static pressure are expanded:

$$\begin{aligned} E_{\psi\,20} &= (\,\overline{J\psi_t} + \widetilde{J\psi_t}\,) \quad (\bar\rho\bar u + \bar\rho\tilde u + \bar\rho u' + \tilde\rho\bar u + \tilde\rho\tilde u + \tilde\rho u')\,, \\ E_{\psi\,21} &= (\,\overline{J\psi_x} + \widetilde{J\psi_x}\,) \quad (\bar\rho\bar u^2 + 2\bar\rho\bar u\tilde u + 2\bar\rho\bar u u' + 2\bar\rho\tilde u u' + \bar\rho\tilde u^2 + \bar\rho\,u'u' \\ &\qquad + \tilde\rho\bar u^2 + 2\tilde\rho\bar u\tilde u + 2\tilde\rho\bar u u' + 2\tilde\rho\tilde u u' + \tilde\rho\tilde u^2 + \tilde\rho\,u'u' \\ &\qquad + \bar p + \tilde p + p')\,, \\ E_{\psi\,22} &= (\,\overline{J\psi_y} + \widetilde{J\psi_y}\,) \quad (\bar\rho\bar u\bar v + \bar\rho\bar u\tilde v + \bar\rho\bar u v' + \bar\rho\tilde u\bar v + \bar\rho\tilde u\tilde v + \bar\rho\tilde u v' \\ &\qquad + \bar\rho u'\bar v + \bar\rho u'\tilde v + \bar\rho u'v' \\ &\qquad + \tilde\rho\bar u\bar v + \tilde\rho\bar u\tilde v + \tilde\rho\bar u v' + \tilde\rho\tilde u\bar v + \tilde\rho\tilde u\tilde v + \tilde\rho\tilde u v' \\ &\qquad + \tilde\rho u'\bar v + \tilde\rho u'\tilde v + \tilde\rho u'v')\,, \\ E_{\psi\,23} &= (\,\overline{J\psi_z} + \widetilde{J\psi_z}\,) \quad (\bar\rho\bar u\bar w + \bar\rho\bar u\tilde w + \bar\rho\bar u w' + \bar\rho\tilde u\bar w + \bar\rho\tilde u\tilde w + \bar\rho\tilde u w' \\ &\qquad + \bar\rho u'\bar w + \bar\rho u'\tilde w + \bar\rho u'w' \\ &\qquad + \tilde\rho\bar u\bar w + \tilde\rho\bar u\tilde w + \tilde\rho\bar u w' + \tilde\rho\tilde u\bar w + \tilde\rho\tilde u\tilde w + \tilde\rho\tilde u w' \\ &\qquad + \tilde\rho u'\bar w + \tilde\rho u'\tilde w + \tilde\rho u'w')\,, \end{aligned} \tag{3.44}$$

wherein products between the erratic fluctuation of the x-directional Cartesian velocity and the erratic fluctuation of each Cartesian velocity novelly occur.

The phase average statistically reduces Eq. (3.44) to

$$\begin{aligned}
\langle\, E_{\psi\,20}\,\rangle &= (\,\overline{J\psi_t} + \widetilde{J\psi_t}\,)\quad (\bar\rho\bar u + \bar\rho\tilde u + \tilde\rho\bar u + \tilde\rho\tilde u)\,,\\
\langle\, E_{\psi\,21}\,\rangle &= (\,\overline{J\psi_x} + \widetilde{J\psi_x}\,)\quad (\bar\rho\bar u^2 + 2\bar\rho\bar u\tilde u + 2\tilde\rho\tilde u\bar u + \tilde\rho\bar u^2 + \bar\rho\tilde u^2 + \tilde\rho\tilde u^2\\
&\qquad\qquad +\langle\,\langle\,\rho\,\rangle\,u'u'\,\rangle + \langle\,p\,\rangle)\,,\\
\langle\, E_{\psi\,22}\,\rangle &= (\,\overline{J\psi_y} + \widetilde{J\psi_y}\,)\quad (\bar\rho\bar u\bar v + \bar\rho\bar u\tilde v + \bar\rho\tilde u\bar v + \bar\rho\tilde u\tilde v + \tilde\rho\bar u\bar v + \tilde\rho\bar u\tilde v + \tilde\rho\tilde u\tilde v\\
&\qquad\qquad +\langle\,\langle\,\rho\,\rangle\,u'v'\,\rangle)\,,\\
\langle\, E_{\psi\,23}\,\rangle &= (\,\overline{J\psi_z} + \widetilde{J\psi_z}\,)\quad (\bar\rho\bar u\bar w + \bar\rho\bar u\tilde w + \bar\rho\tilde u\bar w + \bar\rho\tilde u\tilde w + \tilde\rho\bar u\bar w + \tilde\rho\bar u\tilde w + \tilde\rho\tilde u\tilde w\\
&\qquad\qquad +\langle\,\langle\,\rho\,\rangle\,u'w'\,\rangle)\,;
\end{aligned} \tag{3.45}$$

based on [100]. Terms that are inherently linear with respect to the erratic fluctuation of a Cartesian velocity have again been eliminated, as well as the erratic fluctuation of the static pressure itself. In contrast, the phase-averaged products between the erratic fluctuations of two Cartesian velocities persist; i.e., on account of the first mathematical identity given in Eq. (3.14). Hence, the influence of turbulence on this particular convective instance of the momentum flux has been wholly compounded into $\langle\,\langle\,\rho\,\rangle\,u'u'\,\rangle$, $\langle\,\langle\,\rho\,\rangle\,u'v'\,\rangle$, $\langle\,\langle\,\rho\,\rangle\,u'w'\,\rangle$ [100]. On the basis of both Acharya [1] and Norris [92], these turbulent correlation terms are identified as elements of an organized unsteady Reynolds stress tensor. They are nonlinear with respect to the inherent periodic perturbation:

$$\begin{aligned}
\langle\,\langle\,\rho\,\rangle\,u'u'\,\rangle &= \bar\rho\,\overline{u'u'} + \tilde\rho\,\overline{u'u'} + \bar\rho\,\widetilde{u'u'} + \tilde\rho\,\widetilde{u'u'}\,, \quad \text{with}\quad \widetilde{u'u'} := \langle\,u'u'\,\rangle - \overline{u'u'}\,;\\
\langle\,\langle\,\rho\,\rangle\,u'v'\,\rangle &= \bar\rho\,\overline{u'v'} + \tilde\rho\,\overline{u'v'} + \bar\rho\,\widetilde{u'v'} + \tilde\rho\,\widetilde{u'v'}\,, \quad \text{with}\quad \widetilde{u'v'} := \langle\,u'v'\,\rangle - \overline{u'v'}\,;\\
\langle\,\langle\,\rho\,\rangle\,u'w'\,\rangle &= \bar\rho\,\overline{u'w'} + \tilde\rho\,\overline{u'w'} + \bar\rho\,\widetilde{u'w'} + \tilde\rho\,\widetilde{u'w'}\,, \quad \text{with}\quad \widetilde{u'w'} := \langle\,u'w'\,\rangle - \overline{u'w'}\,.
\end{aligned} \tag{3.46}$$

On account of the second mathematical identity given in Eq. (3.14), time-averaged products between the erratic fluctuations of two Cartesian velocities persist as well. Time-averaging the organized unsteady Reynolds stress tensor renders the inherent time-invariant mean. In this regard, the specific elements provided in Eq. (3.46) yield

$$\begin{aligned}
\overline{\langle\,\rho\,\rangle\,u'u'} &= \overline{\langle\,\langle\,\rho\,\rangle\,u'u'\,\rangle} = \bar\rho\,\overline{u'u'} + \overline{\tilde\rho\,\widetilde{u'u'}}\,, \quad \text{as}\quad \overline{\widetilde{u'u'}} = 0\,;\\
\overline{\langle\,\rho\,\rangle\,u'v'} &= \overline{\langle\,\langle\,\rho\,\rangle\,u'v'\,\rangle} = \bar\rho\,\overline{u'v'} + \overline{\tilde\rho\,\widetilde{u'v'}}\,, \quad \text{as}\quad \overline{\widetilde{u'v'}} = 0\,;\\
\overline{\langle\,\rho\,\rangle\,u'w'} &= \overline{\langle\,\langle\,\rho\,\rangle\,u'w'\,\rangle} = \bar\rho\,\overline{u'w'} + \overline{\tilde\rho\,\widetilde{u'w'}}\,, \quad \text{as}\quad \overline{\widetilde{u'w'}} = 0\,.
\end{aligned} \tag{3.47}$$

Complementarily, the periodic perturbation inherent to the organized unsteady Reynolds

stress tensor is gained by subtracting the inherent time-invariant mean from it; i.e.,

$$\begin{aligned}
\widetilde{\langle\,\rho\,\rangle\,u'u'} &:= \langle\,\langle\,\rho\,\rangle\,u'u'\,\rangle - \overline{\langle\,\rho\,\rangle\,u'u'} &&= \tilde{\rho}\,\overline{u'u'} + \bar{\rho}\,\widetilde{u'u'} + \tilde{\rho}\,\widetilde{u'u'} - \overline{\tilde{\rho}\,\widetilde{u'u'}}\,,\\
\widetilde{\langle\,\rho\,\rangle\,u'v'} &:= \langle\,\langle\,\rho\,\rangle\,u'v'\,\rangle - \overline{\langle\,\rho\,\rangle\,u'v'} &&= \tilde{\rho}\,\overline{u'v'} + \bar{\rho}\,\widetilde{u'v'} + \tilde{\rho}\,\widetilde{u'v'} - \overline{\tilde{\rho}\,\widetilde{u'v'}}\,,\\
\widetilde{\langle\,\rho\,\rangle\,u'w'} &:= \langle\,\langle\,\rho\,\rangle\,u'w'\,\rangle - \overline{\langle\,\rho\,\rangle\,u'w'} &&= \tilde{\rho}\,\overline{u'w'} + \bar{\rho}\,\widetilde{u'w'} + \tilde{\rho}\,\widetilde{u'w'} - \overline{\tilde{\rho}\,\widetilde{u'w'}}
\end{aligned} \tag{3.48}$$

[1] [92]; also established in [100]. The periodic perturbation inherent to the instantaneous static pressure is rendered accordingly:

$$\tilde{p} := \langle p\rangle - \bar{p}\,; \tag{3.49}$$

based on [100]. Taking into account $p(\mathbf{q})$, Eq. (2.16), the organized unsteady static pressure is considered to behave nonlinearly with respect to the periodic perturbation of the density, the Cartesian velocities, and specific total energy. Naturally, this nonlinear behavior extends to both the time-invariant mean and the periodic perturbation inherent to the organized unsteady static pressure. Under linearization, Eq. (3.45) eventually becomes

$$\begin{aligned}
\langle\,E_{\psi\,20}\,\rangle^* &= \overline{J\psi_t}^*\,(\bar{\rho}\bar{u} + \bar{\rho}\tilde{u} + \tilde{\rho}\bar{u})\\
&+ \widetilde{J\psi_t}^*\,\bar{\rho}\bar{u}\,,\\
\langle\,E_{\psi\,21}\,\rangle^* &= \overline{J\psi_x}^*\,(\bar{\rho}\bar{u}^2 + 2\bar{\rho}\bar{u}\tilde{u} + \tilde{\rho}\bar{u}^2 + \langle\,\langle\,\rho\,\rangle\,u'u'\,\rangle^* + \langle\,p\,\rangle^*)\\
&+ \widetilde{J\psi_x}^*\,(\bar{\rho}\bar{u}^2 + \overline{\langle\,\rho\,\rangle\,u'u'}^* + \bar{p}^*)\,,\\
\langle\,E_{\psi\,22}\,\rangle^* &= \overline{J\psi_y}^*\,(\bar{\rho}\bar{u}\bar{v} + \bar{\rho}\bar{u}\tilde{v} + \bar{\rho}\tilde{u}\bar{v} + \tilde{\rho}\bar{u}\bar{v} + \langle\,\langle\,\rho\,\rangle\,u'v'\,\rangle^*)\\
&+ \widetilde{J\psi_y}^*\,(\bar{\rho}\bar{u}\bar{v} + \overline{\langle\,\rho\,\rangle\,u'v'}^*)\,,\\
\langle\,E_{\psi\,23}\,\rangle^* &= \overline{J\psi_z}^*\,(\bar{\rho}\bar{u}\bar{w} + \bar{\rho}\bar{u}\tilde{w} + \bar{\rho}\tilde{u}\bar{w} + \tilde{\rho}\bar{u}\bar{w} + \langle\,\langle\,\rho\,\rangle\,u'w'\,\rangle^*)\\
&+ \widetilde{J\psi_z}^*\,(\bar{\rho}\bar{u}\bar{w} + \overline{\langle\,\rho\,\rangle\,u'w'}^*)\,;
\end{aligned} \tag{3.50}$$

based on [100].

The time average statistically reduces Eq. (3.44) to

$$\begin{aligned}
\overline{E_{\psi\,20}} &= \overline{J\psi_t}\,(\bar\rho\bar u + \overline{\tilde\rho\tilde u}) + \bar\rho\,\overline{\widetilde{J\psi_t}\tilde u} + \bar u\,\overline{\widetilde{J\psi_t}\tilde\rho} + \overline{\widetilde{J\psi_t}\tilde\rho\tilde u}\,,\\
\overline{E_{\psi\,21}} &= \overline{J\psi_x}\,(\bar\rho\bar u^2 + \bar\rho\,\overline{\tilde u^2} + 2\bar u\,\overline{\tilde\rho\tilde u} + \overline{\tilde\rho\tilde u^2} + \overline{\langle\,\rho\,\rangle\,u'u'} + \bar p)\\
&+ 2\bar\rho\bar u\,\overline{\widetilde{J\psi_x}\tilde u} + \bar\rho\,\overline{\widetilde{J\psi_x}\tilde u^2} + \bar u^2\,\overline{\widetilde{J\psi_x}\tilde\rho} + 2\bar u\,\overline{\widetilde{J\psi_x}\tilde\rho\tilde u} + \overline{\widetilde{J\psi_x}\tilde\rho\tilde u^2}\\
&+ \overline{\widetilde{J\psi_x}\widetilde{\langle\,\rho\,\rangle\,u'u'}} + \overline{\widetilde{J\psi_x}\tilde p}\,,\\
\overline{E_{\psi\,22}} &= \overline{J\psi_y}\,(\bar\rho\bar u\bar v + \bar\rho\,\overline{\tilde u\tilde v} + \bar u\,\overline{\tilde\rho\tilde v} + \bar v\,\overline{\tilde\rho\tilde u} + \overline{\tilde\rho\tilde u\tilde v} + \overline{\langle\,\rho\,\rangle\,u'v'})\\
&+ \bar\rho\bar u\,\overline{\widetilde{J\psi_y}\tilde v} + \bar\rho\bar v\,\overline{\widetilde{J\psi_y}\tilde u} + \bar\rho\,\overline{\widetilde{J\psi_y}\tilde u\tilde v} + \bar u\bar v\,\overline{\widetilde{J\psi_y}\tilde\rho} + \bar u\,\overline{\widetilde{J\psi_y}\tilde\rho\tilde v}\\
&+ \bar v\,\overline{\widetilde{J\psi_y}\tilde\rho\tilde u} + \overline{\widetilde{J\psi_y}\tilde\rho\tilde u\tilde v} + \overline{\widetilde{J\psi_y}\widetilde{\langle\,\rho\,\rangle\,u'v'}}\,,\\
\overline{E_{\psi\,23}} &= \overline{J\psi_z}\,(\bar\rho\bar u\bar w + \bar\rho\,\overline{\tilde u\tilde w} + \bar u\,\overline{\tilde\rho\tilde w} + \bar w\,\overline{\tilde\rho\tilde u} + \overline{\tilde\rho\tilde u\tilde w} + \overline{\langle\,\rho\,\rangle\,u'w'})\\
&+ \bar\rho\bar u\,\overline{\widetilde{J\psi_z}\tilde w} + \bar\rho\bar w\,\overline{\widetilde{J\psi_z}\tilde u} + \bar\rho\,\overline{\widetilde{J\psi_z}\tilde u\tilde w} + \bar u\bar w\,\overline{\widetilde{J\psi_z}\tilde\rho} + \bar u\,\overline{\widetilde{J\psi_z}\tilde\rho\tilde w}\\
&+ \bar w\,\overline{\widetilde{J\psi_z}\tilde\rho\tilde u} + \overline{\widetilde{J\psi_z}\tilde\rho\tilde u\tilde w} + \overline{\widetilde{J\psi_z}\widetilde{\langle\,\rho\,\rangle\,u'w'}}\,,
\end{aligned} \tag{3.51}$$

wherein the influence of turbulence has been wholly compounded into $\overline{\langle\,\rho\,\rangle\,u'u'}$, $\overline{\langle\,\rho\,\rangle\,u'v'}$, $\overline{\langle\,\rho\,\rangle\,u'w'}$ [100], as well as $\overline{\widetilde{J\psi_x}\widetilde{\langle\,\rho\,\rangle\,u'u'}}$, $\overline{\widetilde{J\psi_y}\widetilde{\langle\,\rho\,\rangle\,u'v'}}$, $\overline{\widetilde{J\psi_z}\widetilde{\langle\,\rho\,\rangle\,u'w'}}$. Linearization simplifies Eq. (3.51) substantially:

$$\begin{aligned}
\overline{E_{\psi\,20}}^{\,*} &= \overline{J\psi_t}^{\,*}\,\bar\rho\bar u\,, & \overline{E_{\psi\,21}}^{\,*} &= \overline{J\psi_x}^{\,*}\,(\bar\rho\bar u^2 + \overline{\langle\,\rho\,\rangle\,u'u'}^{\,*} + \bar p^{\,*})\,,\\
\overline{E_{\psi\,22}}^{\,*} &= \overline{J\psi_y}^{\,*}\,(\bar\rho\bar u\bar v + \overline{\langle\,\rho\,\rangle\,u'v'}^{\,*})\,, & \overline{E_{\psi\,23}}^{\,*} &= \overline{J\psi_z}^{\,*}\,(\bar\rho\bar u\bar w + \overline{\langle\,\rho\,\rangle\,u'w'}^{\,*})\,;
\end{aligned} \tag{3.52}$$

based on [100].

Subtracting Eq. (3.52) from Eq. (3.50) then yields

$$\begin{aligned}
\widetilde{E_{\psi\,20}}^{\,*} := \langle\,E_{\psi\,20}\,\rangle^* - \overline{E_{\psi\,20}}^{\,*} &= \overline{J\psi_t}^{\,*}\,(\bar\rho\tilde u + \tilde\rho\bar u)\\
&+ \widetilde{J\psi_t}^{\,*}\,\bar\rho\bar u\,,\\
\widetilde{E_{\psi\,21}}^{\,*} := \langle\,E_{\psi\,21}\,\rangle^* - \overline{E_{\psi\,21}}^{\,*} &= \overline{J\psi_x}^{\,*}\,(2\bar\rho\bar u\tilde u + \tilde\rho\bar u^2 + \tilde p^{\,*}) + \widetilde{J\psi_x}^{\,*}(\bar\rho\bar u^2 + \bar p^{\,*})\\
&+ \overline{J\psi_x}^{\,*}\,\widetilde{\langle\,\rho\,\rangle\,u'u'}^{\,*} + \widetilde{J\psi_x}^{\,*}\,\overline{\langle\,\rho\,\rangle\,u'u'}^{\,*}\,,\\
\widetilde{E_{\psi\,22}}^{\,*} := \langle\,E_{\psi\,22}\,\rangle^* - \overline{E_{\psi\,22}}^{\,*} &= \overline{J\psi_y}^{\,*}\,(\bar\rho\bar u\tilde v + \bar\rho\tilde u\bar v + \tilde\rho\bar u\bar v) + \widetilde{J\psi_y}^{\,*}\,\bar\rho\bar u\bar v\\
&+ \overline{J\psi_y}^{\,*}\,\widetilde{\langle\,\rho\,\rangle\,u'v'}^{\,*} + \widetilde{J\psi_y}^{\,*}\,\overline{\langle\,\rho\,\rangle\,u'v'}^{\,*}\,,\\
\widetilde{E_{\psi\,23}}^{\,*} := \langle\,E_{\psi\,23}\,\rangle^* - \overline{E_{\psi\,23}}^{\,*} &= \overline{J\psi_z}^{\,*}\,(\bar\rho\bar u\tilde w + \bar\rho\tilde u\bar w + \tilde\rho\bar u\bar w) + \widetilde{J\psi_z}^{\,*}\,\bar\rho\bar u\bar w\\
&+ \overline{J\psi_z}^{\,*}\,\widetilde{\langle\,\rho\,\rangle\,u'w'}^{\,*} + \widetilde{J\psi_z}^{\,*}\,\overline{\langle\,\rho\,\rangle\,u'w'}^{\,*}\,;
\end{aligned} \tag{3.53}$$

based on [100]. Their summation renders the linearized periodic-perturbation x-directional

contribution of the ψ-directional convective momentum flux:

$$\begin{aligned}
\widetilde{E_{\psi\,2}}^{*} &:= \widetilde{E_{\psi\,20}}^{*} + \widetilde{E_{\psi\,21}}^{*} + \widetilde{E_{\psi\,22}}^{*} + \widetilde{E_{\psi\,23}}^{*} \\
&= \bar{\rho}\bar{u}\,\widetilde{\theta_{\psi}}^{*} + (\bar{\rho}\tilde{u} + \tilde{\rho}\bar{u})\,\overline{\theta_{\psi}}^{*} + \overline{J\psi_{x}}^{*}\,\tilde{p}^{*} + \widetilde{J\psi_{x}}^{*}\,\bar{p}^{*} \\
&+ \overline{J\psi_{x}}^{*}\,\widetilde{\langle\,\rho\,\rangle\,u'u'}^{*} + \overline{J\psi_{y}}^{*}\,\widetilde{\langle\,\rho\,\rangle\,u'v'}^{*} + \overline{J\psi_{z}}^{*}\,\widetilde{\langle\,\rho\,\rangle\,u'w'}^{*} \\
&+ \widetilde{J\psi_{x}}^{*}\,\overline{\langle\,\rho\,\rangle\,u'u'}^{*} + \widetilde{J\psi_{y}}^{*}\,\overline{\langle\,\rho\,\rangle\,u'v'}^{*} + \widetilde{J\psi_{z}}^{*}\,\overline{\langle\,\rho\,\rangle\,u'w'}^{*}\,,
\end{aligned} \tag{3.54}$$

wherein $\widetilde{\langle\,\rho\,\rangle\,u'u'}^{*}$, $\widetilde{\langle\,\rho\,\rangle\,u'v'}^{*}$, $\widetilde{\langle\,\rho\,\rangle\,u'w'}^{*}$, and $\tilde{p}^{*}$, as well as $\overline{\langle\,\rho\,\rangle\,u'u'}^{*}$, $\overline{\langle\,\rho\,\rangle\,u'v'}^{*}$, $\overline{\langle\,\rho\,\rangle\,u'w'}^{*}$, and $\bar{p}^{*}$, remain as additional unknowns.

3.3.2.2 Viscous Instance

The initial deconstruction of $E_{\mathrm{v}\,\psi\,2}$ into summation terms consistent with the generalized metrics becomes

$$E_{\mathrm{v}\,\psi\,2} := J\psi_{x}\tau_{xx} + J\psi_{y}\tau_{yx} + J\psi_{z}\tau_{zx} = E_{\mathrm{v}\,\psi\,21} + E_{\mathrm{v}\,\psi\,22} + E_{\mathrm{v}\,\psi\,23}\,; \tag{3.55}$$

based on [100]. Expressing τ_{xx}, τ_{yx}, and τ_{zx} according to Eq. (2.11), the generalized metrics, as well as the shear stress tensor elements' constituting instantaneous Cartesian velocities and instantaneous dynamic molecular viscosity are subsequently expanded. The latter, however, is considered to have no inherent erratic fluctuation; i.e., behaving simply as an organized unsteady instance:

$$\mu := \langle\mu\rangle = \bar{\mu} + \tilde{\mu}\,, \qquad \text{with} \qquad \tilde{\mu} := \langle\mu\rangle - \bar{\mu} \tag{3.56}$$

familiarly rendering the periodic perturbation inherent to it by way of the time-invariant-mean instance. Taking into account Sutherland's law, Eq. (2.17), the organized unsteady dynamic molecular viscosity is considered to behave nonlinearly with respect to the periodic perturbation of the static temperature. Naturally, this nonlinear behavior extends to both the time-invariant mean and the periodic perturbation inherent to the organized unsteady dynamic molecular viscosity. Furthermore, the instantaneous static temperature is connected to the instantaneous static pressure through the thermal equation of state, Eq. (2.14). Hence, the organized unsteady static temperature itself is considered to behave nonlinearly with respect to the periodic perturbation of the static pressure and the periodic perturbation of the density. This nonlinear behavior again extends to both the time-invariant mean and periodic perturbation inherent to the organized unsteady static temperature.

Foregoing the presentation of the expanded $E_{\mathrm{v}\,\psi\,21}$, $E_{\mathrm{v}\,\psi\,22}$, and $E_{\mathrm{v}\,\psi\,23}$, the statistical

reduction by way of the phase average is

$$\begin{aligned}
\langle E_{\mathrm{v}\,\psi\,21}\rangle &= \left(\overline{J\psi_x}+\widetilde{J\psi_x}\right)\left[\ \frac{2}{3}\,\bar{\mu}\left(2\frac{\partial\bar{u}}{\partial x}-\frac{\partial\bar{v}}{\partial y}-\frac{\partial\bar{w}}{\partial z}\right)+\frac{2}{3}\,\bar{\mu}\left(2\frac{\partial\tilde{u}}{\partial x}-\frac{\partial\tilde{v}}{\partial y}-\frac{\partial\tilde{w}}{\partial z}\right)\right.\\
&\qquad\left.+\frac{2}{3}\,\tilde{\mu}\left(2\frac{\partial\bar{u}}{\partial x}-\frac{\partial\bar{v}}{\partial y}-\frac{\partial\bar{w}}{\partial z}\right)+\frac{2}{3}\,\tilde{\mu}\left(2\frac{\partial\tilde{u}}{\partial x}-\frac{\partial\tilde{v}}{\partial y}-\frac{\partial\tilde{w}}{\partial z}\right)\ \right],\\
\langle E_{\mathrm{v}\,\psi\,22}\rangle &= \left(\overline{J\psi_y}+\widetilde{J\psi_y}\right)\left[\ \bar{\mu}\left(\frac{\partial\bar{u}}{\partial y}+\frac{\partial\bar{v}}{\partial x}\right)+\bar{\mu}\left(\frac{\partial\tilde{u}}{\partial y}+\frac{\partial\tilde{v}}{\partial x}\right)\right.\\
&\qquad\left.+\tilde{\mu}\left(\frac{\partial\bar{u}}{\partial y}+\frac{\partial\bar{v}}{\partial x}\right)+\tilde{\mu}\left(\frac{\partial\tilde{u}}{\partial y}+\frac{\partial\tilde{v}}{\partial x}\right)\ \right],\\
\langle E_{\mathrm{v}\,\psi\,23}\rangle &= \left(\overline{J\psi_z}+\widetilde{J\psi_z}\right)\left[\ \bar{\mu}\left(\frac{\partial\bar{u}}{\partial z}+\frac{\partial\bar{w}}{\partial x}\right)+\bar{\mu}\left(\frac{\partial\tilde{u}}{\partial z}+\frac{\partial\tilde{w}}{\partial x}\right)\right.\\
&\qquad\left.+\tilde{\mu}\left(\frac{\partial\bar{u}}{\partial z}+\frac{\partial\bar{w}}{\partial x}\right)+\tilde{\mu}\left(\frac{\partial\tilde{u}}{\partial z}+\frac{\partial\tilde{w}}{\partial x}\right)\ \right].
\end{aligned}\tag{3.57}$$

Under linearization, Eq. (3.57) eventually becomes

$$\begin{aligned}
\langle E_{\mathrm{v}\,\psi\,21}\rangle^* &= \overline{J\psi_x}^*\,\overline{\tau_{xx}}^* \;+\; \overline{J\psi_x}^*\,\widetilde{\tau_{xx}}^* \;+\; \widetilde{J\psi_x}^*\,\overline{\tau_{xx}}^*,\\
\langle E_{\mathrm{v}\,\psi\,22}\rangle^* &= \overline{J\psi_y}^*\,\overline{\tau_{yx}}^* \;+\; \overline{J\psi_y}^*\,\widetilde{\tau_{yx}}^* \;+\; \widetilde{J\psi_y}^*\,\overline{\tau_{yx}}^*,\\
\langle E_{\mathrm{v}\,\psi\,23}\rangle^* &= \overline{J\psi_z}^*\,\overline{\tau_{zx}}^* \;+\; \overline{J\psi_z}^*\,\widetilde{\tau_{zx}}^* \;+\; \widetilde{J\psi_z}^*\,\overline{\tau_{zx}}^*,
\end{aligned}\tag{3.58}$$

having introduced elements of both a linearized periodic-perturbation and a linearized time-invariant-mean shear stress tensor, respectively,

$$\begin{aligned}
\widetilde{\tau_{xx}}^* &:= \frac{2}{3}\,\bar{\mu}^*\left(2\frac{\partial\tilde{u}}{\partial x}-\frac{\partial\tilde{v}}{\partial y}-\frac{\partial\tilde{w}}{\partial z}\right) \;+\; \frac{2}{3}\,\tilde{\mu}^*\left(\frac{\partial\bar{u}}{\partial x}-\frac{\partial\bar{v}}{\partial y}-\frac{\partial\bar{w}}{\partial z}\right),\\
\widetilde{\tau_{yx}}^* &:= \bar{\mu}^*\left(\frac{\partial\tilde{u}}{\partial y}+\frac{\partial\tilde{v}}{\partial x}\right) \;+\; \tilde{\mu}^*\left(\frac{\partial\bar{u}}{\partial y}+\frac{\partial\bar{v}}{\partial x}\right),\\
\widetilde{\tau_{zx}}^* &:= \bar{\mu}^*\left(\frac{\partial\tilde{u}}{\partial z}+\frac{\partial\tilde{w}}{\partial x}\right) \;+\; \tilde{\mu}^*\left(\frac{\partial\bar{u}}{\partial z}+\frac{\partial\bar{w}}{\partial x}\right),
\end{aligned}\tag{3.59}$$

and

$$\overline{\tau_{xx}}^* := \frac{2}{3}\,\bar{\mu}^*\left(2\frac{\partial\bar{u}}{\partial x}-\frac{\partial\bar{v}}{\partial y}-\frac{\partial\bar{w}}{\partial z}\right),\ \overline{\tau_{yx}}^* := \bar{\mu}^*\left(\frac{\partial\bar{u}}{\partial y}+\frac{\partial\bar{v}}{\partial x}\right),\ \overline{\tau_{zx}}^* := \bar{\mu}^*\left(\frac{\partial\bar{u}}{\partial z}+\frac{\partial\bar{w}}{\partial x}\right).\tag{3.60}$$

Both Eq. (3.59) and Eq. (3.60) are verifiable through the decomposition and subsequent linearization of the instantaneous shear stress tensor, Eq. (2.11), itself.

The statistical reduction of the expanded $E_{\mathrm{v}\,\psi\,21}$, $E_{\mathrm{v}\,\psi\,22}$, and $E_{\mathrm{v}\,\psi\,23}$ by way of the

time average is

$$\begin{aligned}
\overline{E_{\mathrm{v}\,\psi\,21}} &= \overline{J\psi_x}\left[\frac{2}{3}\,\bar{\mu}\left(2\frac{\partial\bar{u}}{\partial x}-\frac{\partial\bar{v}}{\partial y}-\frac{\partial\bar{w}}{\partial z}\right)+\frac{2}{3}\,\overline{\tilde{\mu}\left(2\frac{\partial\tilde{u}}{\partial x}-\frac{\partial\tilde{v}}{\partial y}-\frac{\partial\tilde{w}}{\partial z}\right)}\right] \\
&+ \frac{2}{3}\,\bar{\mu}\,\overline{\widetilde{J\psi}_x\left(2\frac{\partial\tilde{u}}{\partial x}-\frac{\partial\tilde{v}}{\partial y}-\frac{\partial\tilde{w}}{\partial z}\right)}+\frac{2}{3}\left(2\frac{\partial\bar{u}}{\partial x}-\frac{\partial\bar{v}}{\partial y}-\frac{\partial\bar{w}}{\partial z}\right)\overline{\widetilde{J\psi}_x\,\tilde{\mu}} \\
&+ \frac{2}{3}\,\overline{\widetilde{J\psi}_x\,\tilde{\mu}\left(2\frac{\partial\tilde{u}}{\partial x}-\frac{\partial\tilde{v}}{\partial y}-\frac{\partial\tilde{w}}{\partial z}\right)}, \\
\overline{E_{\mathrm{v}\,\psi\,22}} &= \overline{J\psi_y}\left[\bar{\mu}\left(\frac{\partial\bar{u}}{\partial y}+\frac{\partial\bar{v}}{\partial x}\right)+\overline{\tilde{\mu}\left(\frac{\partial\tilde{u}}{\partial y}+\frac{\partial\tilde{v}}{\partial x}\right)}\right] \\
&+ \bar{\mu}\,\overline{\widetilde{J\psi}_y\left(\frac{\partial\tilde{u}}{\partial y}+\frac{\partial\tilde{v}}{\partial x}\right)}+\left(\frac{\partial\bar{u}}{\partial y}+\frac{\partial\bar{v}}{\partial x}\right)\overline{\widetilde{J\psi}_y\,\tilde{\mu}}+\overline{\widetilde{J\psi}_y\,\tilde{\mu}\left(\frac{\partial\tilde{u}}{\partial y}+\frac{\partial\tilde{v}}{\partial x}\right)}, \\
\overline{E_{\mathrm{v}\,\psi\,23}} &= \overline{J\psi_z}\left[\bar{\mu}\left(\frac{\partial\bar{u}}{\partial z}+\frac{\partial\bar{w}}{\partial x}\right)+\overline{\tilde{\mu}\left(\frac{\partial\tilde{u}}{\partial z}+\frac{\partial\tilde{w}}{\partial x}\right)}\right] \\
&+ \bar{\mu}\,\overline{\widetilde{J\psi}_z\left(\frac{\partial\tilde{u}}{\partial z}+\frac{\partial\tilde{w}}{\partial x}\right)}+\left(\frac{\partial\bar{u}}{\partial z}+\frac{\partial\bar{w}}{\partial x}\right)\overline{\widetilde{J\psi}_z\,\tilde{\mu}}+\overline{\widetilde{J\psi}_z\,\tilde{\mu}\left(\frac{\partial\tilde{u}}{\partial z}+\frac{\partial\tilde{w}}{\partial x}\right)},
\end{aligned} \tag{3.61}$$

with linearization simplifying it to

$$\overline{E_{\mathrm{v}\,\psi\,21}}^{*} = \overline{J\psi_x}^{*}\,\overline{\tau_{xx}}^{*}, \quad \overline{E_{\mathrm{v}\,\psi\,22}}^{*} = \overline{J\psi_y}^{*}\,\overline{\tau_{yx}}^{*}, \quad \overline{E_{\mathrm{v}\,\psi\,23}}^{*} = \overline{J\psi_z}^{*}\,\overline{\tau_{zx}}^{*} \tag{3.62}$$

under consideration of Eq. (3.60).

Subtracting Eq. (3.62) from Eq. (3.58) then yields

$$\begin{aligned}
\widetilde{E_{\mathrm{v}\,\psi\,21}}^{*} &:= \langle\, E_{\mathrm{v}\,\psi\,21}\,\rangle^{*}-\overline{E_{\mathrm{v}\,\psi\,21}}^{*} = \overline{J\psi_x}^{*}\,\widetilde{\tau_{xx}}^{*}+\widetilde{J\psi_x}^{*}\,\overline{\tau_{xx}}^{*}, \\
\widetilde{E_{\mathrm{v}\,\psi\,22}}^{*} &:= \langle\, E_{\mathrm{v}\,\psi\,22}\,\rangle^{*}-\overline{E_{\mathrm{v}\,\psi\,22}}^{*} = \overline{J\psi_y}^{*}\,\widetilde{\tau_{yx}}^{*}+\widetilde{J\psi_y}^{*}\,\overline{\tau_{yx}}^{*}, \\
\widetilde{E_{\mathrm{v}\,\psi\,23}}^{*} &:= \langle\, E_{\mathrm{v}\,\psi\,23}\,\rangle^{*}-\overline{E_{\mathrm{v}\,\psi\,23}}^{*} = \overline{J\psi_z}^{*}\,\widetilde{\tau_{zx}}^{*}+\widetilde{J\psi_z}^{*}\,\overline{\tau_{zx}}^{*};
\end{aligned} \tag{3.63}$$

based on [100]. Their summation renders the linearized periodic-perturbation x-directional contribution of the ψ-directional viscous momentum flux:

$$\begin{aligned}
\widetilde{E_{\mathrm{v}\,\psi\,2}}^{*} &:= \widetilde{E_{\mathrm{v}\,\psi\,21}}^{*}+\widetilde{E_{\mathrm{v}\,\psi\,22}}^{*}+\widetilde{E_{\mathrm{v}\,\psi\,23}}^{*} \\
&= \overline{J\psi_x}^{*}\,\widetilde{\tau_{xx}}^{*}+\overline{J\psi_y}^{*}\,\widetilde{\tau_{yx}}^{*}+\overline{J\psi_z}^{*}\,\widetilde{\tau_{zx}}^{*}+\widetilde{J\psi_x}^{*}\,\overline{\tau_{xx}}^{*}+\widetilde{J\psi_y}^{*}\,\overline{\tau_{yx}}^{*}+\widetilde{J\psi_z}^{*}\,\overline{\tau_{zx}}^{*},
\end{aligned} \tag{3.64}$$

wherein $\tilde{\mu}^{*}$ and $\bar{\mu}^{*}$ inherently remain as additional unknowns, and thus $\tilde{T}^{*}$ and $\bar{T}^{*}$ implicitly as well.

3.3.2.3 Resolution of the Reynolds Stress Tensor Elements

As established in [100], the linearized periodic perturbation and the linearized time-invariant mean inherent to the identified elements of the organized unsteady Reynolds stress tensor can be realigned (subscript ra) from $\widetilde{E_{\psi\,2}}^{*}$ to $\widetilde{E_{\mathrm{v}\,\psi\,2}}^{*}$ through subtraction; i.e.,

$$\widetilde{E_{\psi\,2_{\mathrm{ra}}}}^{*} \;:=\; \bar{\rho}\bar{u}\,\widetilde{\theta_{\psi}}^{*} + (\bar{\rho}\tilde{u} + \tilde{\rho}\bar{u})\,\overline{\theta_{\psi}}^{*} + \overline{J\psi_{x}}^{*}\,\tilde{p}^{*} + \widetilde{J\psi_{x}}^{*}\,\bar{p}^{*} \tag{3.65}$$

and

$$\begin{aligned}\widetilde{E_{\mathrm{v}\,\psi\,2_{\mathrm{ra}}}}^{*} \;:=\;& \overline{J\psi_{x}}^{*}(\widetilde{\tau_{xx}}^{*} - \widetilde{\langle\,\rho\rangle\,u'u'}^{*}) + \overline{J\psi_{y}}^{*}(\widetilde{\tau_{yx}}^{*} - \widetilde{\langle\,\rho\rangle\,u'v'}^{*}) + \overline{J\psi_{z}}^{*}(\widetilde{\tau_{zx}}^{*} - \widetilde{\langle\,\rho\rangle\,u'w'}^{*})\\ +\;& \widetilde{J\psi_{x}}^{*}(\overline{\tau_{xx}}^{*} - \overline{\langle\,\rho\rangle\,u'u'}^{*}) + \widetilde{J\psi_{y}}^{*}(\overline{\tau_{yx}}^{*} - \overline{\langle\,\rho\rangle\,u'v'}^{*}) + \widetilde{J\psi_{z}}^{*}(\overline{\tau_{zx}}^{*} - \overline{\langle\,\rho\rangle\,u'w'}^{*})\,.\end{aligned} \tag{3.66}$$

They are further compounded with the linearized periodic perturbation and linearized time-invariant mean inherent to the particular elements of the organized unsteady shear stress tensor into

$$\widetilde{\tau_{tot,xx}}^{*} := \widetilde{\tau_{xx}}^{*} - \widetilde{\langle\,\rho\rangle\,u'u'}^{*},\;\; \widetilde{\tau_{tot,yx}}^{*} := \widetilde{\tau_{yx}}^{*} - \widetilde{\langle\,\rho\rangle\,u'v'}^{*},\;\; \widetilde{\tau_{tot,zx}}^{*} := \widetilde{\tau_{zx}}^{*} - \widetilde{\langle\,\rho\rangle\,u'w'}^{*} \tag{3.67}$$

and

$$\overline{\tau_{tot,xx}}^{*} := \overline{\tau_{xx}}^{*} - \overline{\langle\,\rho\rangle\,u'u'}^{*},\; \overline{\tau_{tot,yx}}^{*} := \overline{\tau_{yx}}^{*} - \overline{\langle\,\rho\rangle\,u'v'}^{*},\; \overline{\tau_{tot,zx}}^{*} := \overline{\tau_{zx}}^{*} - \overline{\langle\,\rho\rangle\,u'w'}^{*}, \tag{3.68}$$

respectively, designated the linearized periodic perturbation and linearized time-invariant mean inherent to the particular elements of an organized unsteady total shear stress tensor. Thus, Eq. (3.66) can be compactly rendered as

$$\begin{aligned}\widetilde{E_{\mathrm{v}\,\psi\,2_{\mathrm{ra}}}}^{*} \;=\;& \overline{J\psi_{x}}^{*}\,\widetilde{\tau_{tot,xx}}^{*} + \overline{J\psi_{y}}^{*}\,\widetilde{\tau_{tot,yx}}^{*} + \overline{J\psi_{z}}^{*}\,\widetilde{\tau_{tot,zx}}^{*}\\ +\;& \widetilde{J\psi_{x}}^{*}\,\overline{\tau_{tot,xx}}^{*} + \widetilde{J\psi_{y}}^{*}\,\overline{\tau_{tot,yx}}^{*} + \widetilde{J\psi_{z}}^{*}\,\overline{\tau_{tot,zx}}^{*}\end{aligned} \tag{3.69}$$

[100].

On the basis of both Acharya [1] and Norris [92], the Boussinesq approximation is subsequently extended to the small disturbance approach. To this end, the linearized organized unsteady dynamic eddy viscosity is introduced:

$$\langle\mu_{t}\rangle^{*} \;=\; \widetilde{\mu_{t}}^{*} \;+\; \overline{\mu_{t}}^{*}, \quad \text{with} \quad \widetilde{\mu_{t}}^{*} \;:=\; \langle\mu_{t}\rangle^{*} - \overline{\mu_{t}}^{*}, \tag{3.70}$$

familiarly rendering the periodic perturbation inherent to it by way of the time-invariant-mean instance. The linearized periodic perturbation inherent to the organized unsteady Reynolds stress tensor can then be expressed through a sum of products between $\widetilde{\mu_{t}}^{*}$ and the Cartesian spatial derivatives of the time-invariant-mean Cartesian velocities as well as products between $\overline{\mu_{t}}^{*}$ and the Cartesian spatial derivatives of the periodic-perturbation

Cartesian velocities [1] [92]. For the diagonal elements, two-thirds of the linearized periodic perturbation inherent to the organized unsteady turbulence kinetic energy per unit volume $\langle \rho \breve{k} \rangle$ are additionally subtracted, ensuring that the expressed tensor's trace still equals $-2\widetilde{\rho \breve{k}}^{*}$; based on Wilcox [139]. In this regard, the linearized periodic perturbation inherent to the particular elements of the organized unsteady total shear stress tensor becomes

$$\begin{aligned}
\widetilde{\tau_{tot,xx}}^{*} &:= \frac{2}{3}\left(\bar{\mu}^{*} + \overline{\mu_t}^{*}\right)\left(2\frac{\partial \tilde{u}}{\partial x} - \frac{\partial \tilde{v}}{\partial y} - \frac{\partial \tilde{w}}{\partial z}\right) + \frac{2}{3}\left(\tilde{\mu}^{*} + \widetilde{\mu_t}^{*}\right)\left(2\frac{\partial \bar{u}}{\partial x} - \frac{\partial \bar{v}}{\partial y} - \frac{\partial \bar{w}}{\partial z}\right) - \frac{2}{3}\widetilde{\rho \breve{k}}^{*}\,, \\
\widetilde{\tau_{tot,yx}}^{*} &:= \quad \left(\bar{\mu}^{*} + \overline{\mu_t}^{*}\right)\left(\frac{\partial \tilde{u}}{\partial y} + \frac{\partial \tilde{v}}{\partial x}\right) \qquad + \quad \left(\tilde{\mu}^{*} + \widetilde{\mu_t}^{*}\right)\left(\frac{\partial \bar{u}}{\partial y} + \frac{\partial \bar{v}}{\partial x}\right)\,, \\
\widetilde{\tau_{tot,zx}}^{*} &:= \quad \left(\bar{\mu}^{*} + \overline{\mu_t}^{*}\right)\left(\frac{\partial \tilde{u}}{\partial z} + \frac{\partial \tilde{w}}{\partial x}\right) \qquad + \quad \left(\tilde{\mu}^{*} + \widetilde{\mu_t}^{*}\right)\left(\frac{\partial \bar{u}}{\partial z} + \frac{\partial \bar{w}}{\partial x}\right)\,;
\end{aligned} \tag{3.71}$$

based on [100] and [102], as well as [98]. Supplementally, the organized unsteady turbulence kinetic energy per unit volume itself can be determined to be

$$\langle \rho \breve{k} \rangle \;:=\; \left(\langle \langle \rho \rangle u'u' \rangle + \langle \langle \rho \rangle v'v' \rangle + \langle \langle \rho \rangle w'w' \rangle \right) / 2\,, \tag{3.72}$$

with its linearized time-invariant mean then being

$$\overline{\rho \breve{k}}^{*} \;=\; \left(\overline{\langle \rho \rangle u'u'}^{*} + \overline{\langle \rho \rangle v'v'}^{*} + \overline{\langle \rho \rangle w'w'}^{*} \right) / 2\,, \tag{3.73}$$

which eventually renders the linearized periodic perturbation as

$$\widetilde{\rho \breve{k}}^{*} \;:=\; \langle \rho \breve{k} \rangle^{*} \;-\; \overline{\rho \breve{k}}^{*} = \left(\widetilde{\langle \rho \rangle u'u'}^{*} + \widetilde{\langle \rho \rangle v'v'}^{*} + \widetilde{\langle \rho \rangle w'w'}^{*} \right) / 2\,. \tag{3.74}$$

The linearized time-invariant mean inherent to the organized unsteady Reynolds stress tensor can be complementarily expressed through a sum of products between $\overline{\mu_t}^{*}$ and the Cartesian spatial derivatives of the time-invariant-mean Cartesian velocities [100]. For the diagonal elements, two-thirds of the linearized time-invariant mean inherent to the organized unsteady turbulence kinetic energy per unit volume are additionally subtracted, ensuring that the expressed tensor's trace still equals $-2\overline{\rho \breve{k}}^{*}$; based on Wilcox [139]. In this regard, the linearized time-invariant mean inherent to the particular elements of the organized unsteady total-shear-stress tensor become

$$\begin{aligned}
\overline{\tau_{tot,xx}}^{*} &:= \frac{2}{3}\left(\bar{\mu}^{*} + \overline{\mu_t}^{*}\right)\left(2\frac{\partial \bar{u}}{\partial x} - \frac{\partial \bar{v}}{\partial y} - \frac{\partial \bar{w}}{\partial z}\right) - \frac{2}{3}\overline{\rho \breve{k}}^{*}\,, \\
\overline{\tau_{tot,yx}}^{*} &:= \quad \left(\bar{\mu}^{*} + \overline{\mu_t}^{*}\right)\left(\frac{\partial \bar{u}}{\partial y} + \frac{\partial \bar{v}}{\partial x}\right)\,, \\
\overline{\tau_{tot,zx}}^{*} &:= \quad \left(\bar{\mu}^{*} + \overline{\mu_t}^{*}\right)\left(\frac{\partial \bar{u}}{\partial z} + \frac{\partial \bar{w}}{\partial x}\right)\,;
\end{aligned} \tag{3.75}$$

based on [100] and [102].

In this manner, the problem of closure regarding the linearized periodic perturbation and linearized time-invariant mean inherent to the organized unsteady Reynolds stress tensor has been simplified to a problem of closure regarding $\widetilde{\mu_t}^*$ and $\widetilde{\rho\breve{k}}^*$, as well as $\overline{\mu_t}^*$ and $\overline{\rho\breve{k}}^*$ [100, 102]. Ultimately, the linearized periodic-perturbation x-directional contribution of the ψ-directional convective momentum flux and that of its viscous counterpart are specified through their realigned instances, respectively,

$$\widetilde{E_{\psi\,2}}^* := \widetilde{E_{\psi\,2_{\mathrm{ra}}}}^* \qquad \text{and} \qquad \widetilde{E_{\mathrm{v}\,\psi\,2}}^* := \widetilde{E_{\mathrm{v}\,\psi\,2_{\mathrm{ra}}}}^* . \tag{3.76}$$

The y- and z-directional contributions, respectively, $\widetilde{E_{\psi\,3}}^*$, $\widetilde{E_{\mathrm{v}\,\psi\,3}}^*$ and $\widetilde{E_{\psi\,4}}^*$, $\widetilde{E_{\mathrm{v}\,\psi\,4}}^*$ can be obtained accordingly.

3.3.3 Energy Flux

Both the generalized convective flux vector and the generalized viscous flux vector contribute to the total-energy-per-unit-volume's time rate of change through a ψ-directional energy flux element; i.e., the respective fifth element, $E_{\psi\,5}$ and $E_{\mathrm{v}\,\psi\,5}$.

3.3.3.1 Convective Instance

The initial deconstruction of $E_{\psi\,5}$ into summation terms consistent with the generalized metrics becomes

$$\begin{aligned} E_{\psi\,5} &:= H\,\theta_\psi - J\psi_t\,p \\ &= J\psi_t\,\rho e + J\psi_x\,(\rho e u + p u) + J\psi_y\,(\rho e v + p v) + J\psi_z\,(\rho e w + p w) \\ &= E_{\psi\,50} + E_{\psi\,51} + E_{\psi\,52} + E_{\psi\,53}\,. \end{aligned} \tag{3.77}$$

The formulation of $\widetilde{E_{\psi\,50}}^*$ can be given outright on the basis of the precedingly derived $\widetilde{E_{\psi\,20}}^*$:

$$\widetilde{E_{\psi\,50}}^* := \overline{J\psi_t}^*\,(\bar{\rho}\tilde{e} + \tilde{\rho}\bar{e}) + \widetilde{J\psi_t}^*\,\bar{\rho}\bar{e}\,, \tag{3.78}$$

which is ultimately expressed as

$$\widetilde{E_{\psi\,50}}^* = \overline{J\psi_t}^*\,(\tilde{H}^* - \tilde{p}^*) + \widetilde{J\psi_t}^*\,(\bar{H}^* - \bar{p}^*)\,, \tag{3.79}$$

having introduced the linearized periodic-perturbation and linearized time-invariant-mean total enthalpy per unit volume, respectively,

$$\tilde{H}^* := \bar{\rho}\tilde{e} + \tilde{\rho}\bar{e} + \tilde{p}^* \qquad \text{and} \qquad \bar{H}^* = \bar{\rho}\bar{e} + \bar{p}^*\,. \tag{3.80}$$

Both instances are verifiable through the triple decomposition and subsequent linearization of H, Eq. (2.10), itself.

The derivations of $\widetilde{E_{\psi\,51}}^{*}$, $\widetilde{E_{\psi\,52}}^{*}$, and $\widetilde{E_{\psi\,53}}^{*}$ conform to one another. Hence, merely the derivation of $\widetilde{E_{\psi\,51}}^{*}$ needs to be focused on. Considering $E_{\psi\,51}$ (the contribution of the x-directional total energy flux and static pressure work per unit time), the expansion of the x-directional generalized metric, the instantaneous density, the instantaneous specific total energy, the x-directional instantaneous Cartesian velocity, and the instantaneous static pressure yields

$$\begin{aligned} E_{\psi\,51} \;=\; (\overline{J\psi_x} + \widetilde{J\psi_x}) \;\; & (\bar{\rho}\bar{e}\bar{u} + \bar{\rho}\bar{e}\tilde{u} + \bar{\rho}\bar{e}u' + \bar{\rho}\tilde{e}\bar{u} + \bar{\rho}\tilde{e}\tilde{u} + \bar{\rho}\tilde{e}u' + \bar{\rho}e'\bar{u} + \bar{\rho}e'\tilde{u} + \bar{\rho}e'u' \\ & + \tilde{\rho}\bar{e}\bar{u} + \tilde{\rho}\bar{e}\tilde{u} + \tilde{\rho}\bar{e}u' + \tilde{\rho}\tilde{e}\bar{u} + \tilde{\rho}\tilde{e}\tilde{u} + \tilde{\rho}\tilde{e}u' + \tilde{\rho}e'\bar{u} + \tilde{\rho}e'\tilde{u} + \tilde{\rho}e'u' \\ & + \bar{p}\bar{u} + \bar{p}\tilde{u} + \bar{p}u' + \tilde{p}\bar{u} + \tilde{p}\tilde{u} + \tilde{p}u' + p'\bar{u} + p'\tilde{u} + p'u') \,, \end{aligned} \tag{3.81}$$

wherein products between the erratic fluctuation of the x-directional Cartesian velocity and both the erratic fluctuation of the specific total energy and the erratic fluctuation of the static pressure novelly occur.

The phase average statistically reduces Eq. (3.81) to

$$\begin{aligned} \langle E_{\psi\,51} \rangle \;=\; (\overline{J\psi_x} + \widetilde{J\psi_x}) \;\; & (\bar{\rho}\bar{e}\bar{u} + \bar{\rho}\bar{e}\tilde{u} + \bar{\rho}\tilde{e}\bar{u} + \bar{\rho}\tilde{e}\tilde{u} + \tilde{\rho}\bar{e}\bar{u} + \tilde{\rho}\bar{e}\tilde{u} + \tilde{\rho}\tilde{e}\bar{u} + \tilde{\rho}\tilde{e}\tilde{u} \\ & + \bar{p}\bar{u} + \bar{p}\tilde{u} + \tilde{p}\bar{u} + \tilde{p}\tilde{u} + \langle\, \langle\, \rho \,\rangle\, e'u' \,\rangle + \langle\, p'u' \,\rangle) \,, \end{aligned} \tag{3.82}$$

with the influence of turbulence having been wholly compounded into $\langle\, \langle\, \rho \,\rangle\, e'u' \,\rangle$ and $\langle\, p'u' \,\rangle$; also see Hoffmann and Chiang [51]. These turbulent correlation terms are identified, respectively, as the organized unsteady turbulent total energy flux and the organized unsteady turbulent static pressure work per unit time in x direction. Their further analysis renders the actually treatable turbulent correlation terms [139]. To this end, the definition of the instantaneous specific total energy, Eq. (2.15), is considered. Its expansion yields

$$\begin{aligned} e \;=\; (\bar{T} + \tilde{T} + T')/\Gamma \;\; & + \;\; (\bar{u}^2 + \tilde{u}^2 + u'u' + 2\bar{u}\tilde{u} + 2\bar{u}u' + 2\tilde{u}u' \\ & + \;\; \bar{v}^2 + \tilde{v}^2 + v'v' + 2\bar{v}\tilde{v} + 2\bar{v}v' + 2\tilde{v}v' \\ & + \;\; \bar{w}^2 + \tilde{w}^2 + w'w' + 2\bar{w}\tilde{w} + 2\bar{w}w' + 2\tilde{w}w')/2 \,, \end{aligned} \tag{3.83}$$

which the phase average statistically reduces to

$$\langle e \rangle \;=\; \langle T \rangle/\Gamma \;+\; (\langle u \rangle^2 + \langle v \rangle^2 + \langle w \rangle^2)/2 \;+\; \langle \breve{k} \rangle \,, \tag{3.84}$$

having determined the organized unsteady specific turbulence kinetic energy:

$$\langle \breve{k} \rangle \;:=\; \langle\, \rho\breve{k} \,\rangle / \langle\, \rho \,\rangle \;=\; (\langle u'u' \rangle + \langle v'v' \rangle + \langle w'w' \rangle)/2 \,. \tag{3.85}$$

Subtracting Eq. (3.84) from Eq. (3.83) then renders the erratic fluctuation of the specific total energy:

$$e' \;:=\; e - \langle e \rangle \;=\; T'/\Gamma \;+\; (u'u' + v'v' + w'w')/2 \;+\; \langle u \rangle u' + \langle v \rangle v' + \langle w \rangle w' - \langle \breve{k} \rangle \tag{3.86}$$

Eventually, its multiplication with $\langle \rho \rangle u'$ and subsequent phase-averaging reveals

$$\begin{aligned} \langle\, \langle\, \rho \,\rangle\, e'u' \,\rangle \;&=\; \langle\, \langle\, \rho \,\rangle\, T'u' \,\rangle/\Gamma \;+\; (\, \langle\, \langle\, \rho \,\rangle\, u'u'u' \,\rangle + \langle\, \langle\, \rho \,\rangle\, v'v'u' \,\rangle + \langle\, \langle\, \rho \,\rangle\, w'w'u' \,\rangle\,)/2 \\ &\quad+\; \langle\, \langle u \rangle \langle\, \rho \,\rangle\, u'u' \,\rangle + \langle\, \langle v \rangle \langle\, \rho \,\rangle\, v'u' \,\rangle + \langle\, \langle w \rangle \langle\, \rho \,\rangle\, w'u' \,\rangle\,, \end{aligned} \tag{3.87}$$

wherein phase-averaged products between the erratic fluctuations of three Cartesian velocities also persist. Furthermore, the thermal equation of state, Eq. (2.14), is considered. Its expansion yields

$$p \;=\; \bar{\rho}\,\bar{T} + \bar{\rho}\,\tilde{T} + \bar{\rho}\,T' + \tilde{\rho}\,\bar{T} + \tilde{\rho}\,\tilde{T} + \tilde{\rho}\,T'\,, \tag{3.88}$$

which the phase average statistically reduces to

$$\langle p \rangle \;=\; \bar{\rho}\,\bar{T} + \bar{\rho}\,\tilde{T} + \tilde{\rho}\,\bar{T} + \tilde{\rho}\,\tilde{T}\,. \tag{3.89}$$

Subtracting Eq. (3.89) from Eq. (3.88) then renders the erratic fluctuation of the static pressure:

$$p' \;:=\; p - \langle p \rangle \;=\; \langle\, \rho \,\rangle\, T'\,. \tag{3.90}$$

Eventually, its multiplication with u' and subsequent phase-averaging reveals

$$\langle\, p'u' \,\rangle \;=\; \langle\, \langle\, \rho \,\rangle\, T'u' \,\rangle\,. \tag{3.91}$$

Adding Eq. (3.91) to Eq. (3.87) then renders the actually treatable turbulent correlation terms; i.e.,

$$\begin{aligned} \langle\, \langle\, \rho \,\rangle\, e'u' \,\rangle + \langle\, p'u' \,\rangle \;&=\; (\, \langle\, \langle\, \rho \,\rangle\, u'u'u' \,\rangle + \langle\, \langle\, \rho \,\rangle\, v'v'u' \,\rangle + \langle\, \langle\, \rho \,\rangle\, w'w'u' \,\rangle\,)/2 \\ &\quad+\; \langle\, \langle u \rangle \langle\, \rho \,\rangle\, u'u' \,\rangle + \langle\, \langle v \rangle \langle\, \rho \,\rangle\, v'u' \,\rangle + \langle\, \langle w \rangle \langle\, \rho \,\rangle\, w'u' \,\rangle \\ &\quad+\; \gamma\, \langle\, \langle\, \rho \,\rangle\, T'u' \,\rangle/\Gamma\,, \end{aligned} \tag{3.92}$$

wherein the organized unsteady turbulent transport of turbulence kinetic energy, the organized unsteady Reynolds stress work, the organized unsteady turbulent heat flux (all in x direction), respectively, $(\, \langle\, \langle\, \rho \,\rangle\, u'u'u' \,\rangle + \langle\, \langle\, \rho \,\rangle\, v'v'u' \,\rangle + \langle\, \langle\, \rho \,\rangle\, w'w'u' \,\rangle\,)/2$, $\langle\, \langle u \rangle \langle\, \rho \,\rangle\, u'u' \,\rangle$, $\langle\, \langle v \rangle \langle\, \rho \,\rangle\, v'u' \,\rangle$, $\langle\, \langle w \rangle \langle\, \rho \,\rangle\, w'u' \,\rangle$, and $\gamma\, \langle\, \langle\, \rho \,\rangle\, T'u' \,\rangle/\Gamma$ are novelly identified, on the basis of Wilcox [139]. All instances are nonlinear with respect to the inherent periodic perturbation. For the organized unsteady turbulent transport of turbulence kinetic energy, it can

be determined that

$$\begin{aligned}
\langle\langle\rho\rangle u'u'u'\rangle &= \bar{\rho}\,\overline{u'u'u'} + \tilde{\rho}\,\overline{u'u'u'} + \bar{\rho}\,\widetilde{u'u'u'} + \tilde{\rho}\,\widetilde{u'u'u'}\,,\\
\langle\langle\rho\rangle v'v'u'\rangle &= \bar{\rho}\,\overline{v'v'u'} + \tilde{\rho}\,\overline{v'v'u'} + \bar{\rho}\,\widetilde{v'v'u'} + \tilde{\rho}\,\widetilde{v'v'u'}\,,\\
\langle\langle\rho\rangle w'w'u'\rangle &= \bar{\rho}\,\overline{w'w'u'} + \tilde{\rho}\,\overline{w'w'u'} + \bar{\rho}\,\widetilde{w'w'u'} + \tilde{\rho}\,\widetilde{w'w'u'}\,,
\end{aligned} \tag{3.93}$$

with

$$\widetilde{u'u'u'} := \langle u'u'u'\rangle - \overline{u'u'u'}\,, \quad \widetilde{v'v'u'} := \langle v'v'u'\rangle - \overline{v'v'u'}\,, \quad \widetilde{w'w'u'} := \langle w'w'u'\rangle - \overline{w'w'u'}\,. \tag{3.94}$$

Time-averaged products between the erratic fluctuations of three Cartesian velocities persist as well. Time-averaging the organized unsteady turbulent transport of turbulence kinetic energy renders the inherent time-invariant mean. In this regard, Eq. (3.93) yields

$$\begin{aligned}
\overline{\langle\rho\rangle u'u'u'} &= \overline{\langle\langle\rho\rangle u'u'u'\rangle} = \bar{\rho}\,\overline{u'u'u'} + \overline{\tilde{\rho}\,\widetilde{u'u'u'}}\,, \quad \text{as} \quad \overline{\widetilde{u'u'u'}} = 0\,;\\
\overline{\langle\rho\rangle v'v'u'} &= \overline{\langle\langle\rho\rangle v'v'u'\rangle} = \bar{\rho}\,\overline{v'v'u'} + \overline{\tilde{\rho}\,\widetilde{v'v'u'}}\,, \quad \text{as} \quad \overline{\widetilde{v'v'u'}} = 0\,;\\
\overline{\langle\rho\rangle w'w'u'} &= \overline{\langle\langle\rho\rangle w'w'u'\rangle} = \bar{\rho}\,\overline{w'w'u'} + \overline{\tilde{\rho}\,\widetilde{w'w'u'}}\,, \quad \text{as} \quad \overline{\widetilde{w'w'u'}} = 0\,.
\end{aligned} \tag{3.95}$$

Complementarily, the periodic perturbation inherent to the organized unsteady turbulent transport of turbulence kinetic energy is gained by subtracting the inherent time-invariant mean from it; i.e.,

$$\begin{aligned}
(\langle\rho\rangle u'u'u')\tilde{} &:= \langle\langle\rho\rangle u'u'u'\rangle - \overline{\langle\rho\rangle u'u'u'}\\
&= \tilde{\rho}\,\overline{u'u'u'} + \bar{\rho}\,\widetilde{u'u'u'} + \tilde{\rho}\,\widetilde{u'u'u'} - \overline{\tilde{\rho}\,\widetilde{u'u'u'}}\,,\\
(\langle\rho\rangle v'v'u')\tilde{} &:= \langle\langle\rho\rangle v'v'u'\rangle - \overline{\langle\rho\rangle v'v'u'}\\
&= \tilde{\rho}\,\overline{v'v'u'} + \bar{\rho}\,\widetilde{v'v'u'} + \tilde{\rho}\,\widetilde{v'v'u'} - \overline{\tilde{\rho}\,\widetilde{v'v'u'}}\,,\\
(\langle\rho\rangle w'w'u')\tilde{} &:= \langle\langle\rho\rangle w'w'u'\rangle - \overline{\langle\rho\rangle w'w'u'}\\
&= \tilde{\rho}\,\overline{w'w'u'} + \bar{\rho}\,\widetilde{w'w'u'} + \tilde{\rho}\,\widetilde{w'w'u'} - \overline{\tilde{\rho}\,\widetilde{w'w'u'}}\,.
\end{aligned} \tag{3.96}$$

For the organized unsteady Reynolds stress work, on the other hand, the nonlinearity of the Reynolds stress with respect to its inherent periodic perturbation permeates, and is even amplified by the periodic perturbation of the particular Cartesian velocity:

$$\begin{aligned}
\langle\langle u\rangle\langle\rho\rangle u'u'\rangle &= \bar{u}\,\overline{\langle\rho\rangle u'u'} + \bar{u}\,\widetilde{\langle\rho\rangle u'u'} + \tilde{u}\,\overline{\langle\rho\rangle u'u'} + \tilde{u}\,\widetilde{\langle\rho\rangle u'u'}\,,\\
\langle\langle v\rangle\langle\rho\rangle v'u'\rangle &= \bar{v}\,\overline{\langle\rho\rangle v'u'} + \bar{v}\,\widetilde{\langle\rho\rangle v'u'} + \tilde{v}\,\overline{\langle\rho\rangle v'u'} + \tilde{v}\,\widetilde{\langle\rho\rangle v'u'}\,,\\
\langle\langle w\rangle\langle\rho\rangle w'u'\rangle &= \bar{w}\,\overline{\langle\rho\rangle w'u'} + \bar{w}\,\widetilde{\langle\rho\rangle w'u'} + \tilde{w}\,\overline{\langle\rho\rangle w'u'} + \tilde{w}\,\widetilde{\langle\rho\rangle w'u'}\,.
\end{aligned} \tag{3.97}$$

The inherent time-invariant mean then is

$$\begin{aligned}
\overline{\langle u\rangle\langle\,\rho\,\rangle\,u'u'} &= \overline{\langle\,\langle u\rangle\langle\,\rho\,\rangle\,u'u'\,\rangle} &&= \bar{u}\,\overline{\langle\,\rho\,\rangle\,u'u'} + \overline{\tilde{u}\,\widetilde{\langle\,\rho\,\rangle\,u'u'}}\,,\\
\overline{\langle v\rangle\langle\,\rho\,\rangle\,v'u'} &= \overline{\langle\,\langle v\rangle\langle\,\rho\,\rangle\,v'u'\,\rangle} &&= \bar{v}\,\overline{\langle\,\rho\,\rangle\,v'u'} + \overline{\tilde{v}\,\widetilde{\langle\,\rho\,\rangle\,v'u'}}\,,\\
\overline{\langle w\rangle\langle\,\rho\,\rangle\,w'u'} &= \overline{\langle\,\langle w\rangle\langle\,\rho\,\rangle\,w'u'\,\rangle} &&= \bar{w}\,\overline{\langle\,\rho\,\rangle\,w'u'} + \overline{\tilde{w}\,\widetilde{\langle\,\rho\,\rangle\,w'u'}}\,.
\end{aligned} \tag{3.98}$$

It renders the periodic perturbation inherent to the organized unsteady Reynolds stress work of Eq. (3.97):

$$\begin{aligned}
(\langle u\rangle\langle\,\rho\,\rangle\,u'u')^{\sim} &:= \langle\,\langle u\rangle\langle\,\rho\,\rangle\,u'u'\,\rangle - \overline{\langle u\rangle\langle\,\rho\,\rangle\,u'u'}\\
&= \bar{u}\,\widetilde{\langle\,\rho\,\rangle\,u'u'} + \tilde{u}\,\overline{\langle\,\rho\,\rangle\,u'u'} + \tilde{u}\,\widetilde{\langle\,\rho\,\rangle\,u'u'} - \overline{\tilde{u}\,\widetilde{\langle\,\rho\,\rangle\,u'u'}}\,,\\
(\langle v\rangle\langle\,\rho\,\rangle\,v'u')^{\sim} &:= \langle\,\langle v\rangle\langle\,\rho\,\rangle\,v'u'\,\rangle - \overline{\langle v\rangle\langle\,\rho\,\rangle\,v'u'}\\
&= \bar{v}\,\widetilde{\langle\,\rho\,\rangle\,v'u'} + \tilde{v}\,\overline{\langle\,\rho\,\rangle\,v'u'} + \tilde{v}\,\widetilde{\langle\,\rho\,\rangle\,v'u'} - \overline{\tilde{v}\,\widetilde{\langle\,\rho\,\rangle\,v'u'}}\,,\\
(\langle w\rangle\langle\,\rho\,\rangle\,w'u')^{\sim} &:= \langle\,\langle w\rangle\langle\,\rho\,\rangle\,w'u'\,\rangle - \overline{\langle w\rangle\langle\,\rho\,\rangle\,w'u'}\\
&= \bar{w}\,\widetilde{\langle\,\rho\,\rangle\,w'u'} + \tilde{w}\,\overline{\langle\,\rho\,\rangle\,w'u'} + \tilde{w}\,\widetilde{\langle\,\rho\,\rangle\,w'u'} - \overline{\tilde{w}\,\widetilde{\langle\,\rho\,\rangle\,w'u'}}\,.
\end{aligned} \tag{3.99}$$

Lastly, for the organized unsteady turbulent heat flux, it can be determined that

$$\gamma\,\langle\,\langle\,\rho\,\rangle\,T'u'\,\rangle/\Gamma = \gamma\left(\bar{\rho}\,\overline{T'u'} + \bar{\rho}\,\widetilde{T'u'} + \tilde{\rho}\,\overline{T'u'} + \tilde{\rho}\,\widetilde{T'u'}\right)/\Gamma\,,\ \text{with}\ \widetilde{T'u'} := \langle\,T'u'\,\rangle - \overline{T'u'}\,. \tag{3.100}$$

The inherent time-invariant mean then is

$$\gamma\,\overline{\langle\,\rho\,\rangle\,T'u'}/\Gamma \;=\; \gamma\,\overline{\langle\,\langle\,\rho\,\rangle\,T'u'\,\rangle}/\Gamma \;=\; \bar{\rho}\,\overline{T'u'} + \overline{\tilde{\rho}\,\widetilde{T'u'}}\,. \tag{3.101}$$

Thus, the periodic perturbation inherent to the organized unsteady turbulent heat flux of Eq. (3.100) is gained as

$$\gamma\widetilde{\langle\,\rho\,\rangle\,T'u'}/\Gamma := \gamma\langle\,\langle\,\rho\,\rangle\,T'u'\,\rangle/\Gamma - \gamma\,\overline{\langle\rho\rangle T'u'}/\Gamma = \gamma\left(\bar{\rho}\,\widetilde{T'u'} + \tilde{\rho}\,\overline{T'u'} + \tilde{\rho}\,\widetilde{T'u'} - \overline{\tilde{\rho}\,\widetilde{T'u'}}\right)/\Gamma\,. \tag{3.102}$$

Refocusing on $\langle E_{\psi\,51}\rangle$, Eq. (3.82), the constituting $\langle\,\langle\,\rho\,\rangle\,e'u'\,\rangle + \langle\,p'u'\,\rangle$ is substituted by Eq. (3.92), and then expanded in accordance with Eqs. (3.93–3.102). Eventually, its lin-

earization yields

$$\begin{aligned}
\langle E_{\psi\,51}\rangle^* &= \overline{J\psi_x}^* \Big\{ \bar\rho\bar e\bar u + \bar\rho\bar e\tilde u + \bar\rho\tilde e\bar u + \tilde\rho\bar e\bar u + \bar p^*\bar u + \bar p^*\tilde u + \tilde p^*\bar u \\
&+ (\,\overline{\langle\,\rho\,\rangle\,u'u'u'}^* + \overline{\langle\,\rho\,\rangle\,v'v'u'}^* + \overline{\langle\,\rho\,\rangle\,w'w'u'}^*\,)/2 \\
&+ [\,(\langle\,\rho\,\rangle\,u'u'u')\tilde{}^* + (\langle\,\rho\,\rangle\,v'v'u')\tilde{}^* + (\langle\,\rho\,\rangle\,w'w'u')\,]\tilde{}^*/2 \\
&+ \overline{\langle u\rangle\langle\,\rho\,\rangle\,u'u'}^* + \overline{\langle v\rangle\langle\,\rho\,\rangle\,v'u'}^* + \overline{\langle w\rangle\langle\,\rho\,\rangle\,w'u'}^* \\
&+ (\langle u\rangle\langle\,\rho\,\rangle\,u'u')\tilde{}^* + (\langle v\rangle\langle\,\rho\,\rangle\,v'u')\tilde{}^* + (\langle w\rangle\langle\,\rho\,\rangle\,w'u')\tilde{}^* \\
&+ \gamma\,\overline{\langle\,\rho\,\rangle\,T'u'}^*/\Gamma + \gamma\,\widetilde{\langle\,\rho\,\rangle T'u'}^*/\Gamma \Big\} \\
&+ \widetilde{J\psi_x}^* \Big[\bar\rho\bar e\bar u + \bar p^*\bar u + (\,\overline{\langle\,\rho\,\rangle\,u'u'u'}^* + \overline{\langle\,\rho\,\rangle\,v'v'u'}^* + \overline{\langle\,\rho\,\rangle\,w'w'u'}^*\,)/2 \\
&+ \overline{\langle u\rangle\langle\,\rho\,\rangle\,u'u'}^* + \overline{\langle v\rangle\langle\,\rho\,\rangle\,v'u'}^* + \overline{\langle w\rangle\langle\,\rho\,\rangle\,w'u'}^* + \gamma\,\overline{\langle\,\rho\,\rangle\,T'u'}^*/\Gamma \Big]\,.
\end{aligned} \tag{3.103}$$

The time average statistically reduces Eq. (3.81) to

$$\begin{aligned}
\overline{E_{\psi\,51}} &= \overline{J\psi_x}\,(\,\bar\rho\bar e\bar u + \bar\rho\overline{\tilde e\tilde u} + \bar e\overline{\tilde\rho\tilde u} + \bar u\overline{\tilde\rho\tilde e} + \overline{\tilde\rho\tilde e\tilde u} + \bar p\bar u + \overline{\tilde p\tilde u} + \overline{\langle\,\rho\,\rangle\,e'u'} + \overline{p'u'}\,) \\
&+ \bar\rho\bar e\overline{\widetilde{J\psi_x}\tilde u} + \bar\rho\bar u\overline{\widetilde{J\psi_x}\tilde e} + \bar\rho\overline{\widetilde{J\psi_x}\tilde e\tilde u} + \bar e\bar u\overline{\widetilde{J\psi_x}\tilde\rho} + \bar e\overline{\widetilde{J\psi_x}\tilde\rho\tilde u} + \bar u\overline{\widetilde{J\psi_x}\tilde\rho\tilde e} + \overline{\widetilde{J\psi_x}\tilde\rho\tilde e\tilde u} \\
&+ \bar p\overline{\widetilde{J\psi_x}\tilde u} + \bar u\overline{\widetilde{J\psi_x}\tilde p} + \overline{\widetilde{J\psi_x}\tilde p\tilde u} + \overline{\widetilde{J\psi_x}\widetilde{\langle\,\rho\,\rangle\,e'u'}} + \overline{\widetilde{J\psi_x}\,\widetilde{p'u'}}\,,
\end{aligned} \tag{3.104}$$

having taken into account that

$$\begin{aligned}
\overline{\langle\,\rho\,\rangle\,e'u'} &= \overline{\langle\,\langle\,\rho\,\rangle\,e'u'\,\rangle} \quad \text{and} \quad \widetilde{\langle\,\rho\,\rangle\,e'u'} := \langle\,\langle\,\rho\,\rangle\,e'u'\,\rangle - \overline{\langle\,\rho\,\rangle\,e'u'}\,; \\
\overline{p'u'} &= \overline{\langle\,p'u'\,\rangle} \quad \text{and} \quad \widetilde{p'u'} := \langle\,p'u'\,\rangle - \overline{p'u'}\,.
\end{aligned} \tag{3.105}$$

The influence of turbulence has been wholly compounded into $\overline{\langle\,\rho\,\rangle\,e'u'}$, $\overline{p'u'}$, as well as $\overline{\widetilde{J\psi_x}\widetilde{\langle\,\rho\,\rangle\,e'u'}}$, $\overline{\widetilde{J\psi_x}\,\widetilde{p'u'}}$. Linearization simplifies Eq. (3.104) substantially:

$$\begin{aligned}
\overline{E_{\psi\,51}}^* &= \overline{J\psi_x}^* \Big[\bar\rho\bar e\bar u + \bar p^*\bar u + (\,\overline{\langle\,\rho\,\rangle\,u'u'u'}^* + \overline{\langle\,\rho\,\rangle\,v'v'u'}^* + \overline{\langle\,\rho\,\rangle\,w'w'u'}^*\,)/2 \\
&+ \overline{\langle u\rangle\langle\,\rho\,\rangle\,u'u'}^* + \overline{\langle v\rangle\langle\,\rho\,\rangle\,v'u'}^* + \overline{\langle w\rangle\langle\,\rho\,\rangle\,w'u'}^* + \gamma\,\overline{\langle\,\rho\,\rangle\,T'u'}^*/\Gamma \Big]\,,
\end{aligned} \tag{3.106}$$

having utilized the time-invariant mean, respectively, inherent to the organized unsteady turbulent transport of turbulence kinetic energy, to the organized unsteady Reynolds stress work, and to the organized unsteady turbulent heat flux (all in x direction).

Subtracting Eq. (3.106) from Eq. (3.103) then yields

$$\begin{aligned}
\widetilde{E_{\psi\,51}}^{*} &:= \langle E_{\psi\,51}\rangle^{*} - \overline{E_{\psi\,51}}^{*} \\
&= \overline{J\psi_x}^{*}\Big\{\,\bar{H}^{*}\tilde{u} + \tilde{H}^{*}\bar{u} \\
&+ \left[\,(\langle\,\rho\,\rangle\,u'u'u')\tilde{}^{\,*} + (\langle\,\rho\,\rangle\,v'v'u')\tilde{}^{\,*} + (\langle\,\rho\,\rangle\,w'w'u')\tilde{}^{\,*}\,\right]/2 \\
&+ (\langle u\rangle\langle\,\rho\,\rangle\,u'u')\tilde{}^{\,*} + (\langle v\rangle\langle\,\rho\,\rangle\,v'u')\tilde{}^{\,*} + (\langle w\rangle\langle\,\rho\,\rangle\,w'u')\tilde{}^{\,*} + \gamma\,\widetilde{\langle\,\rho\,\rangle\,T'u'}^{\,*}/\Gamma\Big\} \\
&+ \widetilde{J\psi_x}^{*}\Big[\,\bar{H}^{*}\bar{u} + \Big(\overline{\langle\,\rho\,\rangle\,u'u'u'}^{\,*} + \overline{\langle\,\rho\,\rangle\,v'v'u'}^{\,*} + \overline{\langle\,\rho\,\rangle\,w'w'u'}^{\,*}\Big)/2 \\
&+ \overline{\langle u\rangle\langle\,\rho\,\rangle\,u'u'}^{\,*} + \overline{\langle v\rangle\langle\,\rho\,\rangle\,v'u'}^{\,*} + \overline{\langle w\rangle\langle\,\rho\,\rangle\,w'u'}^{\,*} + \gamma\,\overline{\langle\,\rho\,\rangle\,T'u'}^{\,*}/\Gamma\Big]\,,
\end{aligned} \tag{3.107}$$

in consideration of Eq. (3.80). The derivation of $\widetilde{E_{\psi\,52}}^{*}$ and $\widetilde{E_{\psi\,53}}^{*}$ is conducted equivalently. Their summation with $\widetilde{E_{\psi\,50}}^{*}$ and $\widetilde{E_{\psi\,51}}^{*}$ renders the linearized periodic-perturbation contribution of the convective energy flux:

$$\begin{aligned}
\widetilde{E_{\psi\,5}}^{*} &:= \widetilde{E_{\psi\,50}}^{*} + \widetilde{E_{\psi\,51}}^{*} + \widetilde{E_{\psi\,52}}^{*} + \widetilde{E_{\psi\,53}}^{*} \\
&= \bar{H}^{*}\,\widetilde{\theta_{\psi}}^{\,*} + \tilde{H}^{*}\,\overline{\theta_{\psi}}^{\,*} - \overline{J\psi_t}^{\,*}\,\tilde{p}^{*} - \widetilde{J\psi_t}^{\,*}\,\bar{p}^{*} \\
&+ \overline{J\psi_x}^{\,*}\,\widetilde{\Xi_x}^{\,*} + \overline{J\psi_y}^{\,*}\,\widetilde{\Xi_y}^{\,*} + \overline{J\psi_z}^{\,*}\,\widetilde{\Xi_z}^{\,*} + \widetilde{J\psi_x}^{\,*}\,\overline{\Xi_x}^{\,*} + \widetilde{J\psi_y}^{\,*}\,\overline{\Xi_y}^{\,*} + \widetilde{J\psi_z}^{\,*}\,\overline{\Xi_z}^{\,*}\,,
\end{aligned} \tag{3.108}$$

with

$$\begin{aligned}
\widetilde{\Xi_x}^{*} &:= \left[\,(\langle\,\rho\,\rangle\,u'u'u')\tilde{}^{\,*} + (\langle\,\rho\,\rangle\,v'v'u')\tilde{}^{\,*} + (\langle\,\rho\,\rangle\,w'w'u')\tilde{}^{\,*}\,\right]/2 \\
&+ (\langle u\rangle\langle\,\rho\,\rangle\,u'u')\tilde{}^{\,*} + (\langle v\rangle\langle\,\rho\,\rangle\,v'u')\tilde{}^{\,*} + (\langle w\rangle\langle\,\rho\,\rangle\,w'u')\tilde{}^{\,*} + \gamma\,\widetilde{\langle\,\rho\,\rangle T'u'}^{\,*}/\Gamma\,, \\
\widetilde{\Xi_y}^{*} &:= \left[\,(\langle\,\rho\,\rangle\,u'u'v')\tilde{}^{\,*} + (\langle\,\rho\,\rangle\,v'v'v')\tilde{}^{\,*} + (\langle\,\rho\,\rangle\,w'w'v')\tilde{}^{\,*}\,\right]/2 \\
&+ (\langle u\rangle\langle\,\rho\,\rangle\,u'v')\tilde{}^{\,*} + (\langle v\rangle\langle\,\rho\,\rangle\,v'v')\tilde{}^{\,*} + (\langle w\rangle\langle\,\rho\,\rangle\,w'v')\tilde{}^{\,*} + \gamma\,\widetilde{\langle\,\rho\,\rangle T'v'}^{\,*}/\Gamma\,, \\
\widetilde{\Xi_z}^{*} &:= \left[\,(\langle\,\rho\,\rangle\,u'u'w')\tilde{}^{\,*} + (\langle\,\rho\,\rangle\,v'v'w')\tilde{}^{\,*} + (\langle\,\rho\,\rangle\,w'w'w')\tilde{}^{\,*}\,\right]/2 \\
&+ (\langle u\rangle\langle\,\rho\,\rangle\,u'w')\tilde{}^{\,*} + (\langle v\rangle\langle\,\rho\,\rangle\,v'w')\tilde{}^{\,*} + (\langle w\rangle\langle\,\rho\,\rangle\,w'w')\tilde{}^{\,*} + \gamma\,\widetilde{\langle\,\rho\,\rangle T'w'}^{\,*}/\Gamma\,,
\end{aligned} \tag{3.109}$$

and

$$\begin{aligned}
\overline{\Xi_x}^* &:= \left(\overline{\langle\,\rho\,\rangle\, u'u'u'}^* + \overline{\langle\,\rho\,\rangle\, v'v'u'}^* + \overline{\langle\,\rho\,\rangle\, w'w'u'}^* \right)/2 \\
&+ \overline{\langle u\rangle\langle\,\rho\,\rangle\, u'u'}^* + \overline{\langle v\rangle\langle\,\rho\,\rangle\, v'u'}^* + \overline{\langle w\rangle\langle\,\rho\,\rangle\, w'u'}^* + \gamma\,\overline{\langle\,\rho\,\rangle T'u'}^*/\Gamma\,, \\
\overline{\Xi_y}^* &:= \left(\overline{\langle\,\rho\,\rangle\, u'u'v'}^* + \overline{\langle\,\rho\,\rangle\, v'v'v'}^* + \overline{\langle\,\rho\,\rangle\, w'w'v'}^* \right)/2 \\
&+ \overline{\langle u\rangle\langle\,\rho\,\rangle\, u'v'}^* + \overline{\langle v\rangle\langle\,\rho\,\rangle\, v'v'}^* + \overline{\langle w\rangle\langle\,\rho\,\rangle\, w'v'}^* + \gamma\,\overline{\langle\,\rho\,\rangle T'v'}^*/\Gamma\,, \\
\overline{\Xi_z}^* &:= \left(\overline{\langle\,\rho\,\rangle\, u'u'w'}^* + \overline{\langle\,\rho\,\rangle\, v'v'w'}^* + \overline{\langle\,\rho\,\rangle\, w'w'w'}^* \right)/2 \\
&+ \overline{\langle u\rangle\langle\,\rho\,\rangle\, u'w'}^* + \overline{\langle v\rangle\langle\,\rho\,\rangle\, v'w'}^* + \overline{\langle w\rangle\langle\,\rho\,\rangle\, w'w'}^* + \gamma\,\overline{\langle\,\rho\,\rangle T'w'}^*/\Gamma\,,
\end{aligned} \tag{3.110}$$

remaining as additional unknowns.

3.3.3.2 Viscous Instance

The initial deconstruction of $E_{\mathrm{v}\,\psi\,5}$ into summation terms consistent with the generalized metrics becomes

$$E_{\mathrm{v}\,\psi\,5} := J\psi_x\,\Pi_x + J\psi_y\,\Pi_y + J\psi_z\,\Pi_z = E_{\mathrm{v}\,\psi\,51} + E_{\mathrm{v}\,\psi\,52} + E_{\mathrm{v}\,\psi\,53}\,. \tag{3.111}$$

The derivations of $\widetilde{E_{\mathrm{v}\,\psi\,51}}^*$, $\widetilde{E_{\mathrm{v}\,\psi\,52}}^*$, and $\widetilde{E_{\mathrm{v}\,\psi\,53}}^*$ conform to one another. Hence, merely the derivation of $\widetilde{E_{\mathrm{v}\psi\,51}}^*$ needs to be focused on. Considering $E_{\mathrm{v}\,\psi\,51}$ (the contribution of the x-directional shear stress work and heat flux), a deconstruction into subsummands can be made:

$$\begin{aligned}
E_{\mathrm{v}\,\psi\,51} &= J\psi_x\,u\,\tau_{xx} + J\psi_x\,v\,\tau_{xy} + J\psi_x\,w\,\tau_{xz} - J\psi_x\,q_x \\
&= E_{\mathrm{v}\,\psi\,511} + E_{\mathrm{v}\,\psi\,512} + E_{\mathrm{v}\,\psi\,513} + E_{\mathrm{v}\,\psi\,514}\,.
\end{aligned} \tag{3.112}$$

Firstly, $E_{\mathrm{v}\,\psi\,511}$, $E_{\mathrm{v}\,\psi\,512}$, and $E_{\mathrm{v}\,\psi\,513}$ are treated. For this purpose, τ_{xx}, τ_{xy}, and τ_{xz} are again expressed according to Eq. (2.11). The x-directional generalized metric, as well as the instantaneous Cartesian velocities and instantaneous dynamic molecular viscosity

are then expanded, with the statistical reduction by way of the phase average being

$$\begin{aligned}
\langle E_{\mathrm{v}\,\psi\,511}\rangle &= (\overline{J\psi_x}+\widetilde{J\psi_x})\left[\bar{u}\,\frac{2}{3}\,\bar{\mu}\,\left(2\frac{\partial\bar{u}}{\partial x}-\frac{\partial\bar{v}}{\partial y}-\frac{\partial\bar{w}}{\partial z}\right)+\bar{u}\,\frac{2}{3}\,\bar{\mu}\,\left(2\frac{\partial\tilde{u}}{\partial x}-\frac{\partial\tilde{v}}{\partial y}-\frac{\partial\tilde{w}}{\partial z}\right)\right]\\
&+ (\overline{J\psi_x}+\widetilde{J\psi_x})\left[\bar{u}\,\frac{2}{3}\,\tilde{\mu}\,\left(2\frac{\partial\bar{u}}{\partial x}-\frac{\partial\bar{v}}{\partial y}-\frac{\partial\bar{w}}{\partial z}\right)+\bar{u}\,\frac{2}{3}\,\tilde{\mu}\,\left(2\frac{\partial\tilde{u}}{\partial x}-\frac{\partial\tilde{v}}{\partial y}-\frac{\partial\tilde{w}}{\partial z}\right)\right]\\
&+ (\overline{J\psi_x}+\widetilde{J\psi_x})\left[\tilde{u}\,\frac{2}{3}\,\bar{\mu}\,\left(2\frac{\partial\bar{u}}{\partial x}-\frac{\partial\bar{v}}{\partial y}-\frac{\partial\bar{w}}{\partial z}\right)+\tilde{u}\,\frac{2}{3}\,\bar{\mu}\,\left(2\frac{\partial\tilde{u}}{\partial x}-\frac{\partial\tilde{v}}{\partial y}-\frac{\partial\tilde{w}}{\partial z}\right)\right]\\
&+ (\overline{J\psi_x}+\widetilde{J\psi_x})\left[\tilde{u}\,\frac{2}{3}\,\tilde{\mu}\,\left(2\frac{\partial\bar{u}}{\partial x}-\frac{\partial\bar{v}}{\partial y}-\frac{\partial\bar{w}}{\partial z}\right)+\tilde{u}\,\frac{2}{3}\,\tilde{\mu}\,\left(2\frac{\partial\tilde{u}}{\partial x}-\frac{\partial\tilde{v}}{\partial y}-\frac{\partial\tilde{w}}{\partial z}\right)\right]\\
&+ (\overline{J\psi_x}+\widetilde{J\psi_x})\left\langle u'\,\frac{2}{3}\,\langle\mu\rangle\,\left(2\frac{\partial u'}{\partial x}-\frac{\partial v'}{\partial y}-\frac{\partial w'}{\partial z}\right)\right\rangle,
\end{aligned}\tag{3.113}$$

$$\begin{aligned}
\langle E_{\mathrm{v}\,\psi\,512}\rangle &= (\overline{J\psi_x}+\widetilde{J\psi_x})\left[\bar{v}\,\bar{\mu}\,\left(\frac{\partial\bar{u}}{\partial y}+\frac{\partial\bar{v}}{\partial x}\right)+\bar{v}\,\bar{\mu}\,\left(\frac{\partial\tilde{u}}{\partial y}+\frac{\partial\tilde{v}}{\partial x}\right)\right]\\
&+ (\overline{J\psi_x}+\widetilde{J\psi_x})\left[\bar{v}\,\tilde{\mu}\,\left(\frac{\partial\bar{u}}{\partial y}+\frac{\partial\bar{v}}{\partial x}\right)+\bar{v}\,\tilde{\mu}\,\left(\frac{\partial\tilde{u}}{\partial y}+\frac{\partial\tilde{v}}{\partial x}\right)\right]\\
&+ (\overline{J\psi_x}+\widetilde{J\psi_x})\left[\tilde{v}\,\bar{\mu}\,\left(\frac{\partial\bar{u}}{\partial y}+\frac{\partial\bar{v}}{\partial x}\right)+\tilde{v}\,\bar{\mu}\,\left(\frac{\partial\tilde{u}}{\partial y}+\frac{\partial\tilde{v}}{\partial x}\right)\right]\\
&+ (\overline{J\psi_x}+\widetilde{J\psi_x})\left[\tilde{v}\,\tilde{\mu}\,\left(\frac{\partial\bar{u}}{\partial y}+\frac{\partial\bar{v}}{\partial x}\right)+\tilde{v}\,\tilde{\mu}\,\left(\frac{\partial\tilde{u}}{\partial y}+\frac{\partial\tilde{v}}{\partial x}\right)\right]\\
&+ (\overline{J\psi_x}+\widetilde{J\psi_x})\left\langle v'\,\langle\mu\rangle\,\left(\frac{\partial u'}{\partial y}+\frac{\partial v'}{\partial x}\right)\right\rangle,
\end{aligned}\tag{3.114}$$

$$\begin{aligned}
\langle E_{\mathrm{v}\,\psi\,513}\rangle &= (\overline{J\psi_x}+\widetilde{J\psi_x})\left[\bar{w}\,\bar{\mu}\,\left(\frac{\partial\bar{u}}{\partial z}+\frac{\partial\bar{w}}{\partial x}\right)+\bar{w}\,\bar{\mu}\,\left(\frac{\partial\tilde{u}}{\partial z}+\frac{\partial\tilde{w}}{\partial x}\right)\right]\\
&+ (\overline{J\psi_x}+\widetilde{J\psi_x})\left[\bar{w}\,\tilde{\mu}\,\left(\frac{\partial\bar{u}}{\partial z}+\frac{\partial\bar{w}}{\partial x}\right)+\bar{w}\,\tilde{\mu}\,\left(\frac{\partial\tilde{u}}{\partial z}+\frac{\partial\tilde{w}}{\partial x}\right)\right]\\
&+ (\overline{J\psi_x}+\widetilde{J\psi_x})\left[\tilde{w}\,\bar{\mu}\,\left(\frac{\partial\bar{u}}{\partial z}+\frac{\partial\bar{w}}{\partial x}\right)+\tilde{w}\,\bar{\mu}\,\left(\frac{\partial\tilde{u}}{\partial z}+\frac{\partial\tilde{w}}{\partial x}\right)\right]\\
&+ (\overline{J\psi_x}+\widetilde{J\psi_x})\left[\tilde{w}\,\tilde{\mu}\,\left(\frac{\partial\bar{u}}{\partial z}+\frac{\partial\bar{w}}{\partial x}\right)+\tilde{w}\,\tilde{\mu}\,\left(\frac{\partial\tilde{u}}{\partial z}+\frac{\partial\tilde{w}}{\partial x}\right)\right]\\
&+ (\overline{J\psi_x}+\widetilde{J\psi_x})\left\langle w'\,\langle\mu\rangle\,\left(\frac{\partial u'}{\partial z}+\frac{\partial w'}{\partial x}\right)\right\rangle.
\end{aligned}\tag{3.115}$$

Therein, the organized unsteady molecular diffusion in x direction is novelly identified,

on the basis of Wilcox [139]:

$$\begin{aligned}
\left\langle u' \frac{2}{3} \langle\mu\rangle \left(2\frac{\partial u'}{\partial x} - \frac{\partial v'}{\partial y} - \frac{\partial w'}{\partial z}\right)\right\rangle &= \frac{2}{3}\bar{\mu}\,\overline{u'\left(2\frac{\partial u'}{\partial x} - \frac{\partial v'}{\partial y} - \frac{\partial w'}{\partial z}\right)} \\
&+ \frac{2}{3}\bar{\mu}\left[u'\left(2\frac{\partial u'}{\partial x} - \frac{\partial v'}{\partial y} - \frac{\partial w'}{\partial z}\right)\right]^{\sim} \\
&+ \frac{2}{3}\tilde{\mu}\,\overline{u'\left(2\frac{\partial u'}{\partial x} - \frac{\partial v'}{\partial y} - \frac{\partial w'}{\partial z}\right)} \\
&+ \frac{2}{3}\tilde{\mu}\left[u'\left(2\frac{\partial u'}{\partial x} - \frac{\partial v'}{\partial y} - \frac{\partial w'}{\partial z}\right)\right]^{\sim},
\end{aligned} \tag{3.116}$$

$$\begin{aligned}
\left\langle v' \langle\mu\rangle \left(\frac{\partial u'}{\partial y} + \frac{\partial v'}{\partial x}\right)\right\rangle &= \bar{\mu}\,\overline{v'\left(\frac{\partial u'}{\partial y} + \frac{\partial v'}{\partial x}\right)} + \bar{\mu}\left[v'\left(\frac{\partial u'}{\partial y} + \frac{\partial v'}{\partial x}\right)\right]^{\sim} \\
&+ \tilde{\mu}\,\overline{v'\left(\frac{\partial u'}{\partial y} + \frac{\partial v'}{\partial x}\right)} + \tilde{\mu}\left[v'\left(\frac{\partial u'}{\partial y} + \frac{\partial v'}{\partial x}\right)\right]^{\sim},
\end{aligned} \tag{3.117}$$

$$\begin{aligned}
\left\langle w' \langle\mu\rangle \left(\frac{\partial u'}{\partial z} + \frac{\partial w'}{\partial x}\right)\right\rangle &= \bar{\mu}\,\overline{w'\left(\frac{\partial u'}{\partial z} + \frac{\partial w'}{\partial x}\right)} + \bar{\mu}\left[w'\left(\frac{\partial u'}{\partial z} + \frac{\partial w'}{\partial x}\right)\right]^{\sim} \\
&+ \tilde{\mu}\,\overline{w'\left(\frac{\partial u'}{\partial z} + \frac{\partial w'}{\partial x}\right)} + \tilde{\mu}\left[w'\left(\frac{\partial u'}{\partial z} + \frac{\partial w'}{\partial x}\right)\right]^{\sim},
\end{aligned} \tag{3.118}$$

with

$$\begin{aligned}
\left[u'\left(2\frac{\partial u'}{\partial x} - \frac{\partial v'}{\partial y} - \frac{\partial w'}{\partial z}\right)\right]^{\sim} &:= \left\langle u'\left(2\frac{\partial u'}{\partial x} - \frac{\partial v'}{\partial y} - \frac{\partial w'}{\partial z}\right)\right\rangle \\
&- \overline{u'\left(2\frac{\partial u'}{\partial x} - \frac{\partial v'}{\partial y} - \frac{\partial w'}{\partial z}\right)}, \\
\left[v'\left(\frac{\partial u'}{\partial y} + \frac{\partial v'}{\partial x}\right)\right]^{\sim} &:= \left\langle v'\left(\frac{\partial u'}{\partial y} + \frac{\partial v'}{\partial x}\right)\right\rangle - \overline{v'\left(\frac{\partial u'}{\partial y} + \frac{\partial v'}{\partial x}\right)}, \\
\left[w'\left(\frac{\partial u'}{\partial z} + \frac{\partial w'}{\partial x}\right)\right]^{\sim} &:= \left\langle w'\left(\frac{\partial u'}{\partial z} + \frac{\partial w'}{\partial x}\right)\right\rangle - \overline{w'\left(\frac{\partial u'}{\partial z} + \frac{\partial w'}{\partial x}\right)},
\end{aligned} \tag{3.119}$$

wholly compounding the influence of turbulence. As evident from Eqs. (3.116–3.118), the nonlinearity of the organized unsteady dynamic viscosity with respect to its inherent periodic perturbation permeates the organized unsteady molecular diffusion, and is even amplified by the periodic perturbation of the Cartesian velocities' particular spatial-derivative turbulent correlation. The time-invariant mean inherent to Eq. (3.116), Eq. (3.117), and Eq. (3.118) then, respectively, is

$$\begin{aligned}\overline{u' \frac{2}{3} \langle \mu \rangle \left(2\frac{\partial u'}{\partial x} - \frac{\partial v'}{\partial y} - \frac{\partial w'}{\partial z} \right)} &= \frac{2}{3} \bar{\mu} \, \overline{u' \left(2\frac{\partial u'}{\partial x} - \frac{\partial v'}{\partial y} - \frac{\partial w'}{\partial z} \right)} \\ &+ \frac{2}{3} \tilde{\mu} \, \widetilde{\overline{\left[u' \left(2\frac{\partial u'}{\partial x} - \frac{\partial v'}{\partial y} - \frac{\partial w'}{\partial z} \right) \right]}} ,\end{aligned} \tag{3.120}$$

$$\overline{v' \langle \mu \rangle \left(\frac{\partial u'}{\partial y} + \frac{\partial v'}{\partial x} \right)} = \bar{\mu} \, \overline{v' \left(\frac{\partial u'}{\partial y} + \frac{\partial v'}{\partial x} \right)} + \widetilde{\overline{\left[v' \left(\frac{\partial u'}{\partial y} + \frac{\partial v'}{\partial x} \right) \right]}} , \tag{3.121}$$

$$\overline{w' \langle \mu \rangle \left(\frac{\partial u'}{\partial z} + \frac{\partial w'}{\partial x} \right)} = \bar{\mu} \, \overline{w' \left(\frac{\partial u'}{\partial z} + \frac{\partial w'}{\partial x} \right)} + \widetilde{\overline{\left[w' \left(\frac{\partial u'}{\partial z} + \frac{\partial w'}{\partial x} \right) \right]}} . \tag{3.122}$$

Under linearization, Eqs. (3.113–3.115) eventually become

$$\begin{aligned}\langle E_{\mathrm{v}\,\psi\,511} \rangle^* &= \overline{J\psi_x}^* \left(\overline{\langle u \rangle \, \tau_{xx}}^* + \overline{u' \tau'_{xx}}^* \right) + \overline{J\psi_x}^* \left(\widetilde{\langle u \rangle \, \tau_{xx}}^* + \widetilde{u' \tau'_{xx}}^* \right) \\ &+ \widetilde{J\psi_x}^* \left(\overline{\langle u \rangle \, \tau_{xx}}^* + \overline{u' \tau'_{xx}}^* \right) , \\ \langle E_{\mathrm{v}\,\psi\,512} \rangle^* &= \overline{J\psi_x}^* \left(\overline{\langle v \rangle \, \tau_{xy}}^* + \overline{v' \tau'_{xy}}^* \right) + \overline{J\psi_x}^* \left(\widetilde{\langle v \rangle \, \tau_{xy}}^* + \widetilde{v' \tau'_{xy}}^* \right) \\ &+ \widetilde{J\psi_x}^* \left(\overline{\langle v \rangle \, \tau_{xy}}^* + \overline{v' \tau'_{xy}}^* \right) , \\ \langle E_{\mathrm{v}\,\psi\,513} \rangle^* &= \overline{J\psi_x}^* \left(\overline{\langle w \rangle \, \tau_{xz}}^* + \overline{w' \tau'_{xz}}^* \right) + \overline{J\psi_x}^* \left(\widetilde{\langle w \rangle \, \tau_{xz}}^* + \widetilde{w' \tau'_{xz}}^* \right) \\ &+ \widetilde{J\psi_x}^* \left(\overline{\langle w \rangle \, \tau_{xz}}^* + \overline{w' \tau'_{xz}}^* \right) ,\end{aligned} \tag{3.123}$$

having introduced both the linearized periodic-perturbation and the linearized time-

invariant-mean shear stress work in x direction, respectively,

$$\begin{aligned}
\widetilde{\langle u\rangle\,\tau_{xx}}^{*} &:= \bar{u}\,\widetilde{\tau_{xx}}^{*} + \tilde{u}\,\overline{\tau_{xx}}^{*}, \\
\widetilde{\langle v\rangle\,\tau_{xy}}^{*} &:= \bar{v}\,\widetilde{\tau_{xy}}^{*} + \tilde{v}\,\overline{\tau_{xy}}^{*}, \\
\widetilde{\langle w\rangle\,\tau_{xz}}^{*} &:= \bar{w}\,\widetilde{\tau_{xz}}^{*} + \tilde{w}\,\overline{\tau_{xz}}^{*}
\end{aligned} \tag{3.124}$$

and

$$\overline{\langle u\rangle\,\tau_{xx}}^{*} := \bar{u}\,\overline{\tau_{xx}}^{*}, \qquad \overline{\langle v\rangle\,\tau_{xy}}^{*} := \bar{v}\,\overline{\tau_{xy}}^{*}, \qquad \overline{\langle w\rangle\,\tau_{xz}}^{*} := \bar{w}\,\overline{\tau_{xz}}^{*}. \tag{3.125}$$

with $\widetilde{\tau_{xy}}^{*} = \widetilde{\tau_{yx}}^{*}$ and $\overline{\tau_{xy}}^{*} = \overline{\tau_{yx}}^{*}$, as well as $\widetilde{\tau_{xz}}^{*} = \widetilde{\tau_{zx}}^{*}$ and $\overline{\tau_{xz}}^{*} = \overline{\tau_{zx}}^{*}$. Additionally, the linearized periodic-perturbation molecular diffusion in x direction is introduced as

$$\begin{aligned}
\widetilde{u'\tau_{xx}'}^{*} &:= \left[u'\,\frac{2}{3}\,\langle\mu\rangle\,\left(2\frac{\partial u'}{\partial x} - \frac{\partial v'}{\partial y} - \frac{\partial w'}{\partial z}\right)\right]^{\sim *} \\
&= \frac{2}{3}\,\tilde{\mu}^{*}\,\overline{u'\left(2\frac{\partial u'}{\partial x} - \frac{\partial v'}{\partial y} - \frac{\partial w'}{\partial z}\right)} + \frac{2}{3}\,\bar{\mu}^{*}\,\left[u'\left(2\frac{\partial u'}{\partial x} - \frac{\partial v'}{\partial y} - \frac{\partial w'}{\partial z}\right)\right]^{\sim}, \\
\widetilde{v'\tau_{xy}'}^{*} &:= \left[v'\,\langle\mu\rangle\,\left(\frac{\partial u'}{\partial y} + \frac{\partial v'}{\partial x}\right)\right]^{\sim *} \\
&= \tilde{\mu}^{*}\,\overline{v'\left(\frac{\partial u'}{\partial y} + \frac{\partial v'}{\partial x}\right)} + \bar{\mu}^{*}\,\left[v'\left(\frac{\partial u'}{\partial y} + \frac{\partial v'}{\partial x}\right)\right]^{\sim}, \\
\widetilde{w'\tau_{xz}'}^{*} &:= \left[w'\,\langle\mu\rangle\,\left(\frac{\partial u'}{\partial z} + \frac{\partial w'}{\partial x}\right)\right]^{\sim *} \\
&= \tilde{\mu}^{*}\,\overline{w'\left(\frac{\partial u'}{\partial z} + \frac{\partial w'}{\partial x}\right)} + \bar{\mu}^{*}\,\left[w'\left(\frac{\partial u'}{\partial z} + \frac{\partial w'}{\partial x}\right)\right]^{\sim},
\end{aligned} \tag{3.126}$$

with its linearized time-invariant-mean counterpart then being

$$\begin{aligned}
\overline{u'\tau_{xx}'}^{*} &:= \overline{u'\,\frac{2}{3}\,\langle\mu\rangle\,\left(2\frac{\partial u'}{\partial x} - \frac{\partial v'}{\partial y} - \frac{\partial w'}{\partial z}\right)}^{*} = \frac{2}{3}\,\bar{\mu}^{*}\,\overline{u'\left(2\frac{\partial u'}{\partial x} - \frac{\partial v'}{\partial y} - \frac{\partial w'}{\partial z}\right)}, \\
\overline{v'\tau_{xy}'}^{*} &:= \overline{v'\,\langle\mu\rangle\,\left(\frac{\partial u'}{\partial y} + \frac{\partial v'}{\partial x}\right)}^{*} = \bar{\mu}^{*}\,\overline{v'\left(\frac{\partial u'}{\partial y} + \frac{\partial v'}{\partial x}\right)}, \\
\overline{w'\tau_{xz}'}^{*} &:= \overline{w'\,\langle\mu\rangle\,\left(\frac{\partial u'}{\partial z} + \frac{\partial w'}{\partial x}\right)}^{*} = \bar{\mu}^{*}\,\overline{w'\left(\frac{\partial u'}{\partial z} + \frac{\partial w'}{\partial x}\right)}.
\end{aligned} \tag{3.127}$$

The statistical reduction of the expanded $E_{\mathrm{v}\,\psi\,511}$, $E_{\mathrm{v}\,\psi\,512}$, and $E_{\mathrm{v}\,\psi\,513}$ by way of the time average is

$$
\begin{aligned}
\overline{E_{\mathrm{v}\,\psi\,511}} &= \overline{J\psi_x}\,\bar{u}\,\frac{2}{3}\,\bar{\mu}\,\left(2\frac{\partial\bar{u}}{\partial x}-\frac{\partial\bar{v}}{\partial y}-\frac{\partial\bar{w}}{\partial z}\right)+\bar{u}\,\frac{2}{3}\,\bar{\mu}\,\overline{\widetilde{J\psi_x}\,\left(2\frac{\partial\tilde{u}}{\partial x}-\frac{\partial\tilde{v}}{\partial y}-\frac{\partial\tilde{w}}{\partial z}\right)}\\
&+ \overline{J\psi_x}\,\bar{u}\,\frac{2}{3}\,\overline{\tilde{\mu}\,\left(2\frac{\partial\tilde{u}}{\partial x}-\frac{\partial\tilde{v}}{\partial y}-\frac{\partial\tilde{w}}{\partial z}\right)}+\bar{u}\,\frac{2}{3}\,\overline{\widetilde{J\psi_x}\,\tilde{\mu}}\,\left(2\frac{\partial\bar{u}}{\partial x}-\frac{\partial\bar{v}}{\partial y}-\frac{\partial\bar{w}}{\partial z}\right)\\
&+ \bar{u}\,\frac{2}{3}\,\overline{\widetilde{J\psi_x}\,\tilde{\mu}\,\left(2\frac{\partial\tilde{u}}{\partial x}-\frac{\partial\tilde{v}}{\partial y}-\frac{\partial\tilde{w}}{\partial z}\right)}+\overline{J\psi_x}\,\frac{2}{3}\,\bar{\mu}\,\overline{\tilde{u}\,\left(2\frac{\partial\tilde{u}}{\partial x}-\frac{\partial\tilde{v}}{\partial y}-\frac{\partial\tilde{w}}{\partial z}\right)}\\
&+ \overline{\widetilde{J\psi_x}\,\tilde{u}}\,\frac{2}{3}\,\bar{\mu}\,\left(2\frac{\partial\bar{u}}{\partial x}-\frac{\partial\bar{v}}{\partial y}-\frac{\partial\bar{w}}{\partial z}\right)+\frac{2}{3}\,\bar{\mu}\,\overline{\widetilde{J\psi_x}\,\tilde{u}\,\left(2\frac{\partial\tilde{u}}{\partial x}-\frac{\partial\tilde{v}}{\partial y}-\frac{\partial\tilde{w}}{\partial z}\right)}\\
&+ \overline{J\psi_x}\,\overline{\tilde{u}\,\tilde{\mu}}\,\frac{2}{3}\,\left(2\frac{\partial\bar{u}}{\partial x}-\frac{\partial\bar{v}}{\partial y}-\frac{\partial\bar{w}}{\partial z}\right)+\overline{J\psi_x}\,\frac{2}{3}\,\overline{\tilde{u}\,\tilde{\mu}\,\left(2\frac{\partial\tilde{u}}{\partial x}-\frac{\partial\tilde{v}}{\partial y}-\frac{\partial\tilde{w}}{\partial z}\right)}\\
&+ \overline{\widetilde{J\psi_x}\,\tilde{u}\,\tilde{\mu}}\,\frac{2}{3}\,\left(2\frac{\partial\bar{u}}{\partial x}-\frac{\partial\bar{v}}{\partial y}-\frac{\partial\bar{w}}{\partial z}\right)+\frac{2}{3}\,\overline{\widetilde{J\psi_x}\,\tilde{u}\,\tilde{\mu}\,\left(2\frac{\partial\tilde{u}}{\partial x}-\frac{\partial\tilde{v}}{\partial y}-\frac{\partial\tilde{w}}{\partial z}\right)}\\
&+ \overline{J\psi_x}\,\frac{2}{3}\,\overline{u'\,\langle\mu\rangle\,\left(2\frac{\partial u'}{\partial x}-\frac{\partial v'}{\partial y}-\frac{\partial w'}{\partial z}\right)}\\
&+ \frac{2}{3}\,\overline{\widetilde{J\psi_x}\,\left[u'\,\langle\mu\rangle\,\left(2\frac{\partial u'}{\partial x}-\frac{\partial v'}{\partial y}-\frac{\partial w'}{\partial z}\right)\right]^{\sim}},
\end{aligned}
\tag{3.128}
$$

$$
\begin{aligned}
\overline{E_{\mathrm{v}\,\psi\,512}} &= \overline{J\psi_x}\,\bar{v}\,\bar{\mu}\,\left(\frac{\partial\bar{u}}{\partial y}+\frac{\partial\bar{v}}{\partial x}\right)+\bar{v}\,\bar{\mu}\,\overline{\widetilde{J\psi_x}\,\left(\frac{\partial\tilde{u}}{\partial y}+\frac{\partial\tilde{v}}{\partial x}\right)}\\
&+ \overline{J\psi_x}\,\bar{v}\,\overline{\tilde{\mu}\,\left(\frac{\partial\tilde{u}}{\partial y}+\frac{\partial\tilde{v}}{\partial x}\right)}+\bar{v}\,\overline{\widetilde{J\psi_x}\,\tilde{\mu}\,\left(\frac{\partial\tilde{u}}{\partial y}+\frac{\partial\tilde{v}}{\partial x}\right)}\\
&+ \bar{v}\,\overline{\widetilde{J\psi_x}\,\tilde{\mu}\,\left(\frac{\partial\tilde{u}}{\partial y}+\frac{\partial\tilde{v}}{\partial x}\right)}+\overline{J\psi_x}\,\bar{\mu}\,\overline{\tilde{v}\,\left(\frac{\partial\tilde{u}}{\partial y}+\frac{\partial\tilde{v}}{\partial x}\right)}\\
&+ \overline{\widetilde{J\psi_x}\,\tilde{v}}\,\bar{\mu}\,\left(\frac{\partial\bar{u}}{\partial y}+\frac{\partial\bar{v}}{\partial x}\right)+\bar{\mu}\,\overline{\widetilde{J\psi_x}\,\tilde{v}\,\left(\frac{\partial\tilde{u}}{\partial y}+\frac{\partial\tilde{v}}{\partial x}\right)}\\
&+ \overline{J\psi_x}\,\overline{\tilde{v}\,\tilde{\mu}}\,\left(\frac{\partial\bar{u}}{\partial y}+\frac{\partial\bar{v}}{\partial x}\right)+\overline{J\psi_x}\,\overline{\tilde{v}\,\tilde{\mu}\,\left(\frac{\partial\tilde{u}}{\partial y}+\frac{\partial\tilde{v}}{\partial x}\right)}\\
&+ \overline{\widetilde{J\psi_x}\,\tilde{v}\,\tilde{\mu}}\,\left(\frac{\partial\bar{u}}{\partial y}+\frac{\partial\bar{v}}{\partial x}\right)+\overline{\widetilde{J\psi_x}\,\tilde{v}\,\tilde{\mu}\,\left(\frac{\partial\tilde{u}}{\partial y}+\frac{\partial\tilde{v}}{\partial x}\right)}\\
&+ \overline{J\psi_x}\,\overline{v'\,\langle\mu\rangle\,\left(\frac{\partial u'}{\partial y}+\frac{\partial v'}{\partial x}\right)}+\overline{\widetilde{J\psi_x}\,\left[v'\,\langle\mu\rangle\,\left(\frac{\partial u'}{\partial y}+\frac{\partial v'}{\partial x},\right)\right]^{\sim}},
\end{aligned}
\tag{3.129}
$$

$$
\begin{aligned}
\overline{E_{\mathrm{v}\,\psi\,513}} &= \overline{J\psi_x}\,\bar{w}\,\bar{\mu}\left(\frac{\partial\bar{u}}{\partial z}+\frac{\partial\bar{w}}{\partial x}\right)+\bar{w}\,\bar{\mu}\,\overline{\widetilde{J\psi_x}\left(\frac{\partial\tilde{u}}{\partial z}+\frac{\partial\tilde{w}}{\partial x}\right)}\\
&+ \overline{J\psi_x}\,\bar{w}\,\overline{\tilde{\mu}\left(\frac{\partial\tilde{u}}{\partial z}+\frac{\partial\tilde{w}}{\partial x}\right)}+\bar{w}\,\overline{\widetilde{J\psi_x}\,\tilde{\mu}\left(\frac{\partial\tilde{u}}{\partial z}+\frac{\partial\tilde{w}}{\partial x}\right)}\\
&+ \bar{w}\,\overline{\widetilde{J\psi_x}\,\tilde{\mu}\left(\frac{\partial\tilde{u}}{\partial z}+\frac{\partial\tilde{w}}{\partial x}\right)}+\overline{J\psi_x}\,\bar{\mu}\,\overline{\tilde{w}\left(\frac{\partial\tilde{u}}{\partial z}+\frac{\partial\tilde{w}}{\partial x}\right)}\\
&+ \overline{\widetilde{J\psi_x}\,\tilde{w}}\,\bar{\mu}\left(\frac{\partial\bar{u}}{\partial z}+\frac{\partial\bar{w}}{\partial x}\right)+\bar{\mu}\,\overline{\widetilde{J\psi_x}\,\tilde{w}\left(\frac{\partial\tilde{u}}{\partial z}+\frac{\partial\tilde{w}}{\partial x}\right)}\\
&+ \overline{J\psi_x}\,\overline{\tilde{w}\,\tilde{\mu}}\left(\frac{\partial\bar{u}}{\partial z}+\frac{\partial\bar{w}}{\partial x}\right)+\overline{J\psi_x}\,\overline{\tilde{w}\,\tilde{\mu}\left(\frac{\partial\tilde{u}}{\partial z}+\frac{\partial\tilde{w}}{\partial x}\right)}\\
&+ \overline{\widetilde{J\psi_x}\,\tilde{w}\,\tilde{\mu}}\left(\frac{\partial\bar{u}}{\partial z}+\frac{\partial\bar{w}}{\partial x}\right)+\overline{\widetilde{J\psi_x}\,\tilde{w}\,\tilde{\mu}\left(\frac{\partial\tilde{u}}{\partial z}+\frac{\partial\tilde{w}}{\partial x}\right)}\\
&+ \overline{J\psi_x}\,\overline{w'\langle\mu\rangle\left(\frac{\partial u'}{\partial z}+\frac{\partial w'}{\partial x}\right)}+\widetilde{\overline{J\psi_x\left[w'\langle\mu\rangle\left(\frac{\partial u'}{\partial z}+\frac{\partial w'}{\partial x}\right)\right]}}\,.
\end{aligned}
\tag{3.130}
$$

with linearization simplifying it to

$$
\begin{aligned}
\overline{E_{\mathrm{v}\,\psi\,511}}^{*} &= \overline{J\psi_x}^{*}\left(\overline{\langle u\rangle\tau_{xx}}^{*}+\overline{u'\tau_{xx}{}'}^{*}\right),\\
\overline{E_{\mathrm{v}\,\psi\,512}}^{*} &= \overline{J\psi_x}^{*}\left(\overline{\langle v\rangle\tau_{xy}}^{*}+\overline{u'\tau_{xy}{}'}^{*}\right),\\
\overline{E_{\mathrm{v}\,\psi\,513}}^{*} &= \overline{J\psi_x}^{*}\left(\overline{\langle w\rangle\tau_{xz}}^{*}+\overline{u'\tau_{xz}{}'}^{*}\right)
\end{aligned}
\tag{3.131}
$$

under consideration of Eq. (3.125) and Eq. (3.127).

Subtracting Eq. (3.131) from Eq. (3.123) then yields

$$
\begin{aligned}
\widetilde{E_{\mathrm{v}\,\psi\,511}}^{*} &:= \langle E_{\mathrm{v}\,\psi\,511}\rangle^{*}-\overline{E_{\mathrm{v}\,\psi\,511}}^{*}\\
&= \overline{J\psi_x}^{*}\left(\widetilde{\langle u\rangle\,\tau_{xx}}^{*}+\widetilde{u'\tau_{xx}{}'}^{*}\right)+\widetilde{J\psi_x}^{*}\left(\overline{\langle u\rangle\,\tau_{xx}}^{*}+\overline{u'\tau_{xx}{}'}^{*}\right),\\
\widetilde{E_{\mathrm{v}\,\psi\,512}}^{*} &:= \langle E_{\mathrm{v}\,\psi\,512}\rangle^{*}-\overline{E_{\mathrm{v}\,\psi\,512}}^{*}\\
&= \overline{J\psi_x}^{*}\left(\widetilde{\langle v\rangle\,\tau_{xy}}^{*}+\widetilde{v'\tau_{xy}{}'}^{*}\right)+\widetilde{J\psi_x}^{*}\left(\overline{\langle v\rangle\,\tau_{xy}}^{*}+\overline{v'\tau_{xy}{}'}^{*}\right),\\
\widetilde{E_{\mathrm{v}\,\psi\,513}}^{*} &:= \langle E_{\mathrm{v}\,\psi\,513}\rangle^{*}-\overline{E_{\mathrm{v}\,\psi\,513}}^{*}\\
&= \overline{J\psi_x}^{*}\left(\widetilde{\langle w\rangle\,\tau_{xz}}^{*}+\widetilde{w'\tau_{xz}{}'}^{*}\right)+\widetilde{J\psi_x}^{*}\left(\overline{\langle w\rangle\,\tau_{xz}}^{*}+\overline{w'\tau_{xz}{}'}^{*}\right).
\end{aligned}
\tag{3.132}
$$

Secondly, the remaining subsummand $E_{\mathrm{v}\,\psi\,514}$ is treated. Representing the instantaneous heat flux in x direction as given in Eq. (2.13), the expansion of the constituting

instantaneous dynamic molecular viscosity and the instantaneous static temperature renders

$$E_{\mathrm{v}\,\psi\,514} = (\overline{J\psi_x} + \widetilde{J\psi_x})\,\frac{\gamma}{\Gamma\,Pr}\left(\bar{\mu}\,\frac{\partial\bar{T}}{\partial x} + \bar{\mu}\,\frac{\partial\tilde{T}}{\partial x} + \bar{\mu}\,\frac{\partial T'}{\partial x} + \tilde{\mu}\,\frac{\partial\bar{T}}{\partial x} + \tilde{\mu}\,\frac{\partial\tilde{T}}{\partial x} + \tilde{\mu}\,\frac{\partial T'}{\partial x}\right). \quad (3.133)$$

The phase average statistically reduces Eq. (3.133) to

$$\langle E_{\mathrm{v}\,\psi\,514}\rangle \;=\; (\overline{J\psi_x} + \widetilde{J\psi_x})\;\frac{\gamma}{\Gamma\,Pr}\left(\bar{\mu}\,\frac{\partial\bar{T}}{\partial x} + \bar{\mu}\,\frac{\partial\tilde{T}}{\partial x} + \tilde{\mu}\,\frac{\partial\bar{T}}{\partial x} + \tilde{\mu}\,\frac{\partial\tilde{T}}{\partial x}\right), \quad (3.134)$$

wholly eliminating the influence of turbulence. Its linearization yields

$$\langle E_{\mathrm{v}\,\psi\,514}\rangle^* \;=\; -\overline{J\psi_x}^*\,\overline{q_x}^* - \overline{J\psi_x}^*\,\widetilde{q_x}^* - \widetilde{J\psi_x}^*\,\overline{q_x}^*, \quad (3.135)$$

having introduced the linearized periodic perturbation and linearized time-invariant mean inherent to the organized unsteady heat flux in x direction, respectively,

$$\widetilde{q_x}^* \;:=\; -\frac{\gamma}{\Gamma\,Pr}\left(\bar{\mu}^*\,\frac{\partial\tilde{T}^*}{\partial x} + \tilde{\mu}^*\,\frac{\partial\bar{T}^*}{\partial x}\right) \qquad \text{and} \qquad \overline{q_x}^* \;:=\; -\frac{\gamma}{\Gamma\,Pr}\,\bar{\mu}^*\,\frac{\partial\bar{T}^*}{\partial x}. \quad (3.136)$$

The time average statistically reduces Eq. (3.133) to

$$\overline{E_{\mathrm{v}\,\psi\,514}} \;=\; \overline{J\psi_x}\,\frac{\gamma}{\Gamma\,Pr}\left(\bar{\mu}\,\frac{\partial\bar{T}}{\partial x} + \overline{\tilde{\mu}\,\frac{\partial\tilde{T}}{\partial x}}\right) + \frac{\gamma}{\Gamma\,Pr}\left(\bar{\mu}\,\overline{\widetilde{J\psi_x}\,\frac{\partial\tilde{T}}{\partial x}} + \overline{\widetilde{J\psi_x}\,\tilde{\mu}}\,\frac{\partial\bar{T}}{\partial x} + \overline{\widetilde{J\psi_x}\,\tilde{\mu}\,\frac{\partial\tilde{T}}{\partial x}}\right), \quad (3.137)$$

wholly eliminating the influence of turbulence as well. Linearization simplifies Eq. (3.137) substantially:

$$\overline{E_{\mathrm{v}\,\psi\,514}}^* \;=\; -\overline{J\psi_x}^*\,\overline{q_x}^*. \quad (3.138)$$

Subtracting Eq. (3.138) from Eq. (3.135) then yields

$$\widetilde{E_{\mathrm{v}\,\psi\,514}}^* \;:=\; \langle E_{\mathrm{v}\,\psi\,514}\rangle^* - \overline{E_{\mathrm{v}\,\psi\,514}}^* \;=\; -\overline{J\psi_x}^*\,\widetilde{q_x}^* - \widetilde{J\psi_x}^*\,\overline{q_x}^*. \quad (3.139)$$

Ultimately, the obtained linearized periodic-perturbation subsummands allow the construction of

$$\begin{aligned}
\widetilde{E_{\mathrm{v}\,\psi\,51}}^* \;&:=\; \widetilde{E_{\mathrm{v}\,\psi\,511}}^* + \widetilde{E_{\mathrm{v}\,\psi\,512}}^* + \widetilde{E_{\mathrm{v}\,\psi\,513}}^* + \widetilde{E_{\mathrm{v}\,\psi\,514}}^* \\
&=\; \overline{J\psi_x}^*\left(\widetilde{\langle u\rangle\,\tau_{xx}}^* + \widetilde{\langle v\rangle\,\tau_{xy}}^* + \widetilde{\langle w\rangle\,\tau_{xz}}^* - \widetilde{q_x}^* + \widetilde{u'\tau_{xx}'}^* + \widetilde{v'\tau_{xy}'}^* + \widetilde{w'\tau_{xz}'}^*\right) \\
&+\; \widetilde{J\psi_x}^*\left(\overline{\langle u\rangle\,\tau_{xx}}^* + \overline{\langle v\rangle\,\tau_{xy}}^* + \overline{\langle w\rangle\,\tau_{xz}}^* - \overline{q_x}^* + \overline{u'\tau_{xx}'}^* + \overline{v'\tau_{xy}'}^* + \overline{w'\tau_{xz}'}^*\right).
\end{aligned} \quad (3.140)$$

The derivation of $\widetilde{E_{\mathrm{v}\,\psi\,52}}^{*}$ and $\widetilde{E_{\mathrm{v}\,\psi\,53}}^{*}$ is conducted equivalently. Their summation with $\widetilde{E_{\mathrm{v}\,\psi\,51}}^{*}$ renders the linearized periodic-perturbation contribution of the viscous energy flux:

$$\begin{aligned}
\widetilde{E_{\mathrm{v}\,\psi\,5}}^{*} &:= \widetilde{E_{\mathrm{v}\,\psi\,51}}^{*} + \widetilde{E_{\mathrm{v}\,\psi\,52}}^{*} + \widetilde{E_{\mathrm{v}\,\psi\,53}}^{*} \\
&= \overline{J\psi_x}^{*}\,\widetilde{\Pi_x}^{*} + \overline{J\psi_y}^{*}\,\widetilde{\Pi_y}^{*} + \overline{J\psi_z}^{*}\,\widetilde{\Pi_z}^{*} + \widetilde{J\psi_x}^{*}\,\overline{\Pi_x}^{*} + \widetilde{J\psi_y}^{*}\,\overline{\Pi_y}^{*} + \widetilde{J\psi_z}^{*}\,\overline{\Pi_z}^{*} \\
&+ \overline{J\psi_x}^{*}\,\widetilde{\Xi_{\mathrm{v}x}}^{*} + \overline{J\psi_y}^{*}\,\widetilde{\Xi_{\mathrm{v}y}}^{*} + \overline{J\psi_z}^{*}\,\widetilde{\Xi_{\mathrm{v}z}}^{*} + \widetilde{J\psi_x}^{*}\,\overline{\Xi_{\mathrm{v}x}}^{*} + \widetilde{J\psi_y}^{*}\,\overline{\Xi_{\mathrm{v}y}}^{*} + \widetilde{J\psi_z}^{*}\,\overline{\Xi_{\mathrm{v}z}}^{*},
\end{aligned} \tag{3.141}$$

having introduced

$$\begin{aligned}
\widetilde{\Pi_x}^{*} &:= \widetilde{\langle u\rangle\,\tau_{xx}}^{*} + \widetilde{\langle v\rangle\,\tau_{xy}}^{*} + \widetilde{\langle w\rangle\,\tau_{xz}}^{*} - \widetilde{q_x}^{*}, \\
\widetilde{\Pi_y}^{*} &:= \widetilde{\langle u\rangle\,\tau_{yx}}^{*} + \widetilde{\langle v\rangle\,\tau_{yy}}^{*} + \widetilde{\langle w\rangle\,\tau_{yz}}^{*} - \widetilde{q_y}^{*}, \\
\widetilde{\Pi_z}^{*} &:= \widetilde{\langle u\rangle\,\tau_{zx}}^{*} + \widetilde{\langle v\rangle\,\tau_{zy}}^{*} + \widetilde{\langle w\rangle\,\tau_{zz}}^{*} - \widetilde{q_z}^{*},
\end{aligned} \tag{3.142}$$

and

$$\begin{aligned}
\overline{\Pi_x}^{*} &:= \overline{\langle u\rangle\,\tau_{xx}}^{*} + \overline{\langle v\rangle\,\tau_{xy}}^{*} + \overline{\langle w\rangle\,\tau_{xz}}^{*} - \overline{q_x}^{*}, \\
\overline{\Pi_y}^{*} &:= \overline{\langle u\rangle\,\tau_{yx}}^{*} + \overline{\langle v\rangle\,\tau_{yy}}^{*} + \overline{\langle w\rangle\,\tau_{yz}}^{*} - \overline{q_y}^{*}, \\
\overline{\Pi_z}^{*} &:= \overline{\langle u\rangle\,\tau_{zx}}^{*} + \overline{\langle v\rangle\,\tau_{zy}}^{*} + \overline{\langle w\rangle\,\tau_{zz}}^{*} - \overline{q_y}^{*},
\end{aligned} \tag{3.143}$$

with

$$\begin{aligned}
\widetilde{\Xi_{\mathrm{v}x}}^{*} &:= \widetilde{u'\tau_{xx}'}^{*} + \widetilde{v'\tau_{xy}'}^{*} + \widetilde{w'\tau_{xz}'}^{*}, \quad & \overline{\Xi_{\mathrm{v}x}}^{*} &:= \overline{u'\tau_{xx}'}^{*} + \overline{v'\tau_{xy}'}^{*} + \overline{w'\tau_{xz}'}^{*}; \\
\widetilde{\Xi_{\mathrm{v}y}}^{*} &:= \widetilde{u'\tau_{yx}'}^{*} + \widetilde{v'\tau_{yy}'}^{*} + \widetilde{w'\tau_{yz}'}^{*}, \quad & \overline{\Xi_{\mathrm{v}y}}^{*} &:= \overline{u'\tau_{yx}'}^{*} + \overline{v'\tau_{yy}'}^{*} + \overline{w'\tau_{yz}'}^{*}; \\
\widetilde{\Xi_{\mathrm{v}z}}^{*} &:= \widetilde{u'\tau_{zx}'}^{*} + \widetilde{v'\tau_{zy}'}^{*} + \widetilde{w'\tau_{zz}'}^{*}, \quad & \overline{\Xi_{\mathrm{v}z}}^{*} &:= \overline{u'\tau_{zx}'}^{*} + \overline{v'\tau_{zy}'}^{*} + \overline{w'\tau_{zz}'}^{*}.
\end{aligned} \tag{3.144}$$

remaining as additional unknowns.

3.3.3.3 Resolution of the Turbulent Transport of Turbulence Kinetic Energy, the Reynolds Stress Work, the Turbulent Heat Flux, and the Molecular Diffusion

The linearized periodic perturbation and the linearized time-invariant mean inherent to the identified instances of the organized unsteady turbulent transport of turbulence kinetic energy and the organized unsteady Reynolds stress work, as well as inherent to the identified elements of the organized unsteady turbulent heat flux vector, can be realigned from $\widetilde{E_{\psi\,5}}^{*}$ to $\widetilde{E_{\mathrm{v}\,\psi\,5}}^{*}$ through subtraction. Specifically,

$$\widetilde{E_{\psi\,5_{\mathrm{ra}}}}^{*} := \bar{H}^{*}\,\widetilde{\theta_{\psi}}^{*} + \tilde{H}^{*}\,\overline{\theta_{\psi}}^{*} - \overline{J\psi_t}^{*}\,\tilde{p}^{*} - \widetilde{J\psi_t}^{*}\,\bar{p}^{*} \tag{3.145}$$

and

$$\begin{aligned}
\widetilde{E_{\mathrm{v}\,\psi\,5_{\mathrm{ra}}}}^{*} &:= \overline{J\psi_x}^{*}\left(\widetilde{\Pi_x}^{*}+\widetilde{\Xi_{\mathrm{v}x}}^{*}-\widetilde{\Xi_x}^{*}\right)+\overline{J\psi_y}^{*}\left(\widetilde{\Pi_y}^{*}+\widetilde{\Xi_{\mathrm{v}y}}^{*}-\widetilde{\Xi_y}^{*}\right)\\
&+ \overline{J\psi_z}^{*}\left(\widetilde{\Pi_z}^{*}+\widetilde{\Xi_{\mathrm{v}z}}^{*}-\widetilde{\Xi_z}^{*}\right)\\
&+ \widetilde{J\psi_x}^{*}\left(\overline{\Pi_x}^{*}+\overline{\Xi_{\mathrm{v}x}}^{*}-\overline{\Xi_x}^{*}\right)+\widetilde{J\psi_y}^{*}\left(\overline{\Pi_y}^{*}+\overline{\Xi_{\mathrm{v}y}}^{*}-\overline{\Xi_y}^{*}\right)\\
&+ \widetilde{J\psi_z}^{*}\left(\overline{\Pi_z}^{*}+\overline{\Xi_{\mathrm{v}z}}^{*}-\overline{\Xi_z}^{*}\right),
\end{aligned} \tag{3.146}$$

with

$$\begin{aligned}
\widetilde{\Pi_x}^{*}+\widetilde{\Xi_{\mathrm{v}x}}^{*}-\widetilde{\Xi_x}^{*} &= \widetilde{\langle u\rangle\,\tau_{xx}}^{*}-\left(\langle u\rangle\langle\rho\rangle u'u'\right)\tilde{}^{*}+\widetilde{\langle v\rangle\,\tau_{xy}}^{*}-\left(\langle v\rangle\langle\rho\rangle v'u'\right)\tilde{}^{*}\\
&+ \widetilde{\langle w\rangle\,\tau_{xz}}^{*}-\left(\langle w\rangle\langle\rho\rangle w'u'\right)\tilde{}^{*}-\widetilde{q_x}^{*}-\gamma\,\widetilde{\langle\rho\rangle T'u'}^{*}/\Gamma\\
&+ \widetilde{u'\tau'_{xx}}^{*}+\widetilde{v'\tau'_{xy}}^{*}+\widetilde{w'\tau'_{xz}}^{*}\\
&- \left[\left(\langle\,\rho\,\rangle u'u'u'\right)\tilde{}^{*}+\left(\langle\,\rho\,\rangle v'v'u'\right)\tilde{}^{*}+\left(\langle\,\rho\,\rangle w'w'u'\right)\tilde{}^{*}\right]/2\,,
\end{aligned} \tag{3.147}$$

$$\begin{aligned}
\widetilde{\Pi_y}^{*}+\widetilde{\Xi_{\mathrm{v}y}}^{*}-\widetilde{\Xi_y}^{*} &= \widetilde{\langle u\rangle\,\tau_{yx}}^{*}-\left(\langle u\rangle\langle\rho\rangle u'v'\right)\tilde{}^{*}+\widetilde{\langle v\rangle\,\tau_{yy}}^{*}-\left(\langle v\rangle\langle\rho\rangle v'v'\right)\tilde{}^{*}\\
&+ \widetilde{\langle w\rangle\,\tau_{yz}}^{*}-\left(\langle w\rangle\langle\rho\rangle w'v'\right)\tilde{}^{*}-\widetilde{q_y}^{*}-\gamma\,\widetilde{\langle\rho\rangle T'v'}^{*}/\Gamma\\
&+ \widetilde{u'\tau'_{yx}}^{*}+\widetilde{v'\tau'_{yy}}^{*}+\widetilde{w'\tau'_{yz}}^{*}\\
&- \left[\left(\langle\,\rho\,\rangle u'u'v'\right)\tilde{}^{*}+\left(\langle\,\rho\,\rangle v'v'v'\right)\tilde{}^{*}+\left(\langle\,\rho\,\rangle w'w'v'\right)\tilde{}^{*}\right]/2\,,
\end{aligned} \tag{3.148}$$

$$\begin{aligned}
\widetilde{\Pi_z}^{*}+\widetilde{\Xi_{\mathrm{v}z}}^{*}-\widetilde{\Xi_z}^{*} &= \widetilde{\langle u\rangle\,\tau_{zx}}^{*}-\left(\langle u\rangle\langle\rho\rangle u'w'\right)\tilde{}^{*}+\widetilde{\langle v\rangle\,\tau_{zy}}^{*}-\left(\langle v\rangle\langle\rho\rangle v'w'\right)\tilde{}^{*}\\
&+ \widetilde{\langle w\rangle\,\tau_{zz}}^{*}-\left(\langle w\rangle\langle\rho\rangle w'w'\right)\tilde{}^{*}-\widetilde{q_z}^{*}-\gamma\,\widetilde{\langle\rho\rangle T'w'}^{*}/\Gamma\\
&+ \widetilde{u'\tau'_{zx}}^{*}+\widetilde{v'\tau'_{zy}}^{*}+\widetilde{w'\tau'_{zz}}^{*}\\
&- \left[\left(\langle\,\rho\,\rangle u'u'w'\right)\tilde{}^{*}+\left(\langle\,\rho\,\rangle v'v'w'\right)\tilde{}^{*}+\left(\langle\,\rho\,\rangle w'w'w'\right)\tilde{}^{*}\right]/2\,,
\end{aligned} \tag{3.149}$$

as well as

$$\begin{aligned}
\overline{\Pi_x}^{*}+\overline{\Xi_{\mathrm{v}x}}^{*}-\overline{\Xi_x}^{*} &= \overline{\langle u\rangle\,\tau_{xx}}^{*}-\overline{\langle u\rangle\langle\rho\rangle u'u'}^{*}+\overline{\langle v\rangle\,\tau_{xy}}^{*}-\overline{\langle v\rangle\langle\rho\rangle v'u'}^{*}\\
&+ \overline{\langle w\rangle\,\tau_{xz}}^{*}-\overline{\langle w\rangle\langle\rho\rangle w'u'}^{*}-\overline{q_x}^{*}-\gamma\,\overline{\langle\rho\rangle T'u'}^{*}/\Gamma\\
&+ \overline{u'\tau'_{xx}}^{*}+\overline{v'\tau'_{xy}}^{*}+\overline{w'\tau'_{xz}}^{*}\\
&- \left(\overline{\langle\,\rho\,\rangle u'u'u'}^{*}+\overline{\langle\,\rho\,\rangle v'v'u'}^{*}+\overline{\langle\,\rho\,\rangle w'w'u'}^{*}\right)/2\,,
\end{aligned} \tag{3.150}$$

$$\begin{aligned}
\overline{\Pi_y}^* + \overline{\Xi_{\mathrm{v}y}}^* - \overline{\Xi_y}^* &= \overline{\langle u\rangle\,\tau_{yx}}^* - \overline{\langle u\rangle\langle\rho\rangle u'v'}^* + \overline{\langle v\rangle\,\tau_{yy}}^* - \overline{\langle v\rangle\langle\rho\rangle v'v'}^* \\
&+ \overline{\langle w\rangle\,\tau_{yz}}^* - \overline{\langle w\rangle\langle\rho\rangle w'v'}^* - \overline{q_y}^* - \gamma\,\overline{\langle\rho\rangle T'v'}^*/\Gamma \\
&+ \overline{u'\tau'_{yx}}^* + \overline{v'\tau'_{yy}}^* + \overline{w'\tau'_{yz}}^* \\
&- \left(\overline{\langle\,\rho\,\rangle\,u'u'v'}^* + \overline{\langle\,\rho\,\rangle\,v'v'v'}^* + \overline{\langle\,\rho\,\rangle\,w'w'v'}^*\right)/2\,,
\end{aligned} \tag{3.151}$$

$$\begin{aligned}
\overline{\Pi_z}^* + \overline{\Xi_{\mathrm{v}z}}^* - \overline{\Xi_z}^* &= \overline{\langle u\rangle\,\tau_{zx}}^* - \overline{\langle u\rangle\langle\rho\rangle u'w'}^* + \overline{\langle v\rangle\,\tau_{zy}}^* - \overline{\langle v\rangle\langle\rho\rangle v'w'}^* \\
&+ \overline{\langle w\rangle\,\tau_{zz}}^* - \overline{\langle w\rangle\langle\rho\rangle w'w'}^* - \overline{q_z}^* - \gamma\,\overline{\langle\rho\rangle T'w'}^*/\Gamma \\
&+ \overline{u'\tau'_{zx}}^* + \overline{v'\tau'_{zy}}^* + \overline{w'\tau'_{zz}}^* \\
&- \left(\overline{\langle\,\rho\,\rangle\,u'u'w'}^* + \overline{\langle\,\rho\,\rangle\,v'v'w'}^* + \overline{\langle\,\rho\,\rangle\,w'w'w'}^*\right)/2\,.
\end{aligned} \tag{3.152}$$

The demonstrated alignment of each Reynolds-stress-work instance with its shear-stress-work counterpart renders a total shear-stress-work entity. In this regard, the linearized periodic-perturbation instances are ascertained to be

$$\begin{aligned}
\widetilde{\langle u\rangle\,\tau_{xx}}^* - \widetilde{(\langle u\rangle\langle\rho\rangle u'u')}^* &= \widetilde{(\langle u\rangle\,\tau_{tot,xx})}^* = \bar{u}\,\widetilde{\tau_{tot,xx}}^* + \tilde{u}\,\overline{\tau_{tot,xx}}^*\,, \\
\widetilde{\langle v\rangle\,\tau_{xy}}^* - \widetilde{(\langle v\rangle\langle\rho\rangle v'u')}^* &= \widetilde{(\langle v\rangle\,\tau_{tot,xy})}^* = \bar{v}\,\widetilde{\tau_{tot,xy}}^* + \tilde{v}\,\overline{\tau_{tot,xy}}^*\,, \\
\widetilde{\langle w\rangle\,\tau_{xz}}^* - \widetilde{(\langle w\rangle\langle\rho\rangle w'u')}^* &= \widetilde{(\langle w\rangle\,\tau_{tot,xz})}^* = \bar{w}\,\widetilde{\tau_{tot,xz}}^* + \tilde{w}\,\overline{\tau_{tot,xz}}^*;
\end{aligned} \tag{3.153}$$

$$\begin{aligned}
\widetilde{\langle u\rangle\,\tau_{yx}}^* - \widetilde{(\langle u\rangle\langle\rho\rangle u'v')}^* &= \widetilde{(\langle u\rangle\,\tau_{tot,yx})}^* = \bar{u}\,\widetilde{\tau_{tot,yx}}^* + \tilde{u}\,\overline{\tau_{tot,yx}}^*\,, \\
\widetilde{\langle v\rangle\,\tau_{yy}}^* - \widetilde{(\langle v\rangle\langle\rho\rangle v'v')}^* &= \widetilde{(\langle v\rangle\,\tau_{tot,yy})}^* = \bar{v}\,\widetilde{\tau_{tot,yy}}^* + \tilde{v}\,\overline{\tau_{tot,yy}}^*\,, \\
\widetilde{\langle w\rangle\,\tau_{yz}}^* - \widetilde{(\langle w\rangle\langle\rho\rangle w'v')}^* &= \widetilde{(\langle w\rangle\,\tau_{tot,yz})}^* = \bar{w}\,\widetilde{\tau_{tot,yz}}^* + \tilde{w}\,\overline{\tau_{tot,yz}}^*;
\end{aligned} \tag{3.154}$$

$$\begin{aligned}
\widetilde{\langle u\rangle\,\tau_{zx}}^* - \widetilde{(\langle u\rangle\langle\rho\rangle u'w')}^* &= \widetilde{(\langle u\rangle\,\tau_{tot,zx})}^* = \bar{u}\,\widetilde{\tau_{tot,zx}}^* + \tilde{u}\,\overline{\tau_{tot,zx}}^*\,, \\
\widetilde{\langle v\rangle\,\tau_{zy}}^* - \widetilde{(\langle v\rangle\langle\rho\rangle v'w')}^* &= \widetilde{(\langle v\rangle\,\tau_{tot,zy})}^* = \bar{v}\,\widetilde{\tau_{tot,zy}}^* + \tilde{v}\,\overline{\tau_{tot,zy}}^*\,, \\
\widetilde{\langle w\rangle\,\tau_{zz}}^* - \widetilde{(\langle w\rangle\langle\rho\rangle w'w')}^* &= \widetilde{(\langle w\rangle\,\tau_{tot,zz})}^* = \bar{w}\,\widetilde{\tau_{tot,zz}}^* + \tilde{w}\,\overline{\tau_{tot,zz}}^*\,,
\end{aligned} \tag{3.155}$$

while their linearized time-invariant-mean counterparts are

$$\begin{aligned}
\overline{\langle u\rangle\,\tau_{xx}}^* - \overline{\langle u\rangle\langle\rho\rangle u'u'}^* &= \overline{\langle u\rangle\,\tau_{tot,xx}}^* = \bar{u}\,\overline{\tau_{tot,xx}}^*\,, \\
\overline{\langle v\rangle\,\tau_{xy}}^* - \overline{\langle v\rangle\langle\rho\rangle v'u'}^* &= \overline{\langle v\rangle\,\tau_{tot,xy}}^* = \bar{v}\,\overline{\tau_{tot,xy}}^*\,, \\
\overline{\langle w\rangle\,\tau_{xz}}^* - \overline{\langle w\rangle\langle\rho\rangle w'u'}^* &= \overline{\langle w\rangle\,\tau_{tot,xz}}^* = \bar{w}\,\overline{\tau_{tot,xz}}^*;
\end{aligned} \tag{3.156}$$

$$\begin{aligned}
\overline{\langle u\rangle\,\tau_{yx}}^{*} - \overline{\langle u\rangle\langle\rho\rangle u'v'}^{*} &= \overline{\langle u\rangle\,\tau_{tot,yx}}^{*} = \bar{u}\,\overline{\tau_{tot,yx}}^{*}\,,\\
\overline{\langle v\rangle\,\tau_{yy}}^{*} - \overline{\langle v\rangle\langle\rho\rangle v'v'}^{*} &= \overline{\langle v\rangle\,\tau_{tot,yy}}^{*} = \bar{v}\,\overline{\tau_{tot,yy}}^{*}\,,\\
\overline{\langle w\rangle\,\tau_{yz}}^{*} - \overline{\langle w\rangle\langle\rho\rangle w'v'}^{*} &= \overline{\langle w\rangle\,\tau_{tot,yz}}^{*} = \bar{w}\,\overline{\tau_{tot,yz}}^{*};
\end{aligned} \tag{3.157}$$

$$\begin{aligned}
\overline{\langle u\rangle\,\tau_{zx}}^{*} - \overline{\langle u\rangle\langle\rho\rangle u'w'}^{*} &= \overline{\langle u\rangle\,\tau_{tot,zx}}^{*} = \bar{u}\,\overline{\tau_{tot,zx}}^{*}\,,\\
\overline{\langle v\rangle\,\tau_{zy}}^{*} - \overline{\langle v\rangle\langle\rho\rangle v'w'}^{*} &= \overline{\langle v\rangle\,\tau_{tot,zy}}^{*} = \bar{v}\,\overline{\tau_{tot,zy}}^{*}\,,\\
\overline{\langle w\rangle\,\tau_{zz}}^{*} - \overline{\langle w\rangle\langle\rho\rangle w'w'}^{*} &= \overline{\langle w\rangle\,\tau_{tot,zz}}^{*} = \bar{w}\,\overline{\tau_{tot,zz}}^{*}\,.
\end{aligned} \tag{3.158}$$

Furthermore, each turbulent-heat-flux instance and its molecular counterpart is compounded into a novel total-heat-flux entity; i.e.,

$$\begin{aligned}
\widetilde{q_{tot,x}}^{*} &:= \widetilde{q_x}^{*} + \gamma\,\widetilde{\langle\rho\rangle T'u'}^{*}/\Gamma \quad \text{and} \quad \overline{q_{tot,x}}^{*} := \overline{q_x}^{*} + \gamma\,\overline{\langle\rho\rangle T'u'}^{*}/\Gamma\,;\\
\widetilde{q_{tot,y}}^{*} &:= \widetilde{q_y}^{*} + \gamma\,\widetilde{\langle\rho\rangle T'v'}^{*}/\Gamma \quad \text{and} \quad \overline{q_{tot,y}}^{*} := \overline{q_y}^{*} + \gamma\,\overline{\langle\rho\rangle T'v'}^{*}/\Gamma\,;\\
\widetilde{q_{tot,z}}^{*} &:= \widetilde{q_z}^{*} + \gamma\,\widetilde{\langle\rho\rangle T'w'}^{*}/\Gamma \quad \text{and} \quad \overline{q_{tot,z}}^{*} := \overline{q_z}^{*} + \gamma\,\overline{\langle\rho\rangle T'w'}^{*}/\Gamma\,,
\end{aligned} \tag{3.159}$$

respectively, being the linearized periodic perturbation and linearized time-invariant-mean inherent to the organized unsteady total heat flux vector. Following Wilcox [139], the aligned instances of the turbulent transport of turbulence kinetic energy and the molecular diffusion are compounded into a Cartesian total-shear-stress equivalent quantity for the specific turbulence kinetic energy:

$$\begin{aligned}
\widetilde{\tau_{\breve{k},x}}^{*} &:= \widetilde{u'\tau'_{xx}}^{*} + \widetilde{v'\tau'_{xy}}^{*} + \widetilde{w'\tau'_{xz}}^{*}\\
&\quad - \left[\,(\langle\,\rho\,\rangle\,u'u'u')^{\sim *} + (\langle\,\rho\,\rangle\,v'v'u')^{\sim *} + (\langle\,\rho\,\rangle\,w'w'u')^{\sim *}\,\right]/2\,,\\
\widetilde{\tau_{\breve{k},y}}^{*} &:= \widetilde{u'\tau'_{yx}}^{*} + \widetilde{v'\tau'_{yy}}^{*} + \widetilde{w'\tau'_{yz}}^{*}\\
&\quad - \left[\,(\langle\,\rho\,\rangle\,u'u'v')^{\sim *} + (\langle\,\rho\,\rangle\,v'v'v')^{\sim *} + (\langle\,\rho\,\rangle\,w'w'v')^{\sim *}\,\right]/2\,,\\
\widetilde{\tau_{\breve{k},z}}^{*} &:= \widetilde{u'\tau'_{zx}}^{*} + \widetilde{v'\tau'_{zy}}^{*} + \widetilde{w'\tau'_{zz}}^{*}\\
&\quad - \left[\,(\langle\,\rho\,\rangle\,u'u'w')^{\sim *} + (\langle\,\rho\,\rangle\,v'v'w')^{\sim *} + (\langle\,\rho\,\rangle\,w'w'w')^{\sim *}\,\right]/2
\end{aligned} \tag{3.160}$$

and

$$\begin{aligned}
\overline{\tau_{\breve{k},x}}^{*} &:= \overline{u'\tau'_{xx}}^{*} + \overline{v'\tau'_{xy}}^{*} + \overline{w'\tau'_{xz}}^{*} \\
&- \left(\overline{\langle\, \rho \,\rangle\, u'u'u'}^{*} + \overline{\langle\, \rho \,\rangle\, v'v'u'}^{*} + \overline{\langle\, \rho \,\rangle\, w'w'u'}^{*} \right) /2 \,, \\
\overline{\tau_{\breve{k},y}}^{*} &:= \overline{u'\tau'_{yx}}^{*} + \overline{v'\tau'_{yy}}^{*} + \overline{w'\tau'_{yz}}^{*} \\
&- \left(\overline{\langle\, \rho \,\rangle\, u'u'v'}^{*} + \overline{\langle\, \rho \,\rangle\, v'v'v'}^{*} + \overline{\langle\, \rho \,\rangle\, w'w'v'}^{*} \right) /2 \,, \\
\overline{\tau_{\breve{k},z}}^{*} &:= \overline{u'\tau'_{zx}}^{*} + \overline{v'\tau'_{zy}}^{*} + \overline{w'\tau'_{zz}}^{*} \\
&- \left(\overline{\langle\, \rho \,\rangle\, u'u'w'}^{*} + \overline{\langle\, \rho \,\rangle\, v'v'w'}^{*} + \overline{\langle\, \rho \,\rangle\, w'w'w'}^{*} \right) /2 \,,
\end{aligned} \tag{3.161}$$

respectively, being the linearized periodic-perturbation and linearized time-invariant-mean directional instances.

All in all, Eq. (3.146) can be compactly rendered as

$$\begin{aligned}
\widetilde{E_{\mathrm{v}\,\psi\,5_{\mathrm{ra}}}}^{*} &:= \overline{J\psi_x}^{*}\, \widetilde{\Pi_{tot,x}}^{*} + \overline{J\psi_y}^{*}\, \widetilde{\Pi_{tot,y}}^{*} + \overline{J\psi_z}^{*}\, \widetilde{\Pi_{tot,z}}^{*} \\
&+ \widetilde{J\psi_x}^{*}\, \overline{\Pi_{tot,x}}^{*} + \widetilde{J\psi_y}^{*}\, \overline{\Pi_{tot,y}}^{*} + \widetilde{J\psi_z}^{*}\, \overline{\Pi_{tot,z}}^{*} \,,
\end{aligned} \tag{3.162}$$

with

$$\begin{aligned}
\widetilde{\Pi_{tot,x}}^{*} &:= \bar{u}\, \widetilde{\tau_{tot,xx}}^{*} + \bar{v}\, \widetilde{\tau_{tot,xy}}^{*} + \bar{w}\, \widetilde{\tau_{tot,xz}}^{*} + \tilde{u}\, \overline{\tau_{tot,xx}}^{*} + \tilde{v}\, \overline{\tau_{tot,xy}}^{*} + \tilde{w}\, \overline{\tau_{tot,xz}}^{*} \\
&- \widetilde{q_{tot,x}}^{*} + \widetilde{\tau_{\breve{k},x}} \,, \\
\widetilde{\Pi_{tot,y}}^{*} &:= \bar{u}\, \widetilde{\tau_{tot,yx}}^{*} + \bar{v}\, \widetilde{\tau_{tot,yy}}^{*} + \bar{w}\, \widetilde{\tau_{tot,yz}}^{*} + \tilde{u}\, \overline{\tau_{tot,yx}}^{*} + \tilde{v}\, \overline{\tau_{tot,yy}}^{*} + \tilde{w}\, \overline{\tau_{tot,yz}}^{*} \\
&- \widetilde{q_{tot,y}}^{*} + \widetilde{\tau_{\breve{k},y}}^{*} \,, \\
\widetilde{\Pi_{tot,z}}^{*} &:= \bar{u}\, \widetilde{\tau_{tot,zx}}^{*} + \bar{v}\, \widetilde{\tau_{tot,zy}}^{*} + \bar{w}\, \widetilde{\tau_{tot,zz}}^{*} + \tilde{u}\, \overline{\tau_{tot,zx}}^{*} + \tilde{v}\, \overline{\tau_{tot,zy}}^{*} + \tilde{w}\, \overline{\tau_{tot,zz}}^{*} \\
&- \widetilde{q_{tot,z}}^{*} + \widetilde{\tau_{\breve{k},z}}^{*} \,,
\end{aligned} \tag{3.163}$$

and

$$\begin{aligned}
\overline{\Pi_{tot,x}}^{*} &:= \bar{u}\, \overline{\tau_{tot,xx}}^{*} + \bar{v}\, \overline{\tau_{tot,xy}}^{*} + \bar{w}\, \overline{\tau_{tot,xz}}^{*} - \overline{q_{tot,x}}^{*} + \overline{\tau_{\breve{k},x}}^{*} \,, \\
\overline{\Pi_{tot,y}}^{*} &:= \bar{u}\, \overline{\tau_{tot,yx}}^{*} + \bar{v}\, \overline{\tau_{tot,yy}}^{*} + \bar{w}\, \overline{\tau_{tot,yz}}^{*} - \overline{q_{tot,y}}^{*} + \overline{\tau_{\breve{k},y}}^{*} \,, \\
\overline{\Pi_{tot,z}}^{*} &:= \bar{u}\, \overline{\tau_{tot,zx}}^{*} + \bar{v}\, \overline{\tau_{tot,zy}}^{*} + \bar{w}\, \overline{\tau_{tot,zz}}^{*} - \overline{q_{tot,z}}^{*} + \overline{\tau_{\breve{k},z}}^{*} \,;
\end{aligned} \tag{3.164}$$

based on [100] and [102]. In this regard, the linearized periodic perturbation inherent to the outstanding elements of the organized unsteady total shear stress tensor is given through

$$\begin{aligned}
\widetilde{\tau_{tot,yy}}^{*} &:= \frac{2}{3} \left(\bar{\mu}^{*} + \overline{\mu_t}^{*} \right) \left(2\frac{\partial \tilde{v}}{\partial y} - \frac{\partial \tilde{u}}{\partial x} - \frac{\partial \tilde{w}}{\partial z} \right) + \frac{2}{3} \left(\tilde{\mu}^{*} + \widetilde{\mu_t}^{*} \right) \left(2\frac{\partial \bar{v}}{\partial y} - \frac{\partial \bar{u}}{\partial x} - \frac{\partial \bar{w}}{\partial z} \right) - \frac{2}{3} \widetilde{\rho\breve{k}}^{*} \,, \\
\widetilde{\tau_{tot,zz}}^{*} &:= \frac{2}{3} \left(\bar{\mu}^{*} + \overline{\mu_t}^{*} \right) \left(2\frac{\partial \tilde{w}}{\partial z} - \frac{\partial \tilde{u}}{\partial x} - \frac{\partial \tilde{v}}{\partial y} \right) + \frac{2}{3} \left(\tilde{\mu}^{*} + \widetilde{\mu_t}^{*} \right) \left(2\frac{\partial \bar{w}}{\partial z} - \frac{\partial \bar{u}}{\partial x} - \frac{\partial \bar{v}}{\partial y} \right) - \frac{2}{3} \widetilde{\rho\breve{k}}^{*} \,,
\end{aligned} \tag{3.165}$$

with $\widetilde{\tau_{tot,xy}}^* = \widetilde{\tau_{tot,yx}}^*$ and $\widetilde{\tau_{tot,xz}}^* = \widetilde{\tau_{tot,zx}}^*$, as well as

$$\widetilde{\tau_{tot,yz}}^* = \widetilde{\tau_{tot,zy}}^* := (\bar{\mu}^* + \overline{\mu_t}^*)\left(\frac{\partial \tilde{v}}{\partial z} + \frac{\partial \tilde{w}}{\partial y}\right) + (\tilde{\mu}^* + \widetilde{\mu_t}^*)\left(\frac{\partial \bar{v}}{\partial z} + \frac{\partial \bar{w}}{\partial y}\right); \tag{3.166}$$

based on [100] and [102]. Complementarily, the linearized time-invariant-mean counterpart is given through

$$\begin{aligned}
\overline{\tau_{tot,yy}}^* &:= \frac{2}{3}(\bar{\mu}^* + \overline{\mu_t}^*)\left(2\frac{\partial \bar{v}}{\partial y} - \frac{\partial \bar{u}}{\partial x} - \frac{\partial \bar{w}}{\partial z}\right) - \frac{2}{3}\overline{\rho \breve{k}}^*, \\
\overline{\tau_{tot,zz}}^* &:= \frac{2}{3}(\bar{\mu}^* + \overline{\mu_t}^*)\left(2\frac{\partial \bar{w}}{\partial z} - \frac{\partial \bar{u}}{\partial x} - \frac{\partial \bar{v}}{\partial y}\right) - \frac{2}{3}\overline{\rho \breve{k}}^*,
\end{aligned} \tag{3.167}$$

with $\overline{\tau_{tot,xy}}^* = \overline{\tau_{tot,yx}}^*$ and $\overline{\tau_{tot,xz}}^* = \overline{\tau_{tot,zx}}^*$, as well as

$$\overline{\tau_{tot,yz}}^* = \overline{\tau_{tot,zy}}^* := (\bar{\mu}^* + \overline{\mu_t}^*)\left(\frac{\partial \bar{v}}{\partial z} + \frac{\partial \bar{w}}{\partial y}\right); \tag{3.168}$$

based on [100] and [102]. As established in [100], the extension of the Boussinesq approximation to the small disturbance approach can be equally applied to the linearized periodic perturbation and linearized time-invariant-mean inherent to the organized unsteady turbulent heat flux vector under consideration of Fourier's law of heat conduction. Introducing the turbulent Prandtl number Pr_t, the linearized periodic perturbation inherent to the organized unsteady turbulent heat flux vector is expressed through the product between $\widetilde{\mu_t}^*/Pr_t$ and the gradient of $\tilde{T}^*$ summed with the product between $\overline{\mu_t}^*/Pr_t$ and the gradient of $\bar{T}^*$ [100]. Consequently, the linearized periodic perturbation inherent to the particular elements of the organized unsteady total heat flux vector becomes

$$\begin{aligned}
\widetilde{q_{tot,x}}^* &:= -\frac{\gamma}{\Gamma}\left[\left(\frac{\bar{\mu}^*}{Pr} + \frac{\overline{\mu_t}^*}{Pr_t}\right)\frac{\partial \tilde{T}^*}{\partial x} + \left(\frac{\tilde{\mu}^*}{Pr} + \frac{\widetilde{\mu_t}^*}{Pr_t}\right)\frac{\partial \bar{T}^*}{\partial x}\right], \\
\widetilde{q_{tot,y}}^* &:= -\frac{\gamma}{\Gamma}\left[\left(\frac{\bar{\mu}^*}{Pr} + \frac{\overline{\mu_t}^*}{Pr_t}\right)\frac{\partial \tilde{T}^*}{\partial y} + \left(\frac{\tilde{\mu}^*}{Pr} + \frac{\widetilde{\mu_t}^*}{Pr_t}\right)\frac{\partial \bar{T}^*}{\partial y}\right], \\
\widetilde{q_{tot,z}}^* &:= -\frac{\gamma}{\Gamma}\left[\left(\frac{\bar{\mu}^*}{Pr} + \frac{\overline{\mu_t}^*}{Pr_t}\right)\frac{\partial \tilde{T}^*}{\partial z} + \left(\frac{\tilde{\mu}^*}{Pr} + \frac{\widetilde{\mu_t}^*}{Pr_t}\right)\frac{\partial \bar{T}^*}{\partial z}\right],
\end{aligned} \tag{3.169}$$

as given in [100] and [102]. Complementarily, the linearized time-invariant mean inherent to the organized unsteady turbulent heat flux vector is expressed through the product between $\overline{\mu_t}^*/Pr_t$ and the gradient of $\bar{T}^*$ [100]. Hence, the linearized time invariant mean inherent to the particular elements of the organized unsteady total heat flux vector be-

comes

$$\begin{aligned}
\overline{q_{tot,x}}^{*} &:= -\frac{\gamma}{\Gamma}\left[\left(\frac{\bar{\mu}^{*}}{Pr}+\frac{\overline{\mu_t}^{*}}{Pr_t}\right)\frac{\partial \bar{T}^{*}}{\partial x}\right], \\
\overline{q_{tot,y}}^{*} &:= -\frac{\gamma}{\Gamma}\left[\left(\frac{\bar{\mu}^{*}}{Pr}+\frac{\overline{\mu_t}^{*}}{Pr_t}\right)\frac{\partial \bar{T}^{*}}{\partial y}\right], \\
\overline{q_{tot,z}}^{*} &:= -\frac{\gamma}{\Gamma}\left[\left(\frac{\bar{\mu}^{*}}{Pr}+\frac{\overline{\mu_t}^{*}}{Pr_t}\right)\frac{\partial \bar{T}^{*}}{\partial z}\right],
\end{aligned} \tag{3.170}$$

as given in [100] and [102]. The setting of Pr_t allows similarity with respect to the relationship between turbulent momentum diffusivity and turbulent thermal diffusivity to be achieved. Pr_t is treated as constant for the particular fluid. Following Wilcox [138, 139], the organized unsteady instance of the Cartesian total-shear-stress equivalent quantities for the turbulence kinetic energy can be expressed through a product between a calibrated organized unsteady total dynamic viscosity and the respective Cartesian spatial derivative of the organized unsteady specific turbulence kinetic energy. The linearized periodic-perturbation and time-invariant-mean directional instances then, respectively, are

$$\begin{aligned}
\widetilde{\tau_{\breve{k},x}}^{*} &:= (\tilde{\mu}^{*}+\sigma_{\breve{k}}\,\widetilde{\mu_t}^{*})\,\frac{\partial \overline{\breve{k}}}{\partial x}+(\bar{\mu}^{*}+\sigma_{\breve{k}}\,\overline{\mu_t}^{*})\,\frac{\partial \widetilde{\breve{k}}}{\partial x}, \\
\widetilde{\tau_{\breve{k},y}}^{*} &:= (\tilde{\mu}^{*}+\sigma_{\breve{k}}\,\widetilde{\mu_t}^{*})\,\frac{\partial \overline{\breve{k}}}{\partial y}+(\bar{\mu}^{*}+\sigma_{\breve{k}}\,\overline{\mu_t}^{*})\,\frac{\partial \widetilde{\breve{k}}}{\partial y}, \\
\widetilde{\tau_{\breve{k},z}}^{*} &:= (\tilde{\mu}^{*}+\sigma_{\breve{k}}\,\widetilde{\mu_t}^{*})\,\frac{\partial \overline{\breve{k}}}{\partial z}+(\bar{\mu}^{*}+\sigma_{\breve{k}}\,\overline{\mu_t}^{*})\,\frac{\partial \widetilde{\breve{k}}}{\partial z}
\end{aligned} \tag{3.171}$$

and

$$\overline{\tau_{\breve{k},x}}^{*} := (\bar{\mu}^{*}+\sigma_{\breve{k}}\,\overline{\mu_t}^{*})\,\frac{\partial \overline{\breve{k}}}{\partial x}, \quad \overline{\tau_{\breve{k},y}}^{*} := (\bar{\mu}^{*}+\sigma_{\breve{k}}\,\overline{\mu_t}^{*})\,\frac{\partial \overline{\breve{k}}}{\partial y}, \quad \overline{\tau_{\breve{k},z}}^{*} := (\bar{\mu}^{*}+\sigma_{\breve{k}}\,\overline{\mu_t}^{*})\,\frac{\partial \overline{\breve{k}}}{\partial z} \tag{3.172}$$

[102], with $\sigma_{\breve{k}}$ being the calibration constant [138]. Since the linearized periodic perturbation and the linearized time-invariant mean of the organized unsteady turbulence kinetic energy per unit volume can be, respectively, defined as

$$\widetilde{\rho\breve{k}}^{*} := \bar{\rho}\,\widetilde{\breve{k}}+\tilde{\rho}\,\overline{\breve{k}} \qquad \text{and} \qquad \overline{\rho\breve{k}}^{*} := \bar{\rho}\,\overline{\breve{k}}, \tag{3.173}$$

their specific-turbulence-kinetic-energy counterparts are gained through simple inversion:

$$\widetilde{\breve{k}} = \left(\widetilde{\rho\breve{k}}^{*}-\tilde{\rho}\,\overline{\breve{k}}\right)/\bar{\rho} \qquad \text{and} \qquad \overline{\breve{k}} = \overline{\rho\breve{k}}^{*}/\bar{\rho} \tag{3.174}$$

[102]. By means of Eq. (3.171) and Eq. (3.172) second-order diffusion of $\widetilde{\rho\breve{k}}^{*}$ is essentially introduced to the linearized periodic-perturbation instance of the energy equation.

Overall, the problem of closure regarding the linearized periodic perturbation and linearized time-invariant mean inherent to the organized unsteady turbulent transport of turbulence kinetic energy, the organized unsteady Reynolds stress work, the organized unsteady molecular diffusion, and the organized unsteady turbulent heat flux vector, has again been reduced to a problem of closure regarding $\widetilde{\mu_t}^*$, $\widetilde{\rho k}^*$, and $\tilde{T}^*$, as well as $\overline{\mu_t}^*$, $\overline{\rho k}^*$, and $\bar{T}^*$. Ultimately, the linearized periodic-perturbation contribution of the ψ-directional convective energy flux and that of its viscous counterpart are specified through their realigned instances, respectively,

$$\widetilde{E_{\psi\,5}}^* := \widetilde{E_{\psi\,5_{\mathrm{ra}}}}^* \qquad \text{and} \qquad \widetilde{E_{\mathrm{v}\,\psi\,5}}^* := \widetilde{E_{\mathrm{v}\,\psi\,5_{\mathrm{ra}}}}^* . \tag{3.175}$$

3.4 Unclosed Time-Domain Formulation

As established by Pechloff and Laschka in 2006, "[c]onsistent application of the triple decomposition to the instantaneous Navier-Stokes equations, while treating higher-order [perturbation] terms and turbulent [correlation terms], results in the [linearized] governing equations of the [periodic-perturbation] flow[field]."[100] They are designated as the small disturbance Navier-Stokes equations in their unclosed time-domain formulation. Cast in nondimensionalized strong conservation form for the curvilinear coordinate system [100],

$$\frac{\partial \widetilde{\mathbf{Q}}^*}{\partial \tau} + \frac{\partial \widetilde{\mathbf{F}}^*}{\partial \xi} + \frac{\partial \widetilde{\mathbf{G}}^*}{\partial \eta} + \frac{\partial \widetilde{\mathbf{H}}^*}{\partial \zeta} = \frac{\partial \widetilde{\mathbf{F}_{\mathbf{v}}}^*}{\partial \xi} + \frac{\partial \widetilde{\mathbf{G}_{\mathbf{v}}}^*}{\partial \eta} + \frac{\partial \widetilde{\mathbf{H}_{\mathbf{v}}}^*}{\partial \zeta} \tag{3.176}$$

is gained in analogy to Eq. (2.3).

$\widetilde{\mathbf{Q}}^*$ represents the linearized periodic perturbation inherent to the organized unsteady curvilinear state vector of dependent conservative variables [100]. It is defined through the linearized periodic perturbation and the linearized time-invariant-mean inherent to the organized unsteady Cartesian state vector of dependent conservative variables; i.e.,

$$\widetilde{\mathbf{Q}}^* := \overline{J}^* \, \tilde{\mathbf{q}}^* + \widetilde{J}^* \, \bar{\mathbf{q}}^* , \tag{3.177}$$

with

$$\tilde{\mathbf{q}}^* := (\tilde{\rho},\, \widetilde{\rho u}^*,\, \widetilde{\rho v}^*,\, \widetilde{\rho w}^*,\, \widetilde{\rho e}^*)^T \quad \text{and} \quad \bar{\mathbf{q}}^* := (\bar{\rho},\, \overline{\rho u}^*,\, \overline{\rho v}^*,\, \overline{\rho w}^*,\, \overline{\rho e}^*)^T , \tag{3.178}$$

respectively [100]. Whereas $\tilde{\mathbf{q}}^*$ becomes the sought-after Cartesian state vector (embodying the organized unsteady flowfield's linearized periodic perturbation), $\bar{\mathbf{q}}^*$ becomes its necessarily known counterpart (embodying the organized unsteady flowfield's linearized time-invariant mean). Concerning $\tilde{\mathbf{q}}^*$, the linearized periodic-perturbation conservative variables supplementing $\tilde{\rho}$ are defined as

$$\widetilde{\rho u}^* := \bar{\rho}\tilde{u} + \tilde{\rho}\bar{u} , \quad \widetilde{\rho v}^* := \bar{\rho}\tilde{v} + \tilde{\rho}\bar{v} , \quad \widetilde{\rho w}^* := \bar{\rho}\tilde{w} + \tilde{\rho}\bar{w} , \quad \widetilde{\rho e}^* := \bar{\rho}\tilde{e} + \tilde{\rho}\bar{e} ; \tag{3.179}$$

i.e., each being a sum of a product between the periodic perturbation and the time-invariant mean of two primitive variables [100]. Complementarily, the linearized time-invariant-mean conservative variables supplementing $\bar{\rho}$ in $\bar{\mathbf{q}}^*$ are defined as

$$\overline{\rho u}^* := \bar{\rho}\bar{u}\,, \quad \overline{\rho v}^* := \bar{\rho}\bar{v}\,, \quad \overline{\rho w}^* := \bar{\rho}\bar{w}\,, \quad \overline{\rho e}^* := \bar{\rho}\bar{e}\,; \tag{3.180}$$

i.e., each being a product between the time-invariant mean of two primitive variables [100]. Hence, the periodic perturbation and the time-invariant mean of the Cartesian velocities, as well as the specific total energy, are, respectively, gained through

$$\tilde{u} = \left(\widetilde{\rho u}^* - \tilde{\rho}\bar{u}\right)/\bar{\rho}, \quad \tilde{v} = \left(\widetilde{\rho v}^* - \tilde{\rho}\bar{v}\right)/\bar{\rho}, \quad \tilde{w} = \left(\widetilde{\rho w}^* - \tilde{\rho}\bar{w}\right)/\bar{\rho}, \quad \tilde{e} = \left(\widetilde{\rho e}^* - \tilde{\rho}\bar{e}\right)/\bar{\rho} \tag{3.181}$$

and

$$\bar{u} = \overline{\rho u}^*/\bar{\rho}\,, \quad \bar{v} = \overline{\rho v}^*/\bar{\rho}\,, \quad \bar{w} = \overline{\rho w}^*/\bar{\rho}\,, \quad \bar{e} = \overline{\rho e}^*/\bar{\rho}\,. \tag{3.182}$$

Lastly, $\overline{J}^*$ and $\widetilde{J}^*$ of Eq. (3.177) denote the linearized periodic perturbation and the linearized time-invariant mean inherent to the determinant of the coordinate transformation's Jacobian; also see Kreiselmaier [70]. The given definition of $\widetilde{\mathbf{Q}}^*$ itself is straightforwardly substantiated. Since the expansion of $\mathbf{Q}$ only renders products of the Cartesian velocities' and the specific total energy's erratic fluctuation with the time-invariant-mean or periodic-perturbation density, no turbulent correlation terms remain after phase- or time-averaging; also see Iatrou [54].

$\widetilde{\mathbf{F}}^*$, $\widetilde{\mathbf{G}}^*$, and $\widetilde{\mathbf{H}}^*$ represent the linearized periodic perturbation inherent to the organized unsteady convective flux vectors, respectively, in ξ, η, and ζ direction. Correspondingly, $\widetilde{\mathbf{F}_\mathbf{v}}^*$, $\widetilde{\mathbf{G}_\mathbf{v}}^*$, and $\widetilde{\mathbf{H}_\mathbf{v}}^*$ represent the linearized periodic perturbation inherent to the organized unsteady viscous flux vectors. Each set can be formulated through the pertinent generalized-curvilinear-coordinate instance; i.e.,

$$\widetilde{\mathbf{E}_\psi}^* = \begin{pmatrix} \bar{\rho}\,\widetilde{\theta_\psi}^* & + & \tilde{\rho}\,\overline{\theta_\psi}^* & & & & \\ \overline{\rho u}^*\,\widetilde{\theta_\psi}^* & + & \widetilde{\rho u}^*\,\overline{\theta_\psi}^* & + & \overline{J\psi_x}^*\,\tilde{p}^* & + & \widetilde{J\psi_x}^*\,\bar{p}^* \\ \overline{\rho v}^*\,\widetilde{\theta_\psi}^* & + & \widetilde{\rho v}^*\,\overline{\theta_\psi}^* & + & \overline{J\psi_y}^*\,\tilde{p}^* & + & \widetilde{J\psi_y}^*\,\bar{p}^* \\ \overline{\rho w}^*\,\widetilde{\theta_\psi}^* & + & \widetilde{\rho w}^*\,\overline{\theta_\psi}^* & + & \overline{J\psi_z}^*\,\tilde{p}^* & + & \widetilde{J\psi_z}^*\,\bar{p}^* \\ \bar{H}^*\,\widetilde{\theta_\psi}^* & + & \tilde{H}^*\,\overline{\theta_\psi}^* & - & \overline{J\psi_t}^*\,\tilde{p}^* & - & \widetilde{J\psi_t}^*\,\bar{p}^* \end{pmatrix} \tag{3.183}$$

or

$$\widetilde{\mathbf{E}_{\mathbf{v}\,\psi}}^{*} = \begin{pmatrix} 0 \\ \overline{J\psi_x}^{*}\widetilde{\tau_{tot,xx}}^{*} + \overline{J\psi_y}^{*}\widetilde{\tau_{tot,yx}}^{*} + \overline{J\psi_z}^{*}\widetilde{\tau_{tot,zx}}^{*} + \widetilde{J\psi_x}^{*}\overline{\tau_{tot,xx}}^{*} + \widetilde{J\psi_y}^{*}\overline{\tau_{tot,yx}}^{*} + \widetilde{J\psi_z}^{*}\overline{\tau_{tot,zx}}^{*} \\ \overline{J\psi_x}^{*}\widetilde{\tau_{tot,xy}}^{*} + \overline{J\psi_y}^{*}\widetilde{\tau_{tot,yy}}^{*} + \overline{J\psi_z}^{*}\widetilde{\tau_{tot,zy}}^{*} + \widetilde{J\psi_x}^{*}\overline{\tau_{tot,xy}}^{*} + \widetilde{J\psi_y}^{*}\overline{\tau_{tot,yy}}^{*} + \widetilde{J\psi_z}^{*}\overline{\tau_{tot,zy}}^{*} \\ \overline{J\psi_x}^{*}\widetilde{\tau_{tot,xz}}^{*} + \overline{J\psi_y}^{*}\widetilde{\tau_{tot,yz}}^{*} + \overline{J\psi_z}^{*}\widetilde{\tau_{tot,zz}}^{*} + \widetilde{J\psi_x}^{*}\overline{\tau_{tot,xz}}^{*} + \widetilde{J\psi_y}^{*}\overline{\tau_{tot,yz}}^{*} + \widetilde{J\psi_z}^{*}\overline{\tau_{tot,zz}}^{*} \\ \overline{J\psi_x}^{*}\widetilde{\Pi_{tot,x}}^{*} + \overline{J\psi_y}^{*}\widetilde{\Pi_{tot,y}}^{*} + \overline{J\psi_z}^{*}\widetilde{\Pi_{tot,z}}^{*} + \widetilde{J\psi_x}^{*}\overline{\Pi_{tot,x}}^{*} + \widetilde{J\psi_y}^{*}\overline{\Pi_{tot,y}}^{*} + \widetilde{J\psi_z}^{*}\overline{\Pi_{tot,z}}^{*} \end{pmatrix}. \tag{3.184}$$

The substitution $\psi = \xi$, η, or ζ then, respectively, yields $\widetilde{\mathbf{F}}^{*} = \widetilde{\mathbf{E}_{\xi}}^{*}$ and $\widetilde{\mathbf{F}_{\mathbf{v}}}^{*} = \widetilde{\mathbf{E}_{\mathbf{v}\,\xi}}^{*}$, $\widetilde{\mathbf{G}}^{*} = \widetilde{\mathbf{E}_{\eta}}^{*}$ and $\widetilde{\mathbf{G}_{\mathbf{v}}}^{*} = \widetilde{\mathbf{E}_{\mathbf{v}\,\eta}}^{*}$, or $\widetilde{\mathbf{H}}^{*} = \widetilde{\mathbf{E}_{\zeta}}^{*}$ and $\widetilde{\mathbf{H}_{\mathbf{v}}}^{*} = \widetilde{\mathbf{E}_{\mathbf{v}\,\zeta}}^{*}$.

The explicit formulation of $\overline{J}^{*}$ and $\widetilde{J}^{*}$, $\overline{\boldsymbol{J\xi}}^{*}$ and $\widetilde{\boldsymbol{J\xi}}^{*}$, $\overline{\boldsymbol{J\eta}}^{*}$ and $\widetilde{\boldsymbol{J\eta}}^{*}$, $\overline{\boldsymbol{J\zeta}}^{*}$ and $\widetilde{\boldsymbol{J\zeta}}^{*}$, had already been provided by Kreiselmaier [70]. It had also been given by Sickmüller [119] and Iatrou [54]. Thus, it is sufficient to note in this dissertation that $\widetilde{J}^{*}$, $\widetilde{\boldsymbol{J\xi}}^{*}$, $\widetilde{\boldsymbol{J\eta}}^{*}$, and $\widetilde{\boldsymbol{J\zeta}}^{*}$ are linear with respect to the curvilinear spatial derivatives of the periodic-perturbation Cartesian spatial coordinates. Further following Kreiselmaier [70], the linearized time-invariant-mean and periodic-perturbation instances of the generalized temporal metric become

$$\overline{J\psi_t}^{*} = 0 \qquad \text{and} \qquad \widetilde{J\psi_t}^{*} = -\frac{\partial\tilde{\boldsymbol{r}}}{\partial\tau}\,\overline{\boldsymbol{J\psi}}^{*}; \tag{3.185}$$

also see [119, 54]. Equivalent to the small disturbance Euler equations' time-domain formulation [70], physical time-dependency is still inherent to Eq. (3.176) through both the sought-after $\tilde{\mathbf{q}}^{*}$ and the known $\widetilde{J}^{*}$, $\widetilde{\boldsymbol{J\psi}}^{*}$, $\widetilde{J\psi_t}^{*}$. Again, all linearized periodic-perturbation entities only appear as products with linearized time-invariant-mean entities [100]. Consequently, the governed flowfield becomes confined to a dynamically linear instance about the linearized time-invariant-mean flowfield. The latter is equal to a steady-state flowfield rendered for the considered body's time-invariant-mean position, and can thus be considered known as well [100].

3.5 Closing the Governing Equation System

The derivation of the small disturbance Navier-Stokes equations' time-domain formulation has been accompanied by the emergence of unresolved systemic field quantities; i.e., the linearized periodic-perturbation and linearized time-invariant-mean instances of the static temperature, the static pressure, the dynamic molecular viscosity, the dynamic eddy viscosity, and the turbulence kinetic energy per unit volume. Providing closure to

the said instances of the static temperature and the static pressure is straightforward. It can be realized by the appropriate treatment of the known instantaneous relationships; i.e., the instantaneous form of the thermal equation of state and the instantaneous static pressure as a function of the instantaneous conservative variables. Likewise, closure of the said instances of the dynamic molecular viscosity can be simply provided through the appropriate treatment of Sutherland's law. For the dynamic eddy viscosity and turbulence kinetic energy, however, achieving closure becomes far more intricate. A governing turbulence model which satisfies the requirements of the considered aerodynamic problem, while being receptive to a small disturbance formulation, needs to be selected. The S/A one-equation turbulence model [121] presents such an instance. The closure of the small disturbance Navier-Stokes equations' time-domain formulation had been initially shown for two dimensions by Pechloff and Laschka [99] in 2004, and was published [100] in 2006.

3.5.1 Static Temperature/Pressure

Connectivity between the static temperature and the static pressure in both their linearized periodic-perturbation and linearized time-invariant-mean instances can be established straightforwardly, as outlined in [100]. Neglecting higher-order perturbation terms within the phase-averaged instance of the thermal equation of state, Eq. (3.89), yields

$$\langle p \rangle^* = \bar{\rho}\,\bar{T}^* + \bar{\rho}\,\tilde{T}^* + \tilde{\rho}\,\bar{T}^* \,. \tag{3.186}$$

Complementarily, time-averaging the expansion of the thermal equation of state, Eq. (3.88), and subsequent linearization produces

$$\bar{p}^* = \bar{\rho}\,\bar{T}^* \,. \tag{3.187}$$

Hence, the linearized periodic-perturbation instance of the thermal equation of state becomes

$$\tilde{p}^* := \langle p \rangle^* - \bar{p}^* = \bar{\rho}\,\tilde{T}^* + \tilde{\rho}\,\bar{T}^* \,. \tag{3.188}$$

Inversely, the linearized periodic-perturbation and linearized time-invariant-mean instances of the static temperature are, respectively, given as

$$\tilde{T}^* = \left(\tilde{p}^* - \tilde{\rho}\,\bar{T}^*\right)/\bar{\rho} \qquad \text{and} \qquad \bar{T}^* = \bar{p}^*/\rho \tag{3.189}$$

[100].

The relationship between the instantaneous static pressure and the instantaneous conservative variables is provided by Eq. (2.16). As further established in [100], its triple decomposition and subsequent linearization allows the relationship between the linearized

periodic-perturbation static pressure and the linearized periodic-perturbation/time-invariant-mean conservative variables to be rendered:

$$\begin{aligned}\tilde{p}^*(\tilde{\mathbf{q}}^*,\,\bar{\mathbf{q}}^*) \;:=\; \Gamma\,\Bigg\{\; \widetilde{\rho e}^{\,*} \;\;+\;\; \tilde{\rho}\,\left[(\overline{\rho u}^{\,*})^2+(\overline{\rho v}^{\,*})^2+(\overline{\rho w}^{\,*})^2\right]/\left(2\,\bar{\rho}^2\right) \\ -\;\; (\overline{\rho u}^{\,*}\,\widetilde{\rho u}^{\,*}+\overline{\rho v}^{\,*}\,\widetilde{\rho v}^{\,*}+\overline{\rho w}^{\,*}\,\widetilde{\rho w}^{\,*})\,/\bar{\rho}\;-\;\widetilde{\breve{\rho k}}^{\,*}\;\Bigg\}\;;\end{aligned} \tag{3.190}$$

also given in [102]. In this regard, the relationship between the linearized time-invariant-mean static pressure and the linearized time-invariant-mean conservative variables has become

$$\bar{p}^*(\bar{\mathbf{q}}^*) \;=\; \Gamma\left\{\; \overline{\rho e}^{\,*} \;\;-\;\; \left[(\overline{\rho u}^{\,*})^2+(\overline{\rho v}^{\,*})^2+(\overline{\rho w}^{\,*})^2\right]/\left(2\,\bar{\rho}\right) \;-\; \overline{\breve{\rho k}}^{\,*}\;\right\}\;; \tag{3.191}$$

also given in [102]. At this point, the linearized periodic-perturbation and linearized time-invariant-mean turbulence kinetic energy per unit volume, respectively, inherent to Eq. (3.190) and Eq. (3.191), still remains unresolved. When discounted, however, these Equations conform to the relationships governing the linearized periodic-perturbation and linearized time-invariant-mean static pressure in closure of the small disturbance Euler equations' time-domain formulation [70] [100].

3.5.2 Dynamic Molecular Viscosity

As established by Pechloff and Laschka, "Sutherland's law defies [the] conventional decomposition into a [linearized periodic-perturbation] and [linearized time-invariant-]mean part because of its mathematical nature[. Thus], an alternative approach based on a first-order Taylor series expansion of Eq. ([2.17]) about the [linearized time-invariant-]mean static temperature is pursued."[100] Ultimately, the linearized periodic-perturbation dynamic molecular viscosity is governed by

$$\tilde{\mu}^*(\tilde{T}^*,\,\bar{T}^*) := \frac{\bar{\mu}^*}{\bar{T}^*+S}\left[\frac{3(\bar{T}^*+S)}{2\bar{T}^*}-1\right]\tilde{T}^*\,, \tag{3.192}$$

with

$$\bar{\mu}^*(\bar{T}^*) := \mu_\infty\;\bar{T}^{*\,\frac{3}{2}}\;(1+S)\,/\left(\bar{T}^*+S\right) \tag{3.193}$$

as its linearized time-invariant-mean counterpart [100].

3.5.3 Dynamic Eddy Viscosity and Turbulence Kinetic Energy

The S/A one-equation turbulence model [121] had been selected to realize the dynamic eddy viscosity closure [100]. In this regard, Spalart and Allmaras summarized that they

> [had assembled a single] transport equation for the [kinematic eddy] viscosity [...], using empiricism and arguments of dimensional analysis, Galilean invariance and selective dependence on the [kinematic] molecular viscosity. [...] Unlike early one-equation models the resulting turbulence model is local (i.e., the equation at one [field] point does not [directly] depend on the solution at other [field] points), and therefore [is] compatible with [structured] grids of [multiblock topology] and Navier-Stokes solvers in two or three dimensions. It is numerically forgiving, in terms of near-wall resolution and stiffness, and yields fairly rapid convergence to the steady state. The wall and freestream boundary conditions are trivial. [121]

The transport equation itself is a PDE of mixed mathematical nature, which actually accounts for the convection, production, diffusion and destruction of a primitive working variable over time, supplemented by a set of algebraic auxiliary functions [121, 100]. In contrast to the kinematic eddy viscosity, the S/A primitive working variable is designed to "[behave] linearly near the wall. [...] Therefore, [this turbulence] model will not require a finer grid than an algebraic [turbulence] model would."[121] A $d^+ \leq 5$ generally is sufficient for aerodynamically smooth surfaces; e.g., similar to the d^+ requirement of the B/L algebraic turbulence model [8], yet less stringent than the $d^+ \approx 1$ of the Wilcox k-omega two-equation turbulence model [138]. The production and destruction of the S/A primitive working variable is devised as a function of the considered field point's distance to the nearest no-slip wall, however, in keeping with the property of locality [121]. In this regard, the B/L algebraic turbulence model [8] exemplifies the deficit of nonlocality: It requires the boundary layer's vorticity profile to be ascertained in a wall-perpendicular sweep in order to switch from an inner- to an outer-layer formulation, while also relying on a separate wake formulation [8]. For complex geometries, this process can become computationally expensive, unwieldily, and render a locally discontinuous/ambiguous eddy viscosity; also stated in [121]. The Wilcox k-omega two-equation turbulence model [138], on the other hand, satisfies the property of locality. It employs a transport equation for both $\rho\breve{k}$ and the turbulence dissipation rate per unit volume $\rho\breve{\omega}$, with the latter eliminating the need to compute a field point's distance to the nearest no-slip wall altogether [138]. As noted by Spalart and Allmaras, such transport-equation models, however, typically "involve strong source terms that often degrade the convergence, and demand [nontrivial] upstream and freestream conditions for the turbulence variables[,]"[121] while their prediction capabilities have been widely shown to be superior only when expansive regions of flow separation occur; e.g., as induced by strong shocks. A circumstance that had likewise been investigated by Pechloff and Laschka [102]. For the transonic flow regime, the S/A one-equation turbulence model is preferably formulated in terms of a conservative working variable [121]. In this regard, the transport equation can be rendered into a strong conservation curvilinear coordinate form, allowing it to be easily incorporated into an equal instance of

the RANS equations [100]. A relationship for determining the specific turbulence kinetic energy was not given by Spalart and Allmaras, as the eddy viscosity per se had been the emphasis of the modeling effort [121]. Over the last decades, the S/A one-equation turbulence model has become a standard in the RANS computations of attached transonic flow for aircraft aerodynamics. Its prediction accuracy with regard to shock/boundary-layer interaction has been well established.

Deriving a small disturbance formulation of the S/A one-equation turbulence model [121], it needs to be considered that the conventional formulation already pertains to a statistically treated flowfield. For the purpose here, this is the phase-averaged flowfield. Hence, the constituting primitive variables merely need to be expanded into a time-invariant-mean and periodic-perturbation part within the transport equation. Time-averaging and subsequent linearization then yields a linearized time-invariant-mean formulation. Eventually, subtraction from the linearized organized unsteady formulation renders the sought-after linearized periodic perturbation of the transport equation [100]. For those auxiliary relationships where this dual decomposition and linearization fails, a Taylor-series expansion about the linearized time-invariant-mean state can be alternatively employed, as all auxiliary relationships are continuously differentiable [100]. In contrast, the B/L algebraic turbulence model [8] employs a nonanalytic switch between the inner- and outer-layer formulation, hindering a straightforward linearization. Clark [28] had originally shown the suitability of the S/A one-equation turbulence model for a complete linearization with regard to the internal flow problem in 1998. With the precedingly discussed practice, Pechloff and Laschka [99] had then obtained the small disturbance formulation of the S/A one-equation turbulence model for the two-dimensional external flow problem in 2004, which was subsequently published [100] in 2006. Because merely fully turbulent boundary layers are to be considered, the S/A one-equation turbulence model's transition tripping functions [121] were disregard from the outset [100].

The extension of the linearized periodic-perturbation instance of the S/A transport equation [121] for the third spatial dimension yields

$$\frac{\partial \widetilde{Q_6}^*}{\partial \tau} + \frac{\partial \widetilde{F_6}^*}{\partial \xi} + \frac{\partial \widetilde{G_6}^*}{\partial \eta} + \frac{\partial \widetilde{H_6}^*}{\partial \zeta} = \frac{\partial \widetilde{F_{\mathrm{v}\,6}}^*}{\partial \xi} + \frac{\partial \widetilde{G_{\mathrm{v}\,6}}^*}{\partial \eta} + \frac{\partial \widetilde{H_{\mathrm{v}\,6}}^*}{\partial \zeta} + \widetilde{T_6}^* \,, \tag{3.194}$$

appending the small disturbance Navier-Stokes equations' unclosed time-domain formulation [100]. In this regard, the sixth elements of the linearized periodic-perturbation curvilinear state vector, the linearized periodic-perturbation generalized convective flux vector, and the linearized periodic-perturbation generalized viscous flux vector, respectively, are

$$\widetilde{Q_6}^* := \overline{J}^* \, \widetilde{q_6}^* + \widetilde{J}^* \, \overline{q_6}^* = \overline{J}^* \, \widetilde{\breve{\mu}}^* + \widetilde{J}^* \, \overline{\breve{\mu}}^* \,, \qquad \widetilde{E_{6\,\psi}}^* := \overline{\breve{\mu}}^* \, \widetilde{\theta_\psi}^* + \widetilde{\breve{\mu}}^* \, \overline{\theta_\psi}^* \,, \quad \text{and}$$

$$\widetilde{E_{\mathrm{v}\,6\psi}}^* := \overline{J\psi_x}^* \, \widetilde{\tau_{\breve{\nu},x}}^* + \overline{J\psi_y}^* \, \widetilde{\tau_{\breve{\nu},y}}^* + \overline{J\psi_z}^* \, \widetilde{\tau_{\breve{\nu},z}}^* + \widetilde{J\psi_x}^* \, \overline{\tau_{\breve{\nu},x}}^* + \widetilde{J\psi_y}^* \, \overline{\tau_{\breve{\nu},y}}^* + \widetilde{J\psi_z}^* \, \overline{\tau_{\breve{\nu},z}}^* \tag{3.195}$$

[100]. Therein, $\widetilde{\breve{\mu}}^*$ and $\overline{\breve{\mu}}^*$, respectively, embody the linearized periodic-perturbation and linearized time-invariant-mean instance of the S/A conservative working variable [121], specified as

$$\widetilde{\breve{\mu}}^* := \bar{\rho}\,\widetilde{\breve{\nu}} + \tilde{\rho}\,\overline{\breve{\nu}} \qquad \text{and} \qquad \overline{\breve{\mu}}^* := \bar{\rho}\,\overline{\breve{\nu}} \tag{3.196}$$

through their primitive counterparts $\widetilde{\breve{\nu}}$ and $\overline{\breve{\nu}}$ [100]. Naturally, Eq. (3.194) merely governs $\widetilde{\breve{\mu}}^*$. In the small disturbance Navier-Stokes equations' closed time-domain formulation, it becomes the sixth sought-after conservative variable. The periodic-perturbation instance of the S/A primitive working variable is then gained through simple inversion:

$$\widetilde{\breve{\nu}} = \left(\widetilde{\breve{\mu}}^* - \tilde{\rho}\,\overline{\breve{\nu}}\right) / \bar{\rho}\,, \qquad \text{with} \qquad \overline{\breve{\nu}} = \overline{\breve{\mu}}^* / \bar{\rho} \tag{3.197}$$

as its time-invariant-mean counterpart. Equal to the five other (linearized) time-invariant-mean conservative variables, $\overline{\breve{\mu}}^*$ is considered a priori known, satisfying the linearized time-invariant-mean instance of the S/A one-equation turbulence model. Ultimately, the required linearized periodic-perturbation dynamic eddy viscosity results from

$$\widetilde{\mu_t}^* := \overline{\breve{\mu}}^* \widetilde{f_{v1}}^* + \widetilde{\breve{\mu}}^* \overline{f_{v1}}^* \tag{3.198}$$

[100], wherein $\widetilde{f_{v1}}^*$ and $\overline{f_{v1}}^*$, respectively, are the linearized periodic-perturbation and linearized time-invariant-mean instance of the S/A first viscous damping function [121]; i.e.,

$$\widetilde{f_{v1}}^* := 3\,(\overline{f_{v1}}^*)^2 c_{v1}^3\,\widetilde{\breve{\chi}}^* / (\overline{\breve{\chi}}^*)^4 \qquad \text{and} \qquad \overline{f_{v1}}^* := (\overline{\breve{\chi}}^*)^3 / \left[(\overline{\breve{\chi}}^*)^3 + c_{v1}^3\right], \tag{3.199}$$

with

$$\widetilde{\breve{\chi}}^* := \overline{\breve{\chi}}^* \left(\widetilde{\breve{\mu}}^* / \overline{\breve{\mu}}^* - \tilde{\mu}^* / \bar{\mu}^*\right) \qquad \text{and} \qquad \overline{\breve{\chi}}^* := \overline{\breve{\mu}}^* / \bar{\mu}^* \tag{3.200}$$

[100]. Furthermore, the required linearized time-invariant-mean eddy viscosity straightforwardly results from

$$\overline{\mu_t}^* := \overline{\breve{\mu}}^* \overline{f_{v1}}^* \tag{3.201}$$

[100]. Allowing for second-order diffusion of $\widetilde{\breve{\mu}}^*$, $\widetilde{E_{\mathrm{v}\,6\psi}}^*$ has become constituted by the linearized periodic-perturbation and linearized time-invariant-mean instances of the S/A Cartesian total-shear-stress equivalent quantities [121], respectively,

$$\begin{aligned}
\widetilde{\tau_{\breve{\nu},x}}^* &:= \overline{\tau_{\breve{\nu},x}}^* \left[\frac{\partial\widetilde{\breve{\nu}}}{\partial x} / \frac{\partial\overline{\breve{\nu}}}{\partial x} + \left(\tilde{\mu}^* + \widetilde{\breve{\mu}}^*\right) / \left(\bar{\mu}^* + \overline{\breve{\mu}}^*\right)\right] \text{ and } \overline{\tau_{\breve{\nu},x}}^* = \left(\bar{\mu}^* + \overline{\breve{\mu}}^*\right) \frac{\partial\overline{\breve{\nu}}}{\partial x} / \sigma_{S/A}\,; \\
\widetilde{\tau_{\breve{\nu},y}}^* &:= \overline{\tau_{\breve{\nu},y}}^* \left[\frac{\partial\widetilde{\breve{\nu}}}{\partial y} / \frac{\partial\overline{\breve{\nu}}}{\partial y} + \left(\tilde{\mu}^* + \widetilde{\breve{\mu}}^*\right) / \left(\bar{\mu}^* + \overline{\breve{\mu}}^*\right)\right] \text{ and } \overline{\tau_{\breve{\nu},y}}^* = \left(\bar{\mu}^* + \overline{\breve{\mu}}^*\right) \frac{\partial\overline{\breve{\nu}}}{\partial y} / \sigma_{S/A}\,; \\
\widetilde{\tau_{\breve{\nu},z}}^* &:= \overline{\tau_{\breve{\nu},z}}^* \left[\frac{\partial\widetilde{\breve{\nu}}}{\partial z} / \frac{\partial\overline{\breve{\nu}}}{\partial z} + \left(\tilde{\mu}^* + \widetilde{\breve{\mu}}^*\right) / \left(\bar{\mu}^* + \overline{\breve{\mu}}^*\right)\right] \text{ and } \overline{\tau_{\breve{\nu},z}}^* = \left(\bar{\mu}^* + \overline{\breve{\mu}}^*\right) \frac{\partial\overline{\breve{\nu}}}{\partial z} / \sigma_{S/A}
\end{aligned} \tag{3.202}$$

[100]. Completing Eq. (3.194), the linearized periodic-perturbations instance of the S/A turbulence source term [121] is gained as

$$\widetilde{T_6}^* := \overline{J}^* (\widetilde{P_{\breve{\mu}}}^* + \widetilde{D_{\breve{\mu}}}^* + \widetilde{F_{\breve{\mu}}}^*) + \widetilde{J}^* (\overline{P_{\breve{\mu}}}^* + \overline{D_{\breve{\mu}}}^* + \overline{F_{\breve{\mu}}}^*) \,, \tag{3.203}$$

accounting for the production, destruction, and first-order diffusion of $\widetilde{\breve{\mu}}^*$ [100]. Given that the small disturbance Navier-Stokes equations' unclosed time-domain formulation has no source term vector to append $\widetilde{T_6}^*$ to,

$$\widetilde{\mathbf{T}}^* := \overline{J}^* \left(0,\, 0,\, 0,\, 0,\, 0,\, \widetilde{P_{\breve{\mu}}}^* + \widetilde{D_{\breve{\mu}}}^* + \widetilde{F_{\breve{\mu}}}^* \right)^T + \widetilde{J}^* \left(0,\, 0,\, 0,\, 0,\, 0,\, \overline{P_{\breve{\mu}}}^* + \overline{D_{\breve{\mu}}}^* + \overline{F_{\breve{\mu}}}^* \right)^T \tag{3.204}$$

is novelly introduced on the RHS of Eq. (3.176) as an additional summand. The linearized periodic-perturbation and linearized time-invariant-mean instance of the S/A production term [121] are, respectively, gained as

$$\widetilde{P_{\breve{\mu}}}^* := \overline{P_{\breve{\mu}}}^* \left(\widetilde{\breve{\mu}}^* / \overline{\breve{\mu}}^* + \widetilde{|\breve{\boldsymbol{\omega}}|}^* / \overline{|\breve{\boldsymbol{\omega}}|}^* \right) \quad \text{and} \quad \overline{P_{\breve{\mu}}}^* = c_{b1} \overline{|\breve{\boldsymbol{\omega}}|}^* \overline{\breve{\mu}}^* \,, \tag{3.205}$$

employing the linearized periodic-perturbation instance of the magnitude of vorticity

$$\begin{aligned} \widetilde{|\boldsymbol{\omega}|}^* \;:=\; & \left[\left(\frac{\partial \bar{w}}{\partial y} - \frac{\partial \bar{v}}{\partial z} \right) \left(\frac{\partial \tilde{w}}{\partial y} - \frac{\partial \tilde{v}}{\partial z} \right) \right. \\ & + \left(\frac{\partial \bar{u}}{\partial z} - \frac{\partial \bar{w}}{\partial x} \right) \left(\frac{\partial \tilde{u}}{\partial z} - \frac{\partial \tilde{w}}{\partial x} \right) \\ & + \left. \left(\frac{\partial \bar{v}}{\partial x} - \frac{\partial \bar{u}}{\partial y} \right) \left(\frac{\partial \tilde{v}}{\partial x} - \frac{\partial \tilde{u}}{\partial y} \right) \right] / \, \overline{|\boldsymbol{\omega}|}^* \end{aligned} \tag{3.206}$$

and its time-invariant-mean counterpart

$$\overline{|\boldsymbol{\omega}|}^* := \sqrt{\left(\frac{\partial \bar{w}}{\partial y} - \frac{\partial \bar{v}}{\partial z} \right)^2 + \left(\frac{\partial \bar{u}}{\partial z} - \frac{\partial \bar{w}}{\partial x} \right)^2 + \left(\frac{\partial \bar{v}}{\partial x} - \frac{\partial \bar{u}}{\partial y} \right)^2} \tag{3.207}$$

under the modifications

$$\widetilde{|\breve{\boldsymbol{\omega}}|}^* := \widetilde{|\boldsymbol{\omega}|}^* + \left(\overline{|\breve{\boldsymbol{\omega}}|}^* - \overline{|\boldsymbol{\omega}|}^* \right) \left(\widetilde{\breve{\nu}} / \overline{\breve{\nu}} + \widetilde{f_{v2}}^* / \overline{f_{v2}}^* - 2\, \tilde{d}^* / \bar{d}^* \right) \tag{3.208}$$

and

$$\overline{|\breve{\boldsymbol{\omega}}|}^* := \overline{|\boldsymbol{\omega}|}^* + \overline{\breve{\nu}}\, \overline{f_{v2}}^* / \left(\kappa\, \bar{d}^* \right)^2 \tag{3.209}$$

[100]. Therein, $\tilde{d}^*$ and $\bar{d}^*$, respectively, stand for the linearized periodic-perturbation and linearized time-invariant-mean instance of the regarded field point's distance to the nearest wall [100]. In addition, $\widetilde{f_{v2}}^*$ and $\overline{f_{v2}}^*$, respectively, are the linearized periodic-perturbation

and linearized time-invariant-mean instance of the S/A second viscous damping function [121]; i.e.,

$$\widetilde{f_{v2}}^{*} := \left(1 - \overline{f_{v2}}^{*}\right)^{2} \left[\widetilde{f_{v1}}^{*} - \widetilde{\breve{\chi}}^{*}/(\overline{\breve{\chi}}^{*})^{2}\right] \quad \text{and} \quad \overline{f_{v2}}^{*} := 1 - \overline{\breve{\chi}}^{*} \,/\, \left(1 + \overline{\breve{\chi}}^{*}\,\overline{f_{v1}}^{*}\right) \tag{3.210}$$

[100]. The linearized periodic-perturbation and linearized time-invariant-mean instance of the S/A destruction term [121], respectively, become

$$\widetilde{D_{\breve{\mu}}}^{*} := \overline{D_{\breve{\mu}}}^{*} \left(\widetilde{f_w}^{*} \,/\, \overline{f_w}^{*} + 2\,\widetilde{\breve{\mu}}^{*} \,/\, \overline{\breve{\mu}}^{*} - 2\,\tilde{d}^{*}/\bar{d}^{*} - \tilde{\rho}/\bar{\rho}\right) \text{ and } \overline{D_{\breve{\mu}}}^{*} := -c_{w1}\overline{f_w}^{*} \left(\overline{\breve{\mu}}^{*}/\bar{d}^{*}\right)^{2}/\bar{\rho}\,, \tag{3.211}$$

employing the linearized periodic-perturbation and linearized time-invariant-mean instance of the S/A wall function [121]:

$$\widetilde{f_w}^{*} := (\overline{f_w}^{*}/\bar{g}^{*})^{7}\, c_{w3}^{6}\, \tilde{g}^{*} / \left(1 + c_{w3}^{6}\right) \quad \text{and} \quad \overline{f_w}^{*} := \bar{g}^{*} \left\{\left(1 + c_{w3}^{6}\right) / \left[(\bar{g}^{*})^{6} + c_{w3}^{6}\right]\right\}^{\frac{1}{6}} \tag{3.212}$$

[100]. Therein, $\tilde{g}^{*}$ and $\bar{g}^{*}$, respectively, are the linearized periodic-perturbation and linearized time-invariant-mean instance of the S/A intermediary limiter function [121]; i.e.,

$$\tilde{g}^{*} := \left\{1 + c_{w2}\left[6(\bar{r}^{*})^{5} - 1\right]\right\} \tilde{r}^{*} \quad \text{and} \quad \bar{g}^{*} := \bar{r}^{*} + c_{w2}\left[(\bar{r}^{*})^{6} - \bar{r}^{*}\right], \tag{3.213}$$

with the linearized periodic-perturbation and linearized time-invariant-mean instance of the S/A wall function argument [121]:

$$\tilde{r}^{*} := \bar{r}^{*} \left(\widetilde{\breve{\nu}}/\,\overline{\breve{\nu}} - \widetilde{|\breve{\boldsymbol{\omega}}|}^{*} \,/\, \overline{|\breve{\boldsymbol{\omega}}|}^{*} - 2\,\tilde{d}^{*}/\,\bar{d}^{*}\right) \quad \text{and} \quad \bar{r}^{*} := \overline{\breve{\nu}} \,/\, \left[\overline{|\breve{\boldsymbol{\omega}}|}^{*} (\kappa\,\bar{d}^{*})^{2}\right] \tag{3.214}$$

[100]. Lastly, the linearized periodic-perturbation and linearized time-invariant-mean instance of the S/A first-order diffusion term [121] are, respectively, obtained to

$$\widetilde{F_{\breve{\mu}}}^{*} := \overline{F_{\breve{\mu}}}^{*} \left(2\,\boldsymbol{\nabla}\widetilde{\breve{\nu}} \,/\, \boldsymbol{\nabla}\overline{\breve{\nu}} + \tilde{\rho}/\bar{\rho}\right) \quad \text{and} \quad \overline{F_{\breve{\mu}}}^{*} = \bar{\rho}\, c_{b2}\, \boldsymbol{\nabla}\overline{\breve{\nu}}\, \boldsymbol{\nabla}\overline{\breve{\nu}}/\sigma_{S/A} \tag{3.215}$$

[100]. The calibration constants of the S/A one-equation turbulence model [121] remain unmodified:

$$\begin{array}{llllllll} \sigma_{S/A} & = & 2/3\,, & \kappa & = & 0.41\,, & & \\ c_{v1} & = & 7.1\,, & c_{b1} & = & 0.1355\,, & c_{b2} & = & 0.622\,, \\ c_{w1} & = & c_{b1}/\kappa^{2} + (1 + c_{b2})/\sigma_{S/A}\,, & c_{w2} & = & 0.3\,, & c_{w3} & = & 2.0 \end{array} \tag{3.216}$$

[100].

Employing the S/A one-equation turbulence model [121] in its small disturbance formulation, both the periodic-perturbation and time-invariant-mean instance of the specific turbulence kinetic energy are permissibly disregarded. Consequently, $\widetilde{\rho\breve{k}}^{*}$ is eliminated from $\widetilde{\tau_{tot,xx}}^{*}$, $\widetilde{\tau_{tot,yy}}^{*}$, and $\widetilde{\tau_{tot,zz}}^{*}$, just as $\overline{\rho\breve{k}}^{*}$ is eliminated from $\overline{\tau_{tot,xx}}^{*}$, $\overline{\tau_{tot,yy}}^{*}$, and $\overline{\tau_{tot,zz}}^{*}$;

see Eq. (3.71) and Eq. (3.165), as well as Eq. (3.75) and Eq. (3.167). Likewise, $\widetilde{\tau_{\check{k},x}}^*$, $\widetilde{\tau_{\check{k},y}}^*$, and $\widetilde{\tau_{\check{k},z}}^*$, as well as $\overline{\tau_{\check{k},x}}^*$, $\overline{\tau_{\check{k},y}}^*$, and $\overline{\tau_{\check{k},z}}^*$ are eliminated; see Eq. (3.171) and Eq. (3.172). Lastly, $\widetilde{\rho\check{k}}^*$ is disregarded in $\tilde{p}^*(\tilde{\mathbf{q}}^*, \bar{\mathbf{q}}^*)$ and $\overline{\rho\check{k}}^*$ is disregarded in $\bar{p}^*(\bar{\mathbf{q}}^*)$, respectively, Eq. (3.190) and Eq. (3.191). Employing the Wilcox k-omega two-equation turbulence model [138] in its small disturbance formulation, however, all these instances would be accounted for [102].

3.6 Closed Frequency-Domain Formulation

The small disturbance Navier-Stokes equations in their S/A-one-equation-turbulence-model-closed time-domain formulation govern the flowfield's dynamically linear perturbation response to the considered body's forced periodic motion (the flowfield's excitation); see Pechloff and Laschka [100]. Since physical time dependence naturally persists throughout the governing equation system, its numerical solution is still associated with a computationally expensive time-accurate deforming grid approach. This deficit can be remedied, however, by constraining both the flowfield's excitation and dynamically linear perturbation response to the same time law, allowing the governing equation system to be transitioned to the frequency domain. Kreiselmaier [70] had originally applied this technique to the small disturbance Euler equations' closed time-domain formulation in 1998. For two-dimensional space, the small disturbance Navier-Stokes equations' partially closed time-domain formulation had been transitioned to the frequency domain by Pechloff et al. [98] in 2002. A particular eddy viscosity turbulence model had not been specified at that time. Pechloff and Laschka [99] initially presented the transition of the S/A-one-equation-turbulence-model-closed two-dimensional instance in 2004, which was then published [100] in 2006. Iatrou et al. [57] had shown the application of this technique as well; i.e., initially for two-dimensional space, with the small disturbance Navier-Stokes equations' partially closed time-domain formulation eventually supplemented by the B/L algebraic turbulence model under a FEVA. The transition of this particular three-dimensional instance was subsequently provided by Iatrou et al. [55], and eventually included in Iatrou's [54] dissertation of 2009.

On the basis of Kreiselmaier [70], the three-dimensional instance of the small disturbance Navier-Stokes equations' S/A-one-equation-turbulence-model-closed time-domain formulation is initially rearranged. With respect to the two-dimensional instance, Pechloff and Laschka already stated that

> [a]s ha[d] become evident, for example, in Eq. [(3.40) and Eq. (3.41)], decomposition and [linearization] yielded two basic sets of terms throughout the equation system: The first group, to be denoted by superscript (1), exclusively contains the unknown [periodic-perturbation field] quantities appearing in linear combination with [the lin-

> earized time-invariant-mean instance of the determinant of the coordinate transformation's Jacobian or the linearized time-invariant-mean spatial metrics, and, yet not necessarily, the (linearized) time-invariant-mean field quantities ...]. The complementary second group, hence distinguished by superscript (2), solely consists of the [linearized periodic-perturbation instance of the determinant of the coordinate transformation's Jacobian or the linearized periodic-perturbation spatial and temporal] metrics in linear combination with the [(linearized) time-invariant-]mean [field] quantities. All terms collected in group [superscript] (2) are designated as known[,] because of the following considerations: The [time-dependent] deformation of the computational grid is [governed] through the [considered] body's [prescribed] periodic motion, consequently supplying the [linearzed periodic-perturbation instance of the determinant of the coordinate transformation's Jacobian, as well as the linearized periodic-perturbation spatial and temporal] metrics. Similar, the [(linearized) time-invariant-]mean [field] quantities can be provided in advance by a steady-state RANS solution for the [considered] body's [time-invariant-]mean[(reference)] position. [100]

In addition, the associated computational grid (with its discrete reference instances of the determinant of the coordinate transformation's Jacobian and the discrete reference spatial metrics) is utilized to express the linearized time-invariant-mean instance of the determinant of the coordinate transformation's Jacobian and the linearized time-invariant-mean spatial metrics composing group superscript (1), once discretized [70]. Distinguishing the individual perturbation terms in the preceding manner, as also noted by Pechloff et al. [98], naturally permeates the three-dimensional constitutive vectors:

$$\begin{aligned} \widetilde{\mathbf{Q}}^{*} &= \widetilde{\mathbf{Q}}^{(1)} + \widetilde{\mathbf{Q}}^{(2)}, & \widetilde{\mathbf{E}_{\psi}}^{*} &= \widetilde{\mathbf{E}_{\psi}}^{(1)} + \widetilde{\mathbf{E}_{\psi}}^{(2)}, \\ \widetilde{\mathbf{E}_{\mathbf{v}\,\psi}}^{*} &= \widetilde{\mathbf{E}_{\mathbf{v}\,\psi}}^{(1)} + \widetilde{\mathbf{E}_{\mathbf{v}\,\psi}}^{(2)}, & \widetilde{\mathbf{T}}^{*} &= \widetilde{\mathbf{T}}^{(1)} + \widetilde{\mathbf{T}}^{(2)}, \end{aligned} \tag{3.217}$$

wherein superscript (1) and superscript (2) have also displaced the original $(\ )^{*}$ modifier as the indicator of linearization. Henceforth, $\widetilde{\mathbf{Q}}^{(1)}$, $\widetilde{\mathbf{E}_{\psi}}^{(1)}$, $\widetilde{\mathbf{E}_{\mathbf{v}\,\psi}}^{(1)}$, and $\widetilde{\mathbf{T}}^{(1)}$ are referred to as the $\widetilde{\mathbf{q}}^{*}$-homogenous constitutive vectors. Complementarily, $\widetilde{\mathbf{Q}}^{(2)}$, $\widetilde{\mathbf{E}_{\psi}}^{(2)}$, $\widetilde{\mathbf{E}_{\mathbf{v}\,\psi}}^{(2)}$, and $\widetilde{\mathbf{T}}^{(2)}$ are referred to as the $\widetilde{J}^{*}/\widetilde{\boldsymbol{J}\boldsymbol{\psi}}^{*}/\widetilde{J\psi_{t}}^{*}$-homogenous constitutive vectors [70].

Rewriting the three-dimensional instance of the small disturbance Navier-Stokes equations' S/A-one-equation-turbulence-model-closed time-domain formulation in this

manner [100] eventually yields

$$\frac{\partial\widetilde{\mathbf{Q}}^{(1)}}{\partial\tau}+\frac{\partial}{\partial\xi}\left(\widetilde{\mathbf{F}}^{(1)}-\widetilde{\mathbf{F}_{\mathbf{v}}}^{(1)}\right)+\frac{\partial}{\partial\eta}\left(\widetilde{\mathbf{G}}^{(1)}-\widetilde{\mathbf{G}_{\mathbf{v}}}^{(1)}\right)+\frac{\partial}{\partial\zeta}\left(\widetilde{\mathbf{H}}^{(1)}-\widetilde{\mathbf{H}_{\mathbf{v}}}^{(1)}\right)=$$
$$-\left[\frac{\partial\widetilde{\mathbf{Q}}^{(2)}}{\partial\tau}+\frac{\partial}{\partial\xi}\left(\widetilde{\mathbf{F}}^{(2)}-\widetilde{\mathbf{F}_{\mathbf{v}}}^{(2)}\right)+\frac{\partial}{\partial\eta}\left(\widetilde{\mathbf{G}}^{(2)}-\widetilde{\mathbf{G}_{\mathbf{v}}}^{(2)}\right)+\frac{\partial}{\partial\zeta}\left(\widetilde{\mathbf{H}}^{(2)}-\widetilde{\mathbf{H}_{\mathbf{v}}}^{(2)}\right)\right] \tag{3.218}$$
$$+\ \widetilde{\mathbf{T}}^{(1)}\ +\ \widetilde{\mathbf{T}}^{(2)}\,,$$

having arranged all the $\widetilde{J}^{*}/\widetilde{\boldsymbol{J\psi}}^{*}/\widetilde{J\psi_t}^{*}$-homogenous constitutive vectors on the RHS. In their entirety, they embody an a priori known source term, which, for the numerical solution of Eq. (3.218), would render the supplied linearized time-invariant-mean flowfield's contribution to the linearized periodic-perturbation flowfield due to the computational grid's linearized periodic-perturbation deformation [100]. Essentially, this circumstance had already been recognized in [70], and was also established in [98].

Further following Kreiselmaier [70], the periodic time law of choice is again specified to be a simple harmonic oscillation of known nondimensional angular frequency. It will govern both the flowfield's excitation and dynamically linear perturbation response, yielding an adequate representation of the time dependence inherent to the flutter problem. A substantial simplification of the mathematical treatment is realized through complex analysis [70]. In this regard, the physical excitation is stipulated to be a sine oscillation; i.e., the employed complex time law becomes

$$e^{i(k\tau-\pi/2)}:=\cos(k\tau-\pi/2)+i\sin(k\tau-\pi/2)=\sin(k\tau)-i\cos(k\tau)\,. \tag{3.219}$$

Hence, the periodic-perturbation Cartesian position vector of the considered body's surface vertices, as well as the instances of the grid internal vertices (induced by the surface's deformation/dislocation) can be said to obey the following:

$$\tilde{\mathbf{r}}(\xi,\,\eta,\,\zeta,\,\tau):=\hat{\mathbf{r}}(\xi,\,\eta,\,\zeta)\,e^{i(k\tau-\pi/2)}\,,\quad\text{with}\quad\hat{\mathbf{r}}(\xi,\,\eta,\,\zeta):=(\hat{x},\,\hat{y},\,\hat{z})^{T}\quad\in\mathbb{R}\,, \tag{3.220}$$

as the novel amplitude Cartesian position vector; based on [70], as well as Pechloff and Laschka [100]. Henceforth, the $\widehat{(\ )}$ modifier will serve to designate the (per se time-invariant) amplitude of any periodic-perturbation entity. As far as such an entity has the property of being linearized, the $(\ )^{*}$ modifier will not be carried over in order to avoid double notation [100]. Kreiselmaier [70] showed that Eq. (3.220) fully permeates the linearized periodic-perturbation instance of the determinant of the coordinate transformation's Jacobian, as well as the linearized periodic-perturbation spatial metric vectors and corresponding temporal metrics. Thus, the formulation

$$\widetilde{J}^{*}=\widehat{J}\,e^{i(k\tau-\pi/2)}\,,\quad\widetilde{\boldsymbol{J\psi}}^{*}=\widehat{\boldsymbol{J\psi}}\,e^{i(k\tau-\pi/2)}\,,\quad\widetilde{J\psi_t}^{*}=\widehat{J\psi_t}\,e^{i(k\tau-\pi/2)} \tag{3.221}$$

becomes equally valid, with

$$\widehat{J}\,, \quad \widehat{\boldsymbol{J\psi}} := \left(\widehat{J\psi_x},\, \widehat{J\psi_y},\, \widehat{J\psi_z}\right)^T \quad \in \mathbb{R}\,, \quad \widehat{J\psi_t} = -i\,k\,\hat{\mathbf{r}}\,\overline{\boldsymbol{J\psi}}^{\,*} \quad \in \mathbb{C}\,, \tag{3.222}$$

respectively, as the novel amplitude instance of the determinant of the coordinate' transformations Jacobian, the amplitude generalized spatial metric vector, and the corresponding temporal metric [70]; also given in [98, 100]. Notably, $\widehat{J\psi_t}$ is purely imaginary [70]. The flowfield's dynamically linear perturbation response is handled equivalently to its excitation [70, 98, 100]. Any periodic-perturbation primitive field quantity can then be said to obey the following:

$$\tilde{\Phi}(\xi,\eta,\zeta,\tau) \;:=\; \hat{\Phi}(\xi,\eta,\zeta)\,e^{i(k\tau-\pi/2)}\,, \quad \text{however, with} \quad \hat{\Phi}(\xi,\eta,\zeta) \quad \in \mathbb{C}\,, \tag{3.223}$$

as the novel amplitude instance of the considered primitive variable. Its imaginary part elegantly accounts for the periodic-perturbation primitive variable's local phase-shift to the excitation [70, 98, 100].

In keeping with Kreiselmaier [70], Pechloff et al. [98], as well as Pechloff and Laschka [100], all periodic-perturbation primitive variables inherent to the $\tilde{\mathbf{q}}^*$-homogenous constitutive vectors of Eq. (3.218) are individually substituted as per Eq. (3.223). Equally, Eq. (3.221) is applied to the $\widetilde{J}^*/\widetilde{\boldsymbol{J\psi}}^*/\widetilde{J\psi_t}^*$-homogenous constitutive vectors. For both groups, the respective amplitude and complex-time-law formulations fully permeate the linearized periodic-perturbation constitutive vectors. Hence, it is permissible to express them accordingly:

$$\begin{aligned}
\widetilde{\mathbf{Q}}^{(1)} &= \widehat{\mathbf{Q}}^{(1)}\,e^{i(k\tau-\pi/2)}\,, & \widetilde{\mathbf{Q}}^{(2)} &= \widehat{\mathbf{Q}}^{(2)}\,e^{i(k\tau-\pi/2)}\,;\\
\widetilde{\mathbf{E}_{\psi}}^{(1)} &= \widehat{\mathbf{E}_{\psi}}^{(1)}\,e^{i(k\tau-\pi/2)}\,, & \widetilde{\mathbf{E}_{\psi}}^{(2)} &= \widehat{\mathbf{E}_{\psi}}^{(2)}\,e^{i(k\tau-\pi/2)}\,;\\
\widetilde{\mathbf{E}_{\mathbf{v}\,\psi}}^{(1)} &= \widehat{\mathbf{E}_{\mathbf{v}\,\psi}}^{(1)}\,e^{i(k\tau-\pi/2)}\,, & \widetilde{\mathbf{E}_{\mathbf{v}\,\psi}}^{(2)} &= \widehat{\mathbf{E}_{\mathbf{v}\,\psi}}^{(2)}\,e^{i(k\tau-\pi/2)}\,;\\
\widetilde{\mathbf{T}}^{(1)} &= \widehat{\mathbf{T}}^{(1)}\,e^{i(k\tau-\pi/2)}\,, & \widetilde{\mathbf{T}}^{(2)} &= \widehat{\mathbf{T}}^{(2)}\,e^{i(k\tau-\pi/2)}
\end{aligned} \tag{3.224}$$

[70, 98, 100]. This allows the temporal derivatives of Eq. (3.218) to be taken; i.e.,

$$\begin{aligned}
\frac{\partial\widetilde{\mathbf{Q}}^{(1)}}{\partial\tau} &= ik\widehat{\mathbf{Q}}^{(1)}\,e^{i(k\tau-\pi/2)}\\
&:= ik\widehat{\mathbf{Q}}^{(1)}\,e^{i(k\tau-\pi/2)} \;+\; \frac{\partial\widehat{\mathbf{Q}}^{(1)}}{\partial\tau^{\circ}}\,e^{i(k\tau-\pi/2)}\,, \quad \text{with} \quad \frac{\partial\widehat{\mathbf{Q}}^{(1)}}{\partial\tau^{\circ}} = 0
\end{aligned} \tag{3.225}$$

for the introduced pseudotime τ°, as well as

$$\frac{\partial\widetilde{\mathbf{Q}}^{(2)}}{\partial\tau} \;=\; ik\widehat{\mathbf{Q}}^{(2)}\,e^{i(k\tau-\pi/2)}\,, \tag{3.226}$$

having both been originally provided by Kreiselmaier [70].

Since $e^{i(k\tau-\pi/2)}$ is linearly inherent to all summands of Eq. (3.218), the instances cancel each other out, eliminating time dependence altogether [70, 98, 100]. Ultimately, the three-dimensional instance of the small disturbance Navier-Stokes equations' S/A-one-equation-turbulence-model-closed time-domain formulation transitions to the frequency domain; i.e., on the basis of Pechloff and Laschka [100],

$$\frac{\partial\widehat{\mathbf{Q}}^{(1)}}{\partial\tau^{\circ}}+\frac{\partial}{\partial\xi}\left(\widehat{\mathbf{F}}^{(1)}-\widehat{\mathbf{F}_{\mathbf{v}}}^{(1)}\right)+\frac{\partial}{\partial\eta}\left(\widehat{\mathbf{G}}^{(1)}-\widehat{\mathbf{G}_{\mathbf{v}}}^{(1)}\right)+\frac{\partial}{\partial\zeta}\left(\widehat{\mathbf{H}}^{(1)}-\widehat{\mathbf{H}_{\mathbf{v}}}^{(1)}\right)=\widehat{\mathbf{S}}^{(1)}+\widehat{\mathbf{S}}^{(2)}\,, \tag{3.227}$$

with the novel amplitude source term vectors

$$\widehat{\mathbf{S}}^{(1)} = -ik\widehat{\mathbf{Q}}^{(1)}+\widehat{\mathbf{T}}^{(1)}\,, \tag{3.228}$$

$$\begin{aligned}\widehat{\mathbf{S}}^{(2)} &= -\left[ik\widehat{\mathbf{Q}}^{(2)}+\frac{\partial}{\partial\xi}\left(\widehat{\mathbf{F}}^{(2)}-\widehat{\mathbf{F}_{\mathbf{v}}}^{(2)}\right)+\frac{\partial}{\partial\eta}\left(\widehat{\mathbf{G}}^{(2)}-\widehat{\mathbf{G}_{\mathbf{v}}}^{(2)}\right)+\frac{\partial}{\partial\zeta}\left(\widehat{\mathbf{H}}^{(2)}-\widehat{\mathbf{H}_{\mathbf{v}}}^{(2)}\right)\right]\\ &+ \widehat{\mathbf{T}}^{(2)}.\end{aligned} \tag{3.229}$$

In this regard, the $\hat{\mathbf{q}}$-homogenous constitutive vectors are

$$\widehat{\mathbf{Q}}^{(1)}=\overline{J}^{*}\,\hat{\mathbf{q}}=\overline{J}^{*}\begin{pmatrix}\hat{\rho}\\ \widehat{\rho u}\\ \widehat{\rho v}\\ \widehat{\rho w}\\ \widehat{\rho e}\\ \widehat{\breve{\mu}}\end{pmatrix},\quad \widehat{\mathbf{E}_{\psi}}^{(1)}=\begin{pmatrix}\bar{\rho}\,\widehat{\theta_{\psi}}^{(1)} & + & \hat{\rho}\,\overline{\theta_{\psi}}^{*} & & \\ \overline{\rho u}^{*}\,\widehat{\theta_{\psi}}^{(1)} & + & \widehat{\rho u}\,\overline{\theta_{\psi}}^{*} & + & \overline{J\psi_x}^{*}\,\hat{p}\\ \overline{\rho v}^{*}\,\widehat{\theta_{\psi}}^{(1)} & + & \widehat{\rho v}\,\overline{\theta_{\psi}}^{*} & + & \overline{J\psi_y}^{*}\,\hat{p}\\ \overline{\rho w}^{*}\,\widehat{\theta_{\psi}}^{(1)} & + & \widehat{\rho w}\,\overline{\theta_{\psi}}^{*} & + & \overline{J\psi_z}^{*}\,\hat{p}\\ \bar{H}^{*}\,\widehat{\theta_{\psi}}^{(1)} & + & \hat{H}\,\overline{\theta_{\psi}}^{*} & & \\ \overline{\breve{\mu}}^{*}\,\widehat{\theta_{\psi}}^{(1)} & + & \widehat{\breve{\mu}}\,\overline{\theta_{\psi}}^{*} & & \end{pmatrix}, \tag{3.230}$$

$$\widehat{\mathbf{E}_{\mathbf{v}\,\psi}}^{(1)}=\begin{pmatrix}0\\ \overline{J\psi_x}^{*}\,\widehat{\tau_{tot,xx}}+\overline{J\psi_y}^{*}\,\widehat{\tau_{tot,yx}}+\overline{J\psi_z}^{*}\,\widehat{\tau_{tot,zx}}\\ \overline{J\psi_x}^{*}\,\widehat{\tau_{tot,xy}}+\overline{J\psi_y}^{*}\,\widehat{\tau_{tot,yy}}+\overline{J\psi_z}^{*}\,\widehat{\tau_{tot,zy}}\\ \overline{J\psi_x}^{*}\,\widehat{\tau_{tot,xz}}+\overline{J\psi_y}^{*}\,\widehat{\tau_{tot,yz}}+\overline{J\psi_z}^{*}\,\widehat{\tau_{tot,zz}}\\ \overline{J\psi_x}^{*}\,\widehat{\Pi_{tot,x}}+\overline{J\psi_y}^{*}\,\widehat{\Pi_{tot,y}}+\overline{J\psi_z}^{*}\,\widehat{\Pi_{tot,z}}\\ \overline{J\psi_x}^{*}\,\widehat{\tau_{\breve{\nu},x}} + \overline{J\psi_y}^{*}\,\widehat{\tau_{\breve{\nu},y}} + \overline{J\psi_z}^{*}\,\widehat{\tau_{\breve{\nu},z}}\end{pmatrix},\quad \widehat{\mathbf{T}}^{(1)}=\overline{J}^{*}\begin{pmatrix}0\\0\\0\\0\\0\\ \widehat{P_{\breve{\mu}}}+\widehat{D_{\breve{\mu}}}+\widehat{F_{\breve{\mu}}}\end{pmatrix}, \tag{3.231}$$

with

$$\widehat{\theta_{\psi}}^{(1)}=\overline{J\psi_x}^{*}\,\hat{u}+\overline{J\psi_y}^{*}\,\hat{v}+\overline{J\psi_z}^{*}\,\hat{w} \tag{3.232}$$

[70], and

$$\widehat{\mathbf{Q}}^{(1)}\,, \quad \widehat{\mathbf{E}_{\psi}}^{(1)}\,, \quad \widehat{\mathbf{E}_{\mathbf{v}\,\psi}}^{(1)}\,, \quad \widehat{\mathbf{T}}^{(1)} \quad \in \mathbb{C}\,. \tag{3.233}$$

Each substitutive amplitude entity inherent to the $\hat{\mathbf{q}}$-homogenous constitutive vectors (e.g., $\hat{p}$, $\hat{H}$, $\widehat{P_{\breve{\mu}}}$, $\widehat{\tau_{tot,xx}}$, $\widehat{\Pi_{tot,x}}$, and $\widehat{\tau_{\breve{\nu}\,x}}$) is formulated by simply replacing the $\widetilde{(\;)}^{*}$ and/or $\widetilde{(\;)}$ modifiers with the $\widehat{(\;)}$ modifier in the respective time domain formulation, as provided in Section 3.3 and Section 3.5. Naturally, this applies to all concealed amplitude entities (e.g., $\widehat{q_{tot,x}}$, $\hat{T}$, and $\hat{\mu}$) likewise. Furthermore, the amplitude primitive variables are gained from the amplitude conservative variables in accordance with the expressions yielding their time-domain counterparts; i.e., Eq. (3.179) and Eq. (3.197). Complementing the $\hat{\mathbf{q}}$-homogenous constitutive vectors, the $\widehat{J}/\widehat{\boldsymbol{J\psi}}/\widehat{J\psi_t}$-homogenous constitutive vectors, which exclusively make up $\widehat{\mathbf{S}}^{(2)}$, are

$$\widehat{\mathbf{Q}}^{(2)} = \widehat{J}\,\bar{\mathbf{q}}^{*} = \widehat{J}\begin{pmatrix} \bar{\rho} \\ \overline{\rho u}^{*} \\ \overline{\rho v}^{*} \\ \overline{\rho w}^{*} \\ \overline{\rho e}^{*} \\ \overline{\breve{\mu}}^{*} \end{pmatrix}, \qquad \widehat{\mathbf{E}_{\psi}}^{(2)} = \begin{pmatrix} \bar{\rho}\,\widehat{\theta_{\psi}}^{(2)} & & \\ \overline{\rho u}^{*}\,\widehat{\theta_{\psi}}^{(2)} & + & \widehat{J\psi_x}\,\bar{p}^{*} \\ \overline{\rho v}^{*}\,\widehat{\theta_{\psi}}^{(2)} & + & \widehat{J\psi_y}\,\bar{p}^{*} \\ \overline{\rho w}^{*}\,\widehat{\theta_{\psi}}^{(2)} & + & \widehat{J\psi_z}\,\bar{p}^{*} \\ \bar{H}^{*}\,\widehat{\theta_{\psi}}^{(2)} & - & \widehat{J\psi_t}\,\bar{p}^{*} \\ \overline{\breve{\mu}}^{*}\,\widehat{\theta_{\psi}}^{(2)} & & \end{pmatrix}, \tag{3.234}$$

$$\widehat{\mathbf{E}_{\mathbf{v}\,\psi}}^{(2)} = \begin{pmatrix} 0 \\ \widehat{J\psi_x}\overline{\tau_{tot,xx}}^{*} + \widehat{J\psi_y}\overline{\tau_{tot,yx}}^{*} + \widehat{J\psi_z}\overline{\tau_{tot,zx}}^{*} \\ \widehat{J\psi_x}\overline{\tau_{tot,xy}}^{*} + \widehat{J\psi_y}\overline{\tau_{tot,yy}}^{*} + \widehat{J\psi_z}\overline{\tau_{tot,zy}}^{*} \\ \widehat{J\psi_x}\overline{\tau_{tot,xz}}^{*} + \widehat{J\psi_y}\overline{\tau_{tot,yz}}^{*} + \widehat{J\psi_z}\overline{\tau_{tot,zz}}^{*} \\ \widehat{J\psi_x}\overline{\Pi_{tot,x}}^{*} + \widehat{J\psi_y}\overline{\Pi_{tot,y}}^{*} + \widehat{J\psi_z}\overline{\Pi_{tot,z}}^{*} \\ \widehat{J\psi_x}\,\overline{\tau_{\breve{\nu},x}}^{*} + \widehat{J\psi_y}\,\overline{\tau_{\breve{\nu},y}}^{*} + \widehat{J\psi_z}\,\overline{\tau_{\breve{\nu},z}}^{*} \end{pmatrix}, \quad \widehat{\mathbf{T}}^{(2)} = \widehat{J}\begin{pmatrix} 0 \\ 0 \\ 0 \\ 0 \\ 0 \\ \overline{P_{\breve{\mu}}}^{*} + \overline{D_{\breve{\mu}}}^{*} + \overline{F_{\breve{\mu}}}^{*} \end{pmatrix}, \tag{3.235}$$

with

$$\widehat{\theta_{\psi}}^{(2)} = \widehat{J\psi_x}\bar{u} + \widehat{J\psi_y}\bar{v} + \widehat{J\psi_z}\bar{w} + \widehat{J\psi_t} \tag{3.236}$$

[70], and

$$\widehat{\mathbf{Q}}^{(2)}\,, \quad \widehat{\mathbf{E}_{\mathbf{v}\,\psi}}^{(2)}\,, \quad \widehat{\mathbf{T}}^{(2)} \quad \in \mathbb{R}\,; \qquad \widehat{\mathbf{E}_{\psi}}^{(2)} \quad \in \mathbb{C} \tag{3.237}$$

[100]. The explicit formulation of $\widehat{J}$, $\widehat{\boldsymbol{J\xi}}$, $\widehat{\boldsymbol{J\eta}}$, and $\widehat{\boldsymbol{J\zeta}}$ had already been provided by Kreiselmaier [70], and was also given by Iatrou [54]. As with FLM-SDEu [70], however, the constituting curvilinear spatial coordinate derivatives of the amplitude Cartesian spatial

coordinates will not actually be evaluated in the FLM-SD.NS implementation to obtain $\widehat{J}$, $\widehat{\boldsymbol{J}\boldsymbol{\xi}}$, $\widehat{\boldsymbol{J}\boldsymbol{\eta}}$, and $\widehat{\boldsymbol{J}\boldsymbol{\zeta}}$.

Pursuant to Pechloff and Laschka, it can be summarized that

> [w]ith the derivation of the small disturbance Navier-Stokes equations[' S/A-one-equation-turbulence-model-closed frequency-domain formulation], the initial unsteady problem has been reduced to a steady one for the complex amplitude[s of the periodic-perturbation conservative variables]. As $\hat{\mathbf{Q}}^{(1)}$ is invariant to time, [...] $\partial\hat{\mathbf{Q}}^{(1)}/\partial\tau$ consequently [does not appear in] Eq. ([3.227]). However, [$\partial\widehat{\mathbf{Q}}^{(1)}/\partial\tau^{\circ}$ has been introduced] in order to construct a [pseudotime-integration] solution scheme[for the sought-after $\hat{\mathbf{q}}$]. Coupling between the in-phase (real) and out-of-phase (imaginary) parts of the complex equation system is solely provided by $ik\hat{\mathbf{Q}}^{(1)}$[within $\widehat{\mathbf{S}}^{(1)}$]. For $k = 0$, [which is] the quasi-steady case, this [coupling] is eliminated, therefore restricting the solution to the real part. [Essentially, it corresponds to $k \to 0$ of the closed RANS equations' application to the considered unsteady problem.] Letting $Re_{\infty} \to \infty$, while disregarding the turbulence model [...], yields the small disturbance Euler equations as given in [[70]]. Thus, implementing the small disturbance Navier-Stokes method FLM-SD.NS on the basis of the existing small disturbance Euler [method] FLM-SDEu becomes reasonable. [100]

Complementarily, restricting Re_{∞} to low values, while again disregarding the turbulence model, the small disturbance Navier-Stokes equations' closed frequency-domain formulation can be employed to treat simple harmonic excitations of fully laminar flow [98, 54], which, however, has only limited use in practice. Under consideration of either inviscid or fully laminar flow conditions, the originally employed phase average would become redundant: The erratic fluctuations otherwise inherent to the instantaneous field quantities can be ruled out a priori. Hence, the triple decomposition reduces to a dual decomposition; i.e., an instantaneous field quantity is merely expanded into a periodic perturbation and a time-invariant mean, with the given time average sufficing to accomplish the decomposition.

Chapter 4

Numerical Method

The general numerical method FLM-SD.NS allowing a case-particular approximative solution of the small disturbance Navier-Stokes equations (frequency-domain formulated) is implemented as an extension of the existing Euler counterpart FLM-SDEu [98, 100, 103]. For its S/A-one-equation-turbulence-model incarnation, the derived amplitude viscous flux and turbulence source term vectors, as well as the pertinent auxiliary functions, are principally incorporated into the FLM-SDEu code [100]. Additionally, the amplitude state and convective flux vectors are supplemented to accommodate the amplitude and linearized time-invariant-mean instances of the S/A conservative working variable [100]. The original boundary conditions are modified accordingly [54], and the inherent pseudo-time integration upgraded for enhanced solution convergence and stability [98, 100, 103]. The intricacies of this particular FLM-SD.NS incarnation are provided, focusing on the extensions made to FLM-SDEu. Naturally, substantial algorithmic commonality exists to the initial laminar incarnation of Pechloff et al. [98], as well as to the B/L-algebraic-turbulence-model incarnation of Iatrou et al. [57] (also subject of Iatrou's [54] dissertation of 2009) originating from it. In the following, the S/A-one-equation-turbulence-model incarnation will simply be referred to as FLM-SD.NS. An extension with the Wilcox k-omega two-equation turbulence model [138] had been made by Pechloff and Laschka [102] beyond this dissertation.

4.1 Overview

Established in [98, 100, 103], a meticulous effort has been made to extend the numerical equivalence already existing between FLM-SDEu and FLM-Eu, as well as between FLM-NS and FLM-Eu, to the FLM-SD.NS implementation; i.e., to likewise realize it between FLM-SD.NS and FLM-SDEu, as well as between FLM-SD.NS and FLM-NS. This is particularly important in the latter instance, because FLM-NS will be appropriated, on one hand, to supply the linearized time-invariant-mean flowfield to FLM-SD.NS, while, on the

other hand, to provide a dynamically fully nonlinear comparative result for the considered unsteady case [98, 100, 103] if required. Concerning the actual FLM-SD.NS implementation, the Fortran 90 programming language utilized in the existing methods' realization is again employed [103] to code the FLM-SDEu extension. In this regard, the intrinsic disjoined treatment of a complex variable's real and imaginary part is retained. As with FLM-SDEu, a number of time-invariant-mean entities need to be stored by FLM-SD.NS during its execution. Again, the greater memory requirements become the trade-off made toward the computational efficiency gain over FLM-NS [98, 100, 103].

4.1.1 Inherited Properties

In accordance with Pechloff et al. [98], as well as Pechloff and Laschka [100, 103], FLM-SD.NS fully inherits the finite volume shock-capturing approach [6] for structured multi-block grids [16] of FLM-SDEu devised by Kreiselmaier [70]. His small disturbance adaptation of a Godunov-type upwind scheme [43, 6, 48], as also described in the dissertation of Sickmüller [119], is continuatively employed. In terms of the governing equations' cell-centroidal discretization, dimensional splitting [48] had been invoked. The multidimensional characteristic of information propagation in continuous space is reduced to an independent instance for each curvilinear coordinate direction respective the individual computational cell. A Riemann initial value problem [6, 48, 50, 16] for the amplitude state vector then exists between the cell and its immediate neighbors. Thus, an accordant utilization of Roe's approximate Riemann-solver [111, 143, 48, 16] was able to render the evaluation of both the $\hat{\mathbf{q}}$- and $\widehat{\boldsymbol{J}\boldsymbol{\psi}}$-homogenous convective flux vectors at each shared bounding surface; i.e., for the considered cell's pertinent directional interface. In this regard, the upwind scheme's inherent first-order spatial accuracy was increased to second-order [6, 48] by directionally extrapolating the amplitude and linearized time-invariant-mean conservative variables accounted on the particular interface's left and right proximate side, respectively, from instances attributed to the two preceding and two succeeding centroids [70]. This practice is based on Van Leer's MUSCL [130, 48]. Conventionally, second-order upwinding is known to produce spurious oscillations in the field quantities for unsmooth regions of a computed flowfield, e.g., in the vicinity of shocks, degrading local resolution and often the overall stability of the solution scheme [6, 48]. In order to nevertheless maintain the total-variation-diminishing property associated with first-order upwinding, spatial accuracy must be locally reduced. This can be accomplished by embedding a limiter function that is responsive to the slope of a particular field quantity into the extrapolation [6, 48]. In this regard, Kreiselmaier [70] employed the instance devised by Van Albada et al. [129]. Specifically, the proximity to local extrema and saddle points of the linearized time-invariant-mean conservative variables gradually put the limiter in effect, reducing the order of both the amplitude and linearized time-invariant-mean conservative

variables' extrapolation in kind [70] [98, 100, 103].

Furthermore, Pechloff and Laschka established that

> [t]he generality of the [FLM-SD.NS] spatial scheme is [again] case-dependently restricted through the application of constraints at both the near- and far-field multiblock boundaries. [... On the basis of the FLM-SDEu implementation, these constraints are] imposed on the [block-interior-]delimiting cell interfaces[, and] accounted for in the constitutive flux [...] vectors' evaluation at these localities[, as well as in the turbulence source term vectors' evaluation at the centroid of the associated interior cell]. [...] Concerning the far[-]field, [Kreiselmaier's [70]] characteristic-based treatment of perturbations at the extents of the regarded physical space is completely retained [...]. [It] avoids an overdetermined in-/outflow constraint, giving the far-field boundary a degree of nonreflectivity [...]. [103]

This far-field approach was derived from the instance employed by Whitfield and Janus [134] in the numerical solution of the Euler equations toward a steady state. The physical mechanism of information propagation is equally accounted for, however, as now inherent to the linearized time-invariant-mean flowfield [70]. It is simply extended for the amplitude S/A primitive working variable by the author.

Since the geometric and kinematic entities constituting the small disturbance Navier-Stokes equations ($\widehat{J}$, $\widehat{\boldsymbol{J}\boldsymbol{\psi}}$, and $\widehat{J\psi_t}$, as well as $\overline{J}^*$ and $\overline{\boldsymbol{J}\boldsymbol{\psi}}^*$) are equal to their Euler counterparts, FLM-SD.NS can retain the FLM-SDEu means of their discrete evaluation [70, 98, 100, 103]; i.e., conducted through the particular association with a physical property of the computational cell [48]. Considering the S/A one-equation turbulence model, the amplitude and linearized time-invariant-mean instances of the distance to the nearest wall need to be additionally rendered [121]. All amplitude geometric and kinematic entities trace back to the discrete Cartesian coordinates given through the supplied reference and extremum grid, with their linearized time-invariant-mean counterparts merely gained from the Cartesian coordinates of the latter [70, 98, 100, 103].

4.1.2 Novel Properties

As originally suggested by Iatrou et al. [58] in 2002, and included by Iatrou [54] in his dissertation of 2009, the $\hat{\mathbf{q}}$- and $\widehat{\boldsymbol{J}\boldsymbol{\psi}}$-homogenous viscous flux vectors are evaluated at the individual computational cell's directional interfaces, just as their convective counterparts. It entails a discrete approximation of Cartesian spatial first-derivatives respective the Cartesian velocities and the static temperature [58, 54], as well as the S/A primitive working variable [100], in both their amplitude and time-invariant-mean instances. For this purpose, Iatrou [58, 54] appropriated Chakravarthy's [21] discrete application of the divergence theorem within a high-resolution viscous numerical method; also stated in [98, 100, 103]. Whereas the Cartesian spatial first-derivatives of a particular time-invariant-

mean primitive quantity are simply obtained through the conventional approach, the corresponding amplitude instances yield from its small disturbance formulation [58, 54, 100]. Interim presentations thereof were made by Iatrou et al. [57] in 2004 and Iatrou et al. [55] in 2005. The suggested means of evaluating the $\hat{\mathbf{q}}$- and $\widehat{\boldsymbol{J}\boldsymbol{\psi}}$-homogenous viscous flux vectors primarily emerged from Cvrlje's [31] successful approach within FLM-NS. Therein, the viscous flux vectors of the RANS equations had already been evaluated at the pertinent directional interfaces with the inherent Cartesian spatial first-derivatives discretely approximated through the divergence theorem. Thus, numerical equivalence between FLM-SD.NS and FLM-NS could be easily maintained [98, 100, 103]. In particular, Cvrlje's [31] implementation of the viscous flux vector evaluation served the author as the template for the small disturbance instance. Next to the $\hat{\mathbf{q}}$- and $\widehat{\boldsymbol{J}\boldsymbol{\psi}}$-homogenous viscous flux vectors, corresponding turbulence source term vectors with inherent Cartesian spatial first-derivatives respective the Cartesian velocities and the S/A primitive working variable, in both their amplitude and time-invariant-mean instances, need to be novelly evaluated as well. Both the conventional and small disturbance formulation of the divergence theorem are again employed for the derivatives' discrete approximation. The collective locality of evaluation, however, shifts from the directional interfaces to the cell centroid itself, as derived and implemented by the author.

Iatrou et al. [58] further provided a small disturbance formulation of both the no-slip- and adiabatic-wall property [6] in order to render the near-field boundary condition (also included by Iatrou [54] in his dissertation of 2009). They replace the slip-wall property utilized with the small disturbance Euler equations, as inherent to FLM-Eu [70]. The near-field boundary condition's implementation by the author for FLM-SD.NS is again based on Cvrlje's [31] conventional instance for FLM-NS. The preceding had also been stated in [100, 103]. With respect to the S/A primitive working variable, in both its amplitude and time-invariant-mean instance, the viscous-sublayer-wall property [121] needs to be novelly satisfied.

In order to improve convergence rates, the FLM-SDEu inherent explicit pseudotime-integration scheme (Runge-Kutta based) [61, 6, 49, 50, 16] is further substituted by an implicit instance. In this regard, the LU-SSOR scheme originating from Jameson and Turkel [62], had already been successfully employed within both FLM-Eu [70] and FLM-NS [31]. It had been historically developed toward maturity by Jameson and Yoon [63], Yoon and Jameson [144, 145], Rieger and Jameson [110], as well as Yoon and Kwak [146, 147]. Typically, the considered governing equation system is reduced to a system of linear equations formulated in terms of an implicit matrix-operator. The LU-SSOR scheme, however, then decomposes the implicit matrix-operator into a diagonally dominant lower- and upper-triangular-matrix factor, allowing a convergent solution by a computationally efficient deferred-correction process for each pseudotime step [145, 147]; also

stated in [98, 100, 103]. Its application to the solution of the small disturbance Navier-Stokes equations, albeit in their two-dimensional laminar form, had been originally derived by the author [95] in 2002, with first results then published by Pechloff et al. [98] in 2004. Kreiselmaier's implementation of the LU-SSOR scheme in FLM-EU [70] had served the author as the basis for the small disturbance appropriation. Characteristically, the numerical effort involved with obtaining the pseudotime update of the amplitude state vector per cell is that of a complex scalar's dual inversion. Following Blazek [14, 15, 16], the FLM-SD.NS-realized LU-SSOR scheme is embedded into a multigrid algorithm in order to additionally accelerate convergence. This capability had been first demonstrated for the solution of the two-dimensional small disturbance Navier-Stokes equations in their S/A-one-equation-turbulence-model closure by Pechloff and Laschka in 2004 [99] (published as [100] in 2006). Subsequently, three-dimensional results were first shown by Iatrou et al. [55] in 2005, as well as by Pechloff and Laschka [101] in 2008 (published as [103] in 2010). The FLOWer implementation [72] of Blazek's [14] suggested multigrid algorithm had served the author as the basis for the small disturbance appropriation. A limitation of the amplitude S/A conservative working variable devised by Pechloff and Laschka [103] allows for the overall pseudotime integration to be stabilized in cases where the underlying linearized time-invariant-mean flowfield exhibits limited regions of flow separation. The option to consider the FEVA, as originally introduced by Clark [28] and Holmes et al. [52], is implemented by the author as well.

Ensuring equivalence between FLM-SD.NS and FLM-NS in both the modeled physics and employed numerics, an upgrade of the original FLM-NS incarnation [31], respectively, with the S/A one-equation turbulence model and the multigrid acceleration technique became necessary [100]. Naturally, the multigrid-embedded LU-SSOR scheme was made available to both FLM-SDEu and FLM-Eu as well, rendering all four methods numerically equivalent; in particular, with respect to the employed pseudotime integration. To date, the computational efficiency gain of FLM-SDEu over FLM-Eu had been assessed on an explicit to implicit basis [70], rendering it overly conservative.

4.2 Spatial Discretization

Inheriting the finite volume framework of FLM-SDEu [70], the disjoined spatial and temporal discretization [16] of the amplitude flowfield's governing equations is likewise considered for FLM-SD.NS [54]. Generally, this measure guarantees a pseudosteady-state solution independent of the utilized pseudotime step [63]. The individual cells constituting the structured reference grid divide the computationally regarded physical domain into discrete control volumes, where an approximated spatial evaluation of the governing equations and subsequent pseudotime integration can take place [6, 70]. The amplitude

flowfield is then gained in its entirety as the composite of the converged control volume solutions. For this purpose, each cell must be assigned a discrete instance of both the amplitude state vector and its linearized time-invariant-mean counterpart. They are formally attributed to the cell's geometric centroid and considered uniform throughout its volume [6, 70].

An individual cell reduces from a convex skewed quadrilateral-faced hexahedron in physical space to a regular hexahedron in computational space [6, 50]. Depicted in Figure 4.1 as employed by Kreiselmaier [70], a unique denotation of the cell, or for that matter its geometric centroid, is introduced by way of the integer triplet (i, j, k). Each of its components exclusively accounts for one of the three index directions running through the geometric centroid. The index directions are specified to correspond with the curvilinear directions of the boundary-fitted coordinate system, allowing for i, j, and k to, respectively, become associated with the ξ, η, and ζ directions. In this regard, the volume bounding surfaces, each representing a unique interface to one of six immediately neighboring cells, can be grouped into three directional pairs. Per pair, a half-integer increment or decrement applied to the directionally corresponding component of the geometric centroid's denoting triplet, respectively, permits the forward or backward interface to be distinguished in terms of the preassigned positive index-direction (Figure 4.1). Additionally, Roman numeral identifiers allow for a more compact distinction [119]. Evidently, any forward interface of the considered cell has its physical and computational equal in the

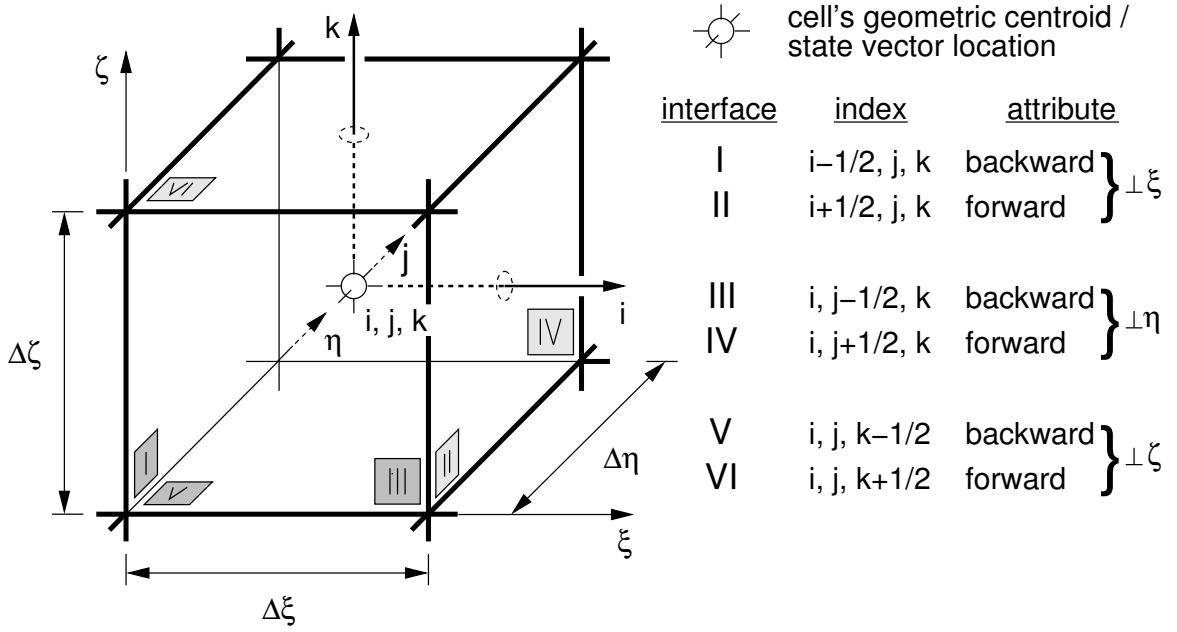

Figure 4.1: Representative computational cell (rendered in computational space); based on [70] and [119], *Abbildung 4.1.*

backward interface of the directionally succeeding cell; e.g., interface II of cell $(i,\, j,\, k)$ will be identical to interface I of cell $(i+1,\, j,\, k)$. Hence, an algorithm employed to evaluate quantities at the individual interfaces can afford to merely consider the backward instances. Ultimately, the directional sweep over the three index ranges renders the evaluation for the entirety of the structured grid [70].

The spatial discretization of the small disturbance Navier-Stokes equations is realized on the basis of Kreiselmaier's [70] treatment of the small disturbance Euler equations, as well as of Iatrou's [54] appropriation of the RANS equations' viscous flux vector evaluation employed by Cvrlje [31]. In preparation, elementary manipulation of Eq. (3.227) isolates the temporal derivative of the sought-after amplitude state vector on the left hand side (LHS):

$$\overline{J}^{*}\,\frac{\partial\hat{\mathbf{q}}}{\partial\tau^{\circ}} = -\widehat{\mathbf{R}}\,, \tag{4.1}$$

with the composited amplitude residual vector

$$\begin{aligned}
\widehat{\mathbf{R}} \;:=\; & \frac{\partial}{\partial\xi}\left(\widehat{\mathbf{F}}^{(1)} \;-\; \widehat{\mathbf{F}_{\mathbf{v}}}^{(1)}\right) \\
+\; & \frac{\partial}{\partial\eta}\left(\widehat{\mathbf{G}}^{(1)} \;-\; \widehat{\mathbf{G}_{\mathbf{v}}}^{(1)}\right) \\
+\; & \frac{\partial}{\partial\zeta}\left(\widehat{\mathbf{H}}^{(1)} \;-\; \widehat{\mathbf{H}_{\mathbf{v}}}^{(1)}\right) \\
-\; & \widehat{\mathbf{S}}^{(1)} \;-\; \widehat{\mathbf{S}}^{(2)}\,.
\end{aligned} \tag{4.2}$$

For a considered computational cell $(i,\, j,\, k)$, each interface-pair is intrinsically equidistant and the edge lengths $\Delta\xi$, $\Delta\eta$, and $\Delta\zeta$ are specified to unity. Assuming the gradient of an amplitude flux vector to be constant between the forward and backward interface of the pertinent index direction, the adhering curvilinear spatial first-derivative is substituted by a first-order central difference operator; all in all,

$$\frac{\partial}{\partial\xi} \approx \delta_{\Delta\xi}\,, \qquad \frac{\partial}{\partial\eta} \approx \delta_{\Delta\eta}\,, \qquad \frac{\partial}{\partial\zeta} \approx \delta_{\Delta\zeta}\,. \tag{4.3}$$

Applied, they will produce a directional balance for the particular amplitude flux vector with respect to the geometric centroid. An amplitude flux vector's discrete evaluation then takes place at both the directionally forward and backward interface, as identified

by a half-integer centroidal-index increment and -decrement:

$$\begin{aligned}
\widehat{\mathbf{R}}_{i,\,j,\,k} \;\approx\; & \left(\delta_{\Delta\xi}\,\widehat{\mathbf{F}}^{(1)}\right)_{i,\,j,\,k} && - \;\; \left(\delta_{\Delta\xi}\,\widehat{\mathbf{F}_{\mathbf{v}}}^{(1)}\right)_{i,\,j,\,k} \\
+ \;\; & \left(\delta_{\Delta\eta}\,\widehat{\mathbf{G}}^{(1)}\right)_{i,\,j,\,k} && - \;\; \left(\delta_{\Delta\eta}\,\widehat{\mathbf{G}_{\mathbf{v}}}^{(1)}\right)_{i,\,j,\,k} \\
+ \;\; & \left(\delta_{\Delta\zeta}\,\widehat{\mathbf{H}}^{(1)}\right)_{i,\,j,\,k} && - \;\; \left(\delta_{\Delta\zeta}\,\widehat{\mathbf{H}_{\mathbf{v}}}^{(1)}\right)_{i,\,j,\,k} \\
- \;\; & \widehat{\mathbf{S}}^{(1)}_{i,\,j,\,k} && - \;\; \widehat{\mathbf{S}}^{(2)}_{i,\,j,\,k} \\
= \;\; & \widehat{\mathbf{F}}^{(1)}_{i+1/2,\,j,\,k} - \widehat{\mathbf{F}}^{(1)}_{i-1/2,\,j,\,k} && - \;\; \left(\widehat{\mathbf{F}_{\mathbf{v}}}^{(1)}_{i+1/2,\,j,\,k} - \widehat{\mathbf{F}_{\mathbf{v}}}^{(1)}_{i-1/2,\,j,\,k}\right) \\
+ \;\; & \widehat{\mathbf{G}}^{(1)}_{i,\,j+1/2,\,k} - \widehat{\mathbf{G}}^{(1)}_{i,\,j-1/2,\,k} && - \;\; \left(\widehat{\mathbf{G}_{\mathbf{v}}}^{(1)}_{i,\,j+1/2,\,k} - \widehat{\mathbf{G}_{\mathbf{v}}}^{(1)}_{i,\,j-1/2,\,k}\right) \\
+ \;\; & \widehat{\mathbf{H}}^{(1)}_{i,\,j,\,k+1/2} - \widehat{\mathbf{H}}^{(1)}_{i,\,j,\,k-1/2} && - \;\; \left(\widehat{\mathbf{H}_{\mathbf{v}}}^{(1)}_{i,\,j,\,k+1/2} - \widehat{\mathbf{H}_{\mathbf{v}}}^{(1)}_{i,\,j,\,k-1/2}\right) \\
- \;\; & \widehat{\mathbf{S}}^{(1)}_{i,\,j,\,k} && - \;\; \widehat{\mathbf{S}}^{(2)}_{i,\,j,\,k}\,,
\end{aligned} \tag{4.4}$$

wherein

$$\widehat{\mathbf{S}}^{(1)}_{i,\,j,\,k} \;=\; -\,ik\,\overline{J}^{*}_{i,\,j,\,k}\,\hat{\mathbf{q}}_{i,\,j,\,k} \;+\; \widehat{\mathbf{T}}^{(1)}_{i,\,j,\,k} \tag{4.5}$$

and

$$\begin{aligned}
\widehat{\mathbf{S}}^{(2)}_{i,\,j,\,k} \;=\; & -\Big[\, ik\,\widehat{J}_{i,\,j,\,k}\,\bar{\mathbf{q}}^{*}_{i,\,j,\,k} \\
+ \;\; & \widehat{\mathbf{F}}^{(2)}_{i+1/2,\,j,\,k} - \widehat{\mathbf{F}}^{(2)}_{i-1/2,\,j,\,k} - \left(\widehat{\mathbf{F}_{\mathbf{v}}}^{(2)}_{i+1/2,\,j,\,k} - \widehat{\mathbf{F}_{\mathbf{v}}}^{(2)}_{i-1/2,\,j,\,k}\right) \\
+ \;\; & \widehat{\mathbf{G}}^{(2)}_{i,\,j+1/2,\,k} - \widehat{\mathbf{G}}^{(2)}_{i,\,j-1/2,\,k} - \left(\widehat{\mathbf{G}_{\mathbf{v}}}^{(2)}_{i,\,j+1/2,\,k} - \widehat{\mathbf{G}_{\mathbf{v}}}^{(2)}_{i,\,j-1/2,\,k}\right) \\
+ \;\; & \widehat{\mathbf{H}}^{(2)}_{i,\,j,\,k+1/2} - \widehat{\mathbf{H}}^{(2)}_{i,\,j,\,k-1/2} - \left(\widehat{\mathbf{H}_{\mathbf{v}}}^{(2)}_{i,\,j,\,k+1/2} - \widehat{\mathbf{H}_{\mathbf{v}}}^{(2)}_{i,\,j,\,k-1/2}\right) \Big] \\
+ \;\; & \widehat{\mathbf{T}}^{(2)}_{i,\,j,\,k}\,.
\end{aligned} \tag{4.6}$$

The Cartesian spatial first-derivatives within the amplitude viscous flux and turbulence source term vectors are initially left untreated [70, 54, 31]. Notably, the latter are set apart from the amplitude flux vectors on grounds of the centroidal assignment, which, however, gives them commonality to both the amplitude and linearized time-invariant-mean state vector. Likewise, the value of the amplitude turbulence source term vectors is deemed to be individually uniform throughout the considered computational cell. With regard to the intended implicit pseudotime integration by means of the LU-SSOR scheme [14], the LHS of Eq. (4.1) is initially left untreated as well.

Naturally, Eq. (4.4) entails a consistently discrete evaluation of the geometric and kinematic entities inherent to its constituting vectors. On the one hand, the amplitude spatial and temporal metrics of the $\widehat{\boldsymbol{J}\boldsymbol{\psi}}$-homogenous flux vectors, as well as the linearized

time-invariant-mean spatial metrics of the $\hat{\mathbf{q}}$-homogenous flux vectors, are assigned to the pertinent directional interface. On the other hand, the determinant of the coordinate transformation's Jacobian in both its amplitude and linearized time-invariant-mean instance is assigned to the centroid, respectively, as apparent in Eq. (4.6) and Eq. (4.5), but also as intrinsic to the $\widehat{\boldsymbol{J}\boldsymbol{\psi}}$- and $\hat{\mathbf{q}}$-homogenous turbulence source term vector. In regard to the latter, the amplitude and linearized time-invariant-mean distance to the nearest wall are considered to be centroidal as well. Again following Hirsch [48], the finite difference approximation of the small disturbance Navier-Stokes equations' curvilinear differential form in computational space can be rendered identical to a finite volume approximation of its Cartesian integral form in physical space. To this end, the discrete determinant of the coordinate transformation's Jacobian in its amplitude and linearized time-invariant-mean instance must become equal, respectively, to the amplitude and linearized time-invariant-mean physical volume of the considered computational cell. In turn, each discrete amplitude and linearized time-invariant-mean spatial metric must become equal, respectively, to the pertinent directional interface's amplitude and linearized time-invariant-mean physical surface normal vector. Hence, an evaluation of the amplitude and linearized time-invariant-mean Cartesian coordinates' curvilinear spatial first-derivatives that actually constitute these geometric entities is equally avoided altogether [48]. This principle had already been invoked by Kreiselmaier [70] for the finite difference approximation of the small disturbance Euler equations' differential form, making the evaluation of the amplitude and linearized time-invariant-mean physical cell volume, as well as the corresponding physical surface normal vectors, already a component of the FLM-SDEu implementation. The pertinent formulae are relegated to Appendix Section A.1. It also includes the formulae for the evaluation of the discrete amplitude temporal metrics, as well as, novelly, for the evaluation of the amplitude and linearized time-invariant-mean distances to the nearest wall. Since all geometric and kinematic entities are invariant with respect to pseudotime, they need to be evaluated only once within the solution algorithm's overall initialization [70].

The sequence governing the evaluation of the amplitude flux vectors and the amplitude turbulence source term vector in either their $\widehat{\boldsymbol{J}\boldsymbol{\psi}}$- or $\hat{\mathbf{q}}$-homogenous instances is essentially the same:

- The appropriate boundary conditions for the far-field, for the symmetry planes, and for the block cuts are imposed on correspondingly designated face segments of each and every block, pursuant to the FLM-SDEu implementation [70].

- For the individual block, the particular amplitude convective flux vector of the first curvilinear direction is evaluated [70]. Subsequently, the appropriate near-field boundary condition is imposed on the correspondingly designated face segments of the same direction. This is realized by correcting the particular amplitude convective

flux vector at the pertinent cell interfaces and setting the particular state vector in the associated ghost cells [70]. The particular amplitude viscous flux vector of the first curvilinear direction is then evaluated, now inherently accounting for the appropriate near-field boundary condition.

- This evaluation procedure is repeated for the remaining two curvilinear directions [70]. Afterward, the particular amplitude turbulence source term vector is evaluated.

- The two preceding steps are successively repeated for all remaining blocks [70].

The given sequence needs to be performed only once for the $\widehat{\boldsymbol{J}\boldsymbol{\psi}}$-homogenous flux vectors and turbulence source term vector as they are invariant with respect to pseudotime, and thus $\widehat{\mathbf{S}}^{(2)}_{i,\,j,\,k}$, Eq. (4.6), is so as well. Its evaluation is part of the algorithm's initialization procedure [70]. For the $\hat{\mathbf{q}}$-homogenous flux vectors and turbulence source term vector, however, the given sequence needs to be repeated prior to every pseudotime step; i.e., as part of the $\widehat{\mathbf{R}}_{i,\,j,\,k}$, Eq. (4.4), update for the current pseudotime level [70]. Again, both the evaluation of the amplitude convective flux vectors and the imposition of the far-field boundary condition are already components of the FLM-SDEu implementation [70]. The pertinent formulae are, respectively, relegated to Appendix Sections A.2 and A.3, as necessarily extended for the small disturbance instance of the S/A one-equation turbulence model.

4.3 Amplitude Viscous Flux/Turbulence Source Term Vector Evaluation

The amplitude viscous flux and turbulence source term vectors constituting $\widehat{\mathbf{R}}_{i,\,j,\,k}$ not only differ in their natural composition, but also in their respective locality of evaluation. While the discrete instances of the amplitude viscous flux vectors are interface associated, those of the amplitude turbulence source term vectors are strictly centroidal. A commonality exists, however, in their intrinsic employment of Cartesian spatial first-derivatives of select amplitude and time-invariant-mean primitive variables. They had initially been left untreated in the discretization of $\widehat{\mathbf{R}}$. For the sake of conciseness, Cartesian spatial first-derivatives will simply be referred to as spatial derivatives (the gradient [16]) in the following.

The discrete instances of the amplitude viscous flux vectors are considered first, with the $\hat{\mathbf{q}}$- and $\widehat{\boldsymbol{J}\boldsymbol{\psi}}$-homogenous-pair pertinent to the ξ-directional backward interface treated

representatively. On the basis of Iatrou [54], they can be functionally expressed as

$$\begin{aligned}
\widehat{\mathbf{F}_{\mathbf{v}}}^{(1)}_{i-1/2,\,j,\,k} &= \widehat{\mathbf{E}_{\mathbf{v}}}^{(1)} \Big(\; \hat{\rho}_{i-1/2,\,j,\,k},\, \hat{\Phi}_{i-1/2,\,j,\,k},\, \hat{T}_{i-1/2,\,j,\,k},\, \boldsymbol{\nabla}\hat{\Phi}\Big|_{i-1/2,\,j,\,k},\, \boldsymbol{\nabla}\hat{T}\Big|_{i-1/2,\,j,\,k}, \\
&\qquad \bar{\rho}_{i-1/2,\,j,\,k},\, \bar{\Phi}_{i-1/2,\,j,\,k},\, \bar{T}^{*}_{i-1/2,\,j,\,k},\, \boldsymbol{\nabla}\bar{\Phi}\big|_{i-1/2,\,j,\,k},\, \boldsymbol{\nabla}\bar{T}^{*}\big|_{i-1/2,\,j,\,k}, \\
&\qquad \overline{\boldsymbol{J}\boldsymbol{\xi}}^{*}_{i-1/2,\,j,\,k} \; \Big) \quad \text{and} \\
\widehat{\mathbf{F}_{\mathbf{v}}}^{(2)}_{i-1/2,\,j,\,k} &= \widehat{\mathbf{E}_{\mathbf{v}}}^{(2)} \Big(\; \bar{\rho}_{i-1/2,\,j,\,k},\, \bar{\Phi}_{i-1/2,\,j,\,k},\, \bar{T}^{*}_{i-1/2,\,j,\,k},\, \boldsymbol{\nabla}\bar{\Phi}\big|_{i-1/2,\,j,\,k},\, \boldsymbol{\nabla}\bar{T}^{*}\big|_{i-1/2,\,j,\,k}, \\
&\qquad \widehat{\boldsymbol{J}\boldsymbol{\xi}}_{i-1/2,\,j,\,k} \; \Big) \,,
\end{aligned} \tag{4.7}$$

wherein Φ (designated the qualified variable) collectively substitutes for those nonderived primitive variables subject to both an interface evaluation and an interface evaluation of their respective spatial derivatives:

$$\Phi \in \{\, u,\, v,\, w,\, \breve{\nu} \,\} \,. \tag{4.8}$$

Any primitive variable's interface value can be straightforwardly determined through the arithmetic average of said variable's preceding and succeeding centroidal instance; i.e.,

$$\begin{aligned}
\hat{\rho}_{i-1/2,\,j,\,k} &:= (\,\hat{\rho}_{i,\,j,\,k} + \hat{\rho}_{i-1,\,j,\,k}\,) \;/\; 2\,, \quad \bar{\rho}_{i-1/2,\,j,\,k} := (\,\bar{\rho}_{i,\,j,\,k} + \bar{\rho}_{i-1,\,j,\,k}\,) \;/\; 2\,; \\
\hat{\Phi}_{i-1/2,\,j,\,k} &:= (\,\hat{\Phi}_{i,\,j,\,k} + \hat{\Phi}_{i-1,\,j,\,k}\,) \;/\; 2\,, \quad \bar{\Phi}_{i-1/2,\,j,\,k} := (\,\bar{\Phi}_{i,\,j,\,k} + \bar{\Phi}_{i-1,\,j,\,k}\,) \;/\; 2\,; \\
\hat{T}_{i-1/2,\,j,\,k} &:= (\,\hat{T}_{i,\,j,\,k} + \hat{T}_{i-1,\,j,\,k}\,) \;/\; 2\,, \quad \bar{T}^{*}_{i-1/2,\,j,\,k} := (\,\bar{T}^{*}_{i,\,j,\,k} + \bar{T}^{*}_{i-1,\,j,\,k}\,) \;/\; 2
\end{aligned} \tag{4.9}$$

[54]. In equivalence to Eq. (4.7), the discrete pair of turbulence source term vectors can be functionally expressed as

$$\begin{aligned}
\widehat{\mathbf{T}}^{(1)}_{i,\,j,\,k} &= \widehat{\mathbf{T}}^{(1)} \Big(\; \hat{\rho}_{i,\,j,\,k},\, \hat{T}_{i,\,j,\,k},\, \widehat{\breve{\nu}}_{i,\,j,\,k},\, \hat{d}_{i,\,j,\,k},\, \boldsymbol{\nabla}\hat{\Phi}\Big|_{i,\,j,\,k}, \\
&\qquad \bar{\rho}_{i,\,j,\,k},\, \bar{T}^{*}_{i,\,j,\,k},\, \overline{\breve{\nu}}_{i,\,j,\,k},\, \bar{d}^{*}_{i,\,j,\,k},\, \boldsymbol{\nabla}\bar{\Phi}\big|_{i,\,j,\,k},\, \overline{J}^{*}_{i,\,j,\,k} \; \Big) \quad \text{and} \\
\widehat{\mathbf{T}}^{(2)}_{i,\,j,\,k} &= \widehat{\mathbf{T}}^{(2)} \Big(\; \bar{\rho}_{i,\,j,\,k},\, \bar{T}^{*}_{i,\,j,\,k},\, \overline{\breve{\nu}}_{i,\,j,\,k},\, \bar{d}^{*}_{i,\,j,\,k},\, \boldsymbol{\nabla}\bar{\Phi}\big|_{i,\,j,\,k},\, \widehat{J}_{i,\,j,\,k} \; \Big) \,,
\end{aligned} \tag{4.10}$$

with Φ now collectively substituting for those nonderived primitive variables subject to a centroidal evaluation of their spatial derivative. It should be noted that by utilizing the $\boldsymbol{\nabla}\hat{\Phi}$ and $\boldsymbol{\nabla}\bar{\Phi}$ notation in Eq. (4.10) the nonconstitutive $\partial\hat{u}/\partial x$, $\partial\hat{v}/\partial y$, $\partial\hat{w}/\partial z$, as well as $\partial\bar{u}/\partial x$, $\partial\bar{v}/\partial y$, $\partial\bar{w}/\partial z$, are formally included, yet exempt from an actual treatment. All in all, once suitable numerical approximations of the spatial derivatives have been instated, the remaining operations involved with either vector pair's discrete evaluation are strictly algebraic.

4.3.1 Small Disturbance Formulation of the Divergence Theorem

As suggested by Iatrou [54], the interface evaluation of both the amplitude and the time-invariant-mean qualified variable's gradient is realized by means of the divergence theorem on the basis of Chakravarthy's [21] original discrete utilization. Furthermore, this approach is novelly appropriated by the author to consistently evaluate both gradient instances at the centroid.

Also known as Gauss's theorem, the volume integral of a vector field's divergence over an arbitrary yet finite control volume V is said to be equal to the surface integral of the vector field over the control volume's delimiting boundary ∂V for continuous physical space. Denoting the vector field with $\mathbf{\Phi}$, this relationship is given by

$$\iiint\limits_{V} \boldsymbol{\nabla}\mathbf{\Phi}\, dV \;=\; \iint\limits_{\partial V} \mathbf{\Phi}\, \mathbf{dS}\,, \tag{4.11}$$

wherein $\mathbf{dS}$ represents the infinitesimal surface normal vector $(\, dS_x,\, dS_y,\, dS_z\,)^T$. If $\mathbf{\Phi}$ is set up as one-directional by multiplying the qualified variable (a scalar field) with one of the Cartesian basis vectors [21, 54], the correspondent spatial derivative becomes isolated within the volume integral. Hence, three directional instances of Gauss's theorem are obtained. They can be composited into the single vector equation

$$\iiint\limits_{V} \boldsymbol{\nabla}\Phi\, dV \;=\; \iint\limits_{\partial V} \Phi\, \mathbf{dS}\,, \tag{4.12}$$

which establishes the relationship between the volume integral of the qualified variable's gradient over V and the surface integral of the qualified variable over ∂V [21, 54].

Considering the problem at hand, Eq. (4.12) is more adequately expressed in terms of the qualified variable's phase average,

$$\iiint\limits_{V} \boldsymbol{\nabla}\langle\Phi\rangle\, dV \;=\; \iint\limits_{\partial V} \langle\Phi\rangle\, \mathbf{dS}\,, \tag{4.13}$$

where the control volume, and thus its delimiting boundary with surface normal vectors, is likewise considered to be time-dependent. Pursuant to Iatrou [54], the small disturbance formulation of Eq. (4.13) is then gained as

$$\iiint\limits_{\bar{V}^*} \boldsymbol{\nabla}\hat{\Phi}\, dV \;=\; \iint\limits_{\partial\bar{V}^*} \hat{\Phi}\, \mathbf{dS} \;+\; \iint\limits_{\partial\hat{V}} \bar{\Phi}\, \mathbf{dS} \;-\; \iiint\limits_{\hat{V}} \boldsymbol{\nabla}\bar{\Phi}\, dV\,, \quad \text{with} \quad \hat{\Phi} \in \mathbb{C}\,, \tag{4.14}$$

having taken into account the linearized time-invariant-mean instance

$$\iiint\limits_{\bar{V}^*} \boldsymbol{\nabla}\bar{\Phi}\, dV \;=\; \iint\limits_{\partial\bar{V}^*} \bar{\Phi}\, \mathbf{dS}\,. \tag{4.15}$$

In preparation of a discrete application, the volume integrals of Eq. (4.14) and Eq. (4.15) are algebraically resolved by considering the amplitude/time-invariant-mean qualified variable's gradient to be uniform within the decomposed control volume, respectively, yielding

$$\boldsymbol{\nabla}\hat{\Phi} \;=\; \left(\iint\limits_{\partial\bar{V}^*} \hat{\Phi}\,\mathbf{dS} \;+\; \iint\limits_{\partial\hat{V}} \bar{\Phi}\,\mathbf{dS} \;-\; \boldsymbol{\nabla}\bar{\Phi}\,\hat{V} \right) / \,\bar{V}^* \tag{4.16}$$

and

$$\boldsymbol{\nabla}\bar{\Phi} \;=\; \iint\limits_{\partial\bar{V}^*} \bar{\Phi}\,\mathbf{dS} \;/\; \bar{V}^* \,. \tag{4.17}$$

Thus, the amplitude qualified variable's gradient, Eq. (4.16), can be uniquely determined from known distributions of the amplitude/time-invariant-mean qualified variable on the decomposed control volume's surfaces, albeit having to take the time-invariant-mean qualified variable's gradient, Eq. (4.17), into account as well. The evaluation of the time-invariant-mean qualified variable's gradient, on the other hand, is elementary, merely requiring the qualified variable's distribution to be known on the linearized time-invariant-mean control volume's surface. Substituting $\hat{\Phi}$ with $\hat{T}$ and $\bar{\Phi}$ with $\bar{T}^*$ in Eq. (4.16) and Eq. (4.17), $\boldsymbol{\nabla}\hat{T}$ and $\boldsymbol{\nabla}\bar{T}^*$ can naturally be determined as well [54].

4.3.2 Application in Discrete Space

The application of Eq. (4.16) and Eq. (4.17) to discrete physical space becomes contingent on a suitable approximation of the constituting surface integrals, and consequently on the respectively employed control volume. Both must be set up to incorporate the considered gradient's desired evaluation locality in discrete computational space, being either the interface or the centroid.

For the gradient's interface-respective evaluation, the ξ-directional backward interface of cell (i, j, k) will again be considered representatively. As depicted in Figure 4.2, an interface-embedding auxiliary cell [21] is initially established in discrete computational space by combining the interface-adjacent half of cell (i, j, k) with the one of cell $(i-1, j, k)$. In agreement with Cvrlje's [31] original FLM-NS-internal designation, each of the auxiliary cell's constituting faces is uniquely denoted by an Arabic numeral m, with $m \in \{1, 2, \ldots, 6\}$. In separate instances, the auxiliary cell allows itself to be physically mapped to both an amplitude and linearized time-invariant-mean control volume, respectively, identified as $\hat{V}_{aux}$ and $\bar{V}^*_{aux}$ [54]. The delimiting boundary of each is embodied by a set of distinct outward-oriented surface normal vectors, summarily designated $\hat{\mathbf{S}}_{m,aux} = (\widehat{S_x}, \widehat{S_y}, \widehat{S_z})^T_{m,aux}$ and $\bar{\mathbf{S}}^*_{m,aux} = (\overline{S_x}^*, \overline{S_y}^*, \overline{S_z}^*)^T_{m,aux}$ [54]. On the basis of Cvrlje's [31] original FLM-NS implementation these geometric entities can be straightforwardly established through arithmetic averages of their cell (i, j, k) and cell $(i-1, j, k)$

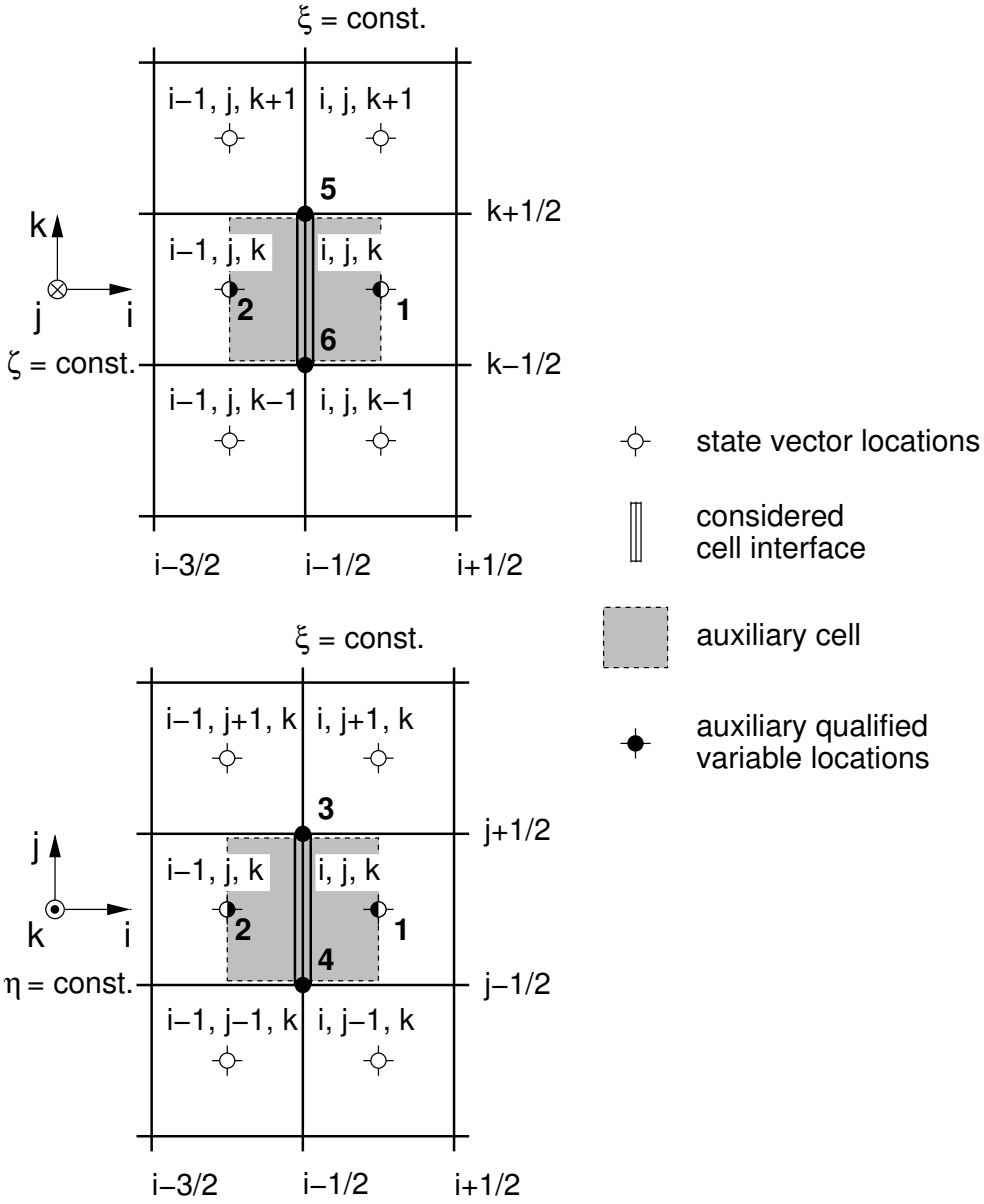

Figure 4.2: Evaluation stencil for the ξ-directional interface-respective Cartesian gradient; based on Chakravarthy [21], Fig. 1, and the original FLM-NS implementation [31].

counterparts. As implemented by the author, the amplitude and linearized time-invariant-mean control volume are ascertained through

$$\hat{V}_{aux} \;:=\; (\,\widehat{J}_{i,j,k} \;+\; \widehat{J}_{i-1,j,k}\,) \;/\; 2\,, \quad \bar{V}^{*}_{aux} \;:=\; (\,\overline{J}^{*}_{i,j,k} \;+\; \overline{J}^{*}_{i-1,j,k}\,) \;/\; 2\,, \tag{4.18}$$

having utilized the determinant of the coordinate transformation's Jacobian. Complementarily, the amplitude and linearized time-invariant-mean set of surface normal vectors

(specified in terms of the interface-associated spatial metrics) are obtained as

$$
\begin{aligned}
\hat{\mathbf{S}}_{1,aux} &:= \quad (\,\widehat{\boldsymbol{J}\boldsymbol{\xi}}_{i+1/2,\,j,\,k} \;+\; \widehat{\boldsymbol{J}\boldsymbol{\xi}}_{i-1/2,\,j,\,k}\,) \quad / \;\; 2\,,\\
\hat{\mathbf{S}}_{2,aux} &:= -\,(\,\widehat{\boldsymbol{J}\boldsymbol{\xi}}_{i-1/2,\,j,\,k} \;+\; \widehat{\boldsymbol{J}\boldsymbol{\xi}}_{i-3/2,\,j,\,k}\,) \quad / \;\; 2\,;\\
\hat{\mathbf{S}}_{3,aux} &:= \quad (\,\widehat{\boldsymbol{J}\boldsymbol{\eta}}_{i,\,j+1/2,\,k} \;+\; \widehat{\boldsymbol{J}\boldsymbol{\eta}}_{i-1,\,j+1/2,\,k}\,) \quad / \;\; 2\,,\\
\hat{\mathbf{S}}_{4,aux} &:= -\,(\,\widehat{\boldsymbol{J}\boldsymbol{\eta}}_{i,\,j-1/2,\,k} \;+\; \widehat{\boldsymbol{J}\boldsymbol{\eta}}_{i-1,\,j-1/2,\,k}\,) \quad / \;\; 2\,;\\
\hat{\mathbf{S}}_{5,aux} &:= \quad (\,\widehat{\boldsymbol{J}\boldsymbol{\zeta}}_{i,\,j,\,k+1/2} \;+\; \widehat{\boldsymbol{J}\boldsymbol{\zeta}}_{i-1,\,j,\,k+1/2}\,) \quad / \;\; 2\,,\\
\hat{\mathbf{S}}_{6,aux} &:= -\,(\,\widehat{\boldsymbol{J}\boldsymbol{\zeta}}_{i,\,j,\,k-1/2} \;+\; \widehat{\boldsymbol{J}\boldsymbol{\zeta}}_{i-1,\,j,\,k-1/2}\,) \quad / \;\; 2\,,
\end{aligned}
\tag{4.19}
$$

and

$$
\begin{aligned}
\bar{\mathbf{S}}^{*}_{1,aux} &:= \quad (\,\overline{\boldsymbol{J}\boldsymbol{\xi}}^{\,*}_{i+1/2,\,j,\,k} \;+\; \overline{\boldsymbol{J}\boldsymbol{\xi}}^{\,*}_{i-1/2,\,j,\,k}\,) \quad / \;\; 2\,,\\
\bar{\mathbf{S}}^{*}_{2,aux} &:= -\,(\,\overline{\boldsymbol{J}\boldsymbol{\xi}}^{\,*}_{i-1/2,\,j,\,k} \;+\; \overline{\boldsymbol{J}\boldsymbol{\xi}}^{\,*}_{i-3/2,\,j,\,k}\,) \quad / \;\; 2\,;\\
\bar{\mathbf{S}}^{*}_{3,aux} &:= \quad (\,\overline{\boldsymbol{J}\boldsymbol{\eta}}^{\,*}_{i,\,j+1/2,\,k} \;+\; \overline{\boldsymbol{J}\boldsymbol{\eta}}^{\,*}_{i-1,\,j+1/2,\,k}\,) \quad / \;\; 2\,,\\
\bar{\mathbf{S}}^{*}_{4,aux} &:= -\,(\,\overline{\boldsymbol{J}\boldsymbol{\eta}}^{\,*}_{i,\,j-1/2,\,k} \;+\; \overline{\boldsymbol{J}\boldsymbol{\eta}}^{\,*}_{i-1,\,j-1/2,\,k}\,) \quad / \;\; 2\,;\\
\bar{\mathbf{S}}^{*}_{5,aux} &:= \quad (\,\overline{\boldsymbol{J}\boldsymbol{\zeta}}^{\,*}_{i,\,j,\,k+1/2} \;+\; \overline{\boldsymbol{J}\boldsymbol{\zeta}}^{\,*}_{i-1,\,j,\,k+1/2}\,) \quad / \;\; 2\,,\\
\bar{\mathbf{S}}^{*}_{6,aux} &:= -\,(\,\overline{\boldsymbol{J}\boldsymbol{\zeta}}^{\,*}_{i,\,j,\,k-1/2} \;+\; \overline{\boldsymbol{J}\boldsymbol{\zeta}}^{\,*}_{i-1,\,j,\,k-1/2}\,) \quad / \;\; 2\,.
\end{aligned}
\tag{4.20}
$$

In the preceding formulations, the spatial metrics' positive orientation in positive index-direction is already accounted for, an even-numbered surface normal vector's proper positive orientation in negative index-direction having been forced through an inserted negative sign.

Pursuant to Iatrou [54], the amplitude and time-invariant-mean qualified variables' distribution on the decomposed control volume's surfaces is considered to be distinct, yet uniform, for each individual face [21]. Embodying this circumstance, auxiliary instances of said variables can be assigned to the respective face's centroid. They are summarily designated $\hat{\Phi}_{m,aux}$ and $\bar{\Phi}_{m,aux}$ [54]. On the basis of Cvrlje's [31] original FLM-NS implementation, the auxiliary amplitude and time-invariant-mean qualified variables are mapped to discrete computational space (Figure 4.2). The locations of the ξ-directional auxiliary amplitude and time-invariant-mean qualified variables coincide, respectively, with the preceding and succeeding centroid of the considered interface. Consequently, the pertinent amplitude and time-invariant-mean qualified variable straightforwardly establishes

its auxiliary counterpart. As implemented by the author,

$$\begin{aligned} \hat{\Phi}_{1,aux} &:= \hat{\Phi}_{i,\,j,\,k}\,, & \hat{\Phi}_{2,aux} &:= \hat{\Phi}_{i-1,\,j,\,k}\,, \quad \text{and} \\ \bar{\Phi}_{1,aux} &:= \bar{\Phi}_{i,\,j,\,k}\,, & \bar{\Phi}_{2,aux} &:= \bar{\Phi}_{i-1,\,j,\,k}\,. \end{aligned} \tag{4.21}$$

The off-directional instances, on the other hand, are gained through arithmetic averaging of the amplitude/time-invariant-mean qualified variables associated with the particular face's adjacent centroids; i.e.,

$$\begin{aligned} \hat{\Phi}_{3,aux} &:= (\,\hat{\Phi}_{1,aux} + \hat{\Phi}_{2,aux} + \hat{\Phi}_{i,\,j+1,\,k} + \hat{\Phi}_{i-1,\,j+1,\,k}\,) \;/\; 4\,, \\ \hat{\Phi}_{4,aux} &:= (\,\hat{\Phi}_{1,aux} + \hat{\Phi}_{2,aux} + \hat{\Phi}_{i,\,j-1,\,k} + \hat{\Phi}_{i-1,\,j-1,\,k}\,) \;/\; 4\,; \\ \hat{\Phi}_{5,aux} &:= (\,\hat{\Phi}_{1,aux} + \hat{\Phi}_{2,aux} + \hat{\Phi}_{i,\,j,\,k+1} + \hat{\Phi}_{i-1,\,j,\,k+1}\,) \;/\; 4\,, \\ \hat{\Phi}_{6,aux} &:= (\,\hat{\Phi}_{1,aux} + \hat{\Phi}_{2,aux} + \hat{\Phi}_{i,\,j,\,k-1} + \hat{\Phi}_{i-1,\,j,\,k-1}) \;/\; 4\,, \end{aligned} \tag{4.22}$$

and

$$\begin{aligned} \bar{\Phi}_{3,aux} &:= (\,\bar{\Phi}_{1,aux} + \bar{\Phi}_{2,aux} + \bar{\Phi}_{i,\,j+1,\,k} + \bar{\Phi}_{i-1,\,j+1,\,k}\,) \;/\; 4\,, \\ \bar{\Phi}_{4,aux} &:= (\,\bar{\Phi}_{1,aux} + \bar{\Phi}_{2,aux} + \bar{\Phi}_{i,\,j-1,\,k} + \bar{\Phi}_{i-1,\,j-1,\,k}\,) \;/\; 4\,; \\ \bar{\Phi}_{5,aux} &:= (\,\bar{\Phi}_{1,aux} + \bar{\Phi}_{2,aux} + \bar{\Phi}_{i,\,j,\,k+1} + \bar{\Phi}_{i-1,\,j,\,k+1}\,) \;/\; 4\,, \\ \bar{\Phi}_{6,aux} &:= (\,\bar{\Phi}_{1,aux} + \bar{\Phi}_{2,aux} + \bar{\Phi}_{i,\,j,\,k-1} + \bar{\Phi}_{i-1,\,j,\,k-1}) \;/\; 4\,. \end{aligned} \tag{4.23}$$

It should be noted that the ξ-directional auxiliary amplitude and time-invariant-mean qualified variables contribute in equal manner to all off-directional instances.

Ultimately, the surface integrals of Eq. (4.16) and Eq. (4.17) are ready to be resolved. Since the amplitude/time-invariant-mean qualified variable's gradient is considered to be uniform within the decomposed control volume [54], it can be considered to be uniform within the auxiliary cell as well, allowing an assignment to the considered interface. This approximation renders

$$\begin{aligned} Re\boldsymbol{\nabla}\hat{\Phi}\Big|_{i-1/2,\,j,\,k} &\approx \left[\sum_{m=1}^{6}\left(Re\hat{\Phi}_m\bar{\mathbf{S}}^*_m\right)_{aux} + \sum_{m=1}^{6}\left(Re\bar{\Phi}_m\hat{\mathbf{S}}_m\right)_{aux} - \boldsymbol{\nabla}\bar{\Phi}\big|_{i-1/2,\,j,\,k}\,\hat{V}_{aux}\right] / \bar{V}^*_{aux}, \\ Im\boldsymbol{\nabla}\hat{\Phi}\Big|_{i-1/2,\,j,\,k} &\approx \left[\sum_{m=1}^{6}\left(Im\hat{\Phi}_m\bar{\mathbf{S}}^*_m\right)_{aux}\right] / \bar{V}^*_{aux} \end{aligned} \tag{4.24}$$

and

$$\boldsymbol{\nabla}\bar{\Phi}\big|_{i-1/2,\,j,\,k} \approx \left[\sum_{m=1}^{6}\left(\bar{\Phi}_m\overline{\mathbf{S}}^*_m\right)_{aux}\right] / \bar{V}^*_{aux} \tag{4.25}$$

[54], with the author having formulated Eq. (4.24) to take into account the implementation's need for a separated evaluation of a complex amplitude quantity's real and imaginary part. Again substituting $\hat{\Phi}$ with $\hat{T}$ and $\bar{\Phi}$ with $\bar{T}^*$ in Eqs. (4.21–4.25), $Re\boldsymbol{\nabla}\hat{T}$, $Im\boldsymbol{\nabla}\hat{T}$, and $\boldsymbol{\nabla}\bar{T}^*$ can naturally be evaluated as well [54].

For the gradients' equivalent evaluation at the representative centroid (i, j, k), the corresponding cell itself is novelly employed by the author as the auxiliary cell. Depicted in Figure 4.3, its formal set-up follows the one established for the interface-respective gradient evaluation. The pertinent geometric entities of the mapped amplitude and linearized

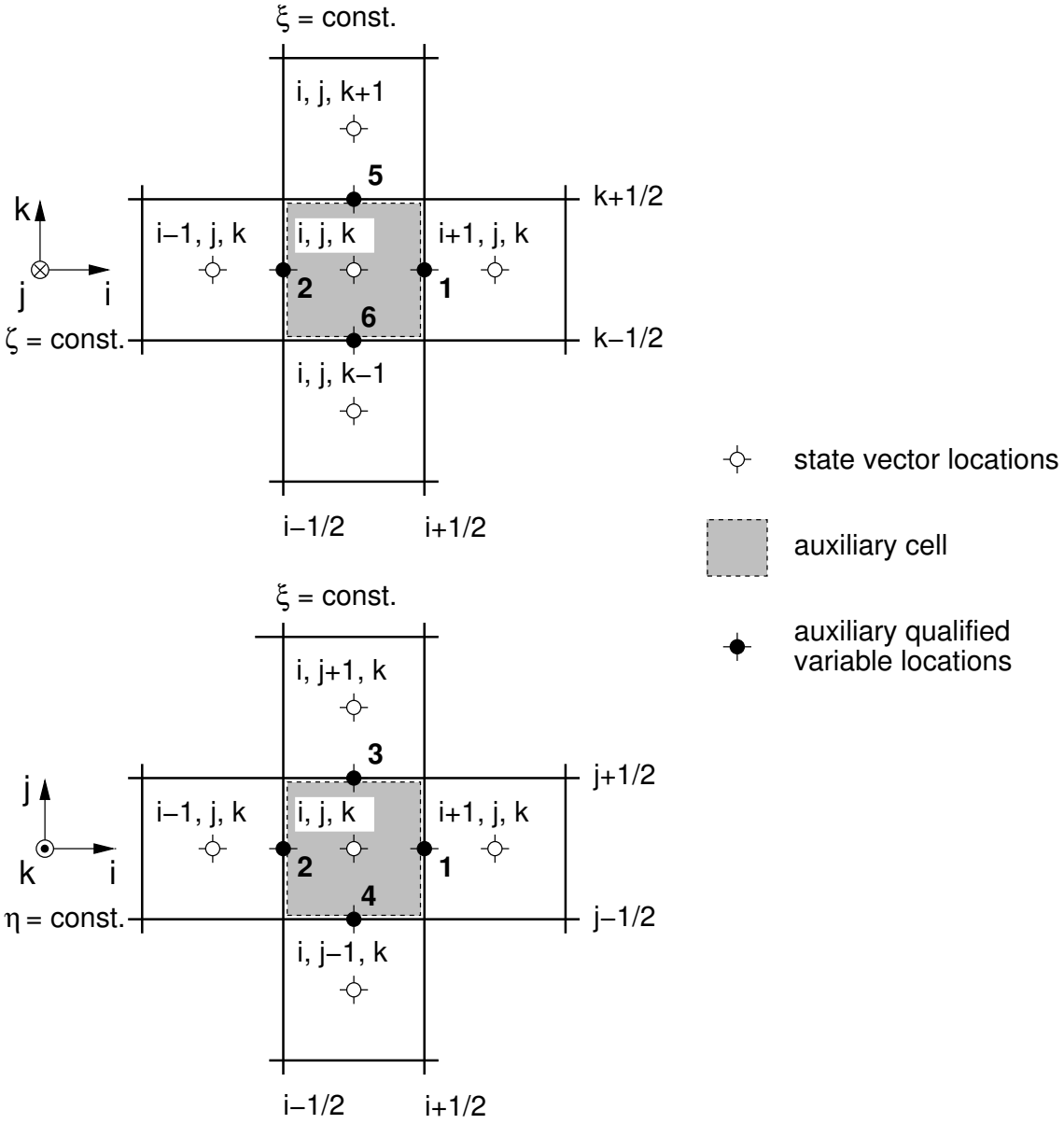

Figure 4.3: Evaluation stencil for the centroid-respective Cartesian gradient.

time-invariant-mean control volume, however, are now identical to their cell (i, j, k) counterparts; i.e.,

$$\hat{V}_{aux} := \widehat{J}_{i,j,k}\,, \qquad \bar{V}^*_{aux} := \overline{J}^*_{i,j,k}\,, \tag{4.26}$$

and

$$\begin{aligned}
\hat{\mathbf{S}}_{1,aux} &:= \widehat{\boldsymbol{J\xi}}_{i+1/2,j,k}\,, & \bar{\mathbf{S}}^*_{1,aux} &:= \overline{\boldsymbol{J\xi}}^*_{i+1/2,j,k}\,;\\
\hat{\mathbf{S}}_{2,aux} &:= -\widehat{\boldsymbol{J\xi}}_{i-1/2,j,k}\,, & \bar{\mathbf{S}}^*_{2,aux} &:= -\overline{\boldsymbol{J\xi}}^*_{i-1/2,j,k}\,;\\
\hat{\mathbf{S}}_{3,aux} &:= \widehat{\boldsymbol{J\eta}}_{i,j+1/2,k}\,, & \bar{\mathbf{S}}^*_{3,aux} &:= \overline{\boldsymbol{J\eta}}^*_{i,j+1/2,k}\,;\\
\hat{\mathbf{S}}_{4,aux} &:= -\widehat{\boldsymbol{J\eta}}_{i,j-1/2,k}\,, & \bar{\mathbf{S}}^*_{4,aux} &:= -\overline{\boldsymbol{J\eta}}^*_{i,j-1/2,k}\,;\\
\hat{\mathbf{S}}_{5,aux} &:= \widehat{\boldsymbol{J\zeta}}_{i,j,k+1/2}\,, & \bar{\mathbf{S}}^*_{5,aux} &:= \overline{\boldsymbol{J\zeta}}^*_{i,j,k+1/2}\,;\\
\hat{\mathbf{S}}_{6,aux} &:= -\widehat{\boldsymbol{J\zeta}}_{i,j,k-1/2}\,, & \bar{\mathbf{S}}^*_{6,aux} &:= -\overline{\boldsymbol{J\zeta}}^*_{i,j,k-1/2}\,.
\end{aligned} \tag{4.27}$$

Each of the auxiliary amplitude and time-invariant-mean qualified variables, on the other hand, is now gained through arithmetic averaging of the face-respective preceding and succeeding centroidal instance; i.e.,

$$\begin{aligned}
\hat{\Phi}_{1,aux} &:= (\,\hat{\Phi}_{i,j,k} + \hat{\Phi}_{i+1,j,k}\,) \;/\; 2\,, & \bar{\Phi}_{1,aux} &:= (\,\bar{\Phi}_{i,j,k} + \bar{\Phi}_{i+1,j,k}\,) \;/\; 2\,;\\
\hat{\Phi}_{2,aux} &:= (\,\hat{\Phi}_{i,j,k} + \hat{\Phi}_{i-1,j,k}\,) \;/\; 2\,, & \bar{\Phi}_{2,aux} &:= (\,\bar{\Phi}_{i,j,k} + \bar{\Phi}_{i-1,j,k}\,) \;/\; 2\,;\\
\hat{\Phi}_{3,aux} &:= (\,\hat{\Phi}_{i,j,k} + \hat{\Phi}_{i,j+1,k}\,) \;/\; 2\,, & \bar{\Phi}_{3,aux} &:= (\,\bar{\Phi}_{i,j,k} + \bar{\Phi}_{i,j+1,k}\,) \;/\; 2\,;\\
\hat{\Phi}_{4,aux} &:= (\,\hat{\Phi}_{i,j,k} + \hat{\Phi}_{i,j-1,k}\,) \;/\; 2\,, & \bar{\Phi}_{4,aux} &:= (\,\bar{\Phi}_{i,j,k} + \bar{\Phi}_{i,j-1,k}\,) \;/\; 2\,;\\
\hat{\Phi}_{5,aux} &:= (\,\hat{\Phi}_{i,j,k} + \hat{\Phi}_{i,j,k+1}\,) \;/\; 2\,, & \bar{\Phi}_{5,aux} &:= (\,\bar{\Phi}_{i,j,k} + \bar{\Phi}_{i,j,k+1}\,) \;/\; 2\,;\\
\hat{\Phi}_{6,aux} &:= (\,\hat{\Phi}_{i,j,k} + \hat{\Phi}_{i,j,k-1}\,) \;/\; 2\,, & \bar{\Phi}_{6,aux} &:= (\,\bar{\Phi}_{i,j,k} + \bar{\Phi}_{i,j,k-1}\,) \;/\; 2\,.
\end{aligned} \tag{4.28}$$

Evidently, the amplitude/time-invariant-mean qualified variable associated with the considered centroid contributes to all six auxiliary instances in equal manner.

All in all, the presented scheme for the interface and centroidal evaluation of the amplitude/time-invariant-mean qualified variable's gradient is quite compact [16], with the employed stencils, respectively, extending over merely ten and seven centroids. For smoothly stretched grids it renders second-order-accurate discretizations of the continuous viscous fluxes [21]. A loss of accuracy is incurred, however, for arbitrarily stretched grids, as the gradients' approximation becomes inconsistent [16].

4.4 Near-Field Boundary Condition

As inherited from FLM-SDEu [70], both artificial and physical boundary conditions (cut and symmetry, on one hand, far-field and near-field, on the other hand) are implemented under utilization of ghost cells [16]. A dual layer of computational cells is exteriorly added to each face of the individual computational block, allowing the spatial scheme's evaluation stencils to extend beyond the rendered physical domain. The amplitude and linearized time-invariant-mean state vectors associated with the first and second exterior centroid are then constructed in such a manner that the stencils properly account for the constraint designated at the pertinent block-interior-delimiting interface. For the stencils employed in the amplitude viscous flux and amplitude turbulence source term vector evaluation, it suffices to set the amplitude and linearized time-invariant-mean state vector associated with the first exterior centroid.

Since the artificial and far-field boundary conditions are not particular to inviscid flow, their FLM-SDEu implementation can be retained for FLM-SD.NS, albeit requiring an extension to accommodate the S/A transport equation. In regard to the near-field boundary condition, however, the existent slip-wall property needs to be replaced by the no-slip instance, while setting the selected adiabatic-wall property as well [6]. The small disturbance formulation of these new constraints have been provided by Iatrou [54], with the actual implementation by the author being based on Cvrlje's [31] original FLM-NS instance. In contrast to the latter, the implementation is realized independent of the block face by formulating the constraints in terms of a generalized boundary-fitted coordinate system. Satisfying the right-hand rule, a block-face-normal curvilinear direction as well as a first and second tangential instance are defined, respectively, with the coordinates $\psi_{wb,\,n}$ as well as $\psi_{wb,\,t1}$ and $\psi_{wb,\,t2}$ then being assigned. Additionally, the pressure-gradient-neutral-wall property implemented by Kreiselmaier [70] for FLM-SDEu needs to be retained, while the S/A one-equation turbulence model's viscous-sublayer-wall constraint [121] requires a novel small disturbance formulation and implementation likewise.

4.4.1 No-Slip Wall

The no-slip-wall property requires zero relative velocity between the designated wall ($\psi_{wb,\,n} = const.$) and the fluid in its immediate proximity [6, 16]. This corresponds to both the normal and tangential contravariant velocities vanishing at the wall [31]. Expressed in terms of the phase-averaged flowfield, the constraint becomes

$$\left(\left\langle \theta_\psi \right\rangle \big|_{wb,\,n} \;,\; \left\langle \theta_\psi \right\rangle \big|_{wb,\,t1} \;,\; \left\langle \theta_\psi \right\rangle \big|_{wb,\,t2} \right)^T = 0 \,, \tag{4.29}$$

which renders a system of linear equations for the associated Cartesian velocities:

$$\begin{pmatrix} J\psi_x|_{wb,\,n} & J\psi_y|_{wb,\,n} & J\psi_z|_{wb,\,n} \\ J\psi_x|_{wb,\,t1} & J\psi_y|_{wb,\,t1} & J\psi_z|_{wb,\,t1} \\ J\psi_x|_{wb,\,t2} & J\psi_y|_{wb,\,t2} & J\psi_z|_{wb,\,t2} \end{pmatrix} \begin{pmatrix} \langle u \rangle_{wb} \\ \langle v \rangle_{wb} \\ \langle w \rangle_{wb} \end{pmatrix} = - \begin{pmatrix} J\psi_t|_{wb,\,n} \\ J\psi_t|_{wb,\,t1} \\ J\psi_t|_{wb,\,t2} \end{pmatrix} . \tag{4.30}$$

Within Eq. (4.30), the spatial metrics reflect the geometry and deformation/deflection of the considered body's surface, while the temporal metrics embody its deformation/deflection velocity as decomposed into the specified curvilinear directions. Since the motion is prescribed, they are collectively known in their time-dependent progression. Hence, Eq. (4.30) can be uniquely solved for any regarded instant of physical time.

4.4.1.1 Small Disturbance Formulation

On the basis of Iatrou [54], the small disturbance formulation of Eq. (4.30) is gained as

$$\begin{pmatrix} \overline{J\psi_x}^*\big|_{wb,\,n} & \overline{J\psi_y}^*\big|_{wb,\,n} & \overline{J\psi_z}^*\big|_{wb,\,n} \\ \overline{J\psi_x}^*\big|_{wb,\,t1} & \overline{J\psi_y}^*\big|_{wb,\,t1} & \overline{J\psi_z}^*\big|_{wb,\,t1} \\ \overline{J\psi_x}^*\big|_{wb,\,t2} & \overline{J\psi_y}^*\big|_{wb,\,t2} & \overline{J\psi_z}^*\big|_{wb,\,t2} \end{pmatrix} \begin{pmatrix} \hat{u}_{wb} \\ \hat{v}_{wb} \\ \hat{w}_{wb} \end{pmatrix} = - \begin{pmatrix} \widehat{J\psi_t}\big|_{wb,\,n} \\ \widehat{J\psi_t}\big|_{wb,\,t1} \\ \widehat{J\psi_t}\big|_{wb,\,t2} \end{pmatrix} , \tag{4.31}$$

having taken into account the linearized time-invariant-mean instance

$$\begin{pmatrix} \overline{J\psi_x}^*\big|_{wb,\,n} & \overline{J\psi_y}^*\big|_{wb,\,n} & \overline{J\psi_z}^*\big|_{wb,\,n} \\ \overline{J\psi_x}^*\big|_{wb,\,t1} & \overline{J\psi_y}^*\big|_{wb,\,t1} & \overline{J\psi_z}^*\big|_{wb,\,t1} \\ \overline{J\psi_x}^*\big|_{wb,\,t2} & \overline{J\psi_y}^*\big|_{wb,\,t2} & \overline{J\psi_z}^*\big|_{wb,\,t2} \end{pmatrix} \begin{pmatrix} \bar{u}_{wb} \\ \bar{v}_{wb} \\ \bar{w}_{wb} \end{pmatrix} = - \begin{pmatrix} \overline{J\psi_t}^*\big|_{wb,\,n} \\ \overline{J\psi_t}^*\big|_{wb,\,t1} \\ \overline{J\psi_t}^*\big|_{wb,\,t2} \end{pmatrix} . \tag{4.32}$$

Apparently, the system matrices of Eq. (4.31) and Eq. (4.32) are identical, with their determinant being

$$\begin{aligned} \bar{D}^*_{wb} \;&:=\; \overline{J\psi_x}^*\big|_{wb,\,n} \left(\overline{J\psi_y}^*\big|_{wb,\,t1}\, \overline{J\psi_z}^*\big|_{wb,\,t2} - \overline{J\psi_z}^*\big|_{wb,\,t1}\, \overline{J\psi_y}^*\big|_{wb,\,t2} \right) \\ &+\; \overline{J\psi_y}^*\big|_{wb,\,n} \left(\overline{J\psi_z}^*\big|_{wb,\,t1}\, \overline{J\psi_x}^*\big|_{wb,\,t2} - \overline{J\psi_x}^*\big|_{wb,\,t1}\, \overline{J\psi_z}^*\big|_{wb,\,t2} \right) \\ &+\; \overline{J\psi_z}^*\big|_{wb,\,n} \left(\overline{J\psi_x}^*\big|_{wb,\,t1}\, \overline{J\psi_y}^*\big|_{wb,\,t2} - \overline{J\psi_y}^*\big|_{wb,\,t1}\, \overline{J\psi_x}^*\big|_{wb,\,t2} \right) \\ &\neq\; 0 \end{aligned} \tag{4.33}$$

[54]. Hence, for Eq. (4.31) Cramer's rule yields

$$\begin{aligned}
\hat{u}_{wb} &= \left[\widehat{J\psi_t}\Big|_{wb,\,n} \left(\overline{J\psi_z}^*\Big|_{wb,\,t1}\, \overline{J\psi_y}^*\Big|_{wb,\,t2} - \overline{J\psi_y}^*\Big|_{wb,\,t1}\, \overline{J\psi_z}^*\Big|_{wb,\,t2} \right) \right. \\
&+ \widehat{J\psi_t}\Big|_{wb,\,t1} \left(\overline{J\psi_y}^*\Big|_{wb,\,n}\, \overline{J\psi_z}^*\Big|_{wb,\,t2} - \overline{J\psi_z}^*\Big|_{wb,\,n}\, \overline{J\psi_y}^*\Big|_{wb,\,t2} \right) \\
&+ \left. \widehat{J\psi_t}\Big|_{wb,\,t2} \left(\overline{J\psi_y}^*\Big|_{wb,\,t1}\, \overline{J\psi_z}^*\Big|_{wb,\,n} - \overline{J\psi_z}^*\Big|_{wb,\,t1}\, \overline{J\psi_y}^*\Big|_{wb,\,n} \right) \right] \;/\; \bar{D}^*_{wb}\,, \\
\hat{v}_{wb} &= \left[\widehat{J\psi_t}\Big|_{wb,\,n} \left(\overline{J\psi_x}^*\Big|_{wb,\,t1}\, \overline{J\psi_z}^*\Big|_{wb,\,t2} - \overline{J\psi_z}^*\Big|_{wb,\,t1}\, \overline{J\psi_x}^*\Big|_{wb,\,t2} \right) \right. \\
&+ \widehat{J\psi_t}\Big|_{wb,\,t1} \left(\overline{J\psi_z}^*\Big|_{wb,\,n}\, \overline{J\psi_x}^*\Big|_{wb,\,t2} - \overline{J\psi_x}^*\Big|_{wb,\,n}\, \overline{J\psi_z}^*\Big|_{wb,\,t2} \right) \\
&+ \left. \widehat{J\psi_t}\Big|_{wb,\,t2} \left(\overline{J\psi_z}^*\Big|_{wb,\,t1}\, \overline{J\psi_x}^*\Big|_{wb,\,n} - \overline{J\psi_x}^*\Big|_{wb,\,t1}\, \overline{J\psi_z}^*\Big|_{wb,\,n} \right) \right] \;/\; \bar{D}^*_{wb}\,, \\
\hat{w}_{wb} &= \left[\widehat{J\psi_t}\Big|_{wb,\,n} \left(\overline{J\psi_y}^*\Big|_{wb,\,t1}\, \overline{J\psi_x}^*\Big|_{wb,\,t2} - \overline{J\psi_x}^*\Big|_{wb,\,t1}\, \overline{J\psi_y}^*\Big|_{wb,\,t2} \right) \right. \\
&+ \widehat{J\psi_t}\Big|_{wb,\,t1} \left(\overline{J\psi_x}^*\Big|_{wb,\,n}\, \overline{J\psi_y}^*\Big|_{wb,\,t2} - \overline{J\psi_y}^*\Big|_{wb,\,n}\, \overline{J\psi_x}^*\Big|_{wb,\,t2} \right) \\
&+ \left. \widehat{J\psi_t}\Big|_{wb,\,t2} \left(\overline{J\psi_x}^*\Big|_{wb,\,t1}\, \overline{J\psi_y}^*\Big|_{wb,\,n} - \overline{J\psi_y}^*\Big|_{wb,\,t1}\, \overline{J\psi_x}^*\Big|_{wb,\,n} \right) \right] \;/\; \bar{D}^*_{wb}\,.
\end{aligned} \tag{4.34}$$

Naturally, the frequency dependence inherent to the amplitude temporal metrics follows through to the amplitude Cartesian velocities. However, as

$$Re\, \widehat{J\psi_t}\Big|_{wb,\,n} = 0\,, \qquad Re\, \widehat{J\psi_t}\Big|_{wb,\,t1} = 0\,, \qquad Re\, \widehat{J\psi_t}\Big|_{wb,\,t2} = 0\,, \tag{4.35}$$

perforce

$$Re\, \hat{u}_{wb} = 0\,, \qquad Re\, \hat{v}_{wb} = 0\,, \qquad Re\, \hat{w}_{wb} = 0\,; \tag{4.36}$$

i.e., the amplitude Cartesian velocities are purely imaginary. In the quasi-steady case, the prescribed frequency of nil value lets the RHS of Eq. (4.31) vanish, permitting only the degenerate solution, where

$$Im\, \hat{u}_{wb} = 0\,, \qquad Im\, \hat{v}_{wb} = 0\,, \qquad Im\, \hat{w}_{wb} = 0 \tag{4.37}$$

is then given as well. Contrarily, the RHS of Eq. (4.32) vanishes in any case, since the linearized time-invariant-mean temporal metrics are always of nil value:

$$\overline{J\psi_t}^*\Big|_{wb,\,n} = 0\,, \qquad \overline{J\psi_t}^*\Big|_{wb,\,t1} = 0\,, \qquad \overline{J\psi_t}^*\Big|_{wb,\,t1} = 0\,. \tag{4.38}$$

Hence, merely the degenerate solution

$$\bar{u}_{wb} = 0\,, \qquad \bar{v}_{wb} = 0\,, \qquad \bar{w}_{wb} = 0 \tag{4.39}$$

is permitted. Accordingly, the supplied linearized time-invariant-mean flowfield only satisfies the no-slip-wall property if its near-field had developed from wall-bounded Cartesian velocities of nil value. This circumstance is naturally given for the supplied steady-state flowfield respective the considered body's reference position [54].

4.4.1.2 Application in Discrete Space

The formulated no-slip-wall property can be applied to a boundary cell-interface of any directionally starting or ending block face. It becomes specific to the particular block face by setting $\psi_{wb,\,n}$, $\psi_{wb,\,t1}$, and $\psi_{wb,\,t2}$ to the actual curvilinear coordinate directions. In this regard, the normal instance associated with the considered block face entails the tangential instances. Summarized in Table 4.1, the individual assignment naturally follows through to the linearized time-invariant-mean spatial matrices and the amplitude temporal metrics constituting Eq. (4.34). On the basis of Cvrlje's [31] original (block-face-specific) FLM-NS implementation, the employed discrete metrics of the block-face-normal direction are directly satisfied by those associated with each considered wall-boundary cell-interface. The complementary metrics of the first and second tangential direction, on the other hand,

$\psi_{wb,\,n}$	$\psi_{wb,\,t1}$	$\psi_{wb,\,t2}$
ξ	η	ζ
η	ζ	ξ
ζ	ξ	η

Table 4.1: Correlation between the block-face-normal curvilinear coordinate direction and the first- and second-tangential instances.

are gained indirectly. Considering the first exterior and first interior cell comprising the wall-boundary cell-interface, the metrics associated with both cell's directionally pertinent forward and backward interface need to be arithmetically averaged.

Denoting the first interior cell with $(i,\,j,\,k)$, the setup is exemplified by way of $\psi_{wb,\,n} := \xi$, and thus, $\psi_{wb,\,t1} := \eta$, $\psi_{wb,\,t2} := \zeta$. For the directionally starting block face, the first exterior cell is identified with $(i-1,\,j,\,k)$. As implemented by the author, the employed discrete metrics are

$$\begin{aligned}
\overline{\boldsymbol{J}\boldsymbol{\psi}}^{\,*}\Big|_{wb,\,n} = \overline{\boldsymbol{J}\boldsymbol{\xi}}^{\,*}\Big|_{wb} &:= \overline{\boldsymbol{J}\boldsymbol{\xi}}^{\,*}_{i-1/2,\,j,\,k}\,, \\
\overline{\boldsymbol{J}\boldsymbol{\psi}}^{\,*}\Big|_{wb,\,t1} = \overline{\boldsymbol{J}\boldsymbol{\eta}}^{\,*}\Big|_{wb} &:= \left(\overline{\boldsymbol{J}\boldsymbol{\eta}}^{\,*}_{i,\,j-1/2,\,k} + \overline{\boldsymbol{J}\boldsymbol{\eta}}^{\,*}_{i,\,j+1/2,\,k} + \overline{\boldsymbol{J}\boldsymbol{\eta}}^{\,*}_{i-1,\,j-1/2,\,k} + \overline{\boldsymbol{J}\boldsymbol{\eta}}^{\,*}_{i-1,\,j+1/2,\,k}\right)/4, \\
\overline{\boldsymbol{J}\boldsymbol{\psi}}^{\,*}\Big|_{wb,\,t2} = \overline{\boldsymbol{J}\boldsymbol{\zeta}}^{\,*}\Big|_{wb} &:= \left(\overline{\boldsymbol{J}\boldsymbol{\zeta}}^{\,*}_{i,\,j,\,k-1/2} + \overline{\boldsymbol{J}\boldsymbol{\zeta}}^{\,*}_{i,\,j,\,k+1/2} + \overline{\boldsymbol{J}\boldsymbol{\zeta}}^{\,*}_{i-1,\,j,\,k-1/2} + \overline{\boldsymbol{J}\boldsymbol{\zeta}}^{\,*}_{i-1,\,j,\,k+1/2}\right)/4\,,
\end{aligned} \tag{4.40}$$

and

$$\begin{aligned}
\widehat{J\psi_t}\Big|_{wb,\,n} &= \widehat{J\xi_t}\Big|_{wb} &:=\quad & \widehat{J\xi}_{t\,i-1/2,\,j,\,k}\,,\\
\widehat{J\psi_t}\Big|_{wb,\,t1} &= \widehat{J\eta_t}\Big|_{wb} &:=\ & \left(\widehat{J\eta}_{t\,i,\,j-1/2,\,k}+\widehat{J\eta}_{t\,i,\,j+1/2,\,k}+\widehat{J\eta}_{t\,i-1,\,j-1/2,\,k}+\widehat{J\eta}_{t\,i-1,\,j+1/2,\,k}\right)/4\,,\\
\widehat{J\psi_t}\Big|_{wb,\,t2} &= \widehat{J\zeta_t}\Big|_{wb} &:=\ & \left(\widehat{J\zeta}_{t\,i,\,j,\,k-1/2}+\widehat{J\zeta}_{t\,i,\,j,\,k+1/2}+\widehat{J\zeta}_{t\,i-1,\,j,\,k-1/2}+\widehat{J\zeta}_{t\,i-1,\,j,\,k+1/2}\right)/4\,,
\end{aligned} \tag{4.41}$$

yielding $\hat{u}_{wb}$, $\hat{v}_{wb}$, and $\hat{w}_{wb}$ at the cell interface $(i-1/2,\ j,\ k)$ through Eq. (4.34). Complementarily, for the directionally ending block face, the first exterior cell is identified with $(i+1,\ j,\ k)$. As implemented by the author, the employed discrete metrics are

$$\begin{aligned}
\overline{\boldsymbol{J\psi}}^{*}\Big|_{wb,\,n} &= \overline{\boldsymbol{J\xi}}^{*}\Big|_{wb} &:=\ & \overline{\boldsymbol{J\xi}}^{*}_{i+1/2,\,j,\,k}\,,\\
\overline{\boldsymbol{J\psi}}^{*}\Big|_{wb,\,t1} &= \overline{\boldsymbol{J\eta}}^{*}\Big|_{wb} &:=\ & \left(\overline{\boldsymbol{J\eta}}^{*}_{i,\,j-1/2,\,k}+\overline{\boldsymbol{J\eta}}^{*}_{i,\,j+1/2,\,k}+\overline{\boldsymbol{J\eta}}^{*}_{i+1,\,j-1/2,\,k}+\overline{\boldsymbol{J\eta}}^{*}_{i+1,\,j+1/2,\,k}\right)/4,\\
\overline{\boldsymbol{J\psi}}^{*}\Big|_{wb,\,t2} &= \overline{\boldsymbol{J\zeta}}^{*}\Big|_{wb} &:=\ & \left(\overline{\boldsymbol{J\zeta}}^{*}_{i,\,j,\,k-1/2}+\overline{\boldsymbol{J\zeta}}^{*}_{i,\,j,\,k+1/2}+\overline{\boldsymbol{J\zeta}}^{*}_{i+1,\,j,\,k-1/2}+\overline{\boldsymbol{J\zeta}}^{*}_{i+1,\,j,\,k+1/2}\right)/4\,,
\end{aligned} \tag{4.42}$$

and

$$\begin{aligned}
\widehat{J\psi_t}\Big|_{wb,\,n} &= \widehat{J\xi_t}\Big|_{wb} &:=\quad & \widehat{J\xi}_{t\,i+1/2,\,j,\,k}\,,\\
\widehat{J\psi_t}\Big|_{wb,\,t1} &= \widehat{J\eta_t}\Big|_{wb} &:=\ & \left(\widehat{J\eta}_{t\,i,\,j-1/2,\,k}+\widehat{J\eta}_{t\,i,\,j+1/2,\,k}+\widehat{J\eta}_{t\,i+1,\,j-1/2,\,k}+\widehat{J\eta}_{t\,i+1,\,j+1/2,\,k}\right)/4\,,\\
\widehat{J\psi_t}\Big|_{wb,\,t2} &= \widehat{J\zeta_t}\Big|_{wb} &:=\ & \left(\widehat{J\zeta}_{t\,i,\,j,\,k-1/2}+\widehat{J\zeta}_{t\,i,\,j,\,k+1/2}+\widehat{J\zeta}_{t\,i+1,\,j,\,k-1/2}+\widehat{J\zeta}_{t\,i+1,\,j,\,k+1/2}\right)/4\,,
\end{aligned} \tag{4.43}$$

yielding $\hat{u}_{wb}$, $\hat{v}_{wb}$, and $\hat{w}_{wb}$ at the cell interface $(i+1/2,\ j,\ k)$ through Eq. (4.34).

4.4.2 Adiabatic/Pressure-Gradient-Neutral/Viscous-Sublayer Wall

The adiabatic-wall property requires the wall-normal gradient of the static temperature to be neutral [6, 16]. Expressed in terms of the phase-averaged flowfield, the constraint becomes

$$\boldsymbol{J\psi}\big|_{wb,\,n}\ \boldsymbol{\nabla}\langle T\rangle_{wb}=0\,. \tag{4.44}$$

Generally, the wall-normal gradient of the static pressure needs to be neutral as well [6, 16]:

$$\boldsymbol{J\psi}\big|_{wb,\,n}\ \boldsymbol{\nabla}\langle p\rangle_{wb}=0\,. \tag{4.45}$$

The viscous-sublayer-wall constraint for the S/A one-equation turbulence model [121], on the other hand, simply requires its primitive working variable to be of nil value at the

wall; i.e.,

$$\langle \breve{\nu} \rangle_{wb} = 0 \,, \tag{4.46}$$

which corresponds to a vanishing dynamic eddy viscosity.

4.4.2.1 Small Disturbance Formulation

Pursuant to Iatrou [54], the small disturbance formulation of Eq. (4.44) is gained as

$$\overline{\boldsymbol{J\psi}}^{*}\Big|_{wb,\,n} \boldsymbol{\nabla}\hat{T}_{wb} + \widehat{\boldsymbol{J\psi}}\Big|_{wb,\,n} \boldsymbol{\nabla}\bar{T}^{*}_{wb} = 0 \,, \tag{4.47}$$

having taken into account the linearized time-invariant-mean instance

$$\overline{\boldsymbol{J\psi}}^{*}\Big|_{wb,\,n} \boldsymbol{\nabla}\bar{T}^{*}_{wb} = 0 \,. \tag{4.48}$$

Correspondingly, Eq. (4.45) leads to

$$\overline{\boldsymbol{J\psi}}^{*}\Big|_{wb,\,n} \boldsymbol{\nabla}\hat{p}_{wb} + \widehat{\boldsymbol{J\psi}}\Big|_{wb,\,n} \boldsymbol{\nabla}\bar{p}^{*}_{wb} = 0 \,, \tag{4.49}$$

with

$$\overline{\boldsymbol{J\psi}}^{*}\Big|_{wb,\,n} \boldsymbol{\nabla}\bar{p}^{*}_{wb} = 0 \,. \tag{4.50}$$

The small disturbance formulation of Eq. (4.46) is otherwise trivial:

$$\widehat{\breve{\nu}}_{wb} = 0 \,, \qquad \text{with} \qquad \overline{\breve{\nu}}_{wb} = 0 \,. \tag{4.51}$$

As with the no-slip-wall property, the computed steady-state flowfield respective the considered body's reference position will a priori satisfy the linearized time-invariant-mean adiabatic-wall property [54], as well as the pressure-gradient-neutral- [70] and viscous-sublayer-wall instances.

4.4.2.2 Application in Discrete Space

Regarding a boundary cell-interface, Eq. (4.47) is numerically satisfied by letting both the amplitude and linearized time-invariant-mean static temperature be equal to their first interior centroid counterpart; i.e.,

$$\boldsymbol{\nabla}\hat{T}_{wb} \approx 0 \quad \text{for} \quad \hat{T}_{wb} := \hat{T}_{int} \qquad \text{and} \qquad \boldsymbol{\nabla}\bar{T}^{*}_{wb} \approx 0 \quad \text{for} \quad \bar{T}^{*}_{wb} := \bar{T}^{*}_{int} \,, \tag{4.52}$$

as based on Cvrlje's [31] original FLM-NS implementation. The amplitude and linearized time-invariant-mean static temperature of the first interior centroid are, respectively, obtained through

$$\hat{T}_{int} = \left(\hat{p}_{int}\, \bar{\rho}_{int} - \hat{\rho}_{int}\, \bar{p}^{*}_{int} \right) / \left(\bar{\rho}_{int} \right)^{2} \qquad \text{and} \qquad \bar{T}^{*}_{int} = \bar{p}^{*}_{int} / \bar{\rho}_{int} \,, \tag{4.53}$$

wherein the frequency-domain formulation of Eq. (3.190) sans $\widetilde{\rho\breve{k}}^{*}$ supplies the amplitude static pressure by means of

$$\begin{aligned}\hat{\mathbf{q}}_{int} &= \left(\hat{\rho}_{int},\, \widehat{\rho u}_{int},\, \widehat{\rho v}_{int},\, \widehat{\rho w}_{int},\, \widehat{\rho e}_{int},\, \widehat{\breve{\mu}}_{int}\right)^{T} \quad \text{and} \\ \bar{\mathbf{q}}^{*}_{int} &= \left(\bar{\rho}_{int},\, \overline{\rho u}^{*}_{int},\, \overline{\rho v}^{*}_{int},\, \overline{\rho w}^{*}_{int},\, \overline{\rho e}^{*}_{int},\, \overline{\breve{\mu}}^{*}_{int}\right)^{T} ,\end{aligned} \tag{4.54}$$

while Eq. (3.191) sans $\overline{\rho\breve{k}}^{*}$ renders its linearized time-invariant-mean counterpart using $\bar{\mathbf{q}}^{*}_{int}$. In equivalence to Eq. (4.52), Eq. (4.49) is numerically satisfied by letting both the amplitude and linearized time-invariant-mean static pressure be equal to their first interior centroid counterpart; i.e.,

$$\boldsymbol{\nabla}\hat{p}_{wb} \approx 0 \quad \text{for} \quad \hat{p}_{wb} := \hat{p}_{int} \qquad \text{and} \qquad \boldsymbol{\nabla}\bar{p}^{*}_{wb} \approx 0 \quad \text{for} \quad \bar{p}^{*}_{wb} := \bar{p}^{*}_{int}\,, \tag{4.55}$$

as retained from Kreiselmaier's [70] original FLM-SDEu implementation. Furthermore, the amplitude and time-invariant-mean density at the boundary cell-interface can be, respectively, obtained through

$$\hat{\rho}_{wb} = \left(\hat{p}_{wb}\,\bar{T}^{*}_{wb} - \bar{p}^{*}_{wb}\,\hat{T}_{wb}\right) / \left(\bar{T}^{*}_{wb}\right)^{2} = \hat{\rho}_{int} \qquad \text{and} \qquad \bar{\rho}_{wb} = \bar{p}^{*}_{wb}/\bar{T}^{*}_{wb} = \bar{\rho}_{int}\,, \tag{4.56}$$

having taken Eq. (4.53) into account.

Ultimately, the amplitude and time-invariant-mean instances of the density, Cartesian velocities, and S/A primitive working variable, as well as the amplitude and linearized time-invariant-mean static temperature, are linearly extrapolated from the interior centroid to the exterior centroid using the pertinent boundary cell-interface specification [48]. The amplitude state vector associated with the exterior centroid is then given through

$$\hat{\mathbf{q}}_{ext} = \begin{pmatrix} \hat{\rho}_{ext} \\ \widehat{\rho u}_{ext} \\ \widehat{\rho v}_{ext} \\ \widehat{\rho w}_{ext} \\ \widehat{\rho e}_{ext} \\ \\ \widehat{\breve{\mu}}_{ext} \end{pmatrix} := \begin{pmatrix} 2\hat{\rho}_{wb} - \hat{\rho}_{int} & & \\ \hat{\rho}_{ext}(2\bar{u}_{wb} - \bar{u}_{int}) & + & \bar{\rho}_{ext}(2\hat{u}_{wb} - \hat{u}_{int}) \\ \hat{\rho}_{ext}(2\bar{v}_{wb} - \bar{v}_{int}) & + & \bar{\rho}_{ext}(2\hat{v}_{wb} - \hat{v}_{int}) \\ \hat{\rho}_{ext}(2\bar{w}_{wb} - \bar{w}_{int}) & + & \bar{\rho}_{ext}(2\hat{w}_{wb} - \hat{w}_{int}) \\ \hat{\rho}_{ext}(2\bar{T}^{*}_{wb} - \bar{T}^{*}_{int})/\Gamma & + & \bar{\rho}_{ext}(2\hat{T}_{wb} - \hat{T}_{int})/\Gamma \\ -\hat{\rho}_{ext}\left[(\overline{\rho u}^{*}_{ext})^{2} + (\overline{\rho v}^{*}_{ext})^{2} + (\overline{\rho w}^{*}_{ext})^{2}\right] / \left[2(\bar{\rho}_{ext})^{2}\right] & & \\ +(\overline{\rho u}^{*}_{ext}\widehat{\rho u}_{ext} + \overline{\rho v}^{*}_{ext}\widehat{\rho v}_{ext} + \overline{\rho w}^{*}_{ext}\widehat{\rho w}_{ext})/\bar{\rho}_{ext} & & \\ \hat{\rho}_{ext}(2\overline{\breve{\nu}}_{wb} - \overline{\breve{\nu}}_{int}) & + & \bar{\rho}_{ext}(2\widehat{\breve{\nu}}_{wb} - \widehat{\breve{\nu}}_{int}) \end{pmatrix}, \tag{4.57}$$

with its linearized time-invariant-mean counterpart being

$$\bar{\mathbf{q}}^*_{ext} = \begin{pmatrix} \bar{\rho}_{ext} \\ \overline{\rho u}^*_{ext} \\ \overline{\rho v}^*_{ext} \\ \overline{\rho w}^*_{ext} \\ \overline{\rho e}^*_{ext} \\ \\ \overline{\breve{\mu}}^*_{ext} \end{pmatrix} := \begin{pmatrix} 2\bar{\rho}_{wb} - \bar{\rho}_{int} \\ \bar{\rho}_{ext}(2\bar{u}_{wb} - \bar{u}_{int}) \\ \bar{\rho}_{ext}(2\bar{v}_{wb} - \bar{v}_{int}) \\ \bar{\rho}_{ext}(2\bar{w}_{wb} - \bar{w}_{int}) \\ \bar{\rho}_{ext}(2\bar{T}^*_{wb} - \bar{T}^*_{int})/\Gamma \\ \quad + \left[(\overline{\rho u}^*_{ext})^2 + (\overline{\rho v}^*_{ext})^2 + (\overline{\rho w}^*_{ext})^2\right]/(2\bar{\rho}_{ext}) \\ \bar{\rho}_{ext}(2\overline{\breve{\nu}}_{wb} - \overline{\breve{\nu}}_{int}) \end{pmatrix} . \tag{4.58}$$

The direct consideration of Eq. (4.56), Eq. (4.39), Eq. (4.51), as well as Eq. (4.52), reduces Eq. (4.57) and Eq. (4.58), respectively, to

$$\hat{\mathbf{q}}_{ext} := \begin{pmatrix} \hat{\rho}_{int} \\ -\widehat{\rho u}_{int} + 2\bar{\rho}_{int}\hat{u}_{wb} \\ -\widehat{\rho v}_{int} + 2\bar{\rho}_{int}\hat{v}_{wb} \\ -\widehat{\rho w}_{int} + 2\bar{\rho}_{int}\hat{w}_{wb} \\ \widehat{\rho e}_{int} \\ -2(\overline{\rho u}^*_{int}\hat{u}_{wb} + \overline{\rho v}^*_{int}\hat{v}_{wb} + \overline{\rho w}^*_{int}\hat{w}_{wb}) \\ -\widehat{\breve{\mu}}_{int} \end{pmatrix} \quad \text{and} \quad \bar{\mathbf{q}}^*_{ext} := \begin{pmatrix} \bar{\rho}_{int} \\ -\overline{\rho u}^*_{int} \\ -\overline{\rho v}^*_{int} \\ -\overline{\rho w}^*_{int} \\ \overline{\rho e}^*_{int} \\ \\ -\overline{\breve{\mu}}^*_{int} \end{pmatrix} , \tag{4.59}$$

as implemented by the author.

4.4.3 Consideration in the Amplitude Residual Vector

The near-field boundary condition is imposed within $\widehat{\mathbf{R}}_{i,j,k}$, Eq. (4.4), through the appropriate evaluation of its constituting amplitude flux and amplitude turbulence source term vectors. It requires the first layer of ghost cells to actually be physical cells; i.e., both their volume and surface normal vectors must exists [16]. On the basis of Cvrlje's [31] original FLM-NS implementation, this is accomplished by the author within FLM-SD.NS by simply assigning the amplitude and linearized time-invariant-mean volume and surface normal vectors of the particular interior cell to the exterior cell. The approximation is adequate barring strong wall curvature. In the case of FLM-Eu/FLM-SDEu, on the other hand, it had sufficed for the first layer of ghost cells to be virtual cells, as solely the slip-wall and pressure-gradient-neutral-wall property needed to be put into effect [70].

4.4.3.1 Amplitude Convective Flux Vector

Equal to the small disturbance formulation of the slip-wall property provided by Kreiselmaier [70], the no-slip instance, Eq. (4.31) and Eq. (4.32), intrinsically requires the amplitude and linearized time-invariant-mean contravariant velocities normal to the wall

boundary to vanish; i.e.,

$$\widehat{\theta_{\psi}}\Big|_{wb,\,n} = \widehat{\theta_{\psi}}^{(1)}\Big|_{wb,\,n} + \widehat{\theta_{\psi}}^{(2)}\Big|_{wb,\,n} = 0 \qquad \text{and} \qquad \overline{\theta_{\psi}}^{*}\Big|_{wb,\,n} = 0\,, \tag{4.60}$$

with

$$\widehat{\theta_{\psi}}^{(1)}\Big|_{wb,\,n} = -\,\widehat{J\psi_t}\Big|_{wb,\,n} \qquad \text{and} \qquad \widehat{\theta_{\psi}}^{(2)}\Big|_{wb,\,n} = \widehat{J\psi_t}\Big|_{wb,\,n}\,. \tag{4.61}$$

On the basis of the FLM-SDEu implementation [70], Eq. (4.60) and Eq. (4.61), as well as Eq. (4.55), Eq. (4.56), and Eq. (4.46), are directly accounted for in the evaluation of $\widehat{\mathbf{E}_{\psi}}^{(1)}$ and $\widehat{\mathbf{E}_{\psi}}^{(2)}$, respectively, Eq. (3.230) and Eq. (3.234), at the boundary cell-interface. They supplant the Roe-accordant instances (Appendix Section A.2) obtained without the constraint in the initial block-face-normal directional sweep. Concretely,

$$\widehat{\mathbf{E}_{\psi}}^{(1)}\Big|_{wb,\,n;\,mod} := \begin{pmatrix} 0 \\ \overline{J\psi_x}^{*}\Big|_{wb,\,n}\,\hat{p}_{wb} \\ \overline{J\psi_y}^{*}\Big|_{wb,\,n}\,\hat{p}_{wb} \\ \overline{J\psi_z}^{*}\Big|_{wb,\,n}\,\hat{p}_{wb} \\ 0 \\ 0 \end{pmatrix} \quad \text{and} \quad \widehat{\mathbf{E}_{\psi}}^{(2)}\Big|_{wb,\,n;\,mod} := \begin{pmatrix} 0 \\ \widehat{J\psi_x}\Big|_{wb,\,n}\,\bar{p}^{*}_{wb} \\ \widehat{J\psi_y}\Big|_{wb,\,n}\,\bar{p}^{*}_{wb} \\ \widehat{J\psi_z}\Big|_{wb,\,n}\,\bar{p}^{*}_{wb} \\ -\,\widehat{J\psi_t}\Big|_{wb,\,n}\,\bar{p}^{*}_{wb} \\ 0 \end{pmatrix} \tag{4.62}$$

are locally applied, having shifted elements of $\widehat{\mathbf{E}_{\psi}}^{(1)}|_{wb,\,n}$ that are invariant throughout the pseudotime integration to $\widehat{\mathbf{E}_{\psi}}^{(2)}|_{wb,\,n}$ [70]. Subsequent to the application of $\widehat{\mathbf{E}_{\psi}}^{(1)}|_{wb,\,n;\,mod}$, $\hat{\mathbf{q}}_{ext}$ is set. The application of $\widehat{\mathbf{E}_{\psi}}^{(2)}|_{wb,\,n;\,mod}$ is correspondingly followed by the setting of $\bar{\mathbf{q}}^{*}_{ext}$ [70], limited to the algorithm's initialization procedure.

4.4.3.2 Amplitude Viscous Flux/Turbulence Source Term Vector

The set $\hat{\mathbf{q}}_{ext}$ and $\bar{\mathbf{q}}^{*}_{ext}$, Eq. (4.59), are indirectly accounted for in the evaluation of $\widehat{\mathbf{E}_{\mathbf{v}\,\psi}}^{(1)}$ and $\widehat{\mathbf{E}_{\mathbf{v}\,\psi}}^{(2)}$, respectively, Eq. (3.231) and Eq. (3.235), during the pertinent block-face-normal and -tangential directional sweeps. This circumstance is illustrated in the following, though, discounting those interior cells that constitute the edges and corners of a block, as they can have more than one wall-boundary cell-interface.

Considering the amplitude viscous flux vector evaluation in the block-face-normal direction, Eq. (4.7) reformulates for a wall-boundary cell-interface of either the directionally

starting or ending block face as

$$\begin{aligned}
\widehat{\mathbf{E}_{\mathbf{v}\,\psi}}^{(1)}\Big|_{wb,\,n} &= \widehat{\mathbf{E}_{\mathbf{v}}}^{(1)}\Big(\ \hat{\rho}_{wb},\,\hat{\Phi}_{wb},\,\hat{T}_{wb},\,\boldsymbol{\nabla}\hat{\Phi}\Big|_{wb},\,\boldsymbol{\nabla}\hat{T}\Big|_{wb},\\
&\qquad\qquad \bar{\rho}_{wb},\,\bar{\Phi}_{wb},\,\bar{T}^{*}_{wb},\,\boldsymbol{\nabla}\bar{\Phi}\big|_{wb},\,\boldsymbol{\nabla}\bar{T}^{*}\big|_{wb},\,\overline{\boldsymbol{J\psi}}^{\,*}\Big|_{wb,\,n}\ \Big) \quad \text{and}\\
\widehat{\mathbf{E}_{\mathbf{v}\,\psi}}^{(2)}\Big|_{wb,\,n} &= \widehat{\mathbf{E}_{\mathbf{v}}}^{(2)}\Big(\ \bar{\rho}_{wb},\,\bar{\Phi}_{wb},\,\bar{T}^{*}_{wb},\,\boldsymbol{\nabla}\bar{\Phi}\big|_{wb},\,\boldsymbol{\nabla}\bar{T}^{*}\big|_{wb},\,\widehat{\boldsymbol{J\psi}}\Big|_{wb,\,n}\ \Big)\,,
\end{aligned} \tag{4.63}$$

with

$$\begin{aligned}
\hat{\rho}_{wb} &:= (\,\hat{\rho}_{int} + \hat{\rho}_{ext}\,) \;/\; 2\,, & \bar{\rho}_{wb} &:= (\,\bar{\rho}_{int} + \bar{\rho}_{ext}\,) \;/\; 2\,;\\
\hat{\Phi}_{wb} &:= (\,\hat{\Phi}_{int} + \hat{\Phi}_{ext}\,) \;/\; 2\,, & \bar{\Phi}_{wb} &:= (\,\bar{\Phi}_{int} + \bar{\Phi}_{ext}\,) \;/\; 2\,;\\
\hat{T}_{wb} &:= (\,\hat{T}_{int} + \hat{T}_{ext}\,) \;/\; 2\,, & \bar{T}^{*}_{wb} &:= (\,\bar{T}^{*}_{int} + \bar{T}^{*}_{ext}\,) \;/\; 2
\end{aligned} \tag{4.64}$$

gained pursuant to Eq. (4.9). Similarly, the amplitude and linearized time-invariant-mean control volume of the employed auxiliary cell become

$$\hat{V}_{aux} := (\,\widehat{J}_{int} + \widehat{J}_{ext}\,) \;/\; 2\,, \qquad \bar{V}^{*}_{aux} := (\,\overline{J}^{\,*}_{int} + \overline{J}^{\,*}_{ext}\,) \;/\; 2\,. \tag{4.65}$$

Additional subscripts $n \pm 1$, $t1 \pm 1$, and $t2 \pm 1$ are introduced to denote an increment/decrement of the centroidal index, respectively, in the block-face-normal, -first-tangential, and -second-tangential direction. The spatial metrics of the corresponding backward cell-interface are then always considered. For both the directionally starting and ending block-face, the amplitude and linearized time-invariant-mean set of surface normal vectors are

$$\begin{aligned}
\hat{\mathbf{S}}_{1,aux} &:= \Big(\ \widehat{\boldsymbol{J\psi}}\Big|_{wb,\,n} + \widehat{\boldsymbol{J\psi}}\Big|_{wb,\,n;\,n+1}\Big) \;/\; 2\,,\\
\hat{\mathbf{S}}_{2,aux} &:= -\Big(\ \widehat{\boldsymbol{J\psi}}\Big|_{wb,\,n} + \widehat{\boldsymbol{J\psi}}\Big|_{wb,\,n;\,n-1}\Big) \;/\; 2\,;\\
\hat{\mathbf{S}}_{3,aux} &:= \Big(\ \widehat{\boldsymbol{J\psi}}\Big|_{wb,\,t1;\,t1+1} + \widehat{\boldsymbol{J\psi}}\Big|_{wb,\,t1;\,t1+1;\,n-1}\Big) \;/\; 2\,,\\
\hat{\mathbf{S}}_{4,aux} &:= -\Big(\ \widehat{\boldsymbol{J\psi}}\Big|_{wb,\,t1} + \widehat{\boldsymbol{J\psi}}\Big|_{wb,\,t1;\,n-1}\Big) \;/\; 2\,;\\
\hat{\mathbf{S}}_{5,aux} &:= \Big(\ \widehat{\boldsymbol{J\psi}}\Big|_{wb,\,t2;\,t2+1} + \widehat{\boldsymbol{J\psi}}\Big|_{wb,\,t2;\,t2+1;\,n-1}\Big) \;/\; 2\,,\\
\hat{\mathbf{S}}_{6,aux} &:= -\Big(\ \widehat{\boldsymbol{J\psi}}\Big|_{wb,\,t2} + \widehat{\boldsymbol{J\psi}}\Big|_{wb,\,t2;\,n-1}\Big) \;/\; 2\,,
\end{aligned} \tag{4.66}$$

and

$$\begin{aligned}
\bar{\mathbf{S}}^{*}_{1,aux} &:= \left(\overline{\boldsymbol{J\psi}}^{*}\Big|_{wb,\,n} + \overline{\boldsymbol{J\psi}}^{*}\Big|_{wb,\,n;\,n+1} \right) / 2\,, \\
\bar{\mathbf{S}}^{*}_{2,aux} &:= -\left(\overline{\boldsymbol{J\psi}}^{*}\Big|_{wb,\,n} + \overline{\boldsymbol{J\psi}}^{*}\Big|_{wb,\,n;\,n-1} \right) / 2\,; \\
\bar{\mathbf{S}}^{*}_{3,aux} &:= \left(\overline{\boldsymbol{J\psi}}^{*}\Big|_{wb,\,t1;\,t1+1} + \overline{\boldsymbol{J\psi}}^{*}\Big|_{wb,\,t1;\,t1+1;\,n-1} \right) / 2\,, \\
\bar{\mathbf{S}}^{*}_{4,aux} &:= -\left(\overline{\boldsymbol{J\psi}}^{*}\Big|_{wb,\,t1} + \overline{\boldsymbol{J\psi}}^{*}\Big|_{wb,\,t1;\,n-1} \right) / 2\,; \\
\bar{\mathbf{S}}^{*}_{5,aux} &:= \left(\overline{\boldsymbol{J\psi}}^{*}\Big|_{wb,\,t2;\,t2+1} + \overline{\boldsymbol{J\psi}}^{*}\Big|_{wb,\,t2;\,t2+1;\,n-1} \right) / 2\,, \\
\bar{\mathbf{S}}^{*}_{6,aux} &:= -\left(\overline{\boldsymbol{J\psi}}^{*}\Big|_{wb,\,t2} + \overline{\boldsymbol{J\psi}}^{*}\Big|_{wb,\,t2;\,n-1} \right) / 2\,.
\end{aligned} \tag{4.67}$$

The directional instances of the amplitude/time-invariant-mean auxiliary qualified variables undergo an assignment depending on the consideration of either the directionally starting or ending block face; i.e., for the former,

$$\begin{aligned}
\hat{\Phi}_{1,aux} &:= \hat{\Phi}_{int}\,, & \hat{\Phi}_{2,aux} &:= \hat{\Phi}_{ext}\,, \quad \text{and} \\
\bar{\Phi}_{1,aux} &:= \bar{\Phi}_{int}\,, & \bar{\Phi}_{2,aux} &:= \bar{\Phi}_{ext}\,,
\end{aligned} \tag{4.68}$$

or, for the latter,

$$\begin{aligned}
\hat{\Phi}_{1,aux} &:= \hat{\Phi}_{ext}\,, & \hat{\Phi}_{2,aux} &:= \hat{\Phi}_{int}\,, \quad \text{and} \\
\bar{\Phi}_{1,aux} &:= \bar{\Phi}_{ext}\,, & \bar{\Phi}_{2,aux} &:= \bar{\Phi}_{int}\,.
\end{aligned} \tag{4.69}$$

The off-directional instances, on the other hand, undergo an assignment common to either directional block face

$$\begin{aligned}
\hat{\Phi}_{3,aux} &:= (\,\hat{\Phi}_{int} + \hat{\Phi}_{ext} + \hat{\Phi}_{int;\,t1+1} + \hat{\Phi}_{ext;\,t1+1}) \;/\; 4\,, \\
\hat{\Phi}_{4,aux} &:= (\,\hat{\Phi}_{int} + \hat{\Phi}_{ext} + \hat{\Phi}_{int;\,t1-1} + \hat{\Phi}_{ext;\,t1-1}) \;/\; 4\,; \\
\hat{\Phi}_{5,aux} &:= (\,\hat{\Phi}_{int} + \hat{\Phi}_{ext} + \hat{\Phi}_{int;\,t2+1} + \hat{\Phi}_{ext;\,t2+1}) \;/\; 4\,, \\
\hat{\Phi}_{6,aux} &:= (\,\hat{\Phi}_{int} + \hat{\Phi}_{ext} + \hat{\Phi}_{int;\,t2-1} + \hat{\Phi}_{ext;\,t2-1}) \;/\; 4\,,
\end{aligned} \tag{4.70}$$

and

$$\begin{aligned}
\bar{\Phi}_{3,aux} &:= (\,\bar{\Phi}_{int} + \bar{\Phi}_{ext} + \bar{\Phi}_{int;\,t1+1} + \bar{\Phi}_{ext;\,t1+1}) \;/\; 4\,, \\
\bar{\Phi}_{4,aux} &:= (\,\bar{\Phi}_{int} + \bar{\Phi}_{ext} + \bar{\Phi}_{int;\,t1-1} + \bar{\Phi}_{ext;\,t1-1}) \;/\; 4\,; \\
\bar{\Phi}_{5,aux} &:= (\,\bar{\Phi}_{int} + \bar{\Phi}_{ext} + \bar{\Phi}_{int;\,t2+1} + \bar{\Phi}_{ext;\,t2+1}) \;/\; 4\,, \\
\bar{\Phi}_{6,aux} &:= (\,\bar{\Phi}_{int} + \bar{\Phi}_{ext} + \bar{\Phi}_{int;\,t2-1} + \bar{\Phi}_{ext;\,t2-1}) \;/\; 4\,.
\end{aligned} \tag{4.71}$$

Naturally, the instances of the amplitude/time-invariant-mean auxiliary static temperatures are gained by substituting $\hat{\Phi}$ with $\hat{T}$ and $\bar{\Phi}$ with $\bar{T}^*$ in Eqs. (4.68–4.71). The manner in which this generalized accounting becomes specific to the directional block face is illustrated for $\psi_{wb,\,n} := \xi$, and thus, $\psi_{wb,\,t1} := \eta$, $\psi_{wb,\,t2} := \zeta$, as well as $n \pm 1 := i \pm 1$, $t1 \pm 1 := j \pm 1$, and $t2 \pm 1 := k \pm 1$, in Figure 4.4.

Considering the amplitude viscous flux vector evaluation in the block-face-tangential directions, Eq. (4.7) reformulates for a cell interface normal to the wall boundary of either a pertinent starting or ending block face as

$$\begin{aligned}
\widehat{\mathbf{E}_{\mathbf{v}\,\psi}}^{(1)}\Big|_{wb,\,t1/t2} \;=\; \widehat{\mathbf{E}_{\mathbf{v}}}^{(1)}\Bigg(& \hat{\rho}_{wb,\,t1/t2},\, \hat{\Phi}_{wb,\,t1/t2},\, \hat{T}_{wb,\,t1/t2},\, \boldsymbol{\nabla}\hat{\Phi}\Big|_{wb,\,t1/t2},\, \boldsymbol{\nabla}\hat{T}\Big|_{wb,\,t1/t2}, \\
& \bar{\rho}_{wb,\,t1/t2},\, \bar{\Phi}_{wb,\,t1/t2},\, \bar{T}^*_{wb,\,t1/t2},\, \boldsymbol{\nabla}\bar{\Phi}\big|_{wb\,t1/t2},\, \boldsymbol{\nabla}\bar{T}^*\big|_{wb\,t1/t2}, \\
& \overline{\boldsymbol{J}\boldsymbol{\psi}}^*\Big|_{wb,\,t1/t2}\Bigg) \quad \text{and} \\
\widehat{\mathbf{E}_{\mathbf{v}\,\psi}}^{(2)}\Big|_{wb,\,t1/t2} \;=\; \widehat{\mathbf{E}_{\mathbf{v}}}^{(2)}\Bigg(& \bar{\rho}_{wb,\,t1/t2},\, \bar{\Phi}_{wb,\,t1/t2},\, \bar{T}^*_{wb,\,t1/t2},\, \boldsymbol{\nabla}\bar{\Phi}\Big|_{wb,\,t1/t2},\, \boldsymbol{\nabla}\bar{T}^*\Big|_{wb,\,t1/t2}, \\
& \widehat{\boldsymbol{J}\boldsymbol{\psi}}\Big|_{wb,\,t1/t2}\Bigg),
\end{aligned} \tag{4.72}$$

with

$$\begin{aligned}
\hat{\rho}_{wb,\,t1/t2} &:= (\,\hat{\rho}_{int} + \hat{\rho}_{t1-1/t2-1}\,) \;/\; 2\,, \quad \bar{\rho}_{wb,\,t1/t2} := (\,\bar{\rho}_{int} + \bar{\rho}_{t1-1/t2-1}\,) \;/\; 2\,; \\
\hat{\Phi}_{wb,\,t1/t2} &:= (\,\hat{\Phi}_{int} + \hat{\Phi}_{t1-1/t2-1}\,) \;/\; 2\,, \quad \bar{\Phi}_{wb,\,t1/t2} := (\,\bar{\Phi}_{int} + \bar{\Phi}_{t1-1/t2-1}\,) \;/\; 2\,; \\
\hat{T}_{wb,\,t1/t2} &:= (\,\hat{T}_{int} + \hat{T}_{t1-1/t2-1}\,) \;/\; 2\,, \quad \bar{T}^*_{wb,\,t1/t2} := (\,\bar{T}^*_{int} + \bar{T}^*_{t1-1/t2-1}\,) \;/\; 2
\end{aligned} \tag{4.73}$$

gained pursuant to Eq. (4.9). Similarly, the amplitude and linearized time-invariant-mean control volume of the employed auxiliary cell become

$$\hat{V}_{aux} := (\,\widehat{J}_{int} + \widehat{J}_{t1-1/t2-1}\,) \;/\; 2\,, \quad \bar{V}^*_{aux} := (\,\overline{J}^*_{int} + \overline{J}^*_{t1-1/t2-1}\,) \;/\; 2\,. \tag{4.74}$$

Merely a single interface of the employed auxiliary cell coincides with the wall boundary. It is constituted by the halves of two neighboring cell interfaces. For the wall-boundary-pertinent starting block face, the amplitude and linearized time-invariant-mean surface normal vector are

$$\begin{aligned}
\hat{\mathbf{S}}_{6,aux} &:= -\left(\widehat{\boldsymbol{J}\boldsymbol{\psi}}\Big|_{wb,\,n} + \widehat{\boldsymbol{J}\boldsymbol{\psi}}\Big|_{wb,\,n;\,t1-1/t2-1} \right) \;/\; 2 \quad \text{and} \\
\bar{\mathbf{S}}^*_{6,aux} &:= -\left(\overline{\boldsymbol{J}\boldsymbol{\psi}}^*\Big|_{wb,\,n} + \overline{\boldsymbol{J}\boldsymbol{\psi}}^*\Big|_{wb,\,n;\,t1-1/t2-1} \right) \;/\; 2\,,
\end{aligned} \tag{4.75}$$

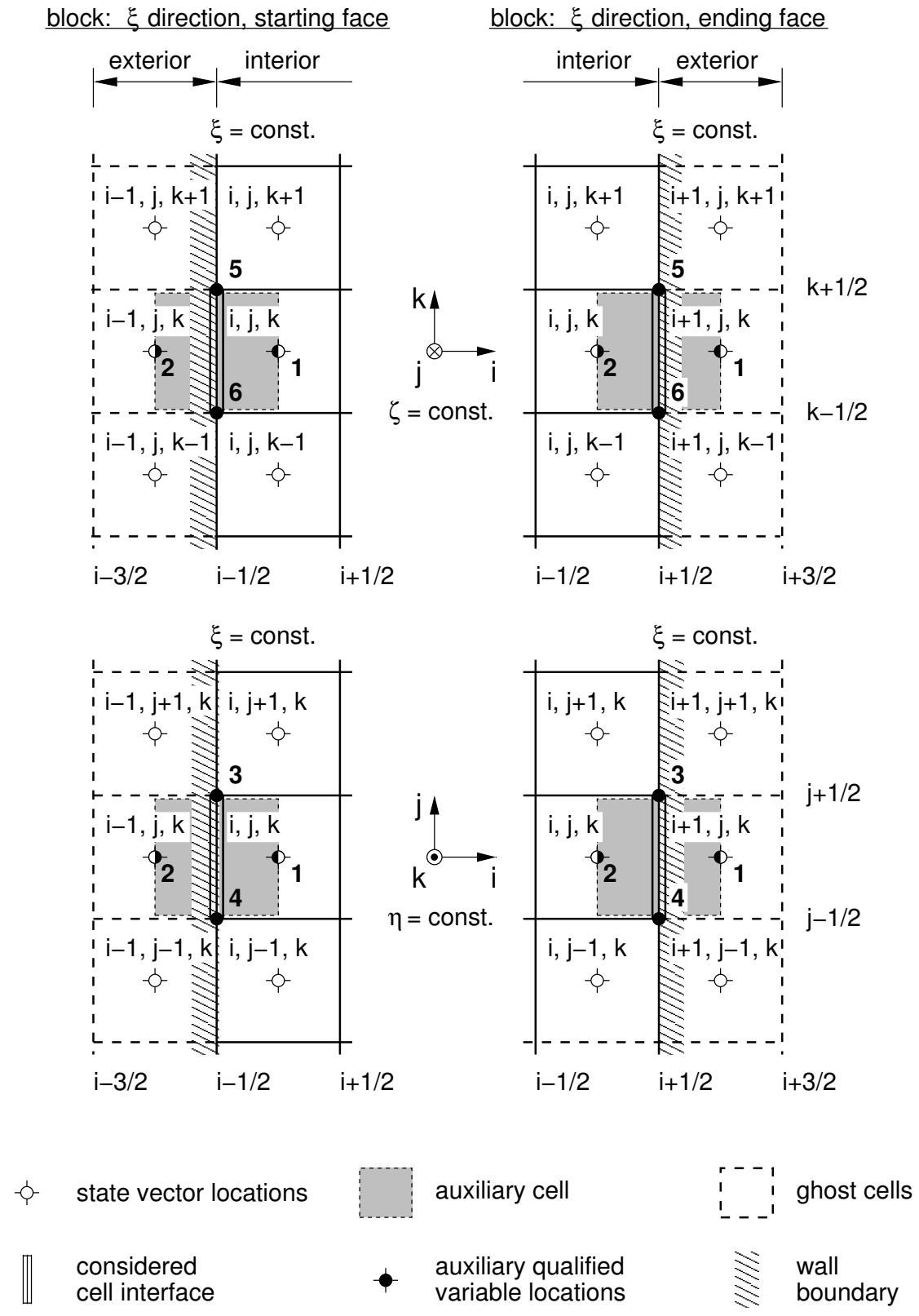

Figure 4.4: Inherent assignment scheme for the cell-interface-respective evaluation of the Cartesian gradient at a ξ-directional block face with wall-boundary segment.

while, for the wall-boundary-pertinent ending block face, being

$$\begin{aligned} \hat{\mathbf{S}}_{5,aux} &:= -\left(\widehat{\boldsymbol{J\psi}}\Big|_{wb,\,n;\,n+1} + \widehat{\boldsymbol{J\psi}}\Big|_{wb,\,n;\,n+1;\,t1-1/t2-1} \right) \;/\; 2 \quad \text{and} \\ \bar{\mathbf{S}}^{*}_{5,aux} &:= -\left(\overline{\boldsymbol{J\psi}}^{*}\Big|_{wb,\,n;\,n+1} + \overline{\boldsymbol{J\psi}}^{*}\Big|_{wb,\,n;\,n+1;\,t1-1/t2-1} \right) \;/\; 2\,. \end{aligned} \tag{4.76}$$

Since $\hat{\mathbf{S}}_{1-4,aux}$ and $\bar{\mathbf{S}}^{*}_{1-4,aux}$ are all strictly gained from arithmetically averaging interior cell-interfaces, the assignment is not explicitly shown. The directional instances of the amplitude/time-invariant-mean auxiliary qualified variables undergo an assignment independent of either the wall-boundary-pertinent starting or ending block face; i.e.,

$$\begin{aligned} \hat{\Phi}_{1,aux} &:= \hat{\Phi}_{int}\,, \qquad \hat{\Phi}_{2,aux} := \hat{\Phi}_{int;\,t1-1/t2-1} \quad \text{and} \\ \bar{\Phi}_{1,aux} &:= \bar{\Phi}_{int}\,, \qquad \bar{\Phi}_{2,aux} := \bar{\Phi}_{int;\,t1-1/t2-1}\,. \end{aligned} \tag{4.77}$$

Only a single off-directional instance of the amplitude/time-invariant-mean auxiliary qualified variables coincides with the wall boundary at either the wall-boundary-pertinent starting or ending block face. It solely accounts for the set $\hat{\mathbf{q}}_{ext}$ and $\bar{\mathbf{q}}^{*}_{ext}$. For the wall-boundary-pertinent starting block face, the assignments are

$$\begin{aligned} \hat{\Phi}_{6,aux} &:= (\,\hat{\Phi}_{int} + \hat{\Phi}_{ext} + \hat{\Phi}_{int;\,t1-1/t2-1} + \hat{\Phi}_{ext;\,t1-1/t2-1}) \;/\; 4 \quad \text{and} \\ \bar{\Phi}_{6,aux} &:= (\,\bar{\Phi}_{int} + \bar{\Phi}_{ext} + \bar{\Phi}_{int;\,t1-1/t2-1} + \bar{\Phi}_{ext;\,t1-1/t2-1}) \;/\; 4\,, \end{aligned} \tag{4.78}$$

while, for the pertinent ending block face, the assignments are

$$\begin{aligned} \hat{\Phi}_{5,aux} &:= (\,\hat{\Phi}_{int} + \hat{\Phi}_{ext} + \hat{\Phi}_{int;\,t1-1/t2-1} + \hat{\Phi}_{ext;\,t1-1/t2-1}) \;/\; 4 \quad \text{and} \\ \bar{\Phi}_{5,aux} &:= (\,\bar{\Phi}_{int} + \bar{\Phi}_{ext} + \bar{\Phi}_{int;\,t1-1/t2-1} + \bar{\Phi}_{ext;\,t1-1/t2-1}) \;/\; 4\,. \end{aligned} \tag{4.79}$$

Naturally, the instances of the amplitude and linearized time-invariant-mean auxiliary static temperatures are gained by substituting $\hat{\Phi}$ with $\hat{T}$ and $\bar{\Phi}$ with $\bar{T}^{*}$ in Eqs. (4.77–4.79). Since $\hat{\Phi}_{3/4,aux}$ and $\bar{\Phi}_{3/4,aux}$, as well as $\hat{T}_{3/4,aux}$ and $\bar{T}^{*}_{3/4,aux}$, are all strictly gained from arithmetically averaging interior-centroid instances, the assignment is not explicitly shown. For the wall-boundary-pertinent starting block face, the same applies to $\hat{\Phi}_{5,aux}$ and $\bar{\Phi}_{5,aux}$, as well as $\hat{T}_{5,aux}$ and $\bar{T}^{*}_{5,aux}$, while, for the wall-boundary-pertinent ending block face, applying to $\hat{\Phi}_{6,aux}$ and $\bar{\Phi}_{6,aux}$, as well as $\hat{T}_{6,aux}$ and $\bar{T}^{*}_{6,aux}$. The manner in which this generalized accounting becomes specific to the wall-boundary-pertinent block face is again illustrated for $\psi_{wb,\,n} := \xi$, and thus, $\psi_{wb,\,t1} := \eta$, $\psi_{wb,\,t2} := \zeta$, as well as $n \pm 1 := i \pm 1$, $t1 \pm 1 := j \pm 1$, and $t2 \pm 1 := k \pm 1$, in Figure 4.5.

Similar to the amplitude viscous flux vector evaluation, the set $\hat{\mathbf{q}}_{ext}$ and $\bar{\mathbf{q}}^{*}_{ext}$ are indirectly accounted for in the evaluation of $\widehat{\mathbf{T}}^{(1)}_{i,\,j,\,k}$ and $\widehat{\mathbf{T}}^{(2)}_{i,\,j,\,k}$, Eq. (4.10), during the pertinent nondirectional sweeps. Since the employed auxiliary cell always coincides with the

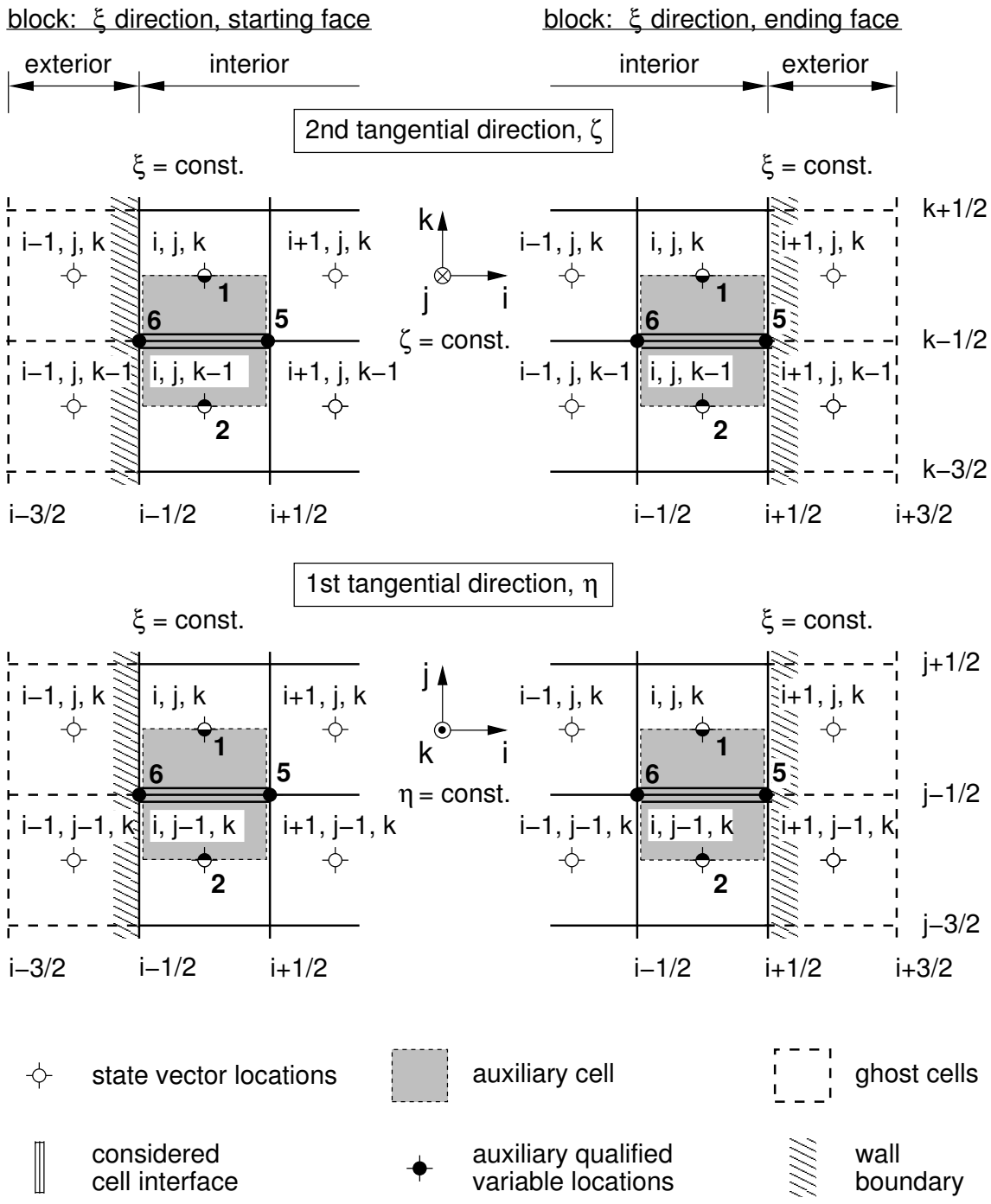

Figure 4.5: Inherent assignment scheme for the tangential cell-interface-respective evaluation of the Cartesian gradient at a ξ-directional block face with wall-boundary segment.

considered computational cell on the basis of Figure 4.3, an interface of the auxiliary cell is always constituted by the particular wall-boundary cell-interface. Correspondingly, only a single instance of the amplitude/time-invariant-mean auxiliary qualified variables again coincides with the wall boundary for a block face. Its assignment then simply occurs through the arithmetical average of the interior and pertinent exterior cell's state vector instances; i.e., in compliance with Eq. (4.28). As this circumstance is deemed straightforward, an additional illustration is forgone.

4.5 Implicit Pseudotime Integration

On the basis of Blazek [14], as well as Kreiselmaier [70], the implicit pseudotime integration of the small disturbance Navier-Stokes equations is set up by approximating the temporal derivative of the amplitude state vector in Eq. (4.1) with a first-order forward difference respective a current pseudotime level ν and an arbitrary pseudotime step $\Delta\tau^{\circ}$:

$$\overline{J}^{*}\,\frac{\Delta\hat{\mathbf{q}}}{\Delta\tau^{\circ}} = -\widehat{\mathbf{R}}^{\nu+1}\,, \qquad \text{wherein} \qquad \Delta\hat{\mathbf{q}} := \hat{\mathbf{q}}^{\nu+1} - \hat{\mathbf{q}}^{\nu}\,, \tag{4.80}$$

being the amplitude state vector's correction between ν and the subsequent pseudotime level $\nu+1$. Since $\hat{\mathbf{q}}^{\nu}$ is considered to be known, all entities rendered by it become equally known. Hence, the amplitude residual vector at $\nu+1$ can be straightforwardly expressed through the first-order Taylor-series expansions of its constituting $\hat{\mathbf{q}}$-homogenous vectors, $\widehat{\mathbf{E}_{\psi}}^{(1)}$, $\widehat{\mathbf{E}_{\mathbf{v}\,\psi}}^{(1)}$, and $\widehat{\mathbf{S}}^{(1)}$, about ν. Ultimately,

$$\widehat{\mathbf{R}}^{\nu+1} = \widehat{\mathbf{R}}^{\nu} + \left.\frac{\partial\widehat{\mathbf{R}}}{\partial\hat{\mathbf{q}}}\right|^{\nu}\Delta\hat{\mathbf{q}}\,, \qquad \text{with} \qquad \widehat{\mathbf{R}}^{\nu} = \widehat{\mathbf{R}}(\hat{\mathbf{q}}^{\nu}) \tag{4.81}$$

and

$$\begin{aligned}
\left.\frac{\partial\widehat{\mathbf{R}}}{\partial\hat{\mathbf{q}}}\right|^{\nu}\Delta\hat{\mathbf{q}} \;:=\; & \frac{\partial}{\partial\xi}\left[\left(\left.\frac{\partial\widehat{\mathbf{F}}^{(1)}}{\partial\hat{\mathbf{q}}}\right|^{\nu} - \left.\frac{\partial\widehat{\mathbf{F}_{\mathbf{v}}}^{(1)}}{\partial\hat{\mathbf{q}}}\right|^{\nu}\right)\Delta\hat{\mathbf{q}}\right] \\
+ \; & \frac{\partial}{\partial\eta}\left[\left(\left.\frac{\partial\widehat{\mathbf{G}}^{(1)}}{\partial\hat{\mathbf{q}}}\right|^{\nu} - \left.\frac{\partial\widehat{\mathbf{G}_{\mathbf{v}}}^{(1)}}{\partial\hat{\mathbf{q}}}\right|^{\nu}\right)\Delta\hat{\mathbf{q}}\right] \\
+ \; & \frac{\partial}{\partial\zeta}\left[\left(\left.\frac{\partial\widehat{\mathbf{H}}^{(1)}}{\partial\hat{\mathbf{q}}}\right|^{\nu} - \left.\frac{\partial\widehat{\mathbf{H}_{\mathbf{v}}}^{(1)}}{\partial\hat{\mathbf{q}}}\right|^{\nu}\right)\Delta\hat{\mathbf{q}}\right] \;-\; \left.\frac{\partial\widehat{\mathbf{S}}^{(1)}}{\partial\hat{\mathbf{q}}}\right|^{\nu}\Delta\hat{\mathbf{q}}\,,
\end{aligned} \tag{4.82}$$

is obtained under utilization of Eq. (4.2). Because $\widehat{\mathbf{R}}$ is merely constituted by entities that are either linear in $\hat{\mathbf{q}}$ or invariant to its temporal change (as composited by $\widehat{\mathbf{S}}^{(2)}$), Eq. (4.81)

a priori has no truncation error. Inserting it into Eq. (4.80), elementary manipulation subsequently isolates $\widehat{\mathbf{R}}^{\nu}$ on the RHS:

$$\frac{\overline{J}^{*}}{\Delta\tau^{\circ}}\Delta\hat{\mathbf{q}} + \left.\frac{\partial\widehat{\mathbf{R}}}{\partial\hat{\mathbf{q}}}\right|^{\nu}\Delta\hat{\mathbf{q}} = -\widehat{\mathbf{R}}^{\nu}\,. \tag{4.83}$$

In order to formulate Eq. (4.83) for the entire computational domain, $\forall\,(i,\,j,\,k)$, the curvilinear spatial-derivatives intrinsic to both $\partial\widehat{\mathbf{R}}/\partial\hat{\mathbf{q}}\,|^{\nu}$ and $\widehat{\mathbf{R}}^{\nu}$ are substituted with the directional first-order central difference operators given in Eq. (4.3). This compactly yields

$$\left[\left(\frac{\overline{J}^{*}}{\Delta\tau^{\circ}}\,\mathbf{I} + \left.\frac{\partial\widehat{\mathbf{R}}}{\partial\widehat{\mathbf{q}}}\right|^{\nu}\right)\Delta\hat{\mathbf{q}}\right]_{\forall\,(i,\,j,\,k)} = -\widehat{\mathbf{R}}^{\nu}_{\forall\,(i,\,j,\,k)}\,, \tag{4.84}$$

rendering a system of linear equations for centroidal instances of $\Delta\hat{\mathbf{q}}$ [14, 70]. Since the Jacobian matrix of any $\hat{\mathbf{q}}$-homogenous flux vector and of the $\hat{\mathbf{q}}$-homogenous source term vector, respectively, the directional instances of $\partial\widehat{\mathbf{E}_{\psi}}^{(1)}/\partial\hat{\mathbf{q}}$ or $\partial\widehat{\mathbf{E}_{\mathbf{v}\,\psi}}^{(1)}/\partial\hat{\mathbf{q}}$ and $\partial\widehat{\mathbf{S}}^{(1)}/\partial\hat{\mathbf{q}}$, are invariant with respect to pseudotime, the spatially discrete coefficients adhering the centroidal instances of $\Delta\hat{\mathbf{q}}$ are invariant as well. Consequently, the $|^{\nu}$ denotation of $\partial\widehat{\mathbf{R}}/\partial\hat{\mathbf{q}}$ within the $\Delta\hat{\mathbf{q}}$-applied implicit matrix-operator has become inapplicable. Following Blazek [14], Eq. (4.84) is designated the unfactored implicit scheme. Its derivation had been corroborated by Iatrou [54] in principle. On the basis of Yoon and Jameson [145], Yoon and Kwak [147], as well as of Blazek [14], a straightforward solution of Eq. (4.84) by Gaussian elimination, however, is prohibitive for the typical three-dimensional case. Essentially, a large complex block-banded matrix would need to be inverted, entailing high operation count and excessive memory requirements [145, 147, 14]. Applying the LU-SSOR scheme [145, 14], on the other hand, allows for an iterative solution of significantly higher efficiency. It relies on the approximate decomposition of the implicit matrix-operator into a diagonally dominant lower- and upper-triangular-matrix factor to ensure convergence [145, 14].

4.5.1 Formulation of the Factored Implicit Scheme

Considering the unfactored implicit scheme, it is permissible to employ differing spatial evaluations on the LHS and RHS according to Blazek [14], because the physical accuracy of an eventually obtained pseudosteady-state solution is merely governed by the RHS. Consequently, scheme-inherent damping can be beneficially manipulated through the design of the implicit matrix-operator without compromise [14]. Likewise, it becomes justifiable to retain only the convective portion of the implicit matrix-operator even for viscous treatments, as suggested by Rieger and Jameson [110]. In particular, the directional instances of $\partial\widehat{\mathbf{E}_{\mathbf{v}\,\psi}}^{(1)}/\partial\hat{\mathbf{q}}$ are discounted within Eq. (4.82), as well as $\widehat{\mathbf{T}}^{(1)}$ within

$\widehat{\mathbf{S}}^{(1)}$, substantially simplifying the LHS of Eq. (4.84). On the basis of Blazek [14], as well as of Kreiselmaier [70], the implicit matrix-operator is initially conditioned for diagonal dominance. For an arbitrary computational cell (i, j, k), the spatially discretizing nature of the implicit matrix-operator allows the LHS to be expanded to

$$\begin{aligned}\left[\left(\frac{\overline{J}^{*}}{\Delta\tau^{\circ}}\mathbf{I}+\frac{\partial\widehat{\mathbf{R}}}{\partial\hat{\mathbf{q}}}\right)\Delta\hat{\mathbf{q}}\right]_{i,j,k} &\approx \frac{\overline{J}^{*}_{i,j,k}}{\Delta\tau^{\circ}}\;\Delta\hat{\mathbf{q}}_{i,j,k}\\ &+\left(\overline{\mathbf{K}_{\xi}}^{*}\Delta\hat{\mathbf{q}}\right)_{i+1/2,j,k}-\left(\overline{\mathbf{K}_{\xi}}^{*}\Delta\hat{\mathbf{q}}\right)_{i-1/2,j,k}\\ &+\left(\overline{\mathbf{K}_{\eta}}^{*}\Delta\hat{\mathbf{q}}\right)_{i,j+1/2,k}-\left(\overline{\mathbf{K}_{\eta}}^{*}\Delta\hat{\mathbf{q}}\right)_{i,j-1/2,k}\\ &+\left(\overline{\mathbf{K}_{\zeta}}^{*}\Delta\hat{\mathbf{q}}\right)_{i,j,k+1/2}-\left(\overline{\mathbf{K}_{\zeta}}^{*}\Delta\hat{\mathbf{q}}\right)_{i,j,k-1/2}\\ &+\;i\,k\,\overline{J}^{*}_{i,j,k}\,\Delta\hat{\mathbf{q}}_{i,j,k}\,,\end{aligned}\tag{4.85}$$

wherein the directional instances of $\overline{\mathbf{K}_{\psi}}^{*}\Delta\hat{\mathbf{q}}=\partial\widehat{\mathbf{E}_{\psi}}^{(1)}/\partial\hat{\mathbf{q}}\;\Delta\hat{\mathbf{q}}$ embody the respective $\hat{\mathbf{q}}$-homogenous convective flux vector's correction between ν and $\nu+1$. It has also been recognized that $\partial\widehat{\mathbf{S}}^{(1)}/\partial\hat{\mathbf{q}}\,|^{\nu}$ reduces to the merely imaginary scalar $i\,k\,\overline{J}^{*}$. The interface-respective evaluation of $\overline{\mathbf{K}_{\xi}}^{*}\Delta\hat{\mathbf{q}}$, $\overline{\mathbf{K}_{\eta}}^{*}\Delta\hat{\mathbf{q}}$, and $\overline{\mathbf{K}_{\zeta}}^{*}\Delta\hat{\mathbf{q}}$ is then approximated by first-order upwind extrapolation from the directionally preceding and succeeding centroid:

$$\begin{aligned}\left(\overline{\mathbf{K}_{\xi}}^{*}\Delta\hat{\mathbf{q}}\right)_{i+1/2,j,k} &\approx \left(\overline{\mathbf{K}_{\xi}}^{*+}\Delta\hat{\mathbf{q}}\right)_{i,j,k}+\left(\overline{\mathbf{K}_{\xi}}^{*-}\Delta\hat{\mathbf{q}}\right)_{i+1,j,k}\,,\\ \left(\overline{\mathbf{K}_{\xi}}^{*}\Delta\hat{\mathbf{q}}\right)_{i-1/2,j\,k} &\approx \left(\overline{\mathbf{K}_{\xi}}^{*+}\Delta\hat{\mathbf{q}}\right)_{i-1,j,k}+\left(\overline{\mathbf{K}_{\xi}}^{*-}\Delta\hat{\mathbf{q}}\right)_{i,j,k}\,;\\ \left(\overline{\mathbf{K}_{\eta}}^{*}\Delta\hat{\mathbf{q}}\right)_{i,j+1/2,k} &\approx \left(\overline{\mathbf{K}_{\eta}}^{*+}\Delta\hat{\mathbf{q}}\right)_{i,j,k}+\left(\overline{\mathbf{K}_{\eta}}^{*-}\Delta\hat{\mathbf{q}}\right)_{i,j+1,k}\,,\\ \left(\overline{\mathbf{K}_{\eta}}^{*}\Delta\hat{\mathbf{q}}\right)_{i,j-1/2,k} &\approx \left(\overline{\mathbf{K}_{\eta}}^{*+}\Delta\hat{\mathbf{q}}\right)_{i,j-1,k}+\left(\overline{\mathbf{K}_{\eta}}^{*-}\Delta\hat{\mathbf{q}}\right)_{i,j,k}\,;\\ \left(\overline{\mathbf{K}_{\zeta}}^{*}\Delta\hat{\mathbf{q}}\right)_{i,j,k+1/2} &\approx \left(\overline{\mathbf{K}_{\zeta}}^{*+}\Delta\hat{\mathbf{q}}\right)_{i,j,k}+\left(\overline{\mathbf{K}_{\zeta}}^{*-}\Delta\hat{\mathbf{q}}\right)_{i,j,k+1}\,,\\ \left(\overline{\mathbf{K}_{\zeta}}^{*}\Delta\hat{\mathbf{q}}\right)_{i,j,k-1/2} &\approx \left(\overline{\mathbf{K}_{\zeta}}^{*+}\Delta\hat{\mathbf{q}}\right)_{i,j,k-1}+\left(\overline{\mathbf{K}_{\zeta}}^{*-}\Delta\hat{\mathbf{q}}\right)_{i,j,k}\,.\end{aligned}\tag{4.86}$$

In this regard, $\overline{\mathbf{K}_{\xi}}^{*}$, $\overline{\mathbf{K}_{\eta}}^{*}$, and $\overline{\mathbf{K}_{\zeta}}^{*}$ have each been separated along the line of their inherent eigenvalues' particular algebraic sign, an accessory $+$ or $-$ superscript distinguishing a split Jacobian matrix, respectively, of either all nonnegative eigenvalues or of all nonpositive eigenvalues. Putting Eq. (4.86) into effect, the assigned centroidal evaluations of $\overline{\mathbf{K}_{\xi}}^{*\pm}$, $\overline{\mathbf{K}_{\eta}}^{*\pm}$, and $\overline{\mathbf{K}_{\zeta}}^{*\pm}$ become intrinsically hybrid. The constituting time-invariant-mean primitive variables draw on the linearized time-invariant-mean state vector of the denoted centroidal index, whereas the constituting linearized time-invariant-mean spatial metrics

are appropriated from the actually considered interface. Exemplifying this circumstance, the upwind extrapolation toward the ξ-directional forward interface requires

$$\begin{aligned} \overline{\mathbf{K}_{\xi}}^{*+}_{i,\,j,\,k} &= \overline{\mathbf{K}_{\xi}}^{*+}\left(\bar{\mathbf{q}}^{*}_{i,\,j,\,k},\, \overline{\boldsymbol{J\xi}}^{*}_{i+1/2,\,j,\,k}\right) \qquad \text{and} \\ \overline{\mathbf{K}_{\xi}}^{*-}_{i+1,\,j,\,k} &= \overline{\mathbf{K}_{\xi}}^{*-}\left(\bar{\mathbf{q}}^{*}_{i+1,\,j,\,k},\, \overline{\boldsymbol{J\xi}}^{*}_{i+1/2,\,j,\,k}\right) , \end{aligned} \tag{4.87}$$

with its backward-interface counterpart being

$$\begin{aligned} \overline{\mathbf{K}_{\xi}}^{*+}_{i-1,\,j,\,k} &= \overline{\mathbf{K}_{\xi}}^{*+}\left(\bar{\mathbf{q}}^{*}_{i-1,\,j,\,k},\, \overline{\boldsymbol{J\xi}}^{*}_{i-1/2,\,j,\,k}\right) \qquad \text{and} \\ \overline{\mathbf{K}_{\xi}}^{*-}_{i,\,j,\,k} &= \overline{\mathbf{K}_{\xi}}^{*-}\left(\bar{\mathbf{q}}^{*}_{i,\,j,\,k},\, \overline{\boldsymbol{J\xi}}^{*}_{i-1/2,\,j,\,k}\right) . \end{aligned} \tag{4.88}$$

Evidently, a commonality exists for the two split Jacobian matrices attributed to the considered cell's centroid; i.e., even though $\overline{\mathbf{K}_{\xi}}^{*+}_{i,\,j,\,k}$ and $\overline{\mathbf{K}_{\xi}}^{*-}_{i,\,j,\,k}$ differ in the appropriated linearized time-invariant-mean spatial metrics, they share the linearized time-invariant-mean state vector. The upwind extrapolation requirements for the remaining split Jacobian matrices can be established in analogy to Eq. (4.87) and Eq. (4.88) [14, 70]. All twelve directional instances are shown in Figure 4.6.

Further following Blazek [14], as well as Kreiselmaier [70], the conditioned implicit matrix-operator can then be formally expressed as the sum of three distinct matrix-operators,

$$\begin{aligned} \left[\left(\frac{\overline{J}^{*}}{\Delta\tau^{\circ}}\mathbf{I} + \frac{\partial\widehat{\mathbf{R}}}{\partial\hat{\mathbf{q}}}\right)\Delta\hat{\mathbf{q}}\right]_{i,\,j,\,k} &\approx \left[\left(\overline{\mathbf{L}}^{*} + \overline{\mathbf{D}}^{*} + \overline{\mathbf{U}}^{*}\right)\Delta\hat{\mathbf{q}}\right]_{i,\,j,\,k} \\ &= \left(\overline{\mathbf{L}}^{*}\Delta\hat{\mathbf{q}}\right)_{i,\,j,\,k} + \left(\overline{\mathbf{D}}^{*}\Delta\hat{\mathbf{q}}\right)_{i,\,j,\,k} + \left(\overline{\mathbf{U}}^{*}\Delta\hat{\mathbf{q}}\right)_{i,\,j,\,k} , \end{aligned} \tag{4.89}$$

with each being responsible for a unique part of the spatially discrete evaluation:

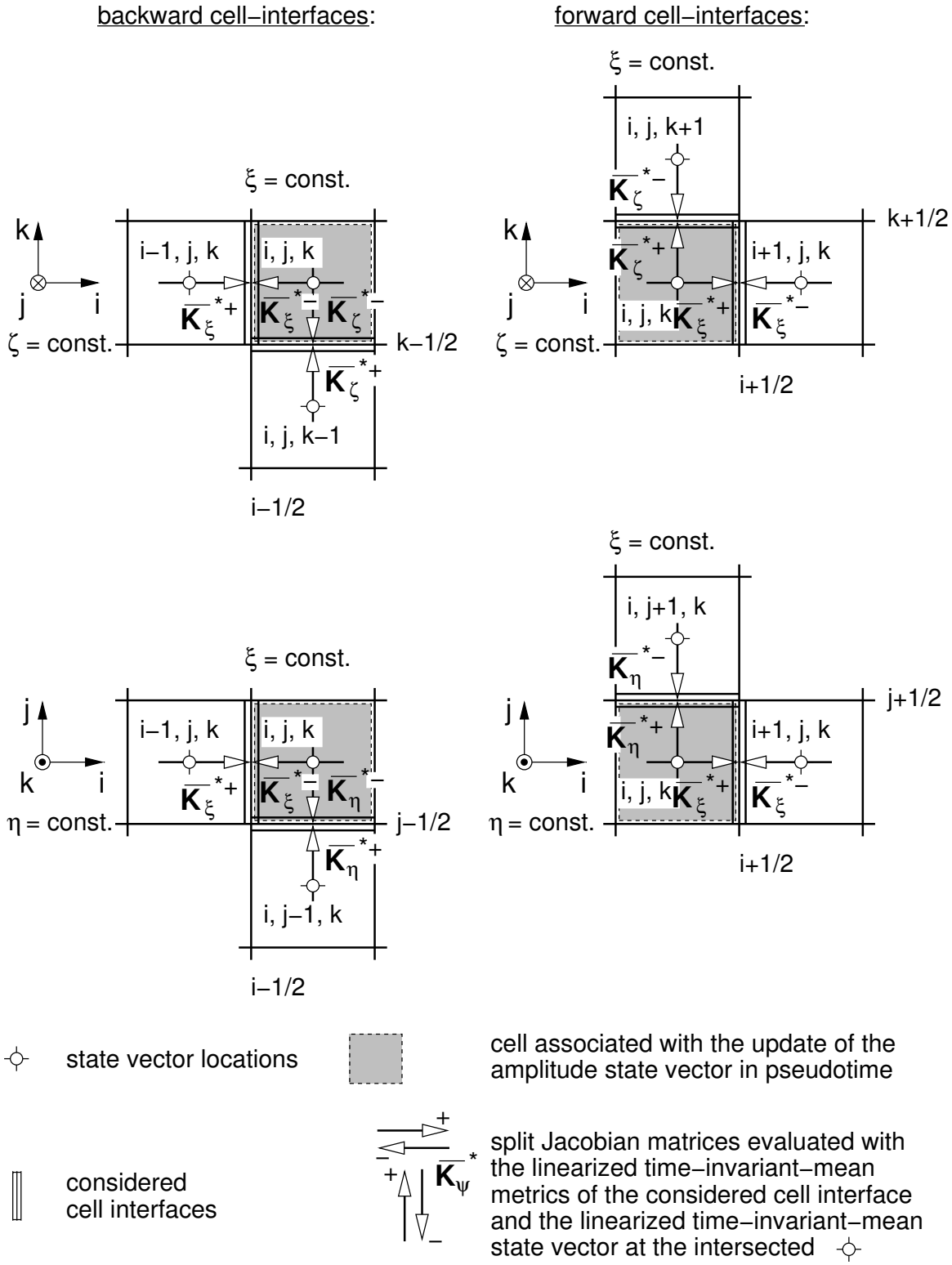

Figure 4.6: Requirement stencil for the split Jacobian matrices employed in the first-order upwind extrapolation of the $\hat{\mathbf{q}}$-homogenous convective flux vector's pseudotime correction; based on [70], *Abb. 3.4.*

$$
\begin{aligned}
\left(\overline{\mathbf{L}}^{*}\Delta\hat{\mathbf{q}}\right)_{i,j,k} &:= -\left[\left(\overline{\mathbf{K}_{\xi}}^{*+}\Delta\hat{\mathbf{q}}\right)_{i-1,j,k} + \left(\overline{\mathbf{K}_{\eta}}^{*+}\Delta\hat{\mathbf{q}}\right)_{i,j-1,k} + \left(\overline{\mathbf{K}_{\zeta}}^{*+}\Delta\hat{\mathbf{q}}\right)_{i,j,k-1}\right], \\
\left(\overline{\mathbf{U}}^{*}\Delta\hat{\mathbf{q}}\right)_{i,j,k} &:= \left(\overline{\mathbf{K}_{\xi}}^{*-}\Delta\hat{\mathbf{q}}\right)_{i+1,j,k} + \left(\overline{\mathbf{K}_{\eta}}^{*-}\Delta\hat{\mathbf{q}}\right)_{i,j+1,k} + \left(\overline{\mathbf{K}_{\zeta}}^{*-}\Delta\hat{\mathbf{q}}\right)_{i,j,k+1}, \\
\left(\overline{\mathbf{D}}^{*}\Delta\hat{\mathbf{q}}\right)_{i,j,k} &:= \frac{\overline{J}^{*}_{i,j,k}}{\Delta\tau^{\circ}}\,\Delta\hat{\mathbf{q}}_{i,j,k} \\
&+ \left(\overline{\mathbf{K}_{\xi}}^{*+}\Delta\hat{\mathbf{q}}\right)_{i,j,k} + \left(\overline{\mathbf{K}_{\eta}}^{*+}\Delta\hat{\mathbf{q}}\right)_{i,j,k} + \left(\overline{\mathbf{K}_{\zeta}}^{*+}\Delta\hat{\mathbf{q}}\right)_{i,j,k} \\
&- \left[\left(\overline{\mathbf{K}_{\xi}}^{*-}\Delta\hat{\mathbf{q}}\right)_{i,j,k} + \left(\overline{\mathbf{K}_{\eta}}^{*-}\Delta\hat{\mathbf{q}}\right)_{i,j,k} + \left(\overline{\mathbf{K}_{\zeta}}^{*-}\Delta\hat{\mathbf{q}}\right)_{i,j,k}\right] \\
&+ i\,k\,\overline{J}^{*}_{i,j,k}\,\Delta\hat{\mathbf{q}}_{i,j,k}\,.
\end{aligned}
\tag{4.90}
$$

In terms of the entire computational domain, $\overline{\mathbf{L}}^{*}$ and $\overline{\mathbf{U}}^{*}$, respectively, comprise the strictly lower- and upper-triangular elements of the conditioned implicit matrix-operator, while $\overline{\mathbf{D}}^{*}$ comprises the elements of its principal diagonal [14, 70]. It can be observed that

$$
\overline{\mathbf{L}}^{*},\ \overline{\mathbf{U}}^{*} \in \mathbb{R}, \qquad \text{however,} \qquad \overline{\mathbf{D}}^{*} \in \mathbb{C}\,, \tag{4.91}
$$

solely due to the coefficient $i\,k\,\overline{J}^{*}$, perforce coupling the real and imaginary part of $\Delta\hat{\mathbf{q}}$. In this regard, the use of $\overline{(\ )}^{*}$ in conjunction with $\mathbf{D}$ represents only a compromise, which is nevertheless appropriate, since all elements of the principal diagonal are composited through linearized time-invariant-mean quantities.

Both Blazek [14] and Kreiselmaier [70] had approximated the split Jacobian matrix of either all nonnegative or all nonpositive eigenvalues in a very computationally efficient manner, respectively, by just adding or subtracting the scaled spectral radius of the actual Jacobian matrix to or from its principal diagonal, as suggested by Jameson and Turkel [62]. Reformulated in terms of the amplitude convective flux vector's correction, the computationally expensive evaluation of the actual Jacobian matrix had been sidestepped likewise [14, 70]. On this basis,

$$
\begin{aligned}
\overline{\mathbf{K}_{\psi}}^{*\pm}\Delta\hat{\mathbf{q}} &\approx \left(\overline{\mathbf{K}_{\psi}}^{*}\Delta\hat{\mathbf{q}} \pm r^{\overline{\mathbf{K}_{\psi}}^{*}}\mathbf{I}\,\Delta\hat{\mathbf{q}}\right) \ / \ 2 \\
&= \left(\Delta\widehat{\mathbf{E}}^{(1)}_{\psi} \pm r^{\overline{\mathbf{K}_{\psi}}^{*}}\Delta\hat{\mathbf{q}}\right) \ / \ 2\,,
\end{aligned}
\tag{4.92}
$$

with

$$\begin{aligned} r^{\overline{\mathbf{K}_\psi}^*} &= \omega_d \left(|\overline{\theta_\psi}^*| + \bar{a}^* \, |\, \overline{\boldsymbol{J}\boldsymbol{\psi}}^* | \right) \qquad \text{and} \\ \Delta\widehat{\mathbf{E}_\psi}^{(1)} &:= \widehat{\mathbf{E}_\psi}^{(1)\,\nu+1} - \widehat{\mathbf{E}_\psi}^{(1)\,\nu} . \end{aligned} \tag{4.93}$$

Ultimately, the scaling parameter $\omega_d \geq 1$ allows user-control over the inherent numerical dissipation [14, 70]. An increase of ω_d will enhance stability, yet may also adversely affect the rate of convergence toward the desired pseudosteady state if it is set too high [14, 70]. Applying Eq. (4.92) in its directional instances to Eq. (4.90), the spatially discrete evaluations rendered by the strictly lower- and upper-triangular matrix-operators, respectively, evolve into

$$\begin{aligned} \left(\overline{\mathbf{L}}^* \Delta\hat{\mathbf{q}}\right)_{i,\,j,\,k} \approx \; - \; \Big[\quad & \Delta\widehat{\mathbf{F}}^{(1)}\Big(\Delta\hat{\mathbf{q}}_{i-1,\,j,\,k},\, \bar{\mathbf{q}}^*_{i-1,\,j,\,k},\, \overline{\boldsymbol{J}\boldsymbol{\xi}}^*_{i-1/2,\,j,\,k}\Big) \\ + \quad & \Delta\widehat{\mathbf{G}}^{(1)}\Big(\Delta\hat{\mathbf{q}}_{i,\,j-1,\,k},\, \bar{\mathbf{q}}^*_{i,\,j-1,\,k},\, \overline{\boldsymbol{J}\boldsymbol{\eta}}^*_{i,\,j-1/2,\,k}\Big) \\ + \quad & \Delta\widehat{\mathbf{H}}^{(1)}\Big(\Delta\hat{\mathbf{q}}_{i,\,j,\,k-1},\, \bar{\mathbf{q}}^*_{i,\,j,\,k-1},\, \overline{\boldsymbol{J}\boldsymbol{\zeta}}^*_{i,\,j,\,k-1/2}\Big) \\ + \quad & r^{\overline{\mathbf{K}_\xi}^*}\Big(\bar{\mathbf{q}}^*_{i-1,\,j,\,k},\, \overline{\boldsymbol{J}\boldsymbol{\xi}}^*_{i-1/2,\,j,\,k}\Big)\, \Delta\hat{\mathbf{q}}_{i-1,\,j,\,k} \\ + \quad & r^{\overline{\mathbf{K}_\eta}^*}\Big(\bar{\mathbf{q}}^*_{i,\,j-1,\,k},\, \overline{\boldsymbol{J}\boldsymbol{\eta}}^*_{i,\,j-1/2,\,k}\Big)\, \Delta\hat{\mathbf{q}}_{i,\,j-1,\,k} \\ + \quad & r^{\overline{\mathbf{K}_\zeta}^*}\Big(\bar{\mathbf{q}}^*_{i,\,j,\,k-1},\, \overline{\boldsymbol{J}\boldsymbol{\zeta}}^*_{i,\,j,\,k-1/2}\Big)\, \Delta\hat{\mathbf{q}}_{i,\,j,\,k-1} \quad \Big] \; / \; 2 \end{aligned} \tag{4.94}$$

and

$$\begin{aligned} \left(\overline{\mathbf{U}}^* \Delta\hat{\mathbf{q}}\right)_{i,\,j,\,k} \approx \quad & \Big[\quad \Delta\widehat{\mathbf{F}}^{(1)}\Big(\Delta\hat{\mathbf{q}}_{i+1,\,j,\,k},\, \bar{\mathbf{q}}^*_{i+1,\,j,\,k},\, \overline{\boldsymbol{J}\boldsymbol{\xi}}^*_{i+1/2,\,j,\,k}\Big) \\ + \quad & \Delta\widehat{\mathbf{G}}^{(1)}\Big(\Delta\hat{\mathbf{q}}_{i,\,j+1,\,k},\, \bar{\mathbf{q}}^*_{i,\,j+1,\,k},\, \overline{\boldsymbol{J}\boldsymbol{\eta}}^*_{i,\,j+1/2,\,k}\Big) \\ + \quad & \Delta\widehat{\mathbf{H}}^{(1)}\Big(\Delta\hat{\mathbf{q}}_{i,\,j,\,k+1},\, \bar{\mathbf{q}}^*_{i,\,j,\,k+1},\, \overline{\boldsymbol{J}\boldsymbol{\zeta}}^*_{i,\,j,\,k+1/2}\Big) \\ - \quad & r^{\overline{\mathbf{K}_\xi}^*}\Big(\bar{\mathbf{q}}^*_{i+1,\,j,\,k},\, \overline{\boldsymbol{J}\boldsymbol{\xi}}^*_{i+1/2,\,j,\,k}\Big)\, \Delta\hat{\mathbf{q}}_{i+1,\,j,\,k} \\ - \quad & r^{\overline{\mathbf{K}_\eta}^*}\Big(\bar{\mathbf{q}}^*_{i,\,j+1,\,k},\, \overline{\boldsymbol{J}\boldsymbol{\eta}}^*_{i,\,j+1/2,\,k}\Big)\, \Delta\hat{\mathbf{q}}_{i,\,j+1,\,k} \\ - \quad & r^{\overline{\mathbf{K}_\zeta}^*}\Big(\bar{\mathbf{q}}^*_{i,\,j,\,k+1},\, \overline{\boldsymbol{J}\boldsymbol{\zeta}}^*_{i,\,j,\,k+1/2}\Big)\, \Delta\hat{\mathbf{q}}_{i,\,j,\,k+1} \quad \Big] \; / \; 2 \, . \end{aligned} \tag{4.95}$$

The principal-diagonal matrix-operator becomes

$$\begin{aligned}
\Big(\overline{\mathbf{D}}^{*}\Delta\hat{\mathbf{q}}\Big)_{i,\,j,\,k} \approx\; & \frac{\overline{J}^{*}{}_{i,\,j,\,k}}{\Delta\tau^{\circ}}\,\Delta\hat{\mathbf{q}}_{i,\,j,\,k} \\
& + \Big\{\Delta\widehat{\mathbf{F}}^{(1)}\Big(\Delta\hat{\mathbf{q}}_{i,\,j,\,k},\,\bar{\mathbf{q}}^{*}_{i,\,j,\,k},\,\overline{\boldsymbol{J\xi}}^{*}_{i-1/2,\,j,\,k}\Big) - \Delta\widehat{\mathbf{F}}^{(1)}\Big(\Delta\hat{\mathbf{q}}_{i,\,j,\,k},\,\bar{\mathbf{q}}^{*}_{i,\,j,\,k},\,\overline{\boldsymbol{J\xi}}^{*}_{i+1/2,\,j,\,k}\Big) \\
& +\; \Delta\widehat{\mathbf{G}}^{(1)}\Big(\Delta\hat{\mathbf{q}}_{i,\,j,\,k},\,\bar{\mathbf{q}}^{*}_{i,\,j,\,k},\,\overline{\boldsymbol{J\eta}}^{*}_{i,\,j-1/2,\,k}\Big) - \Delta\widehat{\mathbf{G}}^{(1)}\Big(\Delta\hat{\mathbf{q}}_{i,\,j,\,k},\,\bar{\mathbf{q}}^{*}_{i,\,j,\,k},\,\overline{\boldsymbol{J\eta}}^{*}_{i,\,j+1/2,\,k}\Big) \\
& +\; \Delta\widehat{\mathbf{H}}^{(1)}\Big(\Delta\hat{\mathbf{q}}_{i,\,j,\,k},\,\bar{\mathbf{q}}^{*}_{i,\,j,\,k},\,\overline{\boldsymbol{J\zeta}}^{*}_{i,\,j,\,k-1/2}\Big) - \Delta\widehat{\mathbf{H}}^{(1)}\Big(\Delta\hat{\mathbf{q}}_{i,\,j,\,k},\,\bar{\mathbf{q}}^{*}_{i,\,j,\,k},\,\overline{\boldsymbol{J\zeta}}^{*}_{i,\,j,\,k+1/2}\Big) \\
& +\; \Big[\,r^{\overline{\mathbf{K}_{\xi}}^{*}}\Big(\bar{\mathbf{q}}^{*}_{i,\,j,\,k},\,\overline{\boldsymbol{J\xi}}^{*}_{i-1/2,\,j,\,k}\Big) + r^{\overline{\mathbf{K}_{\xi}}^{*}}\Big(\bar{\mathbf{q}}^{*}_{i,\,j,\,k},\,\overline{\boldsymbol{J\xi}}^{*}_{i+1/2,\,j,\,k}\Big) \\
& +\quad r^{\overline{\mathbf{K}_{\eta}}^{*}}\Big(\bar{\mathbf{q}}^{*}_{i,\,j,\,k},\,\overline{\boldsymbol{J\eta}}^{*}_{i,\,j-1/2,\,k}\Big) + r^{\overline{\mathbf{K}_{\eta}}^{*}}\Big(\bar{\mathbf{q}}^{*}_{i,\,j,\,k},\,\overline{\boldsymbol{J\eta}}^{*}_{i,\,j+1/2,\,k}\Big) \\
& +\quad r^{\overline{\mathbf{K}_{\zeta}}^{*}}\Big(\bar{\mathbf{q}}^{*}_{i,\,j,\,k},\,\overline{\boldsymbol{J\zeta}}^{*}_{i,\,j,\,k-1/2}\Big) + r^{\overline{\mathbf{K}_{\zeta}}^{*}}\Big(\bar{\mathbf{q}}^{*}_{i,\,j,\,k},\,\overline{\boldsymbol{J\zeta}}^{*}_{i,\,j,\,k+1/2}\Big)\,\Big]\,\Delta\hat{\mathbf{q}}_{i,\,j,\,k}\Big\}\;\;/\;2 \\
& +\; i\,k\,\overline{J}^{*}_{i,\,j,\,k}\,\Delta\hat{\mathbf{q}}_{i,\,j,\,k}\,,
\end{aligned} \tag{4.96}$$

wherein each directional pair of the linearized time-invariant-mean spatial metrics can be substituted by a centroidally assigned instance to reduce operation count [70]; i.e.,

$$\begin{aligned}
\overline{\boldsymbol{J\xi}}^{*}_{i+1/2,\,j,\,k} &:= \overline{\boldsymbol{J\xi}}^{*}_{i,\,j,\,k}\,, \qquad \overline{\boldsymbol{J\xi}}^{*}_{i-1/2,\,j,\,k} := \overline{\boldsymbol{J\xi}}^{*}_{i,\,j,\,k}\,; \\
\overline{\boldsymbol{J\eta}}^{*}_{i,\,j+1/2,\,k} &:= \overline{\boldsymbol{J\eta}}^{*}_{i,\,j,\,k}\,, \qquad \overline{\boldsymbol{J\eta}}^{*}_{i,\,j-1/2,\,k} := \overline{\boldsymbol{J\eta}}^{*}_{i,\,j,\,k}\,; \\
\overline{\boldsymbol{J\zeta}}^{*}_{i,\,j,\,k+1/2} &:= \overline{\boldsymbol{J\zeta}}^{*}_{i,\,j,\,k}\,, \qquad \overline{\boldsymbol{J\zeta}}^{*}_{i,\,j,\,k-1/2} := \overline{\boldsymbol{J\zeta}}^{*}_{i,\,j,\,k}\,.
\end{aligned} \tag{4.97}$$

By this means, the principal-diagonal matrix-operator simplifies to a complex scalar coefficient of the amplitude state vector's correction:

$$\Big(\overline{\mathbf{D}}^{*}\Delta\hat{\mathbf{q}}\Big)_{i,\,j,\,k} \;\approx\; \big(\bar{\beta}^{*}_{Re} + i\,\bar{\beta}^{*}_{Im}\big)\,\Delta\hat{\mathbf{q}}_{i,\,j,\,k}\,, \tag{4.98}$$

with

$$\begin{aligned}
\bar{\beta}^{*}_{Re} &:= \frac{\overline{J}^{*}_{i,\,j,\,k}}{\Delta\tau^{\circ}} + r^{\overline{\mathbf{K}_{\xi}}^{*}}\Big(\bar{\mathbf{q}}^{*}_{i,\,j,\,k},\,\overline{\boldsymbol{J\xi}}^{*}_{i,\,j,\,k}\Big) + r^{\overline{\mathbf{K}_{\eta}}^{*}}\Big(\bar{\mathbf{q}}^{*}_{i,\,j,\,k},\,\overline{\boldsymbol{J\eta}}^{*}_{i,\,j,\,k}\Big) + r^{\overline{\mathbf{K}_{\zeta}}^{*}}\Big(\bar{\mathbf{q}}^{*}_{i,\,j,\,k},\,\overline{\boldsymbol{J\zeta}}^{*}_{i,\,j,\,k}\Big)\,, \\
\bar{\beta}^{*}_{Im} &:= k\,\overline{J}^{*}_{i,\,j,\,k}\,.
\end{aligned} \tag{4.99}$$

Each centroidally assigned directional-instance of the linearized time-invariant-mean spatial metrics is then straightforwardly obtained through the arithmetic average of the

pertinent directional-pair [70]; i.e.,

$$\begin{aligned}
\overline{\boldsymbol{J}\boldsymbol{\xi}}^{*}_{i,\,j,\,k} &:= \left(\overline{\boldsymbol{J}\boldsymbol{\xi}}^{*}_{i+1/2,\,j,\,k} + \overline{\boldsymbol{J}\boldsymbol{\xi}}^{*}_{i-1/2,\,j,\,k}\right) \;\;/\;\; 2\,, \\
\overline{\boldsymbol{J}\boldsymbol{\eta}}^{*}_{i,\,j,\,k} &:= \left(\overline{\boldsymbol{J}\boldsymbol{\eta}}^{*}_{i,\,j+1/2,\,k} + \overline{\boldsymbol{J}\boldsymbol{\eta}}^{*}_{i,\,j-1/2,\,k}\right) \;\;/\;\; 2\,, \\
\overline{\boldsymbol{J}\boldsymbol{\zeta}}^{*}_{i,\,j,\,k} &:= \left(\overline{\boldsymbol{J}\boldsymbol{\zeta}}^{*}_{i,\,j,\,k+1/2} + \overline{\boldsymbol{J}\boldsymbol{\zeta}}^{*}_{i,\,j,\,k-1/2}\right) \;\;/\;\; 2\,.
\end{aligned} \tag{4.100}$$

Refocusing on the entire computational domain, the system of linear equations governing the correction of each discrete amplitude state vector emerges as

$$\left[\left(\overline{\mathbf{L}}^{*} + \overline{\mathbf{D}}^{*} + \overline{\mathbf{U}}^{*}\right)\Delta\hat{\mathbf{q}}\right]_{\forall\,(i,\,j,\,k)} \approx -\widehat{\mathbf{R}}^{\nu}_{\forall\,(i,\,j,\,k)}\,, \tag{4.101}$$

wherein the RHS is evaluated according to the sequence defined in Section 4.2. On the basis of Blazek [14], as well as Kreiselmaier [70], the implicit matrix-operator of Eq. (4.101) can be approximately decomposed into diagonally dominant lower- and upper-triangular-matrix factors, yielding the LU-SSOR-scheme-distinctive

$$\left[\left(\overline{\mathbf{L}}^{*} + \overline{\mathbf{D}}^{*}\right)\overline{\mathbf{D}}^{*-1}\left(\overline{\mathbf{D}}^{*} + \overline{\mathbf{U}}^{*}\right)\Delta\hat{\mathbf{q}}\right]_{\forall\,(i,\,j,\,k)} \approx -\widehat{\mathbf{R}}^{\nu}_{\forall\,(i,\,j,\,k)}\,. \tag{4.102}$$

It is designated the factored implicit scheme.

4.5.2 Solution of the System of Linear Equations

Further following Blazek [14], as well as Kreiselmaier [70], the factored implicit scheme allows a solution of the constructed system of linear equations in two stages. Initially, an interim correction of each discrete amplitude state vector is defined as

$$\Delta\hat{\mathbf{q}}^{\dagger}_{\forall\,(i,\,j,\,k)} := \left[\overline{\mathbf{D}}^{*-1}\left(\overline{\mathbf{D}}^{*} + \overline{\mathbf{U}}^{*}\right)\Delta\hat{\mathbf{q}}\right]_{\forall\,(i,\,j,\,k)}\,, \tag{4.103}$$

reducing Eq. (4.102) to

$$\left[\left(\overline{\mathbf{L}}^{*} + \overline{\mathbf{D}}^{*}\right)\Delta\hat{\mathbf{q}}^{\dagger}\right]_{\forall\,(i,\,j,\,k)} = -\widehat{\mathbf{R}}^{\nu}_{\forall\,(i,\,j,\,k)}\,. \tag{4.104}$$

Since $\overline{\mathbf{L}}^{*}$ is constituted by strictly lower-triangular elements, $(\overline{\mathbf{L}}^{*}\Delta\hat{\mathbf{q}}^{\dagger})_{\forall\,(i,\,j,\,k)}$ can be shifted to the RHS without compromising the feasibility of the inversion; i.e.,

$$\left(\overline{\mathbf{D}}^{*}\Delta\hat{\mathbf{q}}^{\dagger}\right)_{\forall\,(i,\,j,\,k)} = -\left[\widehat{\mathbf{R}}^{\nu}_{\forall\,(i,\,j,\,k)} + \left(\overline{\mathbf{L}}^{*}\Delta\hat{\mathbf{q}}^{\dagger}\right)_{\forall\,(i,\,j,\,k)}\right]. \tag{4.105}$$

It is solved centroid-by-centroid in a forward index-sweep across the entire computational domain. Per centroid, this task merely involves the inversion of the complex scalar coefficient:

$$\Delta\hat{\mathbf{q}}^{\dagger}_{i,\,j,\,k} = -\left[\widehat{\mathbf{R}}^{\nu}_{i,\,j,\,k} + \left(\overline{\mathbf{L}}^{*}\Delta\hat{\mathbf{q}}^{\dagger}\right)_{i,\,j,\,k}\right] / \left(\bar{\beta}^{*}_{Re} + i\,\bar{\beta}^{*}_{Im}\right)\,, \tag{4.106}$$

wherein $(\overline{\mathbf{L}}^{*}\Delta\hat{\mathbf{q}}^{\dagger})_{i,j,k}$ are always known from inversions completed at precedingly indexed centroids [14, 70]. As implemented by the author, Eq. (4.106) is formulated to return the real and imaginary part of $\Delta\hat{\mathbf{q}}^{\dagger}_{i,j,k}$ separately:

$$\begin{aligned} Re\,\Delta\hat{\mathbf{q}}^{\dagger}_{i,j,k} &= -\bar{v}^{*}_{Re}\,Re\left[\widehat{\mathbf{R}}^{\nu}_{i,j,k} + \left(\overline{\mathbf{L}}^{*}\Delta\hat{\mathbf{q}}^{\dagger}\right)_{i,j,k}\right] - \bar{v}^{*}_{Im}\,Im\left[\widehat{\mathbf{R}}^{\nu}_{i,j,k} + \left(\overline{\mathbf{L}}^{*}\Delta\hat{\mathbf{q}}^{\dagger}\right)_{i,j,k}\right], \\ Im\,\Delta\hat{\mathbf{q}}^{\dagger}_{i,j,k} &= \;\; \bar{v}^{*}_{Im}\,Re\left[\widehat{\mathbf{R}}^{\nu}_{i,j,k} + \left(\overline{\mathbf{L}}^{*}\Delta\hat{\mathbf{q}}^{\dagger}\right)_{i,j,k}\right] - \bar{v}^{*}_{Re}\,Im\left[\hat{\mathbf{R}}^{\nu}_{i,j,k} + \left(\overline{\mathbf{L}}^{*}\Delta\hat{\mathbf{q}}^{\dagger}\right)_{i,j,k}\right]. \end{aligned} \tag{4.107}$$

with

$$\bar{v}^{*}_{Re} := \bar{\beta}^{*}_{Re} \,/\, \left[(\bar{\beta}^{*}_{Re})^2 + (\bar{\beta}^{*}_{Im})^2\right] \qquad \text{and} \qquad \bar{v}^{*}_{Im} := \bar{\beta}^{*}_{Im} \,/\, \left[(\bar{\beta}^{*}_{Re})^2 + (\bar{\beta}^{*}_{Im})^2\right]. \tag{4.108}$$

Having computed $\Delta\hat{\mathbf{q}}^{\dagger}_{\forall\,(i,j,k)}$ in this manner, $\Delta\hat{\mathbf{q}}_{\forall\,(i,j,k)}$ can be obtained in the second stage. Since $\overline{\mathbf{U}}^{*}$ is constituted by strictly upper-triangular elements, Eq. (4.103) can be rearranged to

$$\left(\overline{\mathbf{D}}^{*}\Delta\hat{\mathbf{q}}\right)_{\forall\,(i,j,k)} = \left(\overline{\mathbf{D}}^{*}\Delta\hat{\mathbf{q}}^{\dagger}\right)_{\forall\,(i,j,k)} - \left(\overline{\mathbf{U}}^{*}\Delta\hat{\mathbf{q}}\right)_{\forall\,(i,j,k)} \tag{4.109}$$

without compromising the feasibility of the inversion. Similar to Eq. (4.105), Eq. (4.109) is solved centroid-by-centroid, albeit in a backward index-sweep across the entire computational domain. Per centroid this task again merely involves the inversion of the complex scalar coefficient:

$$\Delta\hat{\mathbf{q}}_{i,j,k} = \Delta\hat{\mathbf{q}}^{\dagger}_{i,j,k} - \left(\overline{\mathbf{U}}^{*}\Delta\hat{\mathbf{q}}\right)_{i,j,k} \,/\, \left(\bar{\beta}^{*}_{Re} + i\,\bar{\beta}^{*}_{Im}\right), \tag{4.110}$$

wherein $(\overline{\mathbf{U}}^{*}\Delta\hat{\mathbf{q}})_{i,j,k}$ are known from inversions completed at succeedingly indexed centroids [14, 70], which, however, were conducted precedingly in terms of the backward index-sweep. As implemented by the author, Eq. (4.110) is likewise formulated to return the real and imaginary part of $\Delta\hat{\mathbf{q}}_{i,j,k}$ separately:

$$\begin{aligned} Re\,\Delta\hat{\mathbf{q}}_{i,j,k} &= Re\,\Delta\hat{\mathbf{q}}^{\dagger}_{i,j,k} - \bar{v}^{*}_{Re}\,Re\left(\overline{\mathbf{U}}^{*}\Delta\hat{\mathbf{q}}\right)_{i,j,k} - \bar{v}^{*}_{Im}\,Im\left(\overline{\mathbf{U}}^{*}\Delta\hat{\mathbf{q}}\right)_{i,j,k}, \\ Im\,\Delta\hat{\mathbf{q}}_{i,j,k} &= Im\,\Delta\hat{\mathbf{q}}^{\dagger}_{i,j,k} + \bar{v}^{*}_{Im}\,Re\left(\overline{\mathbf{U}}^{*}\Delta\hat{\mathbf{q}}\right)_{i,j,k} - \bar{v}^{*}_{Re}\,Im\left(\overline{\mathbf{U}}^{*}\Delta\hat{\mathbf{q}}\right)_{i,j,k}. \end{aligned} \tag{4.111}$$

Finally, the amplitude state vector's incremental advancement for $\Delta\tau^{\circ}$ is gained as

$$\hat{\mathbf{q}}^{\nu+1}_{\forall(i,j,k)} = \hat{\mathbf{q}}^{\nu}_{\forall(i,j,k)} + \Delta\hat{\mathbf{q}}_{\forall(i,j,k)}\,. \tag{4.112}$$

In this dissertation, a solution process stabilized purely by the inherent numerical dissipation is favored over the case-dependent ascertainment of the convergence-optimal $\Delta\tau^{\circ}$. Typically, $\Delta\tau^{\circ}$ is stipulated to be of infinite value [14, 110], accomplished in practice

by eliminating $\overline{J}^{*}_{i,j,k}/\Delta\tau^{\circ}$ from $\bar{\beta}^{*}_{Re}$, Eq. (4.99). Equations (4.103–4.112) then embody the LU-SSOR for a single iteration of Newton's method [14, 110]. Trial runs have shown, however, that unexpectedly large values of ω_d are necessary to ensure stability, progressively reducing the rate of convergence. This can be attributed to having discounted the directional instances of $\partial\widehat{\mathbf{E}_{\mathbf{v}\,\psi}}^{(1)}/\partial\hat{\mathbf{q}}$ in the implicit matrix-operator's conditioning. Even though there is no impact on solution accuracy, a level of physical dissipation is absent, degrading the factored implicit scheme's damping behavior. Jameson and Rieger [110], as well as Blazek [14], had similarly recognized this issue for the LU-SSOR-performed pseudotime integration of the RANS equations, inversely observing that the retention of the viscous-flux Jacobian matrices in the implicit matrix-operator can improve solution stability, though, entailing an increased operation count, too.

4.5.3 Multigrid Acceleration, Convergence Criteria, and Limitation of the Amplitude Spalart-Allmaras Conservative Working Variable

On the basis of Blazek [14], the LU-SSOR scheme is embedded into a geometric multigrid algorithm to accelerate convergence toward a pseudosteady solution. Having supplied a reference and amplitude grid of both appropriate cell quantity and boundary segmentation, an equivalent yet coarser grid-pair is generated internally by eliminating every second directional cell-edge. Grid-pairs of even greater coarseness can be gained through consecutive execution, their number only being limited by the properties of the initial instance. Thus, an individual three-dimensional grid comprised of h cells is incrementally reduced to one of $h/8$ cells, $h/64$ cells, etc., as feasible. Brandt's [17] full approximation storage scheme is then applied to these grid-pairs in a predetermined sequence, designated the multigrid schedule. Each grid-pair uniquely corresponds to an operational level within the schedule. The finest grid-pair is attributed to the top level, while successively coarser instances are assigned to successively lower levels [14]. The attainable level depth does not have to be used to full capacity. Trial runs by the author have shown that grid-pairs of the fourth level and deeper are generally too coarse to favorably influence the durative convergence rate, being in contrast to Blazek's experiences [14]. Similar to Blazek [14], merely simple multigrid has been employed for the cases considered in this dissertation; i.e., a multigrid cycle both initiates and terminates on the top level pursuant to Wesseling [133]. The number of LU-SSOR pseudotime steps conducted on each level is within user discretion and may vary between them [14]. The restriction of both the amplitude state vector and the amplitude residual vector to the next-coarser grid-pair is handled through volume-weighted averaging, while the amplitude state vector's correction is prolongated to the next-finer grid-pair by way of trilinear interpolation. In this

regard, Wesseling [133] provides the pertinent cell-centered stencils. For additional stabilization, constant-coefficient implicit smoothing of the prolongated amplitude state vector correction has been made available, as appropriated from Kroll and Jain [73]. Overall, the implementation of the multigrid algorithm by the author followed the FLOWer instance [72].

In combination, the instated measures render a highly adaptable multigrid algorithm, allowing an accelerated pseudotime integration for a wide array of cases. For an individual case, however, the ascertainment of the optimal settings largely relies on empiricism. In this regard, Blazek's [14] systematic investigation of multigrid-embedded LU-SSOR scheme operation provides a valuable starting point. For the majority of cases considered in this dissertation, a three-level V-symmetric multigrid schedule performing dual pseudotime steps on both the top [14] and bottom level, as well as a single instance per coarsening and refinement half-cycle on the intermediate level, has been identified to produce the best durative convergence rate at ample robustness [103]. To this end, implicit smoothing of the amplitude state vector's prolongated coarse-grid correction [73, 72] must also be active on the intermediate level. Designated the $(2_0 \,/\, 1_1 \,/\, 2)$ V-symmetric multigrid schedule, adaptation to the individual case is accomplished by specifying the scheme-inherent dissipation dependent on the level; i.e., letting $(\omega_{d,h} \,/\, \omega_{d,h/8} \,/\, \omega_{d,h/64})$, with $\omega_{d,h} >> \omega_{d,h/8} >> \omega_{d,h/64}$ having emerged as a guideline for achieving stability while avoiding excessive damping on the lower levels. The sequence of procedural calls constituting this select schedule is illustrated in Figure 4.7. Embedding the LU-SSOR scheme into the multigrid algorithm, ν has been formally relegated to tracking the amplitude state vector's level-specific pseudotime advancement within the individual cycle. For each level of the coarsening half-cycle, ν is reinitialized prior to the first LU-SSOR pseudotime step and reaches its predetermined increment on completion of the refinement half-cycle. Ultimately, the amplitude state vector's top-level advancement is of sole interest, and for which convergence needs to be gauged. To this end, a superordinate pseudotime level n (progressively incremented after each multigrid cycle) is introduced. Considering a representative multigrid cycle, n and $n+1$, respectively, denote its initiation and completion, with the associated amplitude state vector then having the top-level equivalence

$$\hat{\mathbf{q}}^{n} \equiv \hat{\mathbf{q}}_h^{\nu=0} \qquad \text{and} \qquad \hat{\mathbf{q}}^{n+1} \equiv \hat{\mathbf{q}}_h^{update} \,. \tag{4.113}$$

Solution convergence is ascertained after each multigrid cycle. As a criterion, the $\hat{\rho}$ residual (ℓ^2-norm) is computed and normalized with its instance after the first multigrid cycle. If it contracts to a value less than a user-specified tolerance of accuracy, the multigrid scheduler terminates [70, 100, 103]. The behavior of the S/A one-equation turbulence model can be concurrently gauged by computing a similarly normalized $\widehat{\tilde{\mu}}$ residual (ℓ^2-norm) [103]. However, it typically need not satisfy a user-specified tolerance of accuracy.

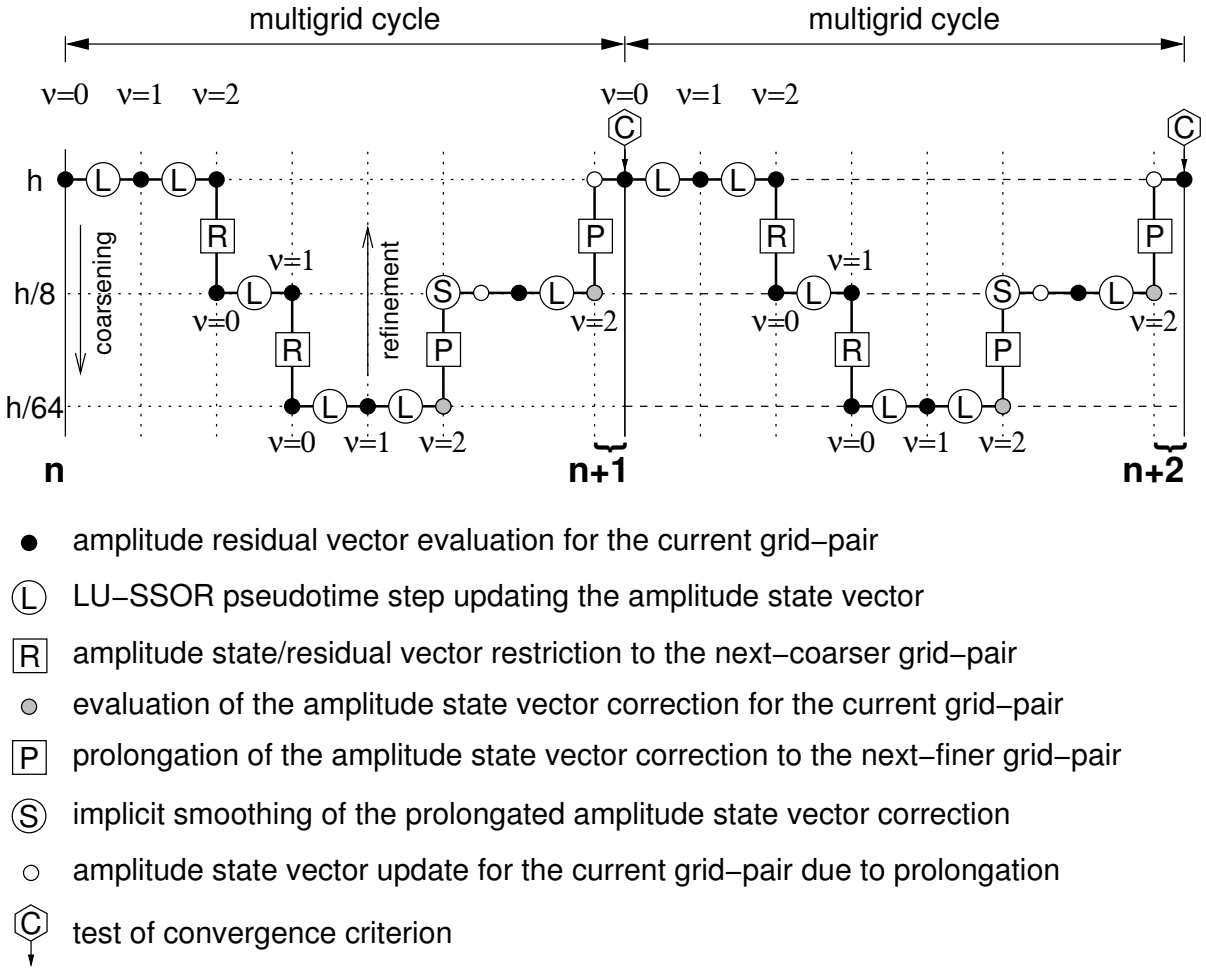

Figure 4.7: $(2_0 \,/\, 1_1 \,/\, 2)$ V-symmetric multigrid schedule; based on [14], and the FLOWer implementation [72].

Both residuals are given through

$$\left|\frac{\Delta\hat{\varsigma}}{\Delta n}\right|_2^{n+1} := \frac{\left\{\sum\limits_{\forall\,(i,j,k)} [(Re\,\hat{\varsigma}^{n+1} - Re\,\hat{\varsigma}^{n})^2 + (Im\,\hat{\varsigma}^{n+1} - Im\,\hat{\varsigma}^{n})^2]\right\}^{1/2}}{\left\{\sum\limits_{\forall\,(i,j,k)} [(Re\,\hat{\varsigma}^{n=1} - Re\,\hat{\varsigma}^{n=0})^2 + (Im\,\hat{\varsigma}^{n=1} - Im\,\hat{\varsigma}^{n=0})^2]\right\}^{1/2}}\,, \text{with } \varsigma \in \{\rho,\, \breve{\mu}\}\,. \tag{4.114}$$

Alternatively, a criterion based on the progression of the global load coefficients' amplitude can be specified. Each instance's relative change after a multigrid cycle is computed and put into comparison with a user-specified tolerance of accuracy. If the relative change of designated instances contract to a value less than the tolerance, the multigrid scheduler terminates [102]. Since this criterion relies on an integral measure of the solution's development, it is considered to be more application-oriented than the former.

Prior to the first multigrid cycle, the top-level amplitude state vector requires initialization:

$$\begin{aligned}\hat{\mathbf{q}}^{n=0} = \hat{\mathbf{q}}_{init} &= \left(\hat{\rho}_{init},\, \widehat{\rho u}_{init},\, \widehat{\rho v}_{init},\, \widehat{\rho w}_{init},\, \widehat{\rho e}_{init},\, \widehat{\breve{\mu}}_{init}\right)^T \\ &:= \left(0,\, 0,\, 0,\, 0,\, 0,\, c_{\widehat{\breve{\mu}}_{init}/\overline{\breve{\mu}}^*_\infty}\overline{\breve{\mu}}^*_\infty\right)^T .\end{aligned} \tag{4.115}$$

Therein, $c_{\widehat{\breve{\mu}}_{init}/\overline{\breve{\mu}}^*_\infty}$ allows user-control over the amplitude S/A conservative working variable's initial setting throughout the computational domain, performed with respect to its linearized time-invariant-mean freestream counterpart [72]. Hence, a means to appropriately normalize the $\widehat{\breve{\mu}}$ residual is given. For values of $c_{\widehat{\breve{\mu}}_{init}/\overline{\breve{\mu}}^*_\infty}$ in the order of Re_∞, large changes of the amplitude S/A conservative working variable are induced throughout the computational domain with the first multigrid cycle [121]. Since the resultant $\widehat{\breve{\mu}}$ residual is employed in its own normalization and the normalization of all succeeding instances, Eq. (4.114), proper adjustment allows the normalized $\widehat{\breve{\mu}}$ residual to develop in the same scale as its $\hat{\rho}$ counterpart.

Campobasso and Giles [19, 20] have shown that conventional pseudotime integration of the small disturbance Navier-Stokes equations leads to instability if the underlying linearized time-invariant-mean solution renders a flowfield with regions of separation. Applying the GMRES approach or the RPM, however, had permitted stabilization [19, 20]. Pursuant to Pechloff and Laschka, "the instability can be traced to the evaluation of the [$\hat{\mathbf{q}}$]-homogenous amplitude S/A [turbulence] source term [vector in that region,]"[103] which produces unwarranted growth of $\widehat{\breve{\mu}}$. It can be kept in check, however, by simply exercising

$$\sigma|_{lim} := \frac{\sigma}{|\sigma|}\, min\left(|\sigma|\,,\, \overline{\breve{\mu}}^*\right), \qquad \text{with} \qquad \sigma \in \left\{ Re\,\widehat{\breve{\mu}}\,,\; Im\,\widehat{\breve{\mu}} \right\}, \tag{4.116}$$

per cell; i.e., imposing a local limitation of the amplitude S/A conservative working variable with respect to its linearized time-invariant-mean counterpart [103]. Pechloff and Laschka further state that "[, i]mplementationwise, Eq. ([4.116]) [is] applied to the amplitude state vector's update within the [LU-SSOR scheme's] backward sweep[, Eq. (4.110)]."[103] Due to the limiter's demonstrated effectivity [103], the more elaborate means of stabilization [19, 20] were not pursued. Naturally, the active limiter disallows the $\widehat{\breve{\mu}}$ residual to serve as a termination criterion at all.

4.5.4 Frozen Eddy-Viscosity Approach

By default, the small disturbance instance of the S/A one-equation turbulence model is fully considered in a computation, retaining the dynamic trait of the original closure under the restriction of linearity. Alternatively, a user-controlled option to effectively discount the $\widehat{\mu}_t$ influence on $\hat{\mathbf{q}}$ (the FEVA) has been made available by the author. To this end,

$\widehat{\breve{\mu}} = 0$ is artificially upheld for each cell, rendering $\widehat{\mu_t}$ solely as a function of $\hat{\mu}$. Specifically, Eq. (3.198) expressed in the frequency domain then reduces to

$$\widehat{\mu_t} = \overline{\breve{\mu}}^* \widehat{f_{v1}}\,, \quad \text{with} \quad \widehat{f_{v1}} = 3\,(\overline{\breve{\chi}}^*)^2 c_{v1}^3\,\widehat{\breve{\chi}} \,/\, \left[(\overline{\breve{\chi}}^*)^3 + c_{v1}^3\right]^2 \quad \text{and} \quad \widehat{\breve{\chi}} = -\overline{\breve{\chi}}^*\,\hat{\mu}/\,\bar{\mu}^*\,, \tag{4.117}$$

which consolidatedly yields

$$\widehat{\mu_t} = f_{\overline{\breve{\chi}}^*}\hat{\mu} \quad \text{with} \quad f_{\overline{\breve{\chi}}^*} := -3\,(\overline{\breve{\chi}}^*)^4 c_{v1}^3 \,/\, \left[(\overline{\breve{\chi}}^*)^3 + c_{v1}^3\right]^2\,. \tag{4.118}$$

Since both $\overline{\breve{\mu}}^*$ and $\bar{\mu}^*$ are invariant to the pseudotime integration, their contribution to $\widehat{\mu_t}$ evidently remains constant in the transient assessment; i.e., by way of $\overline{\breve{\chi}}^*$ constituting $f_{\overline{\breve{\chi}}^*}$. For the regarded transonic problem, the largest occurrence of $\hat{\mu}$ will typically be observed across the linearized time-invariant-mean location of a shock. Far smaller occurrences will be seen within the extents of the postshock boundary layer. Contrarily, $f_{\overline{\breve{\chi}}^*}$ reaches its maximum value at localities where $\overline{\breve{\chi}}^*$ is in the neighborhood of the first-order-of-magnitude value. Following Spalart and Allmaras [121], such localities are present in the boundary layer's defect-layer or at the edges of pronounced off-body shear-flow regions, as attributed to wakes and vortices. For either a $\overline{\breve{\chi}}^*$ increase to second-order-of-magnitude values or a $\overline{\breve{\chi}}^*$ decrease to zero-order-of-magnitude values, as experienced, respectively, in the boundary layer's log-layer or the convectively dominated portions of the linearized time-invariant-mean flowfield, $f_{\overline{\breve{\chi}}^*}$ decreases rapidly and trends toward nil. In case of the log-layer, $f_{\overline{\breve{\chi}}^*}$ thus becomes negligible in a region where $\overline{\breve{\mu}}^*$ is actually most prominent [121]. Under these considerations the significant occurrences of $\hat{\mu}$ and $f_{\overline{\breve{\chi}}^*}$ can be said to have only marginal spatial correlation to one another, with Eq. (4.118) widely rendering $\widehat{\mu_t} \approx 0$ throughout the amplitude flowfield. Consequently, the retention of the original closure's dynamic trait is further diminished. The products between $\overline{\mu_t}^*$ and the gradients of the amplitude velocity and temperature now predominantly influence $\hat{\mathbf{q}}$ during the pseudotime integration. Because $\widehat{\mu_t} := 0$ is not realized directly, however, remnant occurrences of $\widehat{\mu_t}$ may come into effect at localities where $\hat{\mu}$ and $f_{\overline{\breve{\chi}}^*}$ tend to amplify instead of neutralize each other. Such instances are characteristically witnessed in vicinity of the shock's interaction with the boundary layer.

On one hand, the FEVA can be employed to per se isolate the $\widehat{\mu_t}$ contribution to the computed amplitude flowfield of a particular case. On the other hand, it provides an alternative means to stabilize the pseudotime integration when employing a linearized time-invariant-mean flowfield with regions of separation, as $\widehat{\breve{\mu}}$ is kept at nil value from the initial top-level pseudotime step onward. For either case, the FEVA disallows the $\widehat{\breve{\mu}}$ residual to serve as a termination criterion. In its current implementation, no reduction of computational effort is attained over the full consideration. The small disturbance instance of the S/A one-equation turbulence model is still spatially evaluated for each ν and $\widehat{\breve{\mu}}$ subsequently advanced to $\nu + 1$, though, ultimately being multiplied by nil.

In this context, the small disturbance instance of the B/L algebraic turbulence model [8] formulated by Iatrou [54] merely represents a FEVA. Considering

$$\widehat{\mu_t} = \hat{\rho}\,\overline{\nu_t} + \bar{\rho}\,\widehat{\nu_t}\,, \tag{4.119}$$

the original closure supplies the time-invariant-mean kinematic eddy viscosity $\overline{\nu_t}$, while its amplitude counterpart $\widehat{\nu_t}$ is left unresolved. Neglecting $\widehat{\nu_t}$ then renders $\widehat{\mu_t}$ solely as a function of $\hat{\rho}$ [54]. Limiting the B/L algebraic turbulence model to the near-wall region, $\overline{\nu_t}$ becomes most prominent in the log-layer [8]. For the transonic problem of interest, however, the encountered boundary layers can be considered to be incompressible; i.e., locally, $\hat{\rho}$ becomes insignificant. Thus, $\widehat{\mu_t} \approx 0$ is again rendered.

Chapter 5

Results

Before incorporating FLM-SD.NS into a CA tool as the preferred CFD component, its application readiness must be demonstrated. This entails the substantiation of the small disturbance Navier-Stokes approach's validity and attainable computational efficiency gain. For this purpose, an extensive array of forced oscillation cases of both two- and three-dimensional character must be considered. Typically, cases pertaining to the field of aircraft aerodynamics range from the external flow problem of individual airfoils, representing the specialty of merely two-dimensional spatial conditions, over diverse wings, and ultimately to full aircraft configurations. The latter, however, still requires substantially high processing power and storage capabilties. Constraining the number of cases to be taken into consideration, the transonic viscous flow regime intended as the FLM-SD.NS application domain allows a distinct selection on the basis of the exhibited shock/boundary-layer interaction over the course of the considered body's simple harmonic oscillation. Focusing on a low-aspect-ratio wing, suitable cases are amply provided by the experimental campaign conducted by Bennett and Walker [12] for pitching and flap oscillations of the NCDW. Select cases are investigated in the following.

5.1 Overview

Throughout the development of FLM-SD.NS, the validity of the small disturbance Navier-Stokes approach in regard to the two-dimensional external flow problem had been successfully substantiated by means of numerous airfoil cases. To this effect, the local load distribution normal to the airfoil surface, as given through the surface pressure coefficient, had been established by Pechloff et al. [98], Iatrou et al. [57], as well as Pechloff and Laschka [100] to be the primary criterion for evaluating FLM-SD.NS prediction accuracy. Specifically, the linearized time-invariant-mean and amplitude surface pressure coefficient were put into comparison with the zeroth- and first-harmonic instance obtained from the Fourier analysis of the FLM-NS-computed time series and available from an experiment.

In addition, the resultant global loading, as embodied by the lift and pitching-moment coefficient, was investigated. It can be summarized that for FLM-SD.NS the linearized time-invariant-mean and amplitude lift/pitching-moment coefficient

> result directly from the integration of the [underlying surface-]pressure[-coefficient] and skin-friction[-coefficient-vector] distributions over the airfoil [surface] at [its] reference position. Having obtained a converged [pseudosteady]-state solution, the process is conducted only once toward the end of the FLM-SD.NS execution. In case of [...] FLM-NS [...], however, an integration of [its respective surface-]pressure[-coefficient] and skin-friction[-coefficient-vector] distributions [over the deflected airfoil surface] must be performed after each converged physical time step of the [discretized] oscillation [...]. This eventually yields the [lift-/pitching-moment-coefficient] evolution [...] for all cycles[as a series in discrete physical time], including the transient ones. [100]

A cycle of confirmed periodicity is then subjected to Fourier analysis, extracting the zeroth and first harmonic of the particular global load coefficient for the sake of comparison [100]. Regarding FLM-SD.NS, the linearized time-invariant-mean and amplitude local/global load coefficient are again, respectively, referred to as the zeroth- and first-harmonic instance, for the sake of consistency.

It had become common procedure to additionally provide both an FLM-SDEu and FLM-Eu result for the considered case [57, 100]. On the one hand, this allowed the respective impact of disregarded viscosity to be assessed. On the other hand, any deviation between the FLM-SD.NS and FLM-NS result became comparable to the deviation between their inviscid counterparts. In conjunction, an evaluation with respect to both the difference in approach (small disturbance vs. dynamically fully nonlinear) and the difference in phenomenological consideration (viscous vs. inviscid) became possible. Naturally, the best practices that had been established through the two-dimensional investigations were again employed in the three-dimensional investigations.

5.1.1 Preceding Two-Dimensional Investigations

Preceding the dissertation at hand, the two-dimensional investigations conducted by the various researchers can be discerned on the basis of the treatable Reynolds number. Initially, only laminar cases could be considered, with turbulent cases eventually becoming accessible through the implementation of the S/A one-equation turbulence model [121] and the B/L algebraic turbulence model [8].

5.1.1.1 Laminar Cases

In 2002 Pechloff et al. [98] presented the first FLM-SD.NS results for a NACA 0012 pitching-oscillation case, which, however, had no experimental counterpart. It was com-

puted with the initial laminar single-grid incarnation. Naturally, only a very low Reynolds number could be treated. The Mach number was specified in such a manner that the flowfield could be considered incompressible, while a zero angle-of-attack allowed an antisymmetric first-harmonic surface-pressure-coefficient distribution to be obtained. Enabled through the highly viscous flowfield, the case primarily served to verify code integrity, yet also demonstrated the feasibility of the small disturbance Navier-Stokes approach per se. For both the first-harmonic local and the first-harmonic global load coefficients, good agreement to the FLM-NS-obtained instances were ascertained. FLM-SD.NS had realized a computational efficiency gain of half an order of magnitude over FLM-NS, yet at triple its memory allocation. On the basis of this case, an additional frequency variation had been conducted. It revealed a decreasing computational efficiency gain with increasing frequency, though, mostly being attributable to the improving performance of FLM-NS. Inversely, a single decrement from the baseline frequency increased the computational efficiency gain to three-quarters of an order of magnitude [98].

By 2003 Iatrou et al. [59] had extended the initial investigation, considering an even lower Reynolds number, yet somewhat higher Mach number. The latter rendered a compressible flowfield that remained subsonic. A case at the lowest reduced frequency of the established spectrum [98] was computed with FLM-SD.NS/FLM-NS, and another at the highest reduced frequency. For either case, the agreement between the two methods was again deemed to be good with respect to both the first-harmonic local and the first-harmonic global load coefficients. Supplemental FLM-SDEu/FLM-Eu results, however, showed even better intermethod agreement, indicating a minor degradation of prediction accuracy for the small disturbance approach from the inviscid toward the viscous consideration. The benefit of the more complete flow model was readily apparent in the zeroth-harmonic surface-pressure-coefficient distribution, as well as in the real and imaginary part of the first-harmonic instance. Naturally, the substantial deviation of the latter to its inviscidly obtained counterpart had followed through to the first-harmonic global load coefficients. The established decrease of FLM-SD.NS computational efficiency gain from the lowest to the highest frequency [98] was again witnessed for these two cases. Interestingly, FLM-SD.NS required six and a half times more computation time than FLM-SDEu on average, yet allocated only 5% more memory. A positive angle-of-attack pitching-oscillation case at consistent Mach and Reynolds number was computed as well, demonstrating the FLM-SD.NS capability of accurately predicting the unsteady loading of an asymmetrical flowfield. For this case, the baseline reduced frequency [98] had been considered, yet at double the baseline amplitude. The preceding set of cases was also computed for the baseline Reynolds number [98], allowing FLM-SD.NS prediction accuracy and computational efficiency gain to be assessed as a function of the flowfield viscosity. Its lesser degree, however, did not produce a definitive variation in either aspect. On average,

FLM-SD.NS had merely required double the computation time of FLM-SDEu. Lastly, the capability of FLM-SD.NS to accurately and efficiently render the unsteady loading of a plunging oscillation at zero angle-of-attack was demonstrated. For this case, the Mach number was again maintained, while the baseline Reynolds number [98] and the baseline reduced frequency were considered [59].

Iatrou et al. [59] had further computed NACA 64A010 pitching-oscillation cases in the transonic flow regime based on the test cases CT3 through CT7 experimentally investigated by Davis [34]. Ascending in excitation frequency, these test cases are commonly characterized by a weak shock on both the upper and lower surface. The inherent degree of dynamic nonlinearity, however, varies from test case to test case. Experimental data reveals a symmetrical zeroth-harmonic surface-pressure-coefficient distribution featuring the localized discontinuous recompression associated with the shock, as well as an anti-symmetric real and imaginary part of the first-harmonic instance, which exhibit shock-corresponding peaks. Unfortunately, the flight-realistic Reynolds number of these test cases could not be treated with FLM-SD.NS in its laminar incarnation, entailing that the baseline Reynolds number [98] was yet again considered. A substantially thicker boundary layer had then developed in the FLM-NS-computed reference solution, preventing a shock from emerging at all. Naturally, the FLM-SD.NS-obtained zeroth-harmonic surface-pressure-coefficient distribution was continuous, with the real and imaginary part of the first-harmonic instance having no shock peaks. For all cases, the FLM-SD.NS-obtained first-harmonic surface-pressure-coefficient distribution agreed well to its FLM-NS counterpart. A qualitative comparison between the first-harmonic lift coefficients, as well as the first-harmonic pitching-moment coefficients, however, revealed that minor deviations in the first-harmonic surface-pressure-coefficient distributions had visibly amplified for various frequencies. Overall, the agreement between the two methods with respect to the first-harmonic global load coefficients was still good. FLM-SD.NS computational efficiency gain over FLM-NS was ascertained to be highest for the modified CT3 case; i.e., an order of magnitude. Computations with the complementary inviscid methods had merely been conducted for the modified CT7 case. As this is equivalent to a viscous consideration with an infinite Reynolds number, the obtained zeroth- and first-harmonic surface-pressure-coefficient distributions actually exhibited the characteristics of the weak shock. It was also shown, however, that substantial deviations between the FLM-SDEu and FLM-Eu result exist in the shock region, reflecting the degree of dynamic nonlinearity inherent to the case, yet resolved only by FLM-Eu [59]. The FLM-SD.NS-/FLM-NS-obtained zeroth- and first-harmonic surface-pressure-coefficient distributions for the modified CT6 case, as well as the frequency response function of the first-harmonic global load coefficients, were included by Iatrou [54] in his dissertation of 2009.

Under supervision of the author, Steiner [123] had conducted further investigations

on the basis of the initial NACA 0012 pitching-oscillation case [98], which had considered the low-Reynolds-number incompressible flow regime. The results were documented in 2004. For these investigations, both FLM-SD.NS and FLM-NS in their S/A one-equation-turbulence-model incarnation had already been available; see Pechloff and Laschka [99]. However, neither had yet featured the multigrid acceleration technique. Despite the low Reynolds number, the turbulence model was deactivated for the execution of each method in order to guarantee a strictly laminar treatment. Per investigated case, the obtained local and global loading was compared, as well as the CPU-time ratio between FLM-NS and FLM-SD.NS determined. With regard to FLM-SD-NS convergence behavior, the effect of the numerical dissipation inherent to the implicit pseudotime-integration scheme was demonstrated. NACA 0012 pitching-oscillation cases that rendered the frequency and amplitude response functions of the first-harmonic global load coefficients were initially computed. Retaining the freestream conditions and the zero angle-of-attack of these cases, NACA 0012 plunging-oscillation cases that rendered the frequency response functions of the first-harmonic global load coefficients were computed as well. An amplitude of 1% chord length was employed. Finally, NACA 0012 pitching oscillations in the compressible flow regime were considered. For this purpose, the Mach number was increased to yield a barely transonic flowfield, which, however, remained shockless due to the low Reynolds number. Cases that rendered the frequency response functions of the first-harmonic global load coefficients were again computed, drawing on the reduced-frequency spectrum of the incompressible instances. Overall, it was ascertained that the FLM-SD.NS results agreed excellently with their FLM-NS counterparts for both the pitching- and plunging-oscillation cases. Characteristically, the CPU-time ratio between FLM-NS and FLM-SD.NS was observed to increase with either a decrease in reduced frequency or an increase in amplitude across the respective range. The computational efficiency gain of FLM-SD.NS over FLM-NS was up to three quarters of an order of magnitude [123].

5.1.1.2 Turbulent Cases – Spalart-Allmaras One-Equation Turbulence Model

Beyond the laminar investigations, Pechloff and Laschka [99] presented two-dimensional computations of FLM-SD.NS in its S/A-one-equation-turbulence-model incarnation for the first time in 2004. The NACA 64A010 test case CT8 [34] was drawn on. It generally shares the parameters of the test case CT5, with exception of the pitching amplitude, which is only half of the latter's instance. Consequently, the test case CT8 again features a weak shock on both the upper and lower surface, being equal in strength to its test case CT5 counterpart, yet lesser in the inherent degree of dynamic nonlinearity. With FLM-NS in its laminar incarnation having been extended by the S/A one-equation turbulence model first [99], it had become possible to time-accurately compute the test case CT8 for the actual Reynolds number. Both the obtained zeroth- and first-harmonic surface-

pressure-coefficient distributions agreed well with the experimental data, respectively, reproducing the discontinuous recompression of the shock and the shock-corresponding peaks. For the first-harmonic surface-pressure-coefficient distribution, the experimental postshock reversal of sign was properly rendered as well. Hence, FLM-NS in its S/A-one-equation-turbulence-model incarnation could again serve as the comparative method for FLM-SD.NS. Employing the latter, the amplitude S/A conservative working variable is fully accounted for by default. Accordingly, the amplitude dynamic eddy viscosity is put into full effect. On this basis, the FLM-SD.NS-obtained zeroth- and first-harmonic surface-pressure-coefficient distributions showed good agreement to their FLM-NS counterparts. Naturally, the agreement to the experimental data was then ascertained as being equally well, establishing validity of the small disturbance Navier-Stokes approach for a flight-realistic Reynolds number. Nevertheless, minor deviations between the two results became apparent in the shock region. The FLM-SD.NS-obtained zeroth-harmonic surface pressure coefficient of the discontinuous recompression exhibited a slightly steeper gradient than its FLM-NS counterpart, while the first-harmonic surface-pressure-coefficient shock-peaks were of greater absolute value, yet narrower base [99]. This circumstance, however, is typical for the difference in approach when not considering an extremely small amplitude. It had already been observed by Kreiselmaier and Laschka [71] between FLM-SDEu and FLM-Eu results. The supplemental FLM-SDEu computation of the CT8 case provided by Pechloff and Laschka [99] demonstrated that the viscous consideration in principle improves on the inviscid one: Firstly, the FLM-SDEu-obtained zeroth-harmonic surface pressure coefficient exhibited a discontinuous recompression marginally downstream of the FLM-SD.NS instance, which followed through to the location of the first-harmonic surface-pressure-coefficient shock-peaks. Secondly, the discontinuous recompression emerged at a distinctly steeper gradient, characteristically leading to shock peaks of substantially greater absolute value and narrower base. An FLM-Eu result had not been drawn on for an additional comparison [99].

Concerning the global loading of the CT8 case, Pechloff and Laschka [99] ascertained excellent agreement between the FLM-SD.NS- and FLM-NS-obtained first-harmonic lift coefficient. Substantial deviations, however, were observed between the instances of the first-harmonic pitching-moment coefficient. These deviations were attributed to its sensitivity to both the specified reference axis and the differing evaluation techniques: For FLM-SD.NS, the first-harmonic global load coefficients are computed directly from the first-harmonic local-load-coefficient distributions, while for FLM-NS, they are extracted from the time series of the computed global load coefficients. Establishing the CT8 case as the baseline case, FLM-SD.NS prediction accuracy of the first-harmonic global load coefficients was further investigated for a variation in frequency. Both a decrease toward nil value (the quasi-steady case) and an increase toward an order of magnitude greater

value were realized. For the first-harmonic lift coefficient, FLM-SD.NS and FLM-NS again agreed excellently across the entire spectrum. For the first-harmonic pitching-moment coefficient, however, deviations between the two methods had emerged. In particular, the real part of the progressions substantially diverged toward the quasi-steady state, attributable to an increasing deviation in the rendered shock impulse. Inversely, the imaginary part of the progressions converged toward the quasi-steady state, eventually reaching nil value. From the baseline frequency toward the upper end of the spectrum, the prediction accuracy showed no distinct tendency. The real part of the progressions converged up to a frequency of half an order of magnitude greater value, only to diverge from there. The imaginary part of the progressions behaved equally [99]. An FLM-SDEu-/FLM-Eu-rendered frequency response function had not been drawn on for an additional comparison.

Ultimately, Pechloff and Laschka [99] ascertained an FLM-SD.NS computational efficiency gain over FLM-NS of an order of magnitude for the baseline case under consistent utilization of the multigrid acceleration technique. Under consistent single-grid execution, however, a diminished computational efficiency gain of half an order of magnitude was revealed. This circumstance was attributed to a greater effectivity of the multigrid acceleration technique in conjunction with the pseudotime-integration scheme of FLM-SD.NS than when embedded in the dual-time-stepping scheme of FLM-NS. The ratio of allocated memory between FLM-SD.NS and FLM-NS was shown to be three and a half for the multigrid execution [99]. It is only 13% higher than the ratio of allocated memory between FLM-SD.NS and FLM-NS in their laminar single-grid incarnation [98]. For the frequency variation [99], the CPU-time ratio between FLM-NS and FLM-SD.NS increased strongly nonlinearly toward the quasi-steady case, reaching more than double the baseline instance. Toward the upper end of the spectrum, however, the CPU-time ratio decreased linearly, reducing to approximately half the baseline instance [99]. Across the spectrum, this trend of the FLM-SD.NS computational efficiency gain over FLM-NS was consistent with the one established for the laminar single-grid incarnations [98]. Again, the improving performance of FLM-NS toward the upper end of the spectrum and its deteriorating performance toward the quasi-steady case were mainly made responsible [99]. The investigation of the NACA 64A010 CT8 case and the analysis of the frequency variation were eventually published by Pechloff and Laschka [100] in 2006.

Highlighting the benefit of the viscous consideration over the inviscid one, the NLR 7301 transonic pitching-oscillation test case CT5 experimentally investigated by Zwaan [153] was additionally drawn on by Pechloff and Laschka [100]. In contrast to the NACA 64A010, the NLR 7301 is asymmetric, has a blunt LE, and is characterized by its supercritical/rear-loading feature. The specified Mach and Reynolds number of the test case CT5, in conjunction with the positive angle-of-attack, had led to the emergence of a strong shock on the upper surface. Confined flow separation had occurred in the postshock

and trailing-edge (TE) region as well, a circumstance only reproducible under the viscous consideration. Furthermore, the inviscid consideration is expected to render a shock situated farther downstream than either the experimental or viscously gained location. Even though the NACA 64A010 test case CT8 [34] and the NLR 7301 test case CT5 have the same amplitude, the premise of a predominantly dynamically linear flow response to the excitation was thought to possibly be violated by the latter, due to the strength of the shock and the flow separation [100]. The NLR 7301 test case CT5 was again computed with FLM-SD.NS and FLM-NS in their S/A-one-equation-turbulence-model incarnation, as well as with FLM-SDEu, all in multigrid execution [100].

Regarding the local loading of the CT5 case, Pechloff and Laschka stated that

> [e]xamining the zeroth[-]harmonic [surface-]pressure[-coefficient] distribution, good conformity between the [two] viscous methods and the experiment is established. The characteristic suction plateau on the upper [surface] is reproduced excellently, with minor variations apparent for shock initiation and extent[; in particular,] being slightly farther upstream [than the experimental shock location]. At the point of shock initiation, the [zeroth-harmonic surface-pressure-coefficient] distribution gained through FLM-NS exhibits a [shallower] gradient than the steady-state solution utilized by FLM-SD.NS. Even though [both FLM-SD.NS and FLM-NS] agree very well in their prediction of the rear-loading [surface-]pressure[-coefficient] distribution, the localized postshock increase in suction on the upper [surface] as indicated by the experiment is not reproduced. The boundary layer's strong influence on shock formation becomes evident through the [FLM-SDEu] solution, where the shock is situated 20% farther downstream in comparison to the viscous prediction[s].
>
> Adhering directly to the airfoil's upper [surface], [FLM-SDEu] shock resolution is crisp with a very [steep] gradient [of the discontinuous recompression] and the typical [overextension]. Subsequently, the [FLM-SDEu] progression merges into the pressure recovery curve computed by the viscous methods before deviating again toward the trailing edge. [...] Real and imaginary [part] of the first[-]harmonic [surface-]pressure[-coefficient distribution] are clearly dominated by the upper-[surface] peak indicating the extent of the shock's motion in course of the pitch[ing] oscillation. Agreement of FLM-SD.NS to [FLM-NS] and the experimental data is again quite well for the critical shock region, with the peaks displaying the typical narrower progression with a larger absolute maximum value. However, the occurring differences are far greater than those witnessed in the NACA 64A010 CT8 case, correlating to the deviations already observed in the zeroth harmonics. Further investigating this behavior, Fourier analysis of the [...] FLM-NS [time-series] beyond the first harmonic reveals the presence of higher harmonics in the shock region, contributing in a nonneglectable manner to the [...] evolution of [the surface-]pressure[-coefficient distribution]. As FLM-SD.NS is based on the strict decomposition

> of the unsteady flow into a [linearized time-invariant-]mean and [a simple-harmonic] perturbation part, the dynamically nonlinear influences of these higher harmonics naturally are unaccounted for. Outside the region of shock influence, conformity between FLM-SD.NS, FLM-NS, [...] and the experimental data is excellent. [There,] the convective properties of the flow clearly dominate, as put into evidence by the [first-harmonic surface-pressure-coefficient] distribution provided by FLM-SDEu. Yet, the [FLM-SDEu-]predicted location of the [first-harmonic surface-pressure-coefficient] peak [...] distinctly [differs from the viscous instances in both its real and imaginary part], obviously correlating to the inviscid[ly gained] shock position [...]. Because of the [discontinuous recompression's steep] gradient, FLM-SDEu computes a highly defined [first-harmonic surface-pressure-coefficient] peak with an absolute maximum value far exceeding the other[s]. [100]

Despite having ascertained good agreement between FLM-SD.NS and FLM-NS for the local loading of the CT5 case, Pechloff and Laschka [100] had determined that the evaluation of prediction accuracy with regard to the global loading is challenging. As was known from the NACA 64A010 CT8 case [99, 100], deviations between the FLM-SD.NS- and FLM-NS-obtained local-load-coefficient distributions can become either mitigated or amplified toward the global load coefficients. For the first-harmonic lift coefficient [100], the FLM-SD.NS real part was 12% lesser than the FLM-NS instance. This spread was deemed to be on the margin of good agreement. The FLM-SD.NS imaginary part, on the other hand, was one and a half times the FLM-NS instance. Since the imaginary part is nearly half an order of magnitude smaller in absolute value than the real part, the spread was nevertheless deemed acceptable [100]; i.e., it becomes mitigated in the magnitude of the first-harmonic lift coefficient, while still indicating a negative phase angle of barely double-digit degrees. For the first-harmonic pitching-moment coefficient (reference axis at 25% chord length), the FLM-SD.NS real and imaginary part were, respectively, 23% and 31% lesser in absolute value than the FLM-NS instances. These spreads, however, were deemed to be unacceptable [100]; in particular, because the real and imaginary part reside in the same order of magnitude. With hindsight, the consideration of the pitch axis (specified at 40% chord length) as the reference axis could have led to a better agreement between FLM-SD.NS and FLM-NS: As the first-harmonic surface-pressure-coefficient peak is situated close to the pitch axis, existing deviations would become mitigated through less leverage, or even compensated through leverage with an opposing sense of rotation. Additionally, the imaginary part would have been indicative of the free pitching oscillation's stability behavior. The viscously obtained global load coefficients had not been compared with their FLM-SDEu and experimental counterparts.

For the CT5 case, Pechloff and Laschka [100] ascertained the computational efficiency gain of FLM-SD.NS over FLM-NS to be a factor of three, which is substantially lower than

for the NACA 64A010 CT8 case. Surprisingly, an FLM-SD.NS solution had been achieved without resorting to extraordinary techniques. Regions of flow separation inherent to the reference solution are known to destabilize the conventional pseudotime integration of the small disturbance Navier-Stokes equations under the S/A-one-equation-turbulence-model closure [19, 20]. In this regard, neither the limitation of the amplitude S/A conservative working variable nor the FEVA would have been available in the employed FLM-SD.NS version as a remedy.

Pechloff and Laschka [100] had further investigated the sensitivity of the local load coefficients to the employed spatial discretization for both the NACA 64A010 CT8 and the NLR 7301 CT5 case. It was stated that the

> influence on the FLM-SD.NS prediction is primarily an issue of quality in regard to the supplied [reference] solution. Concerning the transonic [viscous] flow regime, good resolution of any occurring discontinuity becomes imperative because the FLM-NS[-]computed location and intensity [...] directly affects the FLM-SD.NS[-computed amplitude solution]. With this in mind, the reference grids respectively employed in [the] NACA 64A010 CT8 and NLR 7301 CT5 [computations] were [already] optimized for capturing the steady-state shock as best as possible. [100]

After a substantially coarser grid-pair had been generated for each the NACA 64A010 CT8 and NLR 7301 CT5 case [100], FLM-NS computations toward a reference solution were again conducted. For the former, it revealed a discontinuous recompression with a slightly shallower gradient than obtained with the baseline reference grid. For the latter, however, both a farther upstream location and a shallower gradient had emerged. On the basis of each reference solution, a new amplitude solution was computed with FLM-SD.NS, though, only converging for the NACA 64A010 CT8 case [100]. In this regard, Pechloff and Laschka ascertained that

> the [shallower] gradient [of the discontinuous recompression] seen in the [zeroth-harmonic surface-]pressure[-coefficient] distribution leads to a decrease of the [first-harmonic surface-]pressure[-coefficient] peak[s' absolute] value by approximately 25% [...], while the extent of the peak region becomes marginally wider. This correlation between [the zeroth-harmonic] and [the first-harmonic surface-pressure-coefficient] is characteristic for FLM-SD.NS, minor [variations on] the [rendered] steady-state shock [...] affecting the order of magnitude smaller [shock impulse] in a distinguishable manner. [100]

The divergence of the amplitude solution for the NLR 7301 CT5 case was attributed to an unsatisfactory spatial resolution of the amplitude S/A conservative working variable near the airfoil's TE [100].

Under supervision of the author, Steiner [123] had conducted further investigations of airfoil pitching oscillations for flight-realistic Reynolds numbers. The results were docu-

mented with the results of his low-Reynolds-number investigations in 2004. Again, FLM-SD.NS and FLM-NS in their S/A one-equation-turbulence-model incarnation [99] had been employed, which, however, had not yet featured the multigrid acceleration technique. Per investigated case, the obtained local and global loading was compared, as well as the CPU-time ratio between FLM-NS and FLM-SD.NS determined. Initially, the NACA 64A010 subsonic test cases CT2 and DI37 experimentally investigated by Davis [34] were considered, featuring, respectively, the reduced frequency of the transonic test case CT8 and a two and a half times higher instance. Furthermore, the transonic test cases CT3, CT5, CT6, and CT7 were drawn on to render frequency response functions of the first-harmonic global load coefficients. The reduced-frequency spectrum was extended beyond the CT7 case through three cases, which, however had no experimental counterparts. The highest reduced frequency was 40 times the CT3 case instance. On the basis of the CT8 case, an amplitude response function was also computed; i.e., by varying the amplitude to one half, to one and a half times, and to double the CT8 case instance. Additionally, the NLR 7301 subsonic test case CT1 experimentally investigated by Zwaan [153] was considered, as well as the NLR 7301 transonic test case CT5 discussed precedingly. For the latter, an initial multigrid-capable version of FLM-SD.NS in its S/A one-equation-turbulence-model incarnation had been employed. Lastly, a parabolic airfoil of 3% relative thickness (at 50% chord length) was considered at zero angle-of-attack in the supersonic flow regime, which, however, had no experimental counterpart. Rather, the flow conditions conformed to those employed by Kreiselmaier [70] in the original FLM-SDEu/FLM-Eu investigations. Cases that rendered the frequency and amplitude response functions of the first-harmonic global load coefficients were computed [123].

Steiner [123] ascertained that the implementation of the S/A one-equation turbulence model allowed for a suitable prediction of the zeroth- and first harmonic surface-pressure-coefficient distributions with respect to the experimental instances. For the considered sub- and supersonic cases, the FLM-SD.NS-obtained local loading showed excellent agreement to its FLM-NS counterpart. For the transonic cases, on the other hand, notable deviations between the two methods occurred in the shock region. It was demonstrated, however, that the consideration of successively smaller amplitudes or higher frequencies brought the FLM-NS result into better conformity with the FLM-SD.NS instance, as the shock motion became more confined. Overall, FLM-SD.NS was deemed to be very well suited to predict the zeroth- and first-harmonic global load coefficients. For the NACA 64A010 transonic cases, the CPU-time ratio between FLM-NS and FLM-SD.NS was again observed to increase with either a decrease in reduced frequency or an increase in amplitude across the respective range. For the parabolic airfoil cases, a minimum CPU-time ratio was exhibited at the median reduced frequency, with the CPU-time ratio still monotonously increasing across the amplitude range. The computational efficiency gain of FLM-SD.NS

over FLM-NS was up to an order of magnitude [123].

5.1.1.3 Turbulent Cases – Baldwin-Lomax Algebraic Turbulence Model and Comparison

By 2004 Iatrou et al. [57] had independently extended FLM-SD.NS in its laminar incarnation with a FEVA formulation of the B/L algebraic turbulence model. Cvrlje's [31] original implementation of the B/L algebraic turbulence model in FLM-NS had served as the template. Naturally, this FLM-NS incarnation was then employed to supply the appropriate reference solution, as well as to render the comparative dynamically fully nonlinear solution. The implicit pseudotime-integration scheme already inherent to FLM-SD.NS in its laminar incarnation [98] had not been retained for its B/L algebraic turbulence model incarnation. Rather, Iatrou et al. [57] resubstituted the explicit instance inherent to the original FLM-SDEu [70]. This FLM-SDEu incarnation was also utilized to highlight the advantages of the viscous consideration over the inviscid one. All three methods were only capable of single-grid execution. The NLR 7301 transonic flap-oscillation test case CT11 experimentally investigated by Zwaan [153] was primarily drawn on to substantiate the validity of this particular small disturbance Navier-Stokes approach [57]. Test case CT11 has a Mach number, Reynolds number, and an angle of attack that are approximately equal to the instances of test case CT5, again yielding a strong shock on the upper surface, with confined flow separation occurring in the postshock and TE region. In contrast to the test case CT5, however, merely the simple harmonic oscillation of the flap induces the organized unsteadiness of the flowfield, and thus the shock motion per se [153]. With most of the airfoil being static, the numerical embodiment for the flap's amplitude deflection was easily rendered by locally deforming the surface of the reference instance. The subsequent regeneration of the grid had then provided the extremum grid, establishing the required grid-pair [57]. The investigation of the test case CT11 constituted the first FLM-SD.NS treatment of a deforming body, instead of the customary rigid-body deflection. The amplitude of the test case CT11 is double the pitching amplitude of test case CT5, however, with the reduced frequency being approximately one third of the latter's instance [153]. Again, a predominantly dynamically linear flow response is not necessarily given.

Regarding the CT11 case, Iatrou et al. [57] established overall good conformity between FLM-SD.NS and FLM-NS in their B/L-algebraic-turbulence-model incarnation for both the zeroth- and first-harmonic surface-pressure-coefficient distribution. Deviations between the particular instances, however, were apparent in the shock region. Similar to the investigation of the CT5 case by Pechloff and Laschka [100], the FLM-SD.NS result [57] exhibited a steeper shock gradient in the zeroth-harmonic surface-pressure-coefficient distribution than its FLM-NS counterpart. Correspondingly, first-harmonic surface-pressure-

coefficient peaks of greater absolute value yet narrower base had emerged [57]. Considering that merely a FEVA had been employed, FLM-SD.NS can be ascertained to have reproduced the FLM-NS result quite satisfactorily in the shock region. Furthermore, both FLM-SD.NS and FLM-NS had rendered the expected marginal secondary peak for the real part of the first-harmonic surface pressure coefficient at the flap hinge (75% chord length), and agreed excellently. As observed by Iatrou et al. [57], the viscously gained surface-pressure-coefficient distributions predominantly showed good conformity to the experimental data. In the shock region, the limited experimental resolution left it inconclusive whether FLM-SD.NS or FLM-NS offered the better prediction. Contrarily, FLM-SDEu had again rendered a shock situated farther downstream than either the experimental or viscously gained location. Of all surface-pressure-coefficient distributions, the FLM-SDEu-obtained instance exhibited the steepest zeroth-harmonic shock gradient, as well as corresponding first-harmonic peaks of the greatest absolute value and narrowest base. Outside of the shock region, the deviation of FLM-SDEu was only marginal. It became more pronounced, though, in the lower-surface zeroth-harmonic toward the TE [57]. Pechloff and Laschka [100] had observed similar characteristics for the FLM-SDEu result of the CT5 case.

Defining the CT11 case as the baseline frequency case, Iatrou et al. [57] had computed two additional flap-oscillation cases, one at half and one at double the baseline frequency. Each case retained the freestream conditions and angle-of-attack of the baseline case. Originally, these two cases had been experimentally investigated by Zwaan [153], however, with merely the first-harmonic lift- and pitching-moment coefficient having been documented. Hence, Iatrou et al. [57] limited their investigation to these instances as well. Rendering frequency response functions, the FLM-SD.NS-obtained first-harmonic global load coefficients agreed very well with their experimental counterparts. The progressions were qualitatively reproduced in both their real and imaginary part. Surprisingly, each FLM-NS-obtained progression deviated quite clearly, although confirming the particular trend. This deviation was most pronounced for the imaginary part of the first-harmonic lift coefficient. In this regard, the FLM-NS-obtained progression nearly coincided with the FLM-SDEu-obtained instance. Each FLM-SDEu-obtained progression had a substantial offset from its experimental counterpart, however, still rendering the particular trend. The computational efficiency gain of FLM-SD.NS over FLM-NS was ascertained to be less than half an order of magnitude. Unexpectedly, the CPU-time ratio between FLM-NS and FLM-SD.NS increased from two to three from the lowest to the highest frequency [57]. The investigations of airfoil pitching oscillations in the sub- and transonic viscous flow regime [98, 59, 100], on the other hand, had shown a monotonously decreasing CPU-time ratio for an increasing frequency, albeit employing the methods' laminar and S/A-one-equation-turbulence-model incarnations. It needs to be taken into account, however, that

the CPU-time ratios given by Iatrou et al. [57] had resulted from an implicit (FLM-NS) to explicit (FLM-SD.NS) solution-technique comparison. Next to the differing oscillation type, this may have contributed to the reversed behavior of the CPU-time ratio across the frequency spectrum. The memory-requirement ratio between FLM-SD.NS and FLM-NS in their B/L-algebraic-turbulence-model incarnation was not reported. FLM-SD.NS solution stability was not addressed either, despite having utilized a reference solution with a region of separated flow. This may not have been an issue, though, as the B/L algebraic turbulence model had merely been implemented in a FEVA instance. The preceding investigation of the CT11 case and of the frequency response functions were included by Iatrou [54] in his dissertation of 2009, supplemented by FLM-Eu results.

Iatrou et al. [57] further revisited the NACA 64A010 transonic pitching-oscillation test case CT4 [34], which had initially been investigated with FLM-SD.NS in its laminar incarnation [59]. To recall, the flight-realistic Reynolds number of this test case had not been treatable, and a substantially lower instance was considered instead. Hence, the weak shock on both the upper and lower surface actually characterizing the test case had not emerged [59]. FLM-SD.NS and FLM-NS in their B/L-algebraic-turbulence-model incarnation, on the other hand, allowed for the shocks to be properly rendered [57]. Outside of the shock region, FLM-SD.NS again showed very good conformity to FLM-NS for both the zeroth- and first-harmonic surface-pressure-coefficient distributions, while also agreeing to the experimental data. Deviations between FLM-SD.NS and FLM-NS were apparent for the discontinuous recompression and the corresponding shock peaks. FLM-SD.NS had rendered a steeper gradient for the former as well as a greater absolute value and narrower base for the latter [57]. In comparison to the test case CT8 investigated by Pechloff and Laschka [100], which has equal freestream conditions and angle of attack, the deviations had increased. The test case CT4, however, has half the frequency and double the amplitude, entailing a higher inherent degree of dynamic nonlinearity. This circumstance was only accounted for by FLM-NS, and had led to the increased deviation between the two results. Pursuant to Iatrou et al. [57], the limited experimental resolution in the shock region again disallowed a conclusive assessment of the prediction quality. Regarding the inviscid consideration, FLM-SDEu had rendered both a zeroth- and first-harmonic surface-pressure-coefficient distribution that deviated only minutely from the viscously obtained instances outside of the shock region. The shocks themselves, however, had been predicted distinctly downstream of the viscously obtained instances and at greater strength. For the zeroth-harmonic surface-pressure-coefficient distribution, the gradient of the discontinuous recompression had become steeper, while for its first-harmonic counterpart the shock peaks had increased in absolute value. Interestingly, the particular experimental data point in the shock region indicated that the FLM-SDEu-predicted shock initiation was the most accurate, yet it allowed no equal assessment with

respect to the shock peaks [57]. The global loading had not been investigated. The computational efficiency gain of FLM-SD.NS over FLM-NS was ascertained to be a factor of two [57].

The preceding investigation of the NACA 64A010 CT4 case was included by Iatrou [54] in his dissertation of 2009. It was supplemented by FLM-SD.NS/FLM-NS zeroth- and first-harmonic surface-pressure-coefficient distributions obtained with the S/A one-equation turbulence model: Again, deviations between the particular instances were merely witnessed in the shock region. Characteristically, FLM-SD.NS had rendered a steeper gradient for the discontinuous recompression than FLM-NS, as well as a greater absolute value and narrower base for the corresponding shock peaks. The shocks themselves had been predicted slightly downstream of the instances obtained with the B/L algebraic turbulence model. Regarding FLM-SD.NS, a steeper gradient had been rendered for the discontinuous recompression than with the B/L algebraic turbulence model. Correspondingly, the shock peaks were of greater absolute value, yet of equally narrow base. Regarding FLM-NS, the rendered gradient, on the other hand, exhibited conformity to the instance obtained with the B/L algebraic turbulence model. The shock peaks did so as well, both in their characteristically lower absolute value and wider base [54].

Iatrou [54] additionally investigated the first-harmonic global load coefficients for the CT4 case. The CT5, CT6, and CT7 cases [34], which had initially been investigated with FLM-SD.NS in its laminar incarnation [59], were revisited as well. This allowed frequency response functions to again be rendered. For the first-harmonic lift coefficient [54], the FLM-SD.NS progression obtained with the B/L algebraic turbulence model showed very good conformity to the FLM-NS instance in the real part, except at the lowest frequency. In the imaginary part, however, an overall deviation was evident. Nevertheless, FLM-SD.NS had reproduced the FLM-NS trend. The FLM-SD.NS progression obtained with the S/A one-equation turbulence model, on the other hand, showed excellent conformity to the FLM-NS instance in both the real and imaginary part. Interestingly, the progressions obtained with the S/A one-equation turbulence model conformed to the FLM-NS progression obtained with the B/L algebraic turbulence model. Supplemental FLM-SDEu/FLM-Eu computations demonstrated that the viscous consideration had improved only marginally on the inviscid one. Generally, the FLM-SDEu progression agreed very well with the FLM-Eu instance. Deviations were merely exhibited toward the lower end of the spectrum [54].

For the first-harmonic pitching-moment coefficient [54], a substantial variation in the real part of the rendered progressions was observed across the entire spectrum. All instances, however, concurred in their trend. Whereas the FLM-SD.NS and FLM-NS real part exhibited conformity at the highest frequency for both turbulence models, deviations increased significantly toward the lower end of the spectrum, yet less pronounced for the

S/A one-equation turbulence model. Regarding FLM-NS, the real part obtained with the S/A one-equation turbulence model again conformed to its B/L-algebraic-turbulence-model counterpart. Surprisingly, the FLM-SDEu and FLM-Eu real part were rendered at a substantial offset to the viscously gained instances. The deviation between the FLM-SDEu and FLM-Eu real part behaved inversely across the spectrum. In the imaginary part of the rendered progressions, all instances again concurred in their trend. The FLM-SD.NS imaginary part obtained with the B/L algebraic turbulence model deviated substantially from its FLM-NS counterpart across the entire spectrum. With respect to the deviation witnessed in the imaginary part of the first-harmonic lift coefficient, an amplification had occurred. For the S/A one-equation turbulence model, the FLM-SD.NS and FLM-NS imaginary part exhibited conformity. Regarding FLM-NS, the imaginary part obtained with the S/A one-equation turbulence model again conformed to its B/L-algebraic-turbulence-model counterpart. The FLM-SDEu imaginary part showed only marginal deviation to the FLM-SD.NS instance obtained with the S/A one-equation turbulence model, while agreeing well to its FLM-Eu counterpart. They merely began to deviate toward the lower end of the spectrum, as already observed for the imaginary part of the first-harmonic lift coefficient [54]. A comparison with experimental data had not been made, nor were CPU-time ratios between corresponding dynamically fully nonlinear and small disturbance methods given.

5.1.2 Preceding Three-Dimensional Investigations

Preceding the dissertation at hand, the three-dimensional investigations conducted by the various researchers can be discerned on the basis of the treated geometry. Cases for two low-aspect-ratio wings (the NCDW [12] and the FTDW [120, 132, 119]) and for two high-aspect-ratio wings (the BAC-13 wing [122] and the LANNW [154]), as well as a case for a nacelle-pylon-rectangular-wing assembly, were considered. The FTDW cases, however, are not elaborated on herein, as they are more application-oriented.

5.1.2.1 Low-Aspect-Ratio Wing Cases

The NCDW experimentally investigated by Bennett and Walker [12] is constituted by a trapezoidal semi-span planform, with a 50 deg swept LE and an unswept TE. Across the semi-span, its volume is rendered by a symmetrical circular-arc section of constant 6% relative thickness ($x_d/c = 0.5$), yielding both a sharp LE and TE, while remaining untwisted [103]. Since Bennett and Walker [12] strictly considered pitching and flap oscillations without sideslip, it had sufficed to employ a wall-mounted semi-span model. As realized in the NASA Langley Transonic Dynamics Tunnel, the flow conditions ranged from the subsonic to the low supersonic regime. Heavy gas was utilized as the test medium

in order to coexistently realize compressible and viscous similarity to actual flight conditions. The parametric studies encompassed the variation of the Mach number, the angle of attack, as well as the oscillation frequency and amplitude, especially with the aim of accentuating the flow response in the transonic regime. This was facilitated by the NCDW geometry. Approaching the speed of sound, the specified relative thickness induces a pronounced aft shock. Additionally, the LE's high sweep and sharpness initiates a vortex for an angle of attack as low as three degrees. Referred to as the LE vortex (LEV), a coincidental occurrence with a shock becomes possible per se. From the entirety of experimentally investigated cases a select number had been included in the campaign report as computationally relevant test cases [12]. Designated the dynamic test cases [12], Table 4 and Table 5, the particular raw data measured at five instrumented spanwise sections had been reduced to the first-harmonic surface-pressure-coefficient distribution, with the real and imaginary part tabulated as normalized with the oscillation amplitude in radians. Supplementally, static test cases [12], Table 3, had been provided. A subset correlates to the dynamic test cases; i.e., each instance was experimentally investigated at flow conditions that conform to those of a particular array of dynamic test case, yet without the oscillation being imposed. The measured raw data was processed to yield the steady surface-pressure-coefficient distribution at each spanwise section [12].

An early utilization of the compiled test cases came in 2003. As the original FLM-NS incarnation had been upgraded with the S/A one-equation turbulence model [121] and the multigrid acceleration technique, the validity of the approach needed to be resubstantiated. For this purpose, Markmiller [82] conducted FLM-NS computations of the static test cases 40S1 (a subsonic case), 90S1 (a weak shock case), 90S38 (a medium-strength shock/LEV case), 96S1 (a strong shock case), as well as 112S1 and 112S6 (two supersonic cases) [12]. Additionally, FLM-NS computations of the pitching-oscillations test case 40D5 (a subsonic case), 90D6 (a weak-shock case), and 112D5 (the supersonic case) [12] were realized. Due to the limited processing power at that time, however, merely three oscillations discretized with eight physical time intervals could be considered for the 40D5 and the 112D5 case, as well as only two oscillations for the case 90D6. Furthermore, the dual-time-stepping scheme needed to be reduced to first-order accuracy to remain stable. For all these case, Markmiller [82] extensively investigated FLM-NS prediction accuracy and convergence behavior under supervision of the author. An FLM-SD.NS computation of each dynamic test case was also performed by Markmiller [82], employing the laminar single-grid incarnation as available then; i.e., neither accounting for the amplitude nor the linearized time-invariant-mean dynamic eddy viscosity. Each underlying steady-state RANS solution, however, was rendered by FLM-NS under a fully turbulent consideration. Hence, the FLM-SD.NS computation did take into account a linearized time-invariant-mean velocity profile in the boundary layer that corresponded to the specified Reynolds

number. Naturally, this practice differs from the FEVA per se. Despite the laminar FLM-SD.NS computation, very good agreement of the obtained first-harmonic surface-pressure-coefficient distribution to its FLM-NS counterpart was ascertained for both the 40D5 and the 112D5 case. Generally, good agreement to the experimental data was established as well. For the 90D6 case, however, only satisfactory agreement between the FLM-SD.NS- and the FLM-NS-obtained first-harmonic surface-pressure-coefficient distribution could be ascertained. Whereas the real parts conformed well, the imaginary parts distinctly deviated. For both methods, agreement to the experimental data was likewise only satisfactory. With respect to the global loading, however, very good agreement between the two methods was determined for the real part of the first-harmonic lift coefficient, as well as for the real part of the first-harmonic pitching-moment coefficient (c_M reference axis given through $x_M/c_r = 0.25$), in all three cases. Substantial deviations were generally witnessed for the corresponding imaginary part. It was typically gained an order of magnitude smaller than the real part, which actually rendered the deviation tolerable. Since both the flow consideration and the employed solution technique still differed between FLM-SD.NS and FLM-NS, the true computational efficiency gain could not yet be established [82].

In 2004 Allen et al. [4] further utilized the 90S1 and the 96S1 case, as well as the 92S1 case (a medium-strength shock case) [12], to put FLM-NS in its S/A-one-equation-turbulence-model incarnation into comparison with its original B/L-algebraic-turbulence-model incarnation. Computed surface-pressure-coefficient distributions were investigated for a median- and an outer-span station, which, respectively, represent a flap-inboard-edge and a flap-median station as well. It revealed only a marginal deviation between the FLM-NS incarnations for the 90S1 and the 96S1 case, yet a notably greater deviation for the 92S1 case in the shock region. Additionally, FLM-NS computations of the flap-oscillation test case 92D36 (a medium-strength shock case) [12] were conducted. The resultant first-harmonic surface-pressure-coefficient distributions were investigated for the specified psan stations, overall yielding good conformity between the FLM-NS incarnations. Similar to the 92S1 case, distinct deviations were witnessed in the shock region, as well as at the span stations' intersection with the flap-hinge line. For the corresponding first-harmonic surface-pressure-coefficient peak, FLM-NS in its S/A-one-equation-turbulence-model incarnation had rendered a lower absolute value than its B/L-algebraic-turbulence-model counterpart. For the novelly considered 92S1 and 92D36 case, agreement of the computational results to the experimental data had again been ascertained to be generally well. Global loading had not been investigated for any of the cases [4].

On the preceding basis, FLM-SD.NS computations of the 92D36 case were presented by Iatrou et al. [55] in 2005. First-harmonic surface-pressure-coefficient distributions obtained from both the S/A-one-equation-turbulence-model incarnation and the

B/L-algebraic-turbulence-model incarnation were put into comparison with their FLM-NS counterparts. The FLM-SD.NS results had been obtained under the pertinent FEVA. Naturally, a comparison between the two FLM-SD.NS incarnations became possible as well. Investigations were conducted for the inner-span and inboard median-span station, as well as for the flap-inboard-edge and flap-median station. Overall, good conformity between FLM-SD.NS and FLM-NS in their S/A-one-equation-turbulence-model incarnation, as well as in their B/L-algebraic-turbulence-model incarnation, had been established. Distinct deviations were merely witnessed for the shock region and the flap hinge-line intersection of the flap-median station. FLM-SD.NS predicted dual peaks of the first-harmonic surface pressure coefficient, where FLM-NS predicted a single instance. Notably, the prediction accuracy exhibited by FLM-SD.NS in its S/A-one-equation-turbulence-model incarnation with respect to its FLM-NS counterpart was observed to be similar to the instance exhibited by FLM-SD.NS in its B/L-algebraic-turbulence-model incarnation. The benefit of the viscous consideration had been shown by additionally providing FLM-SDEu/FLM-Eu results, albeit computed with a coarser grid-pair. For all span stations, either inviscid prediction of the first-harmonic surface-pressure-coefficient peak in the shock region was distinctly greater in absolute value than the particular viscous instance. The FLM-SDEu and FLM-Eu results agreed well for the inner-span and inboard median-span station, equaling the conformity between FLM-SD.NS and FLM-NS. For the flap-inboard-edge and flap-median station, on the other hand, the deviation between the FLM-SDEu and FLM-Eu results was far more substantial than the deviation witnessed between the particular FLM-SD.NS and FLM-NS results. As with FLM-SD.NS, however, FLM-SDEu consistently rendered a first-harmonic surface-pressure-coefficient peak of greater absolute value than its dynamically fully nonlinear counterpart. For any method, the flap-local assessment of the prediction accuracy with respect to the experiment was not feasible. Merely a single experimental data point was provided in proximity to each flap hinge-line intersection. An intermethod comparison of global loading had not been conducted [55].

Ultimately, Iatrou et al. [55] were able to establish the true computational efficiency gain of FLM-SD.NS over FLM-NS in their S/A one-equation-turbulence-model incarnation at an order of magnitude. Both methods had equivalently employed the multigrid-accelerated implicit solution technique. In contrast, the comparison between FLM-SD.NS and FLM-NS in their B/L-algebraic-turbulence-model incarnation, as well as between FLM-SDEu and FLM-Eu, yielded a computational efficiency gain of less than half an order of magnitude. However, both FLM-SD.NS in its B/L-algebraic-turbulence-model incarnation and the employed FLM-SDEu were limited to the explicit solution technique. Thus, the comparison made to the implicit solution technique inherent to their dynamically fully nonlinear counterparts again produced CPU-time ratios that were skewed to

the worse. Furthermore, FLM-SD.NS/FLM-NS in their B/L-algebraic-turbulence-model incarnation, as well as FLM-SDEu/FLM-Eu, were only capable of single-grid execution [55]. From the investigations conducted by Pechloff and Laschka [100] for the NACA 64A010 CT8 case, though, it is known that employing multigrid acceleration can benefit a small disturbance method more than its dynamically fully nonlinear counterpart. Consequently, the CPU-time ratios obtained from the explicit to implicit comparison [55] hold potential to be increased; i.e., by likewise realizing a multigrid-capable incarnation of each method. Results from FLM-SD.NS/FLM-NS in their B/L-algebraic-turbulence-model incarnation, as well as from their FLM-SDEu/FLM-Eu counterparts, had been additionally documented by Allen et al. [3] and Iatrou et al. [56]. The latter report also included the results from FLM-SD.NS/FLM-NS in their S/A-one-equation-turbulence-model incarnation presented in [55]. The 92D36 case is again considered in the dissertation at hand.

Beyond the FEVA, Pechloff and Laschka [101] presented three-dimensional FLM-SD.NS computations that fully accounted for the amplitude S/A conservative working variable in 2008. Again, NCDW pitching oscillations had been considered; in particular, the test cases 90D5 (a weak shock case), 90D29 (the medium-strength shock/LEV case), and 94D5 (a strong shock case) [12]. For each case, FLM-SD.NS-obtained first-harmonic surface-pressure-coefficient distributions were compared with their FLM-NS counterparts, corresponding FLM-SDEu/FLM-Eu results, and experimental data. Merely an inner- and an outer-span station were focused on. An intermethod comparison of the global loading, including a stability assessment with respect to the equivalent free pitching oscillation, had been conducted as well [101]. Subsequently, a frequency variation on the 94D5 case was performed. It was further shown that the instated limitation of the amplitude S/A conservative working variable was an effective means of maintaining FLM-SD.NS solution convergence for a reference solution with inherent flow separation. Extending the investigations of [101] in this manner, eventually led to publication by Pechloff and Laschka [103] in 2010. A grid sensitivity study for the FLM-SD.NS-computed global load coefficients was also included. As summarized,

> [o]verall, [FLM-SD.NS] results are in good agreement with [results] provided by [...] FLM-NS, as well as available experimental data. Reductions in computation time, up to an order of magnitude, in relation to FLM-NS are observed. Limitations of the small disturbance approach, however, become apparent for the [medium-strength shock/LEV] case, in which higher-order harmonics are far less negligible in the flow's response to the excitation. [103]

The benefit of the viscous consideration had distinctly emerged for the strong shock cases, where the equivalent free pitching oscillation was assessed to be in a damped state across the frequency variation. Under the inviscid consideration, however, a reversal from an amplified to a damped state was assessed. The investigations of [103] have been incorporated

into the dissertation at hand.

5.1.2.2 High-Aspect-Ratio Wing Cases

By 2006 Iatrou et al. [56] had merged the FEVA-formulated B/L algebraic turbulence model into FLM-SD.NS in its S/A-one-equation-turbulence-model incarnation. This enabled the option of either turbulence model within one FLM-SD.NS incarnation [56]. Employing it, Iatrou [54] substantiated the validity of the small disturbance Navier-Stokes approach for the high-aspect-ratio wing in his dissertation of 2009. Particularly, a transonic pitching-oscillation test case of the BAC 3-11 wing experimentally investigated by Steimle et al. [122] was drawn on. It featured a pronounced shock on the upper surface. The acquired surface-pressure-coefficient distributions, however, were limited to a single inner-span station. Hence, the investigation conducted by Iatrou [54] was primarily an intermethod comparison. Two plunging-oscillation cases of the BAC 3-11 wing at equal freestream conditions yet higher reduced frequency were considered also, but had no experimental counterparts. Comparing the first-harmonic surface-pressure-coefficient distributions for six span stations [54], overall good conformity between the instances obtained with FLM-SD.NS and FLM-NS under the S/A-one-equation-turbulence-model option had been ascertained. Contrarily, substantial deviations had become apparent between the first-harmonic surface-pressure-coefficient distributions obtained with FLM-SD.NS and FLM-NS under the B/L-algebraic-turbulence-model option, primarily in the shock region. Naturally, this disparity in FLM-SD.NS prediction quality followed through to the global loading. As the FLM-NS predictions agreed well with each other per se, it was assumed that these deviations were attributable to the FEVA formulation of the B/L algebraic turbulence model. Investigating this circumstance, the plunging-oscillation cases were recomputed with FLM-SD.NS under the S/A-one-equation-turbulence-model-FEVA option. The resultant global load coefficients were then put into comparison with their B/L-algebraic-turbulence-model counterparts, establishing remarkable agreement at the baseline reduced frequency. Deviations were still exhibited at the higher reduced frequency, however, less pronounced than before. For the pitching-oscillation case, the computational efficiency gain of FLM-SD.NS over FLM-NS was ascertained to be a factor of two and a half under the S/A-one-equation-turbulence-model option, while being an order of magnitude under the B/L-algebraic-turbulence-model option. For the plunging-oscillation cases, on the other hand, the computational efficiency gain had surprisingly inverted under the S/A-one-equation-turbulence-model option; i.e., to a factor of one half. It normalized, though, under the B/L-algebraic-turbulence-model option, but was still only a factor of two. The benefit of the viscous consideration was again clearly demonstrated through the inclusion of FLM-SDEu/FLM-Eu results, albeit most prominently apparent in the global load coefficients of the pitching-oscillation case. The computational efficiency gain

of FLM-SDEu over FLM-Eu was determined to be three-quarters of an order of magnitude for the pitching-oscillation case, yet merely a factor of two, on average, for its plunging counterparts [54].

Iatrou [54] additionally considered the LANNW LE shock/attached-flow pitching-oscillation test case CT2, as well as the LANNW test case CT5, where experimental surface-pressure-coefficient distributions are given for six span stations [154]. For either case, deviations between the computations and the experiment emerged to some extent for both the location and value of the first-harmonic surface-pressure-coefficient's shock-peak. However, a limited number of experimental data points in the shock region restricted the assessment per se. Typically, the particular FLM-SD.NS predictions were corroborated by their FLM-NS counterparts. FLM-Eu/FLM-SDEu results again clearly demonstrated the benefit of the viscous consideration. The first-harmonic surface-pressure-coefficient peak of the LE shock (for the CT2 case) and of the supersonic-flow-terminating shock (for the CT5 case) was predicted farther aft and greater in absolute value. Considering the global load coefficients, the intermethod comparison for the CT2 case revealed only minor variations. Particularly, the deviation in the first-harmonic surface-pressure-coefficient distributions witnessed between the inviscid considerations and their viscous counterparts had been compensated toward the first-harmonic global load coefficients. For the CT5 case, the global load coefficients obtained with FLM-SD.NS and FLM-NS under the S/A-one-equation-turbulence-model option again agreed well, also to the instances obtained with FLM-NS under the B/L-algebraic-turbulence-model option. The global load coefficients obtained with FLM-SD.NS under the B/L-algebraic-turbulence-model option, on the other hand, deviated significantly, even though the first-harmonic surface-pressure-coefficient distributions deviated only marginally. A similar behavior had been seen in the investigation of the BAC 3-11 wing cases, and was shown to arise from the FEVA formulation of the B/L-algebraic-turbulence-model option. The recomputation of the CT5 case with FLM-SD.NS under the S/A-one-equation-turbulence-model-FEVA option again corroborated this circumstance. Notably, either FEVA led to a more substantial deviation than seen for the BAC 3-11 wing cases. They rendered a reversal in phase for the pitching-moment coefficient; i.e., predicting a lagging pitching-moment coefficient where the dynamically fully nonlinear methods had established a leading instance. The computational efficiency gain of the particular small disturbance method over its dynamically fully nonlinear counterpart conformed for the CT2 and CT5 case. Under the S/A-one-equation-turbulence-model option a factor of three was ascertained, agreeing with the computational efficiency gain exhibited in the investigation of the BAC 3-11 wing pitching-oscillation case. Under the B/L-algebraic-turbulence-model option, on the other hand, a factor of four was ascertained, having having contracted from the order of magnitude witnessed previously. In contrast, the computational efficiency gain of FLM-

SDEu over FLM-Eu had increased from three-quarters of an order of magnitude to an order of magnitude per se. An additional frequency variation on the basis of the CT2 case, as well as the CT5 case, rendered a decreasing computational efficiency gain of the particular small disturbance method over its dynamically fully nonlinear counterpart with increasing frequency. Notably, for substantially higher frequencies the CPU-time ratio between FLM-NS and FLM-SD.NS under the B/L-algebraic-turbulence-model option converged toward the otherwise distinctly lower instance under the S/A-one-equation-turbulence-model option. Ultimately, each CPU-time ratio reduced to parity. Vice versa, a single decrement from the baseline frequencies, disclosed an increase in computational efficiency gain, with either CPU-time ratio being about half an order of magnitude [54]. Generally, this behavior of the computational efficiency gain over the frequency spectrum was consistent with the instance observed by Pechloff and Laschka [100] on the basis of the NACA 64A010 CT8 case. The high-aspect-ratio wing cases investigated by Iatrou [54] had all been computed without utilizing the methods' multigrid acceleration capability.

In 2010 Pechloff and Laschka [102] had expanded FLM-SD.NS in its S/A one-equation-turbulence-model incarnation to feature a small disturbance formulation of the Wilcox k-omega two-equation turbulence model [138] as well. The LANNW test case CT9 [154] had then been selected to highlight the difference between the two options. Merely the results obtained with the S/A-one-equation-turbulence-model option are summarized herein. Employing FLM-NS [102], the rendered region of flow separation had extended from the supersonic-flow-terminating shock all the way to the TE. In this regard, the initial steady-state solution for the reference position had exhibited a region of flow separation that conformed to the zeroth-harmonic instance. Experimental data, however, indicated a substantial overprediction. On the basis of this reference solution, an FLM-SD.NS computation that fully accounted for the amplitude S/A conservative working variable was conducted. Its limitation effectively stabilized the solution process, despite the extensive flow separation. For the two investigated span stations, the FLM-SD.NS- and FLM-NS-obtained first-harmonic surface-pressure-coefficient distributions conformed well, except in the peak associated with the supersonic-flow-terminating shock. Substantial deviations in its width and absolute value were witnessed. Notably, FLM-SD.NS predicted the inversion of the shock motion indicated by both the FLM-NS result and the experimental data. Unfortunately, the exhibited deviations had amplified toward the global load coefficients; in particular, observed in the imaginary part of the first-harmonic lift coefficient and the real part of the first-harmonic pitching-moment coefficient [102]. As ascertained, however, "[b]oth [methods] render a time-dependent [pitching-moment coefficient] that lags the excitation by somewhat more than a quarter cycle: Despite the deviations, they conform surprisingly well in their predicted [phase angle] instances[.]"[102] All in all [102], FLM-SD.NS rendered the unsteady loading of the CT9 case in less than satisfactory agree-

ment to its FLM-NS counterpart. This circumstance was attributed to the high degree of dynamic nonlinearity inherent to the FLM-NS-obtained flow response, and thus inherent to the CT9 case per se. The computational efficiency gain of FLM-SD.NS over FLM-NS was determined to be merely a factor of about two, even though the latter required 12 oscillation cycles to achieve global load coefficient periodicity [102].

5.1.2.3 Nacelle-Pylon-Rectangular-Wing Assembly Case

Iatrou [54] lastly investigated a nacelle-pylon-rectangular-wing assembly case in his dissertation of 2009. This case was characterized by a pitching oscillation at a minutely positive angle-of-attack and zero sideslip angle in the transonic flow regime, which, however, had no experimental counterpart. Computations with FLM-NS under the S/A-one-equation-turbulence-model option revealed a region of flow separation on the lower wing surface, emerging across the semi-span with increasing distance from the nacelle. Additionally, a region of flow separation had developed for the lower interior surface of the nacelle in proximity to its outlet. In this regard, the initial steady-state FLM-NS solution for the reference position had exhibited regions of flow separation that conformed to the FLM-NS-obtained zeroth-harmonic instances. On the basis of this reference solution, an FLM-SD.NS computation that fully accounted for the amplitude S/A conservative working variable was conducted, but expectedly failed to render a stable solution. As the limitation of the amplitude S/A conservative working variable had not yet been implemented in this particular FLM-SD.NS incarnation, the FEVA was employed to achieve convergence nonetheless. The FLM-SD.NS- and FLM-NS-obtained first-harmonic surface-pressure-coefficient distributions were compared at four span stations, as well as a span-perpendicular upper- and lower-nacelle section that corresponded to the innermost span station. Generally, good agreement was exhibited. Deviations were witnessed for the region of flow separation on the lower wing surface, and even more prominently for the interior nacelle surface in proximity to the narrowest cross section; i.e., at the axial location of maximum flow expansion. The exhibited deviations had only partially amplified toward the first-harmonic global load coefficients: Whereas the FLM-SD.NS-obtained real part of the first-harmonic lift coefficient and the imaginary part of the first-harmonic pitching-moment coefficient were in good agreement to their FLM-NS counterparts, the respective imaginary and real part each differed substantially between the two methods. Hence, the overall prediction accuracy of FLM-SD.NS had been classified as being merely satisfactory. In contrast, supplemental FLM-SDEu and FLM-Eu results generally agreed very well with each other for both the first-harmonic surface-pressure-coefficient distributions and the first-harmonic global load coefficients. A substantial deviation, though, was again seen for the real part of the first-harmonic pitching-moment coefficient. Naturally, the flowfield rendered by each of the inviscid methods differed from its viscous counterpart;

in particular, exhibiting attached flow, as well as a strong supersonic-flow-terminating shock within the divergent part of the nacelle interior, where the latter had not. Consequently, the associated first-harmonic surface-pressure-coefficient distributions deviated locally, an occurrence that amplified toward both the first-harmonic lift and first-harmonic pitching-moment coefficient. Whereas the computational efficiency gain of FLM-SD.NS over FLM-NS was merely 30%, the instance of FLM-SDEu over FLM-Eu was a factor of four. Restrictions in the FLM-SD.NS/FLM-NS implementation of the B/L-algebraic-turbulence-model option with respect to multiblock grid topologies had precluded its additional employment. All computations had been conducted without utilizing the methods' multigrid acceleration capability [54].

5.2 Computational Set-up

Refocusing on the NCDW, the investigations discussed herein all employed FLM-SD.NS in its S/A-one-equation-turbulence-model incarnation, again simply referred to as FLM-SD.NS. Under supervision of the author, a digital embodiment of the NCDW had been constructed by Markmiller [82] using the computer-aided-design component of the commercial meshing tool ICEM-CFD Hexa [60]. It was rendered within the confines of the numerically considered nondimensionalized physical space. In agreement with the experimental campaign, merely a semi-span instance (the starboard half) was treated. Both the defining and the derived parameters of the NCDW planform are compiled in Table 5.1. Depicted in the spatial view of Figure 5.1, "[t]he globally [utilized] Cartesian coordinate system is set to originate from the wing's root [LE] at [the] reference position, with the x (chordwise) direction running positively toward the [TE] and the y (spanwise) direction running positively toward the starboard tip."[103] Advantageously, the chosen dimensional reference length limits the nondimensional semi-span to unity, with the individual span stations in turn each representing a fraction thereof. Because the NCDW's geometric properties are analytically defined, the root and tip sections, respectively, span

Defining parameter	Value	Derived parameter	Value
Planform	Trapezoidal	Taper ratio $\check{c}_t/\check{c}_r$	0.142
LE, TE sweep angle	50 deg, 0 deg	$A := \check{A}/\check{L}^2$	0.805
$\check{L} := \check{s}$	1.145 m	Aspect ratio s^2/A	1.242
$s := \check{s}/\check{L}$	1.000	$c_{av} := \check{c}_{av}/\check{L}$	0.805
$c_r := \check{c}_r/\check{L}$	1.410	$c_\mu := \check{c}_\mu/\check{L}$	0.956

Table 5.1: Geometric properties of the semi-span NCDW planform [12, 103].

stations $y_{c1} := y/s = 0.00$ and $y_{c6} = 1.00$, in conjunction with the planform sufficed to construct the NCDW digitally. The equally highlighted wing sections of y_{c2} through y_{c5} merely serve to visualize the rendered wing's volume. Superimposed onto the planform view, two axes of rotation had been separately employed in the experimental campaign, one associated with the pitching oscillations, and the other with the flap oscillations. In this regard, the pitch axis was specified perpendicular to the herein established xz plane (the wing's virtual plane of lateral symmetry), while intersecting the root chord (x_p/c_r) at 65% length, with z_p being nil. The flap's hinge axis, on the other hand, was defined through a local chord intersection (x_h/c) of constant 80% length, with z_h also equaling nil [12]. Its projection onto the rendered wing's upper and lower surface, designated as the respective hinge lines, in combination with interpolated wing sections at $y_{fi} = 0.57$ and $y_{fo} = 0.83$ allows the actual flap surfaces to be delimited for the computation.

The planform view of Figure 5.1 also shows the six span stations utilized in the investigation. They are grouped in terms of their inner ($y_{s1} = 0.05$, $y_{s2} = 0.33$), median ($y_{s3} = 0.54$, $y_{s4} = 0.59$) or outer ($y_{s5} = 0.69$, $y_{s6} = 0.85$) location. With exception of y_{s1}, correspondence to the span stations instrumented on the NCDW test model is given [12], Table 2; also see [103]. Hence, a comparison between the experimentally acquired and the computed values of the surface-pressure-coefficient distributions is readily put into effect for stations y_{s2} through y_{s6}, whereas for y_{s1} a mere comparison between the employed numerical methods will have to suffice. Two out of the five span stations pertinent to the experiment intersect the flap. One (y_{s4}) resides in very close proximity to its inboard edge (y_{fi}), while the other (y_{s5}) divides it into approximately equal parts. Thus, they are also referred to as the flap-inboard-edge station and the flap-median station. The intercept

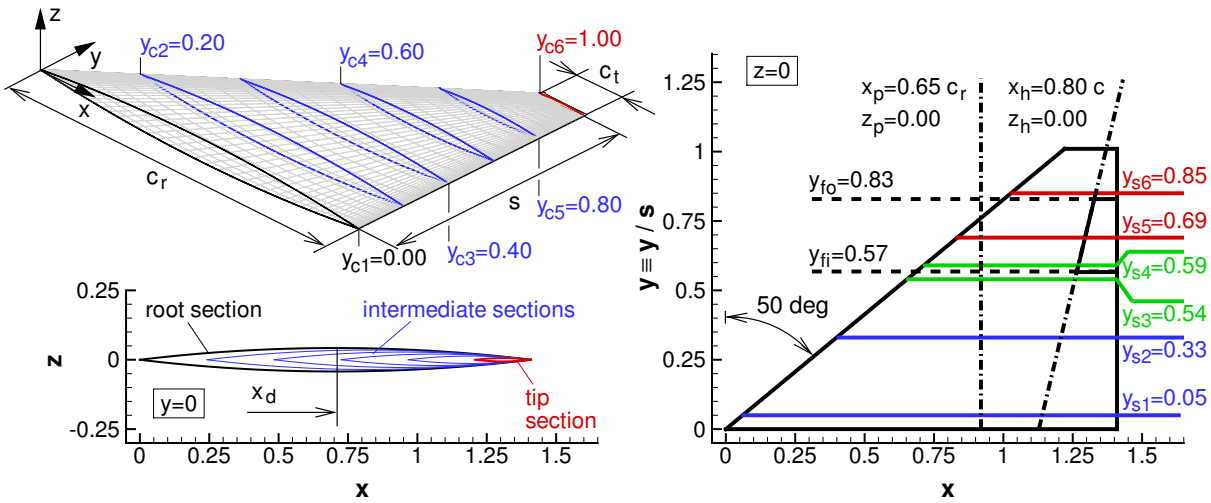

Figure 5.1: Composited spatial view, cross-sectional view, and planform view of the rendered NCDW; based on [103], Fig. 2.

point between any particular span station and either the upper- or lower-surface hinge line is identified as the pertinent hinge-line intersection. Unfortunately, instrumentation constraints had restricted the data acquisition within the extents of the flap to only three chordwise pressure taps per span station [12], Figure 3. Of course, such a resolution can only provide limited detail of the oscillating flap's impact on the local surface-pressure distribution. Lastly, for all experiments conducted at zero angle-of-attack, Walker and Bennett [12] only documented the upper surface-pressure-coefficient distribution, since flow symmetry respective the herein established xy plane (the wing's plane of vertical symmetry) had been preliminarily observed to be sufficiently existent.

Providing an appropriate representation of the digitally rendered NCDW to the numerical methods, the volume bounding upper and lower surfaces underwent a spatial discretization particular to the investigated type of oscillation. Both surfaces were considered to be strictly continuous, and thus exempt of any gaps or skewed edges exhibited by the test model for the flap's undeflected position. The LE as well as the TE were extended beyond the tip section to $y_{c6} + 1\% \, s$, with the wing volume tapering off to a single edge, correspondingly. This modification facilitated the construction of the discrete physical domain of interest. Markmiller [82] realized the surface discretization employed for the pitching oscillations, again using ICEM-CFD Hexa [60]. Depicted in Figure 5.2, "[t]he upper and lower surface of the NCDW's numerical embodiment are each discretized with 72 cells (hyperbolically distributed) in chordwise and 32 cells (Poisson-distributed) in spanwise direction, for a total of 2304 cells per surface." [103] On this basis, Allen et al. [4] realized the surface discretization employed for the flap oscillations. The number of cells in both chordwise and spanwise direction were retained, thus leaving the total number of

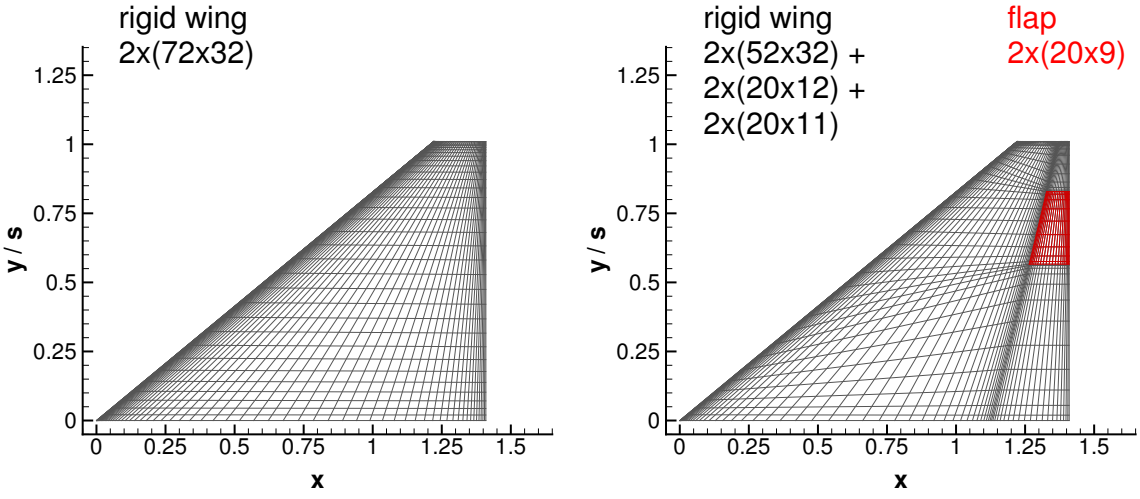

Figure 5.2: NCDW surface grid as rendered for the pitching oscillations (based on [103], Fig. 2) and for the flap oscillations (based on [4], Fig. 1).

cells per surface unchanged. However, the cells were redistributed through agglomeration to better render flowfield gradients in proximity to the hinge lines and the flap edges, as shown in Figure 5.2. Specifically, the upper- and lower-surface grid is constituted through a rigid wing part forward of the hinge line, an inboard and an outboard rigid wing part aft of the hinge line, as well as the flap part itself. These parts are discretized, respectively, with 52 cells in chordwise and 32 cells in spanwise direction, 20 cells in chordwise and 12 cells in spanwise direction, 20 cells in chordwise and 11 cells in spanwise direction, as well as 20 cells in chordwise and 9 cells in spanwise direction, again totaling 2304 cells [4].

For the pitching oscillations, Markmiller [82] embedded the pertinent numerical embodiment of the NCDW at its reference position in a two-block C-H-topology structured volume grid utilizing a boundary-fitted ($\xi\eta\zeta$) coordinate system [103]. Subsequently, it was elliptically smoothed with the tool GRID-FLM, developed by Decker et al. [35]. The resultant volume grid is depicted in Figure 5.3. Pursuant to Pechloff and Laschka, it can be summarized that

> [t]he far-field distances are set to $11 \times s$ in positive chordwise direction from the root LE, to $11 \times s$ in both positive and negative vertical (z) direction from the root TE, as well as to $5 \times s$ in spanwise direction respective the wing's [virtual] plane of [lateral] symmetry. Each block discretizes one half of the numerically treated physical domain as divided by the wing's [...] plane of [vertical] symmetry. Thus, the individual block is associated with strictly one of the wing's surfaces, either the upper or lower[, accounted for through a sole wall-boundary segment on the starting $\zeta = const.$ block face]. [The individual block] discretizes the delimited volume with 96 cells in positive chordwise, 48 cells in spanwise, and 40 cells in [the] wing[-]surface normal direction, translating into 184,320 cells per block or 368,640 cells for the entire grid. Cells in the wing-surface normal direction are hyperbolically distributed, the distance of the first [off-body] grid plane being set to $1 \times 10^{-5} \times s$. For the considered high-Reynolds-number transonic flow[,] this renders a [sublayer-scaled distance of the first off-body grid plane] $d^+ < 5$ as required by the S/A [one-equation] turbulence model. The chosen two[-]block topology allows orthogonality of grid lines emanating from the upper and lower surface in proximity to the LE. [103]

Differing from the experimental set-up, symmetry in y direction is specified on the starting $\eta = const.$ block face instead of a no-slip wall. The volume grid is three-level-multigrid capable. In order to render the extremum grid, the NCDW surface grid was simply rotated by $\breve{\hat{\alpha}}$ about the pitch axis, Figure 5.4, with the delimited volume remeshed, and subsequently smoothed [82]. Consequently, the reference and extremum grid conform in their global properties [103]. Following this process, Allen et al. [4] realized an equivalent reference and extremum grid for the flap oscillations. In this regard, the $\breve{\eta}$ deflection of the flap about the hinge axis was simply rendered by appropriate deformation of the pertinent NCDW surface grid, Figure 5.5. Hence, the gaps exhibited by the test model for the

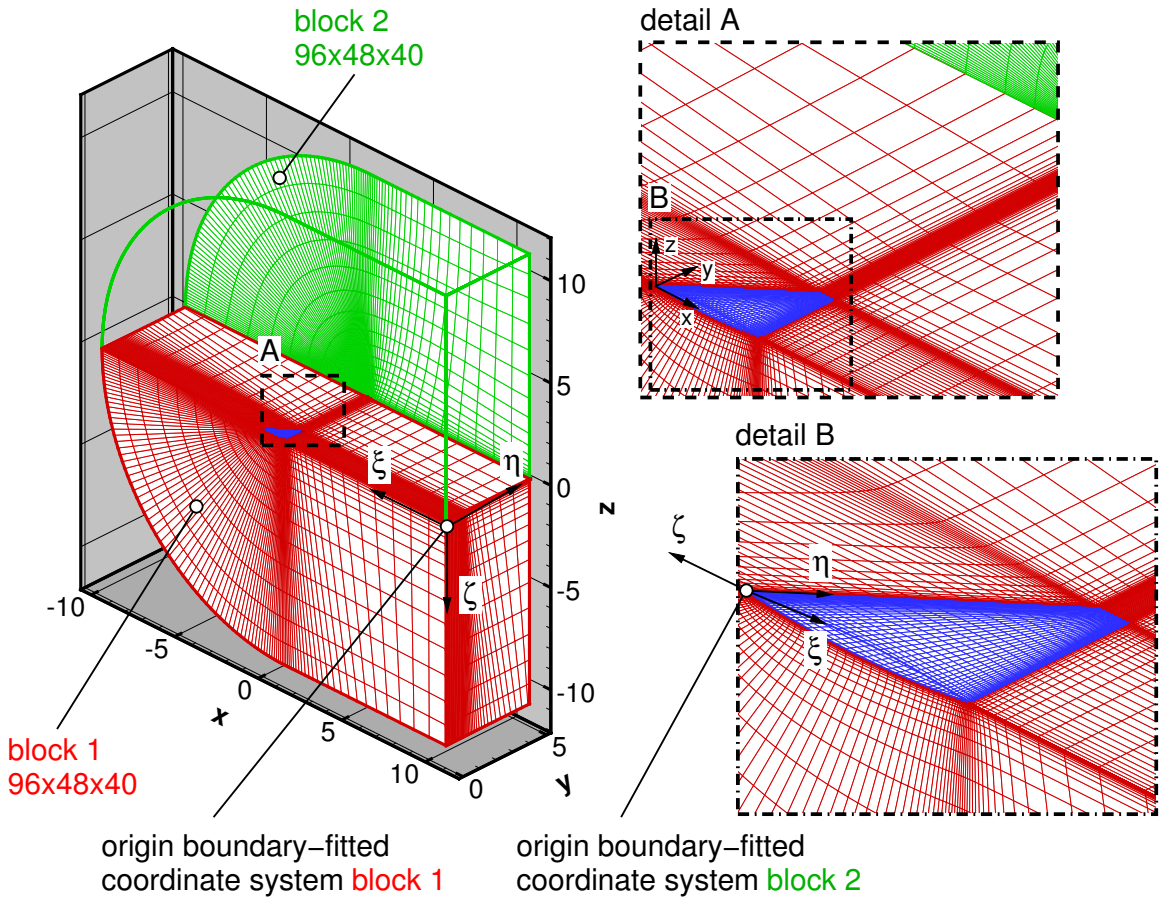

Figure 5.3: NCDW reference grid as rendered for the pitching oscillations [103], Fig. 3.

flap's deflected position (especially between the flap edges and the rigid part of the wing) are not accounted for in its numerical embodiment. Instead the cells that correspond to these particular gaps are both skewed and stretched to accommodate the deflected flap part, as shown in detail A of Figure 5.5. Ultimately, the deformed surface grid retains the coherence of the reference surface grid, with the wall boundary condition likewise applied over its entirety [4].

The pitching oscillations are governed by

$$\begin{aligned} \breve{\alpha}(k_{red}\,\tau_s) \;:=\; \breve{\bar{\alpha}} \;+\; \breve{\tilde{\alpha}}(k_{red}\,\tau_s) \;&=\; \breve{\bar{\alpha}} \;+\; \breve{\hat{\alpha}}\; Re\, e^{i(k_{red}\,\tau_s - \pi/2)} \\ &=\; \breve{\bar{\alpha}} \;+\; \breve{\hat{\alpha}}\; \sin(k_{red}\,\tau_s)\,, \end{aligned} \tag{5.1}$$

with the flap oscillations obeying

$$\breve{\eta}(k_{red}\,\tau_s) \;:=\; \breve{\bar{\eta}} \;+\; \breve{\tilde{\eta}}(k_{red}\,\tau_s) \;=\; \breve{\bar{\eta}} \;+\; \breve{\hat{\eta}}\; \sin(k_{red}\,\tau_s)\,, \tag{5.2}$$

respectively, about the specified pitch and hinge axis. In this regard, a reduced frequency is introduced as

$$k_{red} := 2\pi \breve{f} \breve{L} \sqrt{\breve{\rho}_\infty}/(Ma_\infty \sqrt{\gamma \breve{p}_\infty})\,, \tag{5.3}$$

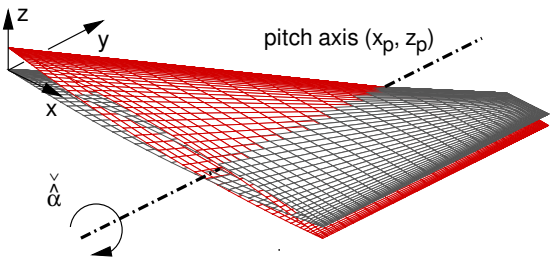

Figure 5.4: Representative amplitude deflection of the NCDW surface grid as rendered for the pitching oscillations ($x_p/c_r = 0.65$, $\check{\hat{\alpha}} > 0$).

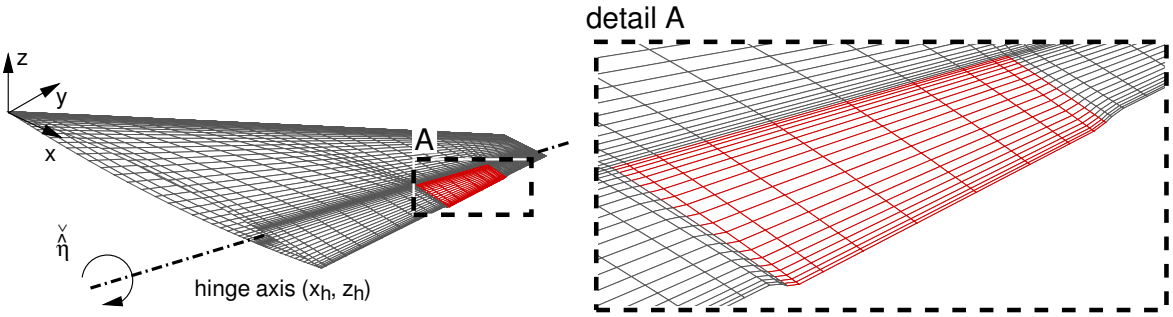

Figure 5.5: Representative amplitude deformation of the NCDW surface grid as rendered for the flap oscillations ($x_h/c = 0.80$, $\check{\hat{\eta}} > 0$).

with the associated time then being

$$\tau_s = \check{t}\, Ma_\infty \sqrt{\gamma \check{p}_\infty}/(\check{L}\sqrt{\check{\rho}_\infty}) \tag{5.4}$$

in order to satisfy $k_{red}\,\tau_s = k\,\tau$. All FLM methods employ k_{red} as the user-supplied input parameter, deriving k from it for internal operations. Their connectivity is given through

$$k = \sqrt{\gamma}\, Ma_\infty\, k_{red}\,. \tag{5.5}$$

The particular test case provides either $\check{\alpha}$ and $\check{\hat{\alpha}}$ or $\check{\eta}$ and $\check{\hat{\eta}}$, as well as k_{red} [103]. For the small disturbance computations, the time-dependent evolution of an arbitrary field quantity can be synthesized by

$$\begin{aligned} < \Phi(k_{red}\,\tau_s) >|_{SD.NS/SDEu} &:= \bar{\Phi}^* + Re\,\tilde{\Phi}^*(k_{red}\,\tau_s) \\ &= \bar{\Phi}^* + Re\left[\hat{\Phi}\, e^{i(k_{red}\,\tau_s - \pi/2)}\right] \\ &= \bar{\Phi}^* + Re\,\hat{\Phi}\sin(k_{red}\,\tau_s) + Im\,\hat{\Phi}\cos(k_{red}\,\tau_s)\,. \end{aligned} \tag{5.6}$$

It becomes evident that for the upstroke zero-crossing ($\check{\alpha}(j\,2\pi) = \check{\hat{\alpha}}$ or $\check{\eta}(j\,2\pi) = \check{\hat{\eta}}$, with $j = 0,\, 1,\, \ldots, \infty$) the field quantity's momentary perturbation is solely rendered by $Im\,\hat{\Phi}$.

Complementarily, for the upper dead center ($\check{\alpha}(j\,2\pi+\pi/2) = \bar{\check{\alpha}}+\hat{\check{\alpha}}$ or $\check{\eta}(j\,2\pi+\pi/2) = \bar{\check{\eta}}+\hat{\check{\eta}}$, with $j = 0,\, 1,\, \ldots, \infty$) the field quantity's momentary perturbation is solely rendered by $Re\,\hat{\Phi}$. In analogy to Eq. (5.6), the time-dependent evolution of any load coefficient can be obtained through

$$\chi(k_{red}\,\tau_s)|_{SD.NS/SDEu} \;:=\; \bar{\chi}^* \;+\; Re\,\hat{\chi}\sin(k_{red}\,\tau_s) \,+\, Im\,\hat{\chi}\cos(k_{red}\,\tau_s) \tag{5.7}$$

[103]. The load coefficient evaluation as pertinent to the small disturbance approach is summarized in Appendix B. In this regard, Section B.1 defines the utilized Cartesian coordinate systems, while Section B.2 and Section B.3, respectively, provide the formulae rendering the local and global load coefficients per se. They are derived from the instances employed in the dynamically fully nonlinear approach; i.e., as originally implemented by Kreiselmaier [70] in FLM-Eu, and extended by Cvrlje [31] on the basis of FLOWer [72] to account for the three-dimensional skin-friction-coefficient vector in FLM-NS.

In the context of the NCDW pitching oscillations, Pechloff and Laschka had specified the Fourier-analysis of a load coefficient's time series in [103]; specifically, Eq. (5) and Eq (6). Originating from the FLM-Eu/FLM-NS usage, it applies to any sinusoidal deformation/deflection of the considered body. Facilitating the investigation, the load coefficients stemming from the small disturbance methods are subsequently designated consistent to their Fourier-analyzed dynamically fully nonlinear counterparts:

$$\chi^0|_{SD.NS/SDEu} := \bar{\chi}^*\,, \qquad \chi^1|_{SD.NS/SDEu} := \hat{\chi} \tag{5.8}$$

[103]. Each pitching oscillation is also discussed with the dynamic stability behavior of its free pitching counterpart in mind. Pechloff and Laschka had specified the necessary criterion in [103]; specifically, Eq. (3) and Eq. (4). It was stated that "for $\hat{\alpha} > 0$ the free pitching oscillation can be classified as unstable if $[Im\,c_M^1] > 0$ or stable if $[Im\,c_M^1] < 0$, respectively, corresponding to a $[\widetilde{c_M}]$ that leads or lags $\tilde{\alpha}$."[103] Singularly, for $Im\,c_M^1 = 0$ the free pitching oscillation can be classified as indifferent, corresponding to a $\widetilde{c_M}$ that is either in phase ($\check{\varphi}_{c_M^1} = 0$ deg) or entirely out of phase ($\check{\varphi}_{c_M^1} = \pm 180$ deg) with $\tilde{\alpha}$.

Finally, it should be noted that as $\check{L} \neq \check{c}_r$ the k_{red} employed in these computation differs from the one generally favored to describe aerodynamic longitudinal motions (subscript: long) at a particular $\check{f}$. Specifically,

$$k_{red}|_{long} = 2\pi\check{f}\check{c}_r\sqrt{\check{\rho}_\infty}/(Ma_\infty\sqrt{\gamma\check{p}_\infty})\,, \tag{5.9}$$

thus letting

$$k_{red} = k_{red}|_{long}\,\check{L}/\check{c}_r\,. \tag{5.10}$$

In retrospect, the particular k_{red} employed in [82], [4], and [55] for the computation of the considered NCDW dynamic test cases each corresponds to an $\check{f}$ that is substantially higher than the one of the actual experiment. Nevertheless, the conducted intermethod comparison remains valid.

5.3 Pitching Oscillations

Bennett and Walker [12] provide an array of NCDW pitching-oscillation test cases, with 90D5 (a weak shock case), 90D29 (the medium-strength shock/LEV case), and 94D5 (a strong shock case) having been selected for the investigation [103] herein. On the basis of each one, both a case at half- and double-frequency are also computed, respectively, 90D4 and 90D6, 90D28 and 90D30, as well as 94D4 and 94D6 [103]. However, only the 90D4 and the 90D6 case have experimental counterparts. Pursuant to Pechloff and Laschka, it can be stated that

> [f]or both the viscous and inviscid small disturbance computations[,] the associated [linearized] time-invariant[-]mean flowfield is, by definition, frequency independent. Therefore, [the half- and double-frequency cases utilize] the same particular steady-state reference-grid solution as employed in the [baseline-frequency] case. Likewise, each solution again serves as the initialization flowfield to the transient process of the corresponding dynamically fully nonlinear computation. [103]

The computation parameters of each case are compiled in Table 5.2, with $Re_\infty = 10.0 \times 10^6$, $L_{Re_\infty} = c_{av}$, $\check{S} = 110.4$ K, $\gamma = 1.132$, $Pr = 0.775$ (heavy gas), and $Pr_t = 0.90$ being shared by all [12, 103]. Accelerating FLM-SD.NS solution convergence, the $(2_0 \,/\, 1_1 \,/\, 2)$ V-symmetric multigrid schedule, as discussed in Subsection 4.5.3, is specified [103]. Solution convergence is accepted when the normalized ℓ^2-norm $\hat{\rho}$ residual, Eq. (4.114), has contracted to a value less than 5.5×10^{-4} (5.0×10^{-4} for the 90D28, 90D29, and 90D30 cases) [103].

The higher solution efficiency of the multigrid scheme with respect to the correspond-

Case	Ma_∞	$\check{\bar{\alpha}}$, deg	$\check{\hat{\alpha}}$, deg	k_{red}	$\check{f}$, Hz	$\check{p}_\infty$, kPa	$\check{\rho}_\infty$, kg/m^3	$\check{T}_\infty$, K
90D4	0.90	0.0	0.5	0.119	4.0	20.7	0.326	298.4
90D5				0.237	8.0			
90D6				0.475	16.0			
90D28	0.90	3.97	0.5	0.120	4.0	20.5	0.329	298.9
90D29				0.240	8.0			
90D30				0.480	16.0			
94D4	0.94	0.0	0.5	0.115	4.0	19.3	0.313	295.5
94D5				0.230	8.0			
94D6				0.460	16.0			

Table 5.2: Computation parameters of the NCDW pitching-oscillation cases [12], Table 4; [103], Table 2.

ing single-grid scheme is exemplified in Figure 5.6 by the $\hat{\rho}$ residual histories of the 90D5 case. At otherwise equal settings, the $(2_0 \,/\, 1_1 \,/\, 2)$ schedule yields a 37% reduction in computational time over the single-grid baseline, while the intermediary $(1_0 \,/\, 1_1 \,/\, 1)$ schedule still yields one of 14%. Surprisingly, for the 90D28, 90D29, and 90D30 cases, solution convergence could not be realized with the single-grid scheme. The subsequently employed multigrid schemes, however, were able to do so without difficulties. In this regard, the $\hat{\rho}$ residual histories of the $(2_0 \,/\, 1_1 \,/\, 2)$ and $(1_0 \,/\, 1_1 \,/\, 1)$ schedule are compared in Figure 5.6 for the 90D29 case, with the latter schedule now becoming the baseline. At otherwise equal settings, a reduction in computational time of merely 8% is exhibited, in contrast to the 27% observed between the two schedules for the 90D5 case. Evidently, the multigrid-realized gain in solution efficiency is highly dependent on the scheme's particular setting, as well as the considered case per se.

With respect to the convergence behavior, it can be further ascertained that

> [i]nstability of the solution process [occurs at first] for [the 94D4, 94D5, and 94D6] cases [...], where a confined region of postshock separation [exists] toward the wing tip in the [linearized] time-invariant[-]mean flowfield. After a number of multigrid cycles the $\hat{\tilde{\mu}}$ residual begins to diverge, eventually leading to its exponential growth. As the incurred distortion of the amplitude flowfield increases in significance, the [$\hat{\rho}$] residual follows suit[(Figure 5.7)]. [...] The localized limitation of $\hat{\tilde{\mu}}$; [i.e., Eq. (4.116)], allowed for stabilization[. ...] In effect, the $\hat{\tilde{\mu}}$ residual decreases and subsequently progresses toward an asymptote, allowing the $\hat{\rho}$ residual to converge to the desired level of accuracy[, Figure 5.7]. As will be shown[in Subsection 5.3.3], the limiter's activation does not lead to any noteworthy degradation of the load prediction. For cases with substantial regions of separation contained in the [linearized] time-invariant[-]mean flowfield[,] the limiter's impact remains to be assessed. [103]

Concerning the comparative FLM-NS computations, it can be established that

> three oscillation cycles suffice to achieve load coefficient periodicity, each discretized with 100 physical time intervals. [...] Multigrid parameters and abort criterion are set equal to those of the FLM-SD.NS computations. The FLM-SD.NS/FLM-NS computation of [the 90D4,] 90D5, and [90D6 cases, as well as the] 90D29 [case], were conducted on a single 1.3 GHz Intel Itanium processor of the Leibniz-Rechenzentrum Linux cluster, with [the 90D28 and the 90D30 case, as well as the 94D4, 94D5, and 94D6 cases] subsequently realized on a 1.6 GHz successor model. The FLM[methods'] machine code was generated with the Intel Fortran Compiler for Linux. [103]

In regard to the additional FLM-SDEu/FLM-Eu computations, it can be said that

> the same reference and extremum grid as [for] the FLM-SD.NS/FLM-NS [computations is generally employed] in order to retain spatial comparability. For [the 90D28,]90D29,

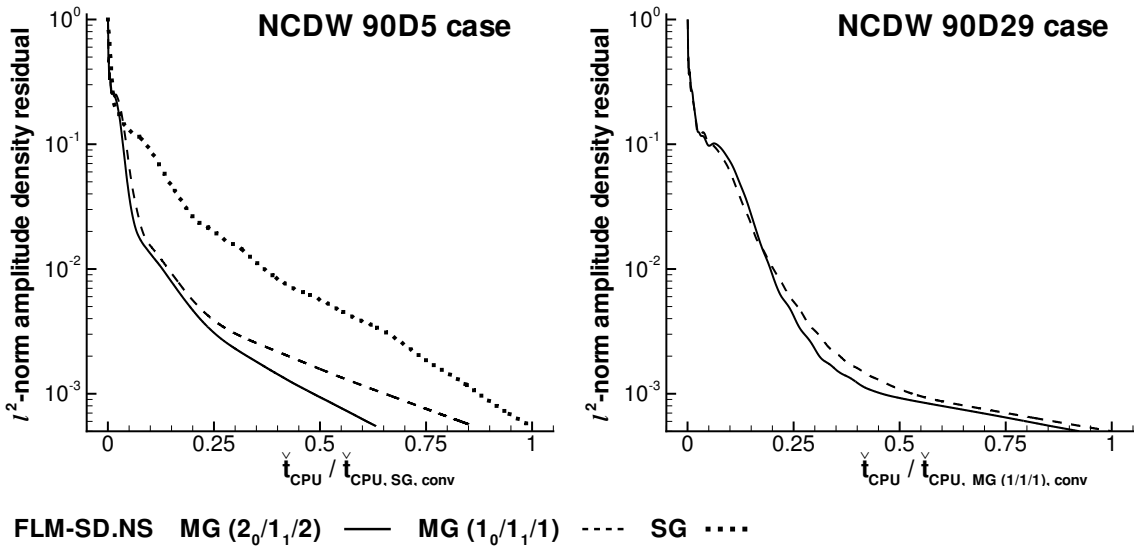

Figure 5.6: Comparison of the FLM-SD.NS $\hat{\rho}$ residual history at two different multigrid (MG) settings and the corresponding single-grid (SG) setting for the NCDW 90D5 case ($Ma_\infty = 0.90$, $Re_\infty = 10.0 \times 10^6$, $\check{\bar{\alpha}} = 0.0$ deg, $\check{\hat{\alpha}} = 0.5$ deg, $k_{red} = 0.237$, $x_p/c_r = 0.65$), and at merely two different MG settings for the NCDW 90D29 case ($Ma_\infty = 0.90$, $Re_\infty = 10.0 \times 10^6$, $\check{\bar{\alpha}} = 3.97$ deg, $\check{\hat{\alpha}} = 0.5$ deg, $k_{red} = 0.240$, $x_p/c_r = 0.65$); subscript conv: converged solution.

> [and 90D30 cases,]however, the high resolution of the wing's near-field destabilized the inviscid solution process, necessitating the consideration of [a] more Euler-typical grid[-pair]. [It is] internally generated from the Navier-Stokes grid[-pair] through elimination of every other cell edge, rendering [a] coarser [reference/extremum grid] of 46,080 cells, with 576 cells per surface. This constitutes a substantial reduction, respectively, by 88% and 75%. Nevertheless, the wing surface and near-field remain sufficiently resolved, with the distance of the first [off-body] grid plane only increasing to $3 \times 10^{-5} \times s$. [103]

Whereas the FLM-SDEu computations of the 90D4, 90D5, and 90D6 cases, as well as the 90D29 case were conducted on a 1.3 GHz Intel Itanium 2 processor, the 90D28 and the 90D30 case, as well as the 94D4, 94D5, and 94D6 cases were realized on a 1.6 GHz successor model, just as all the FLM-Eu computations. Both FLM-NS and FLM-Eu were executed with dual time-stepping set to second-order accuracy.

Demonstrating the higher solution efficiency of the implicit pseudotime-integration scheme over its explicit counterpart [70], FLM-SDEu $\hat{\rho}$ residual histories of the 90D5 and the 90D29 case are presented in Figure 5.8. Both the implicit and explicit pseudotime integration are run, respectively, at the single-grid setting of fastest convergence. For the 90D5 case, implicit pseudotime integration yields a 15% reduction in computational time

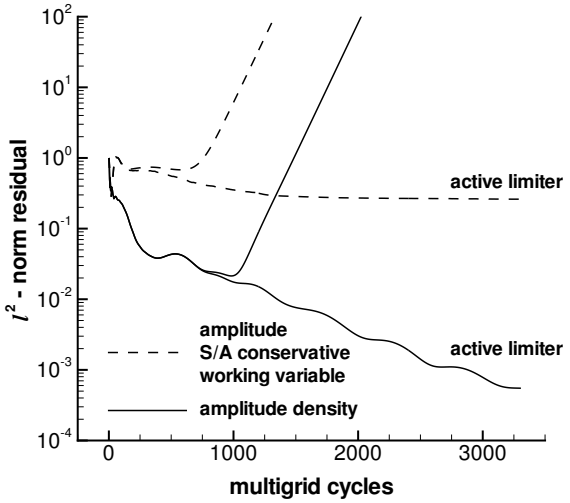

Figure 5.7: Comparison of the FLM-SD.NS $\hat{\rho}$ and $\hat{\breve{\mu}}$ residual histories with and without active limiter for the NCDW 94D5 case ($Ma_\infty = 0.94$, $Re_\infty = 10.0 \times 10^6$, $\breve{\alpha} = 0.0$ deg, $x_p/c_r = 0.65$, $\breve{\hat{\alpha}} = 0.5$ deg, $k_{red} = 0.230$); based on [103], Fig. 4.

with respect to the explicit baseline, while a substantially greater reduction of 44% is witnessed for the 90D29 case between the two schemes. Evidently, the gain in solution efficiency through the implicit pseudotime integration is again highly dependent on the considered case per se, however, with the resolution of the utilized grid-pair (coarser for the 90D29 case) factoring in as well.

Since the experimental surface-pressure data provided by Bennett and Walker [12] for each dynamic test case does not contain the pertinent zeroth harmonic, the corresponding static test case was considered for comparative purposes [103]. Specifically, for the 90D4, 90D5, and 90D6 cases, experimental surface-pressure data of the 90S1 case is drawn on. For the 90D28, 90D29, and 90D30 cases, this is the 90S38 case, while for the 94D4, 94D5, and 94D6 cases, it is the 94S1 case [12]. The sensitivity of the FLM-SD.NS-computed global load coefficients to the employed spatial discretization had been investigated in [103] for the 90D5, 90D29, and 94D5 cases. Subsequently, $\hat{\alpha} := \breve{\hat{\alpha}}\,\pi/180$ deg applies.

5.3.1 Weak Shock Cases

At $Ma_\infty = 0.90$, $Re_\infty = 10.0 \times 10^6$, and $\breve{\alpha} = 0.0$ deg, the FLM-NS-provided linearized time-invariant-mean flowfield underlying the FLM-SD.NS computation of the 90D4, 90D5, and 90D6 cases features "a localized, equally developed supersonic region in proximity to the upper and lower wing surface. It extends, respectively, from the root to the tip, terminating with a weak shock significantly upstream of the TE[, Figure 5.9]."[103] The FLM-SD.NS-obtained surface-pressure-coefficient distributions are compared to their FLM-NS,

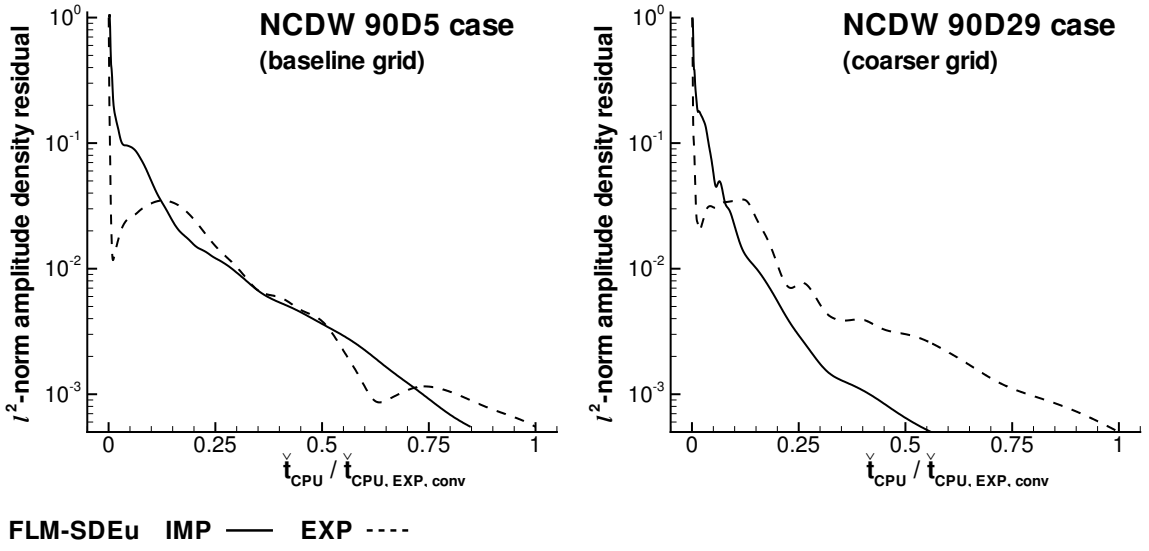

Figure 5.8: Comparison of the FLM-SDEu $\hat{\rho}$ residual histories at implicit (IMP) and explicit (EXP) single-grid settings for the NCDW 90D5 case ($Ma_\infty = 0.90$, $Re_\infty = 10.0 \times 10^6$, $\check{\alpha} = 0.0$ deg, $\check{\hat{\alpha}} = 0.5$ deg, $k_{red} = 0.237$, $x_p/c_r = 0.65$) and the NCDW 90D29 case ($Ma_\infty = 0.90$, $Re_\infty = 10.0 \times 10^6$, $\check{\alpha} = 3.97$ deg, $\check{\hat{\alpha}} = 0.5$ deg, $k_{red} = 0.240$, $x_p/c_r = 0.65$); subscript conv: converged solution.

FLM-SDEu, and FLM-Eu counterparts, as well as to the particular experimental data for the investigated span stations. In this regard, Figures 5.10–5.12, Figures 5.13–5.15, and Figures 5.16–5.18, respectively, correspond to the 90D4, 90D5, and 90D6 cases. For the 90D5 case, the surface-pressure-coefficient distributions of span stations $y/s = 0.33$ and $y/s = 0.69$ were originally presented in [103], Fig. 6.

5.3.1.1 Local Load Coefficients

Focusing on the 90D5 case (the baseline-frequency case) at first, the FLM-SD.NS result as provided in Figures 5.13–5.15 is characterized. Pursuant to Pechloff and Laschka, it can be established that

> [u]pper- and lower-surface c_p^0, of course, exhibit symmetry. From root to tip the onset of supersonic flow moves substantially closer to the LE. In contrast, the termination (indicative of the shock base) varies far less in its chordwise locality, with the weak shock merely imposing a shallow slope onto the c_p^0 progression. Obviously, symmetry of the upper- and lower-surface c_p^0 yields numerically nil c_L^0 and c_M^0 values.
>
> Complementary to c_p^0, upper- and lower-surface $\mathrm{Re}c_p^1$, as well as $\mathrm{Im}c_p^1$, exhibit anti-symmetry. Merely considering the upper-surface distributions, the sharp LE renders an initial primary peak for both $\mathrm{Re}c_p^1$ and $\mathrm{Im}c_p^1$, respectively, being of negative and positive

value. Immediately downstream, $\mathrm{Re}c_p^1$ acutely increases before leveling off. In case of the inner-span station[s], a mild secondary $\mathrm{Re}c_p^1$ peak emerges at the location of minimum c_p^0. It leads into a strong increase across the shock region, culminating in a reversal of sign for $\mathrm{Re}c_p^1$ at the location of the terminating $c_{p,\,crit}^0$. Subsequently, the $\mathrm{Re}c_p^1$ progression follows through to postshock positivity. It reaches a local maximum before decreasing toward the TE, where equalization with the lower-surface $\mathrm{Re}c_p^1$ occurs at nil value. For [both the median- and] outer-span station[s], the further $\mathrm{Re}c_p^1$ progression toward the TE qualitatively corresponds to that of the inner one[s], however, lack[ing] the mild secondary peak. [From root to tip the chordwise locality of the $Re\,c_p^1$ zero-crossing varies consistent with that of the shock base.] Evidently, $\Delta\mathrm{Re}c_p^1$ forward of the zero-crossing supplies the bulk of $\mathrm{Re}c_L^1$. Its positive contribution is only marginally compensated by the aft difference's negative one. Evaluation of $\mathrm{Re}c_M^1$ proves to be more difficult as leverage respective the pitch axis must also be taken into account. [With exception of the outermost span station, t]he positive $\Delta\mathrm{Re}c_p^1$ forward of the zero-crossing can contribute in equal magnitude both positively (pitch up) and negatively (pitch down) to $\mathrm{Re}c_M^1$. The negative $\Delta\mathrm{Re}c_p^1$ aft of the zero-crossing, on the other hand, makes an unambiguous positive (pitch up) contribution through its leverage. Integrating over the entire wing, both a positive $\mathrm{Re}c_L^1$ and $\mathrm{Re}c_M^1$ are ascertained.

For [all span stations], $\mathrm{Im}c_p^1$ acutely decreases from its LE peak, leading into a nearly linear progression that ends slightly upstream of the shock region. Before ending, a reversal of sign is experienced. This places the subsequent shock and postshock

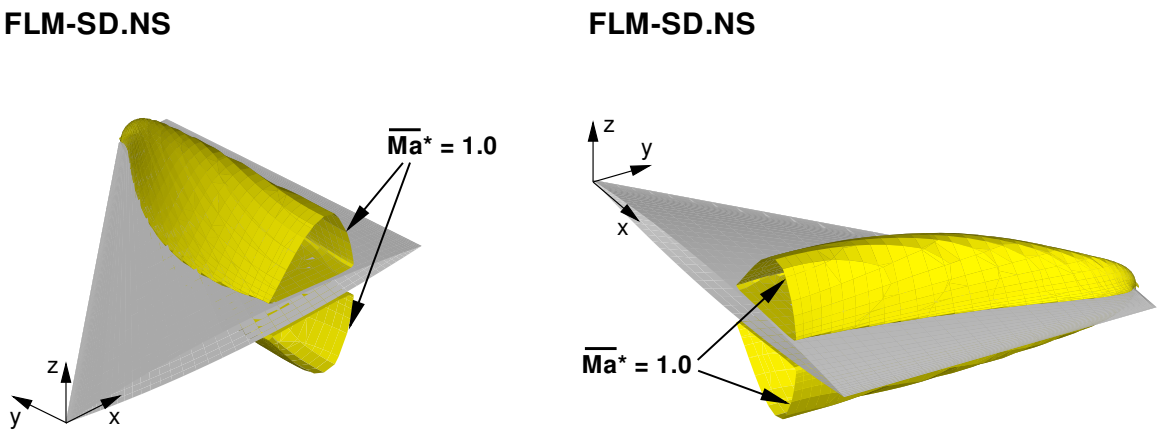

Figure 5.9: Sonic isosurface (LE view and TE view [103], Fig. 5) of the linearized time-invariant-mean flowfield employed by FLM-SD.NS in the NCDW 90D4–6 cases ($Ma_\infty = 0.90$, $Re_\infty = 10.0 \times 10^6$, $\breve{\alpha} = 0.0$ deg, $x_p/c_r = 0.65$, $\hat{\alpha} = 0.5$ deg, $k_{red} = 0.119,\ 0.237,\ 0.475$).

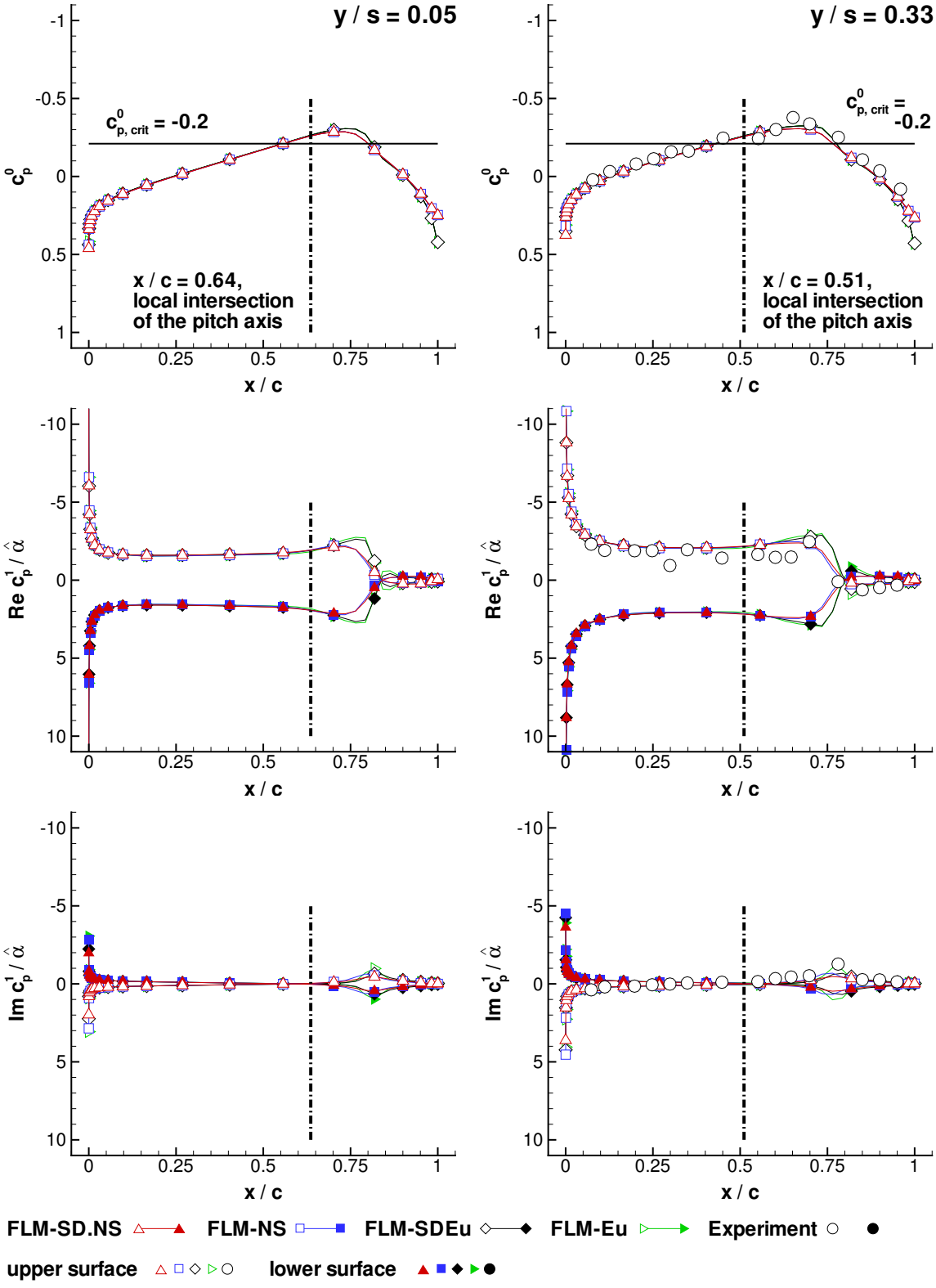

Figure 5.10: Pressure coeff. c_p^0, c_p^1 for a NCDW pitching oscill. at $Ma_\infty = 0.90$, $Re_\infty = 10.0 \times 10^6$, $\breve{\alpha} = 0.0$ deg about $x_p/c_r = 0.65$ w. $\hat{\breve{\alpha}} = 0.5$ deg, $k_{red} = 0.119$ (90D4, inner).

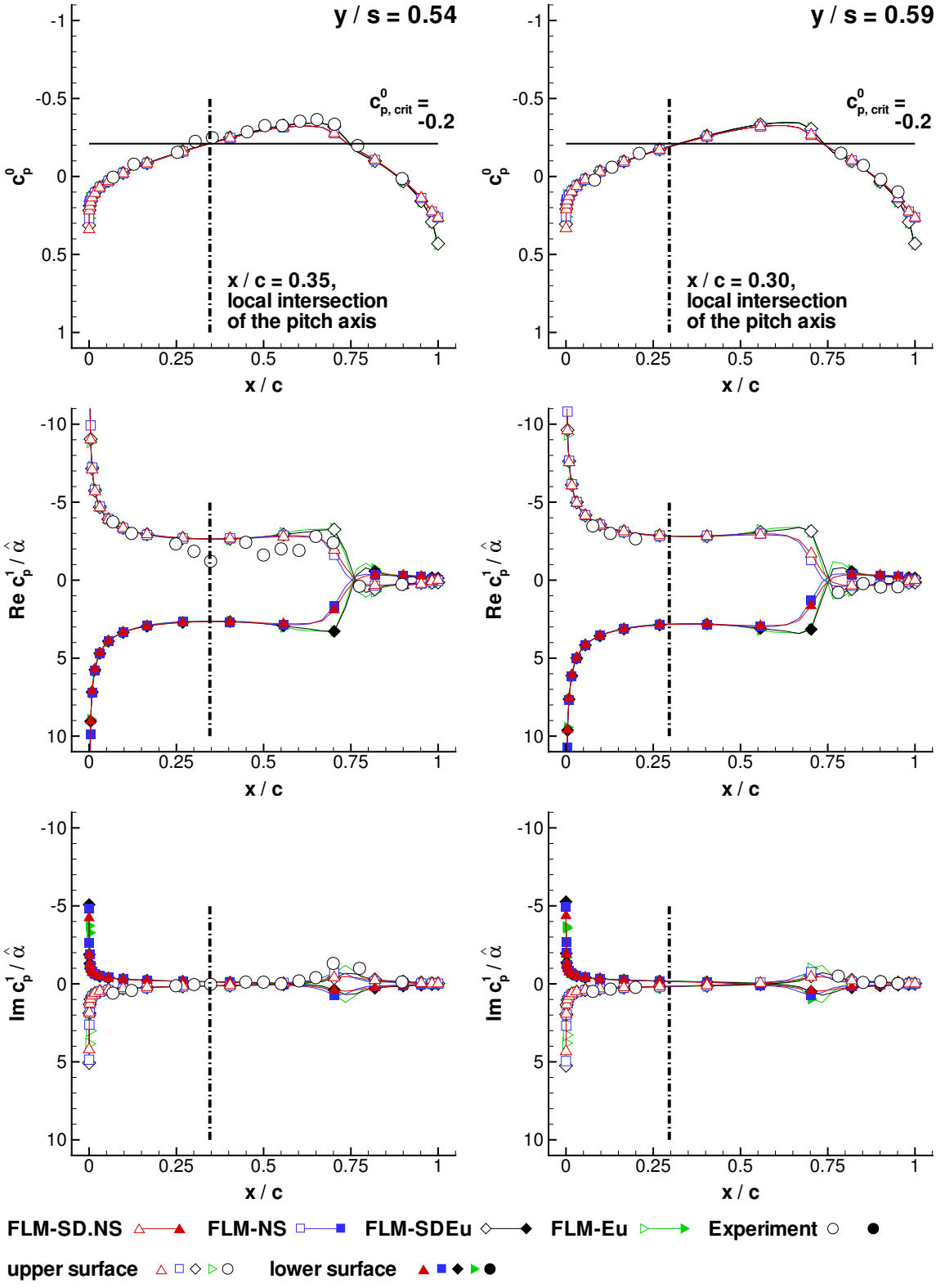

Figure 5.11: Pressure coeff. c_p^0, c_p^1 for a NCDW pitching oscill. at $Ma_\infty = 0.90$, $Re_\infty = 10.0 \times 10^6$, $\breve{\alpha} = 0.0$ deg about $x_p/c_r = 0.65$ w. $\hat{\breve{\alpha}} = 0.5$ deg, $k_{red} = 0.119$ (90D4, median).

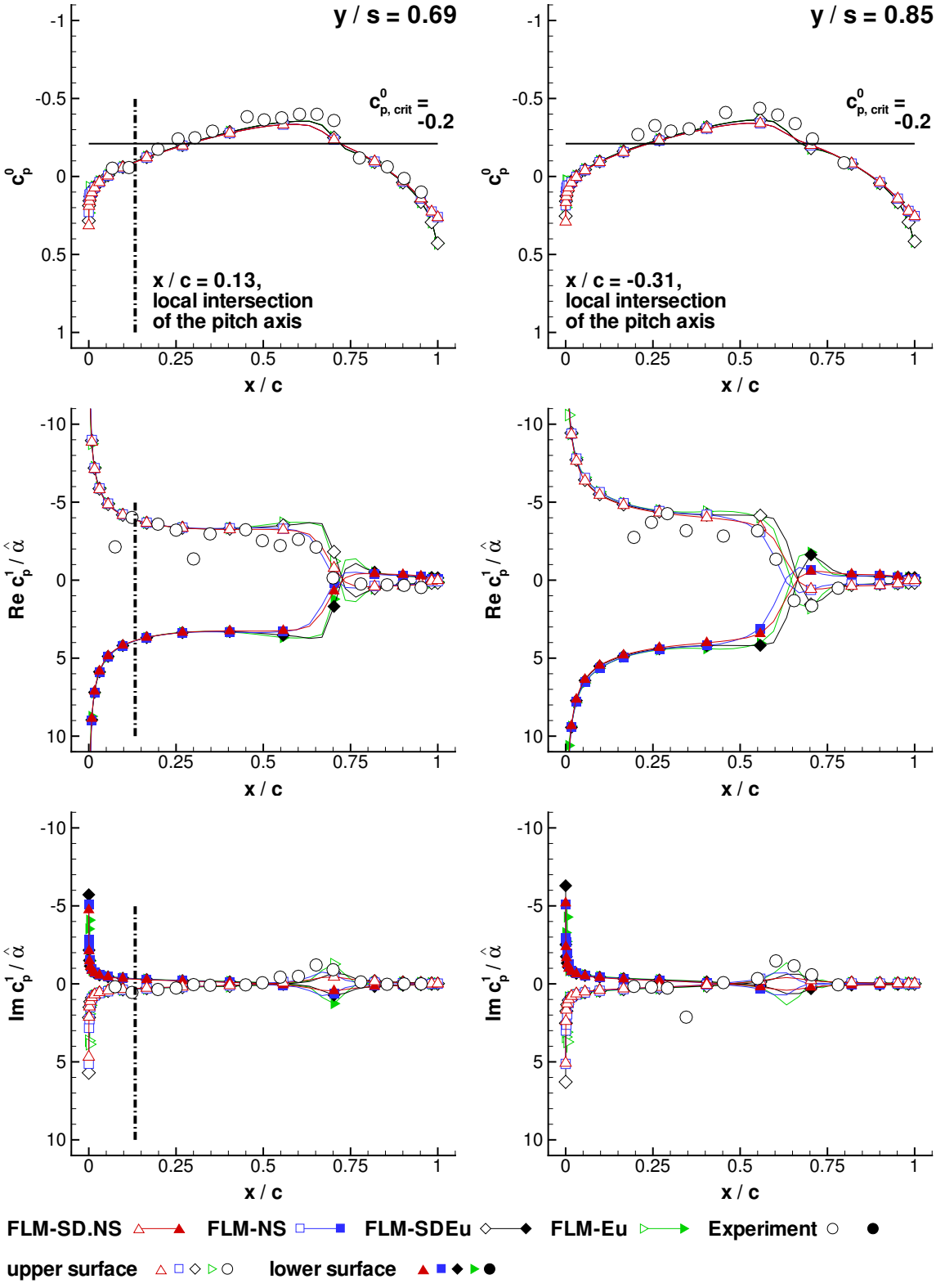

Figure 5.12: Pressure coeff. c_p^0, c_p^1 for a NCDW pitching oscill. at $Ma_\infty = 0.90$, $Re_\infty = 10.0 \times 10^6$, $\breve{\alpha} = 0.0$ deg about $x_p/c_r = 0.65$ w. $\hat{\breve{\alpha}} = 0.5$ deg, $k_{red} = 0.119$ (90D4, outer).

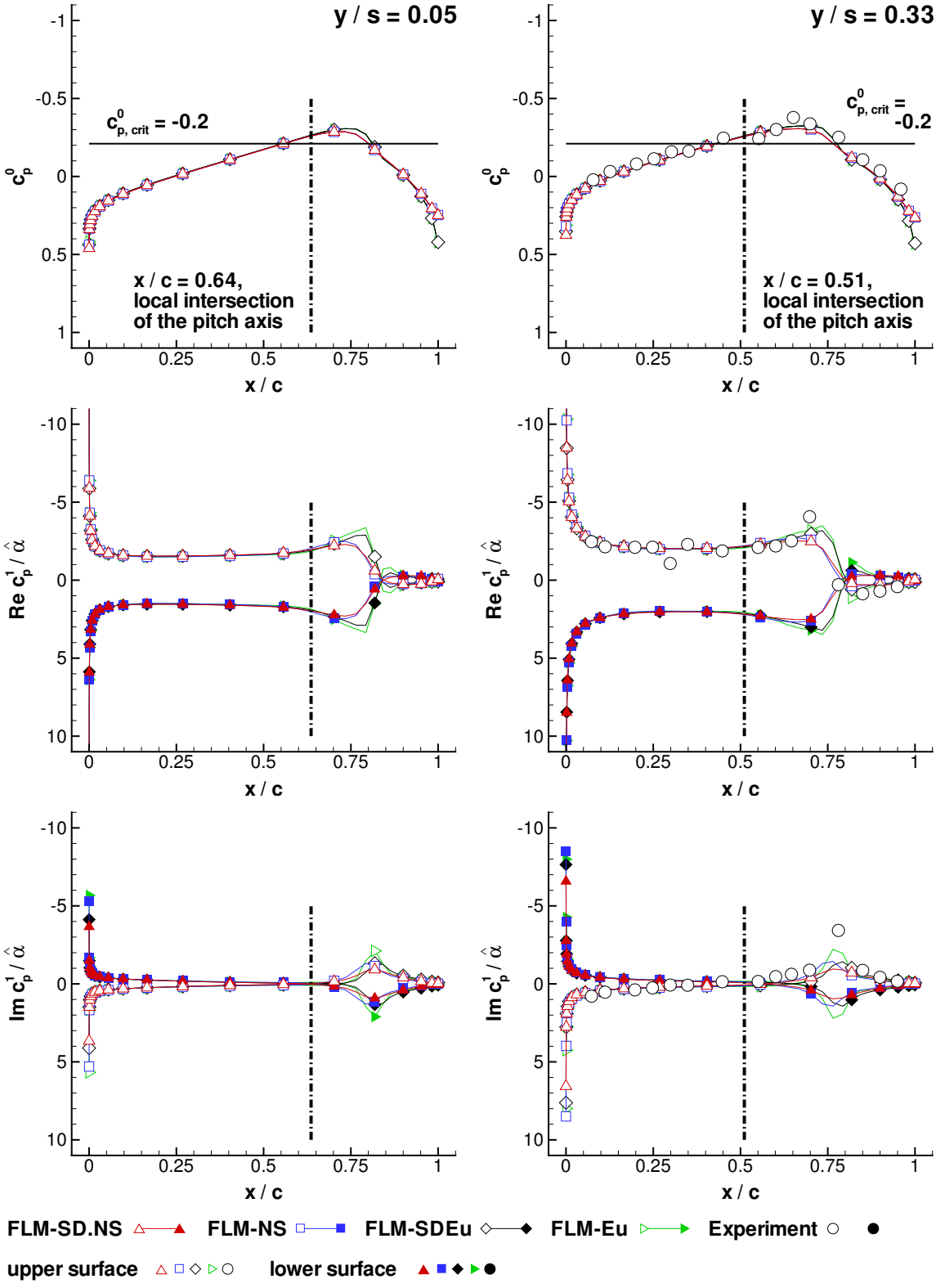

Figure 5.13: Pressure coeff. c_p^0, c_p^1 for a NCDW pitching oscill. at $Ma_\infty = 0.90$, $Re_\infty = 10.0 \times 10^6$, $\breve{\alpha} = 0.0$ deg about $x_p/c_r = 0.65$ w. $\hat{\breve{\alpha}} = 0.5$ deg, $k_{red} = 0.237$ (90D5, inner).

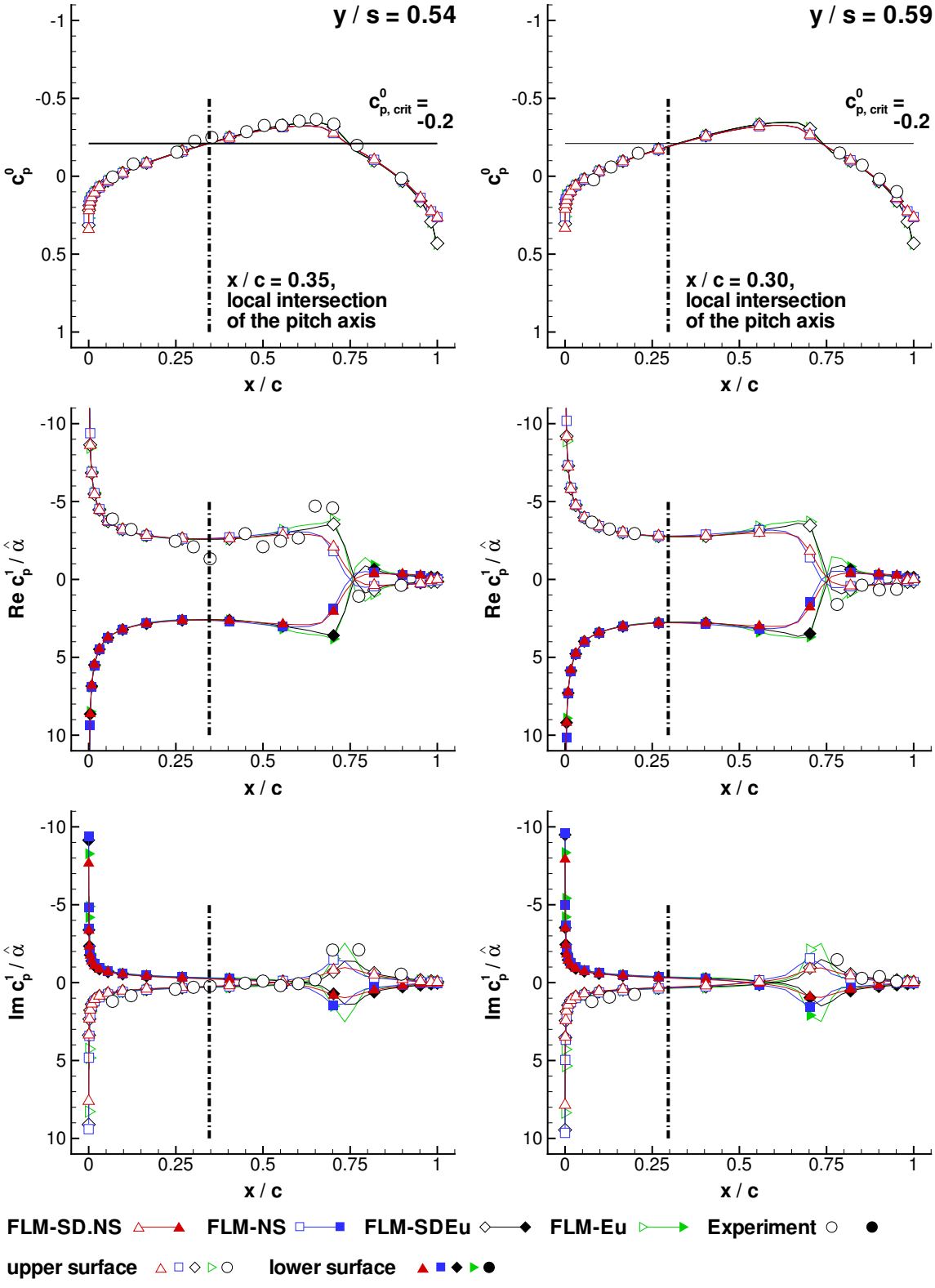

Figure 5.14: Pressure coeff. c_p^0, c_p^1 for a NCDW pitching oscill. at $Ma_\infty = 0.90$, $Re_\infty = 10.0 \times 10^6$, $\breve{\alpha} = 0.0$ deg about $x_p/c_r = 0.65$ w. $\hat{\breve{\alpha}} = 0.5$ deg, $k_{red} = 0.237$ (90D5, median).

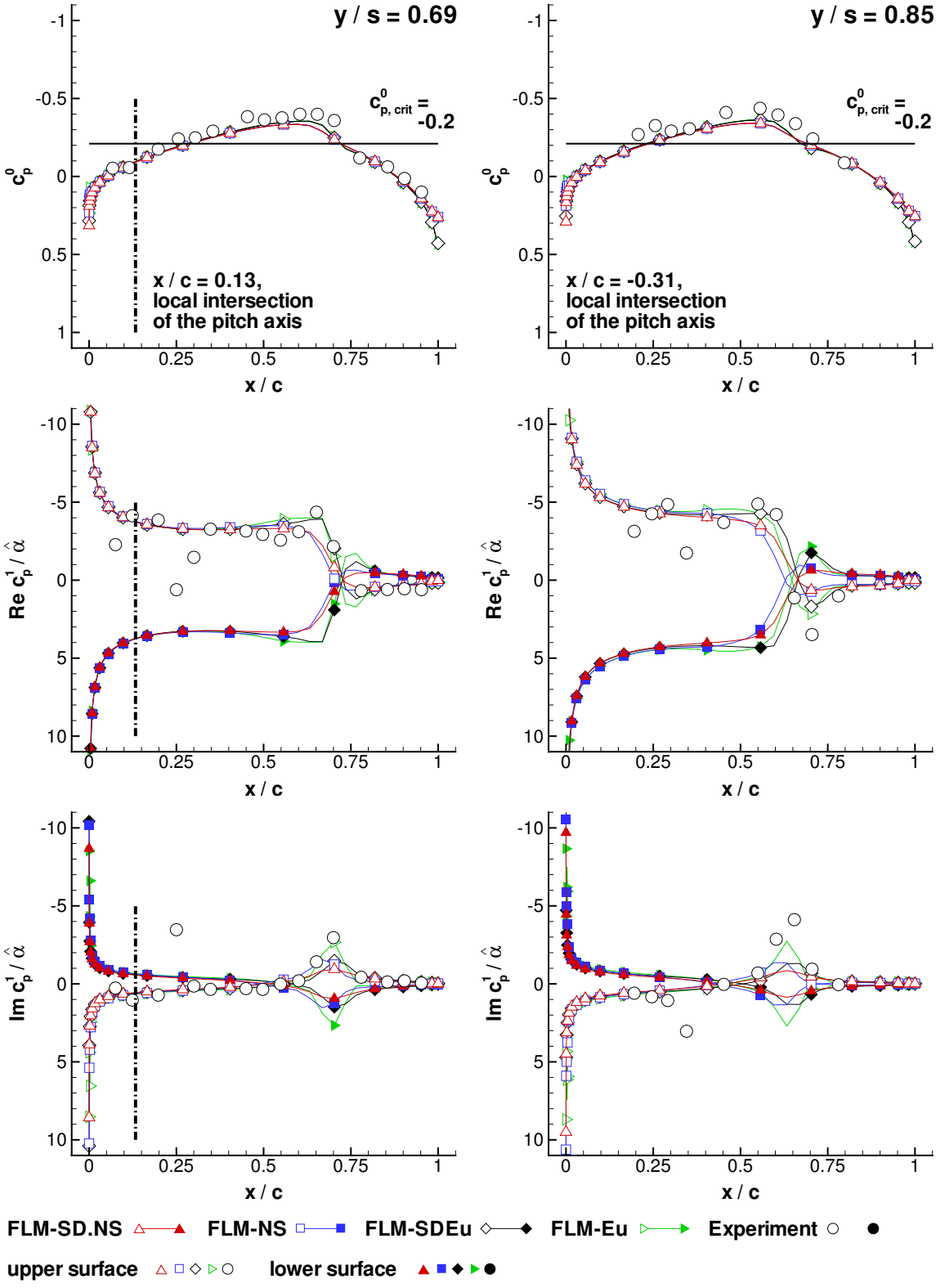

Figure 5.15: Pressure coeff. c_p^0, c_p^1 for a NCDW pitching oscill. at $Ma_\infty = 0.90$, $Re_\infty = 10.0 \times 10^6$, $\breve{\alpha} = 0.0$ deg about $x_p/c_r = 0.65$ w. $\hat{\breve{\alpha}} = 0.5$ deg, $k_{red} = 0.237$ (90D5, outer).

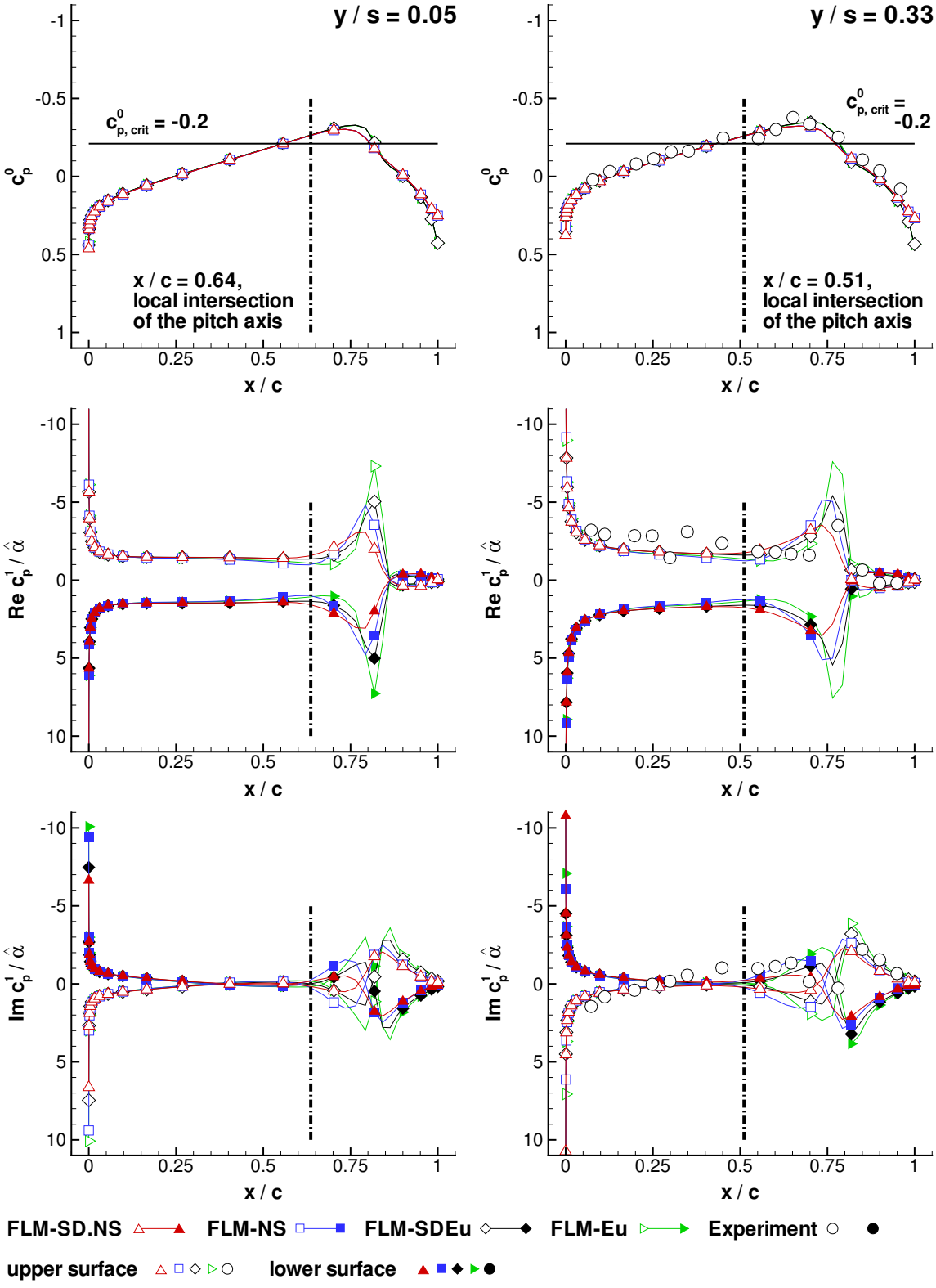

Figure 5.16: Pressure coeff. c_p^0, c_p^1 for a NCDW pitching oscill. at $Ma_\infty = 0.90$, $Re_\infty = 10.0 \times 10^6$, $\breve{\alpha} = 0.0$ deg about $x_p/c_r = 0.65$ w. $\hat{\breve{\alpha}} = 0.5$ deg, $k_{red} = 0.475$ (90D6, inner).

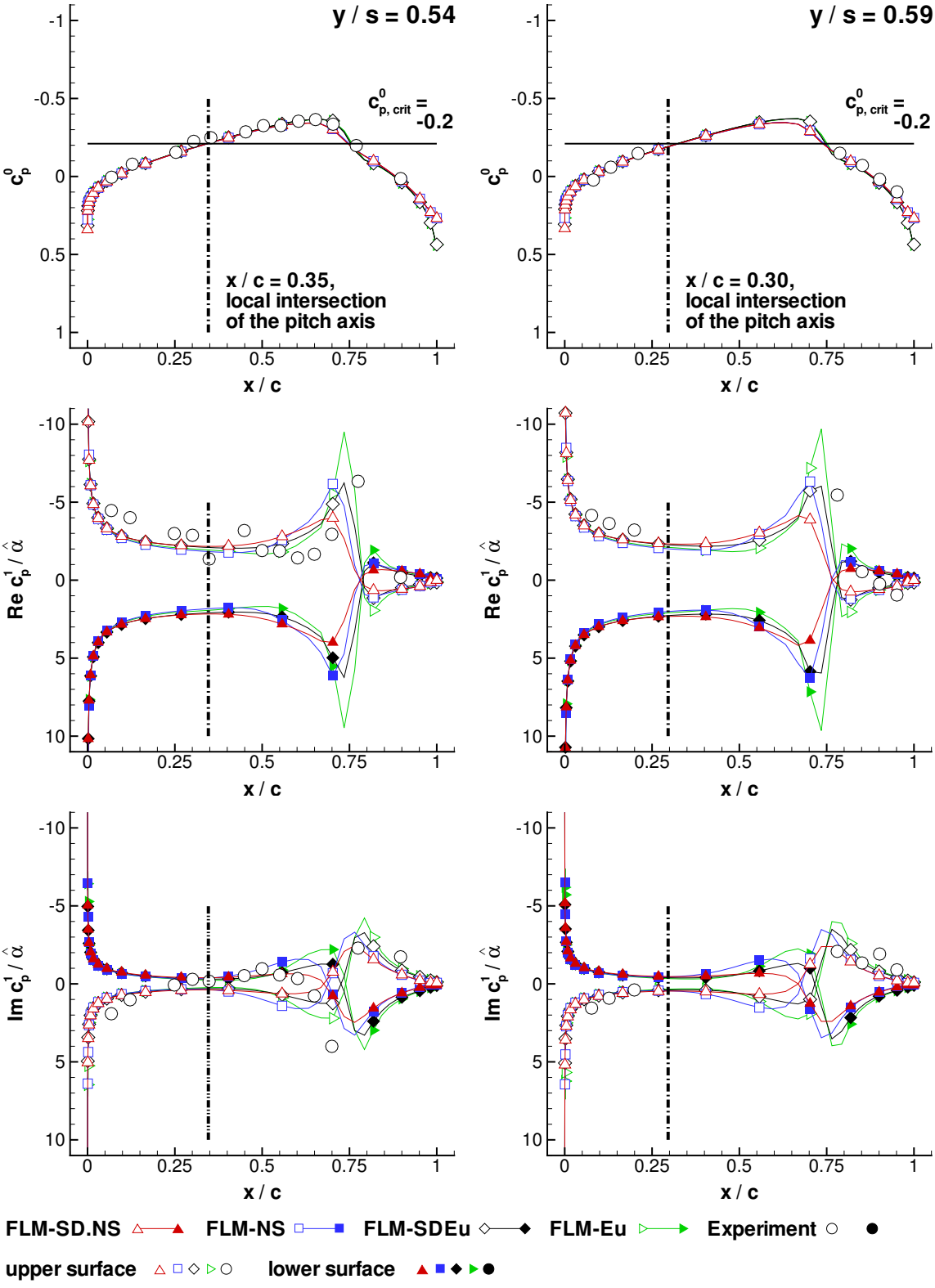

Figure 5.17: Pressure coeff. c_p^0, c_p^1 for a NCDW pitching oscill. at $Ma_\infty = 0.90$, $Re_\infty = 10.0 \times 10^6$, $\breve{\alpha} = 0.0$ deg about $x_p/c_r = 0.65$ w. $\hat{\breve{\alpha}} = 0.5$ deg, $k_{red} = 0.475$ (90D6, median).

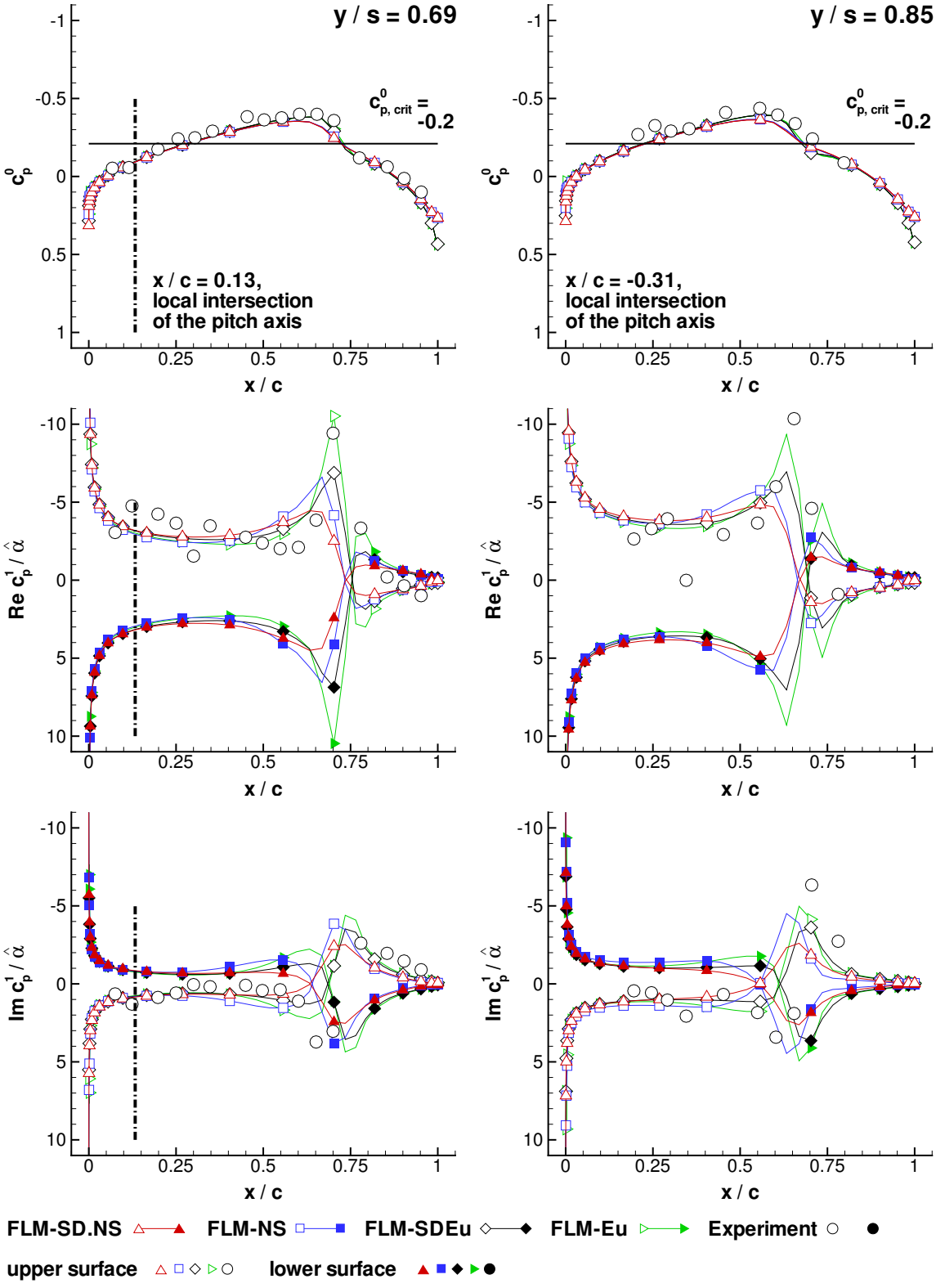

Figure 5.18: Pressure coeff. c_p^0, c_p^1 for a NCDW pitching oscill. at $Ma_\infty = 0.90$, $Re_\infty = 10.0 \times 10^6$, $\breve{\alpha} = 0.0$ deg about $x_p/c_r = 0.65$ w. $\hat{\breve{\alpha}} = 0.5$ deg, $k_{red} = 0.475$ (90D6, outer).

progression into negative territory. A secondary peak is exhibited at the location of the terminating $c_{p,\,crit}^{0}$. $\mathrm{Im}c_p^1$ increases from there toward the TE, where equalization with its lower-surface counterpart takes place. [From root to tip the chordwise locality of the $Im\,c_p^1$ zero-crossing is observed to move closer to the LE.] Forward of the zero-crossing, $\Delta\mathrm{Im}c_p^1$ contributes negatively to $\mathrm{Im}c_L^1$, while its aft counterpart does so positively. Both are approximately equal in magnitude, largely canceling each other out in the sectional $\mathrm{Im}c_L^1$. For the inner-span station[s], the pitch axis intersects closely to the exhibited zero-crossing. Thus, both forward and aft $\Delta\mathrm{Im}c_p^1$ can be said to render a negative (pitch down) contribution to $\mathrm{Im}c_M^1$. As the intersection of the pitch axis moves closer to the LE [from $y/s = 0.54$ to $y/s = 0.69$], merely the aft $\Delta\mathrm{Im}c_p^1$ can be identified to have an unambiguously negative (pitch down) contribution to $\mathrm{Im}\,c_M^1$. [For the outermost span station, however, $\Delta Im\,c_p^1$ forward of the zero-crossing can now be observed to have a solely positive (pitch up) contribution to $Im\,c_M^1$, opposing the solely negative (pitch down) contribution of the aft $\Delta Im\,c_p^1$.] Integrating over the entire wing, both a negative $\mathrm{Im}c_L^1$ and $\mathrm{Im}c_M^1$ (pitch down) are ascertained, however, with $\mathrm{Im}c_L^1$ being an order of magnitude smaller in absolute value than $\mathrm{Re}c_L^1$. [103]

With respect to the prediction accuracy, it can be further determined that

> [f]or [all] span stations, FLM-SD.NS-computed c_p^0, $\mathrm{Re}c_p^1$, and $\mathrm{Im}c_p^1$ agree excellently with those obtained from FLM-NS. Mild discrepancies are observed in the shock and postshock region. Evidently, the small disturbance premise holds up under the dynamic nonlinearity of the weak shock. The conformity between FLM-SD.NS and FLM-NS can be seen equal to that between FLM-SDEu and FLM-Eu. Viscous and inviscid c_p^0 differ only marginally in the shock region, with greater variation becoming noticeable for their $\mathrm{Re}c_p^1$ and $\mathrm{Im}c_p^1$ counterparts. In particular, the inviscid methods predict a mild secondary $\mathrm{Re}c_p^1$ peak that persists from the inner- to the outer-span station[s]. Disregarding outliers, experimental surface pressure is reproduced well. Surprisingly, the data points rendering the secondary $\mathrm{Re}c_p^1$ and $\mathrm{Im}c_p^1$ peak are best met by the FLM-Eu computation. [103]

Considering the 90D4 case (the half-frequency case) next, the FLM-SD.NS result as provided in Figures 5.10–5.12 is characterized. The symmetric upper- and lower-surface c_p^0 are naturally equal to those of the 90D5 case, as both computations employ the same reference solution, while the particular antisymmetric $Re\,c_p^1$ and $Im\,c_p^1$ progressions are gained very similar to their baseline-frequency counterparts. The most noticeable difference is observed in the diminished secondary $Im\,c_p^1$ peak. Hence, $\Delta Im\,c_p^1$ aft of the zero-crossing contributes less positively to $Im\,c_L^1$ and less negatively (pitch down) to $Im\,c_M^1$ than in the 90D5 case.

For the investigated span stations, FLM-SD.NS-computed c_p^0, $Re\,c_p^1$, and $Im\,c_p^1$ agree excellently with those obtained from FLM-NS. The mild discrepancies observed for the 90D5 case in the shock and postshock region have been mitigated toward half-frequency.

Furthermore, the conformity between FLM-SD.NS and FLM-NS can again be seen equal to that between FLM-SDEu and FLM-Eu. The deviation witnessed between the viscous and inviscid instances of $Re\,c_p^1$ in the shock region is similar to the one seen for the 90D5 case. In particular, the inviscid methods still predict a mild secondary $Re\,c_p^1$ peak from the inner- to the outer-span stations. The viscous-inviscid deviation for $Im\,c_p^1$, however, has reduced at half-frequency. Disregarding outliers, experimental surface pressure is again reproduced well. At the outer-span stations, though, data points for $Re\,c_p^1$ no longer imply the existence of a secondary peak in the shock region, now validating the viscous prediction. Data points rendering the secondary $Im\,c_p^1$ peak are now met equally well by the viscous and inviscid consideration.

Lastly, the 90D6 case (the double-frequency case) is regarded. The FLM-SD.NS result as provided in Figures 5.16–5.18 is characterized. The symmetric upper- and lower-surface c_p^0 are again equal to those of the 90D5 case, as both computations employ the same reference solution, while the particular antisymmetric $Re\,c_p^1$ and $Im\,c_p^1$ progressions are gained similar to their baseline-frequency counterparts upstream of the shock region. From the shock region to the TE, however, substantial deviations with respect to the 90D5 case are observed. They increase from the innermost to the outermost span station. Specifically, the mild secondary $Re\,c_p^1$ peak observed for the 90D5 case at the inner-span stations has become very prominent for the 90D6 case and now exists over the entire semi-span. Hence, the shock-region $\Delta Re\,c_p^1$ forward of the zero-crossing now contributes more positively to $Re\,c_L^1$ than in the 90D5 case, with the $\Delta Re\,c_p^1$ aft of the zero-crossing, however, contributing more negatively to $Re\,c_L^1$, in turn. Correspondingly, the shock-region $\Delta Re\,c_p^1$ forward of the zero-crossing now contributes more negatively (pitch down) to $Re\,c_M^1$ than in the 90D5 case, while the $\Delta Re\,c_p^1$ aft of the zero-crossing does so more positively (pitch up). With respect to $Im\,c_p^1$, the upper- and lower-surface progressions forward of the shock region are observed to widen from the innermost to the outermost span station, evolving from intersecting progressions to nonintersecting ones. In comparison, the 90D5 case upper- and lower-surface $Im\,c_p^1$ progressions forward of the shock region are characterized by their singular intersection. Hence, $\Delta Im\,c_p^1$ forward of the zero-crossing now contributes more negatively to $Im\,c_L^1$ than in the 90D5 case. With the secondary $Im\,c_p^1$ peak also emerging more prominently at double-frequency, $\Delta Im\,c_p^1$ aft of the zero-crossing, in turn, contributes more positively to $Re\,c_L^1$. Correspondingly, $\Delta Im\,c_p^1$ aft of the pitch-axis intersection and forward of the zero-crossing now contributes more positively (pitch up) to $Im\,c_M^1$ than in the 90D5 case, while the $\Delta Im\,c_p^1$ aft of the zero-crossing does so more negatively (pitch down).

For the investigated span stations, FLM-SD.NS-computed c_p^0 agrees excellently with the one obtained from FLM-NS. Forward of the shock region the particular $Re\,c_p^1$ and $Im\,c_p^1$ instances do so as well. In the shock and postshock region, however, the intermethod

agreement becomes merely satisfactory: The mild discrepancies observed for the 90D5 case at these localities have been amplified toward double-frequency. However, the conformity between FLM-SD.NS and FLM-NS can still be considered nearly equal to that between FLM-SDEu and FLM-Eu. Merely the inviscid $Re\, c_p^1$-predictions in the shock region appear to deviate stronger than their viscous counterparts. Disregarding outliers, experimental surface pressure is again reproduced well. At the outer-span stations, the data points rendering the secondary $Re\, c_p^1$ and $Im\, c_p^1$ peak are best met by the FLM-Eu computation. This is similar to the behavior witnessed for the 90D5 case across the entire semi-span.

5.3.1.2 Global Load Coefficients

The computed global load coefficients of the 90D4, 90D5, and 90D6 cases are compiled in Table 5.3. The 90D5 case (the baseline-frequency case) is focused on at first. Pursuant to Pechloff and Laschka, it can be established that

> $\mathrm{Re}c_L^1$ gained from FLM-SD.NS agrees excellently to its FLM-NS counterpart. $\mathrm{Im}c_L^1$, on the other hand, is predicted 10% higher in absolute value. This deviation, however, becomes acceptable when taking the two orders of magnitude into account that separate $\mathrm{Re}c_L^1$ from $\mathrm{Im}c_L^1$. [The minutely negative $Im\, c_L^1$ indicates a time-dependent c_L that marginally lags the excitation, or may even be perceived as being entirely in phase.] Both FLM-SDEu- and FLM-Eu-computed $\mathrm{Re}c_L^1$ are 5% higher than their viscous counterparts, attributable to the differing prediction of $\mathrm{Re}c_p^1$ in the shock region. Their mutual deviation is similarly negligible. With FLM-SDEu $\mathrm{Im}c_L^1$ is gained equal to its FLM-SD.NS-predicted instance, disregarded viscosity apparently having no impact. Surprisingly, $\mathrm{Im}c_L^1$ obtained from FLM-Eu exhibits a positive sign, [in principle indicating a reversal of phase,]while remaining within the same order of magnitude as its FLM-SDEu counterpart.
>
> FLM-SD.NS-computed $\mathrm{Re}c_M^1$ and $\mathrm{Im}c_M^1$ are, respectively, 3% and 9% lower in absolute value than their FLM-NS counterparts. Evidently, the deviation exhibited in $\mathrm{Im}c_L^1$ has followed through to $\mathrm{Im}c_M^1$. $\mathrm{Re}c_M^1$ and $\mathrm{Im}c_M^1$ are now in the same order of magnitude. The time-dependent c_M clearly lags the excitation, which in case of a free pitching oscillation would have a damping effect. FLM-SDEu- and FLM-Eu-computed $\mathrm{Re}c_M^1$ are, respectively, 16% and 14% lower than their viscous counterparts. The particular $\mathrm{Im}c_M^1$ instances, on the other hand, are 10% and 13% higher in absolute value. Disregarded viscosity has a more noticeable impact on c_M^1 than on c_L^1, with the inviscid $\mathrm{Im}c_M^1$ indicating greater dynamic stability. [With exception of $Im\, c_L^1$, the d]eviation between FLM-SDEu- and FLM-Eu-computed instances is similar to the one shown by the corresponding viscous methods. [103]

Considering the 90D4 case (the half-frequency case) next, FLM-SD.NS predicts $|c_L^1|$

Case	Method	c_L^0	$Re\, c_L^1/\hat{\alpha}$	$Im\, c_L^1/\hat{\alpha}$	$\lvert c_L^1\rvert/\hat{\alpha}$	$\breve{\varphi}_{c_L^1}$, deg
90D4	FLM-SD.NS	0.000	3.782	-0.016	3.782	-0.24
	FLM-NS	0.000	3.769	-0.012	3.769	-0.18
	FLM-SDEu	0.000	3.984	-0.013	3.984	-0.19
	FLM-Eu	0.000	3.950	-0.007	3.950	-0.10
90D5 [103], Table 3	FLM-SD.NS	0.000	3.748	-0.013	3.748	-0.20
	FLM-NS	0.000	3.762	-0.012	3.762	-0.18
	FLM-SDEu	0.000	3.956	-0.013	3.956	-0.19
	FLM-Eu	0.000	3.962	0.007	3.962	0.11
90D6	FLM-SD.NS	0.000	3.668	-0.064	3.669	-1.00
	FLM-NS	0.000	3.663	-0.228	3.671	-3.56
	FLM-SDEu	0.000	3.872	-0.126	3.874	-1.87
	FLM-Eu	0.000	3.833	-0.241	3.840	-3.60

Case	Method	c_M^0	$Re\, c_M^1/\hat{\alpha}$	$Im\, c_M^1/\hat{\alpha}$	$\lvert c_M^1\rvert/\hat{\alpha}$	$\breve{\varphi}_{c_M^1}$, deg
90D4	FLM-SD.NS	0.000	0.346	-0.093	0.358	-15.09
	FLM-NS	0.000	0.359	-0.099	0.373	-15.46
	FLM-SDEu	0.000	0.301	-0.103	0.318	-18.90
	FLM-Eu	0.000	0.322	-0.110	0.340	-18.86
90D5 [103], Table 3	FLM-SD.NS	0.000	0.322	-0.178	0.368	-28.87
	FLM-NS	0.000	0.333	-0.196	0.387	-30.51
	FLM-SDEu	0.000	0.271	-0.196	0.335	-35.84
	FLM-Eu	0.000	0.285	-0.222	0.361	-37.88
90D6	FLM-SD.NS	0.000	0.221	-0.291	0.365	-52.75
	FLM-NS	0.000	0.155	-0.254	0.297	-58.61
	FLM-SDEu	0.000	0.137	-0.280	0.312	-64.02
	FLM-Eu	0.000	0.097	-0.243	0.261	-68.31

Table 5.3: Global load coefficients for the NCDW 90D4–6 cases ($Ma_\infty = 0.90$, $Re_\infty = 10.0 \times 10^6$, $\breve{\alpha} = 0.0$ deg, $x_p/c_r = 0.65$, $\breve{\hat{\alpha}} = 0.5$ deg, $k_{red} = 0.119, 0.237, 0.475$).

nearly identical to the FLM-NS-gained value, with both methods similarly indicating a time-dependent c_L that minimally lags the excitation. Again, both predictions may even be perceived as being entirely in phase. FLM-SD.NS- and FLM-NS-computed $|c_L^1|$, as well as the mean of $\breve{\varphi}_{c_L^1}$, can be considered unchanged with respect to the 90D5 case. FLM-SDEu- and FLM-Eu-computed $|c_L^1|$ are also observed to be identical, with both methods equivalently indicating a time-dependent c_L that minimally lags the excitation. Similar to the viscous consideration, the behavior of c_L may even be perceived as being entirely in phase. Disregarded viscosity yields a 5% higher $|c_L^1|$, while affecting $\breve{\varphi}_{c_L^1}$ only marginally. For either inviscid computation, both $|c_L^1|$ and $|\breve{\varphi}_{c_L^1}|$ are gained equal to those of the 90D5 case. A reversal of phase, however, is witnessed for the FLM-Eu instance at half-frequency, FLM-SDEu and FLM-Eu now conforming in their marginally lagging c_L prediction, where they had not for the 90D5 case.

Obtained from FLM-SD.NS, $|c_M^1|$ is gained merely 4% lower than its FLM-NS counterpart, with the $\breve{\varphi}_{c_M^1}$ instances deviating by even less. Both methods predict a time-dependent c_M that distinctly lags the excitation, indicating a damping effect on the free pitching oscillation. Whereas the mean of the $|c_M^1|$ instances has decreased only marginally to the mean of their 90D5 case counterparts, the mean of $|\breve{\varphi}_{c_M^1}|$ has decreased by 48%. In case of a free pitching oscillation this combination would indicate a substantially lesser degree of dynamic stability than for the 90D5 case, corroborated by $|Im\, c_M^1|_{90D4} < |Im\, c_M^1|_{90D5}$ for the mean instances as well. The spread between FLM-SD.NS- and FLM-NS-computed $|c_M^1|$ is similar to the one observed for the 90D5 case. Contrarily, the 5% deviation witnessed in $\breve{\varphi}_{c_M^1}$ for the 90D5 case reduces to 2% at half-frequency. Obtained from FLM-SDEu, $|c_M^1|$ is merely 6% lower than its FLM-Eu counterpart, with the $\breve{\varphi}_{c_M^1}$ instances being identical. Disregarded viscosity yields a 10% lower mean $|c_M^1|$ and a 24% higher mean $|\breve{\varphi}_{c_M^1}|$. Again, the time-dependent c_M distinctly lags the excitation. However, the mean $|c_M^1|$ and the mean $|\breve{\varphi}_{c_M^1}|$ in combination indicate a distinctly greater degree of dynamic stability for the free pitching oscillation, corroborated by $|Im\, c_M^1|_{inviscid} > |Im\, c_M^1|_{viscous}$ for the mean instances as well. Evidently, the relative impact of the inviscid consideration on both $|c_M^1|$ and $\breve{\varphi}_{c_M^1}$ is similar to the one observed for the the 90D5 case. Perforce, the mean of the inviscidly computed $|c_M^1|$ decreases by 5% toward half-frequency, while the mean of $|\breve{\varphi}_{c_M^1}|$ has decreased by 49%. This is equal to the decrease seen for the viscous consideration.

Lastly, the 90D6 case (the double-frequency case) is regarded. FLM-SD.NS predicts $|c_L^1|$ nearly identical to the FLM-NS-gained value, with both methods again predicting a lagging $\breve{\varphi}_{c_L^1}$ in the low single-digit degree range. In comparison to the 90D5 case, $|c_L^1|$ is merely 2% lower, with the mean of the $|\breve{\varphi}_{c_L^1}|$ instances having contrarily increased. FLM-SDEu- and FLM-Eu-computed $|c_L^1|$ can also be considered identical, with both methods predicting a lagging $\breve{\varphi}_{c_M^1}$ in the low single-digit degree. Disregarded viscosity yields a

5% higher $|c_L^1|$, while affecting $\check{\varphi}_{c_L^1}$ only marginally. At double-frequency, $|c_L^1|$ has merely decreased by 3%, while the mean of the $|\check{\varphi}_{c_L^1}|$ instances have contrarily increased. This behavior is comparable to the one observed for the viscous instances. However, a reversal of phase is witnessed or the FLM-Eu instance at double-frequency, FLM-SDEu and FLM-Eu now conforming in their slightly lagging c_L prediction, where they had not for the 90D5 case.

Yielding from FLM-SD.NS, $|c_M^1|$ is gained 23% higher than its FLM-NS counterpart. Evidently, the spread between the FLM-SD.NS- and FLM-NS-computed $|c_M^1|$ has increased substantially with respect to the baseline- and half-frequency cases. Even though the viscously predicted $|c_L^1|$ instances had shown a negligible deviation, an extraordinary amplification appears to have occurred toward $|c_M^1|$. In comparison, the spread between the FLM-SD.NS- and FLM-NS-computed $|\check{\varphi}_{c_M^1}|$ has merely increased from 5% to 10% at double-frequency. Both methods again predict a time-dependent c_M that substantially lags the excitation, indicating a damping effect on the free pitching oscillation. Whereas the mean of the $|c_M^1|$ instances has decreased by 12% to the mean of their 90D5 case counterparts, the mean of $|\check{\varphi}_{c_M^1}|$ has increased by 87%. In case of a free pitching oscillation this combination would indicate a substantially higher degree of dynamic stability than for the 90D5 case, corroborated by $|Im\, c_M^1|_{90D6} > |Im\, c_M^1|_{90D5}$ for the mean instances as well. Obtained from FLM-SDEu, $|c_M^1|$ is gained 19% higher than its FLM-Eu counterpart. The spread between the two instances is somewhat lower than the one seen for the corresponding viscous instances, establishing the notion of an inviscidly incurred base deviation between FLM-SD.NS and FLM-NS. This circumstance can also be witnessed in $|\check{\varphi}_{c_M^1}|$, where the FLM-SDEu prediction is 6% lower than the FLM-Eu prediction. Disregarded viscosity yields a 13% lower mean $|c_M^1|$ and a 19% higher mean $|\check{\varphi}_{c_M^1}|$. Again, the time-dependent c_M significantly lags the excitation. However, the mean $|c_M^1|$ and the mean $|\check{\varphi}_{c_M^1}|$ in combination indicate a slightly lesser degree of dynamic stability for the free pitching oscillation, corroborated by $|Im\, c_M^1|_{inviscid} < |Im\, c_M^1|_{viscous}$ for the mean instances as well. Across the investigated frequency range the mean $|\check{\varphi}_{c_M^1}|$ exhibits its greatest value for this particular computation. Notably, the inviscid consideration's relative impact on both $|c_M^1|$ and $\check{\varphi}_{c_M^1}$ is seen to be far more substantial than it had been for the 90D5 case.

5.3.1.3 Overall Assessment

FLM-SD.NS computes the unsteady loading of the 90D4 and 90D5 case [103] in very good agreement to FLM-NS. In regard to the 90D6 case, however, agreement diminishes to only a satisfactory one. In all cases, the viscous consideration improves on the inviscid prediction for both the small disturbance and dynamically fully nonlinear approach. Specifically, the viscously computed $|c_L^1|$ is gained consistently lower than its inviscid counterpart for

the investigated frequency range, while $|c_M^1|$ in turn is gained consistently higher. Furthermore, the viscously computed $|\check{\varphi}_{c_M^1}|$ is observed consistently lower than in the inviscid consideration. In combination, however, the viscous prediction indicates a lesser degree of dynamic stability for the 90D4 and 90D5 case, while a higher one for the 90D6 case. Both the viscous and inviscid consideration produce a $\check{\varphi}_{c_M^1}$ progression over k_{red} that is nearly linear. The gradients between each supporting point are similar: At half-frequency, $|\check{\varphi}_{c_M^1}|$ has decreased by approximately 50%, while having increased by approximately 100% at double-frequency.

5.3.2 Medium-Strength Shock/Leading-Edge-Vortex Cases

At $Ma_\infty = 0.90$, $Re_\infty = 10.0 \times 10^6$, and $\check{\alpha} = 3.97$ deg, it can be ascertained in accordance with Pechloff and Laschka that the FLM-NS-provided linearized time-invariant-mean flowfield underlying the FLM-SD.NS computation of the 90D28, 90D29, and 90D30 cases features

> an expanded supersonic region in proximity to the upper wing surface. It extends from the root to the tip, terminating with a medium-strength shock significantly upstream of the TE[, Figure 5.19]. At the root, the sharp LE additionally initiates a vortex that convects toward the tip[, Figure 5.20]. The LE itself approximately renders the line of separation, while the line of reattachment is observed at a sweep angle of 56 deg. [This LEV] induces a localized suction plateau on the upper surface which increases in both intensity and expansion over the course of the progression, [$\overline{c_p}^*$] reaching its minimum value at the LE and $y/s \approx 0.95$. Toward the tip, the LEV has intersected the shock ($y/s \approx 0.80$), the interaction between the two rendering quite the intricate flow topology. [103]

The FLM-SD.NS-obtained surface-pressure-coefficient distributions of the 90D29 case are compared to their FLM-NS, FLM-SDEu, and FLM-Eu counterparts, as well as to the particular experimental data for the investigated span stations in Figures 5.21–5.23. The surface-pressure-coefficient distributions of span stations $y/s = 0.33$ and $y/s = 0.69$ were originally presented in [103], Fig. 9. Supplementally, the FLM-SD.NS/FLM-NS planform upper-surface zeroth- and first-harmonic pressure coefficient is provided in Figure 5.24, with the FLM-NS planform upper-surface second- and third-harmonic pressure coefficient shown in Figure 5.25.

5.3.2.1 Local Load Coefficients

The FLM-SD.NS result of the 90D29 case (the baseline-frequency case) is characterized for an inner- and an outer-span station, respectively, $y/s = 0.33$ (Figure 5.21) and $y/s = 0.69$ (Figure 5.23). Pursuant to Pechloff and Laschka, it can be established that

[for the particular] inner-span station [...], the sharp LE renders an initial suction peak for the upper-surface c_p^0 progression. It acutely increases immediately downstream, a tightly constrained suction plateau induced by the LEV. As rotational velocity abruptly subsides beyond the line of reattachment ($x/c = 0.10$), c_p^0 again increases steeply, eventually leading into a local maximum. The further acceleration from subsonic to supersonic speeds produces a linearly decreasing c_p^0 that culminates in a local minimum before the discontinuous recompression, the medium-strength shock. As supersonic flow terminates, the remaining recompression toward the TE is strictly continuous. In contrast, the convex lower-surface c_p^0 progression never falls below $c_{p,crit}^0$, indicating subsonic flow from LE to TE. Notably, the continuous recompression toward the TE occurs with a c_p^0 of lesser value than observed for the [upper surface], equalization eventually taking place at the TE. Apparently, the positive contribution to c_L^0 made by Δc_p^0 forward of both progressions' intersection is only marginally compensated by the negative one aft of it. In accordance, Δc_p^0 leveraged respective the pitch axis unambiguously yields a positive (pitch up) net contribution to c_M^0.

The c_p^0 progressions of the [particular] outer-span station are qualitatively similar to their inner counterparts. In regard to the upper surface, the suction plateau is now observed to range farther downstream, as the extent of the LEV has grown. Shortly beyond the line of reattachment ($x/c = 0.27$) the flow has already become supersonic. Accelerating further, c_p^0 again decreases linearly downstream, however, now over a far shorter distance. The local minimum preceding the discontinuous recompression is exhibited far-

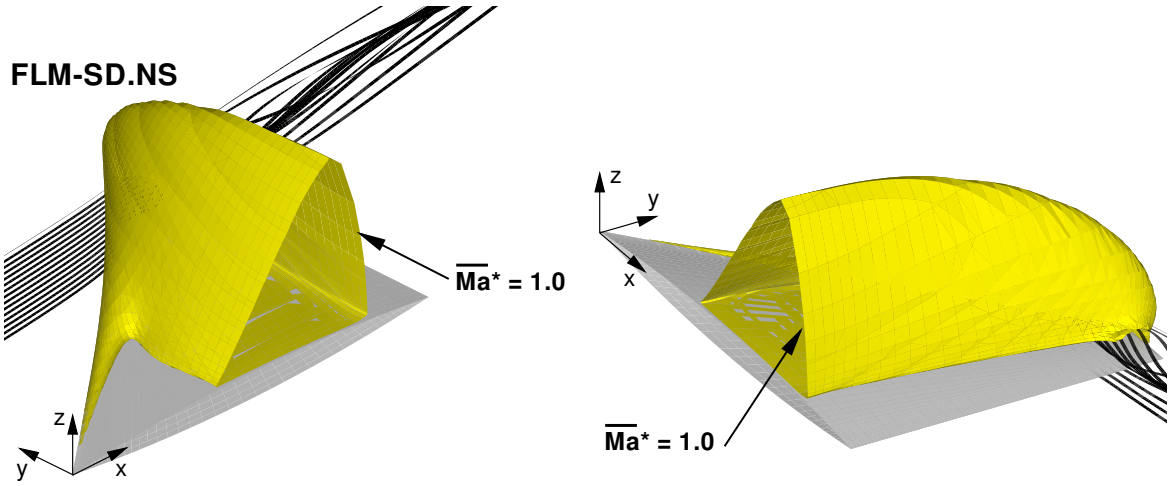

Figure 5.19: Sonic isosurface (LE view and TE view [103], Fig. 7) of the linearized time-invariant-mean flowfield employed by FLM-SD.NS in the NCDW 90D28–30 cases ($Ma_\infty = 0.90$, $Re_\infty = 10.0 \times 10^6$, $\breve{\alpha} = 3.97$ deg, $x_p/c_r = 0.65$, $\hat{\breve{\alpha}} = 0.5$ deg, $k_{red} = 0.120$, 0.240, 0.480).

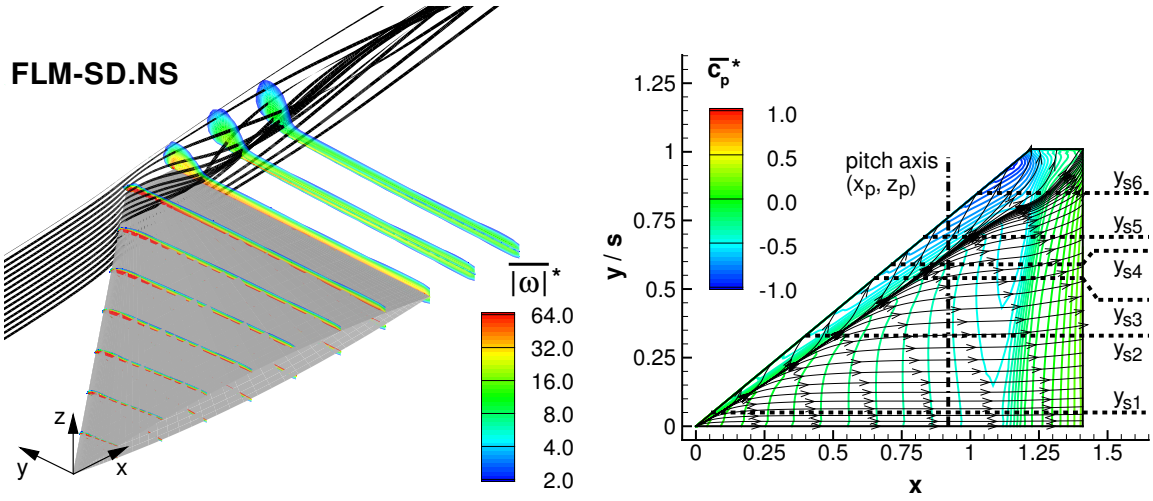

Figure 5.20: Vorticity contours, near-surface streamlines, and surface isobars (based on [103], Fig. 8) of the linearized time-invariant-mean flowfield employed by FLM-SD.NS in the NCDW 90D28–30 cases ($Ma_\infty = 0.90$, $Re_\infty = 10.0 \times 10^6$, $\breve{\alpha} = 3.97$ deg, $x_p/c_r = 0.65$, $\mathring{\alpha} = 0.5$ deg, $k_{red} = 0.120$, 0.240, 0.480).

ther upstream relative to the local chord length than its [particular] inner-span-station counterpart. The latter can also be observed for the $c^0_{p,\,crit}$-indicated shock base. For the lower surface, c^0_p still indicates entirely subsonic flow, with the convex progression now intersecting its upper-surface counterpart farther upstream relative to the chord length. Whereas Δc^0_p again yields a substantial positive contribution to c^0_L, its leverage with respect to the pitch axis now renders a differingly negative (pitch down) contribution to c^0_M. Integrating over the entire wing though, both a positive c^0_L and c^0_M (pitch up) are ascertained.

Common to the [particular] inner- and outer-span station, the upper-surface $\mathrm{Re}c^1_p$ progression is characterized by a forward and aft negative peak, respectively, ascribed to the implied motion of the LEV and shock. They are interconnected by a region of nearly constant $\mathrm{Re}\,c^1_p$. Postshock, $\mathrm{Re}c^1_p$ increases abruptly, leading into a positive value progression which ultimately decreases toward the TE, a reversal of sign occurring again shortly before reaching it. Comparing the $\mathrm{Re}c^1_p$ progression of the [particular] inner- and outer-span station, the LEV-induced peak has moved farther downstream relative to the local chord length for the latter. It exhibits a decrease in value and a greatly widened base. Vice versa, the shock-induced peak is now situated farther upstream while its value has increased. The base of the shock-induced peak, however, widens only slightly. As a consequence of both the LEV- and shock-induced occurrences, the interconnecting region of nearly constant $\mathrm{Re}c^1_p$ has reduced to a small fraction of the chord length. The [particular] inner- and outer-span-station instances of the lower-surface $\mathrm{Re}c^1_p$ progression

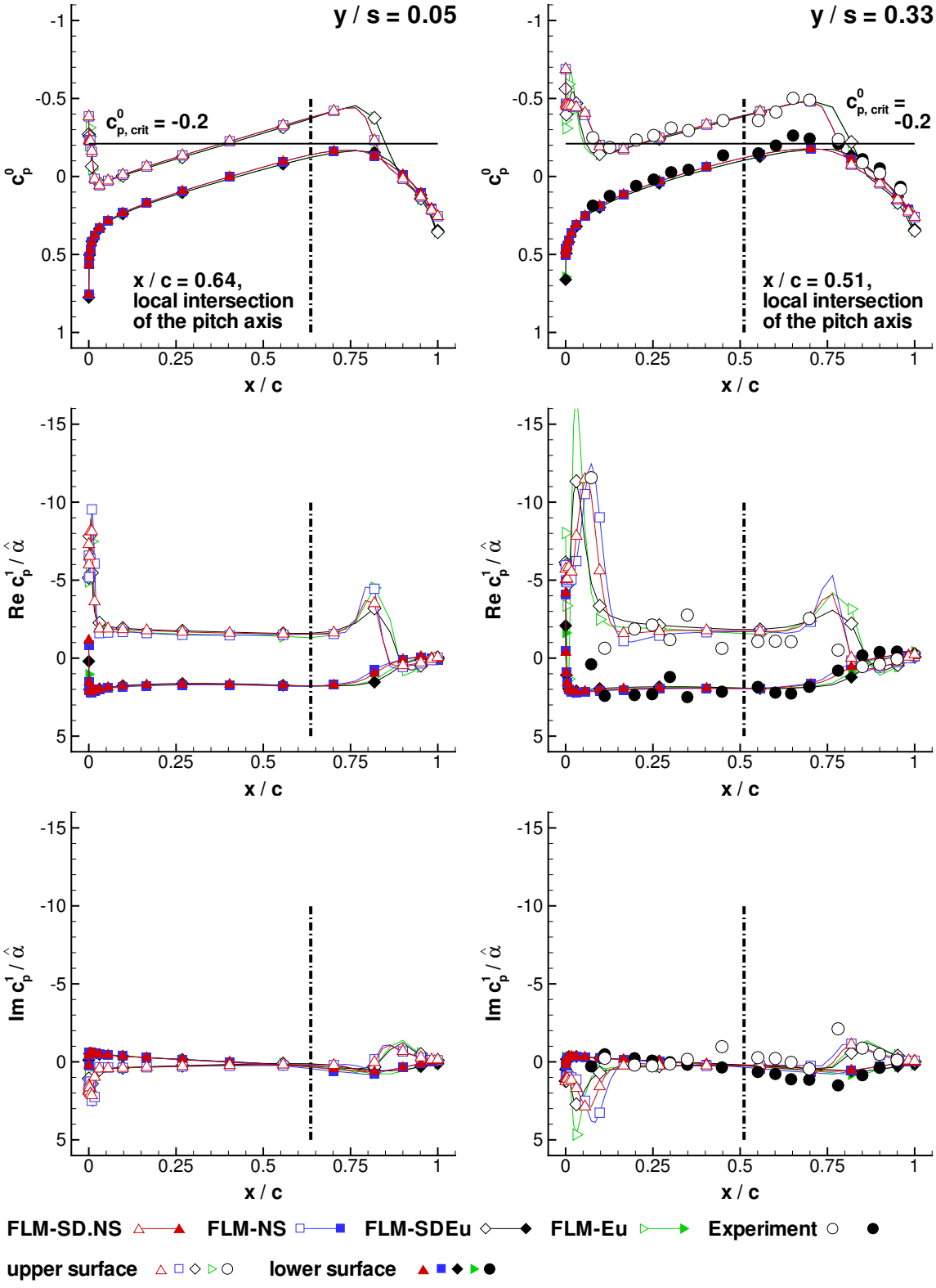

Figure 5.21: Press. coeff. c_p^0, c_p^1 for a NCDW pitching oscill. at $Ma_\infty = 0.90$, $Re_\infty = 10.0 \times 10^6$, $\breve{\alpha} = 3.97$ deg about $x_p/c_r = 0.65$ w. $\hat{\breve{\alpha}} = 0.5$ deg, $k_{red} = 0.240$ (90D29, inner).

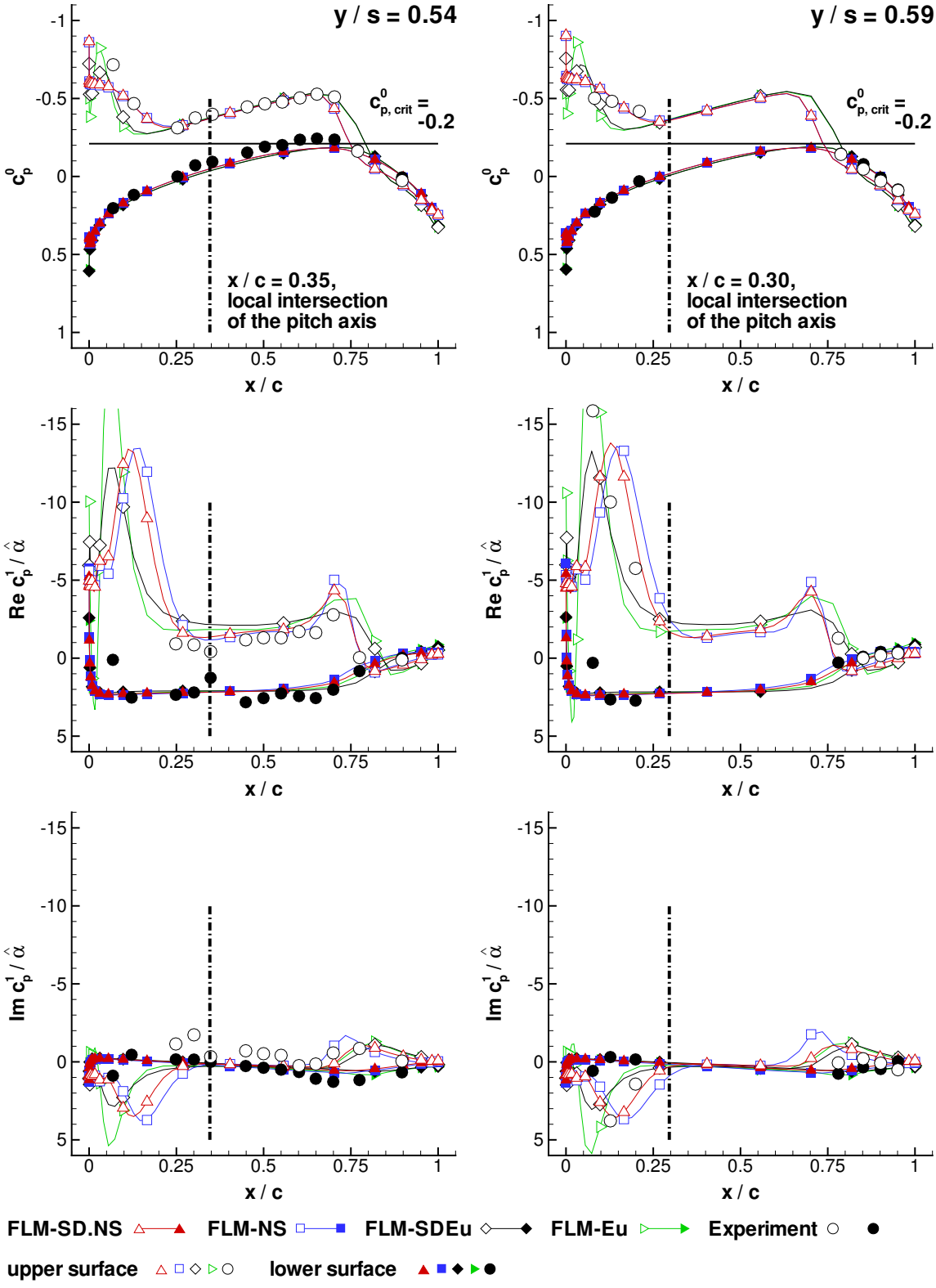

Figure 5.22: Press. coeff. c_p^0, c_p^1 for a NCDW pitching oscill. at $Ma_\infty = 0.90$, $Re_\infty = 10.0 \times 10^6$, $\breve{\alpha} = 3.97$ deg ab. $x_p/c_r = 0.65$ w. $\hat{\breve{\alpha}} = 0.5$ deg, $k_{red} = 0.240$ (90D29, median).

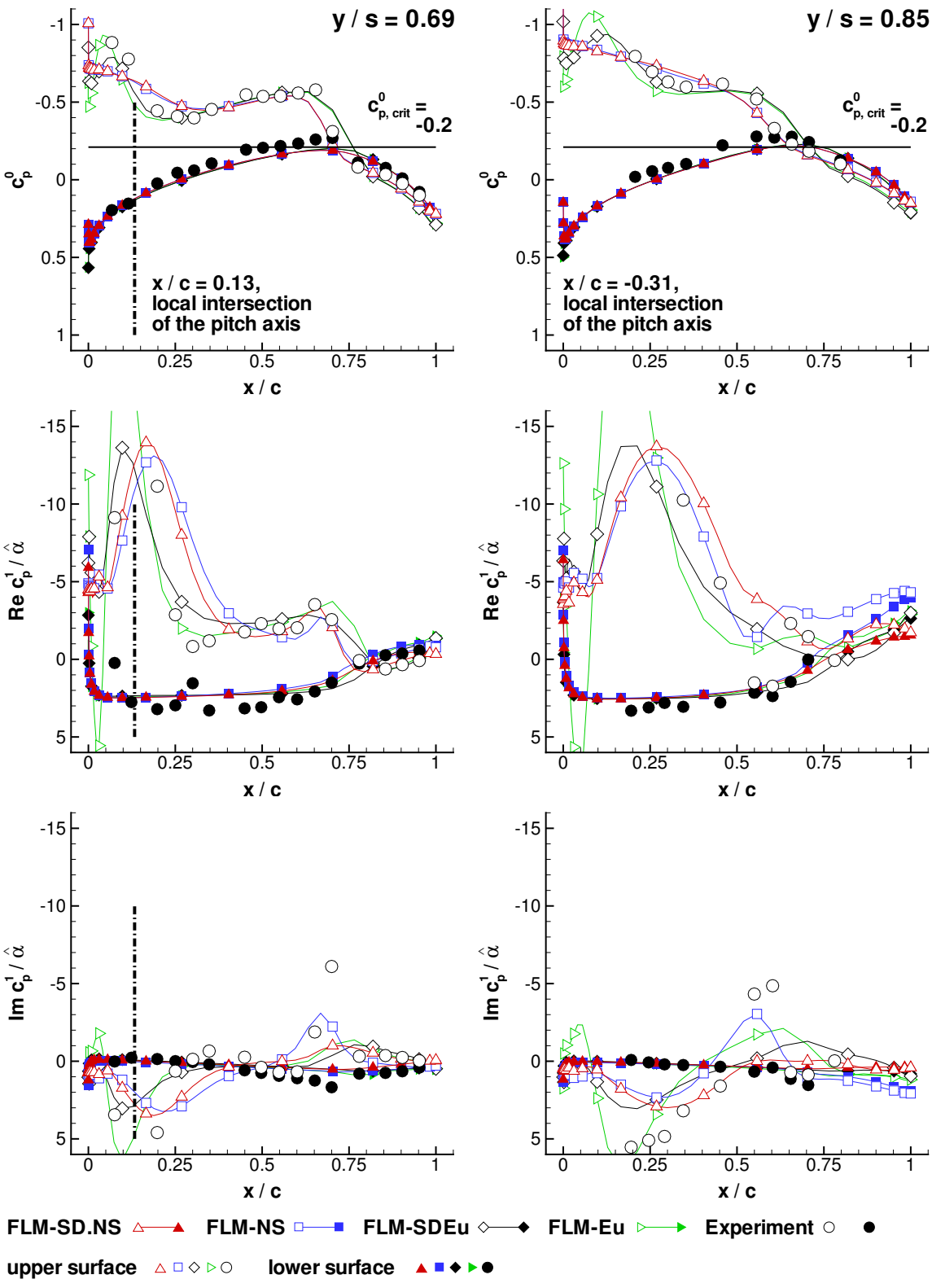

Figure 5.23: Press. coeff. c_p^0, c_p^1 for a NCDW pitching oscill. at $Ma_\infty = 0.90$, $Re_\infty = 10.0 \times 10^6$, $\breve{\alpha} = 3.97$ deg about $x_p/c_r = 0.65$ w. $\hat{\breve{\alpha}} = 0.5$ deg, $k_{red} = 0.240$ (90D29, outer).

are again similar. They increase acutely from the LE toward a nearly constant value that ranges downstream. Subsequently decreasing, the progressions intersect their upper-surface counterparts, reverse sign, and finally equalize at the TE. In either case, the positive $\mathrm{Re}c_L^1$ contribution made by $\Delta\mathrm{Re}c_p^1$ forward of the intersection is only marginally compensated by the negative one aft of it. For the [particular] inner-span station, $\Delta\mathrm{Re}c_p^1$ leveraged respective the pitch axis will unambiguously yield a positive (pitch up) net contribution to $\mathrm{Re}c_M^1$. For the [particular] outer-span station, on the other hand, it will result in a differingly negative (pitch down) net contribution. Integrating over the entire wing though, both a positive $\mathrm{Re}c_L^1$ and $\mathrm{Re}c_M^1$ (pitch up) are ascertained.

Naturally, the implied motion of the LEV and shock also leaves its trace on the upper-surface $\mathrm{Im}c_p^1$ progression. For both the [particular] inner- and outer-span station[,] a forward positive and aft negative peak have developed, however, being of substantially lower absolute value than their upper-surface $\mathrm{Re}c_p^1$ counterparts. They are interconnected by a region of nearly constant $\mathrm{Im}c_p^1$, all in all observed as a progression close to nil value. Comparing the $\mathrm{Im}c_p^1$ progression of the inner- and outer-span station, the LEV-induced peak has again moved downstream relative to the local chord length for the latter, while being higher in $\mathrm{Im}c_p^1$ value. Vice versa, the shock-induced peak is now situated farther upstream relative to the local chord length, with the $\mathrm{Im}c_p^1$ value being nearly unchanged. The base of both the LEV- and shock-induced peak have widened to the point where the decreasing progression of the former directly leads into that of the latter. Notably, the differing sign witnessed in the peak $\mathrm{Im}c_p^1$ values of either span station indicates a reversal in phase, from leading to lagging, between these two instances. For both the [particular] inner- and outer-span station, the lower-surface $\mathrm{Im}c_p^1$ progression can be observed to be close to nil value, allowing the corresponding time-dependent c_p to be considered essentially in phase. $\Delta\mathrm{Im}c_p^1$ resulting from the LEV-induced peak contributes negatively to the sectional $\mathrm{Im}c_L^1$, whereas the one resulting from the shock-induced peak does so positively. With respect to each span station, however, the two largely cancel each other out. Considering leverage to the pitch axis, the forward and aft $\Delta\mathrm{Im}c_p^1$ both render an unambiguous negative (pitch down) contribution to $\mathrm{Im}c_M^1$ for the [particular] inner-span station. In case of the particular outer-span station, the negative $\Delta\mathrm{Im}c_p^1$ resulting from the LEV-induced peak now contributes both negatively (pitch down) and positively (pitch up) to $\mathrm{Im}c_M^1$. The positive $\Delta\mathrm{Im}c_p^1$ resulting from the shock-induced peak, however, still contributes negatively (pitch down) to $\mathrm{Im}c_M^1$. Integrating over the entire wing, both a negative $\mathrm{Im}c_L^1$ and $\mathrm{Im}c_M^1$ (pitch down) are ascertained, however, with $\mathrm{Im}c_L^1$ being an order of magnitude smaller in absolute value than $\mathrm{Re}c_L^1$. From the [particular] outer-span station toward the tip, the occurrences in the c_p^0, $\mathrm{Re}c_p^1$, and $\mathrm{Im}c_p^1$ progressions distinctly associated with the LEV and the shock become more diffuse. They eventually merge into a single instance beyond the span station of intersection[; see Figure 5.24)]. [103]

With respect to the prediction accuracy, it can be further determined that

> [f]or [all] span stations, FLM-SD.NS-computed upper- and lower-surface c_p^0 agrees excellently with those obtained from FLM-NS [(Figures 5.21–5.23)]. Respective $\mathrm{Re}c_p^1$, mild discrepancies are observed for the predicted LEV- and shock-induced peaks of the inner-span station[s], however, growing larger [toward] the [particular] outer one. [There, p]ostshock deviations are also witnessed [...] for both the upper- and lower-surface $\mathrm{Re}c_p^1$ progression toward the TE. [For the outermost span station, where the LEV- and the shock-associated part of the progression have already merged into a single instance, the deviation of upper-surface $Re\, c_p^1$ becomes especially pronounced from the singular peak on toward the TE. The same can be said about its lower-surface counterpart from $x/c = 0.70$ on downstream.] Otherwise, the lower-surface $\mathrm{Re}c_p^1$ agrees excellently, as linear flow physics are dominant. With exception of a localized region from $y/s = 0.80$ to the tip, lower-surface flow remains subsonic over the entire course of an oscillation. Naturally, the lower-surface $\mathrm{Im}c_p^1$ agrees excellently as well. In regard to upper-surface $\mathrm{Im}c_p^1$, mild discrepancies are observed for the predicted LEV-and shock-induced peaks of the inner-span station[s], which yet again increase toward the outer[most] one. [There,] the deviation between the FLM-SD.NS[-] and FLM-NS-predicted shock-induced peak becomes very substantial[. The latter predicts a shock-induced peak where the former does not, an indication] that the premise of the dynamically linear approach may no longer be valid [from $y/s = 0.69$ on to the tip.] Investigating this matter, the FLM-SD.NS-computed planform upper-surface c_p^0, c_p^1 are compared with the planform upper-surface c_p^0, c_p^1, as well as planform upper-surface second[-] and third[-]harmonic pressure[-]coefficient distributions (c_p^2, c_p^3) gained from FLM-NS[, respectively, Figure 5.24 and Figure 5.25]. Apparently, even for a small amplitude of $\breve{\alpha} = 0.5$ deg the imposed motion on the LEV and its dynamic interaction with the shock are sufficient to induce higher-order harmonics within the time-dependent evolution of the upper-surface c_p. It can be observed that both c_p^2 and c_p^3 locally exceed the specified 10% c_p^1 range, in parts significantly. For regions where $c_p^0 \gg c_p^1 \gg c_p^2 \gg c_p^3$ no longer holds true, however, the small disturbance method cannot render an accurate c_p^1 prediction. As higher-order harmonics become dominant in the flowfield they exert influence on those of lower order (nonlinear interaction). Consequently, the [linearized] time-invariant[-]mean flowfield employed by the dynamically linear approach will depart from the actual zeroth-harmonic one. The complex amplitude flowfield computed by FLM-SD.NS can then only deviate from the actual first-harmonic one as well.
>
> Revisiting [Figures 5.21–5.23], the conformity between FLM-SD.NS and FLM-NS can again be seen equal to that between FLM-SDEu and FLM-Eu. An exception is given for the LE region, where the former deviate less. Characteristically, the inviscid methods compute an LEV-induced upper-surface c_p^0 peak instead of the viscous[ly]ob-

served suction plateau. This results from a separation mechanism driven by numerical viscosity instead of a a physical one. Furthermore, the discontinuous c_p^0 recompression is predicted farther downstream by the inviscid methods. Both the LEV-induced $\mathrm{Re}c_p^1$ and $\mathrm{Im}c_p^1$ peak emerge closer to the LE, as well as more pronounced. [For these instances, the FLM-SDEu deviation to FLM-Eu is observed to be the most substantial, increasing from the innermost to the outermost span station. Nevertheless], the experimental data is better reproduced by the inviscid methods, [in this regard,] which is quite surprising. Neither FLM-SD.NS/FLM-NS nor FLM-SDEu/FLM-Eu, however, are able to render the measured $\mathrm{Im}c_p^1$ peak at the shock location of the outer-span station[s]. [103]

5.3.2.2 Global Load Coefficients

The computed global load coefficients of the 90D28, 90D29, and 90D30 cases are compiled in Table 5.4. The 90D29 case (the baseline-frequency case) is focused on at first. Pursuant to Pechloff and Laschka, it can be established that

FLM-SD.NS-predicted c_L^0 equals its FLM-NS counterpart, while $\mathrm{Re}c_L^1$ is merely 3% higher. $\mathrm{Im}c_L^1$, on the other hand, deviates by half an order of magnitude. The minuteness of either $\mathrm{Im}c_L^1$ in comparison to the correspondent $\mathrm{Re}c_L^1$, however, makes this circumstance again tolerable. Both computations still indicate a time-dependent c_L that minimally lags the excitation. The deviation itself can be [attributed] to the differing upper-surface $\mathrm{Im}c_p^1$ predictions in the shock region toward the tip. Disregarding viscosity yields a 4% higher c_L^0, while having only marginal impact on $\mathrm{Re}c_L^1$. Both computations still indicate a time-dependent c_L that minimally lags the excitation. The deviation itself can be made attributable to the differing upper-surface $\mathrm{Im}c_p^1$ predictions in the shock region toward the tip. Disregarding viscosity yields a 4% higher c_L^0, while having only marginal impact on $\mathrm{Re}c_L^1$. The FLM-SDEu- and FLM-Eu-computed instances can be considered identical. [Either] $\mathrm{Im}c_L^1$ [value] fall[s] within the range set up by the FLM-SD.NS and FLM-NS computation, their mutual deviation reducing significantly. [Both the FLM-SDEu and FLM-Eu computation indicate a time-dependent c_L that again minimally lags the excitation. In this regard, the time-dependent c_L may even be perceived as being entirely in phase for both the viscous and inviscid consideration.]

FLM-SD.NS-predicted c_M^0 equals its FLM-NS counterpart, while both $\mathrm{Re}c_M^1$ and $\mathrm{Im}c_M^1$ are gained lower in absolute value, respectively, by 11% and 22%. $\mathrm{Re}c_M^1$ and $\mathrm{Im}c_M^1$ are in the same order of magnitude. The time-dependent c_M clearly lags the excitation, indicating a damping effect on the free pitching oscillation. The deviation between the FLM-SD.NS-computed c_M^1 and its FLM-NS counterpart are attributable to the higher-order harmonics identified in the FLM-NS-computed upper-surface c_p. Their influence follows through to the time-dependent c_M evolution from which c_M^1 is extracted. FLM-SDEu- and FLM-Eu-computed c_M^0 ($\mathrm{Re}c_M^1$) are, respectively, 17% (12%) and 13% (23%)

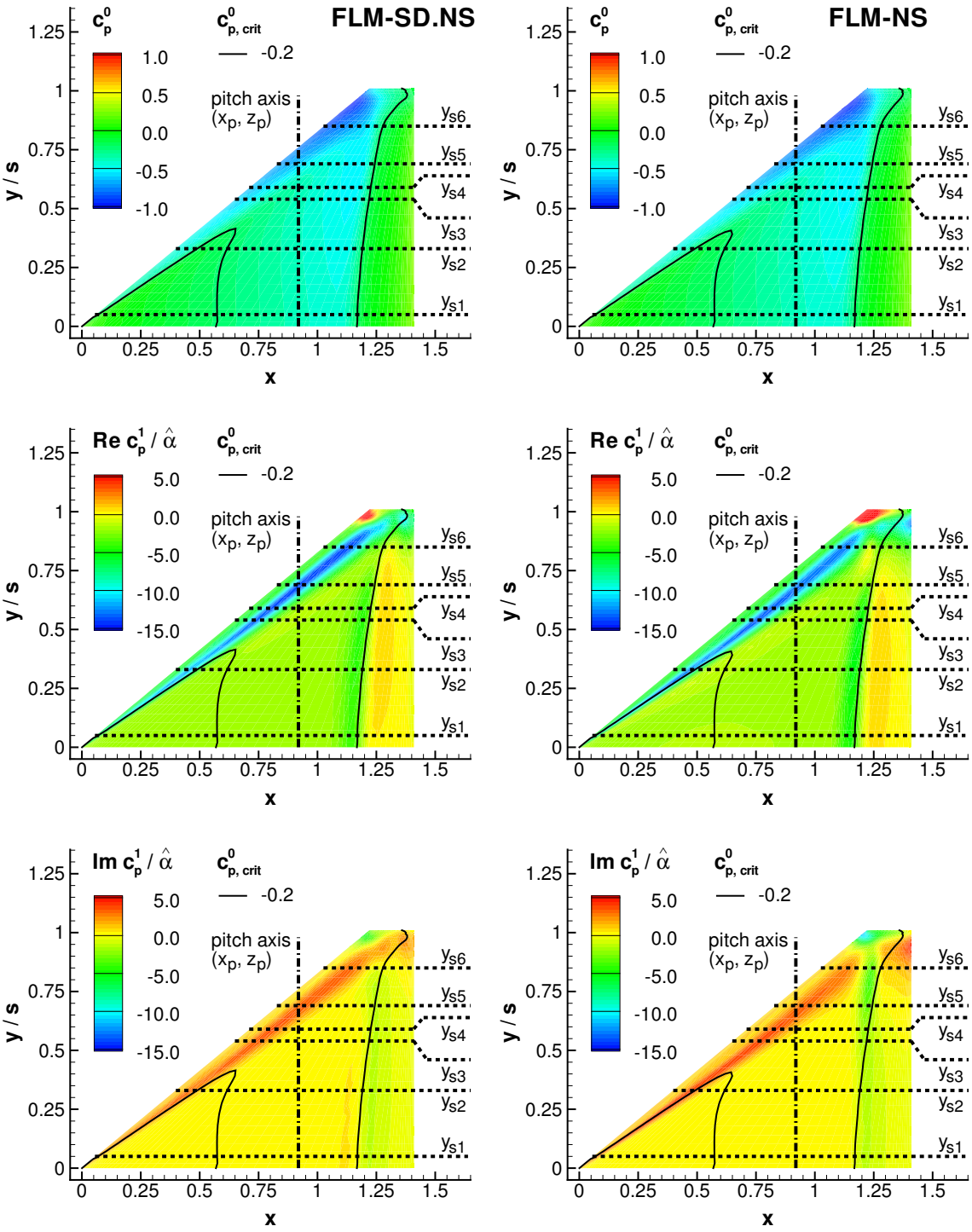

Figure 5.24: Planform pressure coefficients c_p^0, c_p^1 for a NCDW pitching oscillation at $Ma_\infty = 0.90$, $Re_\infty = 10.0 \times 10^6$, $\breve{\alpha} = 3.97$ deg about $x_p/c_r = 0.65$ with $\hat{\breve{\alpha}} = 0.5$ deg, $k_{red} = 0.240$ (90D29, upper surface); based on [103], Fig. 10.

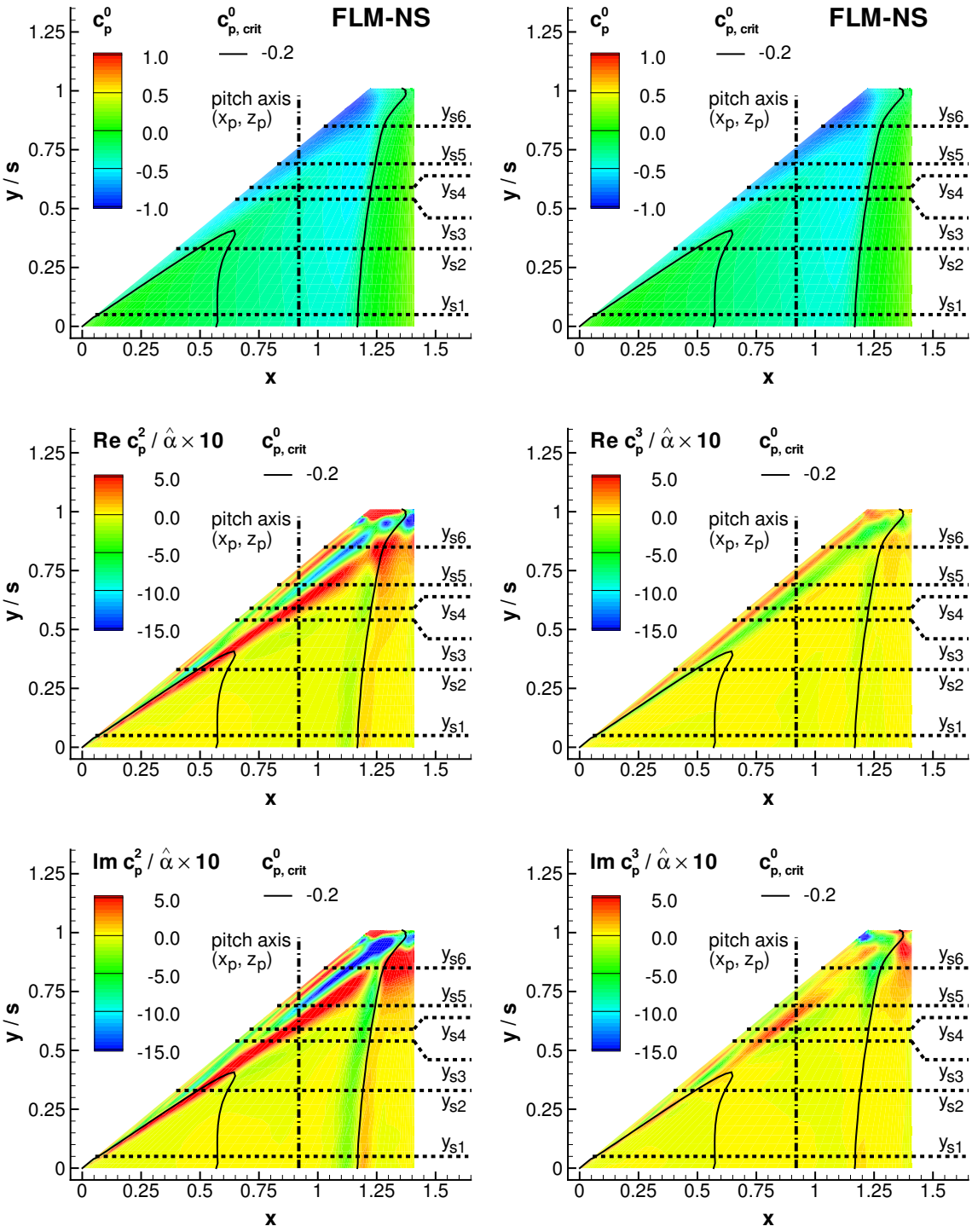

Figure 5.25: Planform pressure coefficients c_p^0, c_p^2, c_p^3 for a NCDW pitching oscillation at $Ma_\infty = 0.90$, $Re_\infty = 10.0 \times 10^6$, $\breve{\alpha} = 3.97$ deg about $x_p/c_r = 0.65$ with $\hat{\breve{\alpha}} = 0.5$ deg, $k_{red} = 0.240$ (90D29, upper surface); based on [103], Fig. 11.

Case	Method	c_L^0	$Re\, c_L^1/\hat{\alpha}$	$Im\, c_L^1/\hat{\alpha}$	$\lvert c_L^1\rvert/\hat{\alpha}$	$\breve{\varphi}_{c_L^1}$, deg
90D28	FLM-SD.NS	0.263	4.159	-0.097	4.160	-1.34
	FLM-NS	0.263	3.965	-0.014	3.965	-0.21
	FLM-SDEu	0.274	4.145	-0.058	4.145	-0.81
	FLM-Eu	0.273	4.065	0.102	4.066	1.43
90D29 [103], Table 4	FLM-SD.NS	0.263	4.065	-0.180	4.069	-2.53
	FLM-NS	0.263	3.958	-0.051	3.959	-0.73
	FLM-SDEu	0.274	4.066	-0.097	4.067	-1.37
	FLM-Eu	0.273	4.062	-0.064	4.063	-0.91
90D30	FLM-SD.NS	0.263	3.819	-0.113	3.821	-1.69
	FLM-NS	0.263	3.839	-0.004	3.839	-0.06
	FLM-SDEu	0.274	3.882	0.021	3.882	0.31
	FLM-Eu	0.273	3.907	0.044	3.907	0.64

Case	Method	c_M^0	$Re\, c_M^1/\hat{\alpha}$	$Im\, c_M^1/\hat{\alpha}$	$\lvert c_M^1\rvert/\hat{\alpha}$	$\breve{\varphi}_{c_M^1}$, deg
90D28	FLM-SD.NS	0.030	0.371	-0.103	0.385	-15.52
	FLM-NS	0.030	0.438	-0.128	0.457	-16.32
	FLM-SDEu	0.025	0.329	-0.109	0.346	-18.41
	FLM-Eu	0.026	0.346	-0.126	0.368	-20.05
90D29 [103], Table 4	FLM-SD.NS	0.030	0.335	-0.178	0.380	-28.02
	FLM-NS	0.030	0.377	-0.229	0.441	-31.27
	FLM-SDEu	0.025	0.294	-0.192	0.351	-33.13
	FLM-Eu	0.026	0.290	-0.221	0.364	-37.25
90D30	FLM-SD.NS	0.030	0.313	-0.290	0.427	-42.79
	FLM-NS	0.030	0.315	-0.341	0.464	-47.28
	FLM-SDEu	0.025	0.257	-0.322	0.412	-51.44
	FLM-Eu	0.026	0.250	-0.340	0.422	-53.68

Table 5.4: Global load coefficients for the NCDW 90D28–30 cases ($Ma_\infty = 0.90$, $Re_\infty = 10.0 \times 10^6$, $\breve{\alpha} = 3.97$ deg, $x_p/c_r = 0.65$, $\breve{\hat{\alpha}} = 0.5$ deg, $k_{red} = 0.120$, 0.240, 0.480).

lower than their viscous counterparts. For $c_M^0[,]$ the deviation experienced between the inviscid methods is 4%, an order of magnitude greater than that of c_L^0. The $\mathrm{Re}c_M^1$ instances can again be considered identical. Disregarding viscosity has only limited impact on $\mathrm{Im}c_M^1$, and thus on the degree of dynamic stability, both values again falling within the range of the FLM-SD.NS and FLM-NS computation. Their mutual deviation, however, reduces to 13%. [103]

Considering the 90D28 case (the half-frequency case) next, FLM-SD.NS predicts $|c_L^1|$ within 5% of the FLM-NS-gained value, with both methods similarly indicating a time-dependent c_L that minimally lags the excitation. Again, the FLM-NS prediction may even be perceived as being entirely in phase. The mean of the FLM-SD.NS- and FLM-NS-computed $|c_L^1|$ remains unchanged, while the mean of the lagging phase angle has decreased only slightly. FLM-SDEu- and FLM-Eu-computed $|c_L^1|$ can be considered identical to one another. In contrast, the $\breve{\varphi}_{c_L^1}$ predictions, while equally being in the low single-digit degree range, now differ in sign: The FLM-SDEu-computed instance falls within the range set up by FLM-SD.NS and FLM-NS before, indicating a time-dependent c_L that minimally lags the excitation, or similarly, may even be perceived as being entirely in phase. The positive sign of the FLM-Eu-computed instance, on the other hand, now indicates a time-dependent c_L that minimally leads the excitation. With exception of this reversal in phase, disregarding viscosity has had negligible impact on the $|c_L^1|$ and $\breve{\varphi}_{c_L^1}$ prediction. At half-frequency, both $|c_L^1|$ and the mean of $|\breve{\varphi}_{c_L^1}|$ remain unchanged. However, where FLM-SDEu and FLM-Eu had agreed in their minimally lagging c_L prediction for the 90D29 case, they now contradict each other.

Obtained from FLM-SD.NS, $|c_M^1|$ is gained 16% lower than its FLM-NS counterpart, with the $\breve{\varphi}_{c_M^1}$ instances, however, deviating by a mere 5%. Both methods predict a time-dependent c_M that distinctly lags the excitation, indicating a damping effect on the free pitching oscillation. Whereas the mean of the $|c_M^1|$ instances has increased only immaterially to the mean of their 90D29 case counterparts, the mean of $|\breve{\varphi}_{c_M^1}|$ has decreased by 46%. In case of a free pitching oscillation this combination would indicate a significantly lesser degree of dynamic stability than for the 90D29 case, corroborated by $|Im\, c_M^1|_{90D28} < |Im\, c_M^1|_{90D29}$ for the mean instances as well. The spread between FLM-SD.NS- and FLM-NS-computed $|c_M^1|$ is similar to the one observed for the 90D29 case. Contrarily, the 10% deviation witnessed in $\breve{\varphi}_{c_M^1}$ for the 90D29 case reduces at half-frequency. Obtained from FLM-SDEu, $|c_M^1|$ is merely 6% lower than its FLM-Eu counterpart, with the $\breve{\varphi}_{c_M^1}$ instances differing by 8%. Disregarded viscosity yields a 15% lower mean $|c_M^1|$ and a 21% higher mean $|\breve{\varphi}_{c_M^1}|$. Again, the time-dependent c_M distinctly lags the excitation. However, the mean $|c_M^1|$ and the mean $|\breve{\varphi}_{c_M^1}|$ in combination indicate a nearly equal degree of dynamic stability for the free pitching oscillation, corroborated by $|Im\, c_M^1|_{inviscid} \approx |Im\, c_M^1|_{viscous}$ for the mean instances as well. Evidently, the relative im-

pact of the inviscid consideration on both $|c_M^1|$ and $|\check{\varphi}_{c_M^1}|$ is similar to the one observed for the 90D29 case. Perforce, the mean of the inviscidly computed $|c_M^1|$ remains unchanged toward half-frequency, while the mean of $|\check{\varphi}_{c_M^1}|$ has decreased by 45%. This is nearly equal to the behavior seen for the viscous consideration.

Lastly, the 90D30 case (the double-frequency case) is regarded. FLM-SD.NS-gained $|c_L^1|$ can be considered identical to its FLM-NS counterpart, with both methods predicting a time-dependent c_L that minimally lags the excitation. The FLM-NS prediction may even be perceived as being entirely in phase. In comparison to the 90D29 case, $|c_L^1|$ is merely 5% lower, with the mean of the $|\check{\varphi}_{c_L^1}|$ instances having decreased likewise, albeit inside the established low single-digit degree range. FLM-SDEu- and FLM-Eu-computed $|c_L^1|$ can also be considered identical. The $\check{\varphi}_{c_L^1}$ instances conform well, both similarly predicting a time-dependent c_L that minimally leads the excitation, or may even be perceived as being entirely in phase. With exception of this reversal in phase, disregarding viscosity has again had negligible impact on the $|c_L^1|$ and $\check{\varphi}_{c_L^1}$ prediction. At double-frequency, $|c_L^1|$ has decreased by merely 4%, comparable to the decrease seen for the viscous consideration. Contrarily, the inviscid computations reveal a reversal in phase, even though not very prominently.

Yielding from FLM-SD.NS, $|c_M^1|$ is gained 8% lower than its FLM-NS counterpart, with the $\check{\varphi}_{c_M^1}$ instances deviating by 10%. Both methods predict a time-dependent c_M that substantially lags the excitation, indicating a damping effect on the free pitching oscillation. Whereas the mean of the $|c_M^1|$ instances has increased by only 9% to the mean of their 90D29 case counterparts, the mean of $|\check{\varphi}_{c_M^1}|$ has increased by 52%. In case of a free pitching oscillation this combination would indicate a significantly higher degree of dynamic stability than for the 90D29 case, corroborated by $|Im\, c_M^1|_{90D30} > |Im\, c_M^1|_{90D29}$ for the mean instances as well. The spread between FLM-SD.NS- and FLM-NS-computed $|c_M^1|$ has narrowed respective the one observed for the 90D29 case. Contrarily, the 10% deviation witnessed in $\check{\varphi}_{c_M^1}$ for the 90D29 case remains unchanged at double-frequency. Obtained from FLM-SDEu, $|c_M^1|$ is merely 2% lower than its FLM-Eu counterpart, with the $\check{\varphi}_{c_M^1}$ instances differing by only 4%. Disregarded viscosity yields a 6% lower mean $|c_M^1|$ and a 17% higher $|\check{\varphi}_{c_M^1}|$. Again, the time-dependent c_M substantially lags the excitation. However, the mean $|c_M^1|$ and the mean $|\check{\varphi}_{c_M^1}|$ in combination indicate a slightly greater degree of dynamic stability for the free pitching oscillation, corroborated by $|Im\, c_M^1|_{inviscid} > |Im\, c_M^1|_{viscous}$ for the mean instances as well. Whereas the relative impact of the inviscid consideration on the mean $|c_M^1|$ has reduced from the 90D29 to the 90D30 case, the one on the mean of $\check{\varphi}_{c_M^1}$ remains nearly unchanged. Consequently, the mean of the inviscidly computed $|c_M^1|$ has increased by 17% toward double-frequency, while the mean of $|\check{\varphi}_{c_M^1}|$ has increased by 49%. This is nearly equal to the behavior seen for the viscous consideration.

5.3.2.3 Overall Assessment

FLM-SD.NS computes the unsteady loading of the 90D28, 90D29 [103], and 90D30 cases in satisfactory agreement to FLM-NS. In all cases, the viscous consideration improves on the inviscid c_M prediction for both the small disturbance and dynamically fully nonlinear approach. Specifically, the viscously computed $|c_M^1|$ is gained consistently higher than its inviscid counterpart for the investigated frequency range, while yielding a consistently lower $|\check{\varphi}_{c_M^1}|$. In combination, however, the viscous prediction indicates a degree of dynamic stability that is nearly equal to the inviscid one for the 90D28 and 90D29 case, yet slightly greater for the 90D30 case. Both the viscous and inviscid consideration produce a $\check{\varphi}_{c_M^1}$ progression over k_{red} that is apparently nonlinear. The gradients between each supporting point are dissimilar: At half-frequency, $|\check{\varphi}_{c_M^1}|$ has decreased by approximately 50%, while having merely increased by approximately 50% at double-frequency.

5.3.3 Strong Shock Cases

At $Ma_\infty = 0.94$, $Re_\infty = 10.0 \times 10^6$, and $\check{\alpha} = 0.0$ deg, the FLM-NS-provided linearized time-invariant-mean flowfield underlying the FLM-SD.NS computation of the 94D4, 94D5, and 94D6 cases features "a sizeable, equally developed supersonic region in proximity to the upper and lower wing surface. It extends, respectively, from the root to considerably beyond the tip, terminating with a strong shock slightly upstream of the TE[, Figure 5.26]. The discontinuous recompression is substantial enough to induce postshock flow separation from $y/s = 0.83$ to $y/s = 0.98$[(Figure 5.27)]."[103] The FLM-SD.NS-obtained surface-pressure-coefficient distributions of the 94D5 case are compared to their FLM-NS, FLM-SDEu, and FLM-Eu counterparts, as well as to the particular experimental data for the investigated span stations in Figures 5.28–5.30. The surface-pressure-coefficient distributions of span stations $y/s = 0.33$ and $y/s = 0.69$ were originally presented in [103], Fig. 13.

5.3.3.1 Local Load Coefficients

The FLM-SD.NS result of the 94D5 case (the baseline-frequency case) is characterized. Pursuant to Pechloff and Laschka, it can be established that

> [u]pper- and lower-surface c_p^0, of course, exhibit symmetry. The onset of supersonic flow occurs significantly upstream of the obtained 90D5 [case] locations. Correspondingly, its termination moves farther downstream, with the strong shock imposing a steep slope onto the c_p^0 progression. Again, symmetry of the upper- and lower-surface c_p^0 yields numerically nil c_L^0 and c_M^0 values.
>
> Complementary to c_p^0, upper- and lower-surface $\mathrm{Re}c_p^1$, as well as $\mathrm{Im}c_p^1$, exhibit anti-symmetry. Merely considering the upper-surface distribution[s], the sharp LE renders an

initial primary peak for both $\mathrm{Re}c_p^1$ and $\mathrm{Im}c_p^1$, respectively, being of negative and positive value. Immediately downstream, $\mathrm{Re}c_p^1$ acutely increases before merging into a positively sloped linear progression that abruptly culminates in a shock region reversal of sign. Whereas the subsequent $\mathrm{Re}c_p^1$ progression conforms to the one of [the] 90D5 [case] for [$y/s = 0.05$ to $y/s = 0.54$], a secondary peak [...] emerges for [$y/s = 0.59$, increasing substantially toward the wing tip.] Integrating over the entire wing, both a positive $\mathrm{Re}c_L^1$ and $\mathrm{Re}c_M^1$ (pitch up) are again ascertained. The $\mathrm{Im}c_p^1$ progression exhibits the characteristics of its 90D5 [case] counterpart, however, with strongly subdued secondary peaks being rendered in the shock region. For the inner-span station[s], an additional zero-crossing is observed before the shock region, reversing the secondary peak's contribution to $\mathrm{Im}c_L^1$ from positive to negative, and thus the contribution to $\mathrm{Im}c_M^1$ vice versa. Integrating over the entire wing, both a negative $\mathrm{Im}c_L^1$ and $\mathrm{Im}c_M^1$ (pitch down) are ascertained, however, each being an order of magnitude lower in absolute value than [the] Re counterpart. [103]

With respect to the prediction accuracy, it can be further determined that

[f]or the investigated span stations, FLM-SD.NS-computed c_p^0, $\mathrm{Re}c_p^1$, and $\mathrm{Im}c_p^1$ agree

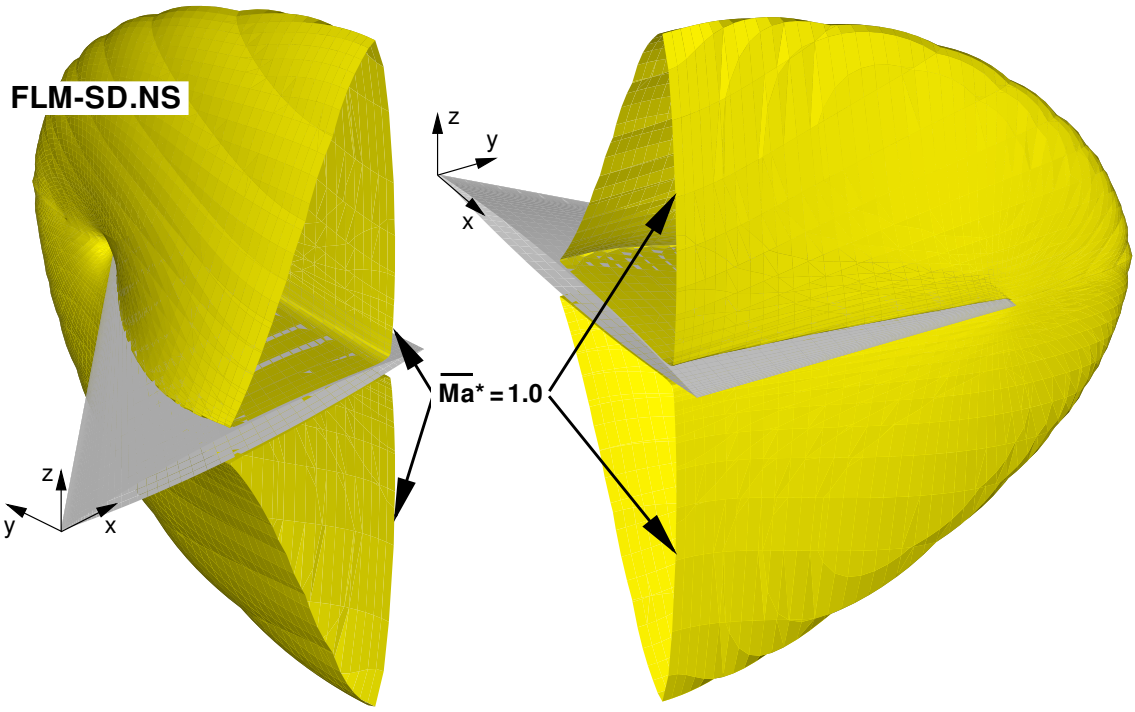

Figure 5.26: Sonic isosurface (LE view [103], Fig. 12, and TE view) of the linearized time-invariant-mean flowfield employed by FLM-SD.NS in the NCDW 94D4–6 cases ($Ma_\infty = 0.94$, $Re_\infty = 10.0 \times 10^6$, $\breve{\alpha} = 0.0$ deg, $x_p/c_r = 0.65$, $\hat{\breve{\alpha}} = 0.5$ deg, $k_{red} = 0.115, 0.230, 0.460$).

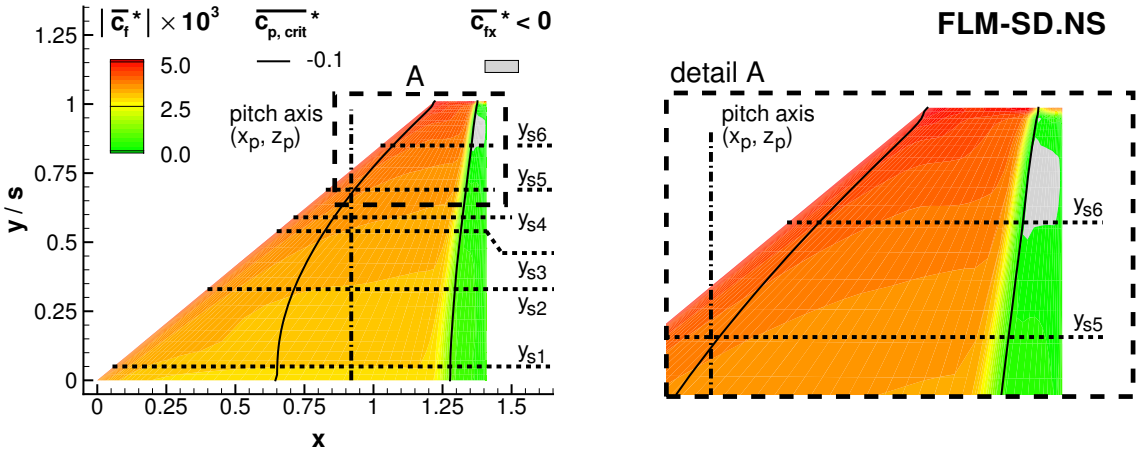

Figure 5.27: Planform upper-surface distribution of the linearized time-invariant-mean skin-friction-coefficient-vector's magnitude (flow separation indicated by $\overline{c_{fx}}^* < 0$) inherent to the FLM-SD.NS consideration of the NCDW 94D4–6 cases ($Ma_\infty = 0.94$, $Re_\infty = 10.0 \times 10^6$, $\breve{\alpha} = 0.0$ deg, $x_p/c_r = 0.65$, $\hat{\breve{\alpha}} = 0.5$ deg, $k_{red} = 0.115, 0.230, 0.460$).

excellently with those obtained from FLM-NS. Discrepancies are merely seen with the farther upstream prediction of the $\mathrm{Re}c_p^1$[zero-crossing] at the inner-span station[s], as well as the value of the [secondary] $\mathrm{Re}c_p^1$[peak] at the [median and] outer-span station[s]. For both [the inner- and outer-span] stations[,] discrepancies in the [secondary] $\mathrm{Im}c_p^1$[peak] are also noticeable. The conformity between FLM-SD.NS and FLM-NS can again be seen equal to that between FLM-SDEu and FLM-Eu. The inviscid methods, however, compute a profoundly differing behavior in the shock and postshock region. Not only is the discontinuous c_p^0 recompression predicted farther downstream, strong $\mathrm{Re}c_p^1$ and $\mathrm{Im}c_p^1$ peaks are rendered at its location, respectively, making substantial $\mathrm{Re}c_L^1$, $\mathrm{Re}c_M^1$, and $\mathrm{Im}c_L^1$, $\mathrm{Im}c_M^1$ contributions. Experimental surface pressure is best reproduced by FLM-SD.NS/FLM-NS, confirming the higher fidelity of the viscous approach. [103]

5.3.3.2 Global Load Coefficients

The computed global load coefficients of the 94D4, 94D5, and 94D6 cases are compiled in Table 5.5. The 94D5 case (the baseline-frequency case) is focused on at first. Pursuant to Pechloff and Laschka, it can be established that

$\mathrm{Re}c_L^1$ obtained from FLM-SD.NS can be considered identical to its FLM-NS counterpart. $\mathrm{Im}c_L^1$, on the other hand, is predicted 17% lower in absolute value, attributable to differingly computed $\mathrm{Im}c_p^1$ in the shock region. Nevertheless, the two viscous methods conform in their prediction of a time-dependent c_L that lags the excitation by only a

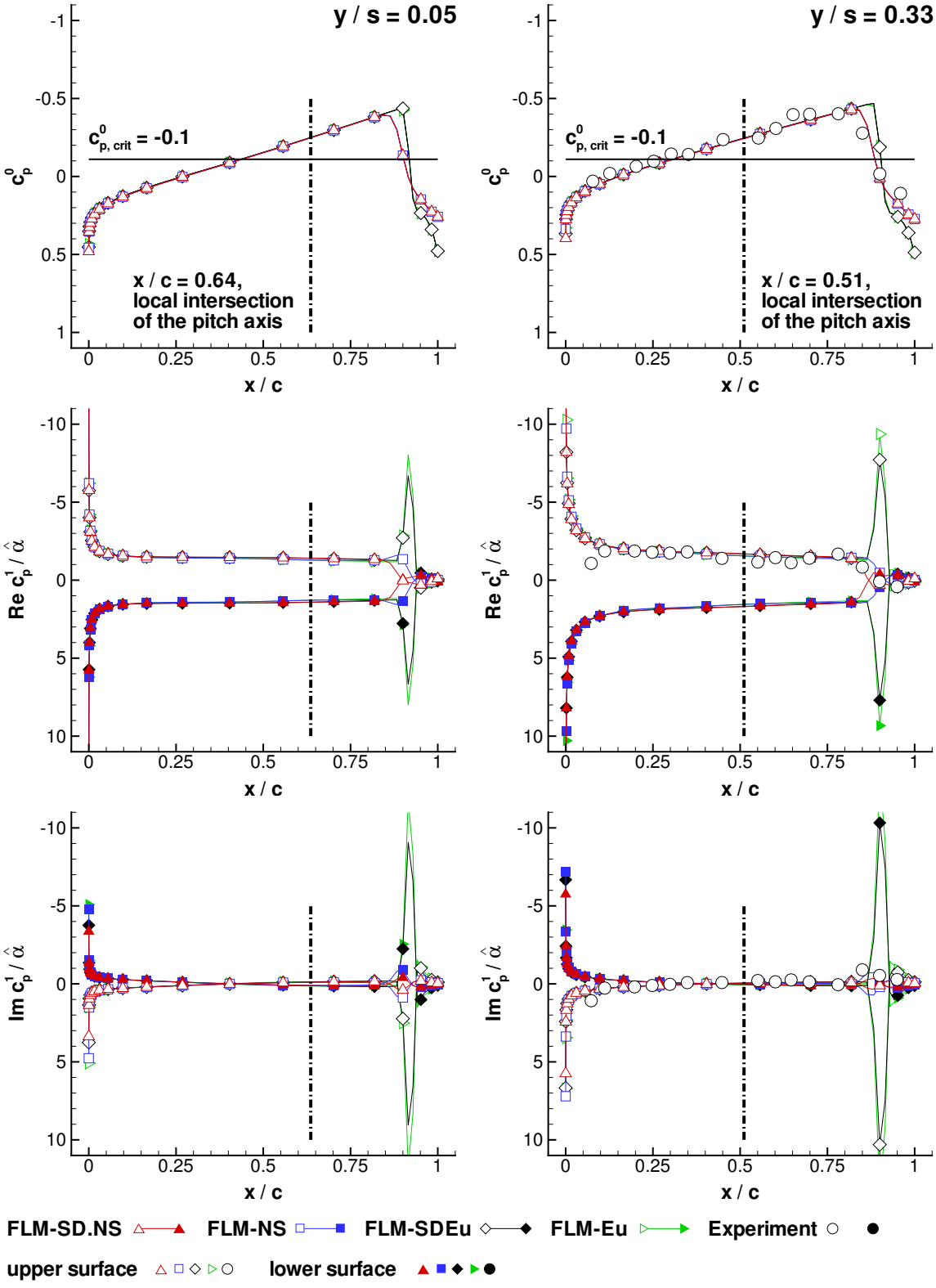

Figure 5.28: Pressure coeff. c_p^0, c_p^1 for a NCDW pitching oscill. at $Ma_\infty = 0.94$, $Re_\infty = 10.0 \times 10^6$, $\breve{\alpha} = 0.0$ deg about $x_p/c_r = 0.65$ w. $\hat{\breve{\alpha}} = 0.5$ deg, $k_{red} = 0.230$ (94D5, inner).

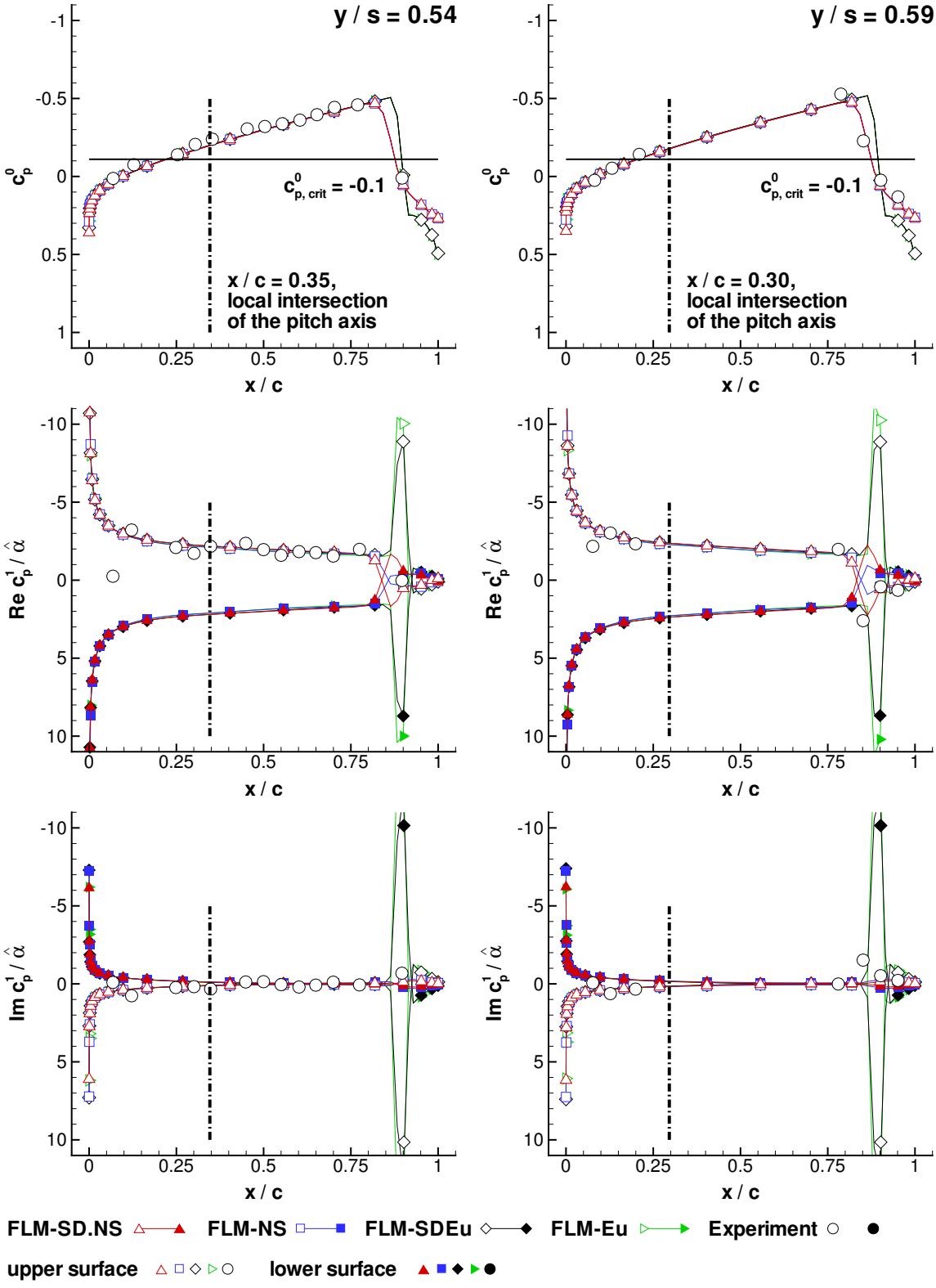

Figure 5.29: Pressure coeff. c_p^0, c_p^1 for a NCDW pitching oscill. at $Ma_\infty = 0.94$, $Re_\infty = 10.0 \times 10^6$, $\breve{\alpha} = 0.0$ deg about $x_p/c_r = 0.65$ w. $\hat{\breve{\alpha}} = 0.5$ deg, $k_{red} = 0.230$ (94D5, median).

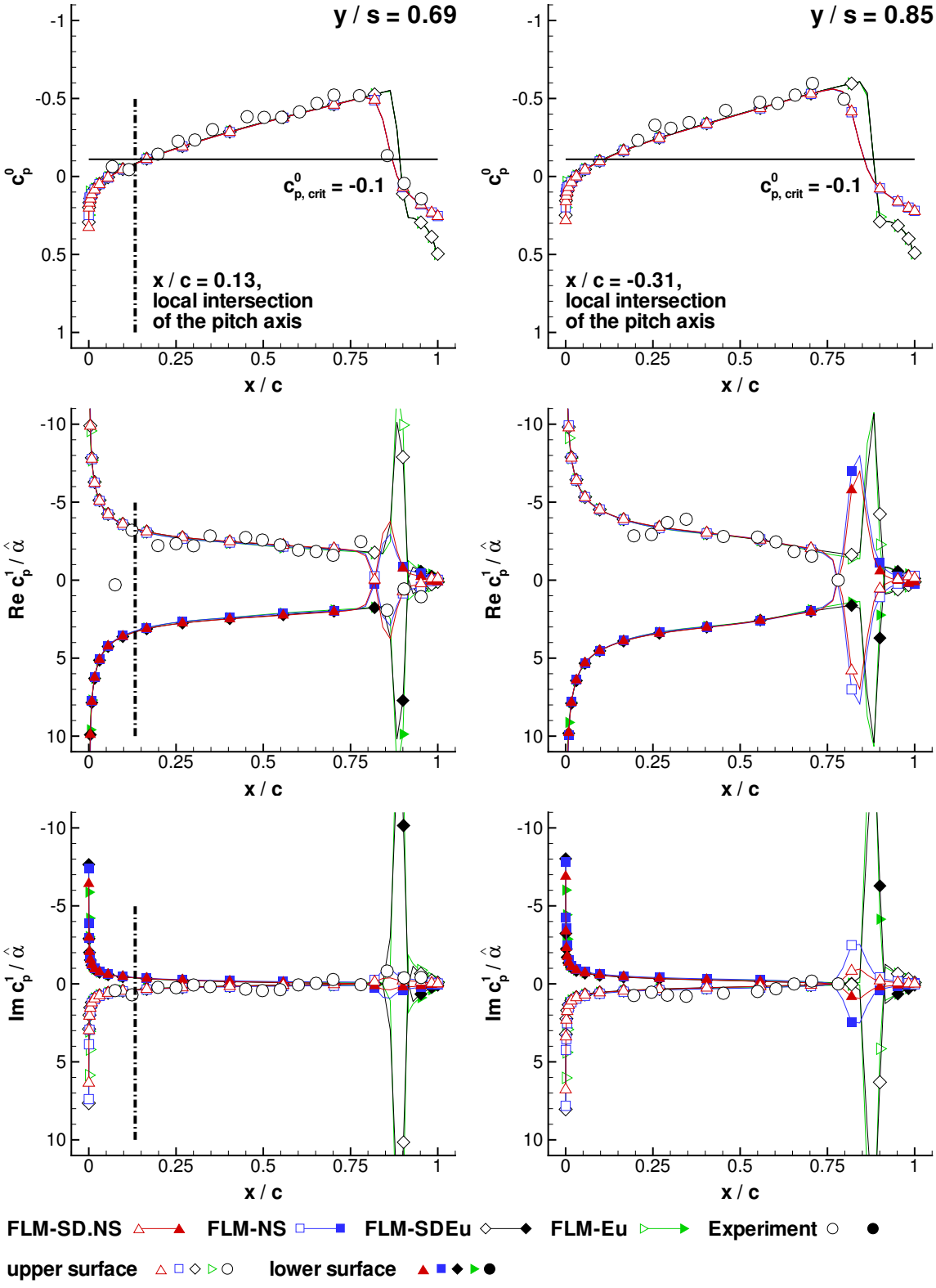

Figure 5.30: Pressure coeff. c_p^0, c_p^1 for a NCDW pitching oscill. at $Ma_\infty = 0.94$, $Re_\infty = 10.0 \times 10^6$, $\breve{\alpha} = 0.0$ deg about $x_p/c_r = 0.65$ w. $\hat{\breve{\alpha}} = 0.5$ deg, $k_{red} = 0.230$ (94D5, outer).

Case	Method	c_L^0	$Re\, c_L^1/\hat{\alpha}$	$Im\, c_L^1/\hat{\alpha}$	$\lvert c_L^1\rvert/\hat{\alpha}$	$\breve{\varphi}_{c_L^1}$, deg
94D4 [103], Table 6	FLM-SD.NS	0.000	3.462	-0.135	3.465	-2.23
	FLM-NS	0.000	3.483	-0.118	3.485	-1.94
	FLM-SDEu	0.000	4.711	-0.661	4.757	-7.98
	FLM-Eu	0.000	4.754	-0.704	4.806	-8.43
94D5 [103], Table 5	FLM-SD.NS	0.000	3.301	-0.181	3.306	-3.13
	FLM-NS	0.000	3.302	-0.218	3.309	-3.77
	FLM-SDEu	0.000	4.087	-0.808	4.166	-11.19
	FLM-Eu	0.000	4.034	-0.947	4.144	-13.21
94D6 [103], Table 7	FLM-SD.NS	0.000	3.113	-0.007	3.113	-0.14
	FLM-NS	0.000	3.123	-0.084	3.124	-1.55
	FLM-SDEu	0.000	3.614	-0.387	3.634	-6.12
	FLM-Eu	0.000	3.585	-0.462	3.615	-7.34

Case	Method	c_M^0	$Re\, c_M^1/\hat{\alpha}$	$Im\, c_M^1/\hat{\alpha}$	$\lvert c_M^1\rvert/\hat{\alpha}$	$\breve{\varphi}_{c_M^1}$, deg
94D4 [103], Table 6	FLM-SD.NS	0.000	0.305	-0.052	0.309	-9.76
	FLM-NS	0.000	0.300	-0.073	0.308	-13.71
	FLM-SDEu	0.000	-0.219	0.157	0.269	144.46
	FLM-Eu	0.000	-0.235	0.158	0.283	146.16
94D5 [103], Table 5	FLM-SD.NS	0.000	0.311	-0.077	0.321	-13.87
	FLM-NS	0.000	0.284	-0.072	0.293	-14.18
	FLM-SDEu	0.000	-0.016	0.197	0.198	96.61
	FLM-Eu	0.000	-0.019	0.254	0.255	94.73
94D6 [103], Table 7	FLM-SD.NS	0.000	0.350	-0.208	0.407	-30.75
	FLM-NS	0.000	0.330	-0.198	0.385	-30.87
	FLM-SDEu	0.000	0.151	-0.050	0.159	-18.35
	FLM-Eu	0.000	0.143	-0.038	0.148	-14.95

Table 5.5: Global load coefficients for the NCDW 94D4–6 cases ($Ma_\infty = 0.94$, $Re_\infty = 10.0 \times 10^6$, $\breve{\alpha} = 0.0$ deg, $x_p/c_r = 0.65$, $\breve{\hat{\alpha}} = 0.5$ deg, $k_{red} = 0.115$, 0.230, 0.460).

small margin. Both FLM-SDEu- and FLM-Eu-computed $\mathrm{Re}c_L^1$ are significantly higher than their viscous counterparts. The strong $\mathrm{Re}c_p^1$ peaks rendered in the shock region yield a large yet chordwise-localized difference between [the] upper- and lower-surface distribution. Contributing positively, its summation over the [semi-span], however, is substantial enough to increase $\mathrm{Re}c_L^1$ by 23% on average. This circumstance emerges even more pronounced in $\mathrm{Im}c_L^1$. Outside of the shock region $\Delta\mathrm{Im}c_p^1$ would merely result in a minutely negative $\mathrm{Im}c_L^1$ similar to that of the viscous computations. Comparatively, the $\mathrm{Re}c_p^1$-corresponding $\mathrm{Im}c_p^1$ peaks contribute strongly negative to $\mathrm{Im}c_L^1$. Supplying the bulk of its value, a fourfold amplification of the viscously obtained $\mathrm{Im}c_L^1$ is experienced. The deviation between FLM-SDEu- and FLM-Eu-computed $\mathrm{Re}c_L^1$, as well as $\mathrm{Im}c_L^1$, becomes similar to that of the respective FLM-SD.NS and FLM-NS counterparts. [Inviscidly, the time-dependent c_L is predicted to distinctly lag the excitation.]

FLM-SD.NS predicts both $\mathrm{Re}c_M^1$ and $\mathrm{Im}c_M^1$ within 10% of the FLM-NS-gained value, the two being separated by merely half an order of magnitude. Even though $\mathrm{Re}c_L^1$ has been established as identical between the two methods, the same cannot be said for $\mathrm{Re}c_M^1$. Inversely, the deviation exhibited by $\mathrm{Im}c_L^1$ does not entirely follow through to $\mathrm{Im}c_M^1$. Considering [the] skin friction contribution to be negligible, deviations in $\mathrm{Re}c_p^1$ are apparently amplified toward $\mathrm{Re}c_M^1$, while deviations in $\mathrm{Im}c_p^1$ are compensated toward $\mathrm{Im}c_M^1$, for the given reference axis. Both viscous methods predict the time-dependent c_M to distinctly lag the excitation, with the $\breve{\varphi}_{c_M^1}$ instances differing by merely 2%.

Disregarding viscosity, the character of c_M becomes significantly altered. FLM-SDEu-/FLM-Eu-computed $\mathrm{Re}c_M^1$ and $\mathrm{Im}c_M^1$ exchange sign as well as order of magnitude given by their viscous counterparts. Through accounted leverage, the inviscidly predicted $\mathrm{Re}c_p^1$ and $\mathrm{Im}c_p^1$ peaks in the shock region, respectively, supply the bulk negative and positive contribution that tip the scale. With $\mathrm{Im}c_M^1 > 0$ the time-dependent c_M now substantially leads the excitation. In case of a free pitching oscillation this would have an amplifying effect. For both $\mathrm{Re}c_M^1$ and $\mathrm{Im}c_M^1$ deviation between the FLM-SDEu and FLM-Eu-computed instance is within 20%, double the one exhibited between the viscous counterparts. Whereas this appears reasonable for $\mathrm{Re}c_M^1$ on grounds of its minuteness, it seems surprisingly high for $\mathrm{Im}c_M^1$. The deviation compensates itself in the phase shift of the time-dependent c_M yet persists in its magnitude. [103]

Considering the 94D4 case (the half-frequency case) next,

[FLM-SD.NS-predicted] $|c_L^1|$ can be considered identical to its FLM-NS counterpart, with both methods similarly predicting a time-dependent c_L that marginally lags the excitation. In comparison [to the] 94D5 [case], $|c_L^1|$ is merely 5% higher, with the lagging phase angle having decreased only slightly. FLM-SDEu- and FLM-Eu-computed $|c_L^1|$ can also be considered identical to one another, with the $\breve{\varphi}_{c_L^1}$ instances differing by a mere 5%. The inviscidly computed $|c_L^1|$ is about 38% higher than its viscous counterpart, with

the lag of the time-dependent c_L having increased as well. Both $\check{\varphi}_{c_L^1}$ instances, however, remain in the single-digit degree range. At half[-]frequency, the inviscidly computed $|c_L^1|$ presents itself about 15% higher, whereas the lagging phase angle has decreased from the low double-digit to the single-digit degree range.

Obtained from FLM-SD.NS, $|c_M^1|$ can be considered identical to its FLM-NS counterpart, with both methods predicting a time-dependent c_M that lags the excitation. Either $\check{\varphi}_{c_M^1}$ instance presents itself in the low double-digit degree range[. In combination with $|c_M^1|$, however,] FLM-SD.NS [indicates a distinctly] lesser degree of dynamic stability for the free pitching oscillation than FLM-NS[, corroborated by $|Im\, c_M^1|_{SD.NS} < |Im\, c_M^1|_{NS}$ as well]. Whereas the $|c_M^1|$ instances can be considered equal to the mean of their 94D5 [case] counterparts, the mean of the [$|\check{\varphi}_{c_M^1}|$] instances has decreased somewhat [...]. [In case of a free pitching oscillation this combination would indicate a lesser degree of dynamic stability than for the 94D5 case, corroborated by $|Im\, c_M^1|_{94D4} < |Im\, c_M^1|_{94D5}$ for the mean instances as well.] Obtained from FLM-SDEu, $|c_M^1|$ is merely 5% lower than its FLM-Eu counterpart, with the $\check{\varphi}_{c_M^1}$ instances being nearly equal. The mean of the inviscidly computed $|c_M^1|$ instances is 11% lower than its viscous counterpart. Similar to [the] 94D5 [case], disregarded viscosity renders a time-dependent c_M that leads the excitation, which in case of a free pitching oscillation would have an amplifying effect. At half[-]frequency, however, the mean of the FLM-SDEu- and FLM-Eu-computed $|c_M^1|$ instances has gained 22%, while [$\check{\varphi}_{c_M^1}$] has increased to slightly more than three-eighths of a cycle. [In case of a free pitching oscillation this combination would indicate a significantly lesser degree of dynamic instability than for the 94D5 case, corroborated by $Im\, c_M^1|_{94D4} < Im\, c_M^1|_{94D5}$.] Notably, the reduction of frequency has had a [significant] impact on the inviscid time-dependent c_M, where it only has had a [minor] one on the viscous counterpart. [103]

Lastly, the 94D6 case (the double-frequency case) is regarded:

[FLM-SD.NS-predicted] $|c_L^1|$ [...] can be considered identical to its FLM-NS counterpart, with both methods predicting a time-dependent c_L that marginally lags the excitation. The FLM-SD.NS prediction may even be perceived as being entirely in phase. $|c_L^1|$ is merely 6% lower than in [the] 94D5 [case], with the phase lag having decreased slightly. FLM-SDEu- and FLM-Eu-computed $|c_L^1|$ can also be considered identical, with the $\check{\varphi}_{c_L^1}$ instances conforming well. The inviscidly computed $|c_L^1|$ is about 16% higher than its viscous counterpart, with the lag of the time-dependent c_L having increased too. Both inviscidly computed $\check{\varphi}_{c_L^1}$ instances, however, remain in the single-digit degree range. At double[-]frequency, $|c_L^1|$ presents itself 13% lower, with the lagging phase angle having decreased from the low double-digit to the single-digit degree range.

FLM-SD.NS predicts $|c_M^1|$ within 6% of the FLM-NS-gained value, while the obtained instances of $\check{\varphi}_{c_M^1}$ can be considered identical. At double[-]frequency, the mean

of the FLM-SD.NS- and FLM-NS-[computed] $|c_M^1|$ has increased by 29%. The time-dependent c_M now lags the excitation even more distinctly,[the combination of the mean $|c_M^1|$ and the mean $\check{\varphi}_{c_M^1}$] indicating a substantially higher degree of dynamic stability for the free pitching oscillation. [A circumstance corroborated by $|Im\, c_M^1|_{94D6} >> |Im\, c_M^1|_{94D5}$ for the mean instances as well.] The deviation between the FLM-SDEu- and FLM-Eu-computed $|c_M^1|$ instances is similar to the one witnessed between the FLM-SD.NS- and FLM-NS-computed counterparts, whereas a greater variation can be observed for $\check{\varphi}_{c_M^1}$. Disregarding viscosity entails a 61% lower mean $|c_M^1|$ and a 46% lower mean $[|\check{\varphi}_{c_M^1}|]$, [in combination] indicating a [substantially] lesser degree of dynamic stability for the free pitching oscillation. [This circumstance is corroborated by $|Im\, c_M^1|_{inviscid} << |Im\, c_M^1|_{viscous}$ for the mean instances as well.] From [the] 94D5 [case] to [the] 94D6 [case], the mean of the inviscidly computed $|c_M^1|$ instances has decreased by 32%. Even more notably, a reversal in sign has occurred for $\check{\varphi}_{c_M^1}$ toward [double-]frequency. Whereas the time-dependent c_M leads the excitation by slightly more than a quarter cycle for [the] 94D5 [case], it distinctly lags the excitation for [the] 94D6 [case]. [Regarding] a free pitching oscillation, c_M goes from having an amplifying to a damping effect, the latter now conforming to the FLM-SD.NS/FLM-NS prediction. [103]

5.3.3.3 Overall Assessment

FLM-SD.NS computes the unsteady loading of the 94D4, 94D5, and 94D6 cases in good agreement to FLM-NS, despite having employed the $\widehat{\tilde{\mu}}$ limitation [103]. In all cases, the viscous consideration improves on the inviscid c_L and c_M prediction for both the small disturbance and dynamically fully nonlinear approach. Specifically, the viscously computed $|c_L^1|$ and $|\check{\varphi}_{c_L^1}|$ are gained consistently lower than their inviscid counterparts for the investigated frequency range. On the other hand, the viscously computed $|c_M^1|$ is gained consistently higher than its inviscid counterpart, with $\check{\varphi}_{c_M^1}$, most notably, differing in sign for the 94D4 and 94D5 case. The viscous prediction indicates dynamic stability for all cases, while the inviscid one only does so for the 94D6 case, though, to a substantially lesser degree [103].

5.4 Flap Oscillations – Medium-Strength Shock Cases

Bennett and Walker [12] provide an array of NCDW flap-oscillation test cases, with 92D33 (a medium-strength shock case) having been selected for the investigation. On this basis, a case at an approximately 40% higher frequency is also considered, 92D36 being its experimental equivalent. With respect to [4, 55], the 92D36 case has been recomputed

and reevaluated for this dissertation. Naturally, both the small disturbance computation of the higher- and the baseline-frequency case are conducted with the same steady-state reference-grid solution, in either its viscous or inviscid instance. Complementarily, each solution is employed to initialize the pertinent dynamically fully nonlinear computation. The computation parameters of each case are compiled in Table 5.6, with $Re_\infty = 10.0 \times 10^6$, $L_{Re_\infty} = c_{av}$, $\check{S} = 110.4$ K, $\gamma = 1.132$, $Pr = 0.775$ (heavy gas), and $Pr_t = 0.90$ being shared by all [12]. Just as with the pitching oscillations, FLM-SD.NS solution convergence is accelerated by specifying the $(2_0 \,/\, 1_1 \,/\, 2)$ V-symmetric multigrid schedule. However, solution convergence is now accepted when the subsequent load tolerance criterion is satisfied. At the current pseudotime step the relative change of $|\widehat{c_L}|$ with respect to each $|\widehat{c_L}|$ of the 15 prior pseudotime steps must be lower in absolute value than 1×10^{-4}.

Instability of the solution process occurs at first for both cases. After a number of multigrid cycles the $\widehat{\check{\mu}}$ residual becomes not-a-number, with the $\hat{\rho}$ residual following suit. This behavior can be traced back to the turbulence transport equation's pseudotime integration in off-body cells proximate to the flap edges. Apparently, it is initiated by the associated amplitude metrics. In the rendered extremum grid, the skew of the spanwise gap-corresponding surface cells naturally follows through to the near-field volume cells, though diminishing with increasing distance to the discretized surface. For the specific deflection amplitude, the values of the locally corresponding amplitude metrics in part exceeded the values of their reference metric counterparts, violating the small disturbance premise per se. The application of the FEVA, Eq. (4.118), provided stabilization, eventually allowing the load tolerance criterion to be satisfied. In the process, the $\widehat{\check{\mu}}$ residual was naturally rendered obsolete as an auxiliary measure of solution convergence. In this regard, Figure 5.31 depicts the $|\widehat{c_L}|$ and $|\widehat{c_M}|$ history, as well as the $\hat{\rho}$ residual history, resulting from the FLM-SD.NS computation of the 92D33 case. Notably, the load tolerance criterion is already satisfied at a $\hat{\rho}$ residual of 3×10^{-3}, being almost an order of magnitude higher than the $\hat{\rho}$ residual tolerance employed in the termination of the pitching-oscillation cases.

Concerning the comparative FLM-NS computations, three oscillation cycles, each discretized with 100 physical time intervals, are again adequate to obtain load coefficient periodicity. Likewise, the specified multigrid parameters and abort criterion conform to those of the FLM-SD.NS computations. A single 1.3 GHz Intel Itanium 2 processor of

Case	Ma_∞	$\check{\alpha}$, deg	$\check{\eta}$, deg	$\check{\hat{\eta}}$, deg	k_{red}	$\check{f}$, Hz	$\check{p}_\infty$, kPa	$\check{\rho}_\infty$, kg/m^3	$\check{T}_\infty$, K
92D33	0.92	0.0	0.0	3.9	0.478	16.0	19.6	0.327	288.2
92D36					0.651	22.0			

Table 5.6: Computation parameters of the NCDW flap-oscillation cases [12], Table 5.

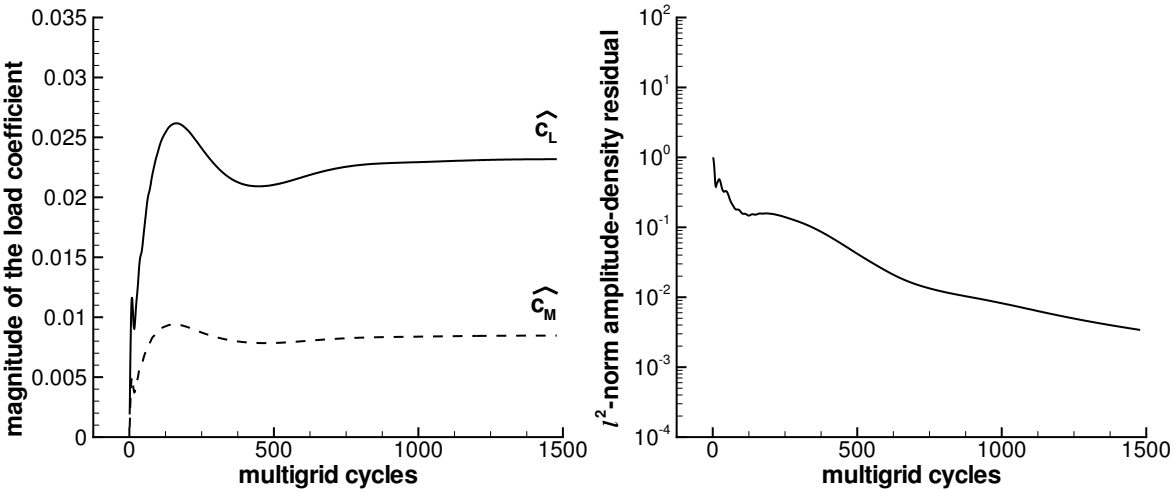

Figure 5.31: FLM-SD.NS-yielding $|\widehat{c_L}|$ and $|\widehat{c_M}|$ history, as well as $\hat{\rho}$ residual history, for the NCDW 92D33 case ($Ma_\infty = 0.92$, $Re_\infty = 10.0 \times 10^6$, $\breve{\alpha} = 0.0$ deg, $x_h/c = 0.80$, $\breve{\eta} = 0.0$ deg, $\breve{\hat{\eta}} = 3.9$ deg, $k_{red} = 0.478$).

the Leibniz-Rechenzentrum Linux cluster was utilized for either methods execution. The additional FLM-SDEu/FLM-Eu computations were realized with the reference and extremum grid employed by their viscous counterparts, allowing for spatial comparability between the solutions. Whereas the FLM-SDEu computations were conducted on the same processor as utilized for the viscous computations, the FLM-Eu instances were realized on a 1.6 GHz successor model. Again, FLM-NS and FLM-Eu were executed with dual time-stepping set to second-order accuracy. For both the 92D33 and 92D36 case, zeroth-harmonic comparison is performed with the experimental surface-pressure-coefficient data of the 92S1 case [12]. The sensitivity of the FLM-SD.NS-computed global load coefficients to the employed spatial discretization has not been investigated. Subsequently, $\hat{\eta} := \breve{\hat{\eta}}\,\pi/180$ deg applies.

At $Ma_\infty = 0.92$, $Re_\infty = 10.0 \times 10^6$, and $\breve{\alpha} = 0.0$ deg, the FLM-NS-provided linearized time-invariant-mean flowfield underlying the FLM-SD.NS computation of the 92D33 and 92D96 case features an expanded, equally developed supersonic region in proximity to the upper and lower wing surface. It extends, respectively, from the root to somewhat beyond the tip, terminating with a medium-strength shock significantly upstream of the TE, Figure 5.32. Flap-locally, the shock base is situated slightly upstream of either hinge line ($x_h/c = 0.80$). The FLM-SD.NS-obtained surface-pressure-coefficient distributions are again compared to their FLM-NS, FLM-SDEu, and FLM-Eu counterparts, as well as to the particular experimental data for the investigated span stations. In this regard, Figures 5.33–5.35, Figure 5.36, and Figure 5.37 correspond to the 92D33 case, while Figures 5.38–5.40, Figure 5.41, and Figure 5.42 correspond to the 92D36 case.

5.4.1 Local Load Coefficients

Focusing on the 92D33 case (the baseline-frequency case) at first, the FLM-SD.NS result as provided in Figures 5.33–5.35 is characterized. Upper- and lower-surface c_p^0, of course, exhibit symmetry. The onset of supersonic flow and its termination consistently occur within the respectively obtained 90D5 and 94D5 case locations. The medium-strength shock imposes a slightly shallower slope onto the c_p^0 progressions than witnessed for the 94D5 case. Again, symmetry of the upper- and lower-surface c_p^0 yields numerically nil c_L^0 and c_M^0 values. Complementary to c_p^0, upper- and lower-surface $Re\, c_p^1$, as well as $Im\, c_p^1$, exhibit antisymmetry. In stark contrast to the pitching oscillations, the flap oscillations induce a tightly confined unsteadiness in the aft surface-pressure-coefficient distribution, specifically, between the shock region and the TE. For both $Re\, c_p^1$ and $Im\, c_p^1$, a peak is rendered between the location of minimum c_p^0 and the location of the supersonic-flow-terminating $c_{p,\,crit}^0$, respectively, being of negative and positive upper-surface value. Indicative of the implied shock motion, the peaks increase in prominence from root to tip; i.e., observed to be fairly subdued at the inner-span stations, they strongly amplify from the flap-inboard-edge station on toward the outermost span station. This behavior is exhibited far more distinctive by $Re\, c_p^1$ than by $Im\, c_p^1$. With exception of the $Re\, c_p^1$ progression at the innermost span station, the base of the peak initiates at the location of minimum c_p^0. From there on upstream, both $Re\, c_p^1$ and $Im\, c_p^1$ can be considered to be of nil value. The thin boundary layer only allows for a very limited propagation of the amplitude dis-

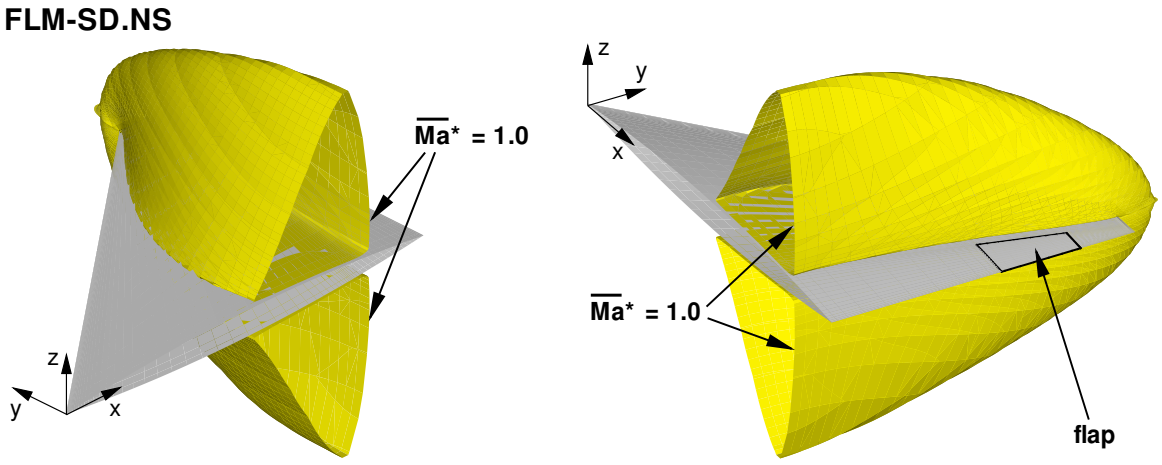

Figure 5.32: Sonic isosurface (LE view and TE view) of the linearized time-invariant-mean flowfield employed by FLM-SD.NS in the NCDW 92D33 and 92D36 case ($Ma_\infty = 0.92$, $Re_\infty = 10.0 \times 10^6$, $\breve{\alpha} = 0.0$ deg, $x_h/c = 0.80$, $\breve{\eta} = 0.0$ deg, $\hat{\breve{\eta}} = 3.9$ deg, $k_{red} = 0.478$, 0.651).

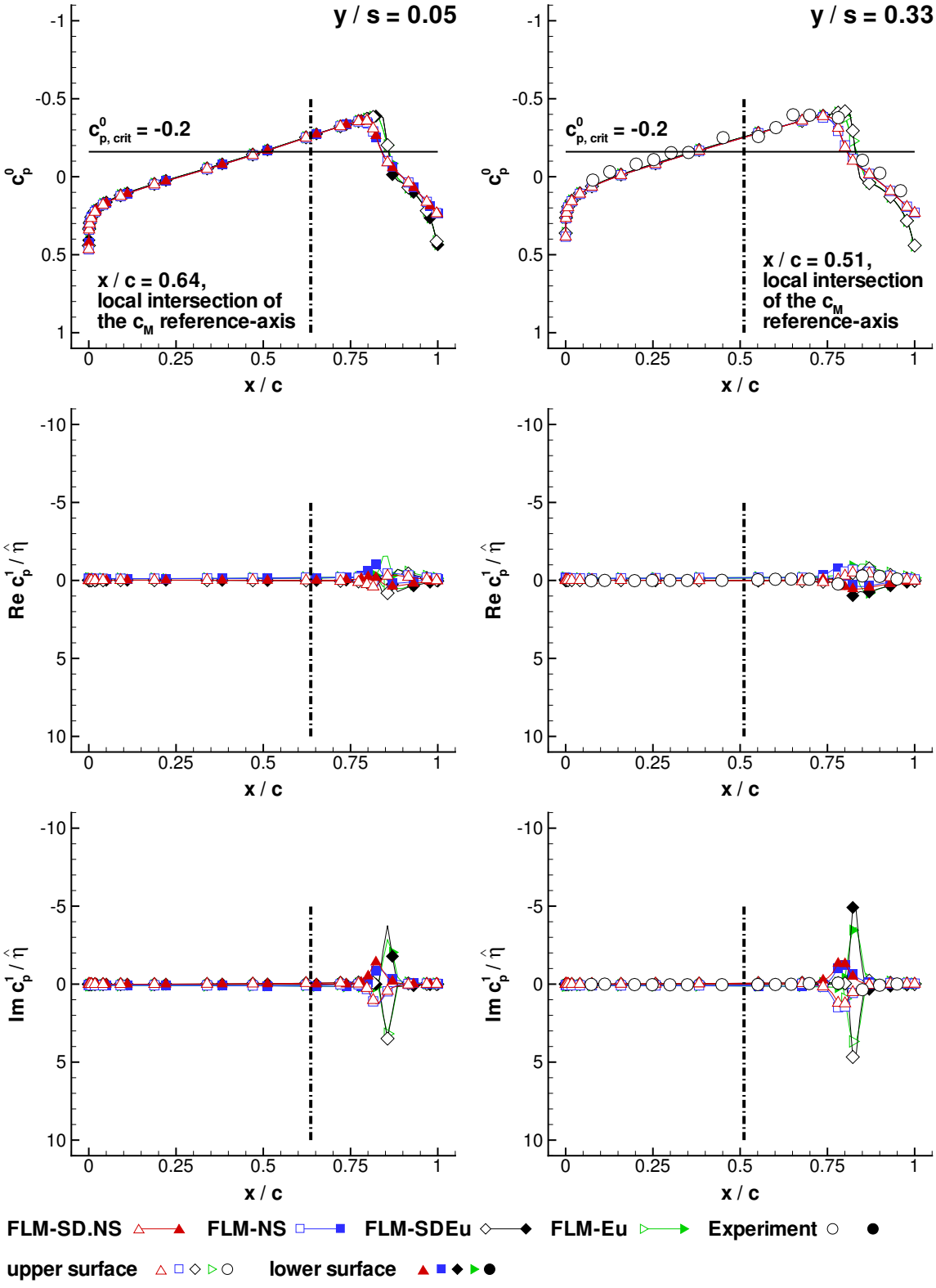

Figure 5.33: Press. coeff. c_p^0, c_p^1 for a NCDW flap oscill. at $Ma_\infty = 0.92$, $Re_\infty = 10.0 \times 10^6$, $\breve{\alpha} = 0.0$ deg ab. $x_h/c = 0.80$ w. $\breve{\eta} = 0.0$ deg, $\hat{\breve{\eta}} = 3.9$ deg, $k_{red} = 0.478$ (92D33, inner).

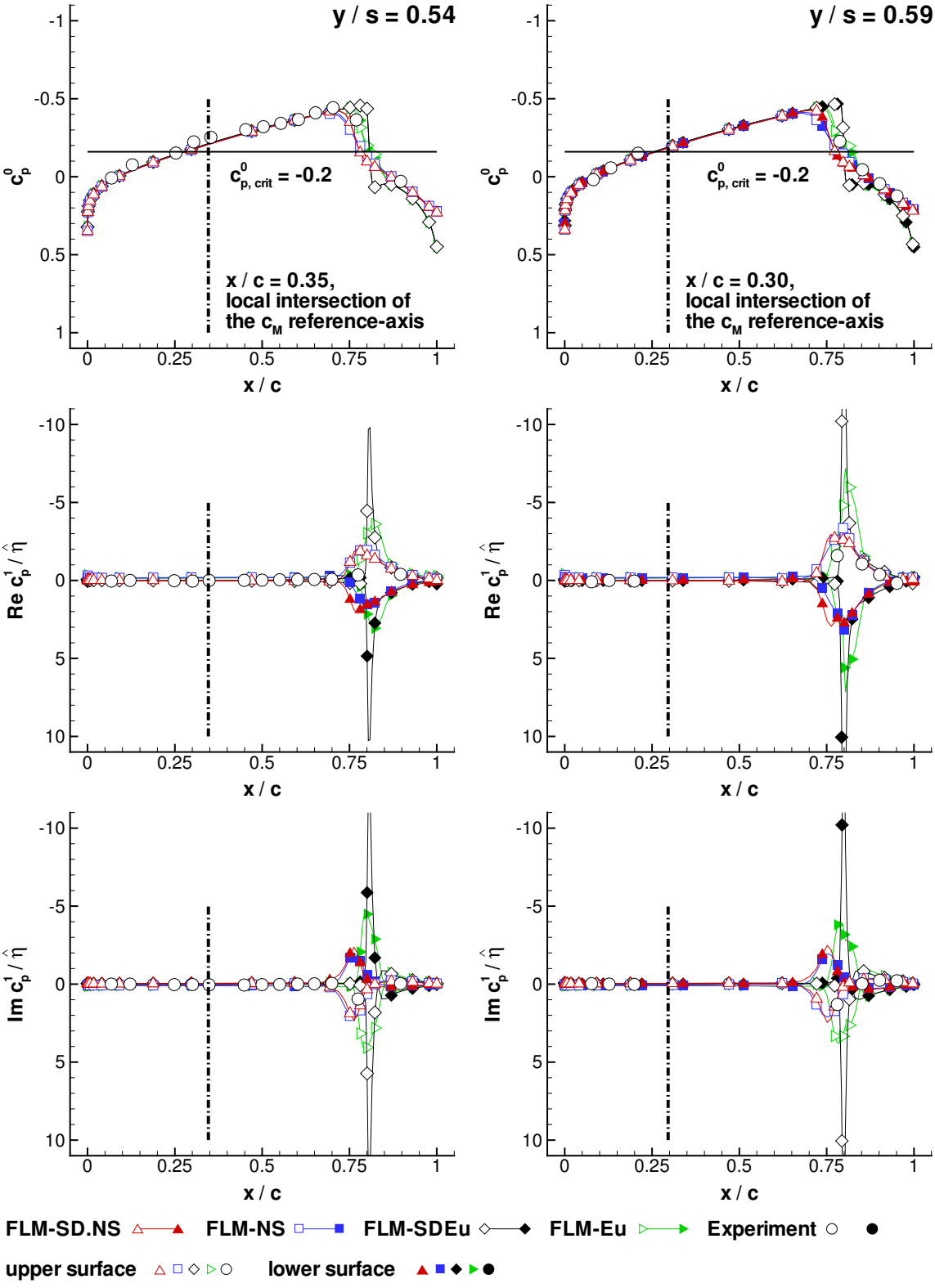

Figure 5.34: Press. coeff. c_p^0, c_p^1 for a NCDW flap oscill. at $Ma_\infty = 0.92$, $Re_\infty = 10.0 \times 10^6$, $\breve{\alpha} = 0.0$ deg ab. $x_h/c = 0.80$ w. $\breve{\eta} = 0.0$ deg, $\hat{\breve{\eta}} = 3.9$ deg, $k_{red} = 0.478$ (92D33, median).

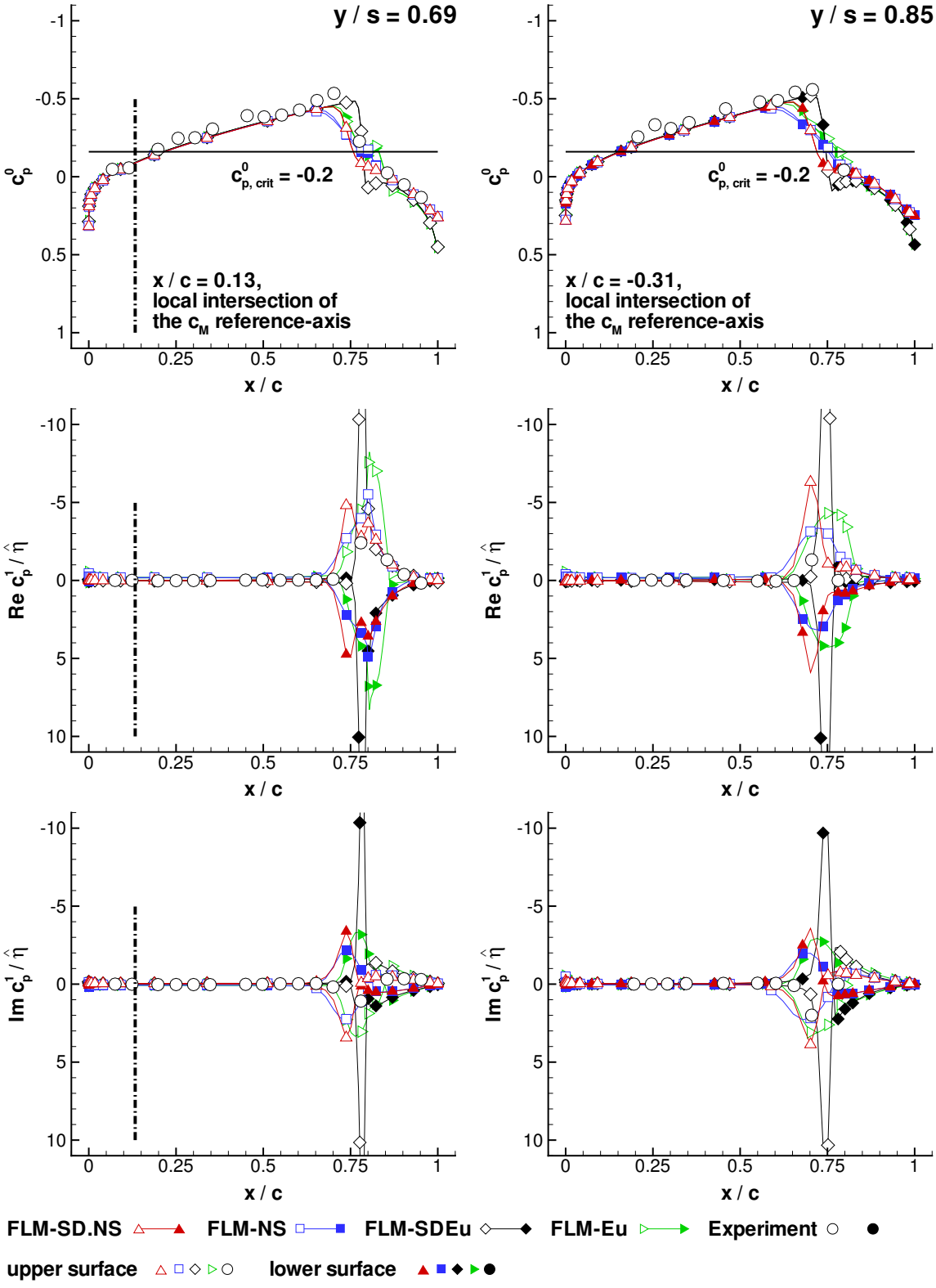

Figure 5.35: Press. coeff. c_p^0, c_p^1 for a NCDW flap oscill. at $Ma_\infty = 0.92$, $Re_\infty = 10.0 \times 10^6$, $\breve{\alpha} = 0.0$ deg ab. $x_h/c = 0.80$ w. $\breve{\eta} = 0.0$ deg, $\hat{\breve{\eta}} = 3.9$ deg, $k_{red} = 0.478$ (92D33, outer).

turbance into the region of supersonic flow. Consequently, the flap oscillation alone will not induce an unsteadiness in the surface-pressure-coefficient distributions upstream of the shock region. For $Re\, c_p^1$, the base of the peak extends to the TE, where equalization between the upper- and lower-surface progressions occurs at nil value. Up to this location, either progression retains the sign of the particular peak value. For the flap-median station, a secondary $Re\, c_p^1$ peak saddles the primary peak's base slightly downstream of the supersonic-flow-terminating $c_{p,\,crit}^0$ location. Closer examination of the shock and postshock region, Figure 5.36, reveals the secondary peak to be of lesser absolute value, with its location actually coinciding with either hinge-line intersection. Thus, the secondary peak embodies a known characteristic of an oscillating flap in subsonic flow; i.e., rendering a quasi-singularity for c_p at the flap's LE for any deflected position. Evidently, the entirety of the sectional $Re\, c_L^1$ is supplied by the positive $\Delta Re\, c_p^1$ of the shock and postshock region. For all span stations, the local intersection of the c_M reference axis resides distinctly upstream of the particular $Re\, c_p^1$ peak's base. Therefore, the associated $\Delta Re\, c_p^1$ will always contribute negatively (pitch down) to the sectional $Re\, c_M^1$ through leverage. Naturally, integrating over the entire wing, a positive $Re\, c_L^1$ and a negative $Re\, c_M^1$ (pitch down) are then ascertained.

In contrast to $Re\, c_p^1$, the $Im\, c_p^1$ peak's base only extends somewhat downstream of the supersonic-flow-terminating $c_{p,\,crit}^0$ location. It is delimited by the upper- and lower-surface progressions' zero-crossing. Merely considering the upper surface, $Im\, c_p^1$ decreases from its positive peak-value, eventually reversing in sign and following through to postshock negativity. The progressions reach a local minimum before increasing toward the TE, where equalization with the lower-surface $Im\, c_p^1$ instances occurs at nil value. These postshock features are again observed to be strongly subdued for the inner-span stations, while becoming increasingly prominent for the median- and the outer-span stations. Most notably, the gradient of the decreasing $Im\, c_p^1$ turns out especially steep for the outermost span station. Furthermore, the zero-crossing shifts from a location downstream of the hinge line to an upstream one. The reversal of sign exhibited by both the upper- and lower-surface $Im\, c_p^1$ progressions indicates a reversal of phase for the particular time-dependent c_p from the shock to the postshock region. Closer examination for the flap-median station, Figure 5.36, reveals that the particular zero-crossing takes place slightly upstream of the hinge-line intersections. Approximately corresponding to the location of the secondary $Re\, c_p^1$ peak, this occurrence conforms to the $Im\, c_p^1$ characteristic of an oscillating flap's LE in subsonic flow. Similar to the relationship between $Re\, c_L^1$ and $\Delta Re\, c_p^1$, the entirety of the sectional $Im\, c_L^1$ is supplied by the $\Delta Im\, c_p^1$ of the shock and postshock region. However, whereas the bulk contribution to the sectional $Im\, c_L^1$ stems from the negative $\Delta Im\, c_p^1$ forward of the zero-crossing, it is partially compensated by the positive $\Delta Im\, c_p^1$ aft of the zero-crossing. For all investigated span stations, Figures 5.33–5.35, the local intersection

of the c_M reference axis again resides distinctly upstream of the shock and postshock region. Therefore, the negative $\Delta Im\, c_p^1$ forward of the zero-crossing will always contribute positively (pitch up) to the sectional $Im\, c_M^1$ through leverage, while its aft counterpart will always do so negatively (pitch down). For the outer-span stations, both the $\Delta Im\, c_p^1$ forward and aft of the zero-crossing are approximately equal in magnitude, largely canceling each other out in the sectional $Im\, c_M^1$. Integrating over the entire wing, however, a negative $Im\, c_L^1$ and a positive $Im\, c_M^1$ (pitch up) are ascertained.

With respect to the prediction accuracy, FLM-SD.NS-computed c_p^0, $Re\, c_p^1$, and $Im\, c_p^1$ agree very well with those obtained from FLM-NS for the inner- and median-span stations. Notable discrepancies are witnessed for the outer-span stations in both the shock and postshock region. Focusing solely on the flap-median station, Figure 5.36, the FLM-NS-gained c_p^0 progression exhibits a minimum located farther upstream of its FLM-SD.NS counterpart, while being of lesser absolute value, although just slightly for both occurrences. In turn, the location of the supersonic-flow-terminating $c_{p,\,crit}^0$ is observed to be farther downstream, now coinciding with the hinge-line intersections. Hence, this progression's gradient across the shock region is visibly shallower than for its FLM-SD.NS counterpart. The variation between the two instances serves as an indication that the small disturbance premise does not completely hold up for the flap-induced motion of the the medium-strength shock. Furthermore, the FLM-NS-gained upper- and lower-surface c_p^0 progressions are observed to be mildly incongruent, a behavior that will be addressed subsequently. The two instances return to congruency at the location of the supersonic-flow-terminating $c_{p,\,crit}^0$, with conformity to the FLM-SD.NS-gained c_p^0 progressions renewed slightly farther downstream.

Concerning $Re\, c_p^1$, the FLM-NS-gained progression features merely a single peak, rendered at the location of the supersonic-flow-terminating $c_{p,\,crit}^0$. Coinciding with the hinge-line intersections, the peak embodies both the effect of the induced shock motion and of the flap deflection itself on the time-dependent c_p. Conformity to the FLM-SD.NS-gained progression is reestablished slightly farther downstream. In contrast to $Re\, c_p^1$, the FLM-NS-gained $Im\, c_p^1$ progression exhibits both characteristics of its FLM-SD.NS counterpart; i.e., the unique peak residing between the location of minimum c_p^0 and the location of the supersonic-flow-terminating $c_{p,\,crit}^0$, as well as the zero-crossing, although now situated exactly at the hinge-line intersections. Nonconformity between the FLM-NS- and FLM-SD.NS-gained progression is merely given for the shock region, yet not overly prominent. For either method, however, the absolute values of the rendered $Re\, c_p^1$ and $Im\, c_p^1$ peaks are in the same order of magnitude as c_p^0 itself, confirming the indicated violation of the small disturbance premise.

Just as the FLM-NS-gained upper- and lower-surface c_p^0 progressions are no longer symmetric for the shock region, the FLM-NS-gained upper- and lower-surface $Re\, c_p^1$ pro-

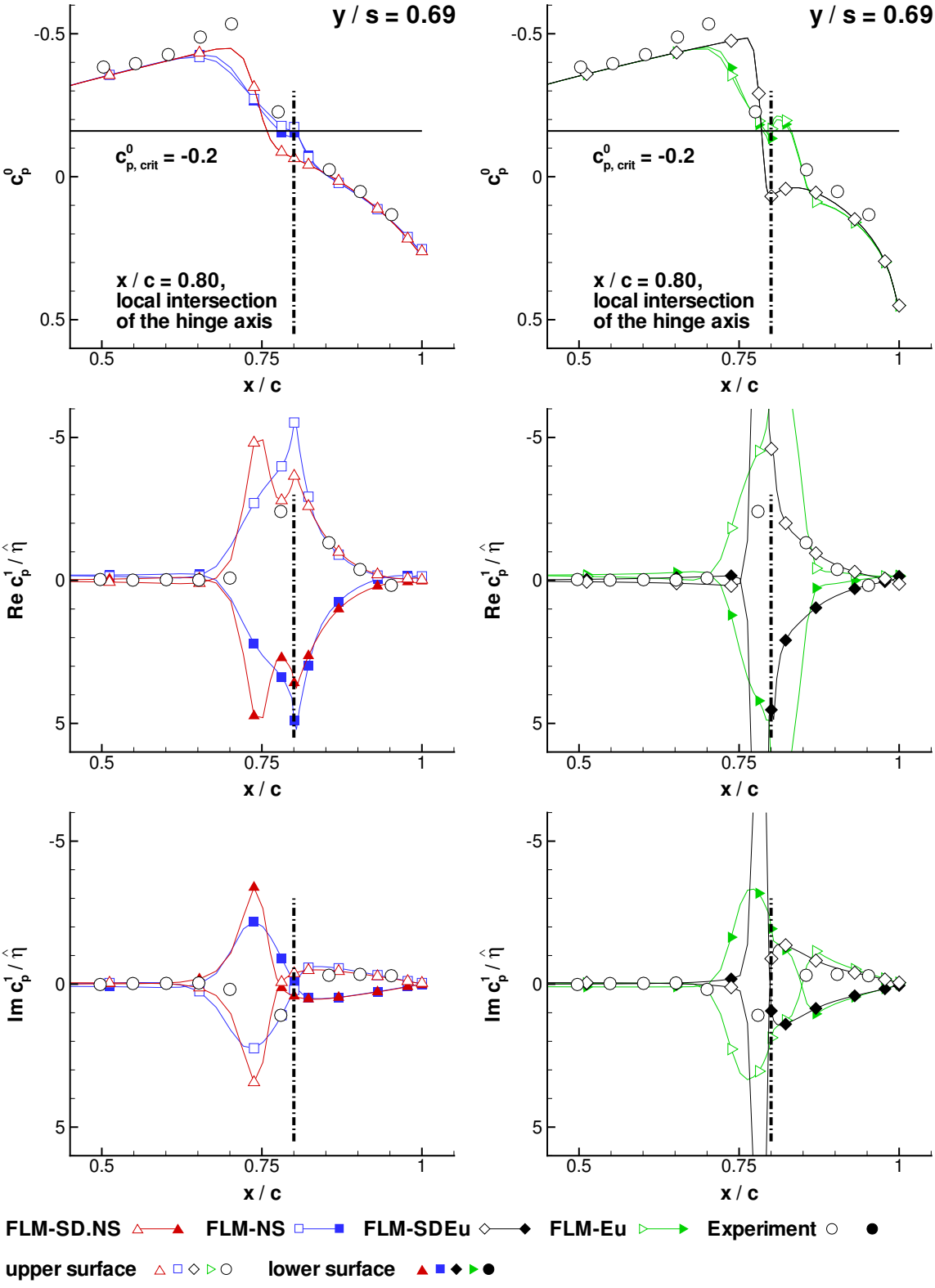

Figure 5.36: Flap-median detail of c_p^0, c_p^1 for the NCDW 92D33 case ($Ma_\infty = 0.92$, $Re_\infty = 10.0 \times 10^6$, $\breve{\alpha} = 0.0$ deg, $x_h/c = 0.80$, $\breve{\eta} = 0.0$ deg, $\hat{\eta} = 3.9$ deg, $k_{red} = 0.478$).

gressions, as well as the particular $Im\, c_p^1$ instances, are no longer antisymmetric. This behavior results from the consideration of merely a reference and an upper-dead-center flap position (the fully downward deflection) to model the locally deforming wing geometry over the course of an entire oscillation cycle. For its first half, the time-accurate interpolation between the two given positions approximates the actual position of a truly rotating rigid flap very well. For the second half of the cycle, however, the extrapolation from the two given positions toward a lower-dead-center position (the fully upward deflection) and back to the reference position, respectively, leads to an elongation and subsequent recontraction of the flap chord. The longitudinal coordinates had been allowed to develop unrestrictedly. With the wing's local deformation not being entirely symmetric for the up- and downstroke, the locally rendered upper- and lower-surface c_p^0 progressions will not be entirely symmetric either. Correspondingly, the upper- and lower-surface $Re\, c_p^1$ and $Im\, c_p^1$ progressions will not be entirely antisymmetric. Considering the FLM-NS-rendered snapshot of the c_p progression for the fully downward-deflected flap, as well as the fully upward-deflected flap, Figure 5.37, however, the incongruity is just marginally observable. The upper-surface c_p progression at $\check{\eta}(\pi/2)$ conforms well to the lower-surface c_p progression at $\check{\eta}(3\pi/2)$, except from the location of minimum c_p to the hinge-line intersections, where the deviation becomes more substantial. The lower-surface c_p progression at $\check{\eta}(\pi/2)$, on the other hand, conforms well to the upper-surface c_p progression at $\check{\eta}(3\pi/2)$ across the considered chord length.

For both the fully downward- and fully upward-deflected flap, the wing surface exhibiting the convex chordwise kink initiates the shock downstream of the hinge line. Complementarily, the wing surface exhibiting the concave chordwise kink initiates the shock upstream of the hinge line. Thus, for either deflection, one surface of the flap's virtual LE always lies in the region of subsonic flow. Nevertheless, both the upper- and lower-surface c_p progression feature a peak at the respective hinge-line intersection, as characteristic of an oscillating flap in subsonic flow. The presence of a thin boundary layer had allowed disturbances caused by the chordwise kink to limitedly propagate upstream of the pertinent hinge line into the region of supersonic flow.

Again considering all investigated span stations, Figures 5.33–5.35, the viscous and inviscid progressions are observed to primarily differ in the shock and postshock region. For both c_p^0 and $Re\, c_p^1$, this variation is only marginally evident at the inner-span stations, yet becomes discontinuously prominent in proximity to the flap's inboard edge (the median-span stations), and increasingly so toward the outermost span station. In particular, the FLM-SDEu-gained c_p^0 progression shows a slightly farther downstream shock initiation than its FLM-SD.NS counterpart, while exhibiting a significantly stronger recompression gradient. This circumstance is expected in absence of a boundary layer. Surprisingly, the FLM-Eu-gained c_p^0 progression follows its FLM-NS counterpart closely. Coinciding with

the location of the supersonic-flow-terminating $c^0_{p,\,crit}$, FLM-SDEu renders unique $Re\,c^1_p$ peaks at the median- and outer-span stations. They are distinctly narrower and of substantially greater absolute value than the FLM-SD.NS-computed instances. These characteristics are retained by the FLM-Eu prediction, with the $Re\,c^1_p$ peaks having a slightly wider base and being of reduced absolute value. At both $y/s = 0.54$ and $y/s = 0.85$ these occurrences even resemble their FLM-NS counterparts more than their FLM-SDEu ones. In contrast to c^0_p and $Re\,c^1_p$, the viscous-inviscid variation of $Im\,c^1_p$ is evident across the entire semi-span. Already for the inner-span stations, distinct shock-induced peaks emerge

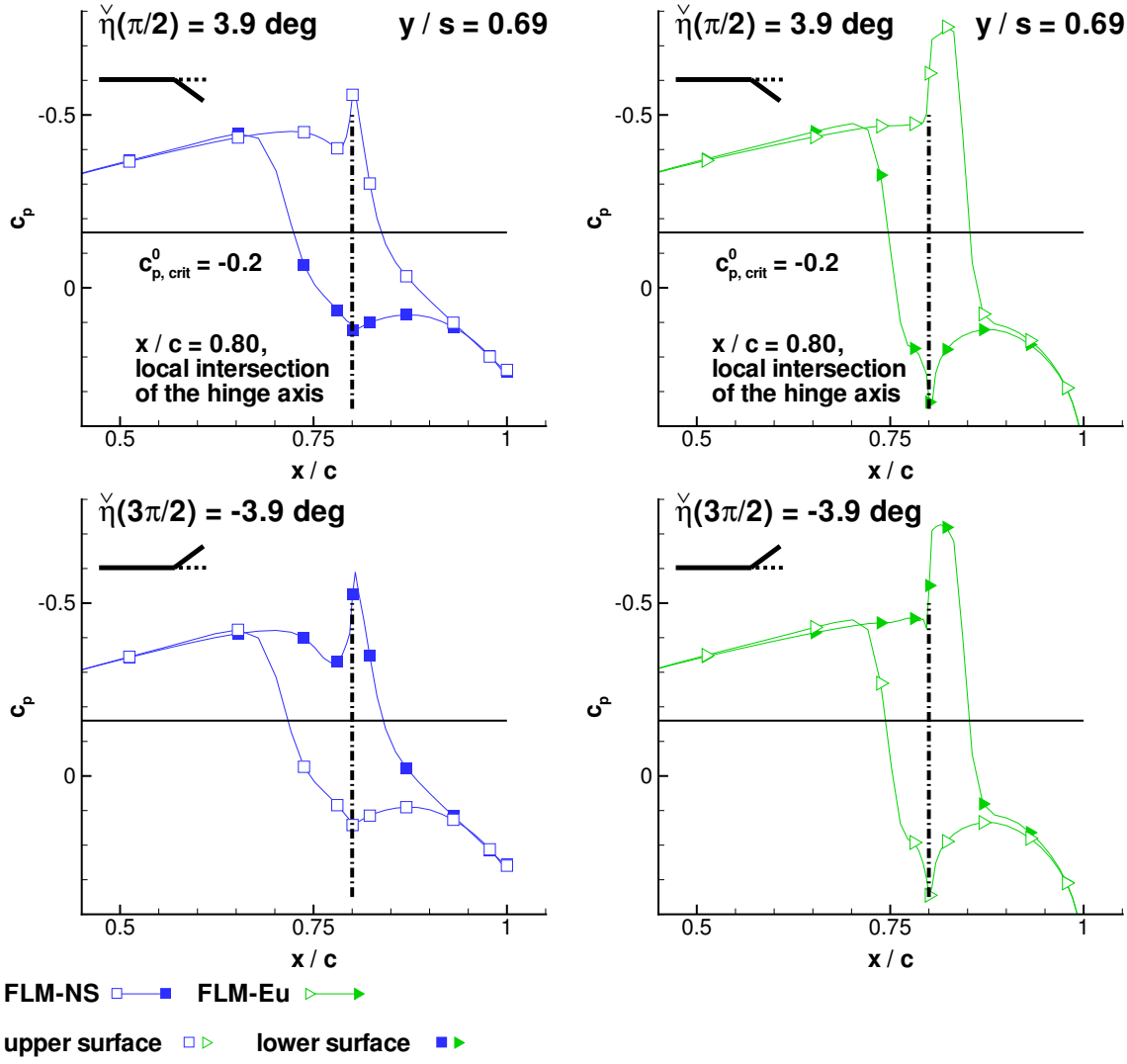

Figure 5.37: Flap-median detail of the FLM-NS-/FLM-Eu-rendered upper- and lower-dead-center pressure coefficient c_p for the NCDW 92D33 case ($Ma_\infty = 0.92$, $Re_\infty = 10.0 \times 10^6$, $\check{\alpha} = 0.0$ deg, $x_h/c = 0.80$, $\check{\bar{\eta}} = 0.0$ deg, $\check{\hat{\eta}} = 3.9$ deg, $k_{red} = 0.478$); i.e., at $\check{\eta}(\pi/2)$ and $\check{\eta}(3\pi/2)$, respectively.

at the locations of the supersonic-flow-terminating $c_{p,\,crit}^{0}$. They are highly constrained, while surpassing the absolute value of their viscous counterparts by more than double. At the median- and outer-span stations both the FLM-SDEu- and FLM-Eu-gained $Im\,c_p^1$ peaks, respectively, reflect their $Re\,c_p^1$ counterparts. Toward the outermost span station, however, the FLM-Eu-gained $Im\,c_p^1$ peaks become notably subdued in respect to their FLM-SDEu-gained counterparts. As witnessed for the FLM-Eu-gained $Re\,c_p^1$ progressions, the corresponding $Im\,c_p^1$ progressions better resemble their FLM-NS-gained counterparts. The agreement between FLM-SDEu and FLM-Eu is best at the innermost span station, monotonically deteriorating from there toward the outermost span station.

Refocusing on the shock and postshock region of the flap-median station, Figure 5.36, the FLM-Eu-gained c_p^0 progression exhibits a minimum located farther upstream of its FLM-SDEu-gained counterpart, while being of lesser absolute value, although just slightly for the latter occurrence. In turn, the successive FLM-Eu-gained supersonic-flow-terminating $c_{p,\,crit}^{0}$ lies slightly farther downstream, coming very close to the hinge-line intersections themselves. Hence, this progression's gradient across the shock region is visibly shallower than for its FLM-SDEu counterpart, yet still steeper than witnessed in the FLM-NS prediction. After forming a local maximum slightly upstream of the hinge-line intersection, the FLM-Eu-gained c_p^0 progression again decreases in value below $c_{p,\,crit}^{0}$, only to form a local minimum slightly downstream of the hinge-line intersection. Subsequently, c_p^0 increases sharply, surpasses $c_{p,\,crit}^{0}$, and finally merges into the FLM-SDEu-gained c_p^0 progression farther downstream. Correlated to a steady-state flowfield, the FLM-Eu-gained c_p^0 progression would indicate that the recompression in proximity to the hinge-line intersection occurs by way of two successive shocks. At first, a shock upstream of the hinge-line intersection discontinuously decelerates the flow to marginally subsonic speeds, allowing a renewed acceleration to supersonic speeds over the flap's virtual LE. As the wing thickness continues to taper off toward the TE, however, the accompanied deceleration of the flow from super- to subsonic speeds again occurs discontinuously; i.e., through another shock, now located slightly downstream of the hinge-line intersection. Subsequently, the flow decelerates continuously for the remaining distance, conforming to the actual steady-state instance of FLM-SDEu. Combined, the apparent dual shock system increases c_p^0 by nearly the same absolute value as the FLM-SDEu-prescribed single shock.

To recall, the FLM-Eu-gained c_p^0 progression is in fact the arithmetic average of the time-discrete c_p progressions rendered over the last oscillation period. Individually, these reveal, however, the existence of merely a single shock for each the upper and lower surface. Considering the FLM-Eu-rendered snapshot of the c_p progression for both the fully downward- and fully upward-deflected flap, Figure 5.37, characteristics similar to the ones established for the FLM-NS-gained c_p progression can initially be ascertained. The upper-surface c_p progression at $\check{\eta}(\pi/2)$ conforms just as well to the lower-surface c_p

progression at $\check{\eta}(3\pi/2)$ as the lower-surface c_p progression at $\check{\eta}(\pi/2)$ does to the upper-surface c_p progression at $\check{\eta}(3\pi/2)$. The incongruity due to the wing's asymmetric local deformation has become even less prominent than before. For both the fully downward- and fully upward-deflected flap, the wing surface exhibiting the convex chordwise kink initiates the shock downstream of the hinge-line intersection. Complementarily, the wing surface exhibiting the concave chordwise kink initiates the shock upstream of the hinge-line intersection. Thus, for either deflection, one surface of the flap's virtual LE once again always lies in the region of supersonic flow, while the other always lies in the region of subsonic flow. Contrary to the FLM-NS instances, however, merely the wing surface exhibiting the concave chordwise kink renders a c_p progression with an actual peak at the hinge-line intersection. In absence of a boundary layer, disturbances caused by the corresponding convex chordwise kink cannot propagate upstream of the hinge line, disallowing any influence on that part of the c_p progression. At the hinge-line intersection itself, however, c_p spikes in negative value, forming a downstream suction plateau, as characteristic of an oscillating flap in inviscid supersonic flow. After only a short distance, the shock eventually does initiate, returning the flow to subsonic speeds, and consequently returning the c_p progression to one typical of a continuous TE recompression. For the wing surface exhibiting the concave chordwise kink, the FLM-Eu-gained compression peak at the hinge-line intersection is observed to be far more pronounced than its FLM-NS-gained counterpart, a trait consequently seen in the convex c_p progression toward the TE as well. Once again, the lower-surface FLM-Eu instance regains conformity to its upper-surface counterpart in proximity to the TE. Ultimately, arithmetic averaging of the time-discrete c_p progressions will invariably yield a c_p^0 progression greater than $c_{p,\,crit}^0$ slightly upstream of the hinge-line intersections (subcritical instance) and one lesser than $c_{p,\,crit}^0$ slightly downstream of the hinge-line intersections (supercritical instance). Thus, the c_p^0-indicated dual shock system is merely an artifact of the arithmetic averaging itself.

Returning to Figure 5.36, the variation between the FLM-SDEu- and FLM-Eu-rendered c_p^0 progression in the shock and postshock region is naturally seen to be far greater than between the FLM-SD.NS- and FLM-NS-rendered counterparts. As precedingly discussed, it results from the varying nature of the upper- and lower-surface c_p progression over the course of an oscillation; i.e., having either a sub- or supersonic characteristic in proximity to the pertinent hinge-line intersection. The FLM-Eu-gained upper- and lower-surface c_p^0 progressions are observed to be mildly incongruent in the shock region, an already established property of the FLM-NS-predicted instances. Likewise, this behavior arises from the asymmetrically rendered flap geometry over the course of an oscillation cycle. Nevertheless, the FLM-SDEu- and FLM-Eu-gained c_p^0 progressions again return to congruency downstream of the hinge-line intersections at the location of the supersonic-flow-terminating $c_{p,\,crit}^0$.

In contrast to the FLM-SD.NS-gained $Re\, c_p^1$ progression, its FLM-SDEu counterpart merely exhibits a unique narrow peak, rendered at the location of the supersonic-flow-terminating $c_{p,\,crit}^0$, an occurrence naturally witnessed in Figure 5.35 for $y/s = 0.69$ as well. Positioned slightly upstream of the hinge-line intersections, it embodies both the effect of the induced shock motion and of the flap deflection itself on the time-dependent c_p. The FLM-Eu-gained $Re\, c_p^1$ progression, on the other hand, resembles its FLM-NS counterpart by featuring a unique peak with a wide base, though rendered downstream of the hinge-line intersections. Equal to the FLM-NS- and FLM-SDEu-gained $Re\, c_p^1$ peak, the FLM-Eu instance embodies both the effect of the induced shock motion and of the flap itself on the time-dependent c_p, as exhibited in Figure 5.37. Conformity to the FLM-SDEu-gained progression is reestablished in proximity to the TE.

The FLM-SDEu-gained $Im\, c_p^1$ progression likewise exhibits the characteristics of its FLM-SD.NS counterpart, namely, the unique peak and the zero-crossing, albeit now at the location of the supersonic-flow-terminating $c_{p,\,crit}^0$ and at the hinge-line intersections, respectively. Corresponding to the FLM-SDEu-gained $Re\, c_p^1$ peak, the $Im\, c_p^1$ instance is again far narrower than its FLM-SD.NS counterpart. The FLM-Eu-gained $Im\, c_p^1$ progression, on the other hand, is once again more in line with its viscous counterpart. Featuring a unique peak in proximity to the location of the primary supersonic-flow-terminating $c_{p,\,crit}^0$, however, its location now differs to that of the FLM-Eu-gained $Re\, c_p^1$ peak. Both the FLM-SDEu- and FLM-Eu-gained $Im\, c_p^1$ peak naturally embody the effect of the induced shock motion and of the flap deflection itself on the time-dependent c_p, as exhibited in Figure 5.37. Contrary to FLM-SDEu, FLM-Eu predicts the characteristic zero-crossing at the location of the secondary supersonic-flow-terminating $c_{p,\,crit}^0$. Conformity to the FLM-SDEu-gained progression is reestablished slightly downstream from there. The FLM-Eu-gained upper- and lower-surface c_p^0 progressions are no longer symmetric in the shock region, while the FLM-Eu-gained upper- and lower-surface $Re\, c_p^1$ and $Im\, c_p^1$ progression are no longer antisymmetric. All in all, the viscous methods improve on the inviscid methods, reproducing the wing's experimental surface-pressure-coefficient well. With only a single experimental data point available in proximity to the hinge-line intersections, however, the flap-local prediction accuracy could not be assessed.

Considering the 92D36 case (the higher-frequency case) next, the FLM-SD.NS result as provided in Figures 5.38–5.40 is characterized. Upper- and lower-surface c_p^0 are naturally equal to those of the 92D33 case, as both computations employ the same reference solution. At higher-frequency the particular antisymmetric $Re\, c_p^1$ and $Im\, c_p^1$ progressions are gained very similar to their baseline-frequency counterparts, with the absolute values of the respective peaks having become slightly diminished. As a consequence, $\Delta Re\, c_p^1$ of the shock and postshock region contributes less positively to $Re\, c_L^1$ and thus less negatively (pitch down) to $Re\, c_M^1$ than in the 92D33 case. Complementarily, $\Delta Im\, c_p^1$ forward

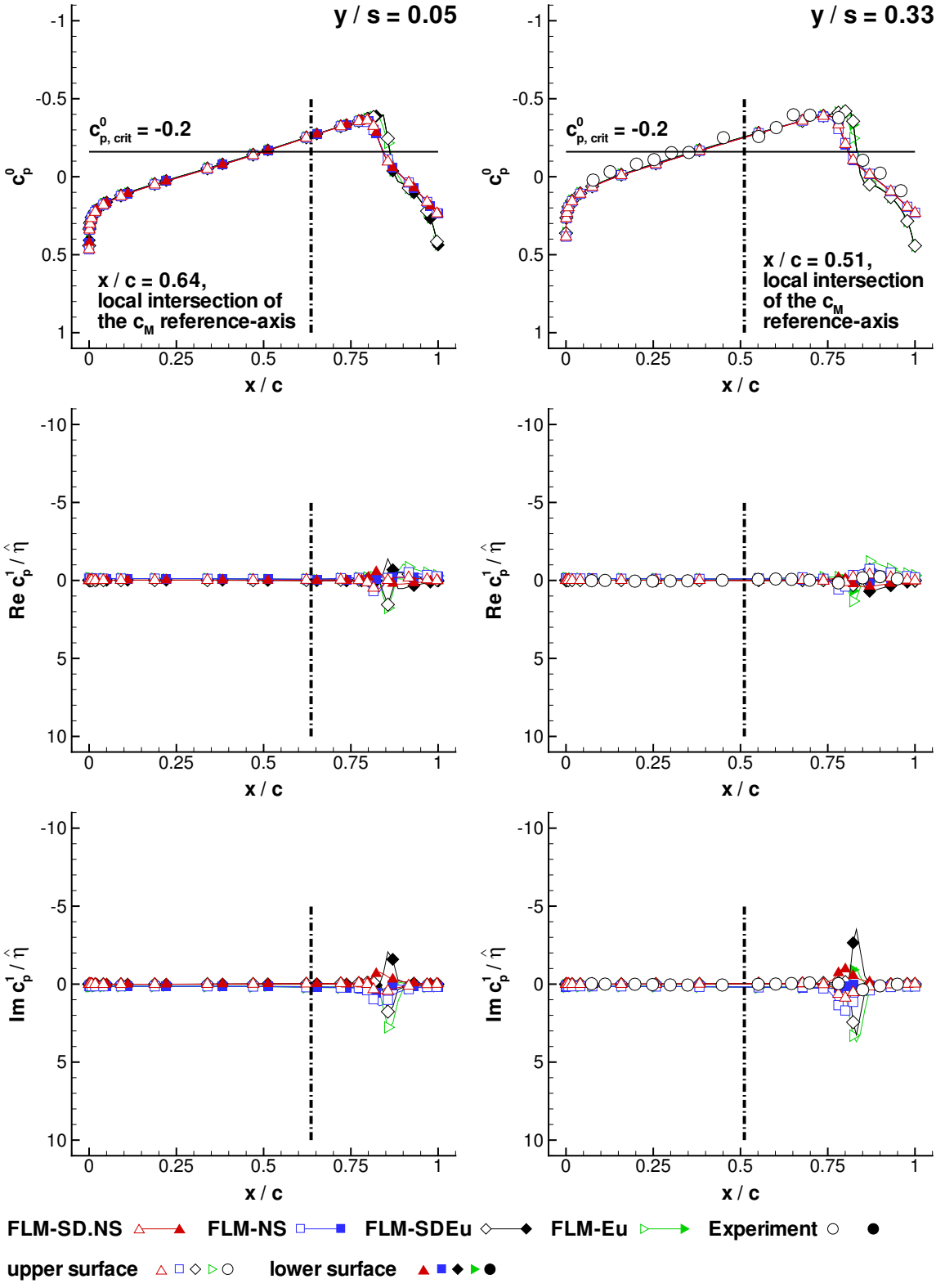

Figure 5.38: Press. coeff. c_p^0, c_p^1 for a NCDW flap oscill. at $Ma_\infty = 0.92$, $Re_\infty = 10.0 \times 10^6$, $\breve{\alpha} = 0.0$ deg ab. $x_h/c = 0.80$ w. $\breve{\eta} = 0.0$ deg, $\hat{\breve{\eta}} = 3.9$ deg, $k_{red} = 0.651$ (92D36, inner).

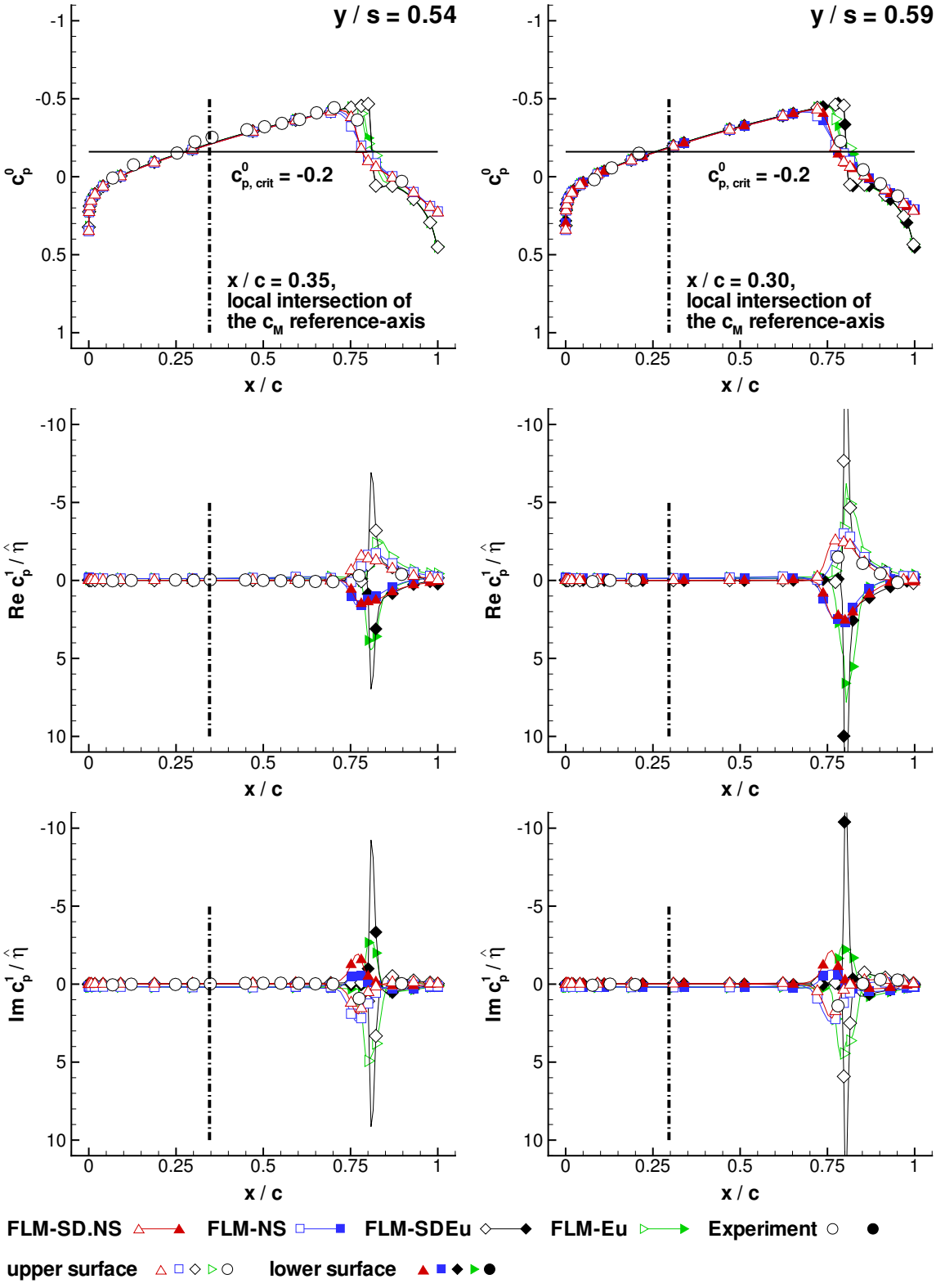

Figure 5.39: Press. coeff. c_p^0, c_p^1 for a NCDW flap oscill. at $Ma_\infty = 0.92$, $Re_\infty = 10.0 \times 10^6$, $\breve{\alpha} = 0.0$ deg ab. $x_h/c = 0.80$ w. $\breve{\eta} = 0.0$ deg, $\hat{\breve{\eta}} = 3.9$ deg, $k_{red} = 0.651$ (92D36, median).

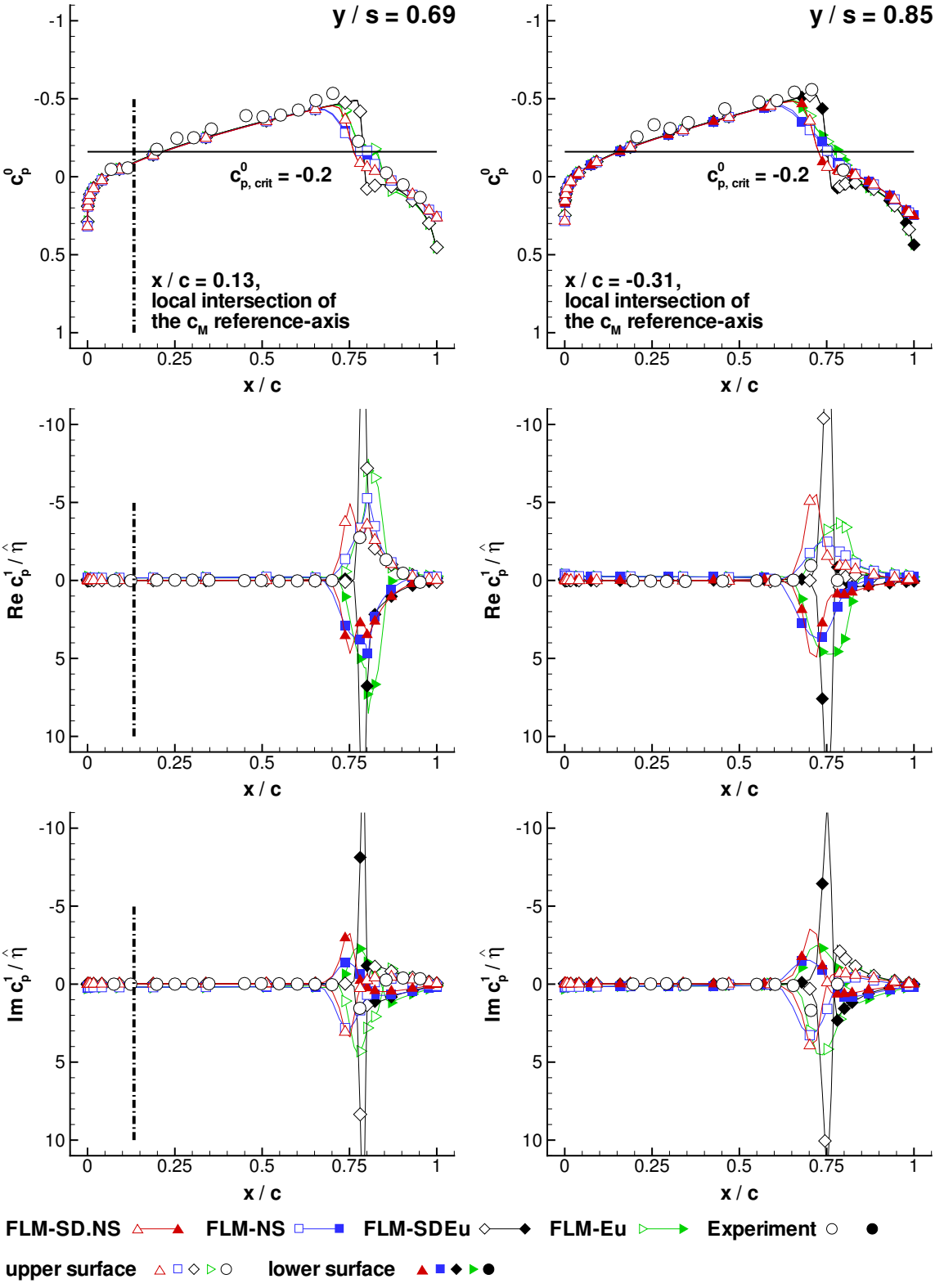

Figure 5.40: Press. coeff. c_p^0, c_p^1 for a NCDW flap oscill. at $Ma_\infty = 0.92$, $Re_\infty = 10.0 \times 10^6$, $\breve{\alpha} = 0.0$ deg ab. $x_h/c = 0.80$ w. $\breve{\eta} = 0.0$ deg, $\hat{\breve{\eta}} = 3.9$ deg, $k_{red} = 0.651$ (92D36, outer).

of the zero-crossing contributes less negatively to $Im\,c_L^1$ and thus less positively (pitch up) to $Im\,c_M^1$. For the flap-median station, a secondary $Re\,c_p^1$ peak of lesser absolute value again saddles the primary peak's base at the hinge-line intersections. Likewise, it embodies the known characteristic of an oscillating flap in subsonic flow; i.e., rendering a quasi-singularity for c_p at the flap's LE for any deflected position. All in all, FLM-SD.NS-computed c_p^0, $Re\,c_p^1$, and $Im\,c_p^1$ agree very well with those obtained from FLM-NS. Similar to the 92D33 case, the FLM-NS-gained upper- and lower-surface $Re\,c_p^1$ progression for both the shock and postshock region of the flap-median station, as well as their $Im\,c_p^1$ progression counterparts, are no longer antisymmetric. This behavior is observed to have even become amplified toward higher-frequency. In particular, the FLM-NS-rendered snapshot of the c_p progression for the fully downward-deflected flap, Figure 5.42, reveals a material incongruity to the instance for the fully upward-deflected flap in the expansion peak's occurrence.

For all investigated span stations, the conformity between the FLM-SD.NS- and FLM-NS-gained c_p^0, $Re\,c_p^1$, and $Im\,c_p^1$ progressions are seen to be significantly better than between their FLM-SDEu- and FLM-Eu-gained counterparts. Especially, the loss of antisymmetry for the FLM-Eu-gained upper- and lower-surface $Re\,c_p^1$ progressions, as well as for the particular $Im\,c_p^1$ instances, in the shock and postshock region of the flap-median station has amplified toward higher-frequency by far more than for the respective FLM-NS instances, Figure 5.41. Corroborated by Figure 5.42, the FLM-Eu-rendered expansion peak substantially differs for the fully downward- and fully upward-deflected flap. In either case, the wing surface exhibiting the convex chordwise kink initiates the shock downstream of the hinge-line intersection, letting the flap's surface-particular virtual LE always lie in the region of supersonic flow. Similar to the 92D33 case, each corresponding c_p progression then features a spike in negative value at the pertinent hinge-line intersection itself. Contrary to the 92D33 case, however, a downstream suction plateau, as characteristic of an oscillating flap in inviscid supersonic flow, has formed at $\check{\eta}(3\pi/2)$. At $\check{\eta}(\pi/2)$, however, it is absent, with the shock having initiated in very close proximity to the hinge-line intersection. Thus, the occurrence actually resembles the characteristic of an oscillating flap in subsonic flow. This variation has naturally followed through to the FLM-Eu-gained $Re\,c_p^1$ and $Im\,c_p^1$ progressions, emerging as a greater loss of antisymmetry than witnessed for the viscous consideration (Figure 5.41). Ultimately, the impact of the wing's asymmetric local deformation is seen to be at its most prominent in the FLM-Eu treatment of the 92D36 case.

The FLM-SDEu-rendered $Re\,c_p^1$ and $Im\,c_p^1$ progressions are gained very similar to their baseline-frequency counterparts, with the absolute values of the respective peaks having become distinctly diminished. As a consequence, $\Delta Re\,c_p^1$ of the shock and postshock region contributes less positively to $Re\,c_L^1$ and thus less negatively (pitch down) to $Re\,c_M^1$

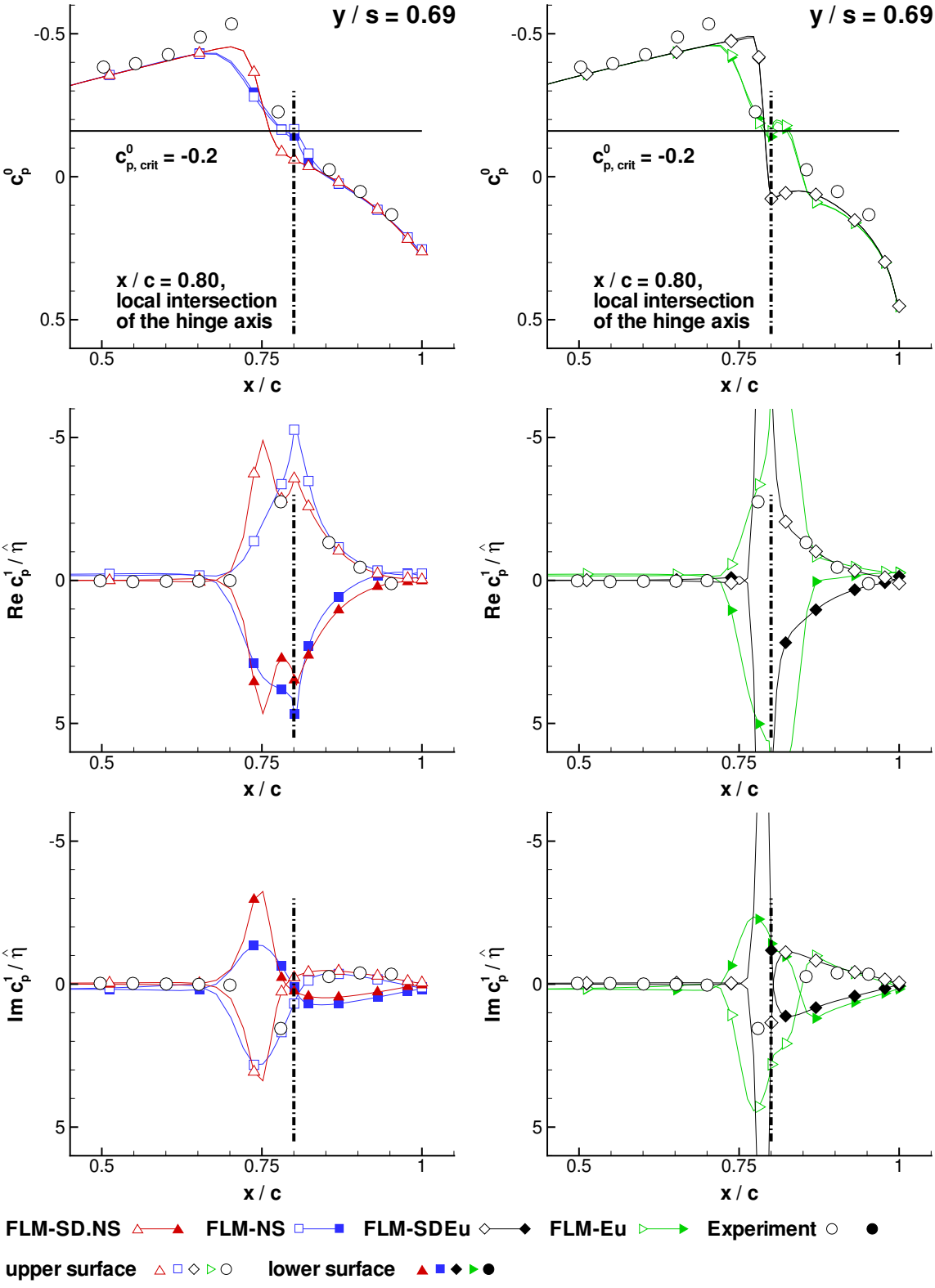

Figure 5.41: Flap-median detail of c_p^0, c_p^1 for the NCDW 92D36 case ($Ma_\infty = 0.92$, $Re_\infty = 10.0 \times 10^6$, $\breve{\alpha} = 0.0$ deg, $x_h/c = 0.80$, $\breve{\eta} = 0.0$ deg, $\hat{\eta} = 3.9$ deg, $k_{red} = 0.651$).

than in the 92D33 case. Complementarily, $\Delta Im\, c_p^1$ forward of the zero-crossing contributes less negatively to $Im\, c_L^1$ and thus less positively (pitch up) to $Im\, c_M^1$. All in all, the viscous methods likewise improve on the inviscid methods for the 92D36 case, reproducing the wing's experimental surface-pressure-coefficient well. Equally, the flap-local prediction accuracy could not be assessed.

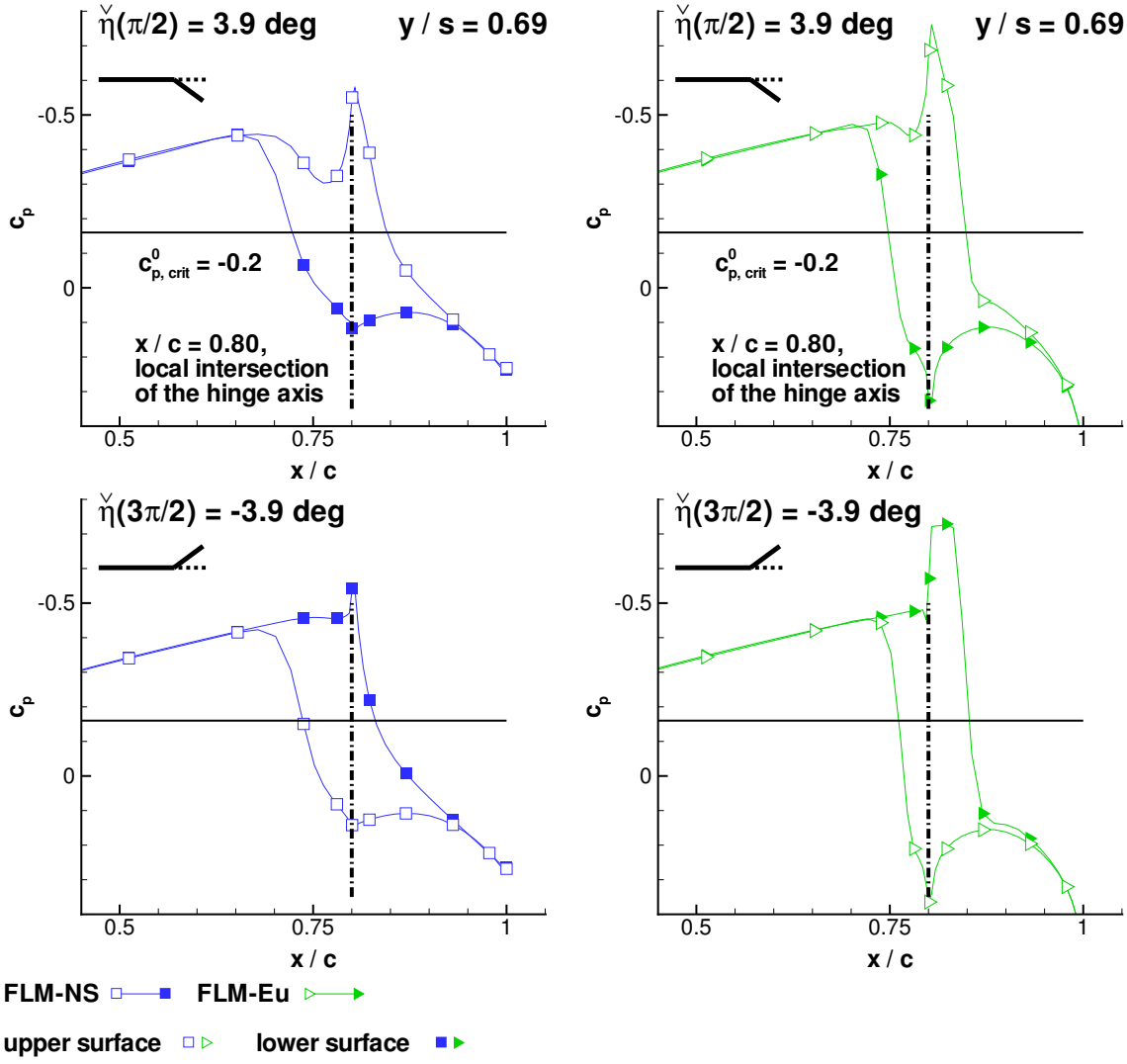

Figure 5.42: Flap-median detail of the FLM-NS-/FLM-Eu-rendered upper- and lower-dead-center pressure coefficient c_p for the NCDW 92D36 case ($Ma_\infty = 0.92$, $Re_\infty = 10.0 \times 10^6$, $\breve{\alpha} = 0.0$ deg, $x_h/c = 0.80$, $\breve{\eta} = 0.0$ deg, $\breve{\eta} = 3.9$ deg, $k_{red} = 0.651$); i.e, at $\breve{\eta}(\pi/2)$ and $\breve{\eta}(3\pi/2)$, respectively.

5.4.2 Global Load Coefficients

The computed global load coefficients of the 92D33 and 92D36 case are compiled in Table 5.7. The 92D33 case (the baseline-frequency case) is focused on at first. $Re\, c_L^1$ and $Im\, c_L^1$ obtained from FLM-SD.NS are, respectively, 5% and 7% higher in absolute value than their FLM-NS instances. Consequently, the two viscous methods conform well in their prediction of a time-dependent c_L that substantially lags the excitation. Both FLM-SDEu- and FLM-Eu-computed $Re\, c_L^1$ are significantly higher in absolute value than their viscous counterparts. From the proximity of the flap's inboard edge on toward the wing tip, stronger $Re\, c_p^1$ peaks are rendered in the shock region, and are observed to amplify along the hinge line. They yield a larger chordwise-localized difference between upper- and lower-surface distribution. Contributing more positively, its summation over the semi-span is substantial enough to increase FLM-SDEu- and FLM-Eu-computed $Re\, c_L^1$ by 23% and

Case	Method	c_L^0	$Re\, c_L^1/\hat{\eta}$	$Im\, c_L^1/\hat{\eta}$	$\lvert c_L^1\rvert/\hat{\eta}$	$\breve{\varphi}_{c_L^1}$, deg
92D33	FLM-SD.NS	0.000	0.302	-0.159	0.341	-27.85
	FLM-NS	0.000	0.287	-0.148	0.323	-27.24
	FLM-SDEu	0.000	0.372	-0.231	0.438	-31.81
	FLM-Eu	0.000	0.365	-0.236	0.435	-32.86
92D36	FLM-SD.NS	0.000	0.268	-0.135	0.300	-26.83
	FLM-NS	0.000	0.265	-0.131	0.295	-26.28
	FLM-SDEu	0.000	0.332	-0.194	0.385	-30.27
	FLM-Eu	0.000	0.331	-0.207	0.390	-32.07

Case	Method	c_M^0	$Re\, c_M^1/\hat{\eta}$	$Im\, c_M^1/\hat{\eta}$	$\lvert c_M^1\rvert/\hat{\eta}$	$\breve{\varphi}_{c_M^1}$, deg
92D33	FLM-SD.NS	0.000	-0.119	0.052	0.130	156.31
	FLM-NS	0.000	-0.110	0.052	0.121	154.83
	FLM-SDEu	0.000	-0.150	0.083	0.172	151.15
	FLM-Eu	0.000	-0.143	0.087	0.167	148.75
92D36	FLM-SD.NS	0.000	-0.104	0.044	0.113	157.32
	FLM-NS	0.000	-0.103	0.041	0.111	158.32
	FLM-SDEu	0.000	-0.133	0.067	0.149	153.15
	FLM-Eu	0.000	-0.133	0.070	0.150	152.41

Table 5.7: Global load coefficients for NCDW cases 92D33 and 92D36 ($Ma_\infty = 0.92$, $Re_\infty = 10.0 \times 10^6$, $\breve{\alpha} = 0.0$ deg, $x_h/c = 0.80$, $\breve{\bar{\eta}} = 0.0$ deg, $\breve{\hat{\eta}} = 3.9$ deg, $k_{red} = 0.478$, 0.651).

27%, respectively. This circumstance emerges even more pronounced in $Im\,c_L^1$. Whereas the $Im\,c_p^1$ peaks rendered in the shock region remain subdued from the innermost span station toward the proximity of the flap's inboard edge for the viscous consideration, the corresponding inviscidly predicted $Im\,c_p^1$ peaks extend across the entire semi-span, while being of greater absolute value. Thus, the resultant $\Delta Im\,c_p^1$ contributes far more negatively to $Im\,c_L^1$, allowing for the one and a half times amplification of the viscous values. The deviation between FLM-SDEu- and FLM-Eu-computed $Re\,c_L^1$, as well as $Im\,c_L^1$, is merely 2%, an improvement on the deviation between their respective FLM-SD.NS and FLM-NS counterparts. Inviscidly, the time-dependent c_L is again predicted to substantially lag the excitation, however, distinctly more than for the viscous consideration.

FLM-SD.NS predicts $Re\,c_M^1$ within 8% of the FLM-NS-gained value, with the $Im\,c_M^1$ instances being identical. Apparently, the difference in $Im\,c_L^1$ does not follow through to $Im\,c_M^1$. Considering the contribution of skin friction to be negligible, deviations in $Im\,c_p^1$ are compensated toward $Im\,c_M^1$ for the given reference axis. In absolute terms, $Re\,c_M^1$ and $Im\,c_M^1$ are separated by half an order of magnitude. Both viscous methods predict the time-dependent c_M to lead the excitation by somewhat more than three-eighth of a cycle. The deviation witnessed for $Re\,c_M^1$ follows through to $|c_M^1|$ yet is compensated in $\check{\varphi}_{c_M^1}$. In case of the latter, the two instances can actually be considered to be identical. FLM-SDEu- and FLM-Eu-computed $Re\,c_M^1$ are, respectively, 26% and 30% higher in absolute value than their viscous counterparts. The particular $Im\,c_M^1$ instances, on the other hand, again amplify by one and a half times from the viscous consideration toward the inviscid one. All in all, disregarded viscosity has similar impact on c_M^1 as it had on c_L^1; i.e., existing differences in c_p^1 intensify only minimally through accounted leverage. For both $Re\,c_M^1$ and $Im\,c_M^1$, the deviation between the FLM-SDEu- and FLM-Eu-computed instance is 5%, only marginally greater than the deviation witnessed between their $Re\,c_L^1$ and $Im\,c_L^1$ counterparts. With $Im\,c_M^1$ still being gained half an order of magnitude smaller than $Re\,c_M^1$ in absolute terms, the impact of the inviscid consideration is naturally observed to be substantial for $|c_M^1|$ yet immaterial for $\check{\varphi}_{c_M^1}$.

Considering the 92D36 case (the higher-frequency case) next, FLM-SD.NS predicts both $|c_L^1|$ and $\check{\varphi}_{c_L^1}$ within 2% of the FLM-NS-gained value. The two viscous methods similarly indicate a time-dependent c_L that substantially lags the excitation. The mean of the FLM-SD.NS- and FLM-NS-computed $|c_L^1|$ is 10% lower than the 92D33 instance, with the mean of $|\check{\varphi}_{c_L^1}|$ being merely 4% lower. FLM-SDEu- and FLM-Eu-computed $|c_L^1|$ are observed to be nearly identical, whereas the two $\check{\varphi}_{c_L^1}$ exhibit a 6% deviation in their prediction of a substantially lagging time-dependent c_L. Disregarded viscosity yields a 30% higher mean $|c_L^1|$ and a 17% higher mean $|\check{\varphi}_{c_L^1}|$. Evidently, the relative impact of the inviscid consideration is equal to the one observed for 92D33. At higher-frequency, the particular mean of $|c_L^1|$ and of $\check{\varphi}_{c_L^1}$ is gained, respectively, 11% and 4% lower than their

92D33 case counterparts.

Obtained from FLM-SD.NS, $|c_M^1|$ is gained merely 2% higher than its FLM-NS counterpart, an improvement over the 7% deviation witnessed for the baseline-frequency case. Again, the spread between the $\check{\varphi}_{c_M^1}$ instances is negligible, with both methods predicting a time-dependent c_M that leads the excitation by somewhat more than three-eighth of a cycle. Whereas the mean of the $|c_M^1|$ instances has decreased by 11% with respect to the mean of their 92D33 case counterparts, the mean of $\check{\varphi}_{c_M^1}$ has increased only marginally. Obtained from FLM-SDEu, both $|c_M^1|$ and $\check{\varphi}_{c_M^1}$ can be considered equal to their respective FLM-Eu counterpart. Disregarded viscosity yields a 33% higher mean $|c_M^1|$ and a merely 3% lower $\check{\varphi}_{c_M^1}$. As already observed for $|c_L^1|$ and $\check{\varphi}_{c_L^1}$, the relative impact of the inviscid consideration on $|c_M^1|$ and $\check{\varphi}_{c_M^1}$ is equal to the one observed for the 92D33 case. At higher-frequency, the particular mean of $|c_M^1|$ and of $\check{\varphi}_{c_M^1}$ is gained, respectively, 12% lower and 2% higher than their 92D33 case counterparts.

5.4.3 Overall Assessment

FLM-SD.NS computes the unsteady loading of the 92D33 and 92D36 case in good agreement to FLM-NS, despite having employed the FEVA. In all cases, the viscous consideration improves on the inviscid prediction for both the small disturbance and dynamically fully nonlinear approach. Specifically, the viscously computed $|c_L^1|$ and $|c_M^1|$ are both gained substantially lower than their inviscid counterparts for the two investigated frequencies. Furthermore, the viscous consideration renders a distinctly lesser $|\check{\varphi}_{c_L^1}|$ and a slightly higher $\check{\varphi}_{c_M^1}$ than the inviscid instance does. Ultimately, the more complete flow model reveals a control surface of reduced efficiency. For both the viscous and inviscid consideration, the variation in frequency impacts the magnitude of the global load coefficients magnitude notably, yet their phase angle only marginally.

5.5 Computational Efficiency Gain

For the individual cases, the computation times of FLM-SD.NS and FLM-NS are compiled in Table 5.8, including their inverse ratio; i.e., $\zeta_{CPU}^{v} = \check{t}_{CPU}^{NS}/\check{t}_{CPU}^{SD.NS}$. Additionally, computation times of FLM-SDEu for the 90D4, 90D5, 90D6 cases, and the 94D4, 94D5, 94D6 cases [103], as well as the 92D33 and 92D36 case are presented. Since each of these computations were realized on the same processor as employed by the particular FLM-SD.NS run, and had utilized the same grid-pair at equal setting of the numerical parameters, a comparison between the FLM-SD.NS and FLM-SDEu computation times is actually permissible. In this regard, FLM-Eu computation times for the 94D4, 94D5, and 94D6 cases [103] are also provided. Likewise realized on the higher-clocking processor, comparability

is not only rendered between the FLM-SDEu and FLM-Eu computation times, but also between the FLM-NS and FLM-Eu instances. Ultimately, ζ^{v}_{CPU} and its inviscid counterpart $\zeta^{i}_{CPU} = \check{t}^{Eu}_{CPU}/\check{t}^{SDEu}_{CPU}$ allow for a direct comparison of the respective computational efficiency gain. For the 90D28, 90D29, and 90D30 cases, on the other hand, FLM-SDEu and FLM-Eu computation times are excluded. In comparison to their viscous treatment, a coarser grid-pair needed to be utilized for stability reasons. Naturally, this skews the obtained computation times to substantially lower values than otherwise observed. The tabulated computation times are supplementally illustrated by Figure 5.43.

Pursuant to Pechloff and Laschka, it can be ascertained that

> FLM-SD.NS realizes reductions up to an order of magnitude. Whereas $\check{t}^{\mathrm{SD.NS}}_{\mathrm{CPU}}$ are all [lower or approximately] 24 h, a far greater range can be observed for $\check{t}^{\mathrm{NS}}_{\mathrm{CPU}}$, the computation of [the 90D4,] 90D5[, and 90D6 cases, as well as of the 94D4, 94D5, and 94D6 cases,] taking longer than [of the 90D28,] 90D29[, and 90D30 cases] by multiples. At

Case	$\check{t}^{SD.NS}_{CPU}$, h	$\check{t}^{NS}_{CPU}$, h	ζ^{v}_{CPU}	$\check{t}^{SDEu}_{CPU}$, h	$\check{t}^{Eu}_{CPU}$, h	ζ^{i}_{CPU}
90D4[a]	25.7	393.5	15.3	4.4	n/a	n/a
90D5[a] [103], Table 8	24.1	419.8	17.4	4.0		
90D6[a]	18.5	277.4	15.0	2.8		
90D28[b]	14.5	47.3	3.3	n/a	n/a	n/a
90D29[a] [103], Table 8	21.2	71.3	3.4			
90D30[b]	13.6	28.1	2.1			
94D4[b] [103], Table 8	16.9	261.0	15.4	3.4	88.3	26.0
94D5[b] [103], Table 8	17.2	242.7	14.1	3.2	78.8	24.6
94D6[b] [103], Table 8	26.4	216.8	8.2	3.7	71.1	19.2
92D33[a]	11.0	120.2	10.9	3.8	n/a	n/a
92D36[a]	11.4	113.6	10.0	8.3		

[a] 1.3 GHz Intel®Itanium®2 processor, [b] 1.6 GHz Intel®Itanium®2 processor

Table 5.8: Quantitive comparison of computational time between FLM-SD.NS and FLM-NS for all NCDW cases, as well as between FLM-SDEu and FLM-Eu for the 94D4, 94D5, and 94D6 cases; FLM-SDEu computational time for the 90D4, 90D5, and 90D6 cases, as well as the 92D33 and the 92D36 case.

> default settings, the dynamically fully nonlinear treatment of the $\breve{\alpha} = 0$ deg [pitching oscillation] had exhibited solution instabilities toward the upper/lower dead center; [i.e.], at physical time steps where the deflected wing experiences strong deceleration and acceleration. Merely very high instances of implicit damping allowed for a remedy, significantly drawing out the computation in turn. Compared to [the 90D4,] 90D5[, and 90D6 cases], the reduced [ζ^{v}_{CPU}] witnessed for [the 94D4,] 94D5[, and 94D6 cases] stems in part from the employed higher-clocking processor, accelerating FLM-NS considerably more than FLM-SD.NS. The frequency variation conducted on the basis of [the] 94D5 [case] further reveals an increase of $\check{t}^{\mathrm{SD.NS}}_{\mathrm{CPU}}$ by 56% from [the] 94D4 to [the] 94D6 [case], with a decrease of $\check{t}^{\mathrm{NS}}_{\mathrm{CPU}}$ by 17% occurring correspondingly. This opposing tendency results in a 47% reduction of [ζ^{v}_{CPU}] across the considered spectrum. Vice versa, it can be said that a 75% decrease of the 94D6 [case] frequency leads to a [nearly] twofold increase of FLM-SD.NS performance over FLM-NS, [reestablishing] a trait already experienced in the investigated airfoil cases [[100]]. [103]

In contrast to the 94D4, 94D5, and 94D6 cases, $\check{t}^{SD.NS}_{CPU}$ decreases from the 90D28 to the 90D30 case by merely 6%. A reduction of $\check{t}^{NS}_{CPU}$ is likewise witnessed, however, at 41%, being far more substantial than the one observed from the 94D4 to the 94D6 case. Ultimately, the concurring tendency of $\check{t}^{SD.NS}_{CPU}$ and $\check{t}^{NS}_{CPU}$ yields a 36% reduction of ζ^{v}_{CPU} across the considered spectrum. Vice versa, it can be said that a 75% decrease of the 90D30

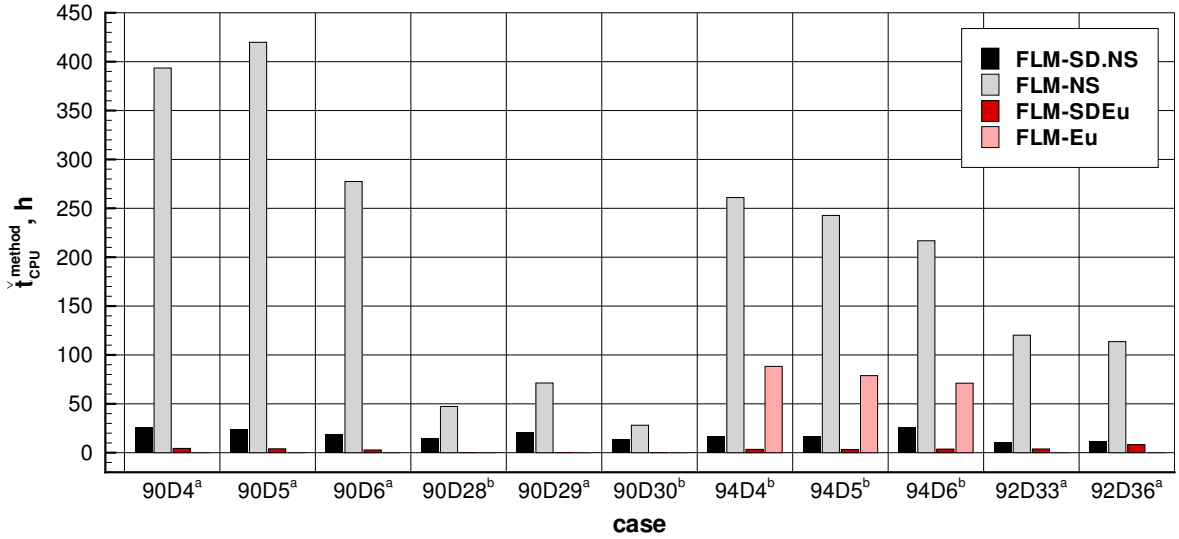

[a] 1.3 GHz Intel®Itanium®2 processor, [b] 1.6 GHz Intel®Itanium®2 processor

Figure 5.43: Qualitative comparison of computational time between FLM-SD.NS and FLM-NS for all NCDW cases, as well as between FLM-SDEu and FLM-Eu for the 94D4, 94D5, and 94D6 cases; FLM-SDEu computational time for the 90D4, 90D5, and 90D6 cases, as well as the 92D33 and the 92D36 case; based on [103], Fig. 14.

case frequency leads to an increase of FLM-SD.NS performance over FLM-NS by one and a half times. In this regard, the 90D29 case has been excluded from the consideration, as it had not been equally computed on the higher-clocking processor. An accordant analysis for the 90D4, 90D5, and 90D6 cases is not permissible, despite having been computed on the same processor. Conducted in the early investigation stages, the setting of the implicit damping and the entropy correction for both the 90D4 and the 90D6 case were varied from the 90D5 case baseline in order to realize the best possible rate of convergence. Thus, comparability across the spectrum for $\check{t}_{CPU}^{SD.NS}$, as well as $\check{t}_{CPU}^{NS}$ becomes skewed. In contrast, the later-performed computations of the 90D28 and the 90D30 case agree in their setting of the implicit damping and the entropy correction, with the 94D4, 94D5, and 94D6 cases, doing so likewise.

The lowest $\check{t}_{CPU}^{SD.NS}$ are exhibited by the flap-oscillation cases (the 92D33 and 92D36 case). These, however, stand somewhat apart from the pitching-oscillation cases, as a load tolerance criterion had been applied to terminate the computation instead of the precedingly employed $\hat{\rho}$ residual tolerance. It was deemed to be more material to the computation of a highly localized near-field disturbance, such as caused by the flap deflection. Shown for the 92D33 case, the employed setting terminates the computation at a $\hat{\rho}$ residual that is nearly an order of magnitude higher than the $\hat{\rho}$ residual tolerance specified for the pitching-oscillation cases (Figure 5.31). This circumstance reduces $\check{t}_{CPU}^{SD.NS}$ for the 92D33 and the 92D36 case substantially. As a matter of course, it also affects the FLM-NS computations. On average, $\check{t}_{CPU}^{NS}$ of the 92D33 and the 92D36 case is the second lowest of all case-group-averaged $\check{t}_{CPU}^{NS}$. In this regard, the considered spectrum also factors in. The 92D33 case frequency is already equal to the maximum frequency of the pitching-oscillation cases, with the 92D36 case frequency being approximately 40% higher. Established previously, the duration of a dynamically fully nonlinear computation, however, typically reduces with increasing frequency. The variation itself has only limited impact on both $\check{t}_{CPU}^{SD.NS}$ and $\check{t}_{CPU}^{NS}$ of the 92D33 and the 92D36 case, rendering a mere 8% decrease in ζ_{CPU}^{v} from the baseline- to the higher-frequency case. All in all, "[w]ith 1.7 GB of RAM, FLM-SD.NS allocates four times more working memory than FLM-NS, as both complex amplitude and [linearized] time-invariant[-]mean entities need to be stored. It is the [trade-off] made toward superior computational efficiency."[103]

For the 90D4, 90D5, and 90D6 cases, $\check{t}_{CPU}^{SDEu}$ is on average 84% lower than $\check{t}_{CPU}^{SD.NS}$, while decreasing by 36% from the lower- to the higher-frequency case. It can be further determined that

> $\check{t}_{\mathrm{CPU}}^{\mathrm{SDEu}}$ [for the 94D4, 94D5, and 94D6 cases] is on average [82%] lower than $\check{t}_{\mathrm{CPU}}^{\mathrm{SD.NS}}$,[however,] increasing by 9% from the [lower- to the higher-frequency case]. In contrast, $\check{t}_{\mathrm{CPU}}^{\mathrm{Eu}}$ (an invariant 66% lower than $\check{t}_{\mathrm{CPU}}^{\mathrm{NS}}$) decreases by 20%, a range approximately equal to the one observed for $\check{t}_{\mathrm{CPU}}^{\mathrm{NS}}$. Apparently, the opposing [trend] witnessed between

> $\check{t}^{\mathrm{SD.NS}}_{\mathrm{CPU}}$ and $\check{t}^{\mathrm{NS}}_{\mathrm{CPU}}$ over the spectrum already exists between $\check{t}^{\mathrm{SDEu}}_{\mathrm{CPU}}$ and $\check{t}^{\mathrm{Eu}}_{\mathrm{CPU}}$; [i.e.], for the computations with the reduced flow model. From [the] 94D4 to [the] 94D6 [case], [ζ^{i}_{CPU}] diminishes by 26%, far less than observed [for ζ^{v}_{CPU}]. On average, [ζ^{v}_{CPU}] is half [ζ^{i}_{CPU}], indicating a relative loss of computational efficiency [gain] toward the more complete flow model's implementation. [103]

For the 92D33 case, $\check{t}^{SDEu}_{CPU}$ is 65% lower than $\check{t}^{SD.NS}_{CPU}$. Surprisingly, $\check{t}^{SDEu}_{CPU}$ lies within the range established for the 90D4, 90D5, and 90D6 cases, despite contrarily employing the load tolerance criterion. At higher-frequency (the 92D36 case), on the other hand, $\check{t}^{SDEu}_{CPU}$ has more than doubled, as the specified load tolerance criterion was not met before the $\hat{\rho}$ residual had reached 8×10^{-4}. In turn, $\check{t}^{SDEu}_{CPU}$ is now merely 27% lower than $\check{t}^{SD.NS}_{CPU}$. All in all, "[w]ith 1.3 GB RAM, FLM-SDEu allocates four times more working memory than FLM-Eu. As FLM-SD.NS scales equally to FLM-NS, no relative penalty can be said to have occurred in its resource need."[103]

Chapter 6

Conclusions

Aircraft flutter analysis within a production environment demands a numerical method that can accurately and yet efficiently predict the unsteady aerodynamic loading of the transonic speed range for a simple harmonic excitation. Both shocks and viscous phenomena need to be treatable. A method based on the frequency-domain solution of the small disturbance Navier-Stokes equations was expected to satisfy this demand. As established by Pechloff and Laschka,

> [f]or problems of dynamic stability, the elastic body's [simple harmonic oscillation] can be regarded as being limited to minor [deformations/]deflections about a reference position. Consequently, the organized [fluctuation] inherent to the flowfield's instantaneous response can be presumed to be a predominantly dynamically linear perturbation about a [linearized] time-invariant[-]mean [(reference)] state. This would entail that the higher-order harmonics present within the response become negligible to the point where a generally phase-shifted first harmonic prevails. Under the preceding assumption, a system of statistically treated linear [PDEs] exclusively governing the complex amplitude of the [periodic perturbation] can be extracted from the instantaneous Navier-Stokes equations. [... T]he necessary computational effort becomes comparable to the one involved with the steady-state solution of the RANS equations. [103]

In this regard, the small disturbance Navier-Stokes method FLM-SD.NS had been developed at TUM [98, 100, 103, 54]. The dissertation at hand had presented a particular incarnation, and substantiated the validity of the approach for the low-aspect-ratio wing, which typifies the high-speed/high-maneuverability aircraft configuration. The flow topological versatility and the computational efficiency gain with respect to the URANS method FLM-NS were also substantiated. The superiority of the viscous treatment over the inviscid treatment was equally demonstrated. In the following, the dissertation is summarized and an outlook of continuative work provided.

6.1 Summary

Realizing FLM-SD.NS per se, a very fundamental path had been taken by the author. It commenced with the triple decomposition of the instantaneous Navier-Stokes equations in their three-dimensional curvilinear coordinate formulation. During this process, higher-order perturbation terms were neglected and turbulent correlation terms were resolved by introducing linearized periodic-perturbation and time-invariant-mean instances of both the dynamic eddy viscosity and the specific turbulence kinetic energy. The particular closure was achieved with a small disturbance formulation of the S/A one-equation turbulence model [100]. Ultimately, the closed time-domain small disturbance Navier-Stokes equations were transitioned to the frequency domain under specification of a simple harmonic time law [70, 100, 54]. This governing equation system of the amplitude flowfield was then discretized by way of a cell-centered structured finite volume upwind scheme of generally second-order accuracy, as devised by Kreiselmaier [70] for the small disturbance Euler equations. The small disturbance formulation of Chakravarthy's viscous flux evaluation scheme as proposed by Iatrou [54] was drawn on, and transfered to the evaluation of the amplitude turbulence source term vectors. Iatrou's [54] small disturbance formulation of the no-slip-/adiabatic-wall boundary condition was considered as well. Innovatively, an implicit pseudotime integration of the governing equation system was devised by means of a multigrid-embedded LU-SSOR scheme. The implementation of the particular instances was conducted by the author on basis of the FLM-SDEu code [70, 71], the FLM-NS code [32, 31], and the FLOWer code [72, 74]. Per default, the amplitude S/A conservative working variable is fully accounted for, and thus the amplitude dynamic eddy viscosity as well. Alternatively, the amplitude S/A conservative working variable can be locally limited for enhanced solution stability, or disregarded entirely, rendering a FEVA.

Substantiating the validity of the small disturbance Navier-Stokes approach, "[FLM-SD.NS] results for NCDW [simple]harmonic pitching [and flap] oscillations [at various frequencies] were presented and compared to those of FLM-NS, FLM-SDEu/FLM-Eu, as well as experimental data."[103] In this regard, "[the induced flowfields] are characterized by shocks of varying strengths and [degree] of motion, as well as [LEV] formation."[103] It was ascertained that "[o]verall, reductions in computational time, up to an order of magnitude, [between FLM-SD.NS and] FLM-NS [were realized]."[103] The trade-off, however, lies in quadrupled memory requirements [103]. Furthermore,

> [both the weak shock and strong shock pitching-oscillation cases, as well as the medium-strength shock flap-oscillation cases,] demonstrated [FLM-SD.NS] accuracy and efficiency in predicting the unsteady local and global loading. [With respect to the pitching-oscillation cases, s]pecial attention had been given to the obtained $\mathrm{Im}c_M^1$, as it is indicative of the corresponding free oscillation's amplified or damped state. [Especially], the strong

> shock case[s] illustrate[d] the benefit of the viscous consideration, FLM-SD.NS/FLM-NS predicting dynamic stability at frequencies where FLM-SDEu/FLM-Eu d[id] not. [For the flap oscillation cases, the viscous consideration complementarily revealed a control surface of reduced efficiency.] The medium-strength shock/LEV case[s], on the other hand, disclose[d] the limitations of the small disturbance approach. [For the baseline frequency,] Fourier analysis of the FLM-NS-computed upper-surface c_p reveale[d] localized higher-order harmonics that are no longer negligible. They result from the LEV itself, as well the LEV's interaction with the shock. With influence exerted on the time-dependent c_M evolution, the Fourier-analysis-obtained $\mathrm{Im}c_M^1$ and the FLM-SD.NS-computed one exhibit the most pronounced deviation among the investigated cases. [103]

6.2 Outlook

Featuring small disturbance appropriations of discretization and solution techniques commonly inherent to current RANS methods, FLM-SD.NS can be considered numerically mature. Nevertheless, a number of avenues for improvement exist. One such avenue is the shared-memory parallelization of the code. This would be realizable in two separate ways. The first pertains to geometries that require a large number of blocks for adequate numerical representation, as typical of full aircraft configurations. In such a case, the entirety of the considered computational domain would best be manually or algorithmically repartitioned into equally sized blocks, with each then distributed to an individual processor thread of a computational node. For unequally sized blocks, thread load imbalance could still be alleviated through dynamic or guided worksharing directives. The feasibility and efficiency of such a shared-memory parallelization had been documented by the author [96] in 2012. The LANNW CT5 case [154] in full span, utilizing a four-block equally sized partitioning of the computational domain was considered. In comparison to the correspondingly parallelized FLM-NS, the parallelization efficiency was demonstrated to be consistently higher for FLM-SD.NS. In contrast, the second manner of shared-memory parallelization would be particular to FLM-SD.NS itself. The real and imaginary part of all complex quantities are implemented separately for better machine code efficiency [70]. Furthermore, the algorithmic interaction between the two instances is limited to the evaluation of the $\hat{\mathbf{q}}$-homogenous source term vector and the LU-SSOR scheme. Hence, it would be feasible to assign the computation of all real parts and all imaginary parts, respectively, to an individual thread. This nested worksharing would be inherently load balanced, since it is particular to each considered block.

Another avenue for improvement concerns the structured grids utilized in the considered physical domain's spatial discretization. The employed nonuniform curvilinear instances allow for a straightforward and accurate imposition of the near-field boundary

condition on curved surfaces and provide good resolution of thin boundary layers. Given a full aircraft configuration, however, the generation of these grids can become overly time-consuming, difficult, and too dependent on user experience. As proposed by Kirshman and Liu [68, 69] for an Euler method, a spatial discretization based on a single uniform Cartesian grid, which becomes refined in vicinity of curved surfaces through a series of embedded instances, can be an alternative that allows for an automated generation. This approach would employ a gridless imposition of the near-field boundary condition through weighted averaging of field quantities within a local cloud of surface-proximate vertices (or centroids). The weighting would be rendered by shape functions. In a forced-motion case, these would also account for the surface's time-dependent deformation/deflection [68, 69]. The applicability within a small disturbance Euler method had already been shown by Zhang et al. [149] in 2012; i.e., with the ZEUS method, where it is known as the transpiration near-field boundary condition. Implementing the approach for the viscous flow consideration, however, some issues may still have to be innovatively tackled; e.g., the sufficient resolution of thin boundary layers under avoidance of excessive grid refinement [69] and the compatibility with the employed turbulence model.

Concerning the turbulence model per se, Pechloff and Laschka [102] had additionally investigated a small disturbance appropriation of the Wilcox k-omega two-equation turbulence model in 2010. It was argued that "[f]or cases where the degree of unsteadiness, flow separation, and involved length scales may not be a priori assessable, employing a model that better represents the physics of turbulence [than the S/A one-equation turbulence model] would be favorable."[102] In this regard, the LANNW CT2, CT5, and CT9 cases [154] were drawn on [102]. Comparing the results of the realized incarnation FLM-SD.NS k-omega, with the instances obtained from its dynamically fully nonlinear counterpart FLM-NS k-omega, as well as FLM-SD.NS/FLM-NS S/A and experimental data, Pechloff and Laschka concluded that

> [f]or the attached-flow cases, FLM-SD.NS [k-omega] yields equally accurate predictions as FLM-SD.NS S/A. Reductions in computation time, up to half an order of magnitude, in relation to FLM-NS [k-omega] are ascertained. Naturally, [the bare computational effort] of FLM-SD.NS [k-omega is considerably] higher than [that] of FLM-SD.NS S/A. For the detached-flow case, the primary benefit of the Wilcox [k-omega two-equation] turbulence model lies in an FLM-NS-supplied [linearized] time-invariant[-]mean flowfield that better represents the actual physical one. Consequently, in production cases where the flowfield's development is not a priori known, FLM-SD.NS [k-omega] can offer an advantage over FLM-SD.NS S/A. Prediction accuracy, however, will be increasingly compromised[,] the more extensive any [underlyingly rendered] flow detachment becomes. [102]

In this context, it was shown that the FLM-SD.NS S/A implicit pseudotime-integration scheme can be stabilized through the local limitation of the amplitude S/A

conservative working variable in cases where the linearized time-invariant-mean flowfield exhibits confined regions of separation [103]. This remedy had also been applied to both the amplitude specific turbulence kinetic energy and the amplitude specific turbulence dissipation rate within FLM-SD.NS k-omega [102]. For either incarnation, however, there are indications that the measure degrades the solution or even is ineffective in cases where the flow separation becomes more extensive. Thus, the application of the GMRES approach or the RPM to the existing pseudotime-integration scheme as demonstrated by Campobasso and Giles [19, 20] should still be considered. Continuatively, the small disturbance Navier-Stokes equations can be formulated in the frequency domain without the amplitude state vector's pseudotime derivative. A fitting spatial discretization would then still yield a system of linear equations governing the amplitude conservative state vector, yet solvable by applying the GMRES approach directly. This had been initially employed by Petrie-Repar [104] for turbomachinery applications in 2002, with Chassaing et al. [25] providing a more fundamental investigation in 2006. Furthermore, in 2012, McCracken et al. [85] had shown that by appropriately preconditioning such a system of linear equations a small disturbance Navier-Stokes method can be accelerated beyond another order of magnitude with respect to required computational time (published by McCracken et al. [84] in 2013). The TAU-LFD method developed by Widhalm et al. [135] had served as the testbed, with McCracken et al. [85], however, utilizing a generalized conjugate residual approach instead of the inherent GMRES instance. Drawbacks were shown to be a loss in parallelization efficiency and excessive memory requirements [85]. In this regard, Thormann and Widhalm [128] had demonstrated a computational efficiency gain of two orders of magnitude between TAU-LFD and TAU-URANS for the LANNW CT5 case [154], when employing the GMRES approach with the suggested preconditioning (2013). The trade-off consisted of approximately twenty times higher memory requirements [128]. These characteristics were also witnessed in the TAU-LFD treatment of DLR's generic transport aircraft FERMAT [127]. As a remedy, Xu et al. [140] proposed a generalized conjugate residual approach with deflated restarting in 2015: Memory requirements were up to 90% less than exhibited by the TAU-LFD baseline GMRES approach for select two- and three-dimensional test cases, while secondarily reducing the computational time by up to 66% [140]; also published in 2016 [141].

Supplementing the NCDW investigations, more application-oriented cases were considered by the author with the FTDW in 2012 [97]. Computing pitching oscillations for a shockless case, an LEV case, and a medium-strength shock case, an intermethod comparison between FLM-SD.NS/FLM-NS and FLM-SD.Eu/FLM-Eu was again made. As stated by the author,

> [the] shockless case, serving as baseline, and [the medium-strength shock] case again demonstrated the small disturbance Navier-Stokes approach's accuracy in predicting the

> unsteady local and global loading. Similarly, the LEV case disclosed the known limitations [...]. However, deviations caused by flow-inherent higher-harmonics are observed to be far less severe than exhibited for the [medium-strength shock]/LEV case of the NCDW. [...] The comparison between the viscous and inviscid global load coefficients [...] revealed that the relative deviation exhibited by the FLM-SD.NS- and FLM-NS-obtained instances is in part already inherent to the FLM-SDEu- and FLM-Eu-predictions.
>
> With exception of the FTDW's [medium-strength shock] case, FLM-SD.NS [computational] efficiency gain over FLM-NS is substantial, however, significantly less than exhibited for the NCDW cases. This circumstance is attributable to the much shorter computational time required by FLM-NS to render the FTDW cases. [102]

Additionally, FTDW flap-oscillation cases were investigated by Iatrou et al. [55] in 2005.

Taking into account the high-aspect-ratio-wing cases as well as the nacelle-pylon-rectangular-wing case investigated by Iatrou [54] in 2009, the validity of the small disturbance Navier-Stokes approach has been substantiated for both the high-speed/high-maneuverability and transport aircraft configuration. Hence, FLM-SD.NS is application ready and can be incorporated into a CA tool. All in all, the boundary of CFD utilization for aircraft flutter analysis within a production environment has been extended considerably by this means.

References

[1] Acharya, M., "Measurements and Predictions of a Fully Developed Turbulent Channel Flow with Imposed Controlled Oscillations," Stanford University, Dissertation (Ph.D.), Stanford, CA, May 1975.

[2] Albano, E., and Rodden, W. P., "A Doublet-Lattice Method for Calculating Lift Distributions on Oscillating Surfaces in Subsonic Flows," *AIAA Journal*, Vol. 7, No. 2, 1969, pp. 279–285.
doi:10.2514/3.5086

[3] Allen, A., Iatrou, M., and Breitsamter, C., "Instationäre Luftkräfte bei Klappenschwingungen an einem Deltaflügel mit Hilfe eines Navier-Stokes Verfahrens bei kleinen Störungen," Institute for Aerodynamics, Technische Universität München, Contract Report TUM-AER-2005/8, unpublished, Garching, Germany, Dec. 2005.

[4] Allen, A., Iatrou, M., Pechloff, A., and Laschka, B., "Computation of Delta Wing Flap Oscillations with a Reynolds-averaged Navier-Stokes Solver," *New Results in Numerical and Experimental Fluid Mechanics V: Contributions to the 14th STAB-DGLR-Symposium, Bremen, Germany 2004*, edited by H.-J. Rath, C. Holze, H.-J. Heinemann, R. Henke, and H. Hönlinger, Notes on Numerical Fluid Mechanics and Multidisciplinary Design, Vol. 92, Springer-Verlag, Berlin, Germany, 2006, pp. 85–93.
doi:10.1007/978-3-540-33287-9_11

[5] Allen, A., Weishäupl, C., and Laschka, B., "Flap Efficiency of a Delta Wing with an External Store Using an Euler Code for Small Disturbances," *New Results in Numerical and Experimental Fluid Mechanics IV: Contributions to the 13th STAB-DGLR-Symposium, Munich, Germany 2002*, edited by C. Breitsamter, B. Laschka, H.-J. Heinemann, and R. Hilbig, Notes on Numerical Fluid Mechanics and Multidisciplinary Design, Vol. 87, Springer-Verlag, Berlin, Germany, 2004, pp. 116–123.
doi:10.1007/978-3-540-39604-8_15

[6] Anderson, Jr., J. D., *Computational Fluid Dynamics: The Basics with Applications*, McGraw-Hill Series in Mechanical Engineering, international ed., McGraw-Hill, New York, NY, 1995.

[7] Anderson, W. K., and Bonhaus, D. L., "An Implicit Upwind Algorithm for Computing Turbulent Flows on Unstructured Grids," *Computers & Fluids*, Vol. 23, No. 1, 1994, pp. 1–21.
doi:10.1016/0045-7930(94)90023-X

[8] Baldwin, B. S., and Lomax, H., "Thin Layer Approximation and Algebraic Model for Separated Turbulent Flows," AIAA Paper 78-257, Jan. 1978.

[9] Batina, J. T., Seidel, D. A., Bland, S. R., and Bennett, R. M., "Unsteady Transonic Flow Calculations for Realistic Aircraft Configurations," NASA TM-1987-89120, 1987.

[10] Bendiksen, O. O., "Review of Unsteady Transonic Aerodynamics: Theory and Applications," *Progress in Aerospace Sciences*, Vol. 47, No. 2, 2011, pp. 135–167.
doi:10.1016/j.paerosci.2010.07.001

[11] Bennett, R. M., Batina, J. M., and Cunningham, H. J., "Wing-Flutter Calculations with the CAP-TSD Unsteady Transonic Small-Disturbance Program," *Journal of Aircraft*, Vol. 26, No. 9, 1989, pp. 876–882.
doi:10.2514/3.45854

[12] Bennett, R. M., and Walker, C. E., "Computational Test Cases for a Clipped Delta Wing with Pitching and Trailing Edge Control Surface Oscillations," NASA TM-1999-209104, 1999.

[13] Bisplinghoff, R., Ashley, H., and Halfman, R. L., *Aeroelasticity*, Dover Publications, New York, NY, 1996.

[14] Blazek, J., "Investigations of the Implicit LU-SSOR Scheme," Institute for Design Aerodynamics, German Aerospace Center, Internal Report DLR-FB 93-51, Braunschweig, Germany, July 1993.

[15] Blazek, J., "A Multigrid LU-SSOR Scheme for the Solution of Hypersonic Flow Problems," AIAA Paper 94-0062, Jan. 1994.

[16] Blazek, J., *Computational Fluid Dynamics: Principles and Applications*, Elsevier Science Ltd., Oxford, UK, 2001.

[17] Brandt, A., "Guide to Multigrid Development," *Multigrid Methods*, edited by E. Hackbush and U. Trottenberg, Lecture Notes in Mathematics, No. 960, Springer-Verlag, Berlin, Germany, 1982, pp. 220–312.

[18] Cambier, L., and Gazaix, M., "elsA: An Efficient Object-oriented Solution to CFD Complexity," AIAA Paper 2002-0108, Jan. 2002.

[19] Campobasso, M. S., and Giles, M. B., "Effects of Flow Instabilities on the Linear Analysis of Turbomachinery Aeroelasticity," *Journal of Propulsion and Power*, Vol. 19, No. 2, 2003, pp. 250–259.
doi:10.2514/2.6106

[20] Campobasso, M. S., and Giles, M. B., "Stabilization of Linear Flow Solver for Turbomachinery Aeroelasticity using Recursive Projection Method," *AIAA Journal*, Vol. 42, No. 9, 2004, pp. 1765–1774.
doi:10.2514/1.1225

[21] Chakravarthy, S. R., "High Resolution Upwind Formulations for the Navier-Stokes Equations," von Karman Institute, Lecture Series on Computational Fluid Dynamics, VKI 1988-05, Brussels, Belgium, March 1988, pp. 1–105.

[22] Chalot, F., and Hughes, T. J. R., "A Consistent Equilibrium Chemistry Algorithm for Hypersonic Flows," *Computer Methods in Applied Mechanics and Engineering*, Vol. 112, No. 1–4, 1994, pp. 25–40.
doi:10.1016/0045-7825(94)90017-5

[23] Chalot, F., Mallet, M., and Ravachol, A., "A Comprehensive Finite Element Navier-Stokes Solver for Low- and High-speed Aircraft Design," AIAA Paper 94-0814, January 1994.

[24] Chassaing, J. C., and Gerolymos, G. A., "Time-Linearized Time-Harmonic 3D Navier-Stokes Shock-Capturing Schemes," *International Journal for Numerical Methods in Fluids*, Vol. 56, No. 3, 2008, pp. 279–303.
doi:10.1002/fld.1523

[25] Chassaing, J. C., Gerolymos, G. A., and Jérémiasz, J. G., "GMRES Solution of Compressible Linearized Navier-Stokes without Pseudo-Time-Marching," AIAA Paper 2006-688, Jan. 2006.

[26] Chen, H. C., and Patel, V. C., "Near-wall Turbulence Models for Complex Flows Including Separation," *AIAA Journal*, Vol. 26, No. 6, 1988, pp. 641–648.
doi:10.2514/3.9948

[27] Chen, P. C., Zhang, Z., Sengupta, A., and Liu, D. D, "Overset Euler/Boundary-Layer Solver with Panel-Based Aerodynamic Modeling for Aeroelastic Applications," *Journal of Aircraft*, Vol. 46, No. 6, 2009, pp. 2054–2068.
doi:10.2514/1.43434

[28] Clark, W. S., "Investigation of Unsteady Viscous Flows in Tubomachinery Using a Linearized Navier-Stokes Analysis," Duke University, Dissertation (Ph.D.), Durham, NC, April 1998.

[29] Clark, W. S., and Hall, K. C., "A Time-linearized Navier-Stokes Analysis of Stall Flutter," International Gas Turbine and Aeroengine Congress & Exhibition, ASME Paper 99-GT-383, Indianapolis, IA, June 1999.

[30] Clark, W. S., and Hall, K. C., "A Time-linearized Navier-Stokes Analysis of Stall Flutter," *Journal of Turbomachinery*, Vol. 122, No. 3, 2000, pp. 467–476.
doi:10.1115/1.1303073

[31] Cvrlje, T., "Instationäre Aerodynamik des Seperationsvorgangs zwischen Träger und Orbiter," Institute for Fluid Mechanics, Technische Universität München, Dissertation (Dr.-Ing.), Garching, Germany, Dec. 2001.

[32] Cvrlje, T., Breitsamter, C., Weishäupl, C., and Laschka, B., "Euler and Navier-Stokes Simulation of Two Stage Hypersonic Vehicle Longitudinal Motions," *Journal of Spacecraft and Rockets*, Vol. 37, No. 2, 2000, pp. 242–251.
doi:10.2514/2.3552

[33] Daumas, L., Chalot, N., Forestier, N., and Johan, Z., "Industrial Use of Linearized CFD Tools for Aeroelastic Problems," International Forum on Aeroelasticity and Structural Dynamics, IFASD Paper 2009-054, Seattle, WA, June 2009.

[34] Davis, S. S., "NACA 64A010 (NASA Ames Model) Oscillatory Pitching," Compendium of Unsteady Aerodynamic Measurements, AGARD-R-702, 1982, pp. 2-1–2-22.

[35] Decker, K., Meyer, E., and Breitsamter, C., "Glätten von strukturierten Multiblockgittern über Blockgrenzen," Institute for Fluid Mechanics, Technische Universität München, Internal Report TUM-FLM-1999/2, unpublished, Garching, Germany, n/a 1999.

[36] Dowell, E., Edwards, J., and Strganac, T., "Nonlinear Aeroelasticity," *Journal of Aircraft*, Vol. 40, No. 5, 2003, pp. 857–874.
doi:10.2514/2.6876

[37] Dufour, G., Sicot, F., Puigt, G., Liauzun, C., and Dugeai, A., "Contrasting the Harmonic Balance and Linearized Methods for Oscillating-Flap Simulations," *AIAA Journal*, Vol. 48, No. 4, 2010, pp. 788–797.
doi:10.2514/1.43401

[38] Dwight, R., and Brezillion, J., "Effect of Approximations of the Discrete Adjoint on Gradient-Based Optimzation," *AIAA Journal*, Vol. 44, No. 12, 2006, pp. 3022–3031.
doi:10.2514/1.21744

[39] Dwight, R., and Brezillion, J., "Effect of Various Approximations of the Discrete Adjoint on Gradient-Based Optimzation," AIAA Paper 2006-0690, Jan. 2006.

[40] Edwards, J. W., "Transonic Shock Oscillations and Wing Flutter Calculated with an Interactive Boundary Layer Coupling Method," NASA TM-1996-110284, 1996.

[41] Ekici, K., Voytovych, D. M., and Hall, K. C., "Time-linearized Navier-Stokes Analysis of Flutter in Multistage Turbomachines," AIAA Paper 2005-836, Jan. 2005.

[42] Gerhold, T., Galle, M., Friedrich, O., and Evans, J., "Calculation of Complex Three-Dimensional Configurations Employing the DLR TAU-code," AIAA Paper 1997-167, January 1997.

[43] Godunov, S., "Finite Difference Method for Numerical Computation of Discontinuos Solutions of the Equations of Fluid Dynamics," *Matematicheski Sbornik*, Vol. 47, No. 3, 1979, pp. 271.

[44] Hall, K. C., and Crawley, E. F., "Calculation of Unsteady Flows in Turbomachinery Using the Linearized Euler Equations," *AIAA Journal*, Vol. 27, No. 6, 1989, pp. 777–787.
doi:10.2514/3.10178

[45] Harten, A., "On a Class of High Resolution Total-Variation-Stable Finite Difference Schemes," *SIAM Journal on Numerical Analysis*, Vol. 21, No. 1, 1984, pp. 1–23.
doi:10.1137/0721001

[46] Hassig, H. J., "An Approximate True Damping Solution of the Flutter Equation by Determinant Iteration," *Journal of Aircraft*, Vol. 8, No. 11, 1971, pp. 885–889.
doi:10.2514/3.44311

[47] Hirsch, C., *Numerical Computation of Internal and External Flows*, Vol. 1, John Wiley & Sons Ltd., Chichester, UK, 1981.

[48] Hirsch, C., *Numerical Computation of Internal and External Flows*, Vol. 2, John Wiley & Sons Ltd., Chichester, UK, 1981.

[49] Hoffmann, K. A., and Chiang, S. T., *Computational Fluid Dynamics for Engineers*, Vol. 1, Engineering Education System, Wichita, KS, 1995.

[50] Hoffmann, K. A., and Chiang, S. T., *Computational Fluid Dynamics*, Vol. 2, 4^{th} ed., Engineering Education System, Wichita, KS, 2000.

[51] Hoffmann, K. A., and Chiang, S. T., *Computational Fluid Dynamics*, Vol. 3, 4^{th} ed., Engineering Education System, Wichita, KS, 2000.

[52] Holmes, D. G., Mitchell, B. E., and Lorence, C. B., "Three Dimensional Linearized Navier-Stokes Calculations for Flutter and Forced Response," *8th International Symposium on Unsteady Aerodynamics and Aeroelasticity of Turbomachines held in Stockholm, Sweden, 14th-18th Sep. 1997*, edited by T. H. Franson, Kluwer Academic Publishers, Dordrecht, Netherlands, 1998, pp. 211–224.

[53] Hübner, A. R., Bergmann, A., and Löser, T., "Experimental and Numerical Investigations of Unsteady Pressure Distributions and Aerodynamic Forces on Moving Transport Aircraft Configurations," AIAA Paper 2009-0091, Jan. 2009.

[54] Iatrou, M., "Ein Navier-Stokes-Verfahren kleiner Störungen für instationäre Vorgänge – Anwendung auf Transportflugzeuge," Institute of Aerodynamics, Technische Universität München, Dissertation (Dr.-Ing.), Garching, Germany, Oct. 2009.

[55] Iatrou, M., Allen, A., Pechloff, A., Breitsamter, C., and Laschka, B., "Small Disturbance Euler/Navier-Stokes Computations for Delta Wing Flap Oscillations," *Flow-Induced Unsteady Loads and the Impact on Military Applications*, RTO-MP-AVT-123, Budapest, Hungary, April 2005, pp. 16–1–16–12.

[56] Iatrou, M., Breitsamter, C., and Laschka, B., "Entwicklung eines Navier-Stokes-Verfahrens bei kleinen Störungen zur Behandlung dynamischer aeroelastischer Probleme komplexer Konfigurationen," Institute for Aerodynamics, Technische Universität München, Deutsche Forschungsgemeinschaft Report TUM-AER-2006/20, unpublished, Garching, Germany, n/a 2006.

[57] Iatrou, M., Breitsamter, C., and Laschka, B., "Small Disturbance Navier-Stokes Equations: Application on Transonic Two-dimensional Flows around Airfoils," *New Results in Numerical and Experimental Fluid Mechanics V: Contributions to the 14th STAB-DGLR-Symposium, Bremen, Germany 2004*, edited by H.-J. Rath, C. Holze, H.-J. Heinemann, R. Henke, and H. Hönlinger, Notes on Numerical Fluid

Mechanics and Multidisciplinary Design, Vol. 92, Springer-Verlag, Berlin, Germany, 2006, pp. 471–478.
doi:10.1007/978-3-540-33287-9_58

[58] Iatrou, M., Weishäupl, C., and Laschka, B., "Entwicklung eines instationären Navier-Stokes-Verfahrens bei kleinen Störungen für aeroelastische Problemstellungen," Institute for Fluid Mechanics, Technische Universität München, Deutsche Forschungsgemeinschaft Report TUM-FLM-2002/9, unpublished, Garching, Germany, April 2002.

[59] Iatrou, M., Weishäupl, C., and Laschka, B., "Entwicklung eines instationären Navier-Stokes-Verfahrens bei kleinen Störungen für aeroelastische Problemstellungen," Aerodynamics Division, Institute for Fluid Mechanics, Technische Universität München, Deutsche Forschungsgemeinschaft Report TUM-FLM-2003/27, unpublished, Garching, Germany, Oct. 2003.

[60] ICEM CFD Engineering, *ICEM CFD Hexa Manual*, ICEM CFD Engineering, Berkley, CA, 2000.

[61] Jameson, A., Schmidt, W., and Turkel, E., "Numerical Solutions of the Euler Equations by Finite Volume Methods Using Runge-Kutta Time-Stepping Schemes," AIAA Paper 81-1259, June 1981.

[62] Jameson, A., and Turkel, E., "Implicit Schemes and LU-Decompositions," *Mathematics of Computation*, Vol. 37, No. 156, 1981, pp. 385–397.
doi:10.1090/S0025-5718-1981-0628702-9

[63] Jameson, A., and Yoon, S., "Lower-Upper Implicit Schemes with Multiple Grids for the Euler Equations," *AIAA Journal*, Vol. 25, No. 7, 1987, pp. 929–935.
doi:10.2514/3.9724

[64] Kalman, T. P., Rodden, W. P., and Giesing, J. P., "Application of the Doublet-Lattice Method to Nonplanar Configurations in Subsonic Flow," *Journal of Aircraft*, Vol. 8, No. 6, 1971, pp. 406–413.
doi:10.2514/2.59117

[65] Kennett, D. J., Timme, S., Angulo, J., and Badcock, K. J., "An Implicit Meshless Method for Application in Computational Fluid Dynamics," *International Journal for Numerical Methods in Fluids*, Vol. 71, No. 8, 2013, pp. 1007–1028.
doi:10.1002/fld.3698

[66] Kersken, H.-P., Frey, C., Voigt, C., and Ashcroft, G., "Time-linearized and Time-accurate 3D RANS Methods for Aeroelastic Analysis in Turbomachinery," *ASME*

Turbo Expo 2010: Power for Land, Sea, and Air, GT2010, Glasgow, UK, 2010, pp. 865–874.
doi:10.1115/GT2010-22940

[67] Kersken, H.-P., Frey, C., Voigt, C., and Ashcroft, G., "Time-linearized and Time-accurate 3D RANS Methods for Aeroelastic Analysis in Turbomachinery," *Journal of Turbomachinery*, Vol. 134, No. 5, 2012, pp. 0001–0008.
doi:10.1115/1.4004749

[68] Kirshman, D. J., and Liu, F., "A Gridless Boundary Condition Method for the Solution of the Euler Equations on Embedded Cartesian Meshes with Multigrid," *Journal of Computational Physics*, Vol. 201, No. 1, 2004, pp. 119–147.
doi:10.1016/j.jcp.2004.05.006

[69] Kirshman, D. J., and Liu, F., "Flutter Prediciton by an Euler Method on Non-moving Cartesian Grids with Gridless Boundary Conditions," *Computers & Fluids*, Vol. 35, No. 6, 2006, pp. 571–586.
doi:10.1016/j.compfluid.2005.04.004

[70] Kreiselmaier, E., "Berechnung instationärer Tragflügelumströmungen auf der Basis der zeitlinearisierten Eulergleichungen," Institute for Fluid Mechanics, Technische Universität München, Dissertation (Dr.-Ing.), Garching, Germany, July 1998.

[71] Kreiselmaier, E., and Laschka, B., "Small Disturbance Euler Equations: Efficient and Accurate Tool for Unsteady Load Predictions," *Journal of Aircraft*, Vol. 37, No. 5, 2000, pp. 770–778.
doi:10.2514/2.2699

[72] Kroll N., *FLOWer Version 116 Installation and User Handbook*, Institute for Design Aerodynamics, German Aerospace Center, Braunschweig, Germany, 2001.

[73] Kroll, N., and Jain, R. K., "Solution of Two-Dimensional Euler Equations- Experience with a Finite Volume Code," Institute for Design Aerodynamics, German Aerospace Center, Internal Report DLR-FB 87-41, Braunschweig, Germany, Oct. 1987.

[74] Kroll, N., Rossow, C. C., Schwamborn, D., Becker, K., and Heller, G., "MEGAFLOW - A Numerical Flow Simulation Tool for Transport Aircraft Design," 23rd Congress of the International Council of the Aeronautical Sciences, ICAS Paper 2002-1.10.5, Toronto, Canada, Sep. 2002.

[75] Laschka, B., "Unsteady Flows - Fundamentals and Applications," *Unsteady Aerodynamics - Fundamentals and Applications to Aircraft Dynamics*, AGARD-CP-386, Göttingen, Federal Republic of Germany, 1985, pp. 1–1–1–21.

[76] Laschka, B., "Zur Theorie der harmonisch schwingenden tragenden Fläche bei Unterschallanströmung," *Zeitschrift für Flugwissenschaften*, Vol. 11, No. 7, 1963, pp. 265–292.

[77] Lee-Rausch, E. M., and Batina, J. T., "Wing Flutter Computations Using an Aerodynamic Model Based on the Navier-Stokes Equations," *Journal of Aircraft*, Vol. 33, No. 6, 1996, pp. 1139–1147.
doi:10.2514/3.47068

[78] Levasseur, V., Chalot, F., Daumas, L., and Forestier, N., "Harmonic Aerodynamics Loads Prediction Including a Linerized Turbulence Model," International Forum on Aeroelasticity and Structural Dynamics, IFASD Paper 2011-129, Paris, France, June 2011.

[79] Liamis, N., "Méthodes Implicites de Résolution des Équations d'Euler pour des Écoulements Tridimensionnels Instationnaires dans des Turbomachines," Université de Paris 06, Dissertation (Doctorat), Paris, France, October 1993.

[80] Liauzun, C., Canonne, E., and Mortchéléwicz, G. D., "Flutter Numerical Computations using the Linearized Navier-Stokes Equations," *Advanced Methods in Aeroelasticity*, RTO-MP-AVT-154, Loen, Norway, May 2008, pp. 8–1–8–12.

[81] Lindquist, D. R., and Giles, M. B., "Validity of Linearized Unsteady Euler Equations with Shock Capturing," *AIAA Journal*, Vol. 32, No. 1, 1994, pp. 46–53.
doi:10.2514/3.11949

[82] Markmiller, J., "Validierung eines zeitechten und eines small disturbance Navier-Stokes Verfahrens an einem schwingenden Deltaflügel," Aerodynamics Division, Institute for Fluid Mechanics, Technische Universität München, Diploma Thesis TUM-FLM-2003/28, unpublished, Garching, Germany, Oct. 2003.

[83] May, M., and Grüber, B., "Realiability of Time-Linearized Flutter Predictions Near the Surge Line," *9th European Conference on Turbomachinery Fluid Dynamics and Thermodynamics*, ETC9, Istanbul, Turkey, 2011, pp. C208–1–C208–12.

[84] McCracken, A., Da Ronch, A., Timme, S., and Badcock, K. J., "Solution of linear systems in Fourier-based methods for aircraft applications," *International Journal of Computational Fluid Dynamics*, Vol. 27, No. 2, 2013, pp. 79–87.
doi:10.1080/10618562.2012.750719

[85] McCracken, A. J., Timme, S., and Badcock, K. J., "Accelerating Convergence of the CFD Linear Frequency Domain Method by a Preconditioned Linear Solver," *European Congress on Computational Methods in Applied Sciences and Engineering*, edited by J. Eberhardsteiner et.al., ECCOMAS 2012, Vienna, Austria, 2012.

[86] Menter, F. R., "Two-Equation Eddy-Viscosity Turbulence Models for Engineering Applications," *AIAA Journal*, Vol. 32, No. 8, 1994, pp. 1598–1605.
doi:10.2514/3.12149

[87] Morkovin, M. V., "Effects of Compressibility on Turbulent Flows," *Mécanique de la Turbulence*, edited by A. Favre, Gordon and Breach, New York, NY, 1962, pp. 367–380.

[88] Mortchéléwicz, G. D., "Application des Équations d'Euler Linéarisées á la Prévision du Flottement," French Aerospace Laboratory, ONERA-TP 97-206, Nov. 1997.

[89] Mortchéléwicz, G. D., "Prediction of Aircraft Transonic Aeroelasticity by the Linearised Euler Equations," French Aerospace Laboratory, ONERA-TP 01-021, Feb. 2001.

[90] Mortchéléwicz, G. D., "Aircraft Aeoelasticity Computed with Linearized RANS Equations," French Aerospace Laboratory, ONERA TP 2003-34, Feb. 2003.

[91] Ning, W., Li, Y. S., and Wells, R. G., "Predicting Bladerow Interactions Using a Multistage Time-Linearized Navier-Stokes Solver," *Journal of Turbomachinery*, Vol. 125, No. 1, 2003, pp. 25–32.
doi:10.1115/1.1516570

[92] Norris, H. L., "Turbulent Channel Flow with a Moving Wavy Boundary," Stanford University, Dissertation (Ph.D.), Stanford, CA, May 1975.

[93] Nürnberger, D., Eulitz, F., Schmitt, S., and Zachcial, A., "Recent Progress in the Numerical Simulation of Unsteady Viscous Multistage Turbomachinery Flow," 15th International Symposium on Air Breathing Engines, ISOABE Paper 2001-1081, Bangalore, India, Sep. 2001.

[94] Pechloff, A., "Triple Decomposition of the Two-dimensional Navier-Stokes Equations in Cartesian Coordinates and Linearization for Small Disturbances," Institute for Fluid Mechanics, Technische Universität München, Internal Report TUM-FLM-2001/4, unpublished, Garching, Germany, March 2001.

[95] Pechloff, A., "An Implicit Method for Solving the Small Disturbance Navier-Stokes Equations," Institute for Fluid Mechanics, Technische Universität München, Internal Report TUM-FLM-2002/21, unpublished, Garching, Germany, Sep. 2002.

[96] Pechloff, A., "Parallelization Effort of the FLM Computational-Fluid-Dynamics Code," Institute for Aerodynamics and Fluid Mechanics, Technische Universität München, Internal Report TUM-AER-2012/01, unpublished, Garching, Germany, March 2012.

[97] Pechloff, A., "Small Disturbance Navier-Stokes Investigations of Fighter-Type-Delta-Wing Pitching Oscillations," 28th Congress of the International Council of the Aeronautical Sciences, ICAS Paper 2012-2.11.3, Brisbane, Australia, Sep. 2012.

[98] Pechloff, A., Iatrou, M., Weishäupl, C., and Laschka, B., "The Small Disturbance Navier-Stokes Equations: Development of an Efficient Method for Calculating Unsteady Air Loads," *New Results in Numerical and Experimental Fluid Mechanics IV: Contributions to the 13th STAB-DGLR-Symposium, Munich, Germany 2002*, edited by C. Breitsamter, B. Laschka, H.-J. Heinemann, and R. Hilbig, Notes on Numerical Fluid Mechanics and Multidisciplinary Design, Vol. 87, Springer-Verlag, Berlin, Germany, 2004, pp. 278–285.
doi:10.1007/978-3-540-39604-8_35

[99] Pechloff, A., and Laschka, B., "Small Disturbance Navier-Stokes Method: An Efficient Tool for Predicting Unsteady Air Loads," 24th Congress of the International Council of the Aeronautical Sciences, ICAS Paper 2004-2.1.3, Yokohama, Japan, Sep. 2004.

[100] Pechloff, A., and Laschka, B., "Small Disturbance Navier-Stokes Method: Efficient Tool for Predicting Unsteady Air Loads," *Journal of Aircraft*, Vol. 43, No. 1, 2006, pp. 17–29.
doi:10.2514/1.14350

[101] Pechloff, A., and Laschka, B., "Small Disturbance Navier-Stokes Computations for Low Aspect Ratio Wing Pitching Oscillations," 26th Congress of the International Council of the Aeronautical Sciences, ICAS Paper 2008-2.10.3, Anchorage, AK, Sep. 2008.

[102] Pechloff, A., and Laschka, B., "Small Disturbance Navier-Stokes Computations Employing the Wilcox k-omega Turbulence Model," 27th Congress of the International Council of the Aeronautical Sciences, ICAS Paper 2010-3.10.5, Nice, France, Sep. 2010.

[103] Pechloff, A., and Laschka, B., "Small Disturbance Navier-Stokes Computations for Low-Aspect-Ratio Wing Pitching Oscillations," *Journal of Aircraft*, Vol. 47, No. 3, 2010, pp. 737–753.
doi:10.2514/1.45233

[104] Petrie-Repar, P., "Development of an Efficient Linearised Navier-Stokes Flow Solver for Turbomachinery Applications," *New Results in Numerical and Experimental Fluid Mechanics IV: Contributions to the 13th STAB-DGLR-Symposium, Munich, Germany 2002*, edited by C. Breitsamter, B. Laschka, H.-J. Heinemann, and R. Hilbig, Notes on Numerical Fluid Mechanics and Multidisciplinary Design, Vol. 87, Springer-Verlag, Berlin, Germany, 2004, pp. 286–293.

[105] Petrie-Repar, P., "Development of an Efficient and Robust Linearised Navier-Stokes Flow Solver," *Unsteady Aerodynamics, Aeroacoustics and Aeroelasticity of Turbomachines*, edited by K. C. Hall, R. E. Kielb and J. P. Thomas, Springer, Netherlands, 2006, pp. 437–448.
doi:10.1007/1-4020-4605-7_32

[106] Petrie-Repar, P., "Three-dimensional Non-reflecting Boundary Condition for Linearized Flow Solvers," *ASME Turbo Expo 2010: Power for Land, Sea, and Air*, GT2010, Glasgow, UK, 2010, pp. 1247–1252.
doi:10.1115/GT2010-23335

[107] Petrie-Repar, P., McGhee, A., and Jacobs, P. A., "Analytical Maps of Aerodynamic Damping as a Function of Operating Condition for a Compressor Profile," *ASME Turbo Expo 2006: Power for Land, Sea, and Air*, GT2006, Barcelona, Spain, 2006, pp. 1133–1144.
doi:10.1115/GT2006-90829

[108] Petrie-Repar, P., McGhee, A., and Jacobs, P. A., "Three-Dimensional Viscous Flutter Analysis of Standard Configuration 10," *ASME Turbo Expo 2007: Power for Land, Sea, and Air*, GT2007, Montreal, Canada, 2007, pp. 665–674.
doi:10.1115/GT2007-27800

[109] Revalor, Y., Daumas, L., and Forestier, N., "Industrial Use of CFD for Loads and Aero-Servo-Elastic Stability Computations at Dassault Aviation," International Forum on Aeroelasticity and Structural Dynamics, IFASD Paper 2011-061, Paris, France, June 2011.

[110] Rieger, H., and Jameson, A., "Solution of Steady Three-Dimensional Compressible Euler and Navier-Stokes Equations by an Implicit LU Scheme," AIAA Paper 88-619, Jan. 1988.

[111] Roe, P. L., "Approximate Riemann Solvers, Parameter Vectors and Difference Schemes," *Journal of Computational Physics*, Vol. 43, No. 2, 1981, pp. 357–372.
doi:10.1016/0021-9991(81)90128-5

[112] Rumsey, C. L., Biedron, R. T., and Thomas, J. L., "CFL3D: Its History and Some Recent Applications," NASA TM-1997-112861, 1997.

[113] Sbardella, L., and Imregun, M., "Linearized Unsteady Viscous Turbomachinery Flows Using Hybrid Grids," *Journal of Turbomachinery*, Vol. 123, No. 3, 2001, pp. 568–582.
doi:10.1115/1.1371777

[114] Schuster, D. M., Liu, D. D., and Huttsell, L. J., "Computational Aeroelasticity: Success, Progress, Challenge," *Journal of Aircraft*, Vol. 40, No. 5, 2003, pp. 843–856.
doi:10.2514/2.6875

[115] Schwamborn, D., Gerhold, T., and Heinrich, R., "The DLR TAU-code: Recent Applications in Research and Industry," *III European Conference on Computational Fluid Dynamics*, edited by P. Wessling et al., ECCOMAS CFD 2006, Egmond aan Zee, Netherlands, 2006.

[116] Sekar, W. K., "Viscous-Inviscid Interaction Methods for Flutter Calculations," Institute of Aerodynamics, Technische Universität München, Dissertation (Dr.-Ing.), Garching, Germany, Sep. 2006.

[117] Sekar, W. K., and Laschka, B., "Calculation of the Transonic Dip of Airfoils Using Visocous-Inviscid Aerodynamic Interaction Method," *Aerospace Science and Technology*, Vol. 9, No. 8, 2005, pp. 661–671.
doi:j.ast.2005.06.004

[118] Sensburg, O., and Laschka, B., "Flutter Induced by Aerodynamic Interference Between Wing and Tail," *Journal of Aircraft*, Vol. 7, No. 4, 1970, pp. 319–324.
doi:10.2514/3.44171

[119] Sickmüller, U., "Luftkräfte höherer Ordnung auf Basis der Euler Gleichungen bei kleinen Störungen," Institute of Aerodynamics, Technische Universität München, Dissertation (Dr.-Ing.), Garching, Germany, Nov. 2005.

[120] Sickmüller, U., Pechloff, A., Weishäupl, C., and Laschka, B, "Aerodynamische Untersuchungen eines Deltaflügels bei verschiedenen Eigenformen mittels eines Euler-Verfahrens bei kleinen Störungen," Deutscher Luft- und Raumfahrtkongress 2001, Paper DGLR.2001-065, Hamburg, Germany, Sep. 2001.

[121] Spalart, P. R., and Allmaras, S. R., "A One-equation Turbulence Model for Aerodynamic Flows," AIAA Paper 92-0439, Jan. 1992.

[122] Steimle, P. C., Schröder, W., and Limberg, W., "Unsteady Pressure Measurements on an Oscillating Swept Wing in Transonic Flow," International Forum on Aeroelasticity and Structural Dynamics, IFASD Paper 2005-117, Munich, Germany, June 2005.

[123] Steiner, H.-J., "Validierung eines Navier-Stokes Verfahrens bei kleinen Störungen für 2D-Profilumströmungen," Institute for Fluid Mechanics, Technische Universität München, Semester Thesis TUM-FLM-2004/13, unpublished, Garching, Germany, July 2004.

[124] Telionis, P. D., "Unsteady Boundary Layers, Separated and Attached," *Unsteady Aerodynamics*, AGARD-CP-227, Ottawa, Canada, 1977, pp. 16–1–16–21.

[125] Telionis, P. D., *Unsteady Viscous Flows*, Springer Series in Computational Physics, Springer-Verlag, New York, NY, 1981.

[126] Thormann, R., Nitzsche, J., and Widhalm, M., "Time-linearized Simulation of Unsteady Transonic Flows with Shock-induced Separation," *European Congress on Computational Methods in Applied Sciences and Engineering*, edited by J. Eberhardsteiner et. al., ECCOMAS 2012, Vienna, Austria, 2012.

[127] Thormann, R., and Widhalm, M., "Forced Motion Simulations Using a Linear Frequency Domain Solver for a Generic Transport Aircraft," International Forum on Aeroelasticity and Structural Dynamics, IFASD Paper 2013-17A, Bristol, UK, June 2013.

[128] Thormann, R., and Widhalm, M., "Linear-Frequency-Domain Predictions of Dynamic-Response Data for Viscous Transonic Flows," *AIAA Journal*, Vol. 51, No. 11, 2013, pp. 2540–2557.
doi:10.2514/1.J051896

[129] Van Albada, G. D., Van Leer, B., and Roberts, Jr., W. W., "A Comparative Study of Computational Methods in Cosmic Gas Dynamics," *Astronomy and Astrophysics*, Vol. 108, 1982, pp. 76–84.

[130] Van Leer, B., "Towards the Ultimate Conservative Difference Scheme V: A Second-Order Sequel to Godunov's Method," *Journal of Computational Physics*, Vol. 32, 1979, pp. 101–136.

[131] Vinokur, M., "An Analysis of Finite-Difference and Finite-Volume Formulations of Conservation Laws," *Journal of Computational Physics*, Vol. 81, 1989, pp. 1–52.
doi:10.1016/0021-9991(89)90063-6

[132] Weishäupl, C., and Laschka, B., "Small Disturbance Euler Simulations for Delta Wing Unsteady Flows due to Harmonic Oscillations," *Journal of Aircraft*, Vol. 41, No. 4, 2004, pp. 782–789.
doi:10.2514/1.12601

[133] Wesseling, P., *An Introduction to Multigrid Methods*, Pure and Applied Mathematics, A Wiley-Interscience Series of Texts, Monographs, and Tracts, John Wiley & Sons Ltd., Chichester, UK, 1992, pp. 60–78.

[134] Whitfield, D. L., and Janus, J. M., "Three-Dimensional Unsteady Euler Equations Solution Using Flux Vector Splitting," AIAA Paper 1984-1552, June 1984.

[135] Widhalm, M., Dwight, R. M., Thormann, R., and Hübner, A., "Efficient Computation of Dynamic Stability Data with a Linearized Frequency Domain Solver," *V European Conference on Computational Fluid Dynamics*, edited by J. C. F. Pereira and A. Sequeira, ECCOMAS CFD 2010, Lisbon, Portugal, 2010.

[136] Widhalm, M., Hübner, A., and Thormann, R., "Linear Frequency Domain Predictions of Dynamic Derivatives for the DLR F12 Wind Tunnel Model," *European Congress on Computational Methods in Applied Sciences and Engineering*, edited by J. Eberhardsteiner et. al., ECCOMAS 2012, Vienna, Austria, 2012.

[137] Widhalm, M., and Thormann, R., "Evaluation of Dynamic Response Data with the DLR-TAU Linearized Frequency Domain Solver for the Viscous Transonic LANN CT9 Case," Institute of Aerodynamics and Flow Technology German Aerospace Center, Internal Report DLR-IB-124-2015/2, Braunschweig, Germany, August 2015.

[138] Wilcox, D. C., "Reassessment of the Scale-Determining Equation for Advanced Turbulence Models," *AIAA Journal*, Vol. 26, No. 11, 1988, pp. 1299–1310.
doi:10.2514/3.10041

[139] Wilcox, D. C., *Turbulence Modelling for CFD*, 2^{nd} ed., DCW Industries, La Cañada, CA, 1998.

[140] Xu, S., Timme, S., and Badcock, K. J., "Krylov Subspace Recycling for Linearised Aerodynamics Analysis using DLR-TAU," International Forum on Aeroelasticity and Structural Dynamics, IFASD Paper 2015-186, Saint Petersburg, Russia, June 2015.

[141] Xu, S., Timme, S., and Badcock, K. J., "Enabling Off-Design Linearised Aerodynamics Analysis using Krylov Subspace Recycling Technique," *Computers & Fluids*, Vol. 140, 2016, pp. 385–396.
doi:10.1016/j.compfluid.2016.10.018

[142] Yang, S., Chen, P. C., and Wang, Z., "Linearized FUN3D for Rapid Aeroelastic Design and Analysis," International Forum on Aeroelasticity and Structural Dynamics, IFASD Paper 2015-97, Saint Petersburg, Russia, June 2015.

[143] Yee, H. C., "A Class of High Resolution Explicit and Implicit Shock Capturing Methods," NASA TM-101088, 1989.

[144] Yoon, S., and Jameson, A., "A Multigrid LU-SSOR Scheme for Approximate Newton-Iteration Applied to the Euler Equations," NASA CR-17954, 1986.

[145] Yoon, S., and Jameson, A., "Lower-Upper Symmetric-Gauss-Seidel Method for the Euler and Navier-Stokes Equations," *AIAA Journal*, Vol. 26, No. 9, Sep. 1988, pp. 1025–1026.
doi:10.2514/3.10007

[146] Yoon, S., and Kwak, D., "Three-Dimensional Incompressible Navier-Stokes Solver Using Lower-Upper Symmetric-Gauss-Seidel Algorithm," *AIAA Journal*, Vol. 29, No. 6, June 1991, pp. 874–875.
doi:10.2514/3.10671

[147] Yoon, S., and Kwak, D., "Implicit Navier-Stokes Solver for Three-Dimensional Compressible Flows," *AIAA Journal*, Vol. 30, No. 11, 1992, pp. 2653–2659.
doi:10.2514/3.48957

[148] Yurkovich, R., "Status of Unsteady Aerodynamic Prediction for Flutter of High-Performance Aircraft," *Journal of Aircraft*, Vol. 40, No. 5, 2003, pp. 832–842.
doi:10.2514/2.6874

[149] Zhang, Z., Yang, S., and Chen, P. C., "Linearized Euler Solver for Rapid Frequency-Domain Aeroelastic Analysis," *Journal of Aircraft*, Vol. 49, No. 3, 2012, pp. 922–932.
doi:10.2514/1.C031611

[150] Zingel, H., "Measurement of Steady and Unsteady Air Loads on a Stiffness Scaled Model of a Modern Transport Aircraft Wing," International Forum on Aeroelasticity and Structural Dynamics, IFASD Paper 1991-069, Aachen, Germany, June 1991.

[151] ZONA Technology, *ZAERO Version 8.3 Theoretical Manual*, ZONA Technology, Scottsdale, CA, 2008.

[152] Zwaan, R. J., "NACA 64A006 Oscillating Flap," Compendium of Unsteady Aerodynamic Measurements, AGARD-R-702, 1982, pp. 1-1–4-15.

[153] Zwaan, R. J., "NLR 7301 Supercritical Airfoil Oscillatory Pitching and Oscillating Flap," Compendium of Unsteady Aerodynamic Measurements, AGARD-R-702, 1982, pp. 4-1–4-25.

[154] Zwaan, R. J., "LANN Wing. Pitching Oscillation," Compendium of Unsteady Aerodynamic Measurements, Addendum No. 1, AGARD-R-702, 1985, pp. 9-1–9-76.

Appendix A

Numerical Method – Supplemental

A.1 Geometric and Kinematic Entity Evaluation

As inherited from FLM-SDEu [70], the FLM-SD.NS evaluation of a computational cell's physical surface normal vectors and physical volume in both their amplitude and linearized time-invariant-mean instances traces back to the vertices of the extremum and reference grid. This likewise holds true for the novel evaluation of the amplitude and linearized time-invariant-mean distances to the nearest wall. Each grid-particular vertex is uniquely given through a position vector, respectively,

$$\mathbf{r}_{v0}^{EG} = \left(x_v^{EG},\, y_v^{EG},\, z_v^{EG} \right)^T \qquad \text{and} \qquad \mathbf{r}_{v0}^{RG} = \left(x_v^{RG},\, y_v^{RG},\, z_v^{RG} \right)^T , \tag{A.1}$$

formulated with regard to the Cartesian coordinate system's origin. Naturally, each vertex corresponds to an intersection between directional line-elements of the curvilinear coordinate system. The amplitude displacement vector and the time-invariant-mean position vector of each vertex are then specified by

$$\hat{\mathbf{r}}_v = \left(\hat{x}_v,\, \hat{y}_v,\, \hat{z}_v \right)^T := \mathbf{r}_{v0}^{EG} - \mathbf{r}_{v0}^{RG} \qquad \text{and} \qquad \bar{\mathbf{r}}_{v0} = \left(\bar{x}_v,\, \bar{y}_v,\, \bar{z}_v \right)^T := \mathbf{r}_{v0}^{RG} . \tag{A.2}$$

Algorithmically, the former embodies the collective subtraction of the reference grid from its extremum counterpart. This is performed only once during the initialization procedure, just as the subsequent evaluation of the geometric and kinematic entities [70].

Again considering the representative computational cell (i, j, k) introduced in Figure 4.1, some further conventions need to be established. In agreement with Kreiselmaier [70], the constituting vertices are distinguished by identifiers that derive from a component-by-component half-integer increment or decrement of the computational cell's denoting triplet as shown in Figure A.1. They are indicative of the individual vertex's relative position to the geometric centroid, respectively, being forward or backward in terms of the particular positive index-direction. On the basis of Vinokur [131], the identifiers $v \in \{1, 2, \ldots, 8\}$ are concurrently employed. It allows each cell interface to be readily distinguished through

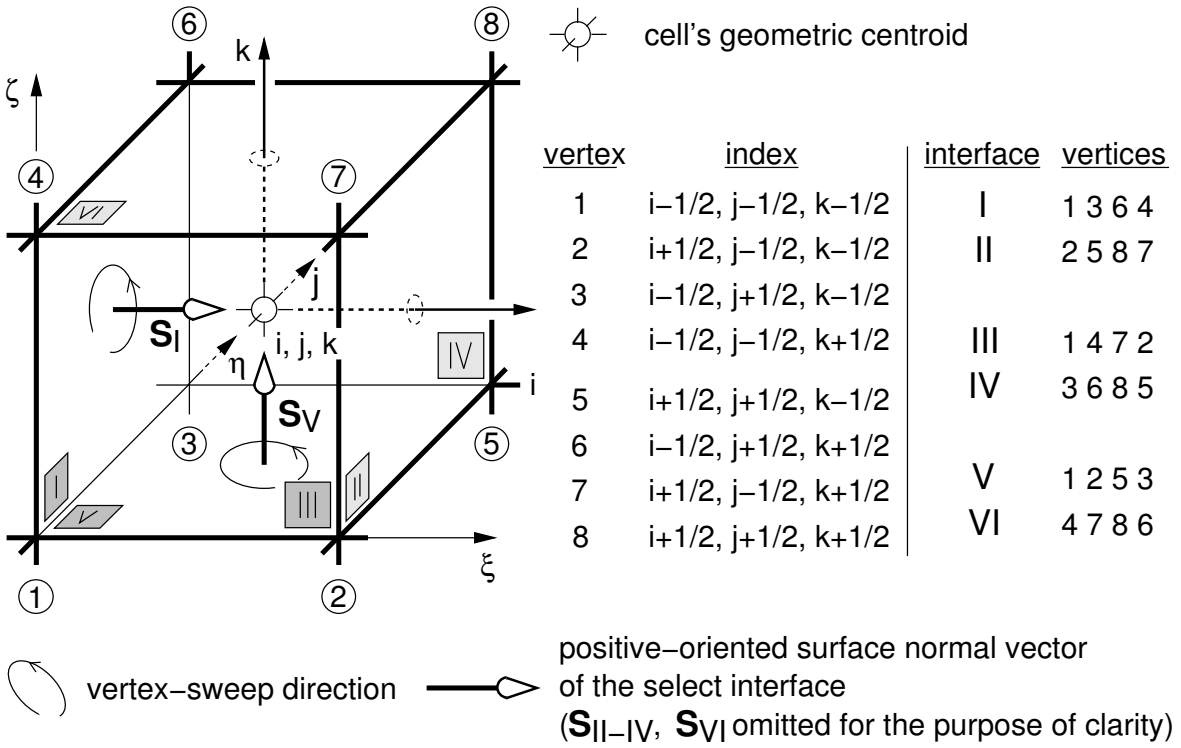

vertex	index
1	i–1/2, j–1/2, k–1/2
2	i+1/2, j–1/2, k–1/2
3	i–1/2, j+1/2, k–1/2
4	i–1/2, j–1/2, k+1/2
5	i+1/2, j+1/2, k–1/2
6	i–1/2, j+1/2, k+1/2
7	i+1/2, j–1/2, k+1/2
8	i+1/2, j+1/2, k+1/2

interface	vertices
I	1 3 6 4
II	2 5 8 7
III	1 4 7 2
IV	3 6 8 5
V	1 2 5 3
VI	4 7 8 6

Figure A.1: Vertex identification and principle surface normal vector definition for the representative computational cell (rendered in computational space); based on [70], *Abbildung 3.6*, [119], *Abbildung 4.1*, as well as [131], Fig. 1.

its constituting vertices; i.e., with their identifiers composited into a four-digit label. The identifiers' sequence in the label follows the vertex-sweep direction employed in the associated physical surface normal vector's evaluation. Being compliant to the right-hand-rule, the positive orientation of each surface normal vector accords to the particular positive coordinate-/index-direction (Figure A.1). Hence, the instances associated with the forward interfaces ($\mathbf{S}_{II}$, $\mathbf{S}_{IV}$, $\mathbf{S}_{VI}$) are outward oriented, while their backward counterparts ($\mathbf{S}_{I}$, $\mathbf{S}_{III}$, $\mathbf{S}_{V}$) are inward oriented [70]. Physically, each computational cell is treated as merely being a convex planar-quadrilateral-faced hexahedron [70, 119]. This simplification allows a less elaborate evaluation of the geometric entities, however, which is still adequately accurate if a pair of smoothed grids is employed [131, 16].

Focusing on the physical surface normal vectors first, any one of the computational cell's backward interfaces can be considered. In generalized terms, it is constituted by the vertices a, b, c, and d, as depicted in Figure A.2. Their identification follows the established vertex-sweep direction. The interface-associated physical surface normal vector $\mathbf{S}_{abcd}$ then results from one-half of the cross product between the quadrilateral's diagonal vectors $\mathbf{r}_{ca}$ and $\mathbf{r}_{db}$ [131, 16, 70, 119]. Furthermore, the interface's geometric centroid is gained

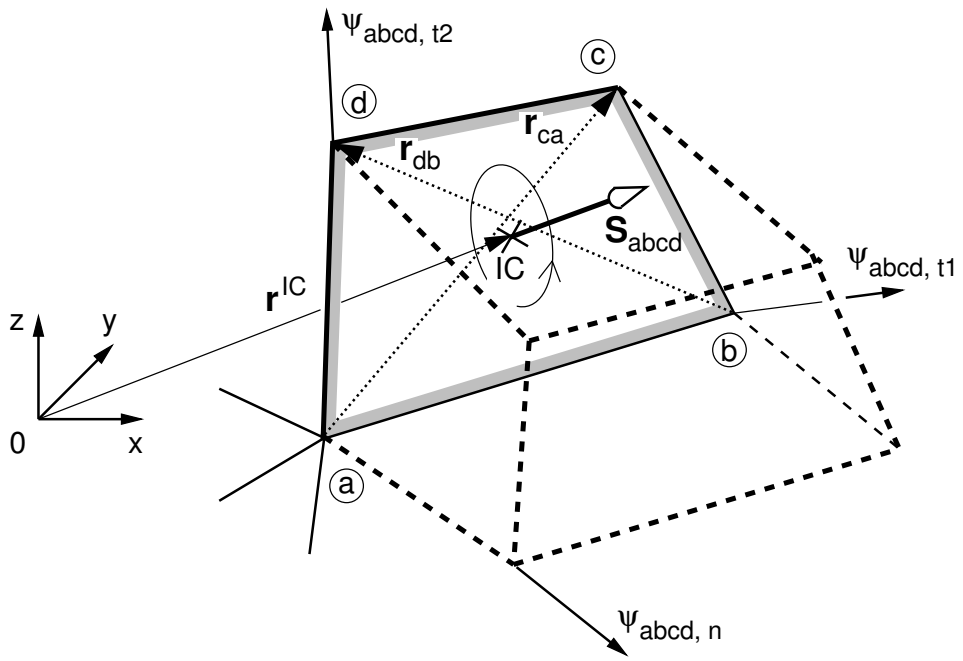

Figure A.2: Physical surface normal vector evaluation for a generalized cell-interface *abcd* (rendered in physical space); based on [70], [119], *Abbildung 4.4*, as well as [131].

through arithmetically averaging the vertex positions [16, 70]. Following Kreiselmaier [70], as well as Sickmüller [119], the amplitude and linearized time-invariant-mean instances of the physical surface normal vector are then, respectively, derived as

$$\begin{aligned}\hat{\mathbf{S}}_{abcd} &= (\bar{\mathbf{r}}_{ca} \times \hat{\mathbf{r}}_{db}) \;/\; 2 + (\hat{\mathbf{r}}_{ca} \times \bar{\mathbf{r}}_{db}) \;/\; 2 \\ &= \begin{pmatrix} \Delta\bar{y}_{ca}\Delta\hat{z}_{db} - \Delta\bar{z}_{ca}\Delta\hat{y}_{db} \\ \Delta\bar{z}_{ca}\Delta\hat{x}_{db} - \Delta\bar{x}_{ca}\Delta\hat{z}_{db} \\ \Delta\bar{x}_{ca}\Delta\hat{y}_{db} - \Delta\bar{y}_{ca}\Delta\hat{x}_{db} \end{pmatrix} \;/\; 2 + \begin{pmatrix} \Delta\hat{y}_{ca}\Delta\bar{z}_{db} - \Delta\hat{z}_{ca}\Delta\bar{y}_{db} \\ \Delta\hat{z}_{ca}\Delta\bar{x}_{db} - \Delta\hat{x}_{ca}\Delta\bar{z}_{db} \\ \Delta\hat{x}_{ca}\Delta\bar{y}_{db} - \Delta\hat{y}_{ca}\Delta\bar{x}_{db} \end{pmatrix} \;/\; 2 \end{aligned} \tag{A.3}$$

and

$$\bar{\mathbf{S}}^{*}_{abcd} = (\bar{\mathbf{r}}_{ca} \times \bar{\mathbf{r}}_{db}) \;/\; 2 = \begin{pmatrix} \Delta\bar{y}_{ca}\Delta\bar{z}_{db} - \Delta\bar{z}_{ca}\Delta\bar{y}_{db} \\ \Delta\bar{z}_{ca}\Delta\bar{x}_{db} - \Delta\bar{x}_{ca}\Delta\bar{z}_{db} \\ \Delta\bar{x}_{ca}\Delta\bar{y}_{db} - \Delta\bar{y}_{ca}\Delta\bar{x}_{db} \end{pmatrix} \;/\; 2\,, \tag{A.4}$$

with

$$\begin{aligned} \Delta\hat{x}_{v2\,v1} &:= \hat{x}_{v2} - \hat{x}_{v1}\,, & \Delta\bar{x}_{v2\,v1} &:= \bar{x}_{v2} - \bar{x}_{v1}\,; \\ \Delta\hat{y}_{v2\,v1} &:= \hat{y}_{v2} - \hat{y}_{v1}\,, & \Delta\bar{y}_{v2\,v1} &:= \bar{y}_{v2} - \bar{y}_{v1}\,; \\ \Delta\hat{z}_{v2\,v1} &:= \hat{z}_{v2} - \hat{z}_{v1}\,, & \Delta\bar{z}_{v2\,v1} &:= \bar{z}_{v2} - \bar{z}_{v1}\,, \end{aligned} \tag{A.5}$$

for $v1 = a$ and $v2 = c$ or $v1 = b$ and $v2 = d$. Applied to the considered cell, the amplitude and linearized time-invariant-mean physical surface normal vector associated with each backward interface are then utilized to set the corresponding instances of the spatial

metric:

$$\begin{aligned}
\widehat{\boldsymbol{J\xi}}_{i-1/2,\,j,\,k} &:= \hat{\mathbf{S}}_{I} = \hat{\mathbf{S}}_{1364}\,, \quad \overline{\boldsymbol{J\xi}}^{\,*}_{i-1/2,\,j,\,k} := \bar{\mathbf{S}}^{*}_{I} = \bar{\mathbf{S}}^{*}_{1364}\,; \\
\widehat{\boldsymbol{J\eta}}_{i,\,j-1/2,\,k} &:= \hat{\mathbf{S}}_{III} = \hat{\mathbf{S}}_{1472}\,, \quad \overline{\boldsymbol{J\eta}}^{\,*}_{i,\,j-1/2,\,k} := \bar{\mathbf{S}}^{*}_{III} = \bar{\mathbf{S}}^{*}_{1472}\,; \\
\widehat{\boldsymbol{J\zeta}}_{i,\,j,\,k-1/2} &:= \hat{\mathbf{S}}_{V} = \hat{\mathbf{S}}_{1253}\,, \quad \overline{\boldsymbol{J\zeta}}^{\,*}_{i,\,j,\,k-1/2} := \bar{\mathbf{S}}^{*}_{V} = \bar{\mathbf{S}}^{*}_{1253}\,.
\end{aligned} \tag{A.6}$$

Thus, the amplitude temporal metric, Eq. (3.222), as rendered for the particular backward interface becomes

$$\widehat{J\xi}_{t\,i-1/2,\,j,\,k} = -ik\,\hat{\mathbf{r}}_{I}^{\,IC}\,\bar{\mathbf{S}}^{*}_{I}\,, \quad \widehat{J\eta}_{t\,i,\,j-1/2,\,k} = -ik\,\hat{\mathbf{r}}_{III}^{\,IC}\,\bar{\mathbf{S}}^{*}_{III}\,, \quad \widehat{J\zeta}_{t\,i,\,j,\,k-1/2} = -ik\,\hat{\mathbf{r}}_{V}^{\,IC}\,\bar{\mathbf{S}}^{*}_{V}, \tag{A.7}$$

wherein the amplitude displacement vector of each interface's geometric centroid is similarly gained through arithmetic averaging of the constituting vertex instances:

$$\begin{aligned}
\hat{\mathbf{r}}_{I}^{\,IC} &:= (\hat{\mathbf{r}}_1 + \hat{\mathbf{r}}_3 + \hat{\mathbf{r}}_6 + \hat{\mathbf{r}}_4)\ /\ 4\,, \\
\hat{\mathbf{r}}_{III}^{\,IC} &:= (\hat{\mathbf{r}}_1 + \hat{\mathbf{r}}_4 + \hat{\mathbf{r}}_7 + \hat{\mathbf{r}}_2)\ /\ 4\,, \\
\hat{\mathbf{r}}_{V}^{\,IC} &:= (\hat{\mathbf{r}}_1 + \hat{\mathbf{r}}_2 + \hat{\mathbf{r}}_5 + \hat{\mathbf{r}}_3)\ /\ 4\,.
\end{aligned} \tag{A.8}$$

The surface normal vector associated with one of the considered cell's forward interfaces always conform to the surface normal vector associated with the directionally adjoining cell's backward interface. Additionally, the interfaces have the same geometric centroid. This circumstance remains valid for both an amplitude and a linearized time-invariant-mean instance. Hence, the amplitude and linearized time-invariant-mean spatial metrics associated with each forward interface are set through

$$\begin{aligned}
\widehat{\boldsymbol{J\xi}}_{i+1/2,\,j,\,k} &:= \hat{\mathbf{S}}_{II} = \hat{\mathbf{S}}_{I;\,i+1,\,j,\,k}\,, \quad \overline{\boldsymbol{J\xi}}^{\,*}_{i+1/2,\,j,\,k} := \bar{\mathbf{S}}^{*}_{II} = \bar{\mathbf{S}}^{*}_{I;\,i+1,\,j,\,k}\,; \\
\widehat{\boldsymbol{J\eta}}_{i,\,j+1/2,\,k} &:= \hat{\mathbf{S}}_{IV} = \hat{\mathbf{S}}_{III;\,i,\,j+1,\,k}\,, \quad \overline{\boldsymbol{J\eta}}^{\,*}_{i,\,j+1/2,\,k} := \bar{\mathbf{S}}^{*}_{IV} = \bar{\mathbf{S}}^{*}_{III;\,i,\,j+1,\,k}\,; \\
\widehat{\boldsymbol{J\zeta}}_{i,\,j,\,k+1/2} &:= \hat{\mathbf{S}}_{VI} = \hat{\mathbf{S}}_{V;\,i,\,j,\,k+1}\,, \quad \overline{\boldsymbol{J\zeta}}^{\,*}_{i,\,j,\,k+1/2} := \bar{\mathbf{S}}^{*}_{VI} = \bar{\mathbf{S}}^{*}_{V;\,i,\,j,\,k+1}\,,
\end{aligned} \tag{A.9}$$

with the particular amplitude temporal metric being

$$\widehat{J\xi}_{t\,i+1/2,\,j,\,k} = -ik\,\hat{\mathbf{r}}_{II}^{\,IC}\,\bar{\mathbf{S}}^{*}_{II}\,, \quad \widehat{J\eta}_{t\,i,\,j+1/2,\,k} = -ik\,\hat{\mathbf{r}}_{IV}^{\,IC}\,\bar{\mathbf{S}}^{*}_{IV}\,, \quad \widehat{J\zeta}_{t\,i,\,j,\,k+1/2} = -ik\,\hat{\mathbf{r}}_{VI}^{\,IC}\,\bar{\mathbf{S}}^{*}_{VI}\,, \tag{A.10}$$

and

$$\hat{\mathbf{r}}_{II}^{\,IC} = \hat{\mathbf{r}}_{I;\,i+1,\,j,\,k}^{\,IC}\,, \quad \hat{\mathbf{r}}_{IV}^{\,IC} = \hat{\mathbf{r}}_{III;\,i,\,j+1,\,k}^{\,IC}\,, \quad \hat{\mathbf{r}}_{VI}^{\,IC} = \hat{\mathbf{r}}_{V;\,i,\,j,\,k+1}^{\,IC} \tag{A.11}$$

[70, 119].

Secondly, the physical cell volume is considered. Pursuant to Vinokur [131], a computational cell is initially divided into three pyramids. The main diagonal constituted by

the entirely forward and backward vertex, respectively, vertex 8 and vertex 1 in Figure A.1, serves as the common edge. Selecting the former as the shared apex of the pyramids, the latter becomes the common point of the three bases, each corresponding to one of the backward interfaces. The physical volume of the individual pyramid results from one third of the dot product between the interface-associated physical surface normal vector and the main diagonal's direction vector. Ultimately, the physical cell volume is obtained as the sum of the three physical pyramid volumes. [131]. In order to maintain a consistent evaluation of the physical cell volume across multiple blocks, Kreiselmaier [70] additionally considers the three pyramids obtained from a transposed vertex-assignment of the shared apex and the common point; i.e., each of the three bases corresponds to one of the forward interfaces. The physical cell volume resulting from this subdivision is then arithmetically averaged with the ordinary instance, yielding the value actually ascribed to the computational cell [70]. Compactly formulated, the dot product between each interface-associated physical surface normal vector and the main diagonal's direction vector is arithmetically averaged [119]. Further following Kreiselmaier [70], as well as Sickmüller [119], the amplitude and linearized time-invariant-mean instances of the physical cell volume are, respectively, derived as

$$\begin{aligned} \hat{V} &= \left(\bar{\mathbf{S}}^{*}_{I} + \bar{\mathbf{S}}^{*}_{II} + \bar{\mathbf{S}}^{*}_{III} + \bar{\mathbf{S}}^{*}_{IV} + \bar{\mathbf{S}}^{*}_{V} + \bar{\mathbf{S}}^{*}_{VI}\right) (\hat{\mathbf{r}}_{8} - \hat{\mathbf{r}}_{1}) \;\; / \; 6 \\ &+ \left(\hat{\mathbf{S}}_{I} + \hat{\mathbf{S}}_{II} + \hat{\mathbf{S}}_{III} + \hat{\mathbf{S}}_{IV} + \hat{\mathbf{S}}_{V} + \hat{\mathbf{S}}_{VI}\right) (\bar{\mathbf{r}}_{80} - \bar{\mathbf{r}}_{10}) \;\; / \; 6 \end{aligned} \tag{A.12}$$

and

$$\bar{V}^{*} = \left(\bar{\mathbf{S}}^{*}_{I} + \bar{\mathbf{S}}^{*}_{II} + \bar{\mathbf{S}}^{*}_{III} + \bar{\mathbf{S}}^{*}_{IV} + \bar{\mathbf{S}}^{*}_{V} + \bar{\mathbf{S}}^{*}_{VI}\right) (\bar{\mathbf{r}}_{80} - \bar{\mathbf{r}}_{10}) \;\; / \; 6 \,. \tag{A.13}$$

They are utilized to set the analogously decomposed determinant of the coordinate transformation's Jacobian:

$$\widehat{J}_{i,\,j,\,k} := \hat{V}_{i,\,j,\,k} \qquad \text{and} \qquad \overline{J}^{\,*}_{i,\,j,\,k} := \bar{V}^{*}_{i,\,j,\,k} \tag{A.14}$$

[70, 119].

Lastly, the amplitude and linearized time-invariant-mean instance of the centroidal distance to the nearest wall are novelly evaluated. For the considered cell, the position of the geometric centroid with respect to the Cartesian coordinate system's origin is simply gained by arithmetically averaging the constituting vertices' positions. It is conducted in both the extremum and reference grid, respectively,

$$\mathbf{r}^{CC,EG}_{i,\,j,\,k} := \left(\sum_{v=1}^{8} \mathbf{r}^{EG}_{v0}\right) \;/\; 8 \qquad \text{and} \qquad \mathbf{r}^{CC,RG}_{i,\,j,\,k} := \left(\sum_{v=1}^{8} \mathbf{r}^{RG}_{v0}\right) \;/\; 8 \,. \tag{A.15}$$

The grid-particular distance of the geometric centroid to an individual wall-boundary cell-interface m (represented by its own geometric centroid) is then specified as

$$d^{EG}_{i,\,j,\,k;\,m} := \left|\mathbf{r}^{CC,EG}_{i,\,j,\,k} - \mathbf{r}^{IC,EG}_{wb,m}\right| \qquad \text{and} \qquad d^{RG}_{i,\,j,\,k;\,m} := \left|\mathbf{r}^{CC,RG}_{i,\,j,\,k} - \mathbf{r}^{IC,RG}_{wb,m}\right| \,. \tag{A.16}$$

Hence, for M wall-boundary cell-interfaces, an equal number of distances can be determined. The distance to the nearest wall is simply gained by a direct comparison within this set:

$$\begin{aligned} d^{EG}_{i,j,k} &= min\left(d^{EG}_{i,j,k;1}\,,\ d^{EG}_{i,j,k;2}\,,\ \ldots\,,\ d^{EG}_{i,j,k;M}\right) \quad \text{and} \\ d^{RG}_{i,j,k} &= min\left(d^{RG}_{i,j,k;1}\,,\ d^{RG}_{i,j,k;2}\,,\ \ldots\,,\ d^{RG}_{i,j,k;M}\right)\,. \end{aligned} \tag{A.17}$$

The amplitude and linearized time-invariant-mean instance of the centroidal distance to the nearest wall then, respectively, yield from

$$\hat{d}_{i,j,k} := d^{EG}_{i,j,k} - d^{RG}_{i,j,k} \qquad \text{and} \qquad \bar{d}^{*}_{i,j,k} := d^{RG}_{i,j,k}\,. \tag{A.18}$$

Overall, the implementation of this algorithm by the author followed the FLOWer instance [72], notably, maintaining the multiblock capability to full extent; i.e., for a particular block, the evaluation of the centroidal distance to the nearest wall takes into account the wall-boundary cell-interfaces of all blocks.

A.2 Amplitude Convective Flux Vector Evaluation

Kreiselmaier [70] had introduced a small disturbance utilization of Roe's approximate Riemann-solver [111, 143] for the interface-local evaluation of both the $\hat{\mathbf{q}}$- and $\widehat{\boldsymbol{J\psi}}$-homogenous convective flux vectors in FLM-SDEu. Also having been described by Sickmüller [119], it is provided here as extended by the author for the incorporation of the S/A one-equation turbulence model [121, 99] into FLM-SD.NS. The formulation is directionally specific, with the ξ instances treated representatively. The pertinent backward interface of cell (i,j,k) merely needs to be focused on.

Initially, $\widehat{\mathbf{F}}^{(1)}_{i-1/2,\,j,\,k}$ is considered. Following Kreiselmaier [70], as well as Sickmüller [119], its evaluation takes into account an interface-proximate left- and right-side state, respectively, $\widehat{\mathbf{F}}^{(1)\,L}$ and $\widehat{\mathbf{F}}^{(1)\,R}$, in conjunction with the $\widehat{\mathbf{F}}^{(1)}$-pertinent Jacobian matrix $\overline{\mathbf{K}_\xi}^{*}$ formulated with the Roe averages [111] of the constituting primitive variables' left- and right-side state at the interface; i.e., $\underline{\overline{\mathbf{K}_\xi}^{*}}_{i-1/2,\,j,\,k}$. Likewise expressing $\widehat{\mathbf{F}}^{(1)\,L}$ and $\widehat{\mathbf{F}}^{(1)\,R}$ through their Jacobian matrices, respectively, $\overline{\mathbf{K}_\xi}^{*L}\,\hat{\mathbf{q}}^{L}$ and $\overline{\mathbf{K}_\xi}^{*R}\,\hat{\mathbf{q}}^{R}$, while eigendecomposing $\underline{\overline{\mathbf{K}_\xi}^{*}}_{i-1/2,\,j,\,k}$ the evaluation can be conveniently written as

$$\widehat{\mathbf{F}}^{(1)}_{i-1/2,\,j,\,k} \;\approx\; \overline{\mathbf{N}_\xi}^{*L}\,\hat{\mathbf{q}}^{L} \;+\; \overline{\mathbf{N}_\xi}^{*R}\,\hat{\mathbf{q}}^{R}\,, \tag{A.19}$$

with

$$\begin{aligned} \overline{\mathbf{N}_\xi}^{*L} &:= \left(\overline{\mathbf{K}_\xi}^{*L} + \mathbf{R}^{\overline{\mathbf{K}_\xi}^{*}}_{i-1/2,\,j,\,k}\left|\boldsymbol{\Lambda}^{\overline{\mathbf{K}_\xi}^{*}}_{i-1/2,\,j,\,k}\right|_{\delta}\mathbf{L}^{\overline{\mathbf{K}_\xi}^{*}}_{i-1/2,\,j,\,k}\right)\ /\ 2 \quad \text{and} \\ \overline{\mathbf{N}_\xi}^{*R} &:= \left(\overline{\mathbf{K}_\xi}^{*R} - \mathbf{R}^{\overline{\mathbf{K}_\xi}^{*}}_{i-1/2,\,j,\,k}\left|\boldsymbol{\Lambda}^{\overline{\mathbf{K}_\xi}^{*}}_{i-1/2,\,j,\,k}\right|_{\delta}\mathbf{L}^{\overline{\mathbf{K}_\xi}^{*}}_{i-1/2,\,j,\,k}\right)\ /\ 2\,, \end{aligned} \tag{A.20}$$

wherein

$$\overline{\mathbf{K}_\xi}^{*L} := \overline{\mathbf{K}}^{*}\Big(\bar{\mathbf{q}}^{*L},\, \overline{\boldsymbol{J\xi}}^{*}_{i-1/2,\,j,\,k}\Big) \quad \text{and} \quad \overline{\mathbf{K}_\xi}^{*R} := \overline{\mathbf{K}}^{*}\Big(\bar{\mathbf{q}}^{*R},\, \overline{\boldsymbol{J\xi}}^{*}_{i-1/2,\,j,\,k}\Big)\,. \tag{A.21}$$

In this regard, $\mathbf{R}^{\underline{\overline{\mathbf{K}_\xi}^{*}}}$ represents the matrix of $\underline{\overline{\mathbf{K}_\xi}^{*}}$-pertinent linearly independent right eigenvectors, $\mathbf{L}^{\underline{\overline{\mathbf{K}_\xi}^{*}}}$ represents its left eigenvector counterpart, and $\left|\boldsymbol{\Lambda}^{\underline{\overline{\mathbf{K}_\xi}^{*}}}\right|_\delta$ represents the matrix of the modified $\underline{\overline{\mathbf{K}_\xi}^{*}}$-eigenvalues. $\overline{\mathbf{N}_\xi}^{*L}$ and $\overline{\mathbf{N}_\xi}^{*R}$ are invariant throughout the pseudotime integration, and thus need to be evaluated only once; i.e., during the algorithm's initialization procedure [70, 119].

Pursuant to the FLM-SDEu implementation [70], the spatial accuracy of Eq. (A.19) is extended for FLM-SD.NS from a first- to a second-order instance through

$$\begin{aligned}
\hat{\mathbf{q}}^{L} &:= \hat{\mathbf{q}}_{i-1,\,j,\,k} + \overline{\boldsymbol{\Psi}_\xi}^{*L}\,(\hat{\mathbf{q}}_{i-1,\,j,\,k} - \hat{\mathbf{q}}_{i-2,\,j,\,k}) \;\; / \; 2\,, \\
\hat{\mathbf{q}}^{R} &:= \hat{\mathbf{q}}_{i,\,j,\,k} - \overline{\boldsymbol{\Psi}_\xi}^{*R}\,(\hat{\mathbf{q}}_{i+1,\,j,\,k} - \hat{\mathbf{q}}_{i,\,j,\,k}) \;\; / \; 2
\end{aligned} \tag{A.22}$$

and

$$\begin{aligned}
\bar{\mathbf{q}}^{*L} &:= \bar{\mathbf{q}}^{*}_{i-1,\,j,\,k} + \overline{\boldsymbol{\Psi}_\xi}^{*L}\,\big(\bar{\mathbf{q}}^{*}_{i-1,\,j,\,k} - \bar{\mathbf{q}}^{*}_{i-2,\,j,\,k}\big) \;\; / \; 2\,, \\
\bar{\mathbf{q}}^{*R} &:= \bar{\mathbf{q}}^{*}_{i,\,j,\,k} - \overline{\boldsymbol{\Psi}_\xi}^{*R}\,\big(\bar{\mathbf{q}}^{*}_{i+1,\,j,\,k} - \bar{\mathbf{q}}^{*}_{i,\,j,\,k}\big) \;\; / \; 2\,,
\end{aligned} \tag{A.23}$$

as based on Van Leer's MUSCL [48, 130]. In Eq. (A.22) and Eq. (A.23), $\overline{\boldsymbol{\Psi}_\xi}^{*}$ embodies a diagonal matrix constituted in each element by the employed limiter function $\overline{\Psi_\xi}^{*}$. It allows spatial accuracy to again be reduced for unsmooth regions of the linearized time-invariant-mean flowfield. Each instance of $\overline{\Psi_\xi}^{*}$ is separately assessed for the pertinent element of the linearized time-invariant-mean state vector. The limiter function itself is defined in accordance with Van Albada et al. [129]:

$$\overline{\Psi_\xi}^{*}(\bar{v}^{*}_{\xi}) := \big[(\bar{v}^{*}_{\xi})^2 + \bar{v}^{*}_{\xi}\big] \,/\, \big[(\bar{v}^{*}_{\xi})^2 + 1\big]\,, \tag{A.24}$$

realizing

$$\begin{aligned}
\overline{\Psi_\xi}^{*L} &:= \overline{\Psi_\xi}^{*}(\bar{v}^{*L}_{\xi}) \quad \text{with} \quad \bar{v}^{*L}_{\xi} = \big(\bar{q}^{*}_{i,\,j,\,k} - \bar{q}^{*}_{i-1,\,j,\,k}\big) \,/\, \big(\bar{q}^{*}_{i-1,\,j,\,k} - \bar{q}^{*}_{i-2,\,j,\,k}\big)\,; \\
\overline{\Psi_\xi}^{*R} &:= \overline{\Psi_\xi}^{*}(\bar{v}^{*R}_{\xi}) \quad \text{with} \quad \bar{v}^{*R}_{\xi} = \big(\bar{q}^{*}_{i,\,j,\,k} - \bar{q}^{*}_{i-1,\,j,\,k}\big) \,/\, \big(\bar{q}^{*}_{i+1,\,j,\,k} - \bar{q}^{*}_{i,\,j,\,k}\big)\,,
\end{aligned} \tag{A.25}$$

wherein

$$\bar{q}^{*} \in \{\bar{\rho},\, \overline{\rho u}^{*},\, \overline{\rho v}^{*},\, \overline{\rho w}^{*},\, \overline{\rho e}^{*},\, \overline{\breve{\mu}}^{*}\}\,. \tag{A.26}$$

The left- and right-side state of a time-invariant-mean primitive variable is, respectively, gained through $\bar{\mathbf{q}}^{*L}$ and $\bar{\mathbf{q}}^{*R}$ [70].

Introducing the weighting factor $\bar{R} := \sqrt{\bar{\rho}^{R}/\bar{\rho}^{L}}$ [111, 70, 119], and novelly $\bar{R}^{\dagger} := \bar{R}+1$, the required Roe averages of the time-invariant-mean density and Cartesian velocities, respectively, are

$$\underline{\bar{\rho}} = \bar{R}\,\bar{\rho}^{L} \tag{A.27}$$

and

$$\underline{\bar{u}} = (\bar{R}\,\bar{u}^R + \bar{u}^L) \;/\; \bar{R}^\dagger\,, \quad \underline{\bar{v}} = (\bar{R}\,\bar{v}^R + \bar{v}^L) \;/\; \bar{R}^\dagger\,, \quad \underline{\bar{w}} = (\bar{R}\,\bar{w}^R + \bar{w}^L) \;/\; \bar{R}^\dagger\,, \tag{A.28}$$

while the instance of the linearized time-invariant-mean specific total enthalpy is

$$\underline{\bar{h}}^* = (\bar{R}\,\bar{h}^{*R} + \bar{h}^{*L}) \;/\; \bar{R}^\dagger\,, \quad \text{with} \quad \bar{h}^{*L/R} = \bar{e}^{L/R} \,+\, \bar{p}^{*L/R} \,/\, \bar{\rho}^{L/R} \tag{A.29}$$

[111, 70, 119]. The consistent extension for the time-invariant-mean S/A primitive working variable, as derived and implemented into FLM-SD.NS by the author, ultimately renders

$$\underline{\breve{\bar{\nu}}} = (\bar{R}\,\breve{\bar{\nu}}^R + \breve{\bar{\nu}}^L) \;/\; \bar{R}^\dagger\,. \tag{A.30}$$

Returning to the generalized notation, the Jacobian matrix of a $\hat{\mathbf{q}}$-homogenous convective flux vector is gained on basis of Kreiselmaier's [70] original formulation as

$$\overline{\mathbf{K}_\psi}^* := \partial\widehat{\mathbf{E}_\psi}^{(1)} / \,\partial\hat{\mathbf{q}} =$$

$$\begin{pmatrix}
0 & \overline{J\psi_x}^* & \overline{J\psi_y}^* & \overline{J\psi_z}^* & 0 & 0 \\
\overline{J\psi_x}^*\,\bar{\phi} - \bar{u}\,\overline{\theta_\psi}^* & \overline{\theta_\psi}^* + (1-\Gamma)\,\overline{J\psi_x}^*\,\bar{u} & \overline{J\psi_y}^*\,\bar{u} - \Gamma\,\overline{J\psi_x}^*\,\bar{v} & \overline{J\psi_z}^*\,\bar{u} - \Gamma\,\overline{J\psi_x}^*\,\bar{w} & \Gamma\,\overline{J\psi_x}^* & 0 \\
\overline{J\psi_y}^*\,\bar{\phi} - \bar{v}\,\overline{\theta_\psi}^* & \overline{J\psi_x}^*\,\bar{v} - \Gamma\,\overline{J\psi_y}^*\,\bar{u} & \overline{\theta_\psi}^* + (1-\Gamma)\,\overline{J\psi_y}^*\,\bar{v} & \overline{J\psi_z}^*\,\bar{v} - \Gamma\,\overline{J\psi_y}^*\,\bar{w} & \Gamma\,\overline{J\psi_y}^* & 0 \\
\overline{J\psi_z}^*\,\bar{\phi} - \bar{w}\,\overline{\theta_\psi}^* & \overline{J\psi_x}^*\,\bar{w} - \Gamma\,\overline{J\psi_z}^*\,\bar{u} & \overline{J\psi_y}^*\,\bar{w} - \Gamma\,\overline{J\psi_z}^*\,\bar{v} & \overline{\theta_\psi}^* + (1-\Gamma)\,\overline{J\psi_z}^*\,\bar{w} & \Gamma\,\overline{J\psi_z}^* & 0 \\
(\bar{\phi} - \bar{h}^*)\,\overline{\theta_\psi}^* & \bar{h}^*\,\overline{J\psi_x}^* - \Gamma\overline{\theta_\psi}^*\,\bar{u} & \bar{h}^*\,\overline{J\psi_y}^* - \Gamma\overline{\theta_\psi}^*\,\bar{v} & \bar{h}^*\,\overline{J\psi_z}^* - \Gamma\overline{\theta_\psi}^*\,\bar{w} & \gamma\,\overline{\theta_\psi}^* & 0 \\
-\breve{\bar{\nu}}\,\overline{\theta_\psi}^* & \overline{J\psi_x}^*\,\breve{\bar{\nu}} & \overline{J\psi_y}^*\,\breve{\bar{\nu}} & \overline{J\psi_z}^*\,\breve{\bar{\nu}} & 0 & \overline{\theta_\psi}^*
\end{pmatrix},$$

$$\text{with} \quad \bar{\phi} = \Gamma\,(\bar{u}^2 + \bar{v}^2 + \bar{w}^2) \;/\; 2\,; \tag{A.31}$$

originally provided in [99, 100] for two dimensions.

The matrix of $\underline{\overline{\mathbf{K}_\psi}^*}$-pertinent linearly independent right eigenvectors then results to

$$\mathbf{R}^{\overline{\mathbf{K}_\psi}^*} =$$

$$\begin{pmatrix}
\overline{J\psi_x}^\star & \overline{J\psi_y}^\star & \overline{J\psi_z}^\star & \underline{\bar\sigma^*} & \underline{\bar\sigma^*} & 0 \\
\underline{\bar u}\,\overline{J\psi_x}^\star & \begin{matrix}\underline{\bar u}\,\overline{J\psi_y}^\star \\ -\underline{\bar\rho}\,\overline{J\psi_z}^\star\end{matrix} & \begin{matrix}\underline{\bar u}\,\overline{J\psi_z}^\star \\ +\underline{\bar\rho}\,\overline{J\psi_y}^\star\end{matrix} & \underline{\bar\sigma^*}\left(\underline{\bar u} + \overline{a_x}^\star\right) & \underline{\bar\sigma^*}\left(\underline{\bar u} - \overline{a_x}^\star\right) & 0 \\
\begin{matrix}\underline{\bar v}\,\overline{J\psi_x}^\star \\ +\underline{\bar\rho}\,\overline{J\psi_z}^\star\end{matrix} & \underline{\bar v}\,\overline{J\psi_y}^\star & \begin{matrix}\underline{\bar v}\,\overline{J\psi_z}^\star \\ -\underline{\bar\rho}\,\overline{J\psi_x}^\star\end{matrix} & \underline{\bar\sigma^*}\left(\underline{\bar v} + \overline{a_y}^\star\right) & \underline{\bar\sigma^*}\left(\underline{\bar v} - \overline{a_y}^\star\right) & 0 \\
\begin{matrix}\underline{\bar w}\,\overline{J\psi_x}^\star \\ -\underline{\bar\rho}\,\overline{J\psi_y}^\star\end{matrix} & \begin{matrix}\underline{\bar w}\,\overline{J\psi_y}^\star \\ +\underline{\bar\rho}\,\overline{J\psi_x}^\star\end{matrix} & \underline{\bar w}\,\overline{J\psi_z}^\star & \underline{\bar\sigma^*}\left(\underline{\bar w} + \overline{a_z}^\star\right) & \underline{\bar\sigma^*}\left(\underline{\bar w} - \overline{a_z}^\star\right) & 0 \\
\begin{matrix}\underline{\bar\phi}\,\Gamma^{-1}\overline{J\psi_x}^\star \\ -\underline{\overline{\Omega_{\psi,x}}^\star}\,\underline{\bar\rho}\end{matrix} & \begin{matrix}\underline{\bar\phi}\,\Gamma^{-1}\overline{J\psi_y}^\star \\ -\underline{\overline{\Omega_{\psi,y}}^\star}\,\underline{\bar\rho}\end{matrix} & \begin{matrix}\underline{\bar\phi}\,\Gamma^{-1}\overline{J\psi_z}^\star \\ -\underline{\overline{\Omega_{\psi,z}}^\star}\,\underline{\bar\rho}\end{matrix} & \underline{\bar\sigma^*}\left(\underline{\bar h}^* + \underline{\bar a^*}\,\overline{\theta_\psi}^\star\right) & \underline{\bar\sigma^*}\left(\underline{\bar h}^* - \underline{\bar a^*}\,\overline{\theta_\psi}^\star\right) & 0 \\
0 & 0 & 0 & \underline{\bar\sigma^*}\,\overline{\breve\nu} & \underline{\bar\sigma^*}\,\overline{\breve\nu} & \overline{\breve\nu}
\end{pmatrix},$$

$$\text{with} \quad \overline{\theta_\psi}^\star = \overline{J\psi_x}^\star\,\underline{\bar u} + \overline{J\psi_y}^\star\,\underline{\bar v} + \overline{J\psi_z}^\star\,\underline{\bar w}\,;$$

$$\underline{\overline{\Omega_{\psi,x}}^\star} = \overline{J\psi_y}^\star\,\underline{\bar w} - \overline{J\psi_z}^\star\,\underline{\bar v}\,,\ \underline{\overline{\Omega_{\psi,y}}^\star} = \overline{J\psi_z}^\star\,\underline{\bar u} - \overline{J\psi_x}^\star\,\underline{\bar w}\,,\ \underline{\overline{\Omega_{\psi,z}}^\star} = \overline{J\psi_x}^\star\,\underline{\bar v} - \overline{J\psi_y}^\star\,\underline{\bar u}\,;$$

$$\underline{\bar\sigma^*} = \underline{\bar\rho}\,/(2\underline{\bar a^*})\,, \quad \underline{\bar a^*} = \sqrt{\Gamma\underline{\bar h^*} - \underline{\bar\phi}}\,;$$

$$\underline{\overline{a_x}^\star} = \underline{\bar a^*}\,\overline{J\psi_x}^\star\,, \quad \underline{\overline{a_y}^\star} = \underline{\bar a^*}\,\overline{J\psi_y}^\star\,, \quad \underline{\overline{a_z}^\star} = \underline{\bar a^*}\,\overline{J\psi_z}^\star\,;$$

$$\overline{J\psi_x}^\star = \overline{J\psi_x}^*/\,|\overline{\boldsymbol{J\psi}}^*|\,, \quad \overline{J\psi_y}^\star = \overline{J\psi_y}^*/\,|\overline{\boldsymbol{J\psi}}^*|\,, \quad \overline{J\psi_z}^\star = \overline{J\psi_z}^*/\,|\overline{\boldsymbol{J\psi}}^*|\,,$$

$$\text{and} \quad |\overline{\boldsymbol{J\psi}}^*| = \sqrt{(\overline{J\psi_x}^*)^2 + (\overline{J\psi_y}^*)^2 + (\overline{J\psi_z}^*)^2}\,. \tag{A.32}$$

Complementarily, its left eigenvector counterpart becomes

$$\mathbf{L}^{\overline{\mathbf{K}_\psi}^*} = (\mathbf{R}^{\overline{\mathbf{K}_\psi}^*})^{-1} =$$

$$\begin{pmatrix}
\begin{matrix}\overline{J\psi_x}^\star\left[1-\bar{\phi}\,(\bar{a}^*)^{-2}\right]\\ +\overline{\Omega_{\psi,x}}^\star\,\bar{\rho}^{-1}\end{matrix} & \overline{J\psi_x}^\star\,\bar{u}\,\bar{\varphi}^* & \begin{matrix}\overline{J\psi_x}^\star\,\bar{v}\,\bar{\varphi}^*\\ +\overline{J\psi_z}^\star\,\bar{\rho}^{-1}\end{matrix} & \begin{matrix}\overline{J\psi_x}^\star\,\bar{w}\,\bar{\varphi}^*\\ -\overline{J\psi_y}^\star\,\bar{\rho}^{-1}\end{matrix} & -\overline{J\psi_x}^\star\,\bar{\varphi}^* & 0\\
\begin{matrix}\overline{J\psi_y}^\star\left[1-\bar{\phi}\,(\bar{a}^*)^{-2}\right]\\ +\overline{\Omega_{\psi,y}}^\star\,\bar{\rho}^{-1}\end{matrix} & \begin{matrix}\overline{J\psi_y}^\star\,\bar{u}\,\bar{\varphi}^*\\ -\overline{J\psi_z}^\star\,\bar{\rho}^{-1}\end{matrix} & \overline{J\psi_y}^\star\,\bar{v}\,\bar{\varphi}^* & \begin{matrix}\overline{J\psi_y}^\star\,\bar{w}\,\bar{\varphi}^*\\ +\overline{J\psi_x}^\star\,\bar{\rho}^{-1}\end{matrix} & -\overline{J\psi_y}^\star\,\bar{\varphi}^* & 0\\
\begin{matrix}\overline{J\psi_z}^\star\left[1-\bar{\phi}\,(\bar{a}^*)^{-2}\right]\\ +\overline{\Omega_{\psi,z}}^\star\,\bar{\rho}^{-1}\end{matrix} & \begin{matrix}\overline{J\psi_z}^\star\,\bar{u}\,\bar{\varphi}^*\\ +\overline{J\psi_y}^\star\,\bar{\rho}^{-1}\end{matrix} & \begin{matrix}\overline{J\psi_z}^\star\,\bar{v}\,\bar{\varphi}^*\\ -\overline{J\psi_x}^\star\,\bar{\rho}^{-1}\end{matrix} & \overline{J\psi_z}^\star\,\bar{w}\,\bar{\varphi}^* & -\overline{J\psi_z}^\star\,\bar{\varphi}^* & 0\\
\bar{\vartheta}^*\left(\bar{\phi}-\bar{a}^*\,\overline{\theta_\psi}^\star\right) & \begin{matrix}\bar{\vartheta}^*\,\overline{a_x}^\star\\ -\bar{\vartheta}^*\,\bar{u}\,\Gamma\end{matrix} & \begin{matrix}\bar{\vartheta}^*\,\overline{a_y}^\star\\ -\bar{\vartheta}^*\,\bar{v}\,\Gamma\end{matrix} & \begin{matrix}\bar{\vartheta}^*\,\overline{a_z}^\star\\ -\bar{\vartheta}^*\,\bar{w}\,\Gamma\end{matrix} & \bar{\vartheta}^*\Gamma & 0\\
\bar{\vartheta}^*\left(\bar{\phi}+\bar{a}^*\,\overline{\theta_\psi}^\star\right) & \begin{matrix}-\bar{\vartheta}^*\overline{a_x}^\star\\ -\bar{\vartheta}^*\,\bar{u}\,\Gamma\end{matrix} & \begin{matrix}-\bar{\vartheta}^*\overline{a_y}^\star\\ -\bar{\vartheta}^*\,\bar{v}\,\Gamma\end{matrix} & \begin{matrix}-\bar{\vartheta}^*\overline{a_z}^\star\\ -\bar{\vartheta}^*\,\bar{w}\,\Gamma\end{matrix} & \bar{\vartheta}^*\Gamma & 0\\
-\bar{\phi}\,(\bar{a}^*)^{-2} & \bar{u}\,\bar{\varphi}^* & \bar{v}\,\bar{\varphi}^* & \bar{w}\,\bar{\varphi}^* & -\bar{\varphi}^* & \bar{\nu}^{-1}
\end{pmatrix},$$

$$\text{with}\quad \bar{\varphi}^* = \Gamma(\bar{a}^*)^{-2}\quad\text{and}\quad \bar{\vartheta}^* = (\bar{\rho}\,\bar{a}^*)^{-1}\,, \tag{A.33}$$

while the matrix of the modified $\overline{\mathbf{K}_\psi}^*$-eigenvalues is

$$\left|\mathbf{\Lambda}^{\overline{\mathbf{K}_\psi}^*}\right|_{\bar{\delta}^*} = \begin{pmatrix}
\left|\overline{\theta_\psi}^*\right|_{\bar{\delta}^*} & & & & & & \\
& \left|\overline{\theta_\psi}^*\right|_{\bar{\delta}^*} & & & 0 & & \\
& & \left|\overline{\theta_\psi}^*\right|_{\bar{\delta}^*} & & & & \\
& & & \left|\begin{matrix}\overline{\theta_\psi}^*\\ +\,\bar{a}^*|\overline{\boldsymbol{J\psi}}^*|\end{matrix}\right|_{\bar{\delta}^*} & & & \\
& & 0 & & \left|\begin{matrix}\overline{\theta_\psi}^*\\ -\,\bar{a}^*|\overline{\boldsymbol{J\psi}}^*|\end{matrix}\right|_{\bar{\delta}^*} & & \\
& & & & & \left|\overline{\theta_\psi}^*\right|_{\bar{\delta}^*}
\end{pmatrix},$$

$$\text{wherein}\quad \overline{\theta_\psi}^* = \overline{J\psi_x}^*\,\bar{u} + \overline{J\psi_y}^*\,\bar{v} + \overline{J\psi_z}^*\,\bar{w}\quad\in\mathbb{R} \tag{A.34}$$

[70].

Further following Kreiselmaier [70], as well as Sickmüller [119], the eigenvalue-applied

modifier is devised as a continuously differentiable approximation of the absolute value function:

$$\left| \underline{\overline{\Lambda_\psi}^*} \right|_{\underline{\bar{\delta}^*}} := \begin{cases} \left| \underline{\overline{\Lambda_\psi}^*} \right| & ; \quad \left| \underline{\overline{\Lambda_\psi}^*} \right| \geq \underline{\bar{\delta}^*} \\ \left[\left(\underline{\overline{\Lambda_\psi}^*} \right)^2 + (\underline{\bar{\delta}^*})^2 \right] / (2\underline{\bar{\delta}^*}) & ; \quad \left| \underline{\overline{\Lambda_\psi}^*} \right| < \underline{\bar{\delta}^*} \end{cases} \tag{A.35}$$

with either

$$\underline{\overline{\Lambda_\psi}^*} := \underline{\overline{\theta_\psi}^*} \quad \text{or} \quad \underline{\overline{\Lambda_\psi}^*} := \underline{\overline{\theta_\psi}^*} \pm \underline{\bar{a}^*} \, |\overline{\boldsymbol{J}\boldsymbol{\psi}}^*| \,, \quad \text{and} \quad \underline{\bar{\delta}^*} > 0 \,. \tag{A.36}$$

On one hand, the eigenvalues positivity is forced in this manner, rendering the desired upwind evaluation of the particular $\hat{\mathbf{q}}$-homogenous convective flux vector. On the other hand, the eigenvalues are limited to a minimum value, which is equivalent to adding an artificial dissipation term. [70, 119]. For $\underline{\bar{\Lambda}^*_\psi} := \underline{\overline{\theta_\psi}^*} \pm \underline{\bar{a}^*} \, |\overline{\boldsymbol{J}\boldsymbol{\psi}}^*|$, Eq. (A.35) traces back to Harten [45], who originally introduced the limitation to restore the entropy inequality [48] violated in Roe's approximate Riemann-solver [111] by a vanishing acoustic eigenvalue [16]. At flowfield localities where the Cartesian velocity vector turns to nil or becomes perpendicular to the surface vector of the considered cell interface, the entropic eigenvalue will equally vanish [16]. Thus, the limitation is reasonably applied to $\underline{\overline{\theta_\psi}^*}$ as well [16, 70, 119]. Pursuant to the FLM-SDEu implementation [70], $\underline{\bar{\delta}^*}$ is specified with respect to the largest locally possible eigenvalue:

$$\underline{\bar{\delta}^*} := \delta_d \left(|\, \underline{\overline{\theta_\psi}^*} \,| + \underline{\bar{a}^*} \, |\overline{\boldsymbol{J}\boldsymbol{\psi}}^*| \right) , \tag{A.37}$$

with the scaling parameter $\delta_d > 0$ then allowing user-control over the artificial dissipation [70]. In contrast to the behavior of the numerical dissipation inherent to the LU-SSOR scheme as adjusted by ω_d, an increase of δ_d [70, 119] will enhance stability, while favorably affecting the rate of convergence toward the desired pseudosteady state. Whereas the value of ω_d does not impact the validity of the solution, the value of δ_d can substantially alter it if the artificial dissipation increases to the order of magnitude of the physical instance. Thus, special care needs to be taken when setting δ_d, i.e., merely high enough to satisfy the entropy inequality [70, 119]. Concerning the computations in this dissertation, δ_d had been empirically set for each particular case, varying between 0.0015 and 0.045.

Lastly, $\widehat{\mathbf{F}}^{(2)}_{i-1/2,\,j,\,k}$ is considered. Its evaluation [70, 119] again takes into account the interface-proximate left- and right-side state, respectively, $\widehat{\mathbf{F}}^{(2)\,L}$ and $\widehat{\mathbf{F}}^{(2)\,R}$, in conjunction with the $\widehat{\mathbf{F}}^{(2)}$-pertinent Jacobian matrix $\widehat{\mathbf{K}_\xi}^{(2)}$ formulated with the Roe averages [111] of the constituting primitive variables' left- and right-side state at the interface; i.e., $\underline{\widehat{\mathbf{K}_\xi}^{(2)}}_{i-1/2,\,j,\,k}$. Equally eigendecomposing the latter and modifying the exposed eigenvalues then yields

$$\widehat{\mathbf{F}}^{(2)}_{i-1/2,\,j,\,k} = \left[\widehat{\mathbf{F}}^{(2)\,L} + \widehat{\mathbf{F}}^{(2)\,R} - \mathbf{R}_{\widehat{\mathbf{K}_\xi}^{(2)}_{i-1/2,\,j,\,k}} \left| \mathbf{\Lambda}_{\widehat{\mathbf{K}_\xi}^{(2)}_{i-1/2,\,j,\,k}} \right|_\delta \mathbf{L}_{\widehat{\mathbf{K}_\xi}^{(2)}_{i-1/2,\,j,\,k}} \left(\bar{\mathbf{q}}^{*R} - \bar{\mathbf{q}}^{*L} \right) \right] \, / \, 2 \,, \tag{A.38}$$

wherein

$$\widehat{\mathbf{F}}^{(2)\,L} := \widehat{\mathbf{F}}^{(2)}\left(\bar{\mathbf{q}}^{*L},\, \widehat{\boldsymbol{J\xi}}_{i-1/2,\,j,\,k}\right) \quad \text{and} \quad \widehat{\mathbf{F}}^{(2)\,R} := \widehat{\mathbf{F}}^{(2)}\left(\bar{\mathbf{q}}^{*R},\, \widehat{\boldsymbol{J\xi}}_{i-1/2,\,j,\,k}\right). \tag{A.39}$$

$\widehat{\mathbf{F}}^{(2)}_{i-1/2,\,j,\,k}$ is invariant throughout the pseudotime integration, likewise evaluated only once during the algorithm's initialization procedure [70, 119].

Returning to the generalized notation, the Jacobian matrix of a $\widehat{\boldsymbol{J\psi}}$-homogenous convective flux vector is defined on basis of Kreiselmaier [70] as

$$\widehat{\mathbf{K}_{\psi}}^{(2)} := \partial\widehat{\mathbf{E}_{\psi}}^{(2)} / \,\partial\bar{\mathbf{q}}^{*}\,. \tag{A.40}$$

Furthermore, the matrix of $\underline{\widehat{\mathbf{K}_{\psi}}^{(2)}}$-pertinent linearly independent right eigenvectors results to

$$\mathbf{R}^{\underline{\widehat{\mathbf{K}_{\psi}}^{(2)}}} =$$

$$\begin{pmatrix}
\widehat{J\psi_x}^{\star} & \widehat{J\psi_y}^{\star} & \widehat{J\psi_z}^{\star} & \underline{\bar{\sigma}^{*}} & \underline{\bar{\sigma}^{*}} & 0 \\
\underline{\bar{u}}\widehat{J\psi_x}^{\star} & \begin{matrix}\underline{\bar{u}}\widehat{J\psi_y}^{\star} \\ -\underline{\bar{\rho}}\widehat{J\psi_z}^{\star}\end{matrix} & \begin{matrix}\underline{\bar{u}}\widehat{J\psi_z}^{\star} \\ +\underline{\bar{\rho}}\widehat{J\psi_y}^{\star}\end{matrix} & \underline{\bar{\sigma}^{*}}\left(\underline{\bar{u}} + \underline{\widehat{a}_x^{(2)\star}}\right) & \underline{\bar{\sigma}^{*}}\left(\underline{\bar{u}} - \underline{\widehat{a}_x^{(2)\star}}\right) & 0 \\
\begin{matrix}\underline{\bar{v}}\widehat{J\psi_x}^{\star} \\ +\underline{\bar{\rho}}\widehat{J\psi_z}^{\star}\end{matrix} & \underline{\bar{v}}\widehat{J\psi_y}^{\star} & \begin{matrix}\underline{\bar{v}}\widehat{J\psi_z}^{\star} \\ -\underline{\bar{\rho}}\widehat{J\psi_x}^{\star}\end{matrix} & \underline{\bar{\sigma}^{*}}\left(\underline{\bar{v}} + \underline{\widehat{a}_y^{(2)\star}}\right) & \underline{\bar{\sigma}^{*}}\left(\underline{\bar{v}} - \underline{\widehat{a}_y^{(2)\star}}\right) & 0 \\
\begin{matrix}\underline{\bar{w}}\widehat{J\psi_x}^{\star} \\ -\underline{\bar{\rho}}\widehat{J\psi_y}^{\star}\end{matrix} & \begin{matrix}\underline{\bar{w}}\widehat{J\psi_y}^{\star} \\ +\underline{\bar{\rho}}\widehat{J\psi_x}^{\star}\end{matrix} & \underline{\bar{w}}\widehat{J\psi_z}^{\star} & \underline{\bar{\sigma}^{*}}\left(\underline{\bar{w}} + \underline{\widehat{a}_z^{(2)\star}}\right) & \underline{\bar{\sigma}^{*}}\left(\underline{\bar{w}} - \underline{\widehat{a}_z^{(2)\star}}\right) & 0 \\
\begin{matrix}\underline{\bar{\phi}}\Gamma^{-1}\widehat{J\psi_x}^{\star} \\ -\underline{\widehat{\Omega}_{\psi,x}^{(2)\star}}\,\underline{\bar{\rho}}\end{matrix} & \begin{matrix}\underline{\bar{\phi}}\Gamma^{-1}\widehat{J\psi_y}^{\star} \\ -\underline{\widehat{\Omega}_{\psi,y}^{(2)\star}}\,\underline{\bar{\rho}}\end{matrix} & \begin{matrix}\underline{\bar{\phi}}\Gamma^{-1}\widehat{J\psi_z}^{\star} \\ -\underline{\widehat{\Omega}_{\psi,z}^{(2)\star}}\,\underline{\bar{\rho}}\end{matrix} & \begin{matrix}\underline{\bar{\sigma}^{*}}\,\underline{\bar{h}^{*}} \\ +\underline{\bar{\sigma}^{*}}\,\underline{\bar{a}^{*}}\,\underline{\widehat{\theta}_{\psi}^{(2)\dagger\star}}\end{matrix} & \begin{matrix}\underline{\bar{\sigma}^{*}}\,\underline{\bar{h}^{*}} \\ -\underline{\bar{\sigma}^{*}}\,\underline{\bar{a}^{*}}\,\underline{\widehat{\theta}_{\psi}^{(2)\dagger\star}}\end{matrix} & 0 \\
0 & 0 & 0 & \underline{\bar{\sigma}^{*}}\,\underline{\bar{\nu}} & \underline{\bar{\sigma}^{*}}\,\underline{\bar{\nu}} & \underline{\bar{\nu}}
\end{pmatrix},$$

$$\text{with} \quad \underline{\widehat{\theta}_{\psi}^{(2)\dagger\star}} = \widehat{J\psi_x}^{\star}\,\underline{\bar{u}} + \widehat{J\psi_y}^{\star}\,\underline{\bar{v}} + \widehat{J\psi_z}^{\star}\,\underline{\bar{w}}\,;$$

$$\underline{\widehat{\Omega}_{\psi,x}^{(2)\star}} = \widehat{J\psi_y}^{\star}\,\underline{\bar{w}} - \widehat{J\psi_z}^{\star}\,\underline{\bar{v}}\,, \quad \underline{\widehat{\Omega}_{\psi,y}^{(2)\star}} = \widehat{J\psi_z}^{\star}\,\underline{\bar{u}} - \widehat{J\psi_x}^{\star}\,\underline{\bar{w}}\,, \quad \underline{\widehat{\Omega}_{\psi,z}^{(2)\star}} = \widehat{J\psi_x}^{\star}\,\underline{\bar{v}} - \widehat{J\psi_y}^{\star}\,\underline{\bar{u}}\,;$$

$$\underline{\widehat{a}_x^{(2)\star}} = \underline{\bar{a}^{*}}\,\widehat{J\psi_x}^{\star}\,, \quad \underline{\widehat{a}_y^{(2)\star}} = \underline{\bar{a}^{*}}\,\widehat{J\psi_y}^{\star}\,, \quad \underline{\widehat{a}_z^{(2)\star}} = \underline{\bar{a}^{*}}\,\widehat{J\psi_z}^{\star}\,;$$

$$\widehat{J\psi_x}^{\star} = \widehat{J\psi_x} \,/\, |\widehat{\boldsymbol{J\psi}}|\,, \quad \widehat{J\psi_y}^{\star} = \widehat{J\psi_y} \,/\, |\widehat{\boldsymbol{J\psi}}|\,, \quad \widehat{J\psi_z}^{\star} = \widehat{J\psi_z} \,/\, |\widehat{\boldsymbol{J\psi}}|\,,$$

$$\text{and} \quad |\widehat{\boldsymbol{J\psi}}| = \sqrt{\widehat{J\psi_x}^{2} + \widehat{J\psi_y}^{2} + \widehat{J\psi_z}^{2}}\,. \tag{A.41}$$

Complementarily, its left eigenvector counterpart becomes

$$\mathbf{L}^{\widehat{\mathbf{K}_\psi}^{(2)}} = (\mathbf{R}^{\widehat{\mathbf{K}_\psi}^{(2)}})^{-1} =$$

$$\begin{pmatrix}
\widehat{J\psi_x}^{\star}\left[1-\underline{\bar{\phi}}\,(\underline{\bar{a}^*})^{-2}\right] & \widehat{J\psi_x}^{\star}\,\underline{\bar{u}}\,\underline{\bar{\varphi}^*} & \widehat{J\psi_x}^{\star}\,\underline{\bar{v}}\,\underline{\bar{\varphi}^*} & \widehat{J\psi_x}^{\star}\,\underline{\bar{w}}\,\underline{\bar{\varphi}^*} & -\widehat{J\psi_x}^{\star}\,\underline{\bar{\varphi}^*} & 0 \\
+\underline{\widehat{\Omega}_{\psi,x}^{(2)\star}}\,\underline{\bar{\rho}}^{-1} & & +\widehat{J\psi_z}^{\star}\,\bar{\rho}^{-1} & -\widehat{J\psi_y}^{\star}\,\underline{\bar{\rho}}^{-1} & & \\
\widehat{J\psi_y}^{\star}\left[1-\underline{\bar{\phi}}\,(\underline{\bar{a}^*})^{-2}\right] & \widehat{J\psi_y}^{\star}\,\underline{\bar{u}}\,\underline{\bar{\varphi}^*} & \widehat{J\psi_y}^{\star}\,\underline{\bar{v}}\,\underline{\bar{\varphi}^*} & \widehat{J\psi_y}^{\star}\,\underline{\bar{w}}\,\underline{\bar{\varphi}^*} & -\widehat{J\psi_y}^{\star}\,\underline{\bar{\varphi}^*} & 0 \\
+\underline{\widehat{\Omega}_{\psi,y}^{(2)\star}}\,\underline{\bar{\rho}}^{-1} & -\widehat{J\psi_z}^{\star}\,\underline{\bar{\rho}}^{-1} & & +\widehat{J\psi_x}^{\star}\,\underline{\bar{\rho}}^{-1} & & \\
\widehat{J\psi_z}^{\star}\left[1-\underline{\bar{\phi}}\,(\underline{\bar{a}^*})^{-2}\right] & \widehat{J\psi_z}^{\star}\,\underline{\bar{u}}\,\underline{\bar{\varphi}^*} & \widehat{J\psi_z}^{\star}\,\underline{\bar{v}}\,\underline{\bar{\varphi}^*} & \widehat{J\psi_z}^{\star}\,\underline{\bar{w}}\,\underline{\bar{\varphi}^*} & -\widehat{J\psi_z}^{\star}\,\underline{\bar{\varphi}^*} & 0 \\
+\underline{\widehat{\Omega}_{\psi,z}^{(2)\star}}\,\underline{\bar{\rho}}^{-1} & +\widehat{J\psi_y}^{\star}\,\underline{\bar{\rho}}^{-1} & -\widehat{J\psi_x}^{\star}\,\underline{\bar{\rho}}^{-1} & & & \\
\underline{\bar{\vartheta}^*}\left(\underline{\bar{\phi}}-\underline{\bar{a}^*}\,\underline{\widehat{\theta}_\psi^{(2)\dagger\star}}\right) & \underline{\bar{\vartheta}^*}\,\underline{\widehat{a}_x^{(2)\star}} & \underline{\bar{\vartheta}^*}\,\underline{\widehat{a}_y^{(2)\star}} & \underline{\bar{\vartheta}^*}\,\underline{\widehat{a}_z^{(2)\star}} & \underline{\bar{\vartheta}^*}\Gamma & 0 \\
 & -\underline{\bar{\vartheta}^*}\,\underline{\bar{u}}\,\Gamma & -\underline{\bar{\vartheta}^*}\,\underline{\bar{v}}\,\Gamma & -\underline{\bar{\vartheta}^*}\,\underline{\bar{w}}\,\Gamma & & \\
\underline{\bar{\vartheta}^*}\left(\underline{\bar{\phi}}+\underline{\bar{a}^*}\,\underline{\widehat{\theta}_\psi^{(2)\dagger\star}}\right) & -\underline{\bar{\vartheta}^*}\,\underline{\widehat{a}_x^{(2)\star}} & -\underline{\bar{\vartheta}^*}\,\underline{\widehat{a}_y^{(2)\star}} & -\underline{\bar{\vartheta}^*}\,\underline{\widehat{a}_z^{(2)\star}} & \underline{\bar{\vartheta}^*}\Gamma & 0 \\
 & -\underline{\bar{\vartheta}^*}\,\underline{\bar{u}}\,\Gamma & -\underline{\bar{\vartheta}^*}\,\underline{\bar{v}}\,\Gamma & -\underline{\bar{\vartheta}^*}\bar{w}\,\Gamma & & \\
-\underline{\bar{\phi}}\,(\underline{\bar{a}^*})^{-2} & \underline{\bar{u}}\,\underline{\bar{\varphi}^*} & \underline{\bar{v}}\,\underline{\bar{\varphi}^*} & \underline{\bar{w}}\,\underline{\bar{\varphi}^*} & -\underline{\bar{\varphi}^*} & \underline{\breve{\nu}}^{-1}
\end{pmatrix}, \tag{A.42}$$

while the matrix of the modified $\underline{\widehat{\mathbf{K}}_\psi^{(2)}}$-eigenvalues is

$$|\,\mathbf{\Lambda}^{\widehat{\mathbf{K}_\psi}^{(2)}}|_{\underline{\bar{\delta}^*}} = \begin{pmatrix}
|\,\underline{\widehat{\theta}_\psi^{(2)}}|_{\underline{\bar{\delta}^*}} & & & & & \\
 & |\,\underline{\widehat{\theta}_\psi^{(2)}}|_{\underline{\bar{\delta}^*}} & & 0 & & \\
 & & |\,\underline{\widehat{\theta}_\psi^{(2)}}|_{\underline{\bar{\delta}^*}} & & & \\
 & & & \left|\,\underline{\widehat{\theta}_\psi^{(2)}} + \underline{\bar{a}^*}|\widehat{\boldsymbol{J\psi}}|\,\right|_{\underline{\bar{\delta}^*}} & & \\
 & 0 & & & \left|\,\underline{\widehat{\theta}_\psi^{(2)}} - \underline{\bar{a}^*}|\widehat{\boldsymbol{J\psi}}|\,\right|_{\underline{\bar{\delta}^*}} & \\
 & & & & & |\,\underline{\widehat{\theta}_\psi^{(2)}}|_{\underline{\bar{\delta}^*}}
\end{pmatrix},$$

$$\text{with} \quad \underline{\widehat{\theta}_\psi^{(2)}} = \widehat{J\psi_x}\,\underline{\bar{u}} + \widehat{J\psi_y}\,\underline{\bar{v}} + \widehat{J\psi_z}\,\underline{\bar{w}} + \widehat{J\psi_t} \quad \in \mathbb{C} \tag{A.43}$$

[70].

The eigenvalue-applied modifier is given as

$$\left| \underline{\widehat{\Lambda_\psi}^{(2)}} \right|_{\underline{\bar{\delta}^*}} := \begin{cases} \underline{\overline{\Lambda_\psi}^*}\, \underline{\widehat{\Lambda_\psi}^{(2)}} \,/\, \left| \underline{\overline{\Lambda_\psi}^*} \right| & ; \quad \left| \underline{\overline{\Lambda_\psi}^*} \right| \geq \underline{\bar{\delta}^*} \\ \underline{\overline{\Lambda_\psi}^*}\, \underline{\widehat{\Lambda_\psi}^{(2)}} \,/\, \underline{\bar{\delta}^*} & ; \quad \left| \underline{\overline{\Lambda_\psi}^*} \right| < \underline{\bar{\delta}^*} \end{cases} \tag{A.44}$$

with either

$$\underline{\overline{\Lambda_\psi}^*} := \underline{\overline{\theta_\psi}^*} \qquad \text{and} \qquad \underline{\widehat{\Lambda_\psi}^{(2)}} := \underline{\widehat{\theta_\psi}^{(2)}} \tag{A.45}$$

or

$$\underline{\overline{\Lambda_\psi}^*} := \underline{\overline{\theta_\psi}^*} \pm \underline{\bar{a}^*}\, |\overline{\boldsymbol{J\psi}}^*| \qquad \text{and} \qquad \underline{\widehat{\Lambda_\psi}^{(2)}} := \underline{\widehat{\theta_\psi}^{(2)}} \pm \underline{\bar{a}^*}\, |\widehat{\boldsymbol{J\psi}}| \,, \tag{A.46}$$

yielding from a first-order Taylor-series expansion of the conventional instance [45, 16] about the linearized time-invariant-mean state [70, 119].

It should be noted that the default evaluation of the $\widehat{\boldsymbol{J\psi}}$-homogenous convective flux vectors in FLM-SDEu had eventually been reduced by Kreiselmaier [70] to the mere arithmetic average between the particular left- and right-side state. To the author's knowledge, all FLM-SDEu computations preceding this dissertation were conducted with it. Maintaining consistency, the setting was retained for both the FLM-SDEu and FLM-SD.NS computations presented herein.

A.3 Far-Field Boundary Condition

In the following, Kreiselmaier's [70] small disturbance adaptation of the Whitfield-and-Janus-formulated far-field boundary condition [134] is provided as extended by the author for the incorporation of the S/A one-equation turbulence model [121, 99] into FLM-SD.NS. For the sake of formality, it takes into account an amplitude freestream state. An individual cell interface of a distinct block's directional starting or ending face is considered.

Pursuant to the FLM-SDEu implementation [70], the constraint is imposed in terms of the block-face-normal generalized curvilinear coordinate $\psi_{ffb,\,n}$. The linearized time-invariant-mean contravariant velocity associated with the first exterior centroid serves as the inflow/outflow criterion. For both the directional starting and ending face, it is evaluated with the linearized time-invariant-mean spatial metrics pertinent to the mutual interface of the first interior and first exterior cell:

$$\overline{\theta_\psi}^\star\Big|_{ext,\,n} := \overline{J\psi_x}^\star\Big|_{ffb,\,n} \bar{u}_{ext} + \overline{J\psi_y}^\star\Big|_{ffb,\,n} \bar{v}_{ext} + \overline{J\psi_z}^\star\Big|_{ffb,\,n} \bar{w}_{ext} \,. \tag{A.47}$$

Being common to an inflow and outflow far-field boundary, it is further stipulated that

$$\begin{aligned} \widehat{\theta_\psi}^{\star\,(1)}\Big|_{\infty,\,n} &:= \overline{J\psi_x}^\star\Big|_{ffb,\,n} \hat{u}_\infty + \overline{J\psi_y}^\star\Big|_{ffb,\,n} \hat{v}_\infty + \overline{J\psi_z}^\star\Big|_{ffb,\,n} \hat{w}_\infty \,, \\ \widehat{\theta_\psi}^{\star\,(1)}\Big|_{int,\,n} &:= \overline{J\psi_x}^\star\Big|_{ffb,\,n} \hat{u}_{int} + \overline{J\psi_y}^\star\Big|_{ffb,\,n} \hat{v}_{int} + \overline{J\psi_z}^\star\Big|_{ffb,\,n} \hat{w}_{int} \,, \end{aligned} \tag{A.48}$$

and

$$\begin{aligned}
\overline{\theta_\psi}^\star\Big|_{\infty,n} &:= \overline{J\psi_x}^\star\Big|_{ffb,n}\bar{u}_\infty + \overline{J\psi_y}^\star\Big|_{ffb,n}\bar{v}_\infty + \overline{J\psi_z}^\star\Big|_{ffb,n}\bar{w}_\infty\,, \\
\overline{\theta_\psi}^\star\Big|_{int,n} &:= \overline{J\psi_x}^\star\Big|_{ffb,n}\bar{u}_{int} + \overline{J\psi_y}^\star\Big|_{ffb,n}\bar{v}_{int} + \overline{J\psi_z}^\star\Big|_{ffb,n}\bar{w}_{int}\,.
\end{aligned} \tag{A.49}$$

An inflow far-field boundary then exists, if either

$\overline{\theta_\psi}^\star\Big|_{ext,n} > 0$ for the ψ-directional starting face, with the upper sign of the succeeding Eqs. (A.51–A.54) then being valid, or

$\overline{\theta_\psi}^\star\Big|_{ext,n} < 0$ for the ψ-directional ending face, with the lower sign of the succeeding Eqs. (A.51–A.54) then being valid. (A.50)

In the particular case of subsonic inflow, where the subsonic state is determined by $(\,\overline{\theta_\psi}^\star\Big|_{ext,n}\,/\,\bar{a}^*_{ext}\,)^2 < 1.0$ with $\bar{a}^*_{ext} = \sqrt{\gamma\,\bar{\rho}_{ext}\,\bar{p}^*_{ext}}\,/\,\bar{\rho}_{ext}$, the interface-corresponding amplitude static pressure, amplitude density, and amplitude Cartesian velocities are subsequently gained as

$$\begin{aligned}
\hat{p}_{ffb} &\approx \left[\hat{p}_\infty + \hat{p}_{int} \pm \bar{\rho}_{ext}\,\bar{a}^*_{ext}\left(\widehat{\theta_\psi}^{\star(1)}\Big|_{\infty,n} - \widehat{\theta_\psi}^{\star(1)}\Big|_{int,n}\right)\right] \;/\; 2\,, \\
\hat{\rho}_{ffb} &\approx \hat{\rho}_\infty - (\hat{p}_\infty - \hat{p}_{ffb})\,/\,(\bar{a}^*_{ext})^2\,, \\
\hat{u}_{ffb} &\approx \hat{u}_\infty \pm \overline{J\psi_x}^\star\Big|_{ffb,n}(\hat{p}_\infty - \hat{p}_{ffb})\,/\,(\bar{\rho}_{ext}\,\bar{a}^*_{ext})\,, \\
\hat{v}_{ffb} &\approx \hat{v}_\infty \pm \overline{J\psi_y}^\star\Big|_{ffb,n}(\hat{p}_\infty - \hat{p}_{ffb})\,/\,(\bar{\rho}_{ext}\,\bar{a}^*_{ext})\,, \\
\hat{w}_{ffb} &\approx \hat{w}_\infty \pm \overline{J\psi_z}^\star\Big|_{ffb,n}(\hat{p}_\infty - \hat{p}_{ffb})\,/\,(\bar{\rho}_{ext}\,\bar{a}^*_{ext})
\end{aligned} \tag{A.51}$$

[70]. The consistent extension for the amplitude S/A primitive working variable renders

$$\widehat{\breve{\nu}}_{ffb} \approx \widehat{\breve{\nu}}_\infty - (\hat{p}_\infty - \hat{p}_{ffb})\,\overline{\breve{\nu}}_{ext}\;/\;[\bar{\rho}_{ext}(\bar{a}^*_{ext})^2]\,. \tag{A.52}$$

Their linearized time-invariant-mean counterparts are

$$\begin{aligned}
\bar{p}^*_{ffb} &= \left[\bar{p}^*_\infty + \bar{p}^*_{int} \pm \bar{\rho}_{ext}\,\bar{a}^*_{ext}\left(\overline{\theta_\psi}^\star\Big|_{\infty,n} - \overline{\theta_\psi}^\star\Big|_{int,n}\right)\right] \;/\; 2\,, \\
\bar{\rho}_{ffb} &= \bar{\rho}_\infty - (\bar{p}^*_\infty - \bar{p}^*_{ffb})\,/\,(\bar{a}^*_{ext})^2\,, \\
\bar{u}_{ffb} &= \bar{u}_\infty \pm \overline{J\psi_x}^\star\Big|_{ffb,n}(\bar{p}^*_\infty - \bar{p}^*_{ffb})\,/\,(\bar{\rho}_{ext}\,\bar{a}^*_{ext})\,, \\
\bar{v}_{ffb} &= \bar{v}_\infty \pm \overline{J\psi_y}^\star\Big|_{ffb,n}(\bar{p}^*_\infty - \bar{p}^*_{ffb})\,/\,(\bar{\rho}_{ext}\,\bar{a}^*_{ext})\,, \\
\bar{w}_{ffb} &= \bar{w}_\infty \pm \overline{J\psi_z}^\star\Big|_{ffb,n}(\bar{p}^*_\infty - \bar{p}^*_{ffb})\,/\,(\bar{\rho}_{ext}\,\bar{a}^*_{ext})
\end{aligned} \tag{A.53}$$

[70], with

$$\overline{\breve{\nu}}_{ffb} \;=\; \overline{\breve{\nu}}_{\infty} - (\bar{p}^{*}_{\infty} - \bar{p}^{*}_{ffb})\,\overline{\breve{\nu}}_{ext} \;/\; [\bar{\rho}_{ext}(\bar{a}^{*}_{ext})^{2}] \tag{A.54}$$

introduced by the author. Complementarily [70], an outflow far-field boundary exists if either

$\overline{\theta_{\psi}}^{\star}\Big|_{ext,\,n} < 0$ for the ψ-directional starting face, with the upper sign of the succeeding Eqs. (A.56–A.59) then being valid, or

$\overline{\theta_{\psi}}^{\star}\Big|_{ext,\,n} > 0$ for the ψ-directional ending face, with the lower sign of the succeeding Eqs. (A.56–A.59) then being valid. (A.55)

In the particular case of subsonic outflow, the interface-corresponding amplitude static pressure, amplitude density, and amplitude Cartesian velocities are subsequently gained as

$$\begin{aligned}
\hat{p}_{ffb} &\approx \left[\hat{p}_{\infty} + \hat{p}_{int} \pm \bar{\rho}_{ext}\,\bar{a}^{*}_{ext}\left(\widehat{\theta_{\psi}}^{\star(1)}\Big|_{\infty,\,n} - \widehat{\theta_{\psi}}^{\star(1)}\Big|_{int,\,n}\right)\right] \;/\; 2\,,\\
\hat{\rho}_{ffb} &\approx \hat{\rho}_{int} + (\hat{p}_{ffb} - \hat{p}_{int}) \,/\, (\bar{a}^{*}_{ext})^{2}\,,\\
\hat{u}_{ffb} &\approx \hat{u}_{int} \pm \overline{J\psi_{x}}^{\star}\Big|_{ffb,\,n}\,(\hat{p}_{ffb} - \hat{p}_{int}) \,/\, (\bar{\rho}_{ext}\,\bar{a}^{*}_{ext})\,,\\
\hat{v}_{ffb} &\approx \hat{v}_{int} \pm \overline{J\psi_{y}}^{\star}\Big|_{ffb,\,n}\,(\hat{p}_{ffb} - \hat{p}_{int}) \,/\, (\bar{\rho}_{ext}\,\bar{a}^{*}_{ext})\,,\\
\hat{w}_{ffb} &\approx \hat{w}_{int} \pm \overline{J\psi_{z}}^{\star}\Big|_{ffb,\,n}\,(\hat{p}_{ffb} - \hat{p}_{int}) \,/\, (\bar{\rho}_{ext}\,\bar{a}^{*}_{ext})
\end{aligned} \tag{A.56}$$

[70]. The consistent extension for the amplitude S/A primitive working variable renders

$$\widehat{\breve{\nu}}_{ffb} \;\approx\; \widehat{\breve{\nu}}_{int} + (\hat{p}_{ffb} - \hat{p}_{int})\,\overline{\breve{\nu}}_{ext} \;/\; [\bar{\rho}_{ext}(\bar{a}^{*}_{ext})^{2}]\;. \tag{A.57}$$

Their linearized time-invariant-mean counterparts are

$$\begin{aligned}
\bar{p}^{*}_{ffb} &= \left[\bar{p}^{*}_{\infty} + \bar{p}^{*}_{int} \pm \bar{\rho}_{ext}\,\bar{a}^{*}_{ext}\left(\overline{\theta_{\psi}}^{\star}\Big|_{\infty,\,n} - \overline{\theta_{\psi}}^{\star}\Big|_{int,\,n}\right)\right] \;/\; 2\,,\\
\bar{\rho}_{ffb} &= \bar{\rho}_{int} + (\bar{p}^{*}_{ffb} - \bar{p}^{*}_{int}) \,/\, (\bar{a}^{*}_{ext})^{2}\,,\\
\bar{u}_{ffb} &= \bar{u}_{int} \pm \overline{J\psi_{x}}^{\star}\Big|_{ffb,\,n}\,(\bar{p}^{*}_{ffb} - \bar{p}^{*}_{int}) \,/\, (\bar{\rho}_{ext}\,\bar{a}^{*}_{ext})\,,\\
\bar{v}_{ffb} &= \bar{v}_{int} \pm \overline{J\psi_{y}}^{\star}\Big|_{ffb,\,n}\,(\bar{p}^{*}_{ffb} - \bar{p}^{*}_{int}) \,/\, (\bar{\rho}_{ext}\,\bar{a}^{*}_{ext})\,,\\
\bar{w}_{ffb} &= \bar{w}_{int} \pm \overline{J\psi_{z}}^{\star}\Big|_{ffb,\,n}\,(\bar{p}^{*}_{ffb} - \bar{p}^{*}_{int}) \,/\, (\bar{\rho}_{ext}\,\bar{a}^{*}_{ext})
\end{aligned} \tag{A.58}$$

[70], with

$$\overline{\breve{\nu}}_{ffb} \;=\; \overline{\breve{\nu}}_{int} + (\bar{p}^{*}_{ffb} - \bar{p}^{*}_{int})\,\overline{\breve{\nu}}_{ext} \;/\; [\bar{\rho}_{ext}(\bar{a}^{*}_{ext})^{2}] \tag{A.59}$$

introduced by the author.

On the basis of the FLM-SDEu implementation [70], the amplitude state vector associated with the first exterior centroid is then set as

$$\hat{\mathbf{q}}_{ext} = \begin{pmatrix} \hat{\rho}_{ext} \\ \widehat{\rho u}_{ext} \\ \widehat{\rho v}_{ext} \\ \widehat{\rho w}_{ext} \\ \widehat{\rho e}_{ext} \\ \\ \widehat{\breve{\mu}}_{ext} \end{pmatrix} := \begin{pmatrix} \hat{\rho}_{ffb} \\ \bar{\rho}_{ffb}\,\hat{u}_{ffb} + \hat{\rho}_{ffb}\,\bar{u}_{ffb} \\ \bar{\rho}_{ffb}\,\hat{v}_{ffb} + \hat{\rho}_{ffb}\,\bar{v}_{ffb} \\ \bar{\rho}_{ffb}\,\hat{w}_{ffb} + \hat{\rho}_{ffb}\,\bar{w}_{ffb} \\ \hat{p}_{ffb}/\Gamma + \hat{\rho}_{ffb}\left(\bar{u}^2_{ffb} + \bar{v}^2_{ffb} + \bar{w}^2_{ffb}\right)/2 \\ +\bar{\rho}_{ffb}\left(\bar{u}_{ffb}\,\hat{u}_{ffb} + \bar{v}_{ffb}\,\hat{v}_{ffb} + \bar{w}_{ffb}\,\hat{w}_{ffb}\right) \\ \bar{\rho}_{ffb}\,\widehat{\breve{\nu}}_{ffb} + \hat{\rho}_{ffb}\,\overline{\breve{\nu}}_{ffb} \end{pmatrix}, \tag{A.60}$$

with its linearized time-invariant-mean counterpart being

$$\bar{\mathbf{q}}^*_{ext} = \begin{pmatrix} \bar{\rho}_{ext} \\ \overline{\rho u}^*_{ext} \\ \overline{\rho v}^*_{ext} \\ \overline{\rho w}^*_{ext} \\ \overline{\rho e}^*_{ext} \\ \overline{\breve{\mu}}^*_{ext} \end{pmatrix} := \begin{pmatrix} \bar{\rho}_{ffb} \\ \bar{\rho}_{ffb}\,\bar{u}_{ffb} \\ \bar{\rho}_{ffb}\,\bar{v}_{ffb} \\ \bar{\rho}_{ffb}\,\bar{w}_{ffb} \\ \bar{p}^*_{ffb}/\Gamma + \bar{\rho}_{ffb}\left(\bar{u}^2_{ffb} + \bar{v}^2_{ffb} + \bar{w}^2_{ffb}\right)/2 \\ \bar{\rho}_{ffb}\,\overline{\breve{\nu}}_{ffb} \end{pmatrix}. \tag{A.61}$$

Whereas $\hat{\mathbf{q}}_{ext}$ needs to be updated prior to the $\hat{\mathbf{q}}$-homogenous convective flux vectors' evaluation inherent to every pseudotime-step, $\bar{\mathbf{q}}^*_{ext}$ is set only once before the $\widehat{\boldsymbol{J}\boldsymbol{\psi}}$-homogenous convective flux vectors' evaluation during the algorithm's initialization procedure [70]. Equivalent to the near-field boundary condition, the computed steady-state flowfield respective the considered body's reference position will a priori satisfy the linearized time-invariant-mean far-field boundary condition [70].

Finally, the freestream conditions of the amplitude and linearized time-invariant-mean flowfield [70] are, respectively, composited into the state vectors

$$\hat{\mathbf{q}}_{\infty} = \begin{pmatrix} \hat{\rho}_{\infty} \\ \widehat{\rho u}_{\infty} \\ \widehat{\rho v}_{\infty} \\ \widehat{\rho w}_{\infty} \\ \widehat{\rho e}_{\infty} \\ \widehat{\breve{\mu}}_{\infty} \end{pmatrix} := 0 \quad \text{and} \quad \bar{\mathbf{q}}^*_{\infty} = \begin{pmatrix} \bar{\rho}_{\infty} \\ \overline{\rho u}^*_{\infty} \\ \overline{\rho v}^*_{\infty} \\ \overline{\rho w}^*_{\infty} \\ \overline{\rho e}^*_{\infty} \\ \overline{\breve{\mu}}^*_{\infty} \end{pmatrix} := \begin{pmatrix} 1 \\ \bar{u}_{\infty} \\ \bar{v}_{\infty} \\ \bar{w}_{\infty} \\ \Gamma^{-1} + \gamma\, Ma^2_{\infty}/2 \\ c_{\overline{\breve{\mu}}^*_{\infty}/\overline{\mu}^*_{\infty}} \sqrt{\gamma}\, Ma_{\infty}\, L_{Re_{\infty}}/Re_{\infty} \end{pmatrix}, \tag{A.62}$$

wherein $c_{\overline{\breve{\mu}}^*_{\infty}/\overline{\mu}^*_{\infty}}$ embodies the user-supplied ratio of the linearized time-invariant-mean S/A conservative working variable to its dynamic molecular viscosity counterpart at freestream conditions [72].

Appendix B

Load Coefficient Evaluation

B.1 Cartesian Coordinate Systems

As inherited from the FLM-SDEu implementation [70], the amplitude and linearized time-invariant-mean global load coefficient vectors are rendered by FLM-SD.NS in terms of three distinct Cartesian coordinate systems: the body-fixed (subscript b), the experimental, and the aerodynamic (subscript a) instance. They are all specified with respect to the considered body's reference position. Following FLOWer's icoord=2 definition [72], the three Cartesian coordinate systems have the same origin, with the experimental instance rotated negatively about the y-axis of the body-fixed instance for a positive angle-of-attack. Hence, both of these Cartesian coordinate systems have a common y-axis. The aerodynamic Cartesian coordinate system, on the other hand, shares the z-axis with the experimental instance, and is rotated negatively about it for a positive side-slip angle. Naturally, the positive direction of the time-invariant-mean freestream velocity vector then conforms to the positive direction of the aerodynamic Cartesian coordinate system's x-axis [72]. The global load coefficient vectors are merely evaluated in the body-fixed Cartesian coordinate system, and subsequently rendered in terms of the experimental and aerodynamic instances through simple transformation [70, 72]. The body-fixed Cartesian coordinate system itself corresponds to the global Cartesian coordinate system utilized in the computational treatment of the considered physical domain; i.e., as intrinsically given by the reference grid [70]. Cvrlje [31] had already employed the outlined coordinate systems within FLM-NS.

In this dissertation, strictly longitudinal motions are considered. Thus, the sideslip angle is nil per se, and the aerodynamic Cartesian coordinate system becomes one with the experimental instance. The resultant interdependence between the body-fixed and the aerodynamic instance is illustrated for the investigated NCDW in Figure B.1. As formulated in the body-fixed Cartesian coordinate system, the time-invariant-mean freestream

velocity vector is then given through

$$\bar{\mathbf{v}}_{\infty,\mathrm{b}} \;=\; \sqrt{\gamma} Ma_{\infty} \left(\cos(\bar{\alpha}),\, 0,\, \sin(\bar{\alpha}) \right)_{\mathrm{b}}^{T} \,. \tag{B.1}$$

This sets up the freestream Cartesian velocities employed in the FLM-SD.NS far-field boundary condition, Eq. (A.62):

$$(\bar{u}_{\infty},\, \bar{v}_{\infty},\, \bar{w}_{\infty})^{T} := \bar{\mathbf{v}}_{\infty,\mathrm{b}} \,, \tag{B.2}$$

also being inherent to FLM-SDEu [70].

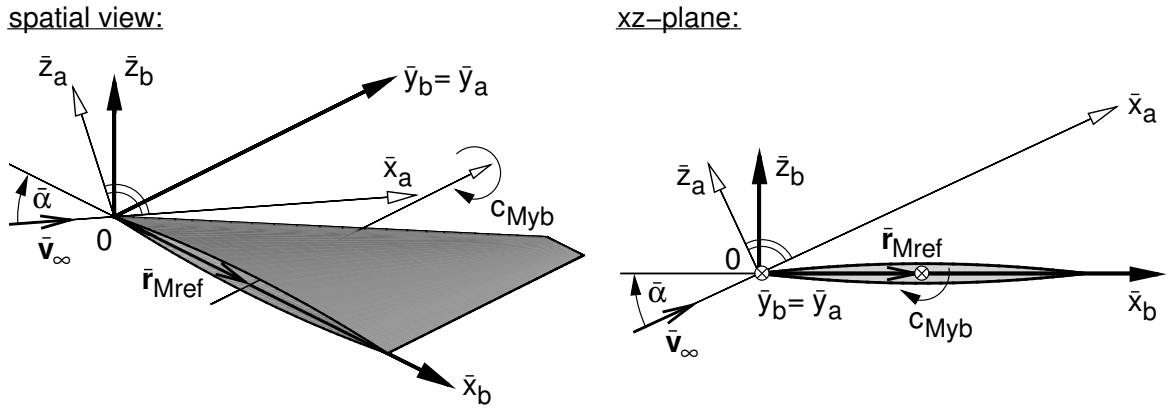

Figure B.1: Body-fixed and aerodynamic Cartesian coordinate system with respect to the NCDW's reference position, including the reference axis for the evaluation of the amplitude and linearized time-invariant-mean pitching-moment coefficient.

B.2 Local Load Coefficients

The amplitude and linearized time-invariant-mean instance of the pressure coefficient for an individual wall-boundary cell-interface is obtained in FLM-SD.NS, respectively, through the amplitude and linearized time-invariant-mean static pressure in the pertinent first interior cell; i.e.,

$$\widehat{c_p}_{\,wb} = c_{Ma_{\infty}}\, \hat{p}_{int} \quad \text{and} \quad \overline{c_p}^{\,*}_{wb} = c_{Ma_{\infty}} \left(\bar{p}^{\,*}_{int} - 1 \right), \quad \text{with} \quad c_{Ma_{\infty}} = 2 \,/\, (\gamma Ma_{\infty}^{2}) \,, \tag{B.3}$$

as already inherent to the FLM-SDEu implementation [70]. In this dissertation, the time-invariant-mean instance of the critical pressure coefficient resulting from one-dimensional compressible flow theory is employed as a comparative threshold:

$$\overline{c_{p,\,crit}}^{\,*} = c_{Ma_{\infty}} \left[\left(\frac{2 + \Gamma Ma_{\infty}^{2}}{2 + \Gamma} \right)^{\frac{\gamma}{\Gamma}} - 1 \right] . \tag{B.4}$$

The amplitude and linearized time-invariant-mean instance of the three-dimensional skin-friction-coefficient vector (body-fixed coordinate system) was derived and implemented by Markmiller [82] under supervision of the author. It is based on FLOWer's conventional treatment [72], which had already been employed by Cvrlje [31] in FLM-NS. For an individual wall-boundary cell-interface these are, respectively, obtained through the pertinent amplitude and linearized time-invariant-mean wall-shear-stress vector; i.e.,

$$\begin{aligned} \widehat{\mathbf{c}_f}_{wb,\mathrm{b}} &:= (\widehat{c_{fx}},\, \widehat{c_{fy}},\, \widehat{c_{fz}})^T_{wb,\mathrm{b}} = c_{Ma_\infty}\, \hat{\boldsymbol{\tau}}_{wb,\mathrm{b}} \quad \text{and} \\ \overline{\mathbf{c}_f}^*_{wb,\mathrm{b}} &:= (\overline{c_{fx}}^*,\, \overline{c_{fy}}^*,\, \overline{c_{fz}}^*)^T_{wb,\mathrm{b}} = c_{Ma_\infty}\, \bar{\boldsymbol{\tau}}^*_{wb,\mathrm{b}}\,, \end{aligned} \tag{B.5}$$

with

$$\begin{aligned} \hat{\boldsymbol{\tau}}_{wb,\mathrm{b}} &= \left[\, \bar{\mu}^*_{int}\, (\hat{\mathbf{v}}_{t,\,int,\,\mathrm{b}} - \hat{\mathbf{v}}_{wb,\mathrm{b}}) \;+\; \hat{\mu}_{int}\, (\bar{\mathbf{v}}^*_{t,\,int,\,\mathrm{b}} - \bar{\mathbf{v}}_{wb,\mathrm{b}}) \,\right] / \bar{d}^*_{int} \quad \text{and} \\ \bar{\boldsymbol{\tau}}^*_{wb,\mathrm{b}} &= \bar{\mu}^*_{int}\, (\bar{\mathbf{v}}^*_{t,\,int,\,\mathrm{b}} - \bar{\mathbf{v}}_{wb,\mathrm{b}}) / \bar{d}^*_{int}\,. \end{aligned} \tag{B.6}$$

The necessary amplitude instance of the Cartesian velocity vector's wall-tangential component in the considered first interior cell results from

$$\begin{aligned} Re\, \hat{\mathbf{v}}_{t,\,int,\,\mathrm{b}} &= Re\, \hat{\mathbf{v}}_{int,\,\mathrm{b}} \\ &- \left(\bar{\mathbf{v}}_{int,\,\mathrm{b}}\; \widehat{\boldsymbol{J\psi}}\Big|_{wb,\,n} + Re\, \hat{\mathbf{v}}_{int,\,\mathrm{b}}\; \overline{\boldsymbol{J\psi}}^*\Big|_{wb,\,n} \right) \overline{\boldsymbol{J\psi}}^*\Big|_{wb,\,n} \,/\, \left| \overline{\boldsymbol{J\psi}}^*\Big|_{wb,\,n} \right|^2 \\ &- \left(\bar{\mathbf{v}}_{int,\,\mathrm{b}}\; \overline{\boldsymbol{J\psi}}^*\Big|_{wb,\,n} \right) \widehat{\boldsymbol{J\psi}}\Big|_{wb,\,n} \,/\, \left| \overline{\boldsymbol{J\psi}}^*\Big|_{wb,\,n} \right|^2 \qquad \text{and} \\ Im\, \hat{\mathbf{v}}_{t,\,int,\,\mathrm{b}} &= Im\, \hat{\mathbf{v}}_{int,\,\mathrm{b}} \\ &- \left(Im\, \hat{\mathbf{v}}_{int,\,\mathrm{b}}\; \overline{\boldsymbol{J\psi}}^*\Big|_{wb,\,n} \right) \overline{\boldsymbol{J\psi}}^*\Big|_{wb,\,n} \,/\, \left| \overline{\boldsymbol{J\psi}}^*\Big|_{wb,\,n} \right|^2 . \end{aligned} \tag{B.7}$$

Its linearized time-invariant-mean counterpart becomes

$$\bar{\mathbf{v}}^*_{t,\,int,\,\mathrm{b}} = \bar{\mathbf{v}}_{int,\,\mathrm{b}} - \left(\bar{\mathbf{v}}_{int,\,\mathrm{b}}\, \overline{\boldsymbol{J\psi}}^*|_{wb,\,n} \right) \overline{\boldsymbol{J\psi}}^*|_{wb,\,n} \,/\, \left| \overline{\boldsymbol{J\psi}}^*|_{wb,\,n} \right|^2 . \tag{B.8}$$

As the computed steady-state flowfield respective the considered body's reference position a priori satisfies the linearized time-invariant-mean no-slip-wall property [54], $\bar{\mathbf{v}}_{wb,\mathrm{b}} = 0$ is implicitly given for Eq. (B.6). Additionally, the amplitude no-slip-wall property renders $Re\, \hat{\mathbf{v}}_{wb,\mathrm{b}} = 0$, as shown by Eqs. (4.34–4.36). By default, the evaluation of the skin-friction-coefficient vector in FLM-NS has been realized under discount of the Cartesian velocity vector at the wall boundary itself. In order to retain equivalence, $Im\, \hat{\mathbf{v}}_{wb,\mathrm{b}}$ is discounted for the evaluation of $\hat{\mathbf{c}}_{f,\,wb,\mathrm{b}}$ in FLM-SD.NS as well. A direct comparison between the FLM-SD.NS- and the FLM-NS-resultant first harmonic of the skin-friction-coefficient vector, as well as the zeroth-harmonic instance, is not provided for the cases investigated in this dissertation.

B.3 Global Load Coefficients

Analytically, the amplitude and linearized time-invariant-mean instance of the Cartesian force-coefficient vector (body-fixed coordinate system) yields from the surface integration of both the pressure-coefficient and skin-friction-coefficient-vector distributions, respectively, in their amplitude and linearized time-invariant-mean instance, for the considered body's reference position; i.e.,

$$\begin{aligned}
\hat{\mathbf{c}}_{\mathrm{b}} &:= (\widehat{c_x},\, \widehat{c_y},\, \widehat{c_z})^T_{\mathrm{b}} \quad \approx \quad -\left(\oint_{\bar{A}^*} \widehat{c_p}\, \overline{\mathbf{dA}}^* - \oint_{\bar{A}^*} \widehat{\mathbf{c}_f}_{\mathrm{b}} \left| \overline{\mathbf{dA}}^* \right| \right) / A \qquad \text{and} \\
\bar{\mathbf{c}}^*_{\mathrm{b}} &:= (\overline{c_x}^*,\, \overline{c_y}^*,\, \overline{c_z}^*)^T_{\mathrm{b}} \;=\; -\left(\oint_{\bar{A}^*} \overline{c_p}^*\, \overline{\mathbf{dA}}^* - \oint_{\bar{A}^*} \overline{\mathbf{c}_f}^*_{\mathrm{b}} \left| \overline{\mathbf{dA}}^* \right| \right) / A\,,
\end{aligned} \tag{B.9}$$

with $\overline{\mathbf{dA}}^* := (\overline{dA_x}^*,\, \overline{dA_y}^*,\, \overline{dA_z}^*)^T$ being the linearized time-invariant-mean instance of an infinitesimal surface element's normal vector. Whereas the integration of the amplitude and linearized time-invariant-mean pressure-coefficient distributions had already been formulated by Kreiselmaier [70] for FLM-SDEu, the additional integration of the skin-friction-coefficient-vector instances was novelly devised by Markmiller [82] for FLM-SD.NS under supervision of the author. It is again based on FLOWer's conventional treatment [72], which had already been employed by Cvrlje [31] in FLM-NS. Naturally, the amplitude and linearized time-invariant-mean instance of the Cartesian moment-coefficient vector (body-fixed coordinate system) are then, respectively, rendered as

$$\begin{aligned}
\widehat{\mathbf{c}_M}_{\mathrm{b}} &:= (\widehat{c_{Mx}},\, \widehat{c_{My}},\, \widehat{c_{Mz}})^T_{\mathrm{b}} \\
&\approx \quad -\left[\oint_{\bar{A}^*} (\bar{\mathbf{r}}_{dA} - \bar{\mathbf{r}}_{Mref}) \times \widehat{c_p}\, \overline{\mathbf{dA}}^* - \oint_{\bar{A}^*} (\bar{\mathbf{r}}_{dA} - \bar{\mathbf{r}}_{Mref}) \times \widehat{\mathbf{c}_f} \left| \overline{\mathbf{dA}}^* \right| \right] / (A\, c_\mu) \quad \text{and} \\
\overline{\mathbf{c}_M}^*_{\mathrm{b}} &:= (\overline{c_{Mx}}^*,\, \overline{c_{My}}^*,\, \overline{c_{Mz}}^*)^T_{\mathrm{b}} \\
&= \quad -\left[\oint_{\bar{A}^*} (\bar{\mathbf{r}}_{dA} - \bar{\mathbf{r}}_{Mref}) \times \overline{c_p}^*\, \overline{\mathbf{dA}}^* - \oint_{\bar{A}^*} (\bar{\mathbf{r}}_{dA} - \bar{\mathbf{r}}_{Mref}) \times \overline{\mathbf{c}_f}^* \left| \overline{\mathbf{dA}}^* \right| \right] / (A\, c_\mu),
\end{aligned} \tag{B.10}$$

with $\bar{\mathbf{r}}_{dA}$ embodying the time-invariant-mean position vector of an infinitesimal surface element [70, 82, 72]. Additionally, $\bar{\mathbf{r}}_{Mref} := (x_{ref},\, y_{ref},\, z_{ref})^T$ defines three moment reference axes (coinciding or being parallel, respectively, to the x_b-, y_b-, and z_b-axis, and replicating the pertinent direction) through a mandatory point of intersection. The positive direction of $\widehat{c_{Mx}}_{\mathrm{b}}$, $\widehat{c_{My}}_{\mathrm{b}}$, and $\widehat{c_{Mz}}_{\mathrm{b}}$, as well as $\overline{c_{Mx}}^*_{\mathrm{b}}$, $\overline{c_{My}}^*_{\mathrm{b}}$, and $\overline{c_{Mz}}^*_{\mathrm{b}}$ is then given through the right-hand rule. For the actual implementation, Eq. (B.9) and Eq. (B.10) underwent a cell-centered discretization; in particular, $\widehat{c_p}$ and $\overline{c_p}^*$, respectively, become $\widehat{c_p}_{wb}$ and $\overline{c_p}^*_{wb}$; $\widehat{\mathbf{c}_f}_{\mathrm{b}}$ and $\overline{\mathbf{c}_f}^*_{\mathrm{b}}$, respectively, become $\widehat{\mathbf{c}_f}_{wb,\mathrm{b}}$ and $\overline{\mathbf{c}_f}^*_{wb,\mathrm{b}}$; $\overline{\mathbf{dA}}^*$ becomes $\left.\overline{\boldsymbol{J\psi}}^*\right|_{wb,n}$; $\bar{\mathbf{r}}_{dA}$ becomes $\bar{\mathbf{r}}^{IC}_{wb}$.

In this dissertation, merely the lift and pitching-moment coefficient (in their first- and zeroth-harmonic instances) are drawn on for comparative purposes. To this effect, the amplitude and linearized time-invariant-mean of the lift coefficient are obtained by transforming $\hat{\mathbf{c}}_{\,\mathrm{b}}$ and $\bar{\mathbf{c}}^{\,*}_{\mathrm{b}}$ into the aerodynamic Cartesian coordinate system, as already inherent to the FLM-SDEu implementation [70]; i.e.,

$$\widehat{c_L} := \widehat{c_{z\,\mathrm{a}}} = \widehat{c_{z\,\mathrm{b}}}\cos(\bar{\alpha}) - \widehat{c_{x\,\mathrm{b}}}\sin(\bar{\alpha}) \quad \text{and} \quad \overline{c_L}^{\,*} := \overline{c_z}^{\,*}_{\mathrm{a}} := \overline{c_z}^{\,*}_{\mathrm{b}}\cos(\bar{\alpha}) - \overline{c_x}^{\,*}_{\mathrm{b}}\sin(\bar{\alpha})\,. \tag{B.11}$$

The amplitude and linearized time-invariant-mean of the pitching-moment coefficient, on the other hand, are gained directly:

$$\widehat{c_M} := \widehat{c_{My\,\mathrm{b}}} \quad \text{and} \quad \overline{c_M}^{\,*} = \overline{c_{My}}^{\,*}_{\mathrm{b}}\,, \tag{B.12}$$

with $\bar{\mathbf{r}}_{Mref} = (x_{ref},\, 0,\, 0)^T$ as depicted in Figure B.1.